Doctoral Dissertation

Doctoral Program in Chemical Engineering (33th Cycle)

# Ceramic open cell foams as catalytic support for endothermic and exothermic reactions: Focus on lean methane combustion

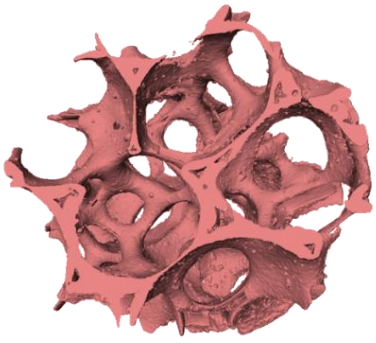

By

Carmen Williana Moncada Quintero

**Doctoral Examination Committee:**

Dr. Francesca Deganello, CNR-ISMN Palermo
Prof. Gianpiero Groppi, Politecnico di Milano
Prof. Hilde Johnsen Venvik, Norwegian University of Science and Technology.
Prof. Klas Engvall, KTH Royal Institute of Technology
Prof. Jean-Marc Tulliani, Politecnico di Torino

**Supervisor:**

Prof. Stefania Specchia

# Declaration

I hereby declare that, the contents and organization of this dissertation constitute my own original work and does not compromise in any way the rights of third parties, including those relating to the security of personal data.

Carmen Williana Moncada Quintero, 2021

* This dissertation is presented in partial fulfillment of the requirements for **Ph.D. degree** in the Graduate School of Politecnico di Torino (ScuDo).

To those who are my core, my encouragement, my light, my safe harbor,

To those who give me their unconditional love,

To those who support me without hesitation,

To those who are the engine of my life,

To those who are my best catalyst for life:

# My Family

I love you

I will always be there for you, wherever I am

# Acknowledgment

My deepest acknowledgement is for my super supervisor, Prof. Stefania Specchia, who has always given me all her love, her patience, her encouragement, her support, her advice, her disposition. She has been not only an excellent supervisor, but also a mother, a sister, a friend and a source of unconditional support.

I would like to thank everyone at IFP with whom I had the pleasure to work and spend hours discussing results: Frederic, Jean-François, Yacine, and Marion. Thank you for your patience and advice.

To everyone I met at the University of the Basque Country, especially Oihane, Mario, Oihana, André, Iñigo, Alvaro and Maria, who made me feel at home, who opened their doors to me from the first day and with whom the hard days of work were much more comfortable.

I would like to thank all those who shared the same office: Giuliana, Lorenzo, Veronica, Paulina, Ana, Ellie and Stefano, thank you for every memory. Thanks also to Corrado De Bortoli, who was always available to help, to solve any laboratory or computer problem.

I would also like to thank Dr. Emidio Grossi, and all the doctors who were there in those moments, always looking for solutions and giving me good energy. Thanks to all the nurses who were the most genuine joy of my days. It is a blessing to have them in the world.

Finally, I would like to thank from the bottom of my heart those who are my whole life: My family. To my dad William, my mom Carmen Rosa, and to the lights of my life, my sisters Carmen G. and Carmen R. for always giving me all their unconditional love, for always being there for me and for simply being the best treasure of my life. To my two nonitas (Felipa and Marta) who are not in this plane. I love them very much and remember them every day.

Part of the research contained in this dissertation was carried out at the IFP Energies Nouvelles facilities in Solaize (France), under the *Erasmus + Traineeship* for PhD candidates program.


Part of the investigation contained in this dissertation was conducted in the laboratory facilities of the University of the Basque Country in San Sebastián (Spain), carried out under the *Erasmus+ PhD Programme Countries.*

# ABSTRACT

The aim of this work is focused on the study of ceramic open cell foams (OCFs) as catalytic support for exothermic and endothermic reactions. In particular, focusing on the methane oxidation reaction under lean conditions. With projection toward process intensification, the research is dedicated to the analysis of the mass transfer effects occurring from the bulk gas phase to the external catalyst surface (external or interphase mass transfer) and within the catalyst layer (internal or intraparticle mass transfer) as well as to evaluate the different controlling regimes (kinetic, internal or external mass transfer) during $CH_4$ oxidation on the coated OCF. In addition, this investigation also explores the heat transfer effects on foams.

In order to study the effects of mass transfer in the gas-solid reaction system, a theoretical low-dimensional model was used. Firstly, the model was applied to exothermic and endothermic reactions catalyzed in ceramic monolithic structures, since this substrate exhibits a much simpler geometry compared to that of OCFs. Specifically, the reactions of nitrous oxide ($N_2O$) decomposition (*Paper I*) and $CH_4$ steam reforming (*Paper II*) catalyzed on cordierite monolith were analyzed. Different controlling regimes were identified by varying the operating conditions and the design parameters of the structured catalyst. Subsequently, the analysis of the OCFs was followed by first examining the steam and oxy-steam reforming reactions of biogas (*Paper III*) catalyzed in ceramic OCFs made of alumina of different pore density (20, 30 and 40 pore per inch). A thin catalytic layer was deposited on the structures via solution combustion synthesis (SCS) and wetness impregnation (WI) techniques. The coated OCFs were physically characterized by SEM/EDX, TEM, XRD, Helium Pycnometry, Stereoscopic measurement and adhesion

test. Besides, pressure drop measurements were performed on all structures. Characteristic times and dimensionless numbers were calculated to analyze the mass transfer effects as well as to evaluate possible heat transfer limitations by varying the flow conditions. Stability tests were performed on both reactions over 200 h of time-on-stream (TOS).

For the intensification of $CH_4$ oxidation in lean conditions, 3 wt. % $PdO/Co_3O_4$ catalyst was deposited on ceramic OCFs made of zirconia (Zir), alumina (Alu) and silicon carbide (SiC) with pore density of 30 ppi (*Paper IV*) using SCS and WI methods. Approximately the same amount of catalyst was deposited on each structure. The catalytic tests were performed at different flow conditions (WHSV of 30 NL $h^{-1}$ $g_{cat}^{-1}$, temperature range of 100-700°C, inlet $CH_4$ concentration of 0.5 and 1 vol. %) and lean conditions were ensured by maintaining a $O_2/CH_4$ molar ratio of 8. In order to verify the stability of the catalyzed OCF, a catalytic test was performed on the best selected catalyst over about 250 h of TOS. All the coated OCFs were characterized by Raman spectroscopy, FESEM, $N_2$ physisorption, EDXS. In addition, adhesion tests were performed on all coated OCFs by ultrasonic treatment. The theoretical low-dimensional model was adapted to the OCF geometry taking into account the characteristic geometrical parameters: pore and strut diameter, specific surface area, tortuosity and open porosity. Thus, the operating regimes were analyzed by studying the evolution of the characteristic resistances as the process temperature varied. Furthermore, possible heat transfer limitations were evaluated using the Mears and Anderson criteria.

The effect of the catalyst content on the catalytic performance and on the various operating regimes during $CH_4$ combustion were also evaluated (*Paper V*). For this purpose, Zir-OCF of 30 ppi was used as catalytic support. Different catalyst loading ($C_{load}^{100}$, $C_{load}^{150}$ and $C_{load}^{250}$ corresponding to 6.1, 8.2 and 13.7 $mg_{cat}$ $cm^{-2}_{OCF}$) and flow conditions were

investigated (0.5 and 1.0 vol.% inlet $CH_4$ concentration, $O_2/CH_4$ molar ratio 8, temperature range of 100-700°C and WHSV of 30, 60 and 90 NL $h^{-1}$ $g_{cat}^{-1}$). Pore and strut dimensions were individuated using SEM and X-CT images. A correlation that describes the mass transfer in coated OCFs at low Reynolds numbers was derived.

Finally, a combination of coated (3 wt. % $PdO/Co_3O_4$) SiC/Zir OCF (of 30 ppi) were tested for $CH_4$ combustion under lean conditions (*Paper VII*). In each combination, the SiC-OCF was placed inside the reactor on the inlet side of reactive gases followed by the Zir-OCF. The catalytic performance, mass and heat transfer effects were evaluated at different flow conditions (0.5 and 1.0 vol.% inlet $CH_4$ concentration, $O_2/CH_4$ molar ratio 8, temperature range of 100-700°C and WHSV of 30, 60 and 90 NL $h^{-1}$ $g_{cat}^{-1}$). Operating regimes of each catalytic combination were evaluated in terms of characteristic resistances using the adapted theoretical model for OCFs. In addition, heat transfer effects were studied by evaluating the Mears and Anderson criteria. The temperature difference between the bulk gas phase and the catalyst surface was also determined theoretically. Lastly, the values of Nusselt number and volumetric heat transfer coefficients were estimated and compared with those obtained in previous work on individual foams.

Zirconia, alumina and silicon carbide OCFs of 30 and 45 ppi were fully characterized by X-ray computed microtomography (*Paper VI*). Characteristic geometrical dimensions such as pore size, length and diameter of strut, node diameter, open porosity and specific surface area were extracted from both 2D slices and 3D foam reconstruction. In addition, the experimental specific surface area values were compared with theoretical models proposed in the literature. Finally, an empirical expression to determine the specific surface area in ceramic OCFs was derived.

Microporosity, dense grains and circular hollow strut were the most relevant characteristics present in the skeletons of all the ceramic OCFs studied. The increase in OCF pore density led to a higher specific surface area. Excellent adhesion of the catalyst to the ceramic foams was found with weight losses below 5%, even at high catalyst contents. All coated alumina foams showed high catalytic activity in the following order 20 ppi < 30 ppi ≈ 40 ppi. Zir-OCF exhibited full $CH_4$ conversion at the lowest temperatures compared to Alu and SiC supports for all flow conditions investigated. At low temperatures, all coated OCFs operated in a kinetic regime independently of the structure material. The diffusion effects within the catalyst become more important at lower temperatures for coated foams with higher thermal conductivity and lower specific surface area in the following order Zir < Alu < SiC. For all flow conditions studied, the best catalytic performance in terms of $CH_4$ conversion and mass transfer was found for the catalyst loading of 6.1 $mg_{cat}$ $cm^{-2}_{OCF}$. The SiC1.5Zir1.5 catalytic combination showed a promising catalytic performance for complete $CH_4$ oxidation in lean conditions, where the $CH_4$ light-off curve was shifted toward lower temperatures than those obtained for individual OCF. According to Anderson's criteria, no temperature gradients were present within the catalytic layer. Nevertheless, the structures could operate in an unstable zone for external heat transfer depending on the structure's nature, caused by the strong exothermicity and fast combustion reaction. The $PdO/Co_3O_4$ catalyst coated on Zir-OCF resulted highly stable after approximately 250 hours of operation.

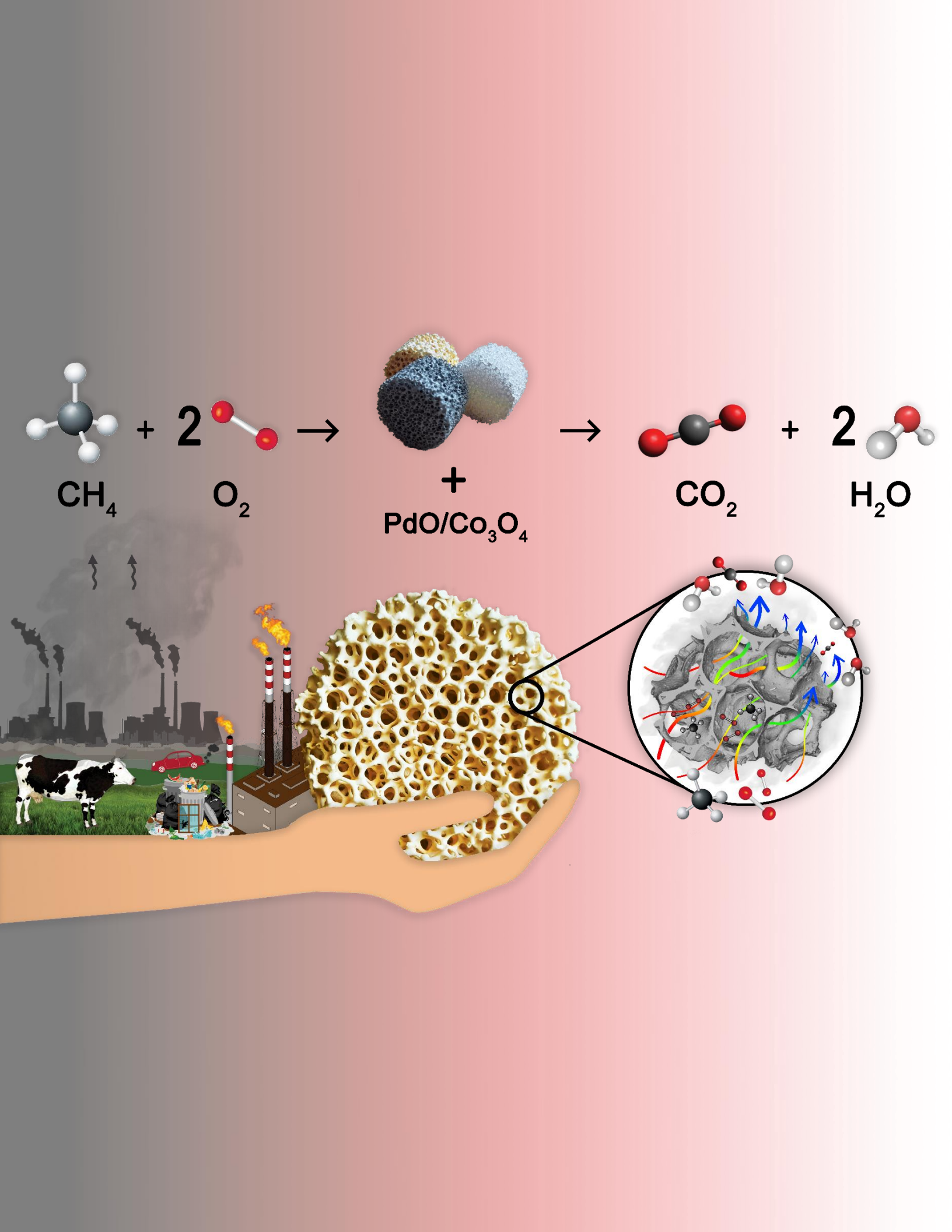
CH4
+
2
O2
→
+
PdO/Co3O4
→
CO2
+
2
H2O

## THIS THESIS IS A SUMMARY OF THE FOLLOWING PAPERS:

**Paper I.** Wójcik, S., Ercolino, G., Gajewska, M., **Moncada Quintero, C. W.**, Specchia, S., & Kotarba, A. (2018). Robust $Co_3O_4|\alpha\text{-}Al_2O_3|$cordierite structured catalyst for $N_2O$ abatement – Validation of the SCS method for active phase synthesis and deposition. *Chemical Engineering Journal, 377*, 120088. https://doi.org/10.1016/j.cej.2018.10.025

**Paper II.** **Moncada Quintero, C. W.**, Babar, R. Z., & Specchia, S. (2021). Performance and Controlling Regimes Analysis of Methane Steam Reforming on $Ru/\gamma\text{-}Al_2O_3$ Cordierite Monoliths. *Green Energy and Technology*, 91–131. https://doi.org/10.1007/978-981-15-5667-8_5

**Paper III.** Italiano, C., Ashraf, M. A., Pino, L., **Moncada Quintero, C. W**., Specchia, S., & Vita, A. (2018). $Rh/CeO_2$ thin catalytic layer deposition on alumina foams: Catalytic performance and controlling regimes in biogas reforming processes. *Catalysts, 8*(10), 1–25. https://doi.org/10.3390/catal8100448

**Paper IV.** **Moncada Quintero, C. W.**, Ercolino, G., Poozhikunnath, A., Maric, R., & Specchia, S. (2020). Analysis of heat and mass transfer limitations for the combustion of methane emissions on $PdO/Co_3O_4$ coated on

ceramic open cell foams. *Chemical Engineering Journal, 405*, 126970. https://doi.org/10.1016/j.cej.2020.126970

**Paper V.** **Moncada Quintero, C. W.**, Ercolino, G., & Specchia, S. (2021). Effect of the $Co_3O_4$ load on the performance of $PdO/Co_3O_4/ZrO_2$ open cell foam catalysts for the lean combustion of methane: kinetic and mass transfer regimes. *Catalysis Today.* In press, https://doi.org/10.1016/j.cattod.2021.03.014 (available online 18/03/2021).

**Paper VI.** **Moncada Quintero, C. W.**, Servel, M., Augier, F., Haroun, Y., Joly, J.F., & Specchia, S. (2021). Imaging ceramic open cell foams by X-ray micro computed tomography. *Under preparation*.

**Paper VII.** **Moncada Quintero, C. W.**, Ercolino, G., & Specchia, S. (2021). Combined silicon carbide and zirconia open cell foams for the process intensification of catalytic methane combustion in lean conditions: impact on heat and mass transfer. *Chemical Engineering Journal, 429, 132448.* https://doi.org/10.1016/j.cej.2021.132448

# AUTHOR'S CONTRIBUTION TO THE APPENDED PAPERS

**Paper I.** Realization of mass transfer calculations, analysis, discussion and interpretation of the obtained results, graphical representation (Figures 7-11) and supplementary information preparation.

**Paper II.** Data processing (catalyst tests, stability measurement, $N_2$ physisorption, X-Ray diffraction and Field-Emission Scanning Electron Microscopy), realization of mass and heat transfer calculations, analysis, discussion and interpretation of the obtained results, graphical representation (Figures 1-13), supplementary information and manuscript preparation.

**Paper III.** Analysis, discussion and interpretation of mass transfer results, supplementary information preparation.

**Paper IV.** Design of experiments and performance of measurements (stability measurement and adhesion test), data preparation (Raman spectroscopy, Field-Emission Scanning Electron Microscopy, and $N_2$ physisorption), apparent kinetic parameters determination, mass and heat transfer analysis, discussion and interpretation of the obtained results, graphical representation (Figures 1-10), supplementary information and manuscript preparation.

**Paper V.** Design of experiments and performance of measurements (catalytic and adhesion tests), data preparation (Scanning Electron Microscope and X-ray Computed Tomography), apparent kinetic parameters determination and mass transfer analysis, discussion and interpretation of the obtained results, graphical representation (Figures 1-10), supplementary information and manuscript preparation.

**Paper VI.** Data processing (pore and strut dimensions, porosity, specific surface area), analysis and conceptualization, discussion and interpretation of the obtained results, graphical representation (Figures 1-10) and manuscript preparation.

**Paper VII.** Design of experiments and performance of measurements (catalytic tests), data processing, apparent kinetic parameters determination and mass and transfer analysis, discussion and interpretation of the obtained results, graphical representation (Figures 1-14) and manuscript preparation.

# TABLE OF CONTENTS

# LIST OF FIGURES

# LIST OF TABLES

# Preface

# 1. Introduction

## 1.1 Background and motivation

Global warming is one of the most serious environmental threats facing the world today. Greenhouse gases (GHGs) such as carbon dioxide ($CO_2$), methane ($CH_4$), and nitrous oxide ($N_2O$) are the main factors responsible for greatly warming the surface of the Earth [1]. In fact, the Fourth Assessment Report (AR4) published by the Intergovernmental Panel on Climate Change (IPCC, 2007) reported an average surface temperature increase of 0.74 °C over the last 100 years (1906-2005), where human activity was "very likely" the primary cause of rising temperatures worldwide [2,3]. The last report presented by IPCC in 2014 (Fifth Assessment Report, AR5) stated with a certainty of more than 90 % that by the end of the 21st century the global surface temperature will exceed 2.0 °C compared to the 1850 to 1900 period [4–6] (**Figure 1.A**). Furthermore, the international scientific committee reported an increase in atmospheric concentrations of GHGs to unprecedented levels (**Figure 1.B)**. Particularly, $CH_4$ recorded an increment of more than 150 % since 1750 as a result of human activities, becoming responsible for approximately a quarter of the global warming that has occurred since then [7–9]. By the end of 2019, the global average $CH_4$ concentration

in the atmosphere reached around 1875 parts per billion (ppb), more than two-and-a-half times pre-industrial levels [10].

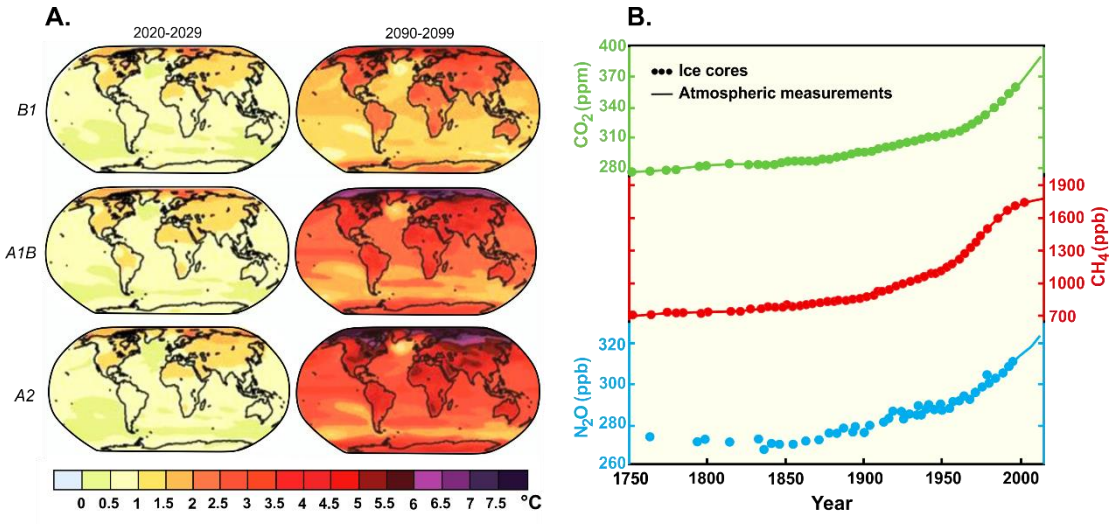


**Figure 1** Projected surface temperatures changes for the 2020-2029 and the 2090-2099 period for three different scenarios: low emissions, B1; intermediate emissions, A1B; and high-emissions future, A2 (A). Global average of greenhouse gas concentration trend for $CO_2$, $N_2O$ and $CH_4$ (B). The images were extracted from the AR5 published by IPCC [5,6,11].

Although methane is about 200 times less abundant in the atmosphere than carbon dioxide, its ability to absorb thermal infrared radiation is much more effective and, in consequence, its impact on the greenhouse effect is much stronger. In fact, the global warming potential (GWP) of $CH_4$ compared to $CO_2$ over a 20-year period is 86 times higher and 28 times more powerful on a 100 year period [5,6]. On the other hand, $CH_4$ plays a role in climate feedback mechanisms that could exacerbate warming and even cause abrupt and

catastrophic climate change in the future [12]. Therefore, the mitigation of $CH_4$ emissions represents a key factor in terms of climate change, health, economy, security and energy. Methane emissions come mainly from agriculture, energy, industry and waste management sectors [13]. The second largest contributor to the overall anthropogenic $CH_4$ emissions is the energy sector (30 %), which includes emissions from natural gas and oil (63 %), coal mines (29 %) and biofuels (8 %) [14] (**Figure 2**).

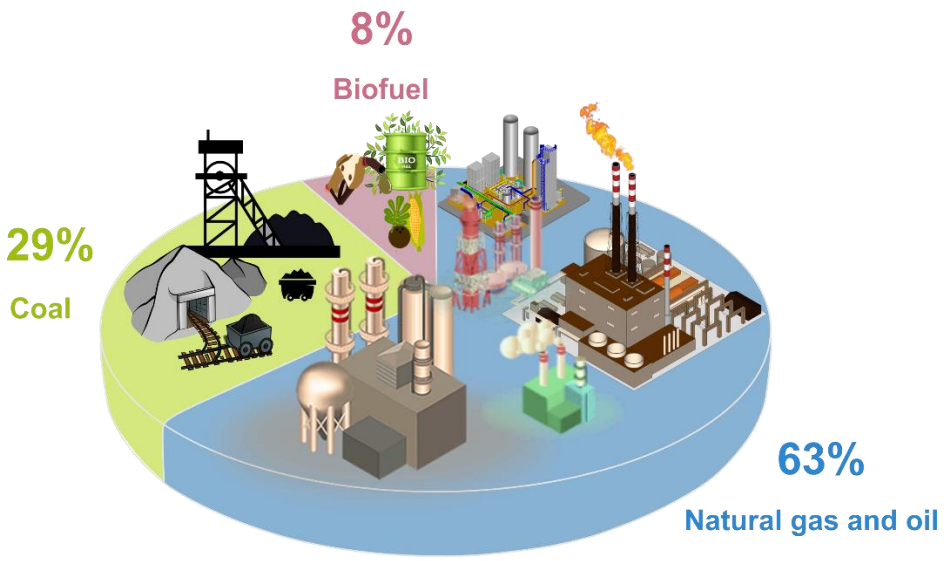


**Figure 2.** $CH_4$ emissions from energy sector [14].

Among the fossil energy sources, the natural gas (NG) is particularly attractive due to its higher energy content (55.7 kJ $g^{-1}$) compared to coal (39.3 kJ $g^{-1}$) and petroleum (43.6 kJ $g^{-1}$) [15]. In recent years, NG has gained widespread use as a consequence of rising oil prices, the need for diversification/security of energy supply and growing global awareness of environmental issues. In fact, among all hydrocarbon fuels, NG (mainly composed of $CH_4$) generates from its combustion, the lowest emissions of $CO_2$, less $NO_x$, and particles in the

exhaust gases compared to gasoline and diesel engines, thus, it is becoming in the most promising and cleanest alternative transport fuel to reduce environmental pollution [16]. The benefits of NG combustion are particularly significant under lean-burn conditions. At these conditions, the thermal efficiency is increased due to the increase in the ratio of specific heats for lean mixtures, further minimizing the typical products of incomplete combustion in comparison to conventional stoichiometric conditions, which reach significantly higher exhaust gas temperatures (up to 1600 °C) resulting in harmful environmental impacts, such as the formation of photochemical smog and acid rain [15,17]. However, these advantages are partially balanced by the emissions of unburned $CH_4$ in the exhaust gases. Such emissions must be necessarily reduced through a catalytic after-treatment of the exhaust gases. Despite the high stability of the $CH_4$ molecule, the catalytic combustion appears as one of the most promising technologies to reduce $CH_4$ emissions and maximize the utilization of rational and clean energy at low temperature. This potential alternative solution can also be implemented for the abatement of $CH_4$ emissions attributed to ventilation air methane (VAM) emitted from coal mines (responsible for 60-70% of total $CH_4$ emissions related to coal mines [18]), which are characterized by the low concentrations of methane. However, to achieve complete oxidation of $CH_4$ from such anthropogenic activities, the catalytic process must be carried out in severe conditions: (i) low temperatures at which the catalyst must operate (typically less than 500–550 °C) [19,20], (ii) low concentrations of $CH_4$ (0.5-1 vol.%) [12,20,21], (iii) large excess of oxygen [19,20]. Therefore, the development of catalysts that exhibit high catalytic activity, low light-off temperatures, good thermal stability and resistance even for such low temperature operations is still a challenging issue [15].

Among all the catalysts investigated in literature, palladium-based catalysts have been reported to be the most active catalytic systems for the total oxidation of $CH_4$, due to their high activity at low temperature [20,22–24]. Nevertheless, the relatively high cost associated with palladium has led researchers to focus on alternative systems such as oxides or mixed oxides [25–27] and perovskites [28–30] that support metal active phase, thus reducing the amount of Pd used. For all cases, the catalytic properties of the supported Pd catalysts depend on both the nature of catalyst carrier and the active phase-support interaction [20,24,31,32]. In recent years, the increasing interest has been focused on the transition metals as catalytic supports owing to their much lower cost and relatively abundant resources. Spinel cobalt oxide ($Co_3O_4$) has demonstrated to be one of the best multifunctional materials for a variety of technological applications and heterogeneous catalysts due to its surface redox reactivity properties [33–40]. Especially, the $Co_3O_4$ exhibits an excellent catalytic activity for the complete combustion of methane [25,31,41–48]. At room temperature, the magnetic structure of the $Co_3O_4$ corresponds to the normal spinel phase (NS), which is defined by the chemical formula $(A)[B]_2O_4$ where A stands for divalent cations ($Co^{2+}$), B for trivalent cations ($Co^{3+}$) and parentheses and brackets represent tetrahedral and octahedral sites respectively [49,50] (see **Figure 3**). Thus, within the NS phase the tetrahedral $Co^{2+}$ and octahedral $Co^{3+}$ ions are found in different local magnetic states. The $Co^{2+}$ ion exhibits a high-spin state presenting a magnetic moment of 3.02 μβ while the $Co^{3+}$ ion is located in the low-spin state with all electron spins paired, and therefore non-magnetic [49,50]. The magnetic structure of the NS $Co_3O_4$ is due to antiferromagnetic ordering of spins in the A sites; each $Co^{2+}$ ion in an A site is surrounded by four nearest neighbors with oppositely directed spins.

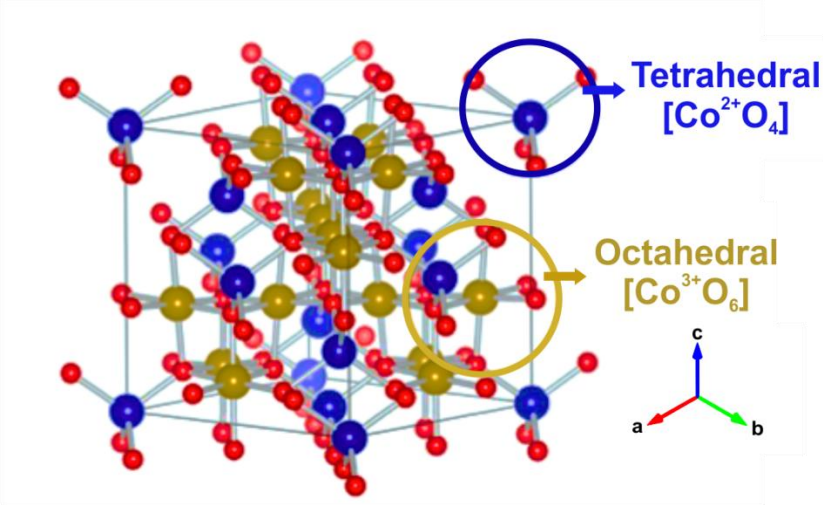


**Figure 3.** Spinel structure of $Co_3O_4$: Tetrahedral and octahedral coordinations [51,52].

Recently, several studies have shown that when a high number of structural defects and a large amount of non-stoichiometric oxygen are available, the catalytic activity is improved [25,32,43]. Moreover, both the tetrahedral coordination of $Co^{2+}$ in $Co_3O_4$ and the oxidation reduction cycle between $Co^{2+}$ and $Co^{3+}$ could play a key role on the catalytic activity for the complete $CH_4$ oxidation [25,53,54]. Cobalt (II,III) oxide $Co_3O_4$ and cobalt (II) oxide (CoO) particles are prepared largely by a broad range of wet chemical techniques such as hydrothermal synthesis, spray pyrolysis, solubility-controlled synthesis, co-precipitation, freeze-drying and sol–gel [55–59].

An attractive alternative for the production of smart materials of high value compared to the more conventional and expensive preparation routes is the solution combustion synthesis (SCS). In fact, SCS allows effective low-cost production of nanomaterials with the desired phase compositions thanks to its relative medium heating temperatures (350-600 °C), fast heating rates and short reaction times [60–62]. The final product obtained from

the synthesis is characterized by high purity, where the size and shape can be perfectly tuned with the synthesis conditions. Besides, a wide variety of structured catalysts can be adapted via in situ SCS [42,46,63–71].

Recently, research areas in chemical engineering have focused on process intensification (PI), which consists of a new and promising strategy for the development of more competitive and sustainable processes, which represent a key factor for the profitability of remote energy sources or for increasing the efficiency and effectiveness of existing processes [72]. In particular, the innovative methodologies of PI are based on a powerful design approach for achieving real manufacturing and processing benefits, such as the reduction of equipment size, energy consumption, waste production and capital cost, and the enhancement of plant efficiency resulting in cheaper and sustainable technology [73,74]. Structured catalysts have become one of the most interesting topics in heterogeneous catalysis, since they represent a fundamental technology for process intensification owing to the potential advantages that they offer for mass and heat transfer, while maintaining limited pressure drops when compared to conventional reactors. During the last few years, monoliths have become the most common and consolidated catalytic support, thanks to their commercial success in the treatment of automobile exhaust gases. [75,76]. Monolithic catalysts are essentially continuous unitary blocks consisting of narrow thin-walled channels that are parallel to each other to facilitate the flow of reagents [77–80] (see **Figure 4**). These parallel channels can be manufactured in different sizes with square, circular, triangular, hexagonal and sinusoidal cross-section areas to provide flow passages for the reactants and products to and from the reactions, respectively. Currently, monoliths are manufactured as ceramic or metal materials which comprise the two main types of supports

used in industry and research. The catalytically active components are dispersed uniformly over the entire porous structure of the monolith or a porous layer containing the catalyst can also be deposited on the channel walls of the monolith structure [74], as shown in **Figure 4**.

When monolithic structures are used as catalytic supports, the relevant geometrical parameters are defined in terms of cell density, cell spacing or wall thickness. The cell density of monoliths is defined as the number of cells per unit of cross-sectional area and expressed as cells per square inch ($cpsi$) [81]. This is determined collectively by the number of channels, their hydraulic diameter ($d_h$), and the void fraction ($\varepsilon$) of the structure, thus providing information on the wall thickness of the monolith [79,82].

Further, the above-mentioned geometric characteristics can be used to determine the geometric surface area ($GSA$), which is a key factor parameter for pressure drop and reactions controlled by mass transfer. Similarly, the hydraulic diameter can be used to determine the effect of channel-scale hydrodynamics [83]. On the other hand, monolithic catalysts show a higher void fraction compared to catalyst pellets, offering lower flow resistance through the channels [77,84,85].

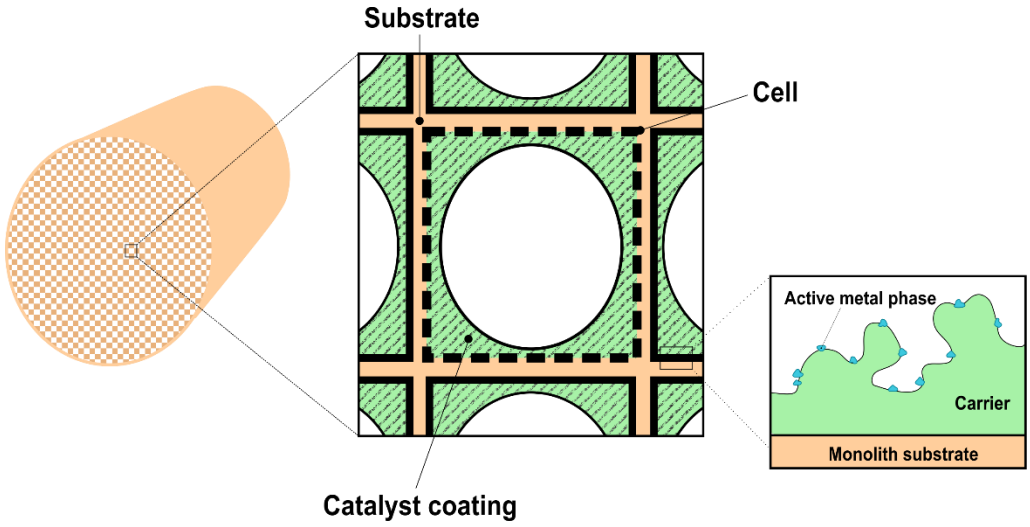


**Figure 4.** Monolith structure as catalyst support.

In general, the most important advantages of these catalytic structures include a short diffusion path in the catalyst layer, high external surface area, high interfacial mass transfer rates and low pressure drop in flow through the monolith channels (compared to conventional packed bed reactors) [74,78,81,82,85,86]. These advantages can result in lower investment and higher productivity of production operations. However, the monolith supports also exhibit some disadvantages such as poor radial heat transfer due to the absence of radial mixing; possible non-uniform distribution of the fluid and, thus, lower reactor effectiveness, misdistribution or lower loading of the catalyst active phase [72,75,82]. Besides, typical parallel channel monoliths are essentially adiabatic, which makes temperature control inherently limited. In recent years, a growing number of researchers have focused their attention on the development of innovative structures as catalytic supports to overcome these limitations [87–91]. Open cell foams (OCFs) are one of the most

promising alternatives as catalytic support for process intensification thanks to their attractive properties such as high specific surface area, low pressure drop, good chemical resistance, high thermal stability and mechanical strength, as well as enhanced heat and mass transfer, due to the tortuous flow paths through the porous matrix [89,92–102] (see **Figure 5**). Indeed, the complex geometry of the foams increases both the local mixing and the gas-to-solid transport properties, as the struts interact strongly with the flow field resulting in continuous boundary layer formation and disruption, leading to improved transport [93,103]. These characteristics can be exploited especially in applications involving not only high flow rates and/or strongly exothermic or endothermic reactions (combustion or reforming processes), but also for low contact time reactions (such as partial oxidation processes). Furthermore, the higher mass and heat transfer coefficients provided by OCFs could lead to the design of more compact and lightweight reactors with better heat management in non-adiabatic applications. Moreover, unlike conventional honeycomb monoliths, OCFs allow radial dispersion of the flow favoring uniform distribution of the reactants across the catalyst bed.

OCFs can be defined as irregular cellular materials made of interconnected solid struts that give rise to a continuous three-dimensional network, which enclose empty regions called cells. This leads to a highly porous structure that provides a flow pathway through the open windows that communicates with neighboring cells [104–110] (**Figure 5**). Pore size is commonly expressed in terms of number of pores per linear inch (ppi) that usually varies from 10 to 100 ppi with typical porosities of 75-90% [105,111]. Moreover, OCFs can be manufactured in a variety of metallic and ceramic materials, cell sizes and porosities, depending on the operating conditions adopted in the specific application. Several

applications of OCFs as catalyst supports have been reported for exothermic reactions, such as volatile organic compounds oxidation [112], methanol [113] and Fischer-Tropsch synthesis [114–116], catalytic wet peroxide oxidation [117,118], preferential oxidation of CO (CO-PROX) [56], partial oxidation of methanol [119], complete combustion of methane [63,71,120,121], and endothermic applications like steam reforming [66,69,97]. Furthermore, their promising functional properties and lightweight have led to their application in numerous other technologies, such as gas filters [122,123], multifunctional heat exchangers [124–126], filtration of molten metals [127,128], mechanical energy absorbers [129,130], compact heat sinks for microelectronic devices [92,131], static mixers for milli-scale plug flow reactors [132–134], porous burners [135,136], and biomedical uses [137–139].

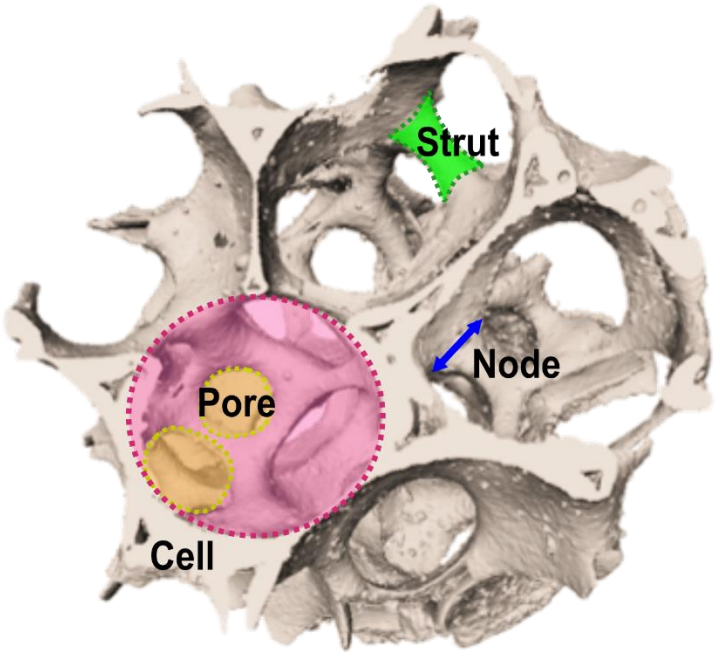


**Figure 5.** Open cell foam structure.

The choice of the structure's nature will depend on the process focus. Ceramic structures are often characterized by better adhesion, high thermal resistance and strength whilst metal structures exhibit greater thermal conductivity and resistance to mechanical shock [104,111,122,128,140–149]. However, ceramic structures can crack with significant temperature changes, while metallic ones can corrode or fuse at high temperatures due to their limited thermal stability [93,111,128,141,144].

On the other hand, it is important to highlight the fundamental role that plays the physical processes of mass and energy transport in solid-catalyzed heterogeneous systems, which can interfere with the chemical (intrinsic) rates to modify the overall reaction rates. Due to their nature, heterogeneous catalytic reactions involve a combination of reaction and transport processes, since the reagents must first be transferred from the bulk of the fluid phase to the catalyst surface, where the reaction takes place (see **Figure 6**). Therefore, the reactants and products undergo a series of chemical and physical processes that include [150,151]:

1. Diffusion of the reactants from the bulk fluid phase to the external catalyst surface (external or interphase diffusion);
2. Diffusion of the reactants within the catalyst pores to the active sites (internal or intra-phase diffusion);
3. Adsorption of the reactants onto active sites;
4. Reaction at specific active sites on the catalyst surface;
5. Desorption of products from catalyst sites;
6. Diffusion of the products from the pores to the exterior catalyst surface (internal or intra-phase diffusion), and

7. Diffusion of the products from the external surface of the catalyst to the bulk fluid phase (external or interphase diffusion).

If the rates of the chemical steps 3-5 are very high compared to the internal diffusion process (very fast reaction), the reaction will take place only in a thin boundary layer near the external surface of the catalyst, thus only the external mass transfer can influence the effective rate of transformation [150–155]. The same scenario will occur in the case of non-porous catalysts where the active phase is placed in a layer near the outer pellet surface. On the other hand, if the diffusion processes (steps 1, 2, 6 and 7) are very fast compared to the intrinsic reaction rates (very slow reaction), the chemical process is kinetically controlled and, thus the mass transfer steps do not affect the overall reaction rate [150–152,155]. Similarly, if the reaction steps are comparable or higher than the diffusion steps, significant concentration profiles of products and reactants will develop both within the catalyst particle (or within the catalyst thickness in the case of catalysts supported in solid structures such as foam and monolith) and in the surrounding layer.

Furthermore, both exothermic and endothermic reactions can release or consume heat and, as a consequence, temperature gradients can occur inside and outside the catalyst particle. Therefore, the control of temperature, heat management and analysis of the transport process are crucial factors in the design and operation of catalytic systems, allowing the process to be intensified through safe operation [156].

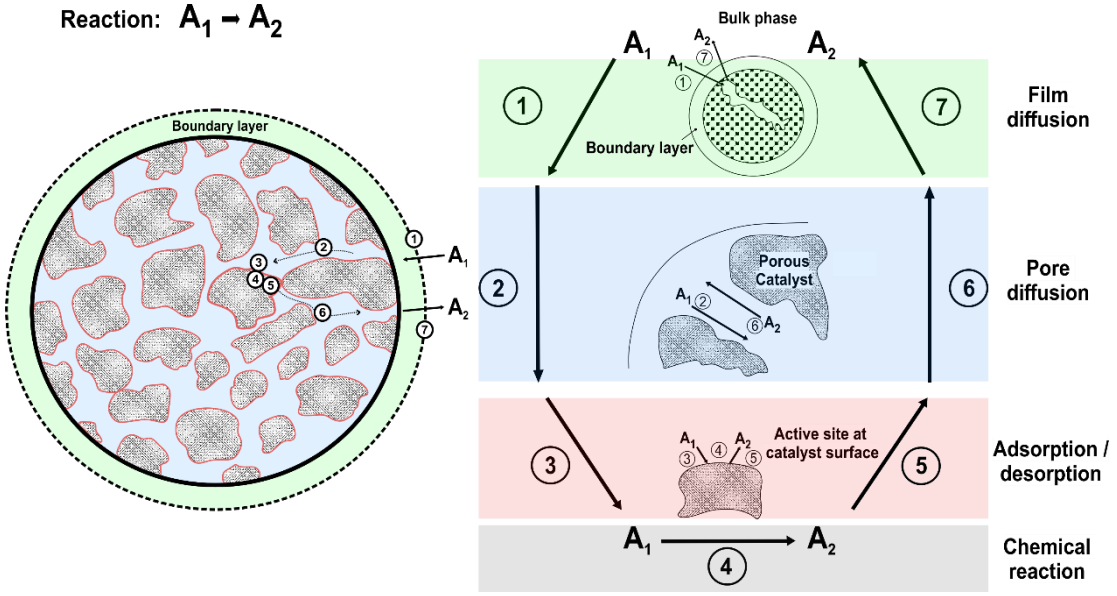


**Figure 6.** Physical and chemical steps involved in heterogeneous catalytic reactions. Images adapted from [151,152,154,155]

## 1.2 Objective and structure of the thesis

The objective of the work is focused on the study of ceramic OCFs as catalytic support for both exothermic and endothermic gas-solid reaction systems. In particular, the investigation is centered on the methane oxidation reaction in lean conditions. With an approach toward process intensification, the research is dedicated to the analysis of mass transfer effects occurring from the bulk gas phase to the external catalyst surface and within the catalyst layer. In addition, the evaluation of the various operating regimes (kinetic, internal and external mass transfer) in coated OCFs. This research also explores the effects of OCF material on the heat transfer of the catalytic process.

For the analysis of mass and heat transfer in open cell foams were studied the following catalytic reactions: Combustion of methane (**Chapters IV**, **V** and **VII**), steam/oxy steam reforming of biogas (**Chapter III**), methane steam reforming (**Chapter II**) and nitrous oxide decomposition (**Chapter I**). These last ones studied in monolithic supports. Since monolithic substrates have a simpler structure than OCFs, they were used as a starting point for the application of the theoretical method for the analysis of transport processes during the catalytic reaction. The model was adapted and applied to the catalyzed reactions using the OCFs as support.

For the process intensification toward methane oxidation (**Chapters IV**, **V**, **VI** and **VII**), the influence of the geometrical properties of the OCFs on the overall catalytic performance was studied. Moreover, the impact of the ceramic foam material type on the exothermic reaction process was also evaluated. The experimental work involved the deposition of the 3 wt. % $PdO/Co_3O_4$ catalyst on ceramic OCF via a two-steps synthesis:

first, solution combustion synthesis (SCS) of the $Co_3O_4$ spinel on the OCF, and second, wetness impregnation (WI) of 3 wt. % Pd on the $Co_3O_4$ spinel. This specific catalyst composition was selected from previous optimization work performed on $PdO/Co_3O_4$ at powder level, in terms of PdO amount and best conditions of synthesis. The influence of catalyst layer thickness was also studied in terms of controlling resistances and catalytic performance. Furthermore, the catalyst performance was evaluated by combining coated OCFs of different materials.

This dissertation is organized as a collection of papers already published during the Ph.D. or submitted for publication. Therefore, the exhaustive analysis of the methods and results are described carefully in each Chapter of the thesis. The sequence of the Chapters is presented as follows:

In **Chapters I** and **II**, the $N_2O$ decomposition and $CH_4$ steam reforming reactions catalyzed on ceramic cordierite monoliths were investigated in terms of catalytic performance and mass transfer effects (**Figure 7**). First of all, the structure was thoroughly analyzed in order to determine the characteristic monolith dimensions as well as the thickness and shape of the catalyst layer. Once the characteristic parameters were determined, a low-dimensional theoretical model was used to describe the various resistances (kinetic, internal and external mass transfer) as the process temperature varied. The effect of deposition method, channel shape and catalyst loading were investigated.

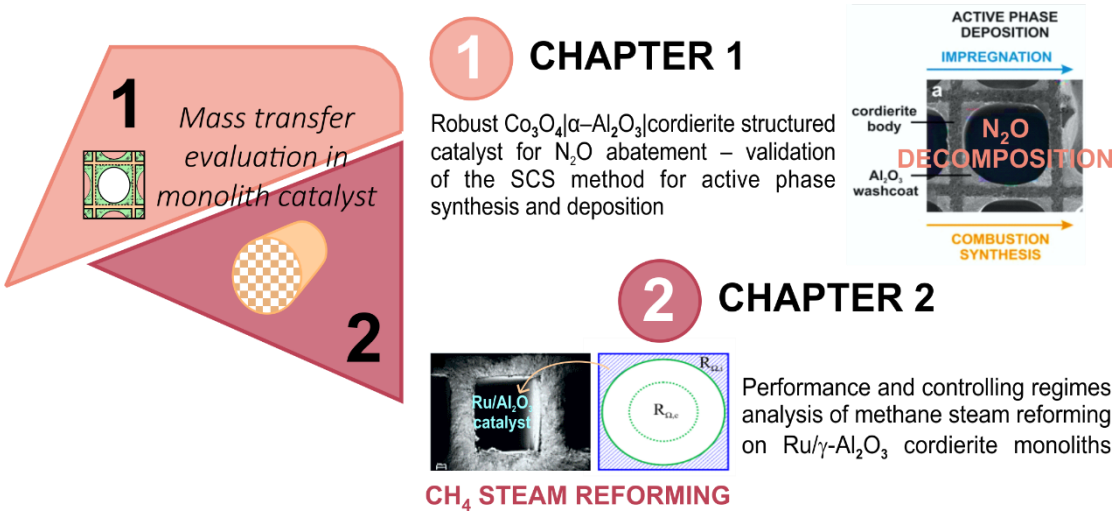


**Figure 7.** Thesis structure portion: Chapter I and Chapter II.

In **Chapter III**, a series of biogas steam reforming and oxy-steam reforming experiments were carried out on alumina ceramic OCF of different pore density (20, 30 and 45 ppi) in order to study the catalytic performance and mass transfer effects (**Figure 8**). Furthermore, the stability of the catalytic foams as well as the pressure drop across the structures were also evaluated. First, the OCFs were carefully characterized using microscopic techniques to define the characteristic lengths such as pore and strut diameter. For describing the trade-off between reaction kinetics and mass transport effects, characteristic Damköhler numbers were estimated for each coated foam. The results were checked using the Carberry and Weisz-Prater criteria.

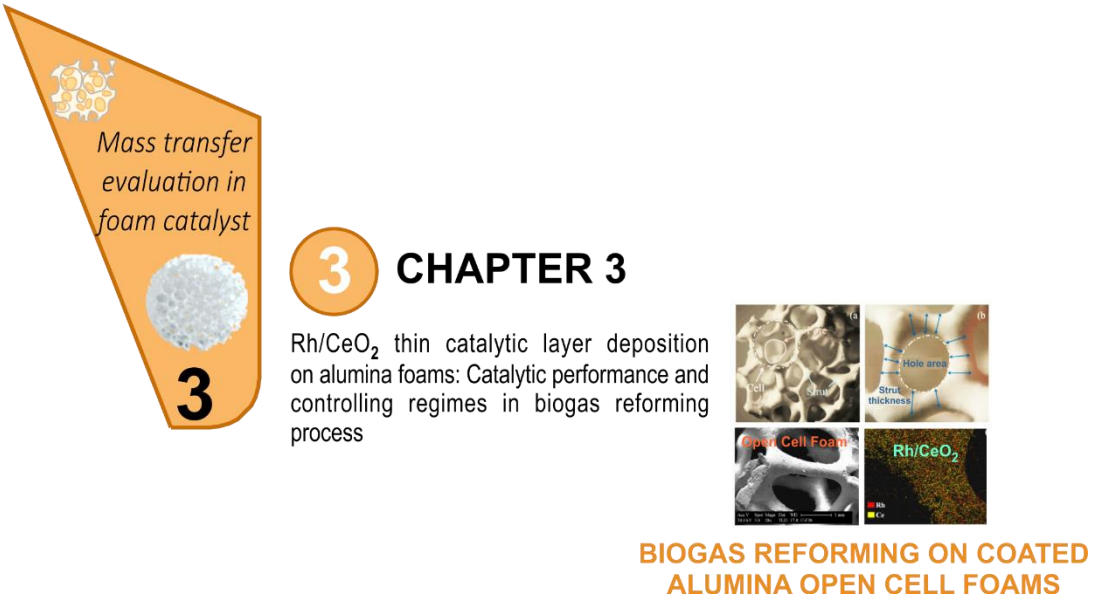


**Figure 8.** Thesis structure portion: Chapter III.

**Chapters IV**, **V** and **VII** were dedicated to the study and intensification of the combustion reaction process under lean conditions conducted on ceramic OCFs made of alumina, silicon carbon and zirconia (**Figure 9**). The foams were coated with 3 wt. % $PdO/Co_3O_4$ as catalyst using SCS and WI techniques. Physico-chemical characterizations were carried out on all structured catalysts. Mass transfer effects were evaluated using a low-dimensional theoretical model adapted to the OCF geometry. First of all, the characteristic lengths of the bare and coated OCFs were carefully estimated. Then, the coated layer shape and catalytic thickness were defined. Subsequently, various resistances (kinetic, internal and external mass transfer) were calculated by varying the gas temperature in order to define the operating regimes of the catalytic process. In **Chapter IV**, the effect of foam material on catalytic performance was studied at varying flow conditions. In addition, a mass and heat transfer analysis was carried out on all structured catalysts. In **Chapter V**,

it was investigated the effect of catalyst loading in terms of catalytic performance and controlling resistances. Then, in **Chapter VII**, three different combinations of coated OCFs made of zirconia and silicon carbide were tested with the aim of intensifying the methane combustion process. Heat transfer measurements were carried out as well as an extensive analysis of mass transfer effects in terms of governing regimes.

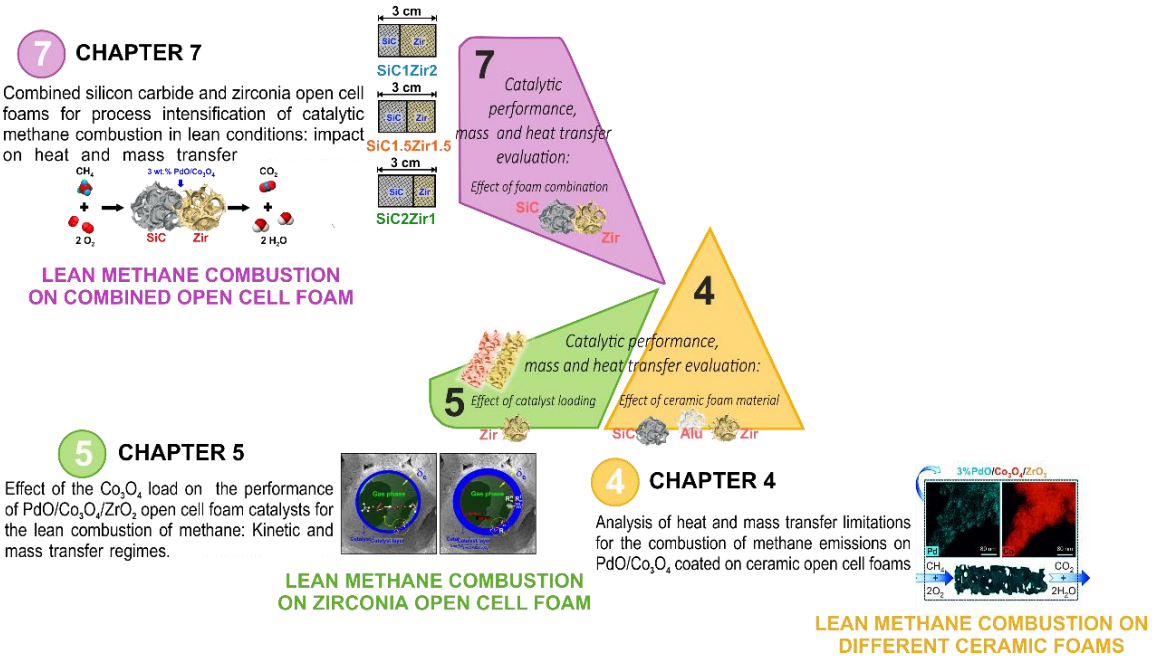


**Figure 9.** Thesis structure portion: Chapter IV, Chapter V and Chapter VII.

In **Chapter VI**, a detailed characterization of ceramic foams at different pore densities is presented using X-ray computed microtomography (**Figure 10**). This technique allowed an exhaustive and quantitative extraction of morphological and geometrical characteristics of the structures such as pore diameter, strut diameter, strut length, open porosity and specific surface area. Pressure drop measurements were performed at different gas

velocities for all structures. Moreover, the validity and suitability of several correlations proposed in the literature to estimate the specific surface area of ceramic foams were evaluated.

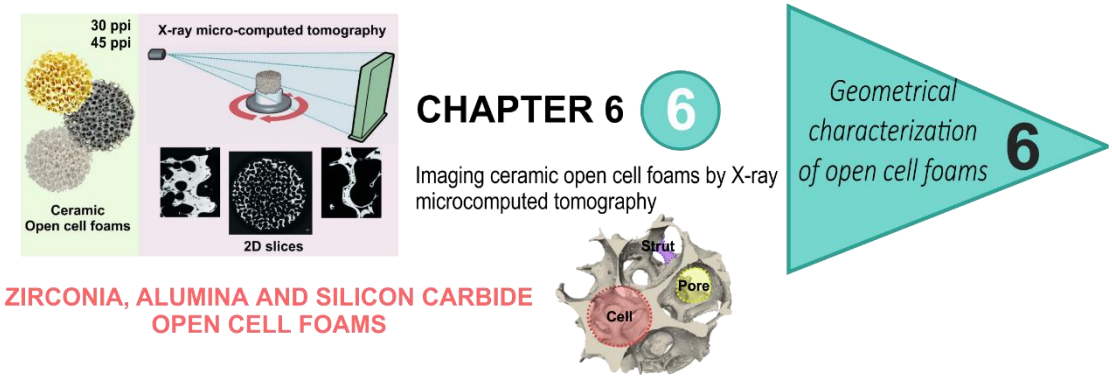


**Figure 10.** Thesis structure portion: Chapter VI.

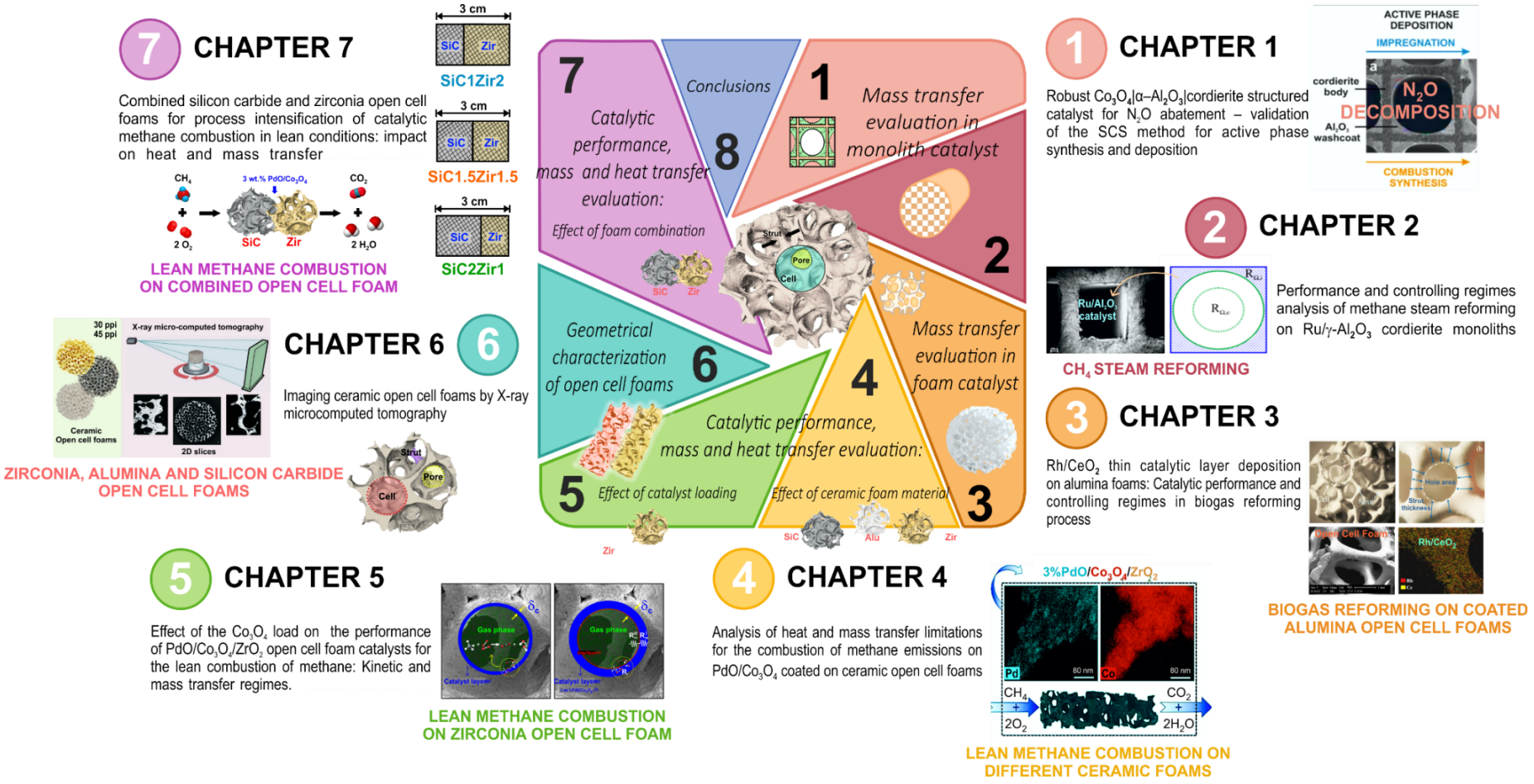


**Figure 11.** General diagram of the thesis structure.

## 1.3 External and internal mass transfer

### 1.3.1 Theoretical low dimensional model

It is well known that the performance of a catalytic structure (such as monoliths and foams) is limited by the kinetic regime at low temperature (or before light-off), pore diffusion regime at intermediate/high temperatures and at sufficiently high temperatures, the external mass transfer controlled regime [89,157–167]. The concept of external mass transfer coefficient is almost a century old and is widely used to simplify mathematical models of convection with diffusion and reaction [150–152,158,168–170]. This model is based on the assumption that all the mass transfer resistance resides entirely in a fictitious thin film where concentration variations occur. Balakotaiah (2008) applied an analogous approach to simplify the process of diffusion and reaction inside the catalyst particle using a hypothetical film model similar to that of external mass transfer, in which the concentration gradients to the inner pore of the catalyst layer occur [161]. Later, Joshi et al. [162] developed a steady-state low-dimensional model (LD) to characterize the controlling regimes during the catalytic reactions in washcoated monoliths of arbitrary shape. The LD model was derived using the concepts of external and internal mass transfer coefficients by averaging the governing equations [161,162]. In this way, the problem of flow and diffusion in the fluid phase is simplified by the coefficient ($Sh_e$) and gradient ($C_f - C_s$) of external mass transfer (**Figure 12**), while the diffusion and reaction in the catalyst layer can be captured by the coefficient ($Sh_i$) and gradient ($C_s - < C_c >$) of internal mass transfer such that the overall process can be described by a two-film model (see **Figure 12**).

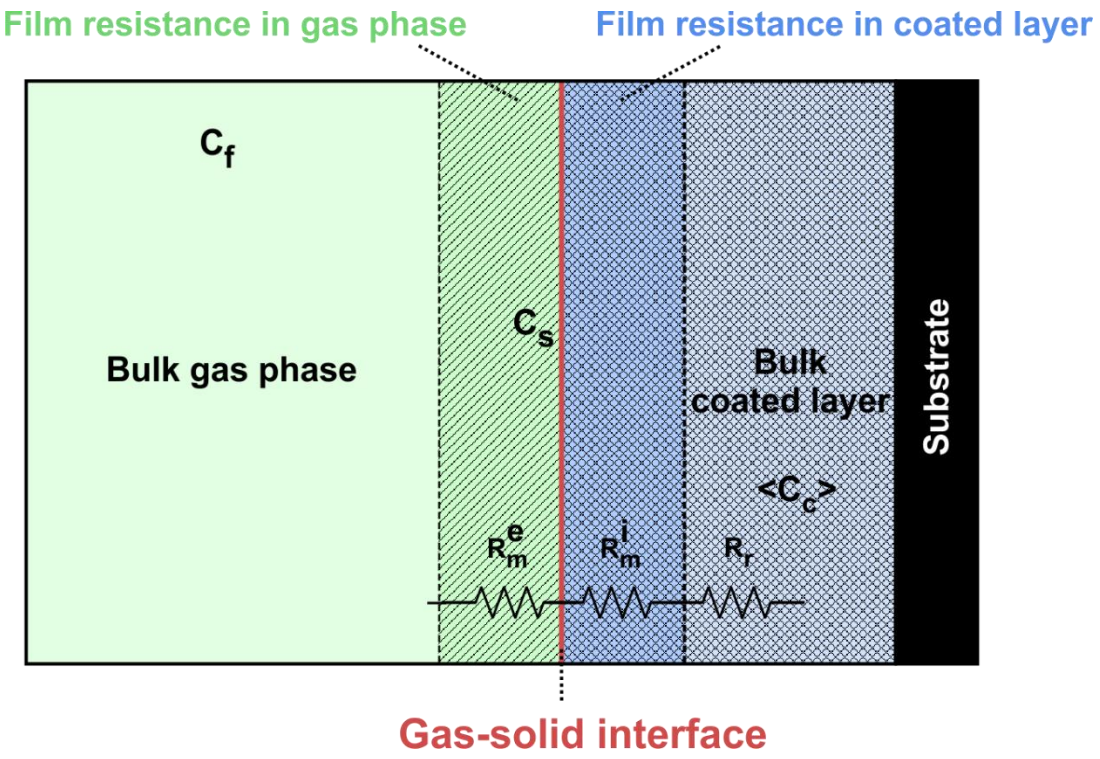


**Figure 12.** Schematic diagram illustrating gas-solid mass transfer with chemical reaction in the coated layer with series resistance approach. Image adapted from [164]

Below, the equations of the low dimensional model developed in detail by the authors for the analysis of the catalytic reactions in washcoated monoliths are presented [162–165]:

- **Gas phase species balance**

As in the conventional approach, the concept of external mass transfer coefficient ($k_m^e$) is used, assuming that the entire mass transport resistance for the gas phase resides in a thin stagnant film in which the concentration drops from $C_f$ to $C_s$. Thus, the steady state equilibrium of species can be expressed as [74,150–153,157,160–162,164,165,168,171–173]:

$$< u >\cdot \frac{dC_f}{dz} = -\frac{k_m^e(z)}{R_{\Omega,e}} \cdot (C_f - C_s) \quad (1)$$

- **Washcoat species balance**

Similar to the gas phase, the process of internal diffusion and reaction in the washcoat is approximated by using the internal mass transfer coefficient assuming that the whole intra-phase resistance resides in a hypothetical washcoat film. Considering no diffusional limitations in the bulk washcoat, the concentration drops from $C_s$ to $< C_c >$. Hence, the steady-state species balance equation in the catalyst is expressed as [162–165]:

$$k_m^i \cdot (C_s - < C_c >) = R_{\Omega,i} \cdot R(< C_c >) \quad (2)$$

- **Interface balance**

As the interface has zero capacitance, there is no accumulation of species at the fluid-washcoat interface. Therefore, the external mass flux from bulk gas phase to the interface must be the same as the internal mass flux from the interface to the bulk washcoat, obtaining [162–165]:

$$k_m^e(z) \cdot (C_f - C_s) = k_m^i \cdot (C_s - < C_c >) \quad (3)$$

- **Boundary conditions**

$$C_f = C_{in} \ \ at\ z = 0 \quad (4)$$

where $< u >$ is the average fluid velocity, $C_f$ is the cup-mixing concentration in fluid phase, $C_s$ is the fluid–washcoat (catalyst layer) interfacial concentration, $< C_c >$ is the volume averaged concentration in the washcoat (catalyst layer), $R_{\Omega,e}$ and $R_{\Omega,i}$ are the characteristic length scales for the gas flow and coated layer areas, respectively. These

characteristic length scales are defined as the ratio of the flow or washcoat cross-sectional area to the gas-solid interfacial perimeter (wetted surface, assuming continuous catalyst layer), which are expressed as [157,160–165,173]:

$$R_{\Omega,e} = \frac{A_{\Omega,e}}{P_{\Omega}} \tag{5}$$

$$R_{\Omega,i} = \frac{A_{\Omega,i}}{P_{\Omega}} \tag{6}$$

where $P_{\Omega}$ is the wetted fluid–washcoat interfacial perimeter, $A_{\Omega,e}$ and $A_{\Omega,i}$ are the cross sectional areas for the fluid phase and coated catalyst layer (washcoat), respectively. **Figure 13** shows the different geometric shapes considered by the authors for the flow path and coated catalyst layer.

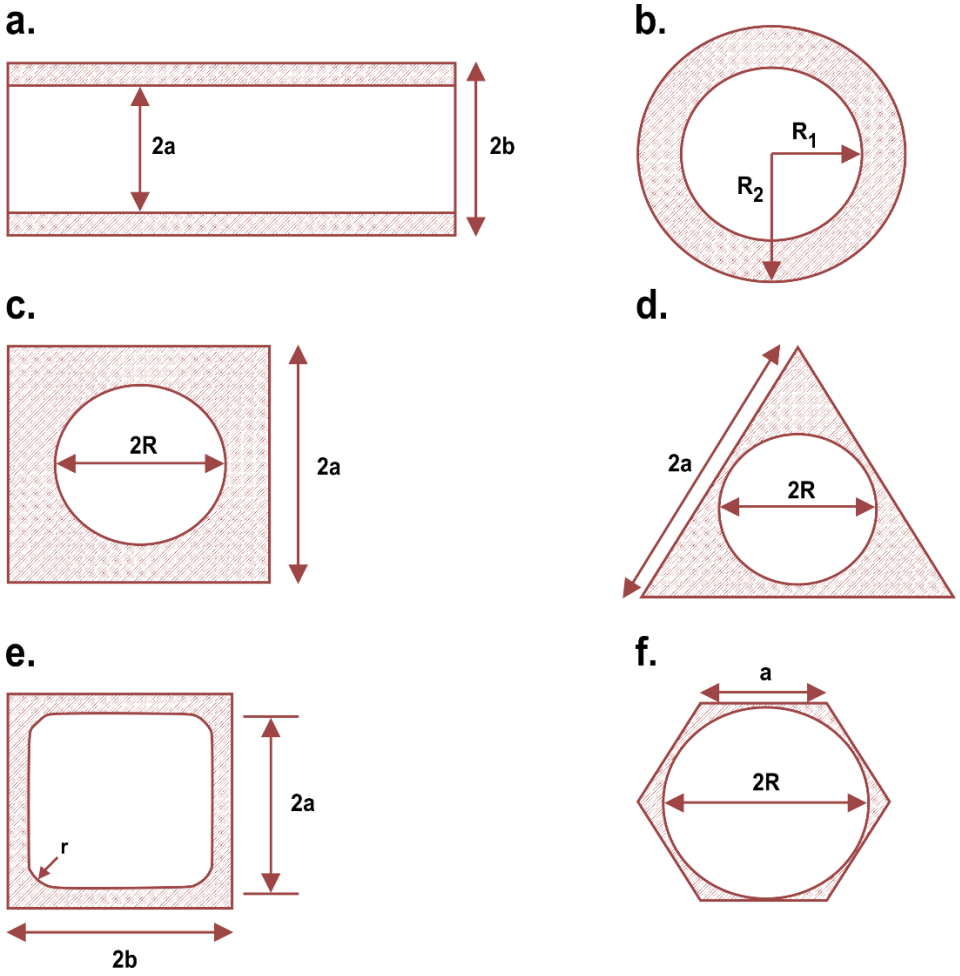


**Figure 13.** Different coated layer and channel geometric shapes for mass transfer. Image adapted from [164].

The mass transfer between the bulk of fluid phase and the fluid-catalyst interface is described by the external mass transfer coefficient $k_m^e$, defined as the ratio of the total flux integrated over the interfacial perimeter to the external mass transfer gradient $(C_f - C_s)$ [74,150–153,158,168,170–172]. Thus, the final expression of $k_m^e$ is given as:

$$k_m^e = \frac{Sh_e \cdot D_f}{4 \cdot R_{\Omega,e}} \tag{7}$$

Similarly, the mass transfer between the fluid-catalyst interface and bulk washcoat is described by the internal mass transfer coefficient $k_m^i$, defined as the ratio of the total flux integrated over the interfacial perimeter to the gradient for the internal mass transfer ($C_s - < C_c >$) according to Balakotaiah [161–164]. Hence, the final expression of $k_m^i$ is given as:

$$k_m^i = \frac{Sh_i \cdot D_e}{R_{\Omega,i}} \tag{8}$$

where $D_f$ is the molecular diffusivity of the reactant in the fluid phase, $D_e$ is the effective diffusivity of the reactant within the catalyst layer, $Sh_e$ and $Sh_i$ are the external and internal Sherwood number, respectively.

A large number of experimental and theoretical correlations have been presented in literature to estimate the dimensionless external mass transfer coefficient ($Sh_e$), which are dependent on the physical properties of the fluid, geometry and fluid velocity [151,157,158,160,170,174–180]. For catalytic monoliths, the external Sherwood number can be estimated by Shah et al.[175] as:

$$Sh_e = Sh_{e,\infty} \cdot \left(1 + 0.095 \cdot Re \cdot Sc \cdot \frac{d_h}{L_m}\right)^{0.45} \tag{9}$$

where $d_h$ is the channel hydraulic diameter ($d_h = 4 \cdot R_{\Omega,e}$); $L_m$ is the monolith length, $Re$ is the Reynold number, $Sc$ is the Schmidt number and $Sh_{e,\infty}$ is the asymptotic external Sherwood number [151,154,155,158,160,161,172,174,181], which depends on the geometry of the channel as summarized in **Table 1**.

**Table 1.** Asymptotic external Sherwood number for some common cross-sectional shapes.

| Geometry | $\boldsymbol{Sh_{e,\infty}}$ |
|---|---|
| Square | 2.98 |
| Circular | 3.66 |
| Ellipse | 3.74 |
| Parallel plates | 7.54 |
| Sinusoidal | 2.47 |
| Hexagonal | 3.66 |
| Equilateral triangle | 2.47 |

Similarly, Balakotaiah and West [160] presented a simple approximation to determine the dimensionless external mass transfer coefficient valid for any arbitrary geometry:

$$Sh_e(z) = Sh_{e,\infty} + \frac{1.4}{Sc^{\frac{1}{6}}} \cdot \sqrt{\frac{R_{\Omega,e}^2 \cdot <u>}{z \cdot D_f}} \tag{10}$$

Thus, for a structure of length $L$ the average value of $Sh_e$ is given by [165]:

$$Sh_e(L) = \frac{1}{L}\int_0^L Sh_e(z)dz = Sh_{e,\infty} + \frac{2.8}{Sc^{\frac{1}{6}}} \cdot \sqrt{\frac{R_{\Omega,e}^2 \cdot <u>}{L \cdot D_f}} = Sh_{e,\infty} + \frac{2.8}{Sc^{\frac{1}{6}}} \cdot \sqrt{P} \tag{11}$$

where $P$ is the transverse Peclet number.

In **Chapters I** and **II**, **Equations 9** and **11** were used to estimate the external Sherwood number ($Sh_e$) in cordite monoliths of square channels with 400 and 100 cpsi, respectively. On the other hand, the dimensionless internal mass transfer coefficient ($Sh_i$) was determined assuming that all the pore diffusion resistance resides in a hypothetical thin film within the catalytic layer as described by Balakotaiah [161]. In this way, the internal Sherwood number can be related to the Thiele module using the following general approximation proposed by the author [161,163]:

$$Sh_i = Sh_{i,\infty} + \frac{\Lambda \cdot \phi^2}{1+\Lambda \cdot \phi} \tag{12}$$

where $\Lambda$ is a constant that depends on the coated catalytic layer geometry and the order reaction[163], $\phi$ is the Thiele modulus and $Sh_{i,\infty}$ is the asymptotic internal Sherwood number[161,163].

Thiele modulus for an *n*th order reaction is defined as:

$$\phi = \sqrt{\frac{(n+1)}{2} \cdot \frac{k_r \cdot R_{\Omega,i}^2 \cdot C_{A,s}^{n-1}}{D_e}} \tag{13}$$

where $n$ is the order reaction, $k_r$ is the reaction rate constant and $C_{A,s}$ is the concentration at the catalyst surface.

For the case of first order kinetics, the Thiele modulus is given by [74,150,152–154,164,168,171,172,182]:

$$\phi = \sqrt{\frac{k_r \cdot R_{\Omega,i}^2}{D_e}} \tag{14}$$

Thus, the effectiveness factor ($\eta$) for a first order reaction can be defined using the concept of dimensionless internal mass transfer coefficient ($Sh_i$) reported by Balakotaiah as [161]:

$$\eta = \frac{1}{1+\frac{\phi^2}{Sh_i}} \tag{15}$$

It is interesting to note that similar to the conventional approach, the number of $Sh_i$ (**Equation 12**) presents two limiting cases:

I. When the reaction is very slow ($\phi << 1$; $\eta \to 1$), the process is governed by the kinetic regime and thus the $Sh_i$ is approximately equal to the asymptotic internal Sherwood number [163–165]:

$$Sh_i \cong Sh_{i,\infty} \qquad \text{for } \phi << 1$$

II. When the reaction is very fast ($\phi >> 1$; $\eta \to 1/\phi$), the process is governed by the diffusion, whereby the $Sh_i$ is nearly equal to the Thiele number [163–165]:

$$Sh_i \cong \phi \qquad \text{for } \phi >> 1$$

In **Table 2** are shown the characteristic length scales, Λ constants and the asymptotic internal ($Sh_{i,\infty}$) and external ($Sh_{e,\infty}$) Sherwood number values for the most common channels and catalytic thickness shapes in the case of first order kinetic reactions [150,151,157,158,161,163].

The effective diffusivity within the catalytic layer was estimated using the random-pore model proposed by Wakao and Smith [183] for layers with bimodal pore size distributions. This model has been widely used in the literature to estimate the effective diffusivity of a bidisperse porous material. However, recently Novak et al.[184] have reported that the model proposed by the authors tends to predict a lower effective diffusivity coefficient and hence a greater impact on catalyst performance. This is especially significant for layers of low macroporosity, while the differences decrease for highly macroporous layers [184–186]. Such results suggest that the correlation underestimates the macropore connectivity at low macroporosities, giving more weight to slow Knudsen diffusion in mesopores.

**Table 2.** Characteristic diffusion lengths, asymptotic internal Sherwood number and Λ for some common cross-sectional shapes for first order kinetics [163].

| Geometry | $R_{\Omega,e}$ | $R_{\Omega,i}$ | $R_2/R_1$; $a/R$; $b/a$ | $Sh_{i,\infty}$ | Λ |
|---|---|---|---|---|---|
| Fig. 7a | a | b-a | - | 3 | 0.32 |
| Fig. 7b | $R_1/2$ | $(R_2^2 - R_1^2)/2\,R_1$ | 1.01[¤] | 3.013 | 0.38 |
| | | | 1.1[¤] | 3.153 | 0.36 |
| | | | 1.2[¤] | 3.311 | 0.34 |
| Fig. 7c | $R/2$ | $(4a^2 - \pi R^2)/2\pi R$ | 1* | 0.826 | 0.67 |
| | | | 1.1* | 1.836 | 1.20 |
| | | | 1.2* | 2.533 | 0.73 |
| Fig. 7d | $R/2$ | $(\sqrt{3}a^2 - \pi R^2)/2\pi R$ | 1.7321* | 0.84 | 0.62 |
| | | | 1.9245* | 1.45 | 1.25 |
| | | | 2.4744* | 2.92 | 0.85 |
| Fig. 7e | $\frac{4a^2 - r^2 + \pi r^2}{2\pi r + 8a - 8r}$ | $\frac{4b^2 - 4a^2 + 4r^2 - \pi r^2}{2\pi r + 8a - 8r}$ | 1.11[x] | 2.645 | 0.58 |
| | | | 1.25[x] | 3.088 | 0.39 |
| Fig. 7f | $R/2$ | $(3\sqrt{3}a^2 - 2\pi R^2)/4\pi R$ | 1.155* | 0.814 | 0.77 |
| | | | 1.17* | 1.16 | 2.08 |
| | | | 1.2* | 1.74 | 1.60 |

[¤] is referred to $R_2/R_1$. * is referred to $a/b$. [x] is referred to $b/a$

## 1.3.2 Resistances in series: Transport-reaction

Considering that the flux continuity equation is linear in the concentrations, the fluid catalyst layer interfacial concentration ($C_s$) from **Equations 1** and **2** can be simplified

using the interface balance (**Equation 3**), obtaining a two-mode low-dimensional model given by:

$$< u >\cdot \frac{dC_f}{dz} = -\frac{k_m^o(z)}{R_{\Omega,e}} \cdot (C_f - < C_c >) \tag{16}$$

$$k_m^o(z) \cdot (C_f - < C_c >) = R_{\Omega,i} \cdot R(< C_c >) \tag{17}$$

It is worth noting that the **Equation 16** and **Equation 17** describe the overall process of mass transfer, that is, the mass transport from the fluid phase to the external catalyst surface as the internal diffusion and reaction within the catalyst layer. Thus, the overall mass transfer coefficient ($k_m^o$) that describes the transport phenomena is given by:

$$\frac{1}{k_m^o} = \frac{1}{k_m^e} + \frac{1}{k_m^i} \tag{18}$$

$$k_m^o = \frac{k_m^e \cdot k_m^i}{k_m^e + k_m^i} \tag{19}$$

Hence, the various resistances for mass transfer can be written as:

$$R_m^o = R_m^e + R_m^i \tag{20}$$

Joshi et al.[163] derived an explicit expression to determine the experimentally observable mass transfer coefficient ($k_{m,app}$) for first order reactions. Assuming fully developed laminar flow, very large axial Peclet number (convection is dominant over axial diffusion), isothermal monolith and steady state operating conditions; the **Equation 17** can be written as:

$$< C_c > = C_f \cdot \left(\frac{k_m^o}{k_r \cdot R_{\Omega,i} + k_m^o}\right) \tag{21}$$

Substituting **Equation 21** into **Equation 16**, the following expression is obtained:

$$< u >\cdot \frac{dC_f}{dz} = -\frac{C_f}{R_{\Omega,e}} \cdot \left( \frac{1}{\frac{1}{k_m^o} + \frac{1}{k_r \cdot R_{\Omega,i}}} \right) \quad (22)$$

Replacing $k_m^o$ (**Equation 19**) in **Equation 22**:

$$< u >\cdot \frac{dC_f}{dz} = -\frac{C_f}{R_{\Omega,e}} \cdot \left( \frac{1}{\frac{1}{k_m^e} + \frac{1}{k_m^i} + \frac{1}{k_r \cdot R_{\Omega,i}}} \right) \quad (23)$$

Now, considering the definition of overall experimentally observable apparent mass transfer coefficient derived by Joshi et al.[163,164]:

$$\frac{1}{k_{m,app}^o} = \frac{1}{k_m^e} + \frac{1}{k_m^i} + \frac{1}{k_r \cdot R_{\Omega,i}} \quad (24)$$

In this way, the overall apparent process resistance ($\frac{1}{k_{m,app}^o}$) is given by the sum of three resistance contributions (series approach): the film fluid phase resistance ($\frac{1}{k_m^e}$), the internal pore diffusion resistance ($\frac{1}{k_m^i}$) and reaction resistance ($\frac{1}{k_r \cdot R_{\Omega,i}}$).

According to the definitions of external (**Equation 7**) and internal (**Equation 8**) mass transfer coefficients, the resistances can be defined as [78,151,152,161–164,177]:

$$R_m^e = \frac{1}{k_m^e} = \frac{4 \cdot R_{\Omega,e}}{Sh_e \cdot D_f} \quad (25)$$

$$R_m^i = \frac{1}{k_m^i} = \frac{R_{\Omega,i}}{Sh_i \cdot D_e} \quad (26)$$

$$R_r = \frac{1}{k_r \cdot R_{\Omega,i}} \quad (27)$$

$$R_t = \frac{1}{k_{m,app}^o} \quad (28)$$

Thus, the **Equation 24** can be written in terms of resistance as:

$$R_t = R_m^e + R_m^i + R_r \quad (29)$$

### 1.3.3 Overall Sherwood number

Previously, the apparent overall mass transfer coefficient ($k^o_{m,app}$) that describes the transport-reaction effects of the catalytic process has been defined as the sum of two diffusional contributions (external and internal) and one contribution related to the reaction kinetics (**Equation 24**). Such definition can also be written in dimensionless form, that is, in terms of Sherwood numbers. According to West et al.[160], the experimentally observable apparent global Sherwood number can be expressed as:

$$Sh^o_{app} = \frac{4 \cdot k^o_{m,app} \cdot R_{\Omega,e}}{D_f} \tag{30}$$

Thus, by replacing $k^o_{m,app}$ (**Equation 24**), $k^e_m$ (**Equation 7**) and $k^i_m$ (**Equation 8**) in **Equation 30** gives:

$$\frac{1}{Sh^o_{app}} \cdot \frac{4 \cdot R_{\Omega,e}}{D_f} = \frac{1}{Sh_e} \cdot \frac{4 \cdot R_{\Omega,e}}{D_f} + \frac{1}{Sh_i} \cdot \frac{R_{\Omega,i}}{D_e} + \frac{1}{k_r \cdot R_{\Omega,i}} \tag{31}$$

Dividing the above expression by $\frac{4 \cdot R_{\Omega,e}}{D_f}$:

$$\frac{1}{Sh^o_{app}} = \frac{1}{Sh_e} + \frac{1}{Sh_i} \cdot \frac{1}{4} \cdot \frac{R_{\Omega,i}}{R_{\Omega,e}} \cdot \frac{D_f}{D_e} + \frac{1}{k_r \cdot R_{\Omega,i}} \cdot \frac{1}{4} \cdot \frac{D_f}{R_{\Omega,e}} \tag{32}$$

Now, introducing Thiele's module definition (**Equation 14**) in **Equation 32** gives:

$$\frac{1}{Sh^o_{app}} = \frac{1}{Sh_e} + \frac{1}{Sh_i} \cdot \frac{1}{4} \cdot \frac{D_f}{D_e} \cdot \frac{R_{\Omega,i}}{R_{\Omega,e}} + \frac{1}{4} \cdot \frac{1}{\phi^2} \cdot \frac{D_f}{D_e} \cdot \frac{R_{\Omega,i}}{R_{\Omega,e}} \tag{33}$$

By defining the following dimensionless groups [163,164]:

$$\lambda = \frac{R_{\Omega,i}}{R_{\Omega,e}}; \quad \mu = \frac{D_f}{D_e} \tag{34}$$

The **Equation 33** can be written as:

$$\frac{1}{Sh^o_{app}} = \frac{1}{Sh_e} + \frac{\mu \cdot \lambda}{4} \cdot \frac{1}{Sh_i} + \frac{\mu \cdot \lambda}{4} \cdot \frac{1}{\phi^2} \tag{35}$$

where $\lambda$ is the ratio of characteristic length scales for washcoat (or catalytic layer) and fluid phase and $\mu$ is the ratio of the molecular and effective diffusivity of the reagents in the fluid phase and within the catalyst layer, respectively.

It is interesting to note that at low temperatures (kinetic regime conditions), the reaction rate constant ($k_r$) is very low and the Thiele modulus ($\phi$) is much lower than unity. Thus, the reaction resistance ($R_r$) becomes dominant while the ($R_m^i$) reaches a characteristic asymptotic value for slow reactions ($R_m^i \rightarrow \frac{R_{\Omega,i}}{Sh_{i,\infty} \cdot D_e}$). In this case, the apparent overall mass transfer coefficient can be written as:

$$Sh_{app}^o \approx \frac{4 \cdot \phi^2}{\mu \cdot \lambda} \tag{36}$$

Likewise, as the temperature increases the transport effects begin to be important. Particularly, the diffusion phenomena inside the catalytic layer become significant when the effective diffusivity within the catalyst is low or when a very thick washcoat is deposited on the structure, as can be clearly seen from **Equation 8**. At this point, $R_m^i$ dominates the catalytic process and hence the catalytic structure operates in a pore diffusion controlled regime.

Finally, at sufficiently high temperatures, $R_r$ declines exponentially due to its dependence on the Arrhenius equation while $R_m^i$ reaches a fast reaction asymptote ($R_m^i \rightarrow \frac{1}{\sqrt{k_r \cdot D_e}}$; with $Sh_i \approx \phi$ for $\phi >> 1$). Thus, $R_m^e$ dominates the process and the catalytic structure operates in a regime controlled by external mass transfer. In this case, the apparent overall mass transfer coefficient can be written as:

$$Sh_{app}^o \approx Sh_e \tag{37}$$

## 1.4 External and internal heat transfer

In addition to mass transfer effects, heat transfer limitations can also occur in catalytic processes, especially in highly exothermic or endothermic reactions such as combustion and steam reforming. Temperature gradients can be originated within the catalyst pores (internal heat transfer) or, more frequently, between the bulk of the fluid phase and the external catalyst surface (external heat transfer), which can lead to catalyst deactivation due to thermal sintering. Thus, both for the development and optimization of the catalysts and for the correct design of the reactor, it is of vital importance to determine the influence of heat transfer phenomena on the reaction kinetics.

External heat transfer effects can be evaluated using the criteria derived by Mears in 1971 [187] using the perturbation approach, in which the resistance to heat transfer in the fluid phase is assumed to be lumped at the surface:

$$\chi = \left|\frac{(-\triangle H_r)\cdot R^{obs}\cdot R_{\Omega e}}{h_e \cdot T_b}\right| < \frac{0.15}{\gamma_b} \tag{38}$$

$$\gamma_b = \frac{E_{app}}{R_g \cdot T_b} \tag{39}$$

where $\Delta H_r$ is the heat of reaction, $h_e$ is the heat transfer coefficient associated to the gas phase, $T_b$ is the temperature in the bulk of the gas phase, $\gamma_b$ is the Arrhenius number evaluated at the bulk of the gas phase, $R_g$ is the universal gas constant and $\chi$ is the Damköhler for interphase heat transport [150,155,158,168,181,187]. If $\chi$ is less than $\frac{0.15}{\gamma_b}$, the temperature gradients between the bulk gas phase and the catalyst surface can be neglected.

Internal heat transfer effects can be evaluated using the criteria proposed by Anderson in 1963 [188], where temperature gradients within the pores of the catalyst can be assumed absent if:

$$\psi = \left|\frac{\left(-\triangle H_r \cdot R^{obs} \cdot R_{\Omega i}^2\right)}{\lambda_e \cdot T_s}\right| < \frac{0.75}{\gamma_s} \tag{40}$$

$$\gamma_s = \frac{E_{app}}{R_g \cdot T_s} \tag{41}$$

where $\lambda_e$ is the effective thermal conductivity, $T_s$ is the temperature at the surface of the catalyst layer, $\gamma_s$ is the Arrhenuis number evaluated at the surface of the gas phase, and $\psi$ is the Damköhler for intraparticle heat transport [150,155,158,168,181,188].

On the other hand, the impact between the degree of mass transfer control of a surface reaction and the external temperature gradient can be easily analyzed in steady state conditions. Under these conditions, by assuming that the outer surface of the catalyst is uniformly accessible to the reactants, the mass transfer rate of the reactant from the bulk fluid to the external catalyst surface must be equal to the rate of reactant conversion by surface reaction [151–154,171,172]:

$$k_m^e \cdot a_m \cdot \left(C_{A,b} - C_{A,s}\right) = k_{sr} \cdot a_m \cdot C_{A,s}^n \tag{42}$$

Because each section of the outer surface behaves kinetically as all other parts, the analysis in steady state is essentially one-dimensional. Therefore, even when the functional form of the rate equation or the order of the reaction is not known, the heat generated or consumed by the surface reaction can be determined by multiplying the mass transfer rate by the heat of the reaction per mole of reactant [151,152,154,155,158,171,172] Considering the $CH_4$ combustion

reaction, the heat generation rate derived from the surface reaction must be equal to the energy removal rate by heat transfer from the external catalyst surface to the bulk fluid in steady state conditions, as follows:

$$k_m^e \cdot a_m \cdot (C_{CH_4,b} - C_{CH_4,s}) \cdot (-\Delta H_r) = h_e \cdot a_m \cdot (T_s - T_b) \quad (43)$$

Now, using the Chilton-Colburn analogy between heat and mass transfer [151,152,154,155,158,172]:

$$\frac{h_e}{\rho \cdot C_p} \cdot Pr^{\frac{2}{3}} = k_m^e \cdot Sc^{\frac{2}{3}} \quad (44)$$

The ratio between the mass and heat transfer coefficient can be obtained as:

$$\frac{h_e}{k_m^e} = \rho \cdot C_p \cdot \left(\frac{Sc}{Pr}\right)^{\frac{2}{3}} \quad (45)$$

Thus, replacing **Equation 45** in **Equation 43** and considering that for simple gas mixtures $(Sc)^{\frac{2}{3}} \approx (Pr)^{\frac{2}{3}}$, the following expression is obtained:

$$(T_s - T_b) = \left(\frac{-\Delta H_r}{\rho \cdot C_p}\right) \cdot \left(C_{CH_4,b} - C_{CH_4,s}\right) \quad (46)$$

Now, by defining the degree of external mass transfer control as the ratio between the observed reaction rate and the maximum mass transfer rate [168], gives:

$$Ca = \frac{C_{CH_4,b} - C_{CH_4,s}}{C_{CH_4,b}} \quad (47)$$

where $Ca$ is the Carberry number.

Thus, **Equation 46** can be rewritten as:

$$(T_s - T_b) = \left(\frac{-\Delta H_r \cdot C_{CH_4,b}}{\rho \cdot C_p}\right) \cdot Ca \quad (48)$$

As can be noted, the temperature difference between the bulk gas and the outer catalyst surface $(T_s - T_b)$ is directly proportional to the heat of reaction per mole of diffusing reactant $(-\Delta H_r)$ as well as the degree of control of mass transfer $(Ca)$.

Now, introducing the concept of adiabatic temperature rise $(\Delta T_{ad})$ as [151,152,154,155,158,171,172]:

$$\Delta T_{ad} = \frac{-\Delta H_r \cdot C_{CH_4,b}}{\rho \cdot C_p} \tag{49}$$

where $\Delta T_{ad}$ is the ratio between the heat released of combustion by complete reaction for unit volume of the reacting gas mixture $(-\Delta H_r \cdot C_{CH_4,b})$ and the volumetric heat capacity of the reacting gas mixture $(\rho \cdot C_p)$. Thus, **Equation 48** is rewritten as:

$$(T_s - T_b) = \Delta T_{ad} \cdot Ca \tag{50}$$

Hence, the temperature difference is maximum when the reaction is limited by mass transfer $(Ca = 1)$. It is worth noting that at higher heat reaction values the temperature gradients $(\Delta T)$ may be significant, even when concentration gradients are small [151,152,154,155,158,172].

## 1.5 Open cell foam: geometrical considerations

As mentioned in *Section 1.1*, OCFs exhibit remarkable properties such as large external surface area, high porosity and mechanical strength, which make them an excellent candidate for a wide variety of industrial applications [92,98,100,105,116,136,189,190]. Due to their particular geometric architecture, foams have become a novel and attractive support for catalysts.

In order to carry out an analysis of mass and heat transfer in catalytic OCFs, it was required to define a geometrical model to describe the complex structure of the foams. In this regard, an accurate evaluation of the specific surface area is fundamental for further study and interpretation of the catalytic processes occurring in such a structure. Different geometrical models have been derived in literature to describe the idealized structure of foams based on repetitive arrangements of single unit cells such as [91,96,110,191–194]: cubic, dodecahedral and tetrakaidekahedral (TTKD) cell. Among all these, the best model that describes the foam structure reconstruction is the TTKD form. The tetrakaidecahedron, also called the Kelvin cell is a polyhedron composed of 14 faces consisting of six quadrilaterals and eight hexagons (see **Figure 14**) that allows the study of the elastic behavior of the foams partitioning the space into identical-volume units with minimal surface energy [96,105,144,193,195,196].

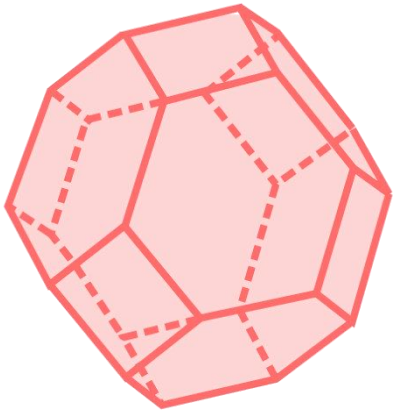

**Figure 14.** Kelvin cell unit cell.

Different correlations based on the periodic assembly of the Kelvin cell have been proposed to determine the specific surface of the foams using different geometrical

parameters as input [105,109,111,141,192,196,197]. According to the work reported by Gibson and Ashby (1988), the relative density of the foams ($\rho_r$) can be determined as a function of the strut dimensions by [198]:

$$\rho_r = 1.06 \cdot \left(\frac{t_s}{l}\right)^2 \tag{51}$$

where $l$ represents the length and $t_s$ the edge width (diameter) of the struts for an average number of edges per face on a single cell of 5.14. The authors also assumed a triangular prism shape for the strut. However, due to the difficulty to evaluate the strut length ($l$), Buciuman and Kraushaar-Czarnetzki [104] proposed the introduction of the face diameter ($d_f$) as an input parameter in the **Equation 51**. Since the faces of the tetrakaidecahedron are not equal, the average area of faces can be calculated as:

$$A_f = \frac{n_{sq} \cdot A_{sq} + n_{hex} \cdot A_{hex}}{n_f} \tag{52}$$

where $n_f$ is the number of faces on a single Kelvin cell, $n_{sq}$ ($n_{hex}$) and $A_{sq}$ ($A_{hex}$) are the number and area of quadrilaterals (hexagons) present in a Kelvin cell, respectively. Thus, the above equation can be written as:

$$A_f = \frac{6 \cdot (l^2) + 8 \cdot (\frac{3\sqrt{3}}{2} \cdot l^2)}{14} = \frac{26.78 \cdot l^2}{14} = 1.91 \cdot l^2 \tag{53}$$

Now, assuming a circular pore (window) of diameter $d_f$, the **Equation 53** is written as:

$$A_f = \frac{\pi \cdot d_f^2}{4} = 1.91 \cdot l^2 \tag{54}$$

$$l = 0.64 \cdot d_f \tag{55}$$

Replacing **Equation 55** in **Equation 51** gives:

$$\rho_r = 2.59 \left(\frac{t_s}{d_f}\right)^2 \tag{56}$$

The above equation was validated by Buciuman and Kraushaar-Czarnetzki approximating the irregular structure of real sintered alumina-mullite foams by a regular body pack [104].

The face diameter ($d_f$) is calculated as [104]:

$$d_f = d_p + t_s \tag{57}$$

where $d_p$ is the pore diameter and $t_s$ is the strut diameter.

Since the Kelvin cell unit consists of 36 struts, considering only the lateral surface of the triangular prism-shaped struts, the surface of a single strut ($S_{s,s}$) can be determined as [104,198]:

$$S_{s,s} = 3 \cdot t_s \cdot l \tag{58}$$

As each edge pertains to three cells, the average number of struts per cell is 12. Thus, the total surface area of the struts per cell ($S_{t,s}$) is calculated as [104,198]:

$$S_{t,s} = 36 \cdot t_s \cdot l \tag{59}$$

Considering that the Kelvin cell volume ($V_{TTKD}$) can be calculated as [198]:

$$V_{TTKD} = 11.31 \cdot l^3 \tag{60}$$

Thus, the geometric surface area per unit volume ($S_{ga}$) is determined as [198]:

$$S_{ga} = \frac{36 \cdot t_s \cdot l}{11.31 \cdot l^3} = 3.18 \cdot \frac{t_s}{l^2} \tag{61}$$

Finally, by substituting **Equations 56** in **Equation 61**, the geometric surface area per unit volume of the foams ($S_{ga}$) can be expressed as a function of relative density and face diameter as follows [104,144,198]:

$$S_{ga} = \frac{4.82}{d_f} \cdot \sqrt{\rho_r} \tag{62}$$

The calculated surface area of the foam ($S_a$) was calculated using the following expression:

$$S_a = V_{OCF} \cdot S_{ga} \tag{63}$$

where $V_{OCF}$ is the total OCF volume. Since in this study the foams were cut into a cylindrical shape, $V_{OCF}$ was calculated as [120,121]:

$$V_{OCF} = \frac{\pi \cdot d_{OCF}^2}{4} \cdot L_{OCF} \tag{64}$$

where $d_{OCF}$ is the foam diameter and $L_{OCF}$ is the foam length.

The foam open porosity (or voidage) was calculated as [104,144,198]:

$$\varepsilon = 1 - \rho_r \tag{65}$$

The OCF tortuosity was determined using the correlation proposed by Inayat et al. [106] for Kelvin cells as:

$$\tau = 1 + \alpha \cdot \frac{[1 - 0.971 \cdot (1-\varepsilon)^{0.5}]}{4 \cdot \varepsilon \cdot (1-\varepsilon)^{0.5}} \cdot (1 - \varepsilon) \tag{66}$$

where $\alpha$ is a non-empirical geometric constant that depends on the shape of the strut cross section. For cylindrical struts $\alpha$ is 4.87, for triangular struts $\alpha$ is 5.62 and for concave triangular struts $\alpha$ is 6.49.

The catalyst loading was determined as:

$$C_{load} = \frac{m_{cat}}{S_a} \tag{67}$$

where $m_{cat}$ is the mass of catalyst deposited on the foam.

The theoretical value of the catalyst thickness in coated OCF was calculated as:

$$\delta_{cat} = \frac{C_{load}}{\rho_{cat}} \tag{68}$$

where $\rho_{cat}$ is the catalyst density.

The low-dimensional model proposed by Joshi et al. [162,163] was adapted to OCFs considering the following assumptions:

i) The flow is laminar and fully developed.

ii) The catalyst is uniformly distributed inside the pore of the foams.

iii) Axial diffusion is negligible both in the gas phase and within the coated layer when compared to the convective transport (axial Peclet number very large).

iv) Isothermal foam

v) First order reaction

vi) Steady state conditions

Then, the characteristic lengths of foams ($R_{\Omega,e}, R_{\Omega,i}$) were defined. For this purpose, the bare and coated OCFs were carefully characterized using techniques such as optical microscopy, scanning electron microscopy and X-ray computed microtomography. The pore diameter was assumed to be circular (as shown in **Figure 15**), although the case of oval pores was also studied in **Chapter IV**. Using such characterization methods, it was possible to estimate both the pore diameter ($d_p$) and the catalyst thickness ($\delta_{cat}$) required to define $R_{\Omega,e}$ and $R_{\Omega,i}$ (in **Chapters IV**, **V** and **VII** the estimation of these dimensions was described in detail). Briefly, for circular pore diameter, using **Equation 5** and **Equation 6**, $R_{\Omega,e} = \frac{d_p}{4}$ and $R_{\Omega,i} = \delta_{cat}$. It is important to note that $R_{\Omega,e}$ is related to the hydraulic diameter $d_h$ by the expression $d_h = 4 \cdot R_{\Omega,e}$, as defined in **Chapters IV**, **V** and **VII**. [Remark: Although in **Chapter V** the definition of $R_{\Omega,e}$ has been correctly described, a typing error was made in **Equation 3**, thus the correct expression is $R_{\Omega,e} = \frac{A_{\Omega,e}}{P_\Omega} = \frac{d_p^c}{4} = \frac{d_h^c}{4}$]. Subsequently, using **Table 1** and **Table 2** (**Figure 13.b**), the asymptotic mass transfer coefficients were defined based on the geometrical ratios ($R_2/R_1$).

In all calculations the tortuosity, open porosity and specific surface area of the foams were considered.

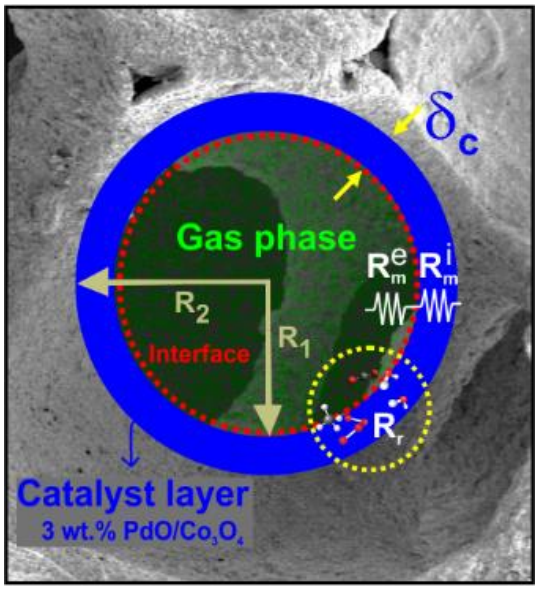


**Figure 15.** Representation of catalyst-coated OCF pore showing characteristic dimensions and resistances.

## 1.6 Materials and experimental methods

### 1.6.1 Powder catalyst

In order to characterize the physical-chemical properties, the catalysts were prepared in powder form by solution combustion synthesis (SCS) and wetness impregnation (WI). Undoped cobalt spinel was synthesized using a precursor solution for combustion synthesis constituted of glycine as organic fuel that acts as reducing agent and cobalt nitrate as metal source and oxidizing agent, according to the following reaction [61,62]:

$$3\,Co(NO_3)_2 \cdot 6H_2O + \frac{28}{9}\,NH_2CH_2COOH \rightarrow Co_3O_4 + \frac{56}{9}\,CO_2 + \frac{232}{9}\,H_2O + \frac{41}{9}N_2$$

Glycine was added at 25% of the necessary stoichiometric amount, to obtain a relatively high specific surface [27,44,68,120,199]. The solution was stirred at 120 °C to favor the complete dissolution of the reagents and then placed in an electric oven at 250 °C for 15 minutes to allow the reaction to occur. The obtained spinels were calcined at 600 °C for 4 hours in calm air. Pd-doped catalysts (with active metal loading of 3 wt. %) were prepared by WI using an aqueous solution of the palladium nitrate deposited drop by drop on the carrier, meanwhile thoroughly mixing the whole mass at about 140 °C in order to let water evaporate and $N_2$ escape. Finally, a posterior calcination was performed in static air at 600 °C for 4 hours. **Figure 16** illustrates a scheme of the experimental process for the powder catalyst preparation.

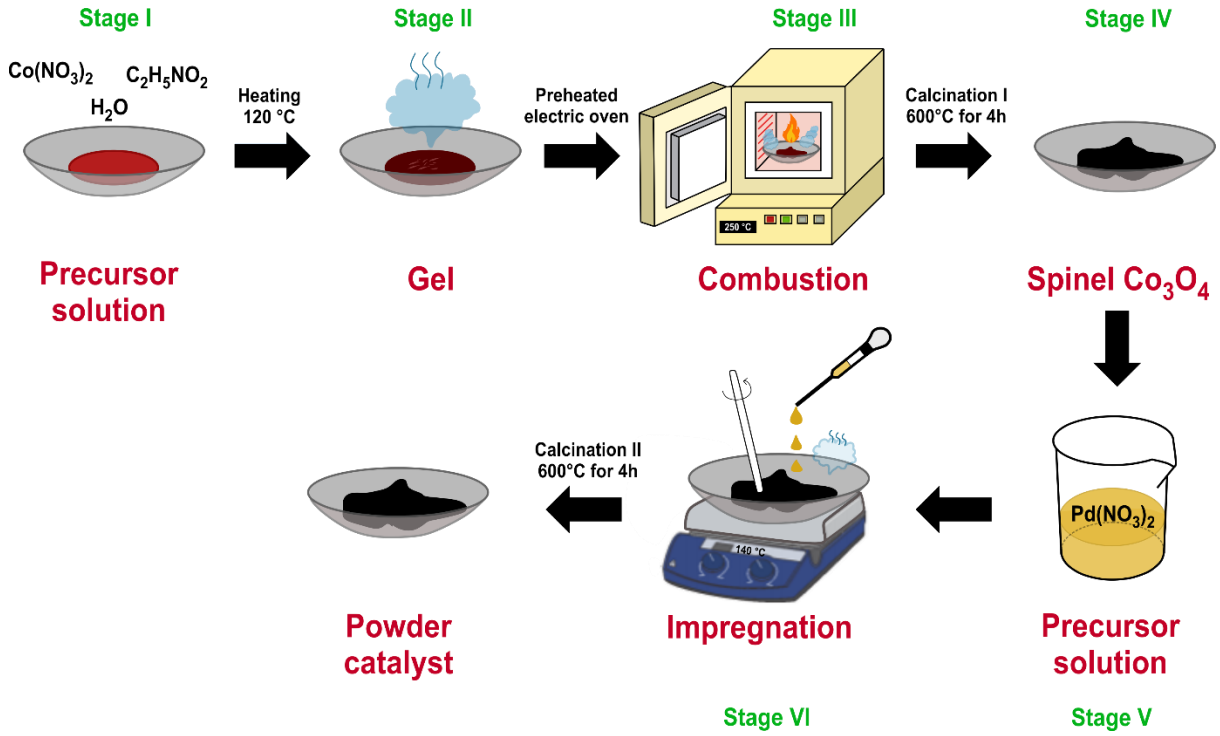


**Figure 16.** Scheme of solution combustion synthesis procedure for powder catalyst.

### 1.6.2 OCF catalyst

Ceramic OCFs made of zirconia (Zir), alumina (Alu) and silicon carbide (SiC) with pore densities of 30 and 45 ppi were used as catalytic support. Prior to use, all structures were cleaned to remove any type of contamination present on the surface, such as grease, dirt, dust, stains, fingerprints, etc., and thus ensure a surface clean of impurities before catalyst deposition. For this purpose, the foams were washed in a solution of water/acetone (50/50 vol. %) for at least 30 min using an ultrasonic bath at room temperature and dried at 140 °C for 30 - 60 min. After cleaning the structures, a thin layer of $Co_3O_4$ catalyst was deposited on the foams by the SCS method. First of all, a solution 3 M of cobalt nitrate and glycine was prepared with a cobalt nitrate/glycine stoichiometric ratio equal to 0.25. Subsequently, the coating procedure was carried out as follows: i) immersion of each OCF in the prepared solution for at least 3 min, ii) removal of the excess of solution with a flow of compressed air and iii) combustion reaction in an furnace at 250 °C for 15 min. The coating process was repeated several times until the desired amount of $Co_3O_4$ spinel was reached. Finally, the coated OCFs were calcined at 600 °C for 4 hours in static air. Then, 3 wt. % PdO was deposited on the $Co_3O_4$-coated OCF by WI using an aqueous solution of palladium nitrate. After each immersion, the wet OCF were dried at 140 °C for 1 h. The coating procedure was repeated until the desired amount of active metal was reached. Finally, the foams were calcined at 600°C for 4 hours. A diagram of the different steps for the preparation of structured catalysts using SCS and WI is shown in **Figure 17**.

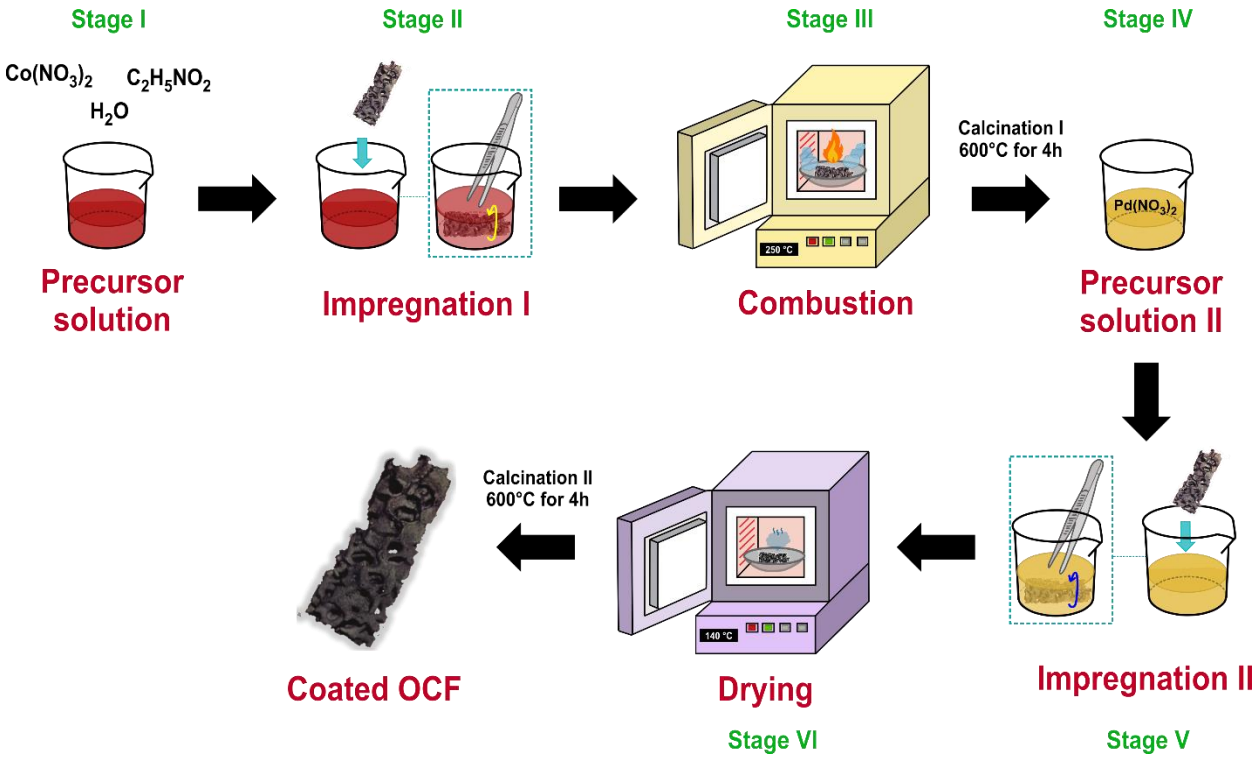


**Figure 17.** Scheme of solution combustion synthesis procedure for structured catalyst.

### 1.6.3 Catalytic test

A series of catalytic tests were performed to evaluate the activity of OCFs coated with 3 wt. % $PdO/Co_3O_4$ catalyst toward $CH_4$ combustion in lean conditions. A lab-scale fixed bed reactor consisting of a straight quartz tube, 10 mm ID, placed into a PID-regulated electrical oven was used to this purpose (as shown in **Figure 18**). Each OCF, was wrapped in a thin vermiculite foil to avoid channeling and heat dispersion phenomena. Then, the structure was placed at the center of the reactor and the oven was heated up to 700 °C flowing 0.1 NL $min^{-1}$ of $N_2$ with a heating rate of 10 °C $min^{-1}$. Once the set temperature has been reached, the reactive $CH_4/O_2/N_2$ gas mixture was fed. Different runs were

performed at inlet $CH_4$ concentrations of 0.5 or 1 vol. %, 4.0 or 8.0 vol. % of $O_2$ in $N_2$, keeping constant the $O_2/CH_4$ molar ratio to 8 to assure lean conditions. When steady state conditions were reached, the reactor was cooled to room temperature (5 °C $min^{-1}$), while the outlet dry gas concentrations were monitored as a function of temperature (measured by K-type thermocouple located a few mm inside the inlet side of each foam configuration) using an ABB analyzer equipped with a Uras 14 NDIR module for $CO/CO_2/CH_4$ and a Magnos 106 paramagnetic module for $O_2$. The water vapor generated by the reaction was removed before entering the analyzer in a condenser set at 3 °C. The reagent flow rate was varied to allow the catalytic tests to be carried out at weight hourly space velocity (WHSV) of 30, 60 and 90 NL $h^{-1}$ $g_{cat}^{-1}$. All catalytic runs were repeated at least three times to ensure reproducibility of the results. Sigma-shaped curves were obtained by plotting the $CH_4$ conversion versus temperature. Generally, three parameters have been taken into account for data comparison: $T_{10}$, $T_{50}$, and $T_{90}$, the conversion temperatures of 10%, 50% and 90% of CH4, respectively.

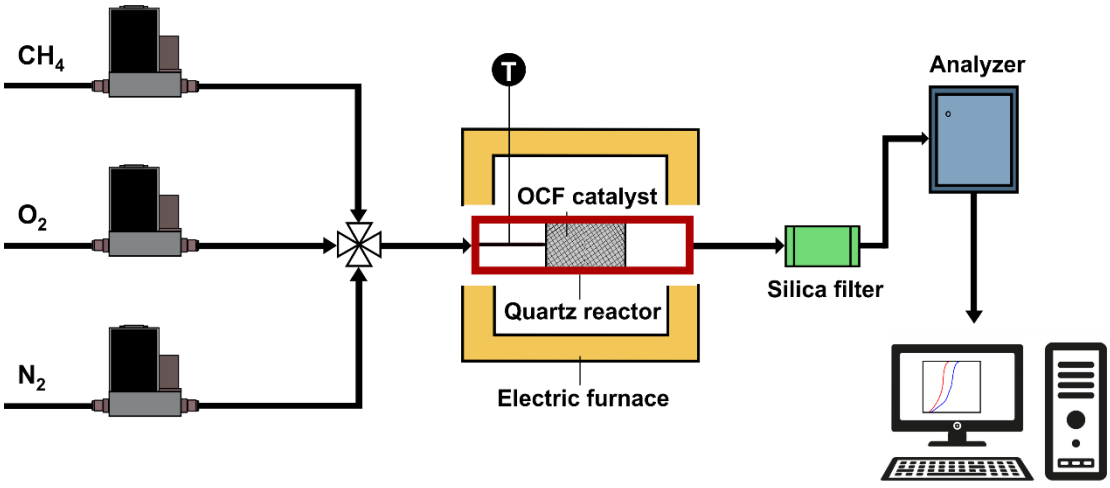


**Figure 18.** Schematic diagram of lab-scale plant for $CH_4$ oxidation.

## 1.6.4 Characterization techniques

### 1.6.4.1 Physisorption of nitrogen ($N_2$)

$N_2$ physisorption is a mature and widely used technique to measure the specific surface area, pore volume and pore size distribution of materials. The principle is based on the physical adsorption of gas molecules on a solid surface. When nitrogen gas comes in contact with a solid at 77 K (boiling point of $N_2$), a specific number of gas molecules will be attracted to the surface of the solid by Van der Waals forces [200–202].The number of physisorbed molecules depends on the nitrogen-relative pressure ($P/P_0$), that is, the ratio between the partial pressure of nitrogen $P$ and the saturated vapor pressure $P_0$ (pressure at which the unconfined gas condenses; $P_0$=1 atm at 77K). Thus, for a given $P/P_0$, the amount of gas molecules on a specific part of the solid surface depends on the local surface energetic properties and the surface geometry. In porous systems, physisorption measurements are typically interpreted assuming homogeneous surfaces, where the amount adsorbed at a certain relative pressure is determined by the pore size/geometry [200,201]. For a $P/P_0$ range between 0.05-0.35, the multilayer adsorption system theory proposed by Brunauer–Emmett–Teller (BET) is commonly applied, which allows to determine the specific surface area of materials [203].

$N_2$ physisorption was performed at -196 °C (77 K) using an Autosorb-1 Quantachrome apparatus (**Paper I**) and a Micromeritics ASAP 2020 instrument (**Paper III**, **Paper IV**, **Paper V** and Paper **VII**). The surface area of the samples was calculated according to the BET method in the range of $P/P_0$ between 0.05 and 0.30. The total pore volume and pore size distribution was obtained by Barrett-Joyner-Halenda (BJH) model using the

desorption isotherm. Powder sample measurements were carried out in conventional physisorption sample holders, whereas a special sample holder was used for structured substrates. Before analysis, the samples were vacuum outgassed as follows:

- In **Paper I**, at 100 °C for 18 h.
- In **Paper III**, at 300 °C for 6 h.
- In **Paper IV**, **Paper V** and **Paper VII**, at 150°C for 12 h.

### 1.6.4.2 Chemisorption analysis

Chemisorption is the adsorption process involving a chemical bond between adsorbed molecules and specific locations on the solid surface of a material, known as active sites. Since the chemisorbed molecules are linked to reactive parts of the surface, the process ceases when all the active sites on the solid surface are occupied, thus adsorption is necessarily confined to a monolayer [204,205]. This interaction is much stronger than physical adsorption, because the chemisorbed species will be irreversibly bound to the surface, that is, they will not be readily desorbed under ambient temperature conditions. This technique provides quantitative information on the physical and chemical properties of the active metal phase that are fundamental to correlate the properties of the catalyst with its catalytic performance, such as metal surface area, metal dispersion and metal crystallite size. The gas employed as adsorbate, typically $H_2$ or CO, must rapidly form the monolayer and the metal-adsorbate interaction stoichiometry must be considered [205].

CO pulse chemisorption measurements were performed in an ASAP 2020 instrument for the $Ru/Al_2O_3$ catalyst (**Paper II**) and an AutoChemII 2920 station for the $PdO/Co_3O_4$ catalyst (*Section 2.5*), both devices from Micromeritics. Prior to the measurement, all the samples were evacuated at 120 °C for 2 h. Then, the samples were treated as follows:

- For the $Ru/Al_2O_3$ catalyst, the sample was treated in a pure $H_2$ flow (20 $Ncm^3$ $min^{-1}$) at 350 °C for 2h, fed with a He flow ( 20 $Ncm^3$ $min^{-1}$ ) at 370 °C for 1.5 h, and finally cooled down to room temperature for chemisorption. The CO pulse chemisorption analysis was performed by dosing a 10% CO/He gas mixture at room temperature (with pulses of 500 NμL). The amount of adsorbed gas was determined as the difference between the total injected volume and the residual escaped one, assuming that each Ru atom adsorbs one molecule of CO (stoichiometric factor equal to one).
- For the $Pd/Co_3O_4$ catalyst, the sample was treated in a pure $H_2$ flow a 150 °C for 1.25 h, evacuated at 150 °C for 1.5 h, and finally cooled down at 35 °C for analysis. To measure the Pd dispersion by the chemisorbed CO, a 1:1 stoichiometry between CO and Pd was assumed.

### 1.6.4.3 X-ray diffraction

X-ray diffraction (XRD) is a powerful non-destructive technique for characterizing the crystalline properties of solids. This technique provides information on both crystalline phases and preferred crystal orientations, as well as estimates of average grain size, crystallinity, strain and crystal defects. The principle is based on the diffraction of a

monochromatic X-ray beam scattered at specific angles from each set of lattice planes in a crystalline sample [206–208]. This phenomenon is described by the Bragg law, which predicts the direction of X-ray beams in the constructive interferences of a crystalline sample, leading to a strict connection between the wavelength of the incident X-rays, the angle of incidence and the distance between the crystal lattice planes of atoms (interatomic distance) according to the following equation [209]:

$$n \cdot \lambda = 2 \cdot d \cdot sin\,\theta \tag{69}$$

where $\lambda$ is the wavelength of the X-ray beam, $d$ is the spacing of the crystal layers (path difference), $\theta$ is the angle between incident beam and the scatter plane. The constructive interference occurs when $n$ is an integer.

The Scherrer equation (**Equation 70**) is widely used to estimate the crystal size. According to this equation, the crystal size is inversely related to broadening of the reflection [207]:

$$\mathcal{D} = \frac{\mathcal{K} \cdot \lambda}{\beta \cdot \cos\theta} \tag{70}$$

where $\mathcal{D}$ is the mean size of the crystal, $\mathcal{K}$ is the dimensionless shape factor which is normally assumed to be 0.9 for spherical particles, $\beta$ is the line broadening at half maximum intensity (FWHM) and $\theta$ is the Bragg angle.

X-ray diffraction patterns were collected using a Philips X-Pert diffractometer (**Paper II** and **Paper III**) and a Bruker D8-advance X-Ray diffractometer (**Paper I** and *Section 2.5*), equipped with a copper Kα radiation source ($\lambda$ = 0.15406 nm) and operated at 40 kV. Measurement specifications are described as follows:

- In *Chapter I* (**Paper I**), the data collection was carried out in the 2θ range of 10 and 90° with the step of 0.2° $s^{-1}$ and a current of 20 mA.
- In *Chapter II* (**Paper II**), the powder samples were scanned in the 2θ range of 20-70° at a rate of 0.02 ° $s^{-1}$ and a current of 30 mA.
- In *Chapter III* (**Paper III**), the XRD patterns were recorded over the 2θ range of 20-75° with a scanning speed of 1.50° $min^{-1}$ and a current of 20 mA.
- In the *Section 2.5*, all samples were scanned in the 2θ range of 5-85° and 30-50°, with a step size of 0.05° and 0.02°, respectively; and a step time of 5s. The current was set at 30 mA.

The peaks were assigned according to the PCPFWIN database. The crystallite size was calculated by the Scherrer equation using the most intense observed reflection for crystallographic structures.

### 1.6.4.4 Scanning electron microscopy

The scanning electron microscopy (SEM) technique has become one of the most powerful and versatile tools for the characterization of materials, providing information on the external morphology, chemical composition, crystalline structure and orientations of the materials that compose a solid surface. This technique uses a focused beam of electrons to scan the surface of a sample and create a high-resolution image. It is based on the principle of applying kinetic energy to generate a variety of signals on the interaction of the electrons [210,211]. These electrons are secondary electrons, backscattered electrons and diffracted backscattered electrons that are used to visualize crystallized elements and photons. The

secondary electrons emitted by the sample are responsible for detecting the morphology and topography of the sample, while the backscattered electrons show the contrast in the composition of the elements in the sample [210,211]

The surface morphologies of powder and structured catalysts were analyzed using the following instruments: a FESEM JEOL-JSM-6700F apparatus (**Paper II**, **Paper IV**, **Paper V**), a FESEM FEI Versa 3D equipment (**Paper I**), a Philips XL-30 FEG ESEM device (**Paper III**) and a FESEM HITACHI S-4800 scanning microscope (*Section 2.5*). All instruments were equipped with an energy dispersive spectrometer (EDAX system) with an accelerating voltage of 8-20 kV, which allowed the elemental composition analysis of the samples.

### 1.6.4.5 Transmission electron microscopy

Transmission electron microscopy (TEM) is a microscopy technique capable of obtaining images with a much higher resolution than optical microscopes, since the wavelength of electrons is much smaller than that of light. Thus, TEMs can reveal valuable information on the inner structure of the sample, such as crystal structure, morphology and stress state information. The technique is based on the transmission of a beam of electrons through a very thin sample, in which the interactions between electrons and atoms allow the formation of an image [212,213]. Since the electrons must penetrate through the material, the TEM uses much higher electron energies compared to SEM (typically 80-300 keV). Due to the requirement for transmitted electrons, the TEM specimens must be sufficiently thin (generally below 100 nm) [212,213].

The measurements were performed using a Philips CM12 instrument (**Paper III**) and a Talos F200X FEG S/TEM microscopy (**Paper IV**) operated at 80-200kV. The specimens for TEM analysis were dispersed in isopropyl alcohol/ethanol by ultrasonic treatment and placed on a copper grid with holey carbon film. The samples were then covered and allowed to dry overnight at room temperature before analysis.

### 1.6.4.6 Raman spectroscopy

Raman spectroscopy is a powerful analytical method for determining vibrational, rotational and other low-frequency modes in a system. The technique is based on the inelastic scattering of photons through their interaction with vibrating molecules, known as Raman scattering. The sample is illuminated with a monochromatic light source, usually from a laser in the visible, near infrared or near ultraviolet range, although X-rays can also be used [214–216]. The laser light interacts with the molecules of sample and originates a scattered light, resulting in an energy change which provides information about the vibrational modes of the system [214,215,217]. The Raman spectra result from the inelastic collision between the incident monochromatic radiation and the molecules of the sample. Thus, this technique allows probing the chemical structure of a material providing information about the structural fingerprint, phase and polymorphism, crystallinity, molecular interactions, intrinsic stress and deformation, contamination and impurities of the sample [214].

Raman analysis was carried out using a Renishaw InVia spectrometer (**Paper I**) and a Renishaw's Micro-Raman spectroscopy (**Paper IV**) equipped with a CCD detector and a

wavelength excitation of 785nm and 514 nm, respectively. The Raman scattered light was recorded at room temperature in the spectral range of 100–1000 $cm^{-1}$. The signal-to-noise ratio was optimized by accumulating 12 scans for each measurement.

### 1.6.4.7 Energy dispersive X-ray spectroscopy

Energy dispersive X-ray spectroscopy (EDX) is an analytical method used for chemical characterization and elemental analysis of a sample. X-ray emission is stimulated by irradiating the surface with a beam of high-energy charged particles (electrons or protons) or a focused X-ray beam. Excitation of the electronic structure of an atom can produce X-ray emission, whose energy signature allows for a unique set of peaks in its electromagnetic emission spectrum, creating the elemental map of a sample [218–220]. EDX are usually coupled to an electron microscopy instrument, which is equipped with the required technology to generate a beam of high-energy charged particles.

EDX analysis was carried out using a STEM Talos F200X FEG S/TEM (200kV) microscopy coupled with energy dispersive X-ray spectroscopy (EDXS) mapping (**Paper IV**) and a Philips CM12 instrument (**Paper III**). The analysis procedure has been described above for the TEM technique (*Section 1.6.4.5*).

### 1.6.4.8 Thermogravimetric analysis (TGA)

Thermogravimetric analysis (TGA) is a thermal analysis technique dedicated to recording the mass variations of a sample as a function of temperature (with constant heating rate) or time (with constant temperature or mass loss) as the sample specimen is subjected to a controlled temperature program in a controlled atmosphere. Therefore, this technique is often used by researchers as a means of predicting the stability, durability and strength of a material, having a wide impact on industry, technology and construction.

Water adsorption capacity was measured with a thermogravimetric analysis (TGA) method on a Mettler Toledo TGA/DSC1. The experiments were carried out under an Ar atmosphere (flow rate 50 ml $min^{-1}$) at the constant temperatures of 30° and 350 °C. Sample weights were similar in each case, approximately 25 mg. The experiment was designed to test the adsorption of water in $H_2O$ flow at or near equilibrium conditions, since water is a reaction product of methane combustion. Saturation of the Ar gas with water was performed by bubbling gas through the gas wash bottle containing water, resulting in ~ 1 vol.% $H_2O$/Ar. The samples were equilibrated in the gas flow, and then the water saturated Ar was introduced to the sample at the same gas flow rate. When the stable signal was reached, the dry Ar flow was restored. To evaluate the buoyancy effect, an empty crucible was tested with the same experimental procedure.

### 1.6.4.9 Temperature-programmed reduction

Temperature programmed reduction (TPR) is a powerful analytical technique that examines the surface chemistry of metal oxides under varying thermal conditions,

providing quantitative information on the reducibility of the oxide surface as well as the heterogeneity of the reducible surface. The principle is based on submitting an oxidized catalyst precursor to a programmed temperature rise while a reducing gas mixture (typically 3 to 17% hydrogen diluted in argon or nitrogen) flows over it [221–223]. A thermal conductivity detector (TCD) is used to measure changes in the thermal conductivity of the gas stream. The signal is then converted into gas concentration using a level curve. Finally, the signal is recorded by a computer, plotted as a function of time (or temperature) and the area under the curve is integrated to obtain the total gas consumed.

$H_2$-TPR measurements were carried out in a Micrometrics Autochem II 2920 apparatus equipped with a TCD detector (*Section 2.5*). Typically, about 160 mg of sample was placed in a U-shaped quartz tube on a bed of quartz wool, and a thermocouple was positioned at about 5 mm from the catalyst bed in order to control the temperature of the analysis. The sample was treated with a reducing mixture (50 $cm^3$ $min^{-1}$) composed of 10% $H_2$/Ar from 0° to 900 °C. An ice/salt bath (-18 °C approx.) downstream of the reactor was used to trap the water produced during the reduction. After calibration, $H_2$ consumption profiles were recorded by monitoring the TCD signal.

### 1.6.4.10 Laser diffraction

Laser diffraction is a technology that measures the size distribution of particles by measuring the angular variation of the scattered light intensity as a laser beam is passed through a dispersed particulate sample [224,225]. Thus, the larger the particle, the smaller the angle and the greater the intensity of the scattering. The detectors (placed at fixed angles)

are responsible for measuring the intensity of the scattered light at different positions where subsequently using a mathematical model it is possible to generate the particle size distribution.

The measurements (*Section 2.5*) were carried out in a Martersizer 2000 (Malvern). Approximately 100 mg of the powdered sample was dispersed in 20 mL of distilled water. The suspension was sonicated for 2 hours at room temperature and then the pH was adjusted to the desired value. Finally, the sample was measured by adding dropwise the required amount of solution to the instrument. The particle size was defined by assuming that all the particles are spherical where $d_{(4,3)}$ is the volume weighted mean.

### 1.6.4.11 Zeta potential

Zeta potential is a key parameter for characterizing the surface functionality or stability of dispersed particles, since it allows to understand the behavior of solid materials in slurry and colloidal systems. This technique reflects the ability of particles to repel each other electrostatically. The principle is based on the double layer theory, where the surface of a charged particle attracts a thin layer of opposite charge and tightly binds to it, forming a thin liquid layer called the Stern layer [226,227]. Once the particle diffuses into the solution, it will be enveloped by a diffuse outer layer consisting of loosely associated ions, as a result an electric double layer is created. The potential at the boundary of the Stern layer and the diffuse layer is known as the zeta potential [227]. This is measured by the electrophoretic mobility, that is, the ratio between the velocity of the charged particles and the external

applied electric field. Large positive or negative values of zeta potential lead to stable slurries in which particles repeal each other. Nevertheless, if the particles present a zeta potential value very small or even zero (isoelectric point), aggregation and flocculation of the particles could occur due to the Van der Waals forces of attraction acting on them [226,227].

The zeta-potential was measured using a Zetasizer Nano ZS (Malvern Instrument) apparatus (*Section 2.5*). The samples were prepared by dispersing 20 mg of solid ($Co_3O_4$) in 50 mL of a NaCl solution (0.001M) and they were sonicated for 1 h at room temperature to obtain highly dispersed solutions. Then, six solutions were prepared by adjusting the pH values to 2, 4, 6, 8, 10, and 12 with $HNO_3$ or $NH_4OH$. Finally, the solutions were stirred overnight to ensure a stable pH before performing the measurement.

#### 1.6.4.12 Viscosity

Viscosity is a fundamental characteristic of fluids that describes the resistance of a material to flow. It can also be defined as drag force which provides information on the frictional properties of the fluid. According to their viscous behavior, fluids can be classified as Newtonian and non-Newtonian. In Newtonian fluids, the ratio of shear stress to shear rate is constant, thus the viscosity will be independent of the shear rate [166,170]. However, for non-Newtonian fluids, the viscosity of the fluid will be dependent on temperature, shear rate and time. Slurries are characteristic fluids of non-Newtonian viscous behavior, hence viscosity is a crucial factor during the preparation of structured catalysts using the washcoating method [166,228]. A slurry with high viscosity has poor fluidity and can cause heterogeneity of the washcoat loaded on the surface of the structure, as well as a clogging

of channels (monolith) or pores (OCF) of the support. On the other hand, a slurry with low viscosity also results in a low washcoat loading which may not be sufficient to cover the entire structure.

Slurry viscosity (*Section 2.5*) was measured at 25 °C using an AR 1500ex rheometer from TA Instruments with a rotor HA AL Recessed (diameter of 28 mm, length of 42 mm). Measurements were performed using approximately 8 mL of the sample which was subjected to an increasing shear rate between 3 and 3715 $s^{-1}$.

### 1.6.4.13 Adhesion measurements

One of the essential properties that the coating catalyst layer must possess is the ability to remain on the structured surface during reaction and handling. The adhesion of the catalyst layer on the substrate is measured by the weight loss of the coated structure after exposure to sonication.

The adhesion properties of the prepared structured catalysts were performed using a USC 900D ultrasonic bath (**Paper III**) and a S3M 2200 device by Sonica (**Paper I**, **Paper IV**, **Paper V**) operated at 40-45 kHz and 130 W for 1-2 h. The coated structures were immersed in a solution of 50/50 water/isopropyl alcohol and sonicated at operating conditions. The structured catalysts were weighed before and after sonication treatment (after 30 min drying in a static oven at 120 °C), to evaluate the weight loss after sonication.

### 1.6.4.14 Stability measurements

In heterogeneous catalysis, not only the activity of the catalyst plays a fundamental role in the evaluation for a possible application, but also the stability of the catalyst throughout its lifetime. Typically, the deactivation of heterogeneous catalysts is caused by poisoning of the active sites or damage to the catalytic structure [24,229–234]. Overcoming such limitations remains a challenge for the synthesis of efficient heterogeneous catalysts. Generally, the evaluation of the stability of catalysts is performed by evaluating the performance as a function of operating time. The procedure used to carry out the catalyst stability measurements are described below.

- In *Chapter II* (**Paper II**), the stability test was performed for the best-selected catalyst over 70 h of time on stream (TOS) at 800 °C. The reactor was fed with the reactant gas mixture at WHSV of 750 NL $h^{-1}$ $g_{cat}^{-1}$. After 30 h of TOS, the WHSV was increased to 1500 NL $h^{-1}$ $g_{cat}^{-1}$ for 20 h. Finally, at 50 h of TOS, the WHSV was reported back to the initial value (750 NL $h^{-1}$ $g_{cat}^{-1}$) until the end of the experiment.
- In *Chapter III* (**Paper III**), the catalyst stability was evaluated over 200 h of TOS at 900 °C and WHSV of 70 NL $h^{-1}$ $g_{cat}^{-1}$ with consecutive start-up and shut-down cycles as accelerated stress test.
- In *Chapter IV* (**Paper IV**), the stability measurements were performed on the best-selected OCF catalyst over approximately 250 h of TOS at 400 °C. The test was carried out by feeding the reactor with the reactive mixture containing 0.5

vol. % of inlet $CH_4$ concentration ($O_2/CH_4$ molar ratio equal to 8) and WHSV of 30 NL $h^{-1}$ $g_{cat}^{-1}$.

#### 1.6.4.15 Pressure drop measurements

One of the most important parameters for the design of catalytic processes is the pressure drop of the fluid along the reactor length. Since mass and heat transfer are strongly related to pressure losses, the catalyst shape for a determined process is chosen in such a way that by combining the desired mass and heat transport, the pressure losses are as low as possible [133,235–237].

The pressure drop across the OCF catalysts (placed inside a straight quartz tube reactor) was measured using a U-tube manometer connected directly to the reactor. (**Paper III**). At room temperature, the reactor was fed with a flow of $N_2$ at different velocities using a mass flow-meter (Brooks Instrument). The difference of level of fluid in the U-tube manometer was converted according to the Stevin's law equation into pressure drop values as [238]:

$$\Delta z = \frac{\Delta P}{g \cdot \rho_{H_2O}} \quad (71)$$

where $\Delta z$ is the height difference between the two columns of water in the two branches of the U-tube manometer, $g$ is the gravitational acceleration, $\rho_{H_2O}$ is the density of water and $\Delta P$ is the pressure drop across the reactor. The measurements were repeated for the bare structures and the coated ones.

#### 1.6.4.16 X-ray Computed Tomography

X-ray computed tomography is a non-destructive imaging technique that allows to inspect and visualize the internal characteristics and composition of a solid material, as it has the capability to recreate the internal structure in 3D providing a detailed analysis of the structural properties of the object [239]. The technique is based on the principle of radiation released from a source into a material, in which a series of 2D radiographs are taken at different angles as the material rotates around an axis through 360° revolution [240–243]. An array of detectors are responsible for measuring the attenuation of the X-rays entering the sample, allowing the projection of the 2D images. The CT scans are then used to reconstruct the 3D image of the material.

The X-CT measurements of the OCF were performed using a Xradia MicroXCT 400 scanner (**Paper V**) and an EasyTom RX Solutions system (**Paper VI**) as follows:

- In *Chapter V* (**Paper V**), high resolution scans of the Zir-OCF (30 ppi) were obtained using an objective lens of 1X with voxel size of 22 μm. The X-ray power was set at 80 kV and 8 watts, while images were collected by rotating the sample 360° with an angular rotation interval of 0.3 degrees and exposure time of 4 s.
- In *Chapter VI* (**Paper VI**), ceramic OCFs made of zirconia, silicon carbide and alumina with pore densities of 30 and 45 ppi were analyzed using two X-ray generators: (i) a 150 kV microfocus X-ray tube, with X-ray power set at 80 kV, current of 142 μA with a pixel size of 22 μm and a 160 kV microfocus X-ray

tube, where the X-ray source was operated at 70/100 kV, current of 200/50 μA with a pixel size of 5 μm. The sample was rotated 360° to transmit X-rays from all possible directions with an angular rotation interval of 0.25 degrees and an exposure time of 2 s

# 2. Main results

In this section the main results and conclusions obtained in the dissertation are described. Therefore, it has a short, collective and comparative character of the principal outcomes achieved.

## 2.1 Ceramic OCFs as catalytic support

The catalytic performance for $CH_4$ oxidation in lean conditions was carried out on coated ceramic open cell foams made of alumina, zirconia and silicon carbide. All ceramic OCFs were covered with 3 wt. % $PdO/Co_3O_4$ as catalyst using SCS and WI techniques. The catalytic tests were carried out at different space velocities (WHSV of 30, 60, 90 NL $h^{-1}$ $g_{cat}^{-1}$) and inlet $CH_4$ concentrations (0.5 and 1 vol. %). In order to guarantee lean operating conditions, the $O_2/CH_4$ molar ratio was maintained at a value of 8. For all catalytic tests the only products formed during methane combustion were $CO_2$ and $H_2O$. The latter was removed prior to entering the analyzer in a condenser set at 3 °C. None of the catalytic tests performed detected carbon monoxide in the reactor effluent gas. The effect of the foam material, the catalyst content and the combination of foams of different material were analyzed considering the catalytic performance toward methane oxidation.

On the other hand, the effect of OCF pore density on catalytic performance was investigated for steam reforming and oxidative steam reforming processes of biogas for syngas production. For this purpose, alumina OCFs with pore densities of 20, 30 and 40 ppi were investigated as potential catalytic supports. A thin layer of $Rh/CeO_2$ catalyst was deposited on each structure by combining techniques of: (i) solution combustion synthesis

(SCS) to deposit in situ the $CeO_2$ support and (ii) wet impregnation (WI) of the Rh active phase. The catalytic performance of the coated foams was evaluated at atmospheric pressure by varying the temperature (800-900 °C) and space velocity (35-140 $NL \cdot g^{-1} \cdot h^{-1}$).

### 2.1.1 Effect of OCF material

Here (**Paper IV***)*, the performance of 3 wt. % $PdO/Co_3O_4$ catalyst supported on three different ceramic materials made of silicon carbide (SiC), alumina (Alu) and zirconia (Zir) with pore densities of 30 ppi was studied. The catalytic tests were carried out at the following flow conditions: WHSV of 30 NL $h^{-1}$ $g_{cat}^{-1}$, temperature range of 100-700 °C, atmospheric pressure and inlet $CH_4$ concentration of 0.5 and 1 vol. %. **Figure 19** shows the light-off curves for $CH_4$ oxidation in lean conditions.

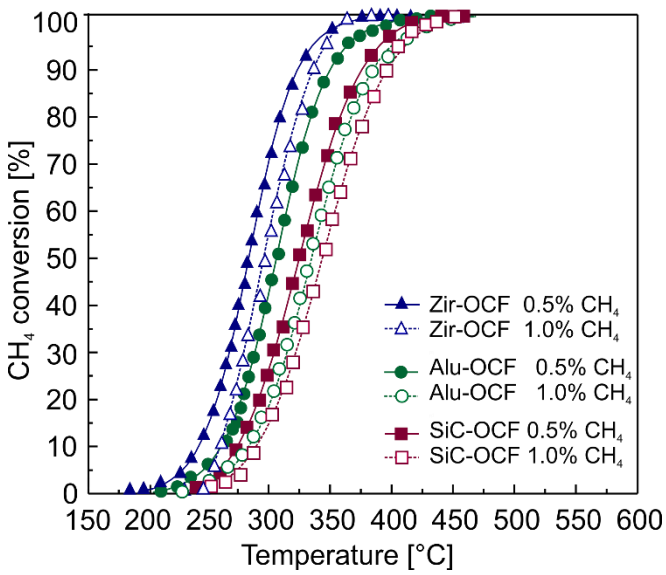


**Figure 19.** $CH_4$ conversion versus temperature of the three OCFs coated with 3 wt. % PdO on 200 mg $Co_3O_4$, tested at 30 NL $h^{-1}$ $g_{cat}^{-1}$ with two different $CH_4$ inlet concentrations (**Paper IV**).

Overall, all three coated OCFs achieved complete $CH_4$ conversion at temperatures below 460 °C, for both inlet $CH_4$ concentrations studied. In particular, Zir-OCF showed the best catalytic performance compared to Alu-OCF and SiC-OCF, reaching full conversion at temperatures lower than 380 °C. The light-off temperatures ($T_{10}$, temperature at which the catalyst reached 10% of $CH_4$ conversion) were very similar for all OCFs, while the difference was more evident on light-on temperatures ($T_{90}$, temperature at which the catalyst reached 90% of $CH_4$ conversion), which range from a minimum of 323 °C for Zir-OCF (0.5% $CH_4$ inlet) to a maximum of 392 °C for SiC-OCF (1.0% $CH_4$ inlet). These results can be explained taking into account the different thermal conductivity values of the foams. In previous work [121], volumetric heat transfer coefficients were measured for each foam, where the values for the SiC-OCF were roughly 25 times higher than those obtained for the Zir-OCF. Hence, the Zir-OCF favors convective heat removal via the combustion gases. However, as reported in previous work [121], as the WHSV increased, the foams with higher thermal conductivity exhibited similar or even lower $T_{10}$ values (particularly for the SiC-OCF) than those obtained by the Zir OCF. This is because in these conditions (low temperatures and high WHSV), when the reaction is starting, the heat produced by combustion is still negligible due to the low methane conversion. In this case, a foam with higher thermal conductivity and higher volumetric heat transfer coefficient (as SiC-OCF) are useful to retain the heat of reaction and, consequently, provide the necessary energy to drive the ignition of the first reacting molecules on the OCF surface. Therefore, a low temperature and high WHSV, the SiC-OCF favors the kinetic aspects while depressing the $CH_4$ conversion at elevated temperatures due to thermodynamic hindrance of the reaction.

## 2.1.2 Effect of catalyst content

In this part of the research (**Paper V**), the effect of catalyst content on the catalytic activity toward $CH_4$ combustion was studied. For this purpose, Zir-OCF (with pore density of 30 ppi) was selected as catalyst support. Three different amounts of $Co_3O_4$ were studied: 100 ($C_{load}^{100}$), 150 ($C_{load}^{150}$) and 250 ($C_{load}^{250}$) mg corresponding 6.1, 8.2 and 13.7 $mg_{cat}$ $cm^{-2}_{OCF}$, respectively. The catalytic tests were carried out at the following flow conditions: WHSV of 30, 60 and 90 NL $h^{-1}$ $g_{cat}^{-1}$ (WHSV is referred to the amount of effective mass of catalyst, that is,$W_{cat} = W_{PdO} + W_{Co_3O_4}$), temperature range of 100-700 °C, atmospheric pressure and inlet $CH_4$ concentration of 0.5 and 1 vol. %. **Figure 20** shows the catalytic performance in lean methane combustion for the three $PdO/Co_3O_4$-coated Zir-OCF catalysts (with 3 wt. % of PdO on $Co_3O_4$ carrier) at different WHSV (30, 60, and 90 NL $h^{-1}$ $g_{cat}^{-1}$) and inlet $CH_4$ concentrations.

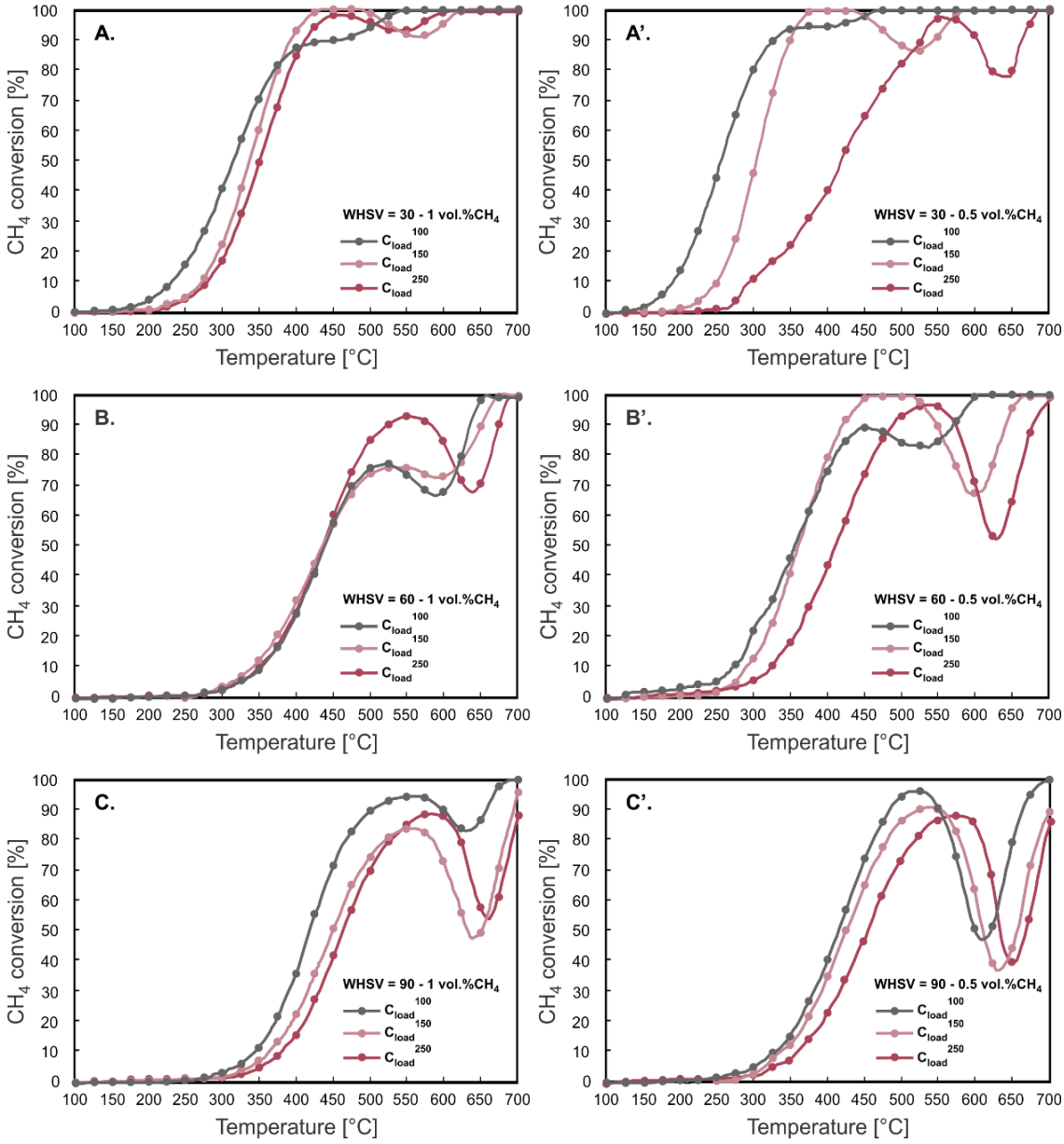


**Figure 20.** $CH_4$ conversion versus temperature by varying the $Co_3O_4$ load in the $PdO/Co_3O_4$ catalyst coated Zir-OCF at different WHSV and inlet CH4 concentration (**Paper V***)*.

As expected, an increase in WHSV leads to a worsening of the combustion process, with a shift of the $CH_4$ conversion curves toward higher temperatures, because of the reduction

of the contact time between the catalyst and the reactants. At the lowest WHSV (30 NL $h^{-1}$ $g_{cat}^{-1}$), full $CH_4$ conversion is achieved at temperatures between 380° and 630 °C depending on both the amount of catalyst and the inlet $CH_4$ concentration. On the other hand, when the reactor operates at the highest WHSV (90 NL $h^{-1}$ $g_{cat}^{-1}$), only the Zir-OCF with lower catalyst content ($C_{load}^{100}$, 6.1 $mg_{cat}$ $cm^{-2}_{OCF}$) achieved complete conversion of $CH_4$ at temperatures below 700 °C for both inlet $CH_4$ concentrations studied. A further interesting point to note from **Figure 20** is that as the catalyst content increases (keeping the flow conditions constant), the light-off curves tend to shift towards higher temperatures, which could suggest possible internal diffusional limitations.

When comparing the characteristic temperatures ($T_{10}$, $T_{50}$, and $T_{90}$) corresponding to 10, 50, and 90% of $CH_4$ conversion (see **Figure 21**), higher $T_{10}$ and $T_{50}$ were obtained as the amount of $Co_3O_4$ increased. Conversely, it was more difficult to establish a specific trend for $T_{90}$ values due to Pd-PdO transformation at high temperatures.

It is also worth mentioning that for all catalytic tests a decrease in $CH_4$ conversion is observed at medium/high temperatures. This decrease in catalytic activity has been observed in numerous studies on $CH_4$ oxidation over Pd-based catalysts, and has been attributed to the decomposition of PdO into Pd and the consequent reoxidation of Pd during the heating and cooling ramps, negatively affecting the catalytic reaction. Moreover, as the methane concentration and hence the oxygen concentration increases, the hysteresis of the curve is less pronounced. Several authors suggest that the increase in partial pressure of $O_2$ helps to stabilize the intermediate compounds identified as surface or interfacial $PdO_x$, which are the key species in the complete redox decomposition/re-oxidation reaction [229,244–248].

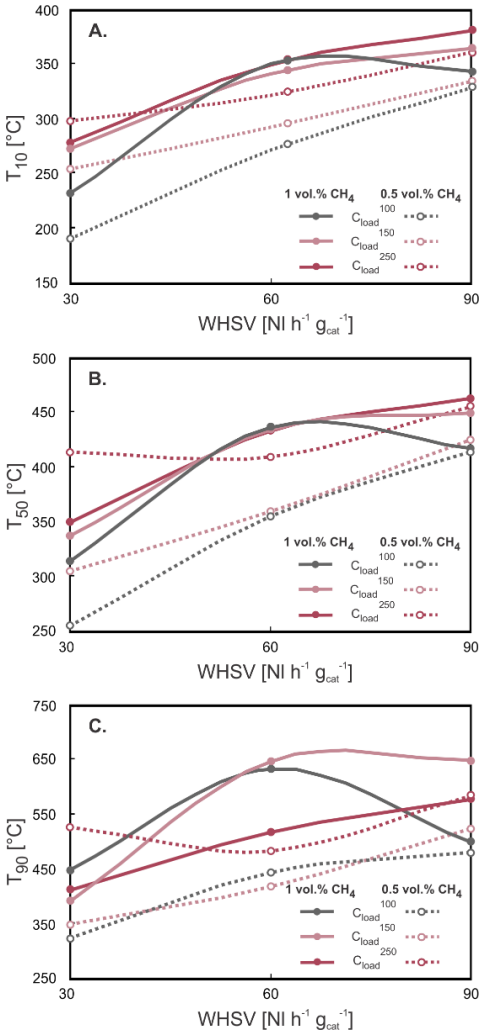


**Figure 21.** Characteristic temperatures $T_{10}$ (A), $T_{50}$ (B) and $T_{90}$ (C) corresponding to 10, 50 and 90% of $CH_4$ conversion by increasing WHSV for the three different catalyst loading (**Paper V**, Supporting information).

## 2.1.3 Effect of OCF combination

In this section of the research (**Paper VII**), on the basis of the results obtained in *Sections 2.1.1* and *2.1.2* (*Chapters IV*, *V*), the catalytic activity toward methane oxidation under lean

conditions was evaluated using three different combinations of coated foams made of SiC and Zir with pore densities of 30 ppi: SiC1Zir2; SiC1.5Zir1.5 and SiC2Zir1. The SiC-OCF was positioned inside the reactor at the inlet side of the reactive gases, followed by the Zir-OCF. The catalytic tests were carried out at the following flow conditions: WHSV of 30 and 90 NL $h^{-1}$ $g_{cat}^{-1}$, temperature range of 100-700 °C, atmospheric pressure and inlet $CH_4$ concentration of 0.5 and 1 vol. %. **Figure 22** shows the extinction curves of $CH_4$ combustion for all flow conditions (inlet $CH_4$ concentration of 0.5 and 1 vol.%; WHSV of 30 and 90 NL $h^{-1}$ $g_{cat}^{-1}$) and coated SiC/Zir OCF combinations (SiC1Zir2; SiC1.5Zir1.5 and SiC2Zir1) studied.

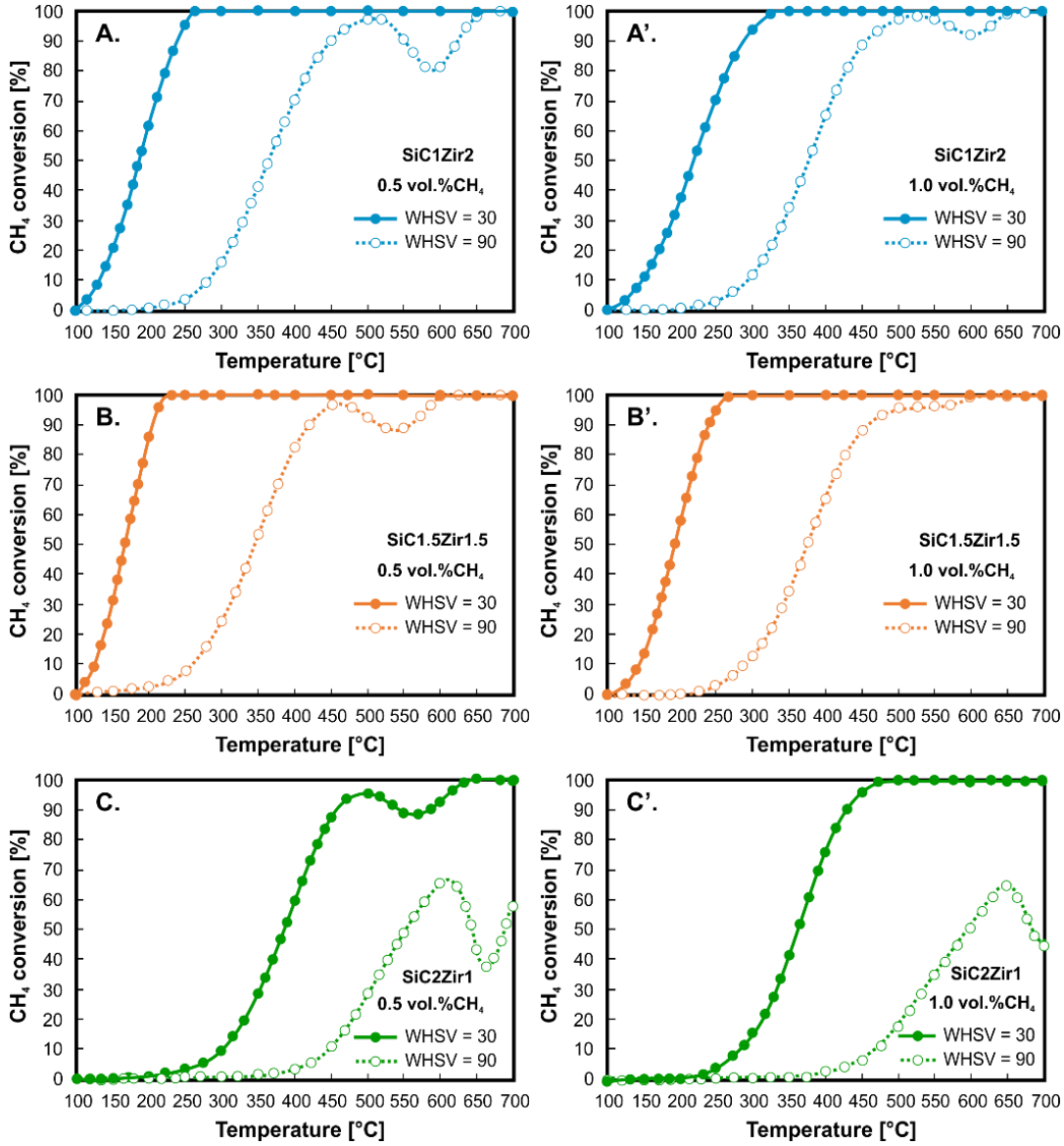


**Figure 22.** Extinction curves of $CH_4$ oxidation on 3 wt.% $PdO/Co_3O_4$ catalyst coated on SiC1Zir2 (A, A'), SiC1.5Zir1.5 (B, B') and SiC2Zir1 (C, C') OCF combinations at WHSV of 30 and 90 NL $h^{-1}$ $g_{cat}^{-1}$ and intel $CH_4$ concentration of 0.5 and 1 vol.% (**Paper VII**).

A shift of the extinction curves toward higher temperatures is obtained by increasing the WHSV, due to the reduction of the contact time between reactants and catalyst. At WHSV

of 30 NL $h^{-1}$ $g_{cat}^{-1}$, all OCF combinations achieved complete $CH_4$ conversion independently of the inlet concentration in the following order: SiC1.5Zir1.5 < SiC1Zir2 < SiC2Zir1. However, with increasing space velocity of 90 NL $h^{-1}$ $g_{cat}^{-1}$, only the SiC1Zir2 and SiC1.5Zir1.5 combinations reached full conversion at temperatures below 700 °C. Interestingly, when carrying out the catalytic $CH_4$ oxidation by combining the coated SiC/Zir OCFs at WHSV of 30 NL $h^{-1}$ $g_{cat}^{-1}$, the $CH_4$ conversion is unaffected by the Pd-PdO transformation at medium/high temperatures (no hysteresis is present, except for the SiC2Zir1 combination at inlet $CH_4$ concentration of 0.5 vol.% ). Nevertheless, at WHSV of 90 NL $h^{-1}$ $g_{cat}^{-1}$, the drop in catalytic activity becomes present in all the foam combinations. Attractively, the SiC1.5Zir1.5 combination showed less accentuated hysteresis compared to the other combinations, even with those reported in our previous work at the same flow conditions on the coated Zir-OCF [63]. In addition, it is possible to observe that by feeding the reactor with a higher concentration of $CH_4$ and hence, $O_2$, the hysteresis of the shut-down curve is less pronounced. This characteristic is in line with the results obtained in *Section 2.1.2* and in literature [229,244–248].

The characteristic temperatures $T_{10}$ and $T_{50}$ are shown in **Figure 23** for the three OCF combinations studied. As observed, $T_{10}$ is favored in the SiC1.5Zir1.5 and SiC1Zir2 combinations, while it is slowed down for the SiC2Zir1 configuration for all flow conditions. Regarding $T_{50}$, at higher space velocity (WHSV of 90 NL $h^{-1}$ $g_{cat}^{-1}$), the SiC1Zir2 and SiC1.5Zir1.5 combinations exhibited similar values with a $T_{50}$ difference below 15°C. However, at WHSV of 30 NL $h^{-1}$ $g_{cat}^{-1}$, the difference between the latter increased to around 30 °C. These results are in line with those obtained in *Section 2.1.1* (*Chapter IV*), since as mentioned above, the SiC foam favors reaction kinetics at low

temperatures and high space velocities. Thus, according to the catalytic test results, it is possible to deduce that combining equal lengths of the coated SiC and Zir OCF pieces, favors the catalytic performance of $CH_4$ oxidation, since it allows maintaining the reaction and the complete $CH_4$ conversion at lower temperatures.

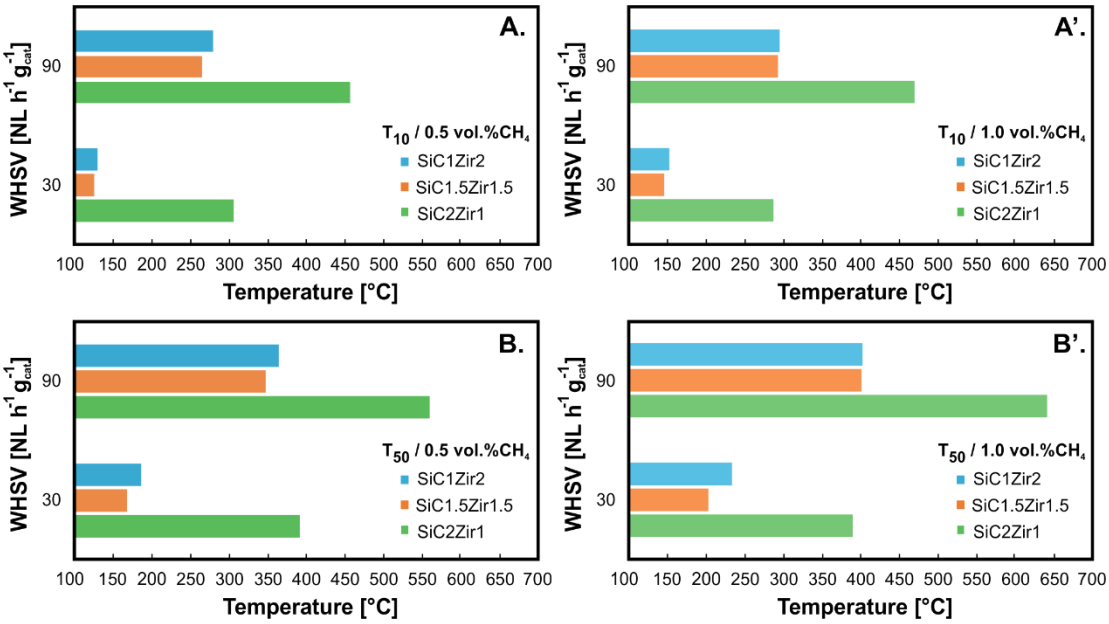


**Figure 23**. $T_{10}$ and $T_{50}$ of the three OCF combinations for all flow conditions studied (**Paper VII**).

## 2.1.4 Effect of OCF pore density

In this part of the research (**Paper III**), a series of biogas steam reforming (SR) and oxy-steam reforming (OSR) experiments were carried out on alumina ceramic OCFs with different pore density (20, 30 and 40 ppi). For this purpose, a thin layer of 1.5 wt. % $Rh/CeO_2$ catalyst was deposited on the structures using the SCS and WI techniques. The

catalytic tests were carried out at the following flow conditions: For SR, $S/CH_4$=3, temperature of 800° and 900 °C, atmospheric pressure and WHSV = 35-140 NL $h^{-1}$ $g_{cat}^{-1}$. For OSR, $S/CH_4$=1, $O_2/CH_4$=0.2, temperature of 800° and 900 °C, atmospheric pressure and WHSV = 35-140 NL $h^{-1}$ $g_{cat}^{-1}$. In **Figure 24** is shown the biogas SR and OSR activity ($S/CH_4$ = 3) over alumina OCF of different pore densities (F20, F30 and F40) in terms of $CH_4$ conversion and $H_2$/CO molar ratio.

As a general trend, in both catalytic tests, the OCF with lower pore density (F20) showed a decrease in $CH_4$ and $CO_2$ conversion with decreasing temperature and increasing WHSV. In particular, the $CH_4$ conversion of F20 decreased from 98% at 800 °C and 35 NL $h^{-1}$ $g_{cat}^{-1}$ to 92% at WHSV of 140 NL $h^{-1}$ $g_{cat}^{-1}$, due to the reduction of contact time between the reagents and the catalyst. On the other hand, for the coated OCFs with higher pore density (F30 and F40), the decline in catalytic activity with increasing WHSV was less pronounced, showing a stable $CH_4$ conversion of about 99 % and 99.6 % for SR and OSR, respectively. This improvement on the catalytic performance could be due to the fact that the higher the pore density, the smaller the pore size and the larger exposed surface area of OCFs. These features allow to improve the turbulence of the reactants in the gas phase and thus the mass transfer properties, as well as leading to longer residence times of the reactants. In both experiments, the order of activity towards SR and OSR is F20<F30≈F40.

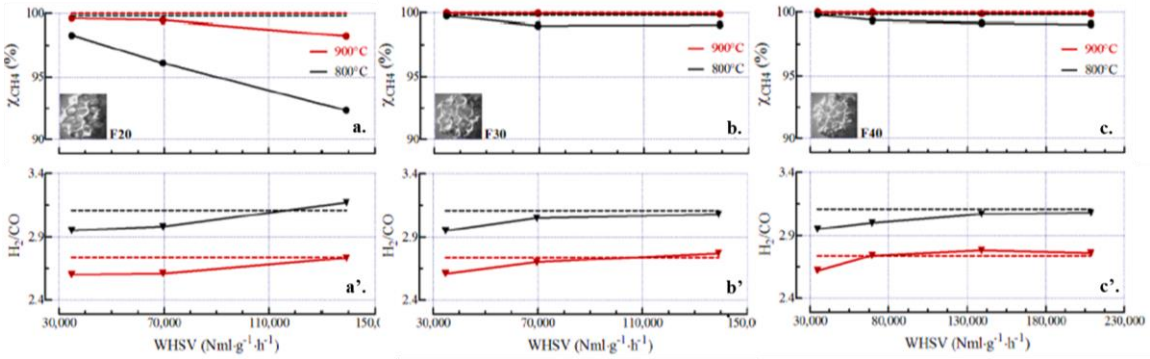


**Figure 24.** Biogas SR and OSR activity (S/$CH_4$ = 3) over F20 (a, a'), F30 (b, b') and F40 (c, c') catalysts. Influence of temperature ($T_{SET}$ = 800-900 °C) and space velocity (WHSV = 35-140 $NL \cdot g^{-1} \cdot h^{-1}$) on $CH_4$ and $CO_2$ conversion (**Paper III**).

## 2.1.5 Stability test on coated OCFs

In order to study the stability of $PdO/Co_3O_4$ catalyst, a catalytic test was carried out on the coated Zir-OCF (30 ppi) after approximately 250h of stream operating time (**Paper IV**). The stability test was carried out at the following flow conditions: WHSV of 30 NL $h^{-1}$ $g_{cat}^{-1}$, atmospheric pressure, inlet $CH_4$ concentration of 0.5 vol. %, temperature of 400 °C (for 250h). The catalytic activity was evaluated as at the beginning and at the end of the stability test. **Figure 25** shows the comparison of the catalytic activity of the coated Zir-OCF before and after the stability test (fresh and aged status).

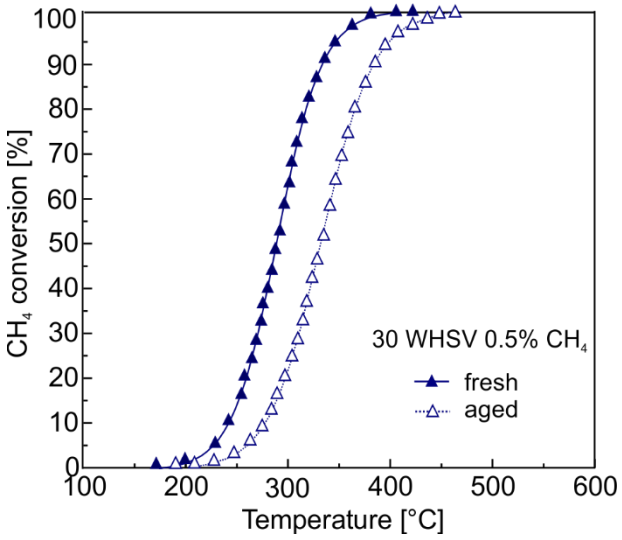


**Figure 25.** Stability performance: $CH_4$ conversion versus temperature of the Zir-OCF coated with 3 wt.% PdO on 200 mg $Co_3O_4$ (tested at 30 NL $h^{-1}$ $g_{cat}^{-1}$ and 0.5 vol. % $CH_4$ inlet concentration) in the fresh and aged status (after 250 h of time on stream) (**Paper IV**).

The catalytic activity suffers of a slight worsening, with a shift of the $CH_4$ light-off curve to higher temperatures. The stability of such a structured catalyst can be considered good. The full $CH_4$ conversion on the aged catalyst was achieved at 40 °C above that obtained for the fresh catalyst. Various authors have reported that the deactivation of Pd-based catalysts in $CH_4$ combustion at temperatures below 450 °C, in a low fuel environment could be related to the accumulation of hydroxyls on the oxide supports [24,42,119].

The stability of the coated OCF was also evaluated in highly endothermic processes for $CH_4$ emission mitigation such as steam reforming (SR) and oxy-steam reforming (OSR), conducted under extreme operating conditions (**Paper III**). For this purpose, the $Rh/CeO_2$ catalyst was supported on alumina OCF with pore density of 40 ppi. Stability measurements were performed over 200 h of time-on-stream via consecutive start-up and

shut-down cycles. Before the catalytic test, the coated OCF was reduced in-situ with a $H_2/N_2$ flow (50/50 vol.% in 30 NmL $min^{-1}$) at 300 °C for 1 h. The stability test was carried out at the following flow conditions: WHSV of 70 NL $h^{-1}$ $g_{cat}^{-1}$, atmospheric pressure, temperature of 900 °C (for 200h). **Figure 26** shows the results as $CH_4$ and $CO_2$ conversion, and effluent composition over 200 h TOS for both SR and OSR experiments.

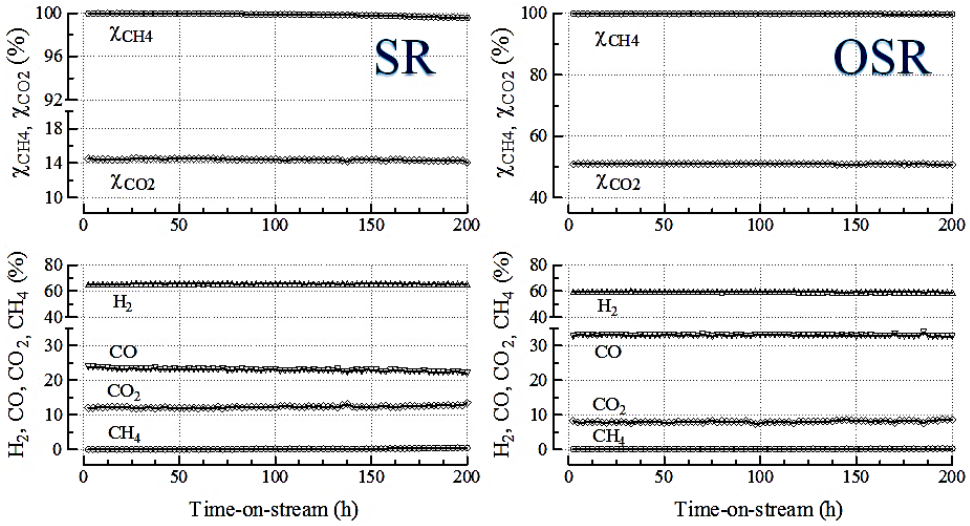


**Figure 26.** Biogas SR and OSR stability over alumina OCF catalyst with 40 ppi (F40). $CH_4$ conversion, $CO_2$ conversion, and effluent composition as a function of time-on-stream (**Paper III**).

As observed, the coated foam showed a steady performance, with negligible changes during the stability tests. This suggest that the $Rh/CeO_2$ catalytic phase is not deactivated at the applied conditions. However, a slight deactivation was obtained in the SR experiment after 150 h, which could be caused by a slight sintering of the Rh active phase induced by the high reaction temperature [70,230].

## 2.2 External and internal mass transfer effects

This section is focused on the study of the internal and external mass transfer effects occurring in a structured catalyst, particularly in OCFs. For this purpose, the low-dimensional theoretical model developed by Joshi et al. [162–164] was implemented. As a starting point, the method was applied to monolithic structures coated with different techniques and tested in different catalytic processes (**Paper I** and **Paper II**). Then, the model was adapted and applied to the coated OCFs to analyze the operating regimes for methane oxidation under lean conditions (**Paper III**, **Paper IV**, **Paper V**, **Paper VII**). The most relevant results obtained are described below.

### 2.2.1 Coated cordierite monolith

#### • $N_2O$ decomposition reaction

In this contribution (**Paper I**), cylindrical cordierite monoliths with square channels (400 cpsi) were used as catalyst supports for $N_2O$ decomposition. First, the monoliths were coated with a thin layer of $\alpha$-$Al_2O_3$ to prevent the migration of ions ($Mg^{2+}$, $Al^{3+}$) from cordierite to the cobalt spinel active phase ($Co_3O_4$). Then, $Co_3O_4$ was deposited on the structure using the SCS or impregnation techniques. This allowed comparison of the structured catalysts in terms of catalytic activity, morphological properties and mass transfer. The principal results obtained from the latter will be discussed in the subsequent paragraphs. The catalytic tests were carried out at the following flow conditions: GHSV of 1600 $h^{-1}$, temperature below 600 °C, atmospheric pressure and a gas flow of 30 mL $min^{-1}$ (5% $N_2O$/He).

In order to evaluate the mass transfer effects, it was assumed that the catalyst was uniformly distributed inside the monolith channel with circular flow area as shown in **Figure 27a**. In addition, fully developed laminar flow, convection dominant over axial diffusion (axial Peclet number very large) and isothermal monolith were considered. In **Figure 27** are shown the main results obtained in terms of controlling resistances: reaction, internal and external mass transfer resistances.

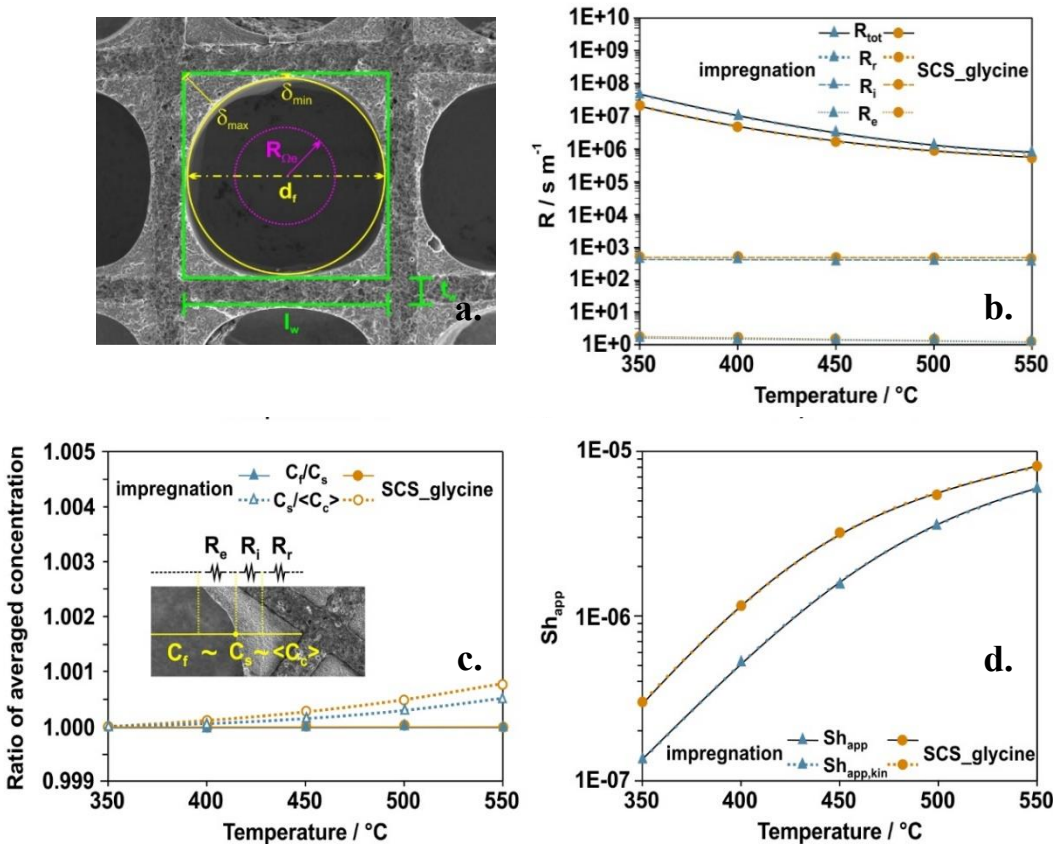


**Figure 27**. Characteristic geometric dimensions (estimated by SEM measurements) of a single monolith channel with circular flow area (a), evolution of the various resistances as a function of temperature (b), calculated ratios of transverse average concentrations profiles (c) and global apparent Sherwood number (d) of the structured catalyst prepared via SCS (orange) and impregnation (blue) methods (**Paper I**).

It is clear that for both structured catalysts, the overall resistance of the catalytic process is dominated by $R_r$ for the whole temperature range studied. While the mass transfer resistances ($R_i$ and $R_e$) are negligible when compared to $R_r$. This is also confirmed by the $Da_{II}$ and $Da_{III}$ values obtained, indicating the absence of mass transfer limitations. Since both coated monoliths operate in a kinetic regime, the reaction rate is much lower than the bulk diffusion rate from the gas to the external catalyst surface and from the external catalyst surface to the interior of the catalytic layer. Thus, the $N_2O$ decomposition reaction occurs throughout the catalyst layer and the concentration profile in the transverse direction of the monolith is nearly uniform (see **Figure 27c**.). On the other hand, by describing the overall process in dimensionless form it is possible to obtain the overall Sherwood number. Clearly, the $Sh_{app}$ values obtained for both catalysts are much lower than the asymptotic value corresponding to the external mass transfer regime ($Sh_e$). In particular, $Sh_{app}$ coincides with the values for the limiting case of slow reaction ($Sh_{app,kin} \approx \frac{4 \cdot \phi^2}{\mu \cdot \lambda}$) [164].

In this work, a hypothetical case was also considered in which the catalyst is uniformly distributed inside the channel wall without accumulations of catalyst at the corners. Therefore, a square distribution of the catalyst thickness (with square flow area) was proposed (see **Figure 28a**.). A detailed description of the hypothesis is reported in **Paper I**. This square distribution in coated monoliths has been observed experimentally in other studies [166,249–251]. Based on this hypothesis, the characteristic resistances were estimated maintaining constant the previously used parameters at the same GHSV. **Figure 28b**. shows the evolution of $R_r$ and $R_i$ with increasing catalyst thickness estimated at different temperatures.

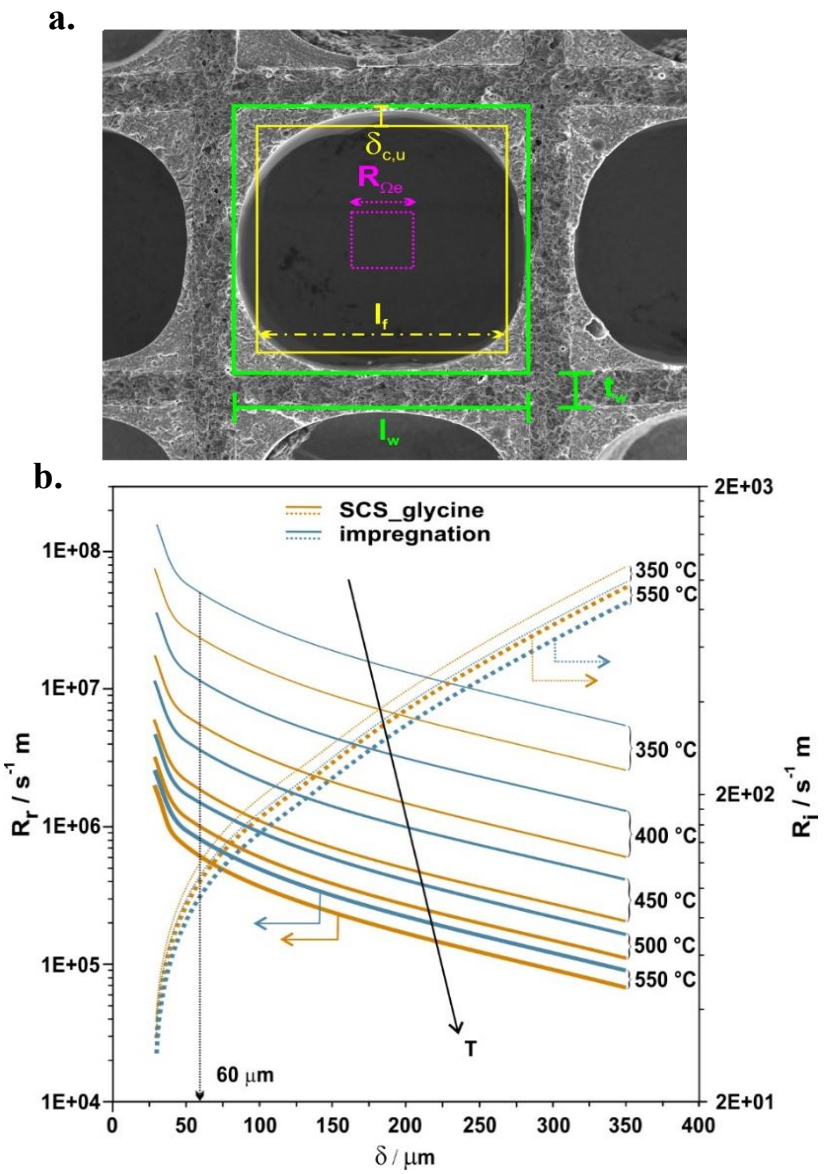


**Figure 28.** Hypothetical case (uniform catalyst deposition) with square flow area (a) and the evolution of $R_r$ and $R_i$ with increasing catalyst thickness estimated at different temperatures (b) (**Paper I**).

The increase of temperature and catalyst thickness leads to a progressive decrease of $R_r$, due to the Arrhenius equation dependence and the definition of kinetic resistance (**Equation 27**). On the other hand, $R_i$ increases progressively with increasing catalyst thickness, although its contribution is still << compared to $R_r$ (three orders of magnitude difference, and $R_r/R_t \approx 1$)

## • $CH_4$ steam reforming reaction

In this work (**Paper II**), mass transfer effects were evaluated in a highly endothermic catalytic process such as $CH_4$ steam reforming. For this scope, ceramic cordierite monoliths of square channels (100 cpsi) were utilized as catalyst support. The metal active phase (1.5 wt. % of Ru and Rh) supported on the carrier ($\gamma$-$Al_2O_3$) was coated on the structure via in-situ SCS. The catalytic performance was compared in terms of $CH_4$ conversion, $H_2$ production, CO selectivity and $H_2$/CO molar ratio, obtaining the best catalytic activity for the Ru-based catalyst. Then, the catalyst loading was varied as 3.20, 6.45 and 12.89 mg $cm^{-2}$, and the catalytic activity as well as mass transfer effects were evaluated. The flow conditions studied were as follows: WHSV of 750 NL $h^{-1}$ $g_{cat}^{-1}$, atmospheric pressure, temperature range of 550 to 850 °C and S/C molar ratio of 3.0. The catalytic performance results are discussed in detail in **Paper II**, thus the following paragraphs will illustrate the main findings of mass transport evaluation. Before discussing the mass transfer results, it is necessary to point out that the calculations were performed assuming an observed reaction rate for methane (under steady state conditions) estimated as: $r_{CH_4}^{obs} = \frac{F_{CH_4} \cdot X_{CH4}}{W_{cat}}$; where $F_{CH_4}$ is the molar flow rate of methane, $X_{CH4}$ is the conversion of methane and $W_{cat}$ is the catalyst weight.

Clearly, this expression is purely simplifying and considers only the kinetic factor of the reaction as a function of methane. As it is well known, the steam reforming process of methane is also accompanied by a moderately exothermic reaction such as the water-gas shift reaction, hence methane steam reforming is a limited-equilibrium process that involves three reversible reactions. As a consequence, carbon dioxide production can come not only from the water-gas shift reaction but also from the reforming reaction. Thus, while reforming is favored at high temperature and low pressure (volume expansion), the exothermic water-gas shift reaction is favored by low temperature, while it is not affected by pressure changes. In order to perform an exhaustive analysis of the reforming process, not only the kinetic factor must be taken into account, but also the driving force and adsorption terms, which are represented by the equilibrium and adsorption constants. However, in this work, to simplify the calculations and to evaluate the effect of resistance due to mass transfer, only the desired reforming reaction was considered and under steady state conditions, the methane disappearance rate expressed per unit mass of catalyst was determined.

In **Figure 29** are shown the evolution of the characteristic resistances (a, b, c) and the resistance ratios (d) as a function of temperature.

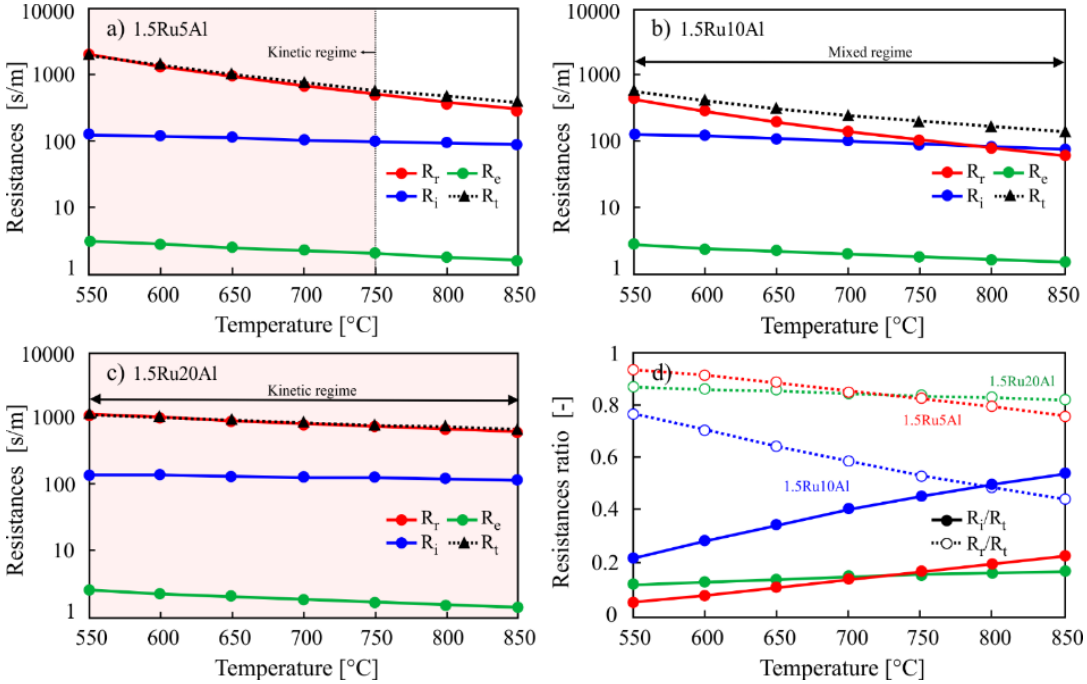


**Figure 29**. Evolution of the various resistances for the catalyst 1.5Ru5Al (a);1.5Ru10Al (b); 1.5Ru20Al (c), and resistance ratios (d) as a function of temperature (**Paper II**).

As can be seen, the mass transfer resistances ($R_i, R_e$) are much less sensitive to temperature because the molecular and effective diffusivities are much weaker functions of temperature compared to the $R_r$, which is strongly dependent on the Arrhenius equation. Clearly, as the catalyst loading varies, the operating regimes of the catalyst change. Particularly, with lower catalyst loading (1.5Ru5Al, 3.20 mg $cm^{-2}$), the process is governed by a kinetic regime at temperatures below 750 °C. However, as the catalyst loading increases to 6.2 mg $cm^{-2}$ (1.5Ru10Al), the process operates in a mixture of regimes in which $R_r$, $R_i$ and $R_e$ co-exist with $R_e << R_r$, $R_i$. On the other hand, with a catalyst loading of 12.89 mg $cm^{-2}$ (1.5Ru20Al), the process is completely controlled by the reaction throughout the entire

temperature range. Thus, when comparing these results with those obtained during the catalytic test reported in detail in **Paper II**. It is clear that optimizing the loading of catalyst allows to guarantee a better catalytic performance in terms of conversion and production of the species, besides playing a key role for mass transfer, particularly those related to internal diffusion.

### 2.2.2 Coated ceramic OCF

Here, the mass transfer effects during the catalytic combustion of $CH_4$ on 3 wt. % $PdO/Co_3O_4$ catalyst were evaluated for the process intensification. Below, the main results obtained by investigating the impact on mass transfer when varying the OCF material (**Paper IV**), the catalyst content (**Paper V**) and by conducting the catalytic test combining ceramic OCFs of different material (**Paper VII**) will be discussed. In addition, the effect of pore density on mass transfer for biogas SR and OSR processes (**Paper III**) will also be addressed.

#### 2.2.2.1 Effect of OCF material

In this contribution (**Paper IV**), the theoretical method for evaluating mass transfer effects discussed in *Section 1.3* was applied and adapted to OCF structures. In this way, it was possible to investigate the different operating regimes of the structured catalysts by varying the support material. For this purpose, as mentioned above, 3 wt. % $PdO/Co_3O_4$ catalyst (about 200 mg) was deposited on each foam using the SCS and WI techniques. OCFs made

of zirconia (Zir), alumina (Alu) and silicon carbide (SiC) with pore density of 30 ppi were used for such scope. Mass transfer effects were evaluated at the following flow conditions: WHSV of 30 NL $h^{-1}$ $g_{cat}^{-1}$, temperature range of 100-700 °C, atmospheric pressure and inlet $CH_4$ concentration of 0.5 vol. %. **Figure 30** displays the evolution of the individual and overall resistances as a function of the temperature for all the structured catalysts.

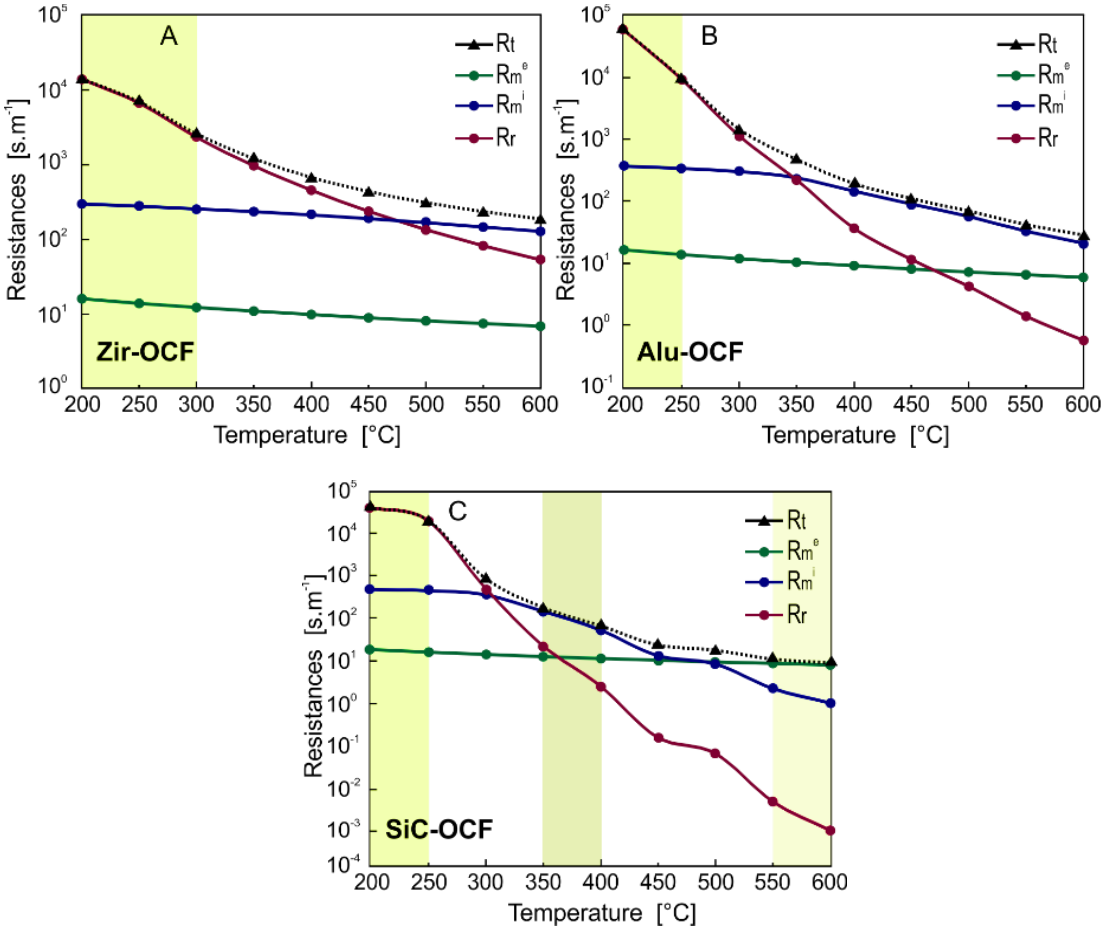


**Figure 30.** Various resistances for the three OCF catalysts in the process of mass transfer with chemical reaction: A. Zir-OCF, B. Alu-OCF and C. SiC-OCF (**Paper IV**).

Clearly, the temperature increase results in a much sharper drop of the reaction resistance ($R_r$) compared to the mass transfer resistances (${R_m}^i, {R_m}^e$), due to the strong dependence of the Arrhenius equation on the kinetic resistance. On the contrary, the diffusivities of reactant species in the gas phase and within the catalyst layer are much weaker functions of temperature, thus the (external and internal) mass transfer rates vary only slightly. Particularly, for the three coated OCFs, ${R_m}^e$ is nearly independent of temperature. As far as the evolution of ${R_m}^i$ is concerned, at temperatures below 350° and 300 °C, ${R_m}^i$ is practically invariant for the Alu- and SiC-OCF catalysts, respectively. In addition, these structures exhibit a higher dominance of internal resistance at medium/high temperatures. Specifically, the ${R_m}^i$ is more significant for Alu-OCF at temperatures above 400 °C, while for SiC-OCF in the temperature range from 350 to 400 °C. This can be explained considering the values of thermal conductivity and catalyst layer of the OCFs: at low temperatures, when the combustion is initiating, the heat generated by reaction is still negligible because of the low $CH_4$ conversion. At these conditions, foams with a higher thermal conductivity help to retain heat, supplying the energy needed to drive the ignition of the first reacting molecules in the coated OCF. As a result, the $R_r$ drops more sharply and the diffusion effects start to become much more important at lower temperatures. Since all three catalysts were coated with the same amount of catalyst, OCFs with a smaller external surface area will exhibit thicker catalyst thicknesses ($\delta_{SiC} > \delta_{Alu} > \delta_{Zir}$). This is in line with the results shown in **Figure 30**, as the internal diffusion effects become significant in catalysts with thicker thickness.

For further analysis, the Thiele modulus and effectiveness factor values were studied for the three coated OCFs, as illustrated in **Figure 31**. The Zir-OCF displayed the lowest

Thiele modulus values ($\phi_{max,@600°C} = 3.5$) resulting in effectiveness factors very close to unity. Thus, according to the results obtained in **Figures 30** and **31**, the catalyst operates in a combination between kinetic ($T < 300°C$; $\phi \ll 1$) and transition regime ($T > 300°C$). For OCFs with higher thermal conductivity (Alu and SiC), the reaction rate tends to be faster, leading to higher Thiele modulus values. In fact, Alu-OCF operates in a kinetic regime at lower temperatures of about 250 °C, and then passes into a transition regime in which at temperatures between 250-400 °C, $R_r$ and ${R_m}^i$ are comparable and, at temperatures above 400 °C, ${R_m}^i$ dominates the catalytic process. On the other hand, the SiC-OCF s $\phi > 100$ at temperatures above 550 °C, becoming the diffusion in the dominant process at $T > 350\ °C$, while operating in a kinetic regime at $T < 250\ °C$ with $\phi \ll 1$ and $\eta \to 1$.

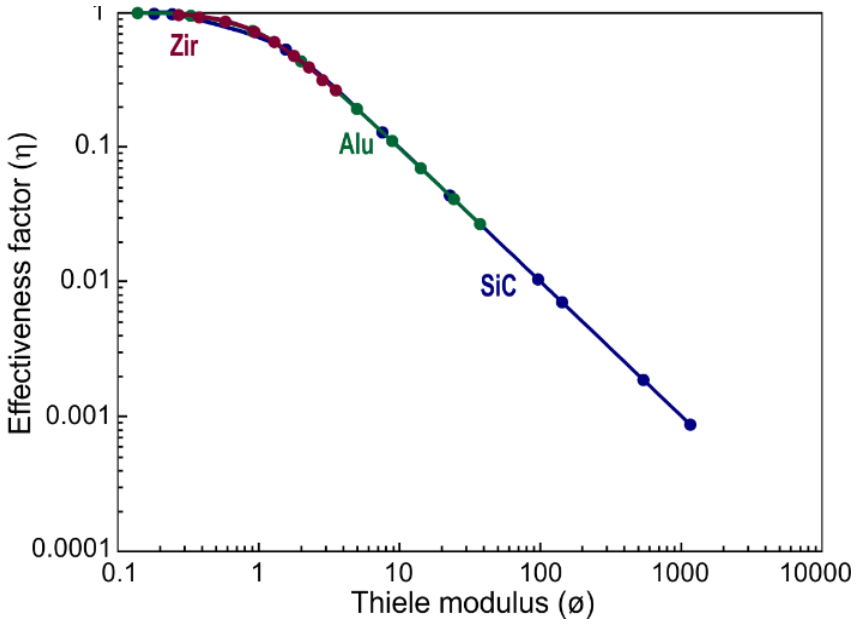


**Figure 31.** Effectiveness factor vs Thiele modulus for all the OCF catalyst (**Paper IV**).

#### 2.2.2.2 Effect of catalyst content

This part of the research (**Paper V**) focused on studying the different controlling resistances (kinetic, pore and interphase diffusion) by varying the content of catalyst deposited ($C_{load}^{100}$, $C_{load}^{150}$ and $C_{load}^{250}$) on the OCF. For this scope, Zir-OCF with pore density of 30 ppi was coated with 3 wt. % $PdO/Co_3O_4$ catalyst using the SCS and WI methods. The catalytic tests toward $CH_4$ combustion in lean conditions were carried out at different flow conditions, as listed in *Section 2.1.2*. The characteristic resistances were determined at the following flow conditions: WHSV of 30, 60 and 90 NL $h^{-1}$ $g_{cat}^{-1}$, temperature range of 100-700 °C, atmospheric pressure and inlet $CH_4$ concentration of 1 vol. %. For comparison, the results obtained at the highest and lowest WHSV studied (30 and 90 NL $h^{-1}$ $g_{cat}^{-1}$) are shown below. The evolution of the characteristic resistances for the three catalyst loadings at WHSV of 30 and 90 (NL $h^{-1}$ $g_{cat}^{-1}$) are shown in **Figure 32**.

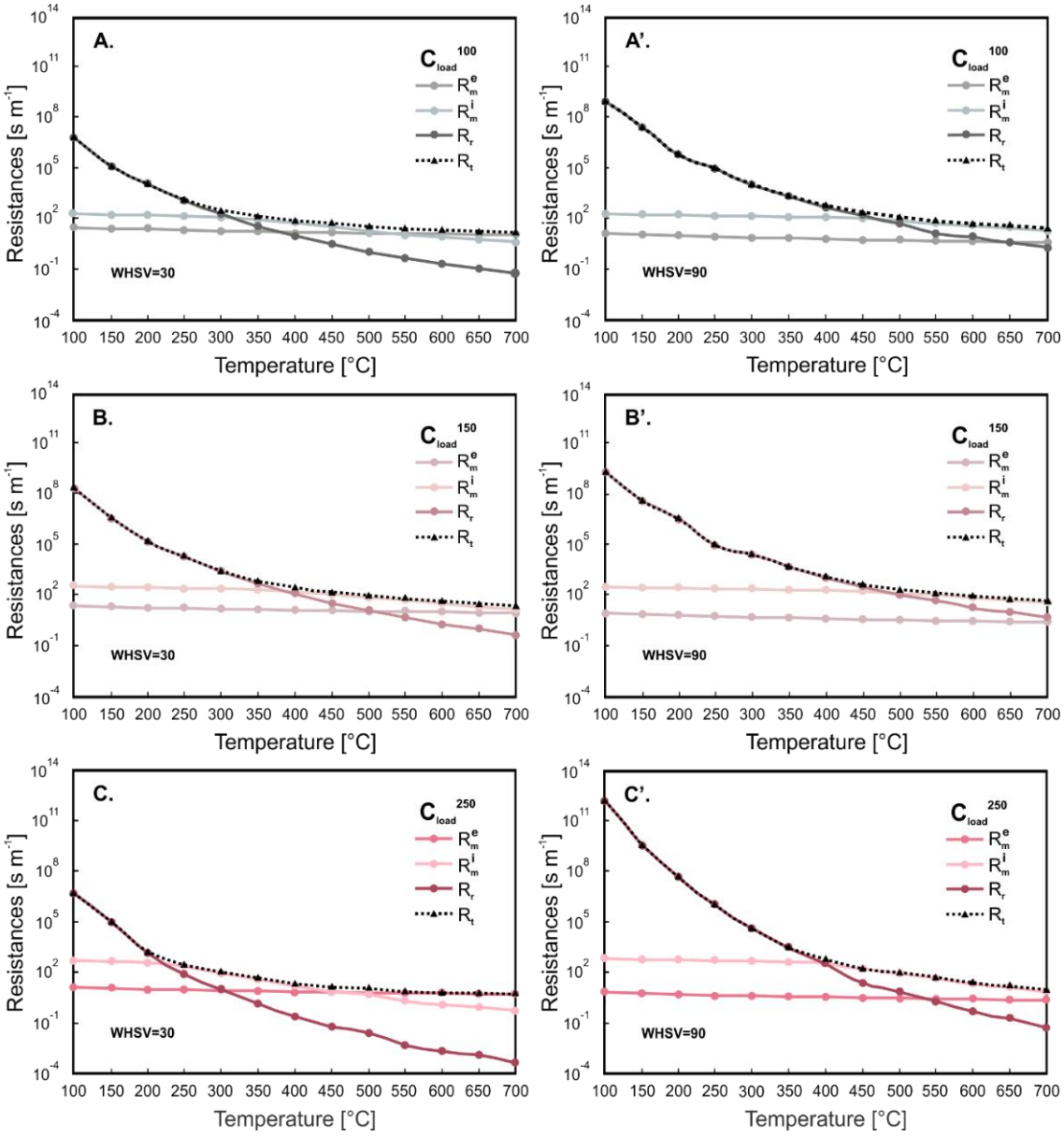


**Figure 32.** Various resistances versus temperature for the three catalyst contents at WHSV of 30 (**A,B** and **C**) and 90 (**A'**,**B'** and **C'**) for $C_{load}^{100}$, $C_{load}^{150}$ and $C_{load}^{250}$, respectively (**Paper V**).

At low temperatures, the reaction rate is much slower than the external and internal diffusion rates and thus the kinetics control the process. In particular, the highest

temperature range under kinetic control for both WHSV was $C_{load}^{150}$ at T < 300 °C for WHSV of 30 NL $h^{-1}$ $g_{cat}^{-1}$ and at T < 388 °C for WHSV of 90 NL $h^{-1}$ $g_{cat}^{-1}$. As the temperature increases, the diffusive resistances ($R_m{}^i, R_m{}^e$) start to become significant mainly in catalysts with higher catalyst thickness. Furthermore, increasing the catalyst loading from 6.1 to 13.7 $mg_{cat}$ $cm^{-2}_{OCF}$, $R_m{}^i$ tends to be more dominant at lower temperatures. Such results are also consistent with those obtained in *Section 2.1.2* during the catalytic test, where increasing the catalyst content shifted the light-curve to higher temperatures (at the same flow conditions). On the other hand, at elevated temperatures, the catalytic tests conducted at the lowest WHSV show a dominance of $R_m{}^e$ for $C_{load}^{100}$ and $C_{load}^{250}$ catalysts. In order to establish the operating regime for each catalyst, the resistance ratios were plotted as a function of temperature in **Figure 33**. First of all, it is worth mentioning that a controlling regime is considered here as the ratio between $\frac{R_x}{R_t} > 0.85 - 0.90$ and a dominant regime or mixed/transitional regime where $0.50 < \frac{R_x}{R_t} < 0.85$, with $R_x = R_r$ or $R_m{}^i$ or $R_m{}^e$. Overall, the three catalyst contents supported on the Zir-OCF operated in a kinetic regime at low temperatures: at temperatures below 240° and 365 °C for $C_{load}^{100}$, of 300° and 370 °C for $C_{load}^{150}$ and of 170° and 338 °C for $C_{load}^{250}$, at WHSV of 30 and 90 NL $h^{-1}$ $g_{cat}^{-1}$, respectively. With increasing temperature and hence reaction rate, the diffusive effects became important and the catalyst, once it overcame the kinetic regime, began to operate in a mixed or transitional regime in which the three resistances coexist. In this case, as the temperature varies, $R_m{}^i$ or $R_m{}^e$ predominates while $R_r$ becomes increasingly negligible. Particularly the $C_{load}^{100}$ and $C_{load}^{150}$ catalysts, once the temperature under kinetic control was exceeded, operated in a mixed regime, where $R_m{}^i$ was more

dominant for the coated Zir-OCF with thicker catalyst layer. However, in the case of $C_{load}^{250}$, the catalyst achieved ${R_m}^i$ control at temperatures between 450° and 600 °C at WHSV 90, while at WHSV 30, the ${R_m}^e$ dominated the process at temperatures above 463 °C, reaching $\frac{{R_m}^i}{R_t} > 0.85$ at temperatures nearer to 700 °C.

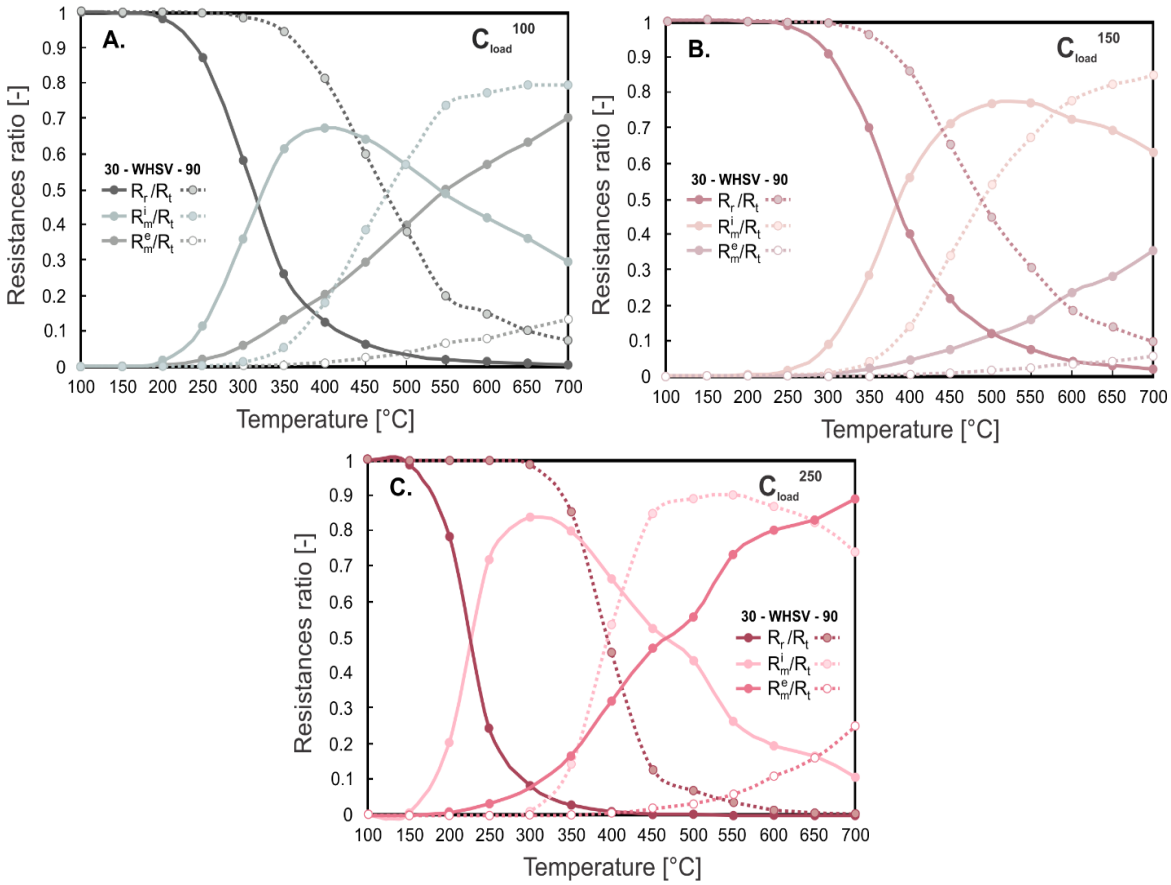


**Figure 33.** Ratio resistances as a function of temperature at WHSV of 30 and 90 NL $h^{-1}$ $g_{cat}^{-1}$ for $C_{load}^{100}$ (**A**), $C_{load}^{150}$ (B) and $C_{load}^{250}$ (C) (**Paper V**).

Furthermore, in this contribution was also derived a correlation to estimate the external mass transfer coefficient at low Reynolds number, taking into consideration the coated

OCF parameters and assuming a Kelvin cell model. The external diffusion control was confirmed by the constancy of $CH_4$ conversion at elevated temperatures (temperatures above the temperature range where the Pd-PdO transformation occurs) with $\frac{R_m^e}{R_t} > 0.9$. Thus, the mass transfer coefficients were estimated according to the steady-state $CH_4$ mass balance, expressed in dimensionless form and plotted as a function of the Reynold's number on a logarithmic scale. **Figure 34** shows the fitting of the values obtained at different flow conditions to a single correlation of the form: $Sh = A \cdot Re^m \cdot Sc^{1/3}$.

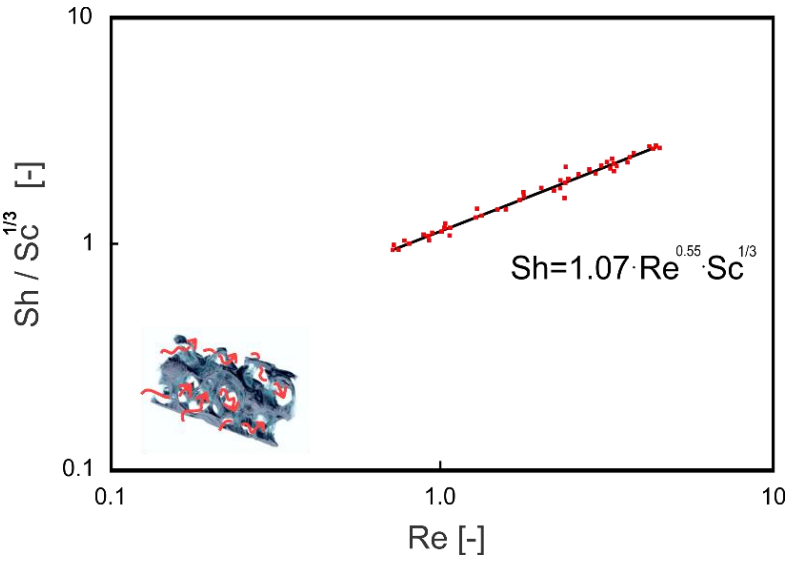


**Figure 34.** Mass-transfer coefficients versus inlet flow rate estimated for different catalyst loadings and flow conditions (**Paper V**).

In this correlation, the obtained parameter $A$, which is a function of the porosity and geometric properties of the OCFs is in line with those reported in literature derived using different foam materials and pore densities [149,194,252]. However, the exponent $m$ was slightly

higher than those reported in other studies [89,176,253,254]. This could be due to the low Reynolds numbers at which the experiments were conducted.[89]

#### 2.2.2.3 Effect of OCF combination

The impact on the mass transport effects of combining SiC and Zir OCFs was investigated in this part of the research (**Paper VII**). For this purpose, as mentioned in *Section 2.1.3*, a combination of SiC and Zir OCFs with pore density of 30 ppi were used as support for the 3 wt. % $PdO/Co_3O_4$ catalyst. Each SiC/Zir combination was 3 cm in total length, while the lengths of each foam piece were varied to obtain the following coated combinations: SiC1Zir2, SiC1.5Zir1.5 and SiC2Zir1. The catalytic tests were conducted by placing the SiC-OCF on the inlet side of the reactive gases followed by the Zir-OCF. Mass transfer effects were evaluated at the following flow conditions: WHSV of 30 and 90 NL $h^{-1}$ $g_{cat}^{-1}$, temperature range of 100-700 °C, atmospheric pressure and inlet $CH_4$ concentration of 1 vol. %. **Figure 35** shows the Arrhenius curves for all coated SiC/Zir OCF combinations, at WHSV of 30 NL $h^{-1}$ $g_{cat}^{-1}$.

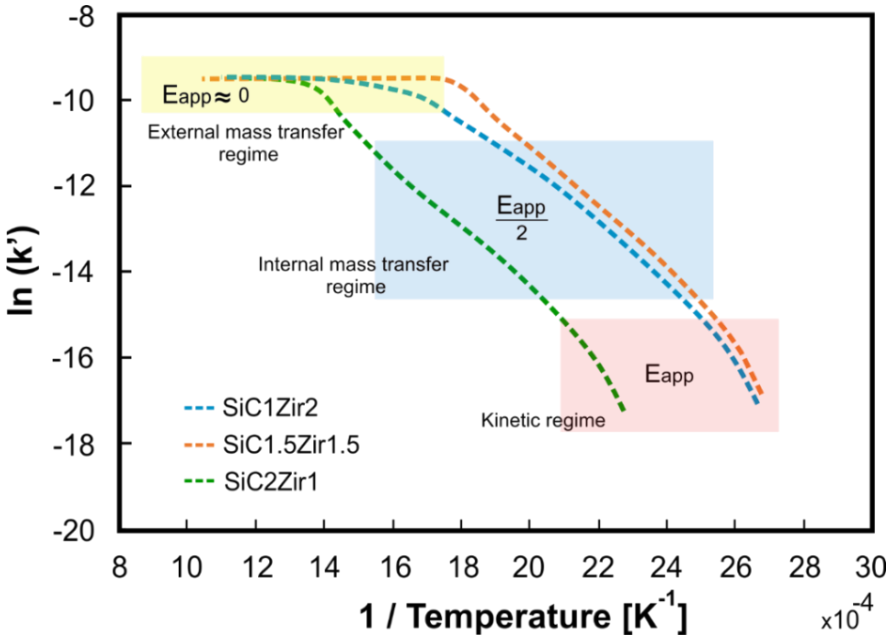


**Figure 35**. Arrhenius plots for the various OCF combinations (SiC1Zir2, SiC1.5Zir1.5, and SiC2Zir1) at WHSV of 30 NL $h^{-1}$ $g_{cat}^{-1}$ and inlet $CH_4$ concentration of 1 vol. % (**Paper VII**).

It is observed that the curves of the SiC1Zir2 and SiC1.5Zir1.5 combinations were fairly similar, showing a slight shift towards lower temperatures for the SiC1.5Zir1.5 combination. Conversely, the SiC2Zir1 combination was shifted towards higher temperatures (lower 1/T values) indicating a slower ignition of reaction. The activation energy values were estimated at $CH_4$ conversions below 10 % to guarantee a kinetic regime in the structured catalysts. The estimated apparent activation energy ($E_{app}$) values were as follows: 104.30 kJ $mol^{-1}$, 102.42 kJ $mol^{-1}$ and 108.82 kJ $mol^{-1}$ for the combinations of SiC1Zir2, SiC1.5Zir1.5 and SiC2Zir1, respectively.

From **Figure 35**, it is also possible to note the change of slope of the Arrhenius curve as the temperature varies. It is well known that these slope variations are caused by the

different controlling regimes during the catalytic process. At low temperatures, when the reaction rate constant is very low, the reaction is controlled by the kinetic regime and it is in this zone that $E_{app} \approx E_a$. As the temperature increases, the slope of the curve changes, passing through a transition zone and then maintains a constant slope at medium temperatures. At this point, the catalyst is governed by internal diffusion regime and here $E_a^{id} \approx E_{app}/2$. Finally at very high temperatures, the slope of the curve drops to values very close to zero, indicating the external mass transfer control $E_a^{ed} \approx 0$.

For the evaluation of the operating regime of each catalytic OCF combination, the ratio of the resistances to the total resistance was plotted as a function of temperature, at WHSV of 30 and 90 NL $h^{-1}$ $g_{cat}^{-1}$, as illustrated in **Figure 36**.

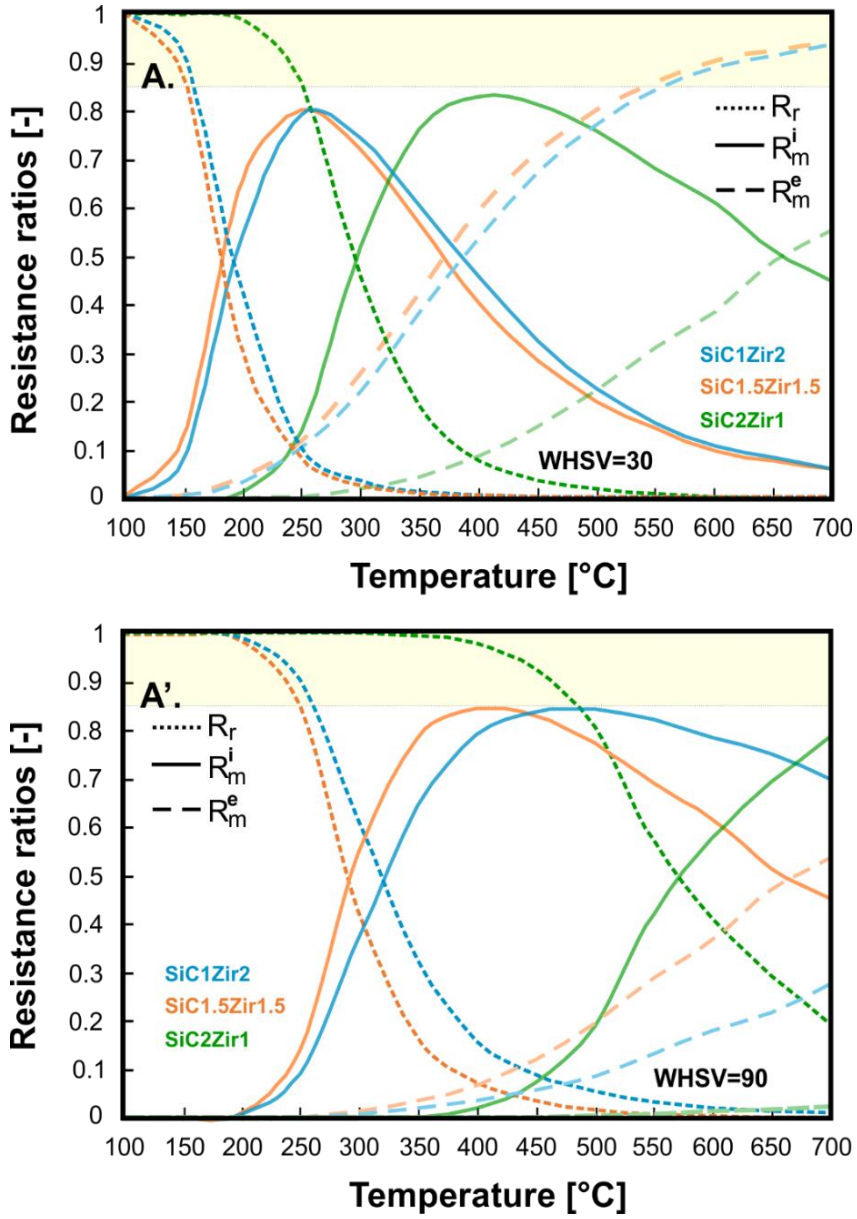


**Figure 36.** Various resistance ratios as a function of temperature showing the different operating regimes for the three OCF combinations at inlet $CH_4$ concentration of 1 vol. % and WHSV of 30 (A) and 90 (A') NL $h^{-1}$ $g_{cat}^{-1}$ (**Paper VII**).

At the lowest WHSV, the three catalytic OCF combinations operate in a kinetic regime with $\frac{R_r}{R^{ov}} > 0.85$. Particularly, at lower temperatures of 148°, 160° and 255 °C for the

SiC1.5Zir1.5, SiC1Zir2 and SiC2Zir1 combination, respectively. With increasing temperatures, all catalyst operated in a mixed regime, in which the intraparticle diffusion effects dominated at temperatures between 180-370 °C, 190-395 °C and 295-660 °C for the SiC1.5Zir1.5, SiC1Zir2 and SiC2Zir1 combinations, respectively. On the other hand, only the SiC1Zir2 and SiC1.5Zir1.5 combinations showed an external diffusion regime at temperatures above 550°C.

On the other hand, when operating the reactor at the highest WHSV (90 NL $h^{-1}$ $g_{cat}^{-1}$), the kinetic regime of all catalysts shifts toward higher temperatures due to the reduction of the contact time between the catalyst and the surface of the catalyzed OCF. Specifically at temperatures below 250°, 260° and 485 °C for the SiC1.5Zir1.5, SiC1Zir2 and SiC2Zir1 catalysts, respectively. Once the kinetic control was overcome, all the catalysts operated in a mixed regime in which the internal resistance dominated at medium/high temperatures. Moreover, due to the increase in gas turbulence, no control of external resistance was found in any of the catalysts.

For further analysis, the effectiveness factor and the evolution of $R_r$ and ${R_m}^i$ as a function of the Thiele modulus ($\phi$) at WHSV of 30 NL $h^{-1}$ $g_{cat}^{-1}$ were plotted in **Figure 37**. It is well known that a catalytic reaction is bounded by two extreme cases: very slow reaction ($\phi \ll 1, \eta \to 1$) and very fast reaction ($\phi \gg 1; \eta \to \frac{1}{\phi}$). In the first case, the kinetics of the reaction controls the process and ${R_m}^i$ reaches the asymptotic value of $\frac{R_{\Omega,i}}{Sh_{c,\infty} \cdot D_e}$, being independent of the reaction kinetics and strongly dependent on the catalytic thickness [163]. In the second case, $R_r$ is practically insignificant because of the high values of kinetic rate constant and at this point ${R_m}^i$ tends to the value of $\frac{1}{\sqrt{k \cdot D_e}}$ [164]. Thus, the combustion reaction

is completed in a thin boundary layer near the gas-coated layer interface. Hence, the $R_m{}^i$ is independent of the catalytic thickness and depends only on the combustion kinetics and effective diffusivity the catalyst layer [150–152,155,163,164,168]

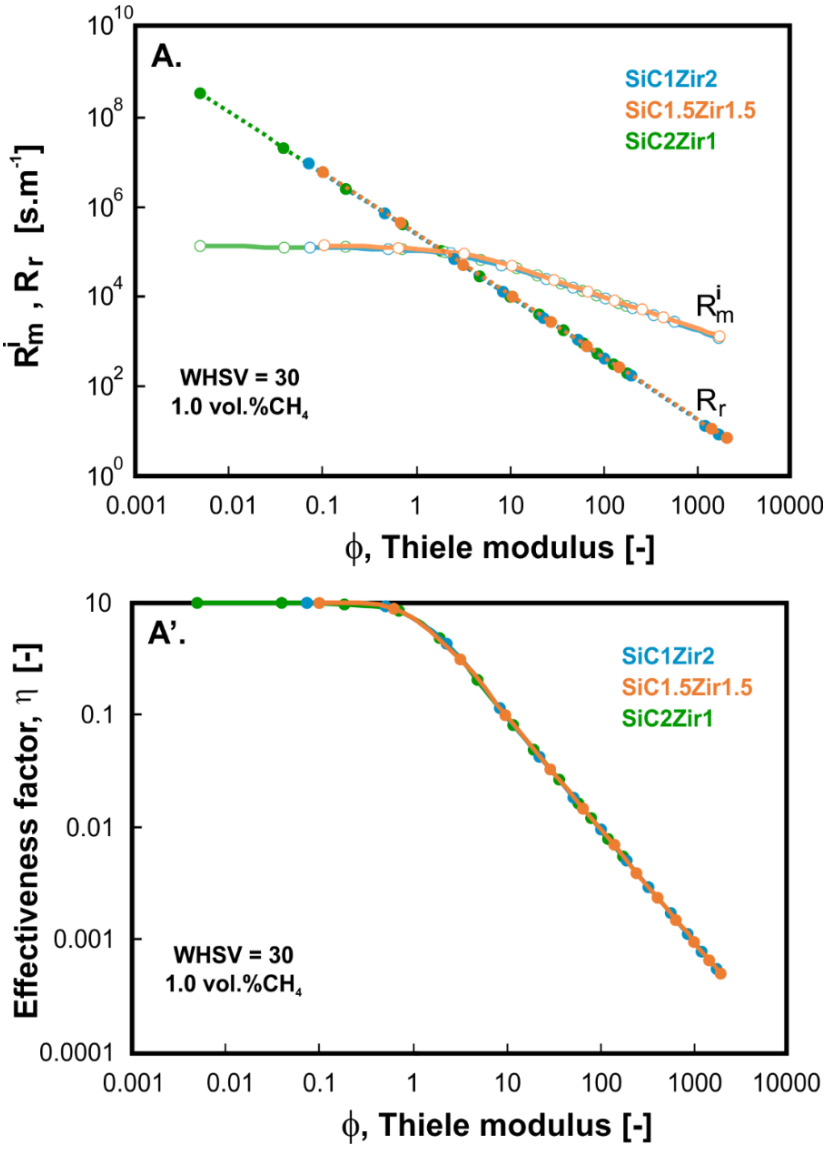


**Figure 37.** Evolution of $R_r$ and $R_m{}^i$ (A) and effectiveness factor (A') as a function of the Thiele modulus ($\phi$) at WHSV of 30 and inlet $CH_4$ concentration of 1 vol.% (**Paper VII**).

### 2.2.2.4 Effect of OCF pore density

In this part of the research (**Paper III**), the diffusive effects related to the fluid phase and coated catalyst layer were evaluated by varying the pore density of alumina OCF (20, 30 and 40 ppi). For this purpose, the $Rh/CeO_2$ catalyst was coated by SCS (for $CeO_2$ carrier) and WI (for Rh active phase) on each of the alumina foams (referred in **Paper III** as F20, F30 and F40). Then, catalytic tests were performed toward biogas SR and OSR. The experiments were carried out at the following flow conditions: S/C of 3 (for SR) and S/C of 1 with $O_2/CH_4$ molar ratio of 0.2 (for OSR), atmospheric pressure, temperature of 800° and 900 °C and WHSV of 35-140 NL $h^{-1}$ $g_{cat}^{-1}$. In order to describe the trade-off between reaction kinetics and convective transport flux, the first Damköhler number (Da-I) was estimated for all the catalysts studied (F20, F30 and F40). The calculated Da-I values were found to be greater than 1 (2.8-3.2), because of the high voidage of alumina OCFs (0.86-0.89), confirming that the reactive gas mixture had sufficient time to react on the catalyst within the pores of the OCFs. Moreover, the Da-I values were higher than unity even when operating the reforming processes at the highest WHSV (140 NL $h^{-1}$ $g_{cat}^{-1}$). This condition is necessary to guarantee a high reforming performance of the investigated catalysts.

On the other hand, the second (Da-II) and third (Da-III) Damköhler numbers were determined to evaluate the possible external and internal mass transfer limitations. **Figure 38** shows the Da-II and Da-III values for the biogas SR and OSR reactions.

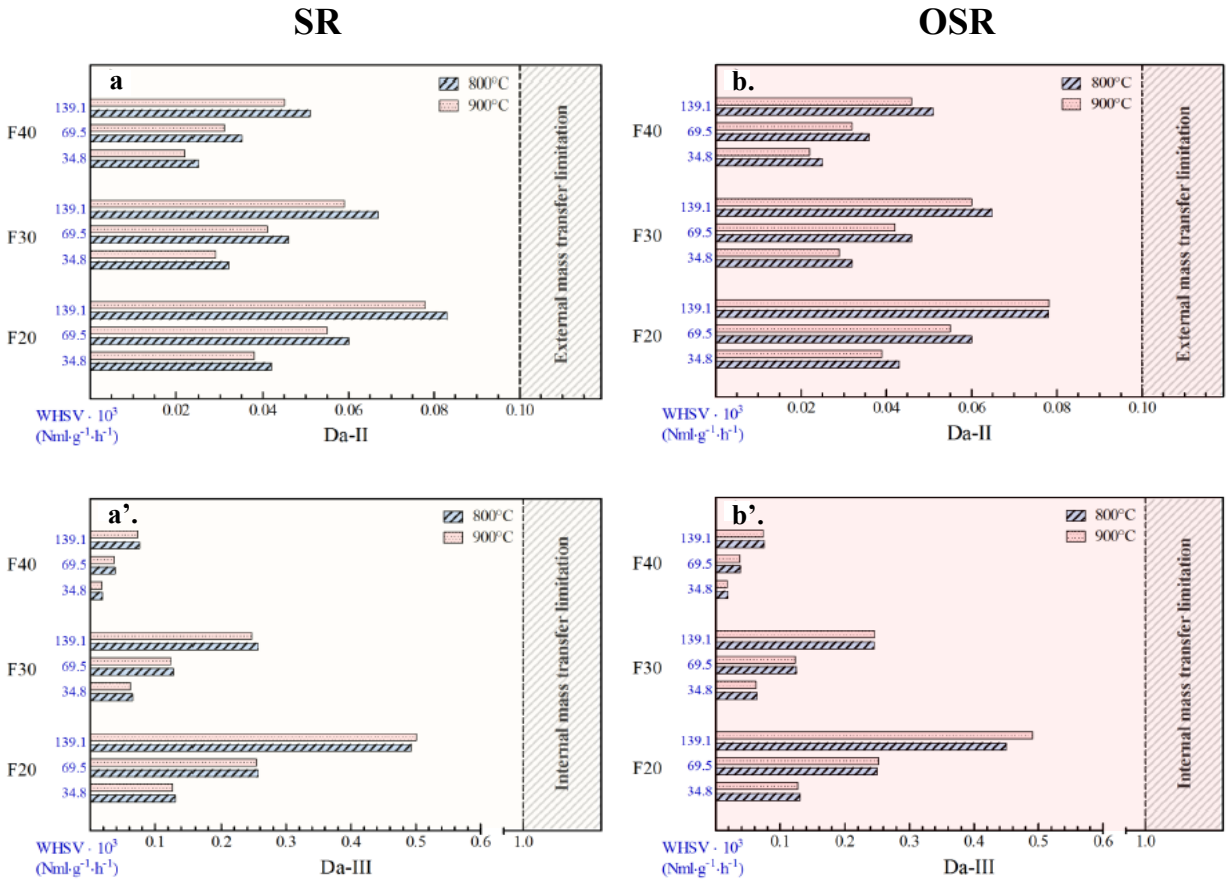


**Figure 38.** Influence of temperature and space velocity on Da-II and Da-III dimensionless numbers on biogas SR (a,a') and OSR (b,b') experiments over F20, F30, and F40 catalysts (**Paper III**).

As can be seen, in both catalytic processes the Da-II values increases with increasing WHSV and decreases with pore density, while they are not greatly affected by varying temperature. Moreover, all Da-II values were below the criterion limit (0.02-0.08) < 0.1, indicating the absence of external mass transfer limitations. However, the OCF with the lowest pore density (F20) showed the highest Da-II values, especially at the highest WHSV studied. This is because the lower the pore density the larger the pore size and hence the lower the flow velocity through the pores of the OCFs. In fact, as reported in detail in

**Paper III**, the high external mass transfer time of F20 affected the catalytic performance, leading to a drop in reactant conversion. These results were also confirmed by applying Carberry's criteria (see **Figures 39a** and **39b)**, which verify the absence of external diffusion limitations ($Ca < 0.05$)

On the other hand, when analyzing the Da-III values related to the internal mass transfer limitations, it is observed that for both catalytic tests all the values were lower than unity, excluding some limitation associated to the internal diffusion. Thus, the reactants rapidly diffused through the pores of the coated layer, avoiding the formation of a concentration gradient between catalyst surface and active sites [164,255]. These results were also checked using the Weisz-Prater criterion (0.02-0.5) <1, indicating the absence of internal mass transfer effects (see **Figures 39a'** and **39b'**). It is also worth noting that Da-III values increase with decreasing OCF pore density. Since the same amount of catalyst was deposited on each foam, OCFs with lower specific surface area or external surface area will exhibit higher catalyst thicknesses. This can be seen in more detail in **Paper III**, in which the estimated values for each OCF are reported. It is evident that the increase of pore density leads to a much more compact structure due to the greater number of cells and

struts per unit volume present in the foam and thus greater exposed surface area (F40>F30>20).

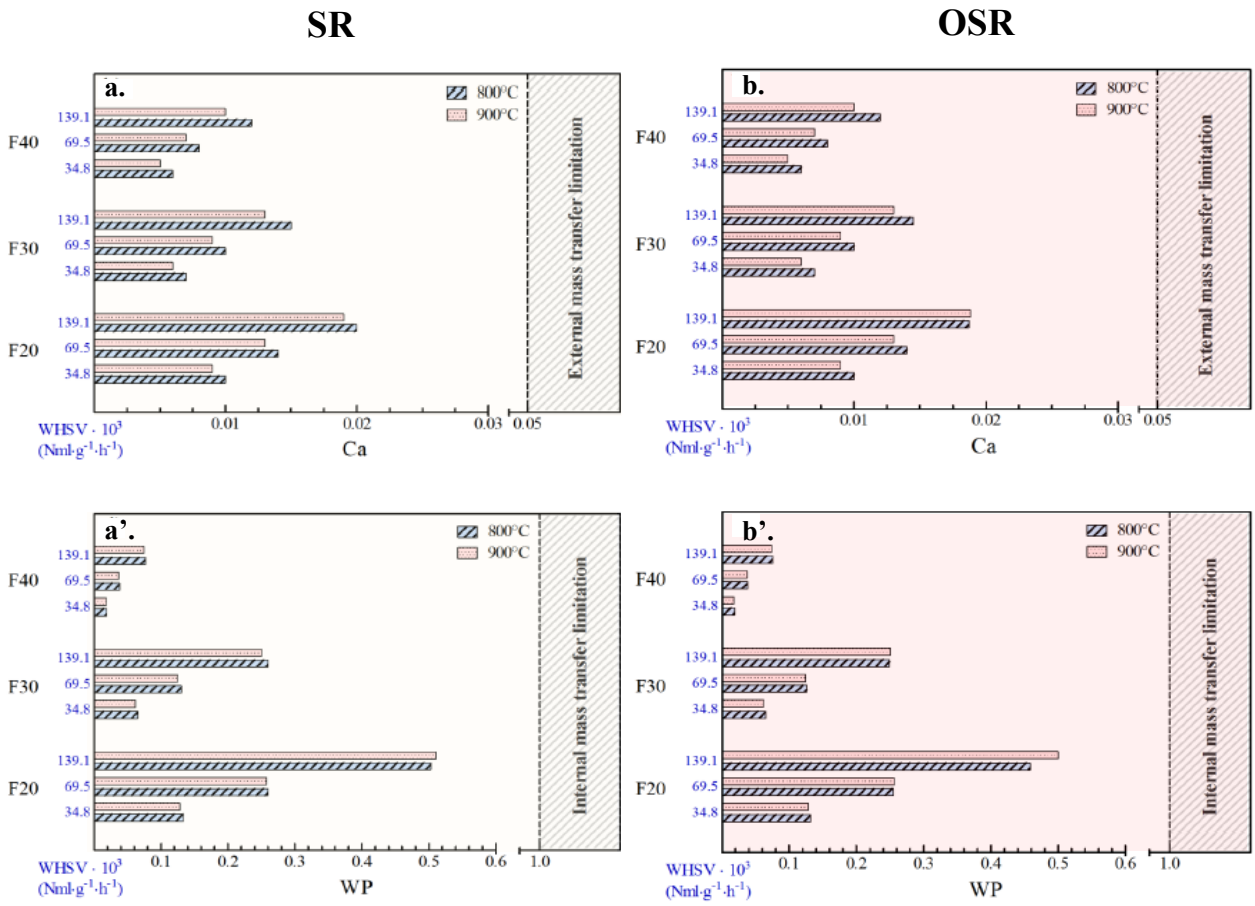


**Figure 39**. Influence of temperature and space velocity on Ca and WP dimensionless numbers on biogas SR (a,a') and OSR (b,b') experiments over F20, F30, and F40 catalysts (**Paper III**).

## 2.3 External and internal heat transfer effects

This section is aimed to study the external and internal heat transfer effects occurring during highly endothermic and exothermic catalytic processes carried out in structured catalysts, especially in OCFs. First, the potential heat limitations were evaluated in highly endothermic processes such as steam reforming and oxy-steam reforming supported on cordierite monolith (**Paper II**) and ceramic OCFs made of alumina (**Paper III**). Then, heat transfer effects were evaluated during the catalytic combustion of $CH_4$ in lean conditions (highly exothermic reaction) on structured catalysts in ceramic OCFs of different materials (**Paper IV**) and OCF combinations (**Paper VII**).

### 2.3.1 Coated cordierite monolith

In this part of the research (**Paper II**), it was carried out a study of the possible external and internal heat transfer limitations that could be present during the evolution of $CH_4$ steam reforming reaction supported on cordierite monoliths. For this purpose, various contents of 1.5 wt. % $Ru/Al_2O_3$ catalyst were deposited on the structure (cordierite monolith of square channel, 100 cpsi) via in-situ SCS. The catalysts were labelled as follows: 1.5Ru5Al (3.20 mg $cm^{-2}$), 1.5Ru10Al (6.45 mg $cm^{-2}$) and 1.5Ru20Al (12.89 mg $cm^{-2}$) and were tested towards $CH_4$ SR at the following flow conditions: WHSV of 750 NL $h^{-1}$ $g_{cat}{}^{-1}$, atmospheric pressure, temperature range of 550 to 850 °C, and S/C molar ratio of 3.0.

External heat transfer limitations were evaluated using the Mears criterion (**Equation 38**) derived on the basis of the perturbation approach in which the gas phase heat transfer

resistance is assumed to be lumped to the surface. In **Figure 40**, the Mears criterion expressed in terms of external Damköhler number were evaluated for the three catalyst contents.

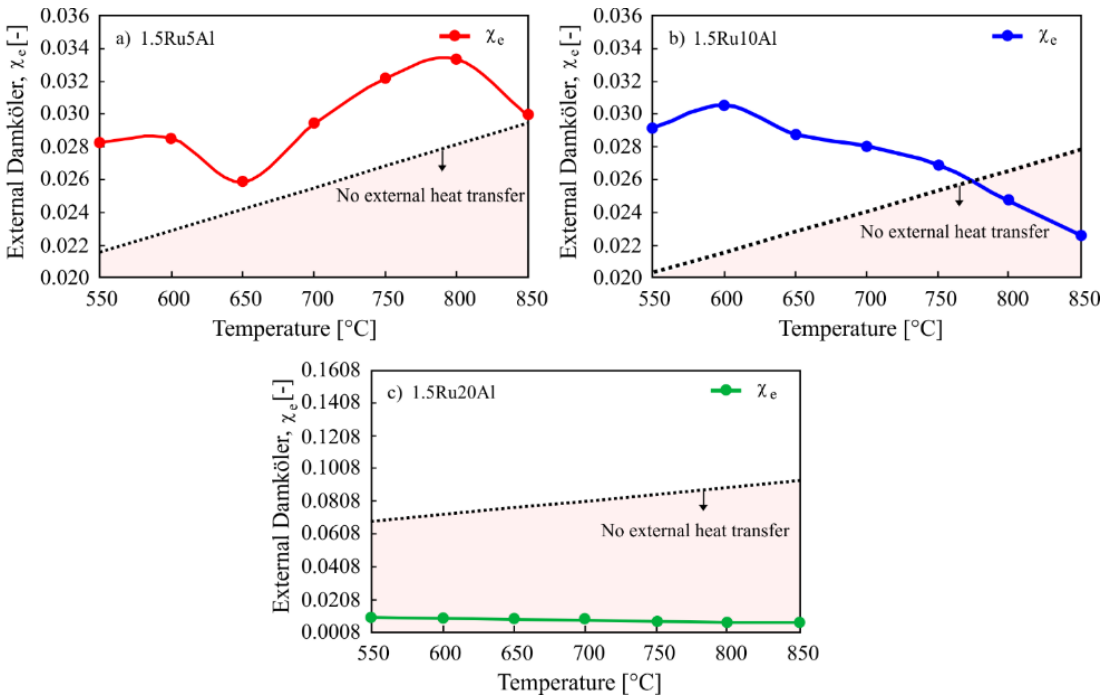


**Figure 40.** Evaluation of external heat transfer limitations using the Mears criterion for the three different catalyst contents: a) 1.5Ru5Al; b) 1.5Ru10Al; c) 1.5Ru20Al (**Paper II**).

As can be observed, only the 1.5Ru5Al and 1.5Ru10Al catalysts exhibited external heat transfer limitations. In particular, the 1.5Ru5Al catalyst displayed thermal limitations over the entire temperature range, while for 1.5Ru10Al catalyst, heat limitations were present at temperatures lower than 775 °C. On the other hand, the structure with higher catalyst content operated without heat transfer limitations related to the fluid phase. It is interesting

to note the remarkable increase of the external Damköhler number of 1.5Ru5Al catalyst at temperatures between 650-800 °C, probably caused by the WGS reaction which due to its exothermicity could lead to an increase of $T_s$. For the 1.5Ru10Al and 1.5Ru20Al catalysts, the $\Delta T$ (evaluated using **Equation 50**) was practically constant as the temperature of the reactant gases increased, approximately 70 and 25 K, respectively.

Internal heat transfer effects were evaluated using Anderson's criterion (**Equation 40**) as shown in **Figure 41**.

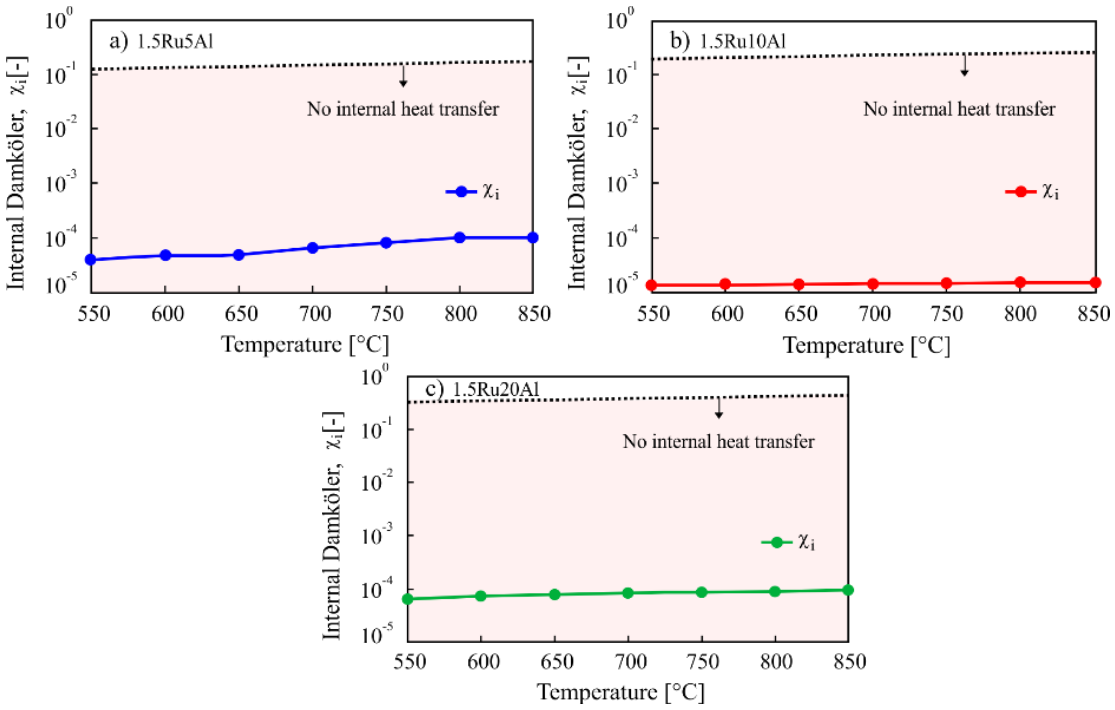


**Figure 41.** Evaluation of external heat transfer limitations using the Anderson criterion for the three different catalyst contents: a) 1.5Ru5Al; b) 1.5Ru10Al; c) 1.5Ru20Al (**Paper II**).

Clearly, neither catalyst exhibited heat transfer limitations related to catalyst layer. These results were also confirmed by the values of the internal Prater number ($\beta_{in}$), which were

much smaller than unity, indicating the complete absence of temperature gradients within the catalyst.

### 2.3.2 Coated ceramic OCF

In order to intensify the methane combustion process under lean conditions carried out in coated foams, the heat transfer effects were analyzed. First, the influence of the catalytic support on heat transport properties was evaluated (**Paper IV**). Then, the effect of the ceramic OCF combination of different thermal conductivity was studied (**Paper VII**). For this scope, the 3 wt. % $PdO/Co_3O_4$ catalyst was coated on three different OCF materials with pore density of 30 ppi. On the other hand, the effect of the foam pore density on heat transfer on biogas steam / oxy-steam reforming reactions was also investigated (**Paper III**). For this aim, alumina ceramic OCFs with different pore densities (20, 30 and 40 ppi) were coated with a thin layer of 1.5 wt. % $Rh/CeO_2$. In this way, it is intended to obtain a much broader vision of the catalyst performance when it is supported on OCF and thus promote and potentiate the catalytic process.

#### 2.3.2.1 Effect of OCF material

In this part of the investigation (**Paper IV**), both the internal and external heat transfer effects were evaluated using the Anderson and Mears criteria, described in *Section 1.4*. Furthermore, a comparative analysis of the heats of reaction and removal of each catalyst was performed. For this purpose, ceramic OCFs made of Alumina (Alu), silicon carbide (SiC) and zirconia (Zir) with pore density of 30 ppi were investigated. About the same

amount of 3 wt.% $PdO/Co_3O_4$ catalyst was deposited on each OCF by SCS and WI techniques. The heat transfer effects were investigated at the following flow conditions: WHSV of 30 NL $h^{-1}$ $g_{cat}^{-1}$, temperature range of 100-700 °C, atmospheric pressure and inlet $CH_4$ concentration of 0.5 vol. %. **Figure 42A** shows the evaluation of external and internal heat transfer effects using the Mears and Anderson criteria for all coated foams.

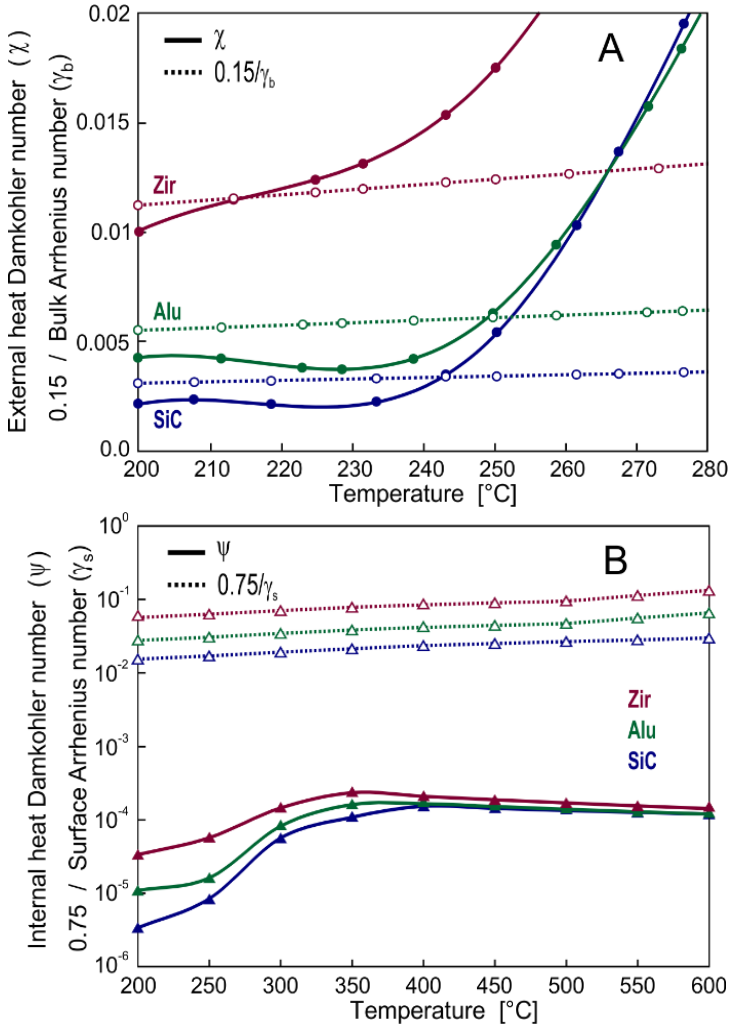


**Figure 42.** Criteria for evaluating the effects of external heat transfer (A) and internal heat transfer (B) for all the OCF catalyst (**Paper IV**).

As observed, the three structured catalysts exhibit external heat transfer limitations at higher temperatures of 215°, 250° and 242 °C for Zir-, Alu- and SiC-OCF, respectively. These possible gas phase-catalyst surface temperature gradients could be due to the strong exothermicity of combustion reaction after ignition. It is also worth noting that the lower the thermal conductivity of OCF, the lower the temperature at which external mass transfer limitations are exhibited. For further analysis, the heat of removal ($Q$) and reaction ($Q_r$) rates were plotted as a function of bulk gas phase temperature, as illustrated in **Figure 43**.

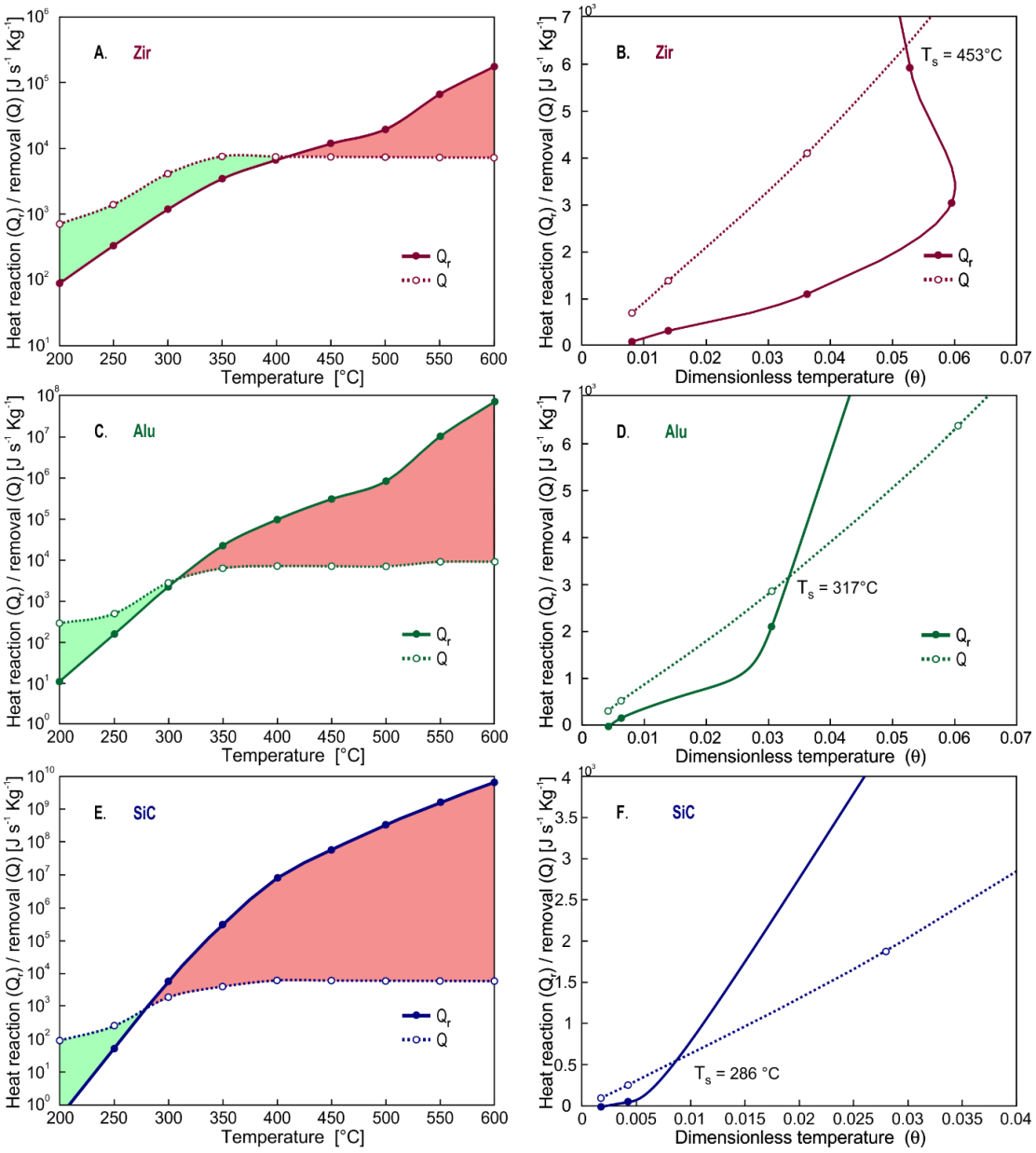


**Figure 43.** Heat reaction and removal rates as a function of bulk and dimensionless temperatures for Zir-OCF (A/B), Alu-OCF (C/D) and SiC-OCF (E/F) (**Paper IV**).

At the flow conditions studied, the Zir-, Alu- and SiC- OCFs operate in a stable zone (in which the heat removed by the effluent gases is greater than the generated heat of reaction)

at temperatures below 400°, 304 and 278 °C, respectively. Moreover, under the steady state condition (point at which the $Q$ and $Q_r$ curves intersect), the temperature at the catalyst surface ($T_s$) for the three coated foams are as follows: $T_{s,Zir-OCF} = 453\ °C$, $T_{s,Alu-OCF} = 317\ °C$, $T_{s,SiC-OCF} = 286\ °C$.

On the other hand, eventual concentration gradients within the catalysts thickness can be ignored based on Anderson's criterion (**Equation 40**), where the values of the internal Damköhler number were found to be much smaller than $0.75/\gamma_s$ (see **Figure 42B**)

### 2.3.2.2 Effect of OCF combination

Considering the promising catalytic performance obtained by combining ceramic SiC/Zir OCFs (described in *Section 2.1.3*), this part of the research is dedicated to the study of heat transfer effects during the catalytic $CH_4$ oxidation in lean conditions conducted on each OCF combination (**Paper VII**). For this purpose, all OCF combinations with pore density of 30 ppi were coated with 3 wt. % $PdO/Co_3O_4$ catalyst using the SCS and WI techniques. The three combinations studied were as follows: SiC1Zir2, SiC1.5Zir1.5 and SiC2Zir1, where the SiC-OCF was placed inside the reactor on the inlet side of reactive gases, followed by the Zir-OCF. Heat transfer effects were evaluated at the following flow conditions: WHSV of 30 and 90 NL $h^{-1}$ $g_{cat}^{-1}$; temperature range of 100-700 °C, atmospheric pressure and inlet $CH_4$ concentration of 0.5 or 1 vol. %. **Figure 44** plots the Nusselt number (**Figure 44A**) and volumetric heat transfer coefficient (**Figure 44A'**) as a function of Reynolds number defined at temperatures of 200°,400° and 600 °C for the three

OCF combinations and for each individual SiC- and Zir- OCF reported in previous work [121].

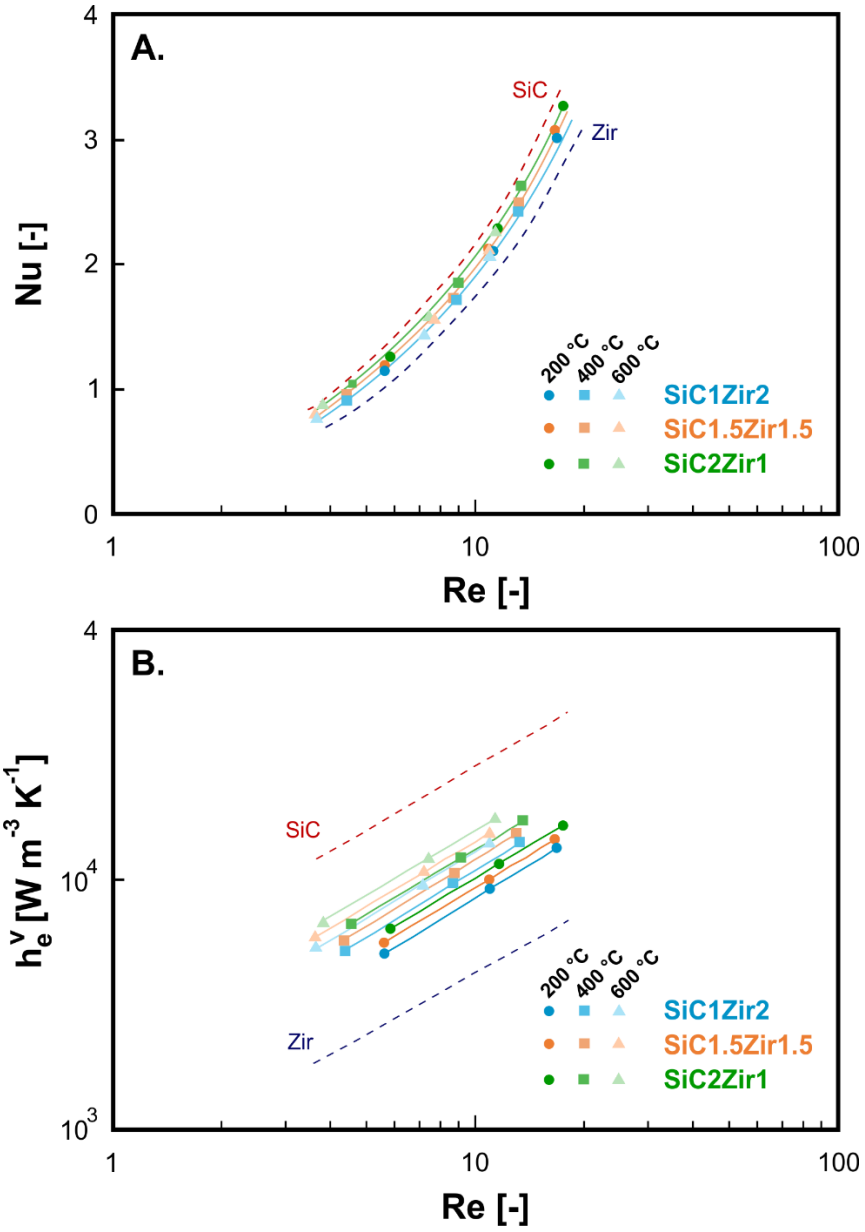


**Figure 44.** Nusselt number and volumetric heat transfer coefficient as a function of Reynolds number defined at temperatures of 200°,400° and 600 °C for the three OCF combinations and for each individual SiC- and Zir- OCF reported in previous work [121] (**Paper VII**).

Clearly, the increase of gas velocity leads to higher fluid turbulence and thus an increase of convective heat transfer. In addition, as the length of the SiC-OCF piece increases in each combination, the higher the superficial gas velocity, at the same flow conditions. This can be explained by the average pore diameter dimensions, which are lower for the SiC-OCF (according to the results extracted from X-ray microtomography, reported in **Paper VI**), thus as the length of SiC-OCF increases in each combination, a larger volume of flow passes through the structure at a higher velocity. Analyzing the Nusselt number results, it is observed that at lower temperatures the Nu number is higher for catalysts with longer SiC-OCF length (SiC2Zir1 > SiC1.5Zir1.5 > SiC1Zir2). However, as the temperature increased, all Nu values were very similar due to the decrease in viscosity of the reactive mixture. Evidently, owing to the higher thermal conductivity offered by the SiC-OCF, the volumetric heat transfer coefficients increased in the following order: SiC2Zir1 > SiC1.5Zir1.5 > SiC1Zir2.

Using the Mears criteria described in *Section 1.4*, the possible external heat transfer limitations for each OCF combination were evaluated. In **Figure 45** are plotted the external Damköhler numbers for the three OCF combinations, at WHSV of 30 and 90 NL $h^{-1}$ $g_{cat}^{-1}$ and inlet $CH_4$ concentration of 1 vol. %.

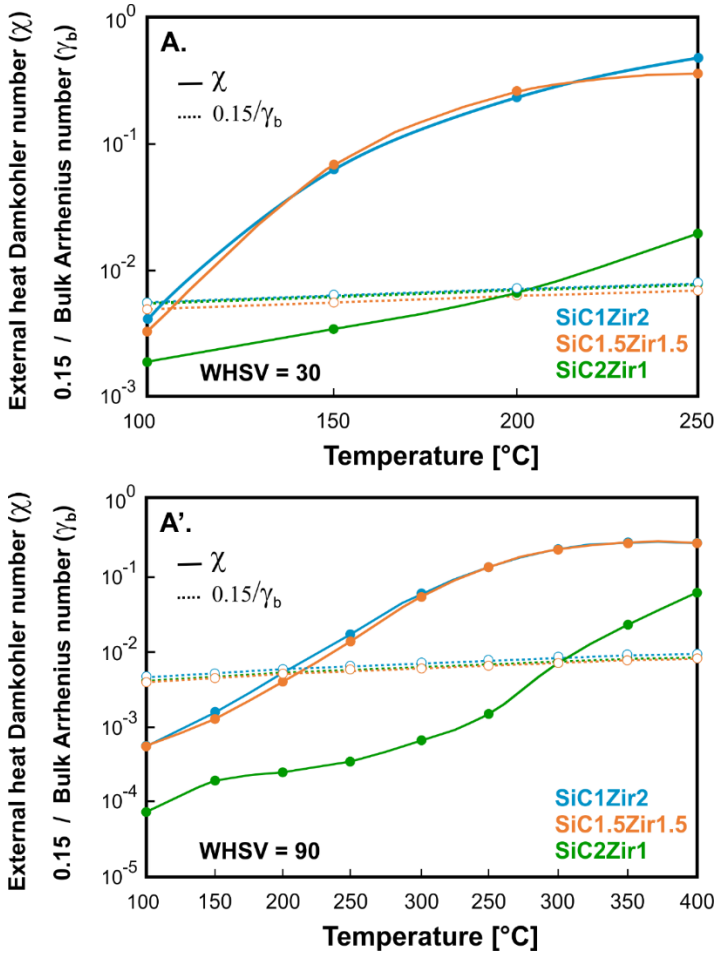


**Figure 45.** Mears criterion to evaluate external heat transfer for all OCF combinations at inlet $CH_4$ concentration of 1 vol. % and WHSV of 30 NL $h^{-1}$ $g_{cat}^{-1}$ (A) and 90 (A') (**Paper VII**).

As observed, interphase heat limitations were found at higher temperatures of 105°, 115° and 200 °C for the combinations SiC1Zir2, SiC1.5Zir1.5 and SiC2Zir1, respectively. Expectedly, the increased gas velocity led to a higher turbulence of the fluid, thus enhancing the convective heat and consequently shifting the external heat transfer limitations towards higher temperatures. As mentioned above, such limitations could be due to the rapid ignition of the reaction resulting in higher heat generation due to the combustion process exothermicity with respect to the heat removed by the flue gases.

The heats of reaction and removal were also analyzed for all the structures studied at WHSV of 30 and 90 NL $h^{-1}$ $g_{cat}^{-1}$, as illustrated in **Figure 46**. Similar $Q$ and $Q_r$ values were found for the SiC1Zir2 and SiC1.5Zir1.5 combinations at both WHSV, with slightly higher values for the latter, which operates in a stable operating zone at temperatures below 160° and 272 °C at WHSV of 30 and 90 NL $h^{-1}$ $g_{cat}^{-1}$, respectively. On the contrary, the SiC2Zir1 combination showed the lowest $Q$ and $Q_r$ values when compared to the other combinations, operating in a stable operating zone at temperatures below 230° and 650 °C at WHSV of 30 and 90 NL $h^{-1}$ $g_{cat}^{-1}$, respectively. These low heat of reaction values could be due to the slowing down of the ignition combustion reaction, as explained in *Section 2.1.3*.

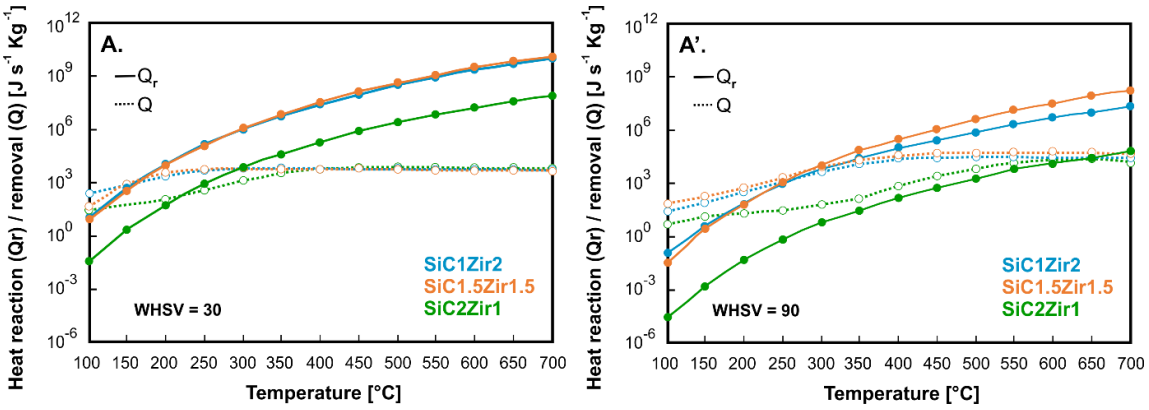


**Figure 46.** Heat reaction and removal rates as a function of bulk temperature for all the three OCF combinations at WHSV of 30 (A) and 90 NL $h^{-1}$ $g_{cat}^{-1}$ (A') and inlet $CH_4$ concentration of 1 vol. % (**Paper VII**).

For a deeper analysis were evaluated the temperature differences between the bulk gas phase and the external catalyst surface (at inlet $CH_4$ concentration of 0.5 vol. %) according to **Equation 50** (see **Figure 47**). As can be seen, the highest $(T_s - T_b)$ were found in the following order: SiC1.5Zir1.5 ≈ SiC1Zir2 > SiC2Zir1. In particular for the SiC1.5Zir1.5

combination, the $(T_s - T_b)_{max}$ was 63° and 92 °C at WHSV of 30 and 90 NL $h^{-1}$ $g_{cat}^{-1}$, respectively. Moreover, it is important to point out that the increase of inlet $CH_4$ concentration led to higher $(T_s - T_b)$ values (for more details see **Paper VII**).

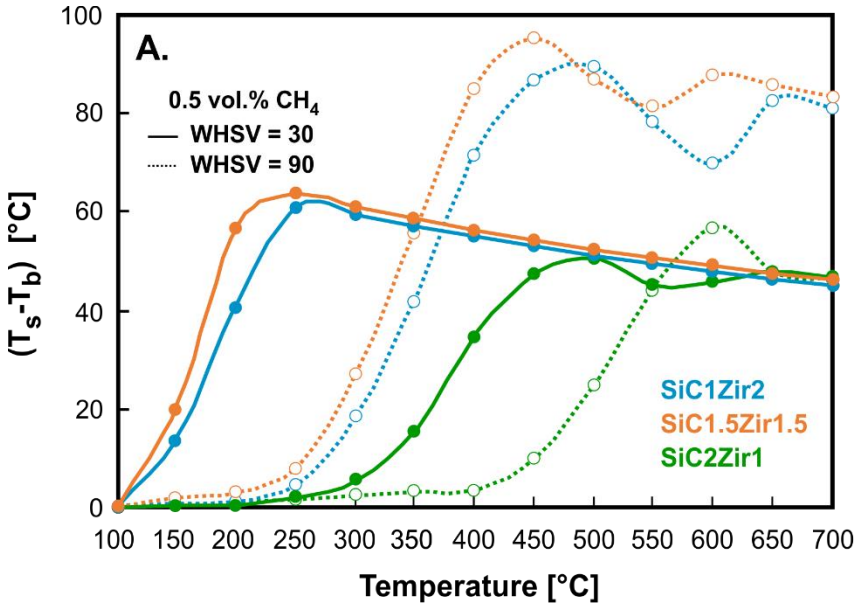


**Figure 47**. Temperature difference between the bulk gas phase and the external catalyst surface as a function of temperature at WHSV of 30 and 90 NL $h^{-1}$ $g_{cat}^{-1}$ and inlet $CH_4$ concentration of 0.5 vol. % for all the OCF combinations investigated (**Paper VII**).

Finally, the possible temperature gradients within the catalyst layer were evaluated using Anderson's criterion, as plotted in **Figure 48**. It is clear that for three OCF combinations, the internal Damköhler numbers are much lower than the limiting value $(\frac{0.75}{\gamma_s})$, at both WHSV studied, indicating the absence of temperature gradients across the catalyst thickness.

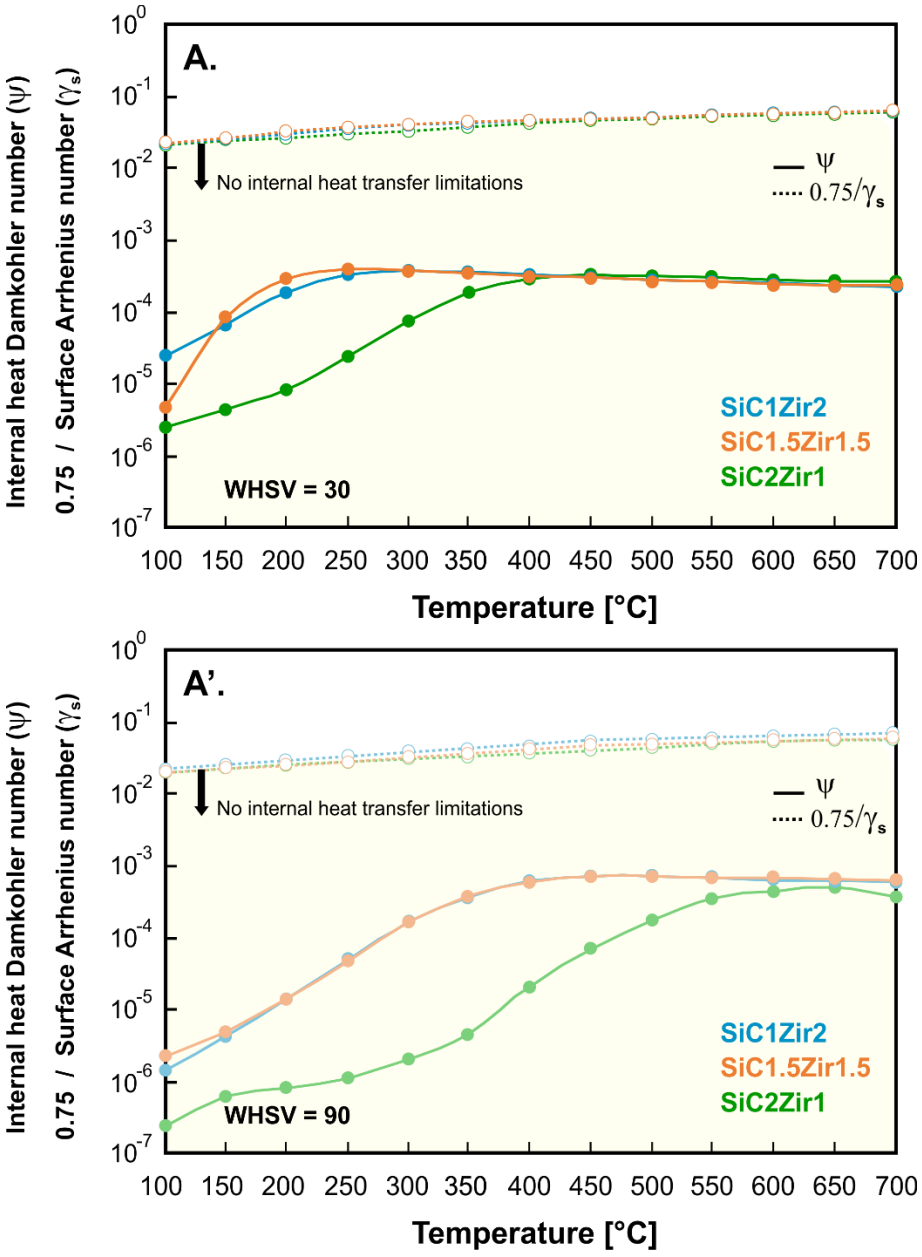


**Figure 48**. Anderson criterion to evaluate internal heat transfer for all OCF combinations at inlet $CH_4$ concentration of 1 vol.% and WHSV of 30 (A) and 90 (A') NL $h^{-1}$ $g_{cat}^{-1}$ (**Paper VII**).

#### 2.3.2.3 Effect of OCF pore density

In this section (**Paper III**), the heat transfer effects on biogas steam / oxy-steam reforming reactions were studied. For this purpose, ceramic OCFs made of alumina with different pore densities (20, 30 and 40 ppi) were coated with a thin layer of 1.5 wt.% $Rh/CeO_2$ catalyst using the SCS and WI methods, as mentioned in *Section 2.1.4*. The experiments were carried out at the following flow conditions: S/C of 3 (for SR) and S/C of 1 with $O_2/CH_4$ molar ratio of 0.2 (for OSR), atmospheric pressure, temperature of 800° and 900 °C and WHSV of 35-140 NL $h^{-1}$ $g_{cat}^{-1}$.

Interestingly, all the coated OCFs satisfied the Mears criterion, indicating the absence of heat transfer limitations between the gas phase and the outer catalyst surface. Nevertheless, it is important to highlight that higher values were obtained as the OCF pore density decreased (F20>F30>F40). This is due to the fact that the lower the pore density, the smaller the specific surface area and the larger the pore dimensions. Therefore, OCFs with a smaller pore size favor the velocity of the reactive gases and thus the turbulence, improving the transfer of both heat and mass.

Likewise, for all structured catalysts, the temperature gradients within the catalyst thickness can be neglected, thanks to the satisfaction of the Anderson criterion. The values obtained were much lower than 0.75, mainly due to the extremely thin coating layer.

## 2.4 Physico-Chemical characterization

This section is dedicated to present the most relevant results obtained from the physico-chemical characterization of both powder and structured catalysts. In particular, it is focused on OCFs as a support for catalysts.

### 2.4.1 Raman spectroscopy

**Figure 49** shows the Raman spectra of all the coated ceramic foams (of 30 ppi) investigated in **Paper IV**. As observed, the three recorded spectra are almost identical, indicating that the catalyst deposition method allowed to coat the structures while maintaining its chemical characteristics, independently of the foam material. The lines located at 487, 526, 624 and 694 $cm^{-1}$, correspond respectively to the $E_g$, $2xF_{2g}$ and $A_{1g}$ vibrational modes of the crystalline spinel of $Co_3O_4$ [41,256], thus confirming its presence in all the structures. These spectra are almost coincident with those obtained for the $PdO/Co_3O_4$ catalyst synthesized as powder in previous works [42]. On the other hand, due to the low concentration of deposited PdO, it was not possible to detect the expected Raman spectra of PdO around 467, 640 and 680 $cm^{-1}$ ($E_g$ and $B_{1g}$ vibrational modes) [42,217]

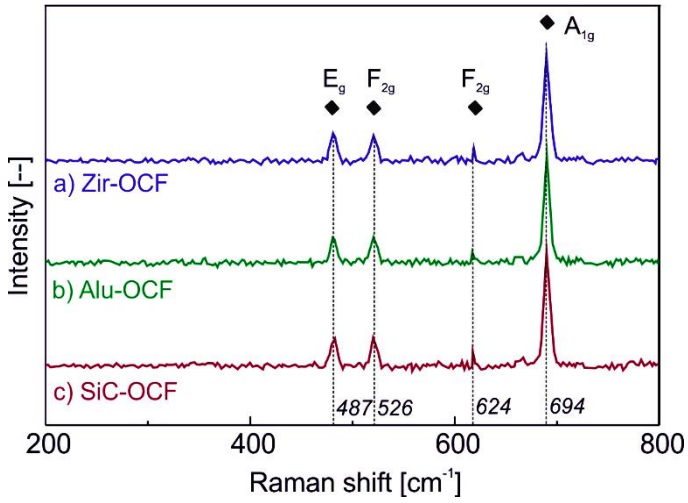


**Figure 49.** Raman spectra of the three OCF coated with 3 wt. % PdO on 200 mg $Co_3O_4$ (**Paper IV**).

## 2.4.2 FESEM / SEM

### 2.4.2.1 PdO/$Co_3O_4$ on OCF

The morphology and homogeneity of the catalyst coating on Zir-OCF was investigated. **Figure 50** shows the bare and 3 wt. % PdO/$Co_3O_4$ catalyst coated structure.

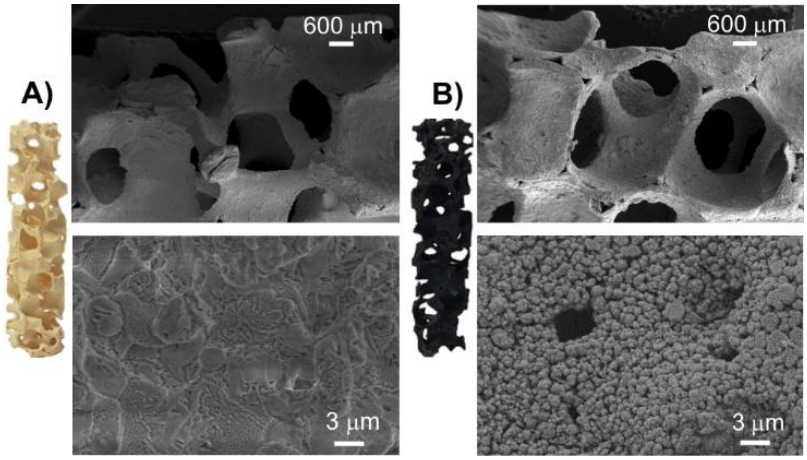


**Figure 50**. Zir-OCF of 30 ppi: A) bare structure, and B) coated structure with 3 wt,% PdO/$Co_3O_4$. FESEM images at 40X and 10,000X magnification (**Paper IV**).

The surface of bare Zir-OCF shows an apparently flat appearance while once coated with the catalyst its surface becomes rough, due to the gases released during the SCS reaction [60,199]. Moreover, as can be observed, the catalyst layer is homogeneously distributed throughout the foam and very well anchored, with an average thickness of about 55 ± 15 μm. These results are in agreement with those obtained in literature for similar structures. SiC- and Alu-OCF showed similar morphology and thickness.

### 2.4.2.2 $Rh/CeO_2$ on OCF

**Figure 51** shows the SEM micrographs of alumina OCF coated with 1.5 wt. % $Rh/CeO_2$ at different magnifications.

A homogeneous catalyst coating fully covered the alumina OCFs (of different pore densities: 20, 30 and 40 ppi) without clogging of cells or pores. Moreover, a good interconnection between the OCF structure and the coated catalyst layer can be observed from the cross-sectional view (**Figure 51a'**, **51b'** and **51c'**). Catalyst thicknesses of 5-20 μm, 15-30 μm and 25-40 μm for F40, F30 and F20 were found respectively.

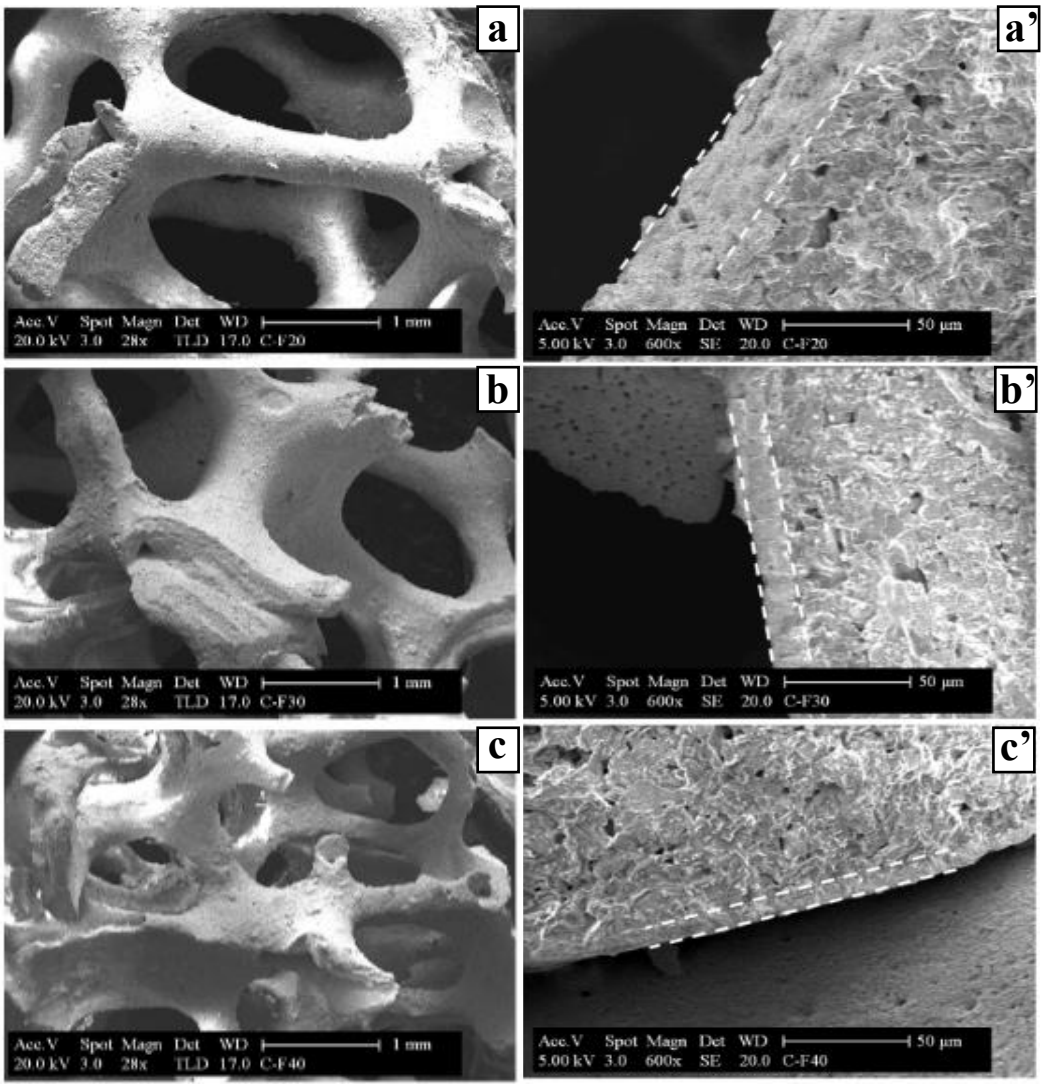


**Figure 51**. SEM micrographs at different magnification and cross sectional view of the $Rh/CeO_2$-coated F20 (a,a'), F30 (b,b') and F40 (c,c') (**Paper III**).

## 2.4.3 HAADF STEM and EDX

### 2.4.3.1 $PdO/Co_3O_4$ on OCF

PdO dispersion on the spinel $Co_3O_4$ coated on Zir-OCF was studied before and after the stability test (**Paper IV**). **Figure 52** shows the HAADF images of the fresh and aged structured catalyst.

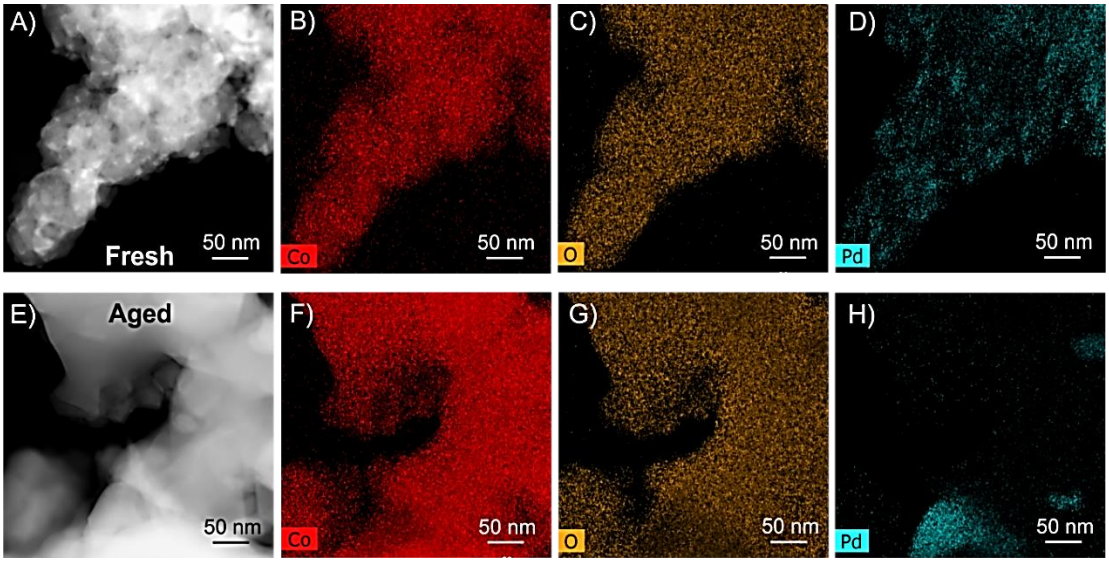


**Figure 52.** HAADF STEM images and EDXS mappings showing Co, O, and Pd distribution in (A/B/C/D) freshly prepared Pd/Co3O4 and, (E/F/G/H) 250 hours aged $PdO/Co_3O_4$, collected from Zir-OFC tested in Figure 12 (**Paper IV**).

Since it was difficult to distinguish the Pd particles from $Co_3O_4$, because of the inadequate contrast difference between them, it was not sufficient to use the Z-contrast in the HAADF images. Therefore, EDX mapping was used to identify the Pd-rich regions. **Figure 52D**, shows that Pd is homogeneously distributed on the surface of the spinel $Co_3O_4$ covering

the analyzed region to a large extent for the fresh catalyst. Moreover, the EDX maps of Co and O overlap each other, indicating the absence of Co segregation in both samples (see **Figure 52 B/C**). In addition, their distribution does not seem to vary as the catalyst is aged, suggesting that the $Co_3O_4$ crystals are conserved. However, when the catalyst is fresh, the $Co_3O_4$ presents a rough morphology, whereas in the aged sample it appears to be denser. On the other hand, unlike $Co_3O_4$, the distribution of Pd is not homogeneously distributed after use, but is concentrated only in preferential areas. A possible local segregation of Pd is observed in **Figure 52H**, with a slight reduction of PdO dispersion in the aged catalyst.

#### 2.4.3.2 Rh/$CeO_2$ on OCF

The dispersion of Rh on the $CeO_2$ coated on alumina OCFs of different pore densities was investigated (**Paper III**). **Figure 53** shows the EDX mapping for the three structures (F20, F30 and F40).

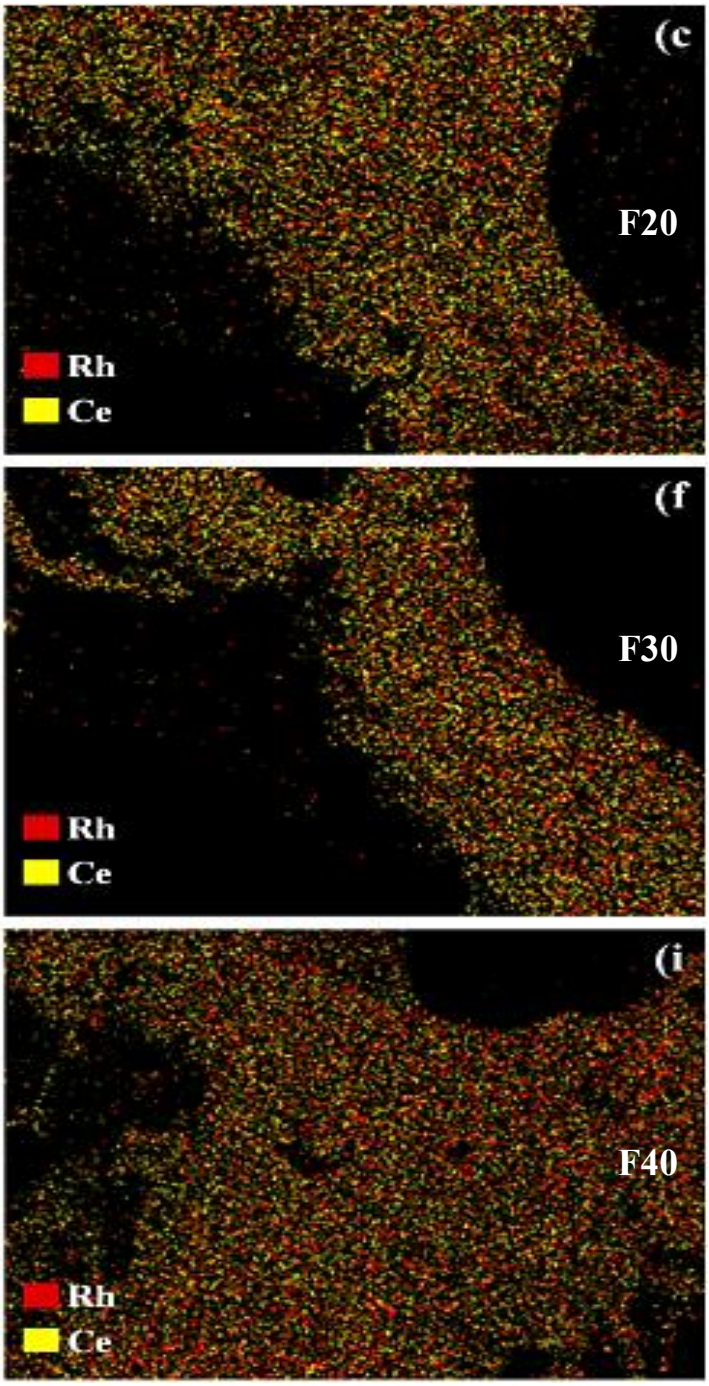


**Figure 53**. EDX mapping for F20 (c), F30 (f) and F40 (i) coated with 1.5 wt. % Rh/$CeO_2$ (**Paper III)**.

As can be seen, the three coated OCFs evidenced that $CeO_2$ is well deposited on the foam surface. Moreover, the active metal seems to be well dispersed along the surface of ceria.

### 2.4.4 XRD

The XRD patterns of $Rh/CeO_2$ as a powder, bare and $Rh/CeO_2$-coated alumina OCF of 30 ppi. **Figure 54** shows the XRD pattern of Rh $Rh/CeO_2$ as a powder, bare and $Rh/CeO_2$-coated F30.

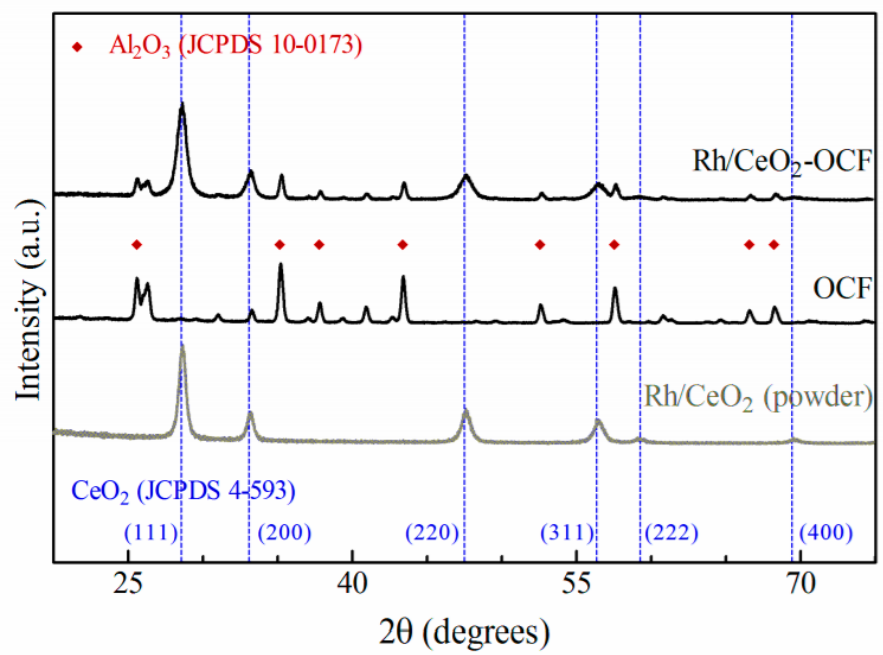


**Figure 54.** XRD pattern of $Rh/CeO_2$ as a powder, bare and $Rh/CeO_2$-coated F30 (included also reference peaks of $CeO_2$: JPDS 4-593 and reference peaks of $Al_2O_3$: JPDS 10-0173) (**Paper III**, Supporting Information).

The diffraction peaks related to the bare alumina OCF can be assigned to the α-$Al_2O_3$ phase (JCPDS 10-0173), with peaks located at 25.59° (012), 35.16° (104) 37.81° (110), 43.38° (113) 52.58° (024), 57.52° (116), 66.57° (214) and 68.27° (306) [257,258]. After depositing the Rh/$CeO_2$ catalyst layer on the OCF, both cubic $CeO_2$ fluorite type and α-$Al_2O_3$ phase were identified. Similar results were found for the F20 and F40 structured catalysts. On the other hand, the diffraction pattern analysis of the powder catalyst identified the crystalline planes of the face-centered cubic $CeO_2$ (JCPDS 4-593) with typical diffraction peaks at 28.55° (111), 33.08° (200), 47.50° (220), 56.33° (311), 59.26° (222) and 69.41° (400) [259]. No diffraction peaks of Rh oxides were detected, due to the low charge and high dispersion of the noble metal [260].

## 2.4.5 Thermogravimetric analysis (TGA)

The results of the TGA water adsorption experiments are shown in **Figure 55**. As mentioned in *Section 1.6.4.8*, the response of the system to the introduction of 1 vol. % $H_2O$ saturated with Ar was evaluated by performing a blank test with an empty crucible. The apparent change in mass for the blank test was about 0.007 mg (see **Fig. 55**). This value was subtracted from the masses of adsorbed water determined for undoped and 5 wt. % PdO-doped $Co_3O_4$ (**Fig. 55A** and **55B**). Considering the specific surface area of the catalysts, a surface concentration of reversibly adsorbed water was estimated, resulting in 0.5 and 2.5 $H_2O$ molecules per $nm^2$, for the undoped and 5 wt. % PdO/$Co_3O_4$ catalysts, respectively. The stronger interaction with water for 5% PdO/$Co_3O_4$ could be the result of a higher basicity of oxygen ions on the $Co_3O_4$ surface, or the high abundance of PdO nanocrystals, as demonstrated by the FESEM images previously reported by our same

research group [44]. At 350 °C, the TGA apparatus could not detect water adsorption on any of the samples (**Fig. 55D**, only 5% $PdO/Co_3O_4$ is shown). The observed effect may be due not only to the high process temperature [261] but also because of the relatively small specific surface areas of the catalysts. Thus, since the amounts adsorbed by the catalysts were quite small, it can be concluded that water interferences have a minimal influence on the detection process.

It is also important to highlight that all catalytic tests toward methane combustion in lean conditions were carried out under dry conditions, i.e. without water in the feed. Although, it has been well reported that the presence of $H_2O$ has a strong inhibitory effect on palladium-based catalysts during methane oxidation. A recent study by Nasr et al.[246] has shown that the activity of $Co_3O_4$ is not affected by water concentration and the $Pd/Co_3O_4$ catalyst is less susceptible to water poisoning compared to PdO and $Pd/Al_2O_3$, which tend to exhibit negative first order behavior with respect to $H_2O$. These results appear to be in line with those obtained in **Figure 55**, where the amount of water absorbed by $Co_3O_4$ was very small, suggesting little interaction with the catalyst active sites. The authors also reported that $Co_3O_4$ exhibited first order behavior with respect to methane and zero order for water, with activation energies similar to those obtained in dry methane combustion studies on $Co_3O_4$. However, during hydrothermal aging the catalyst progressively lost its active sites by sintering (BET surface area dropped from 12 to 7 $m^2\ g^{-1}$). Evidently, the presence of water could have an impact not only on the evaluation of the catalyst activation energy but also on the controlling regimes of the catalytic process (kinetics/internal mass transfer). Since multiple sites with different affinity to water are involved in the activation of methane on $Co_3O_4$ and that in Pd-based catalysts, water is an accepted most abundant

surface-dominated intermediate. A near future goal of this research will be to evaluate the effect of water on the fed reactive gas mixture from the point of view of catalytic performance, catalyst stability, kinetics and internal catalyst mass transfer, thus encompassing a more realistic evaluation of the combustion process.

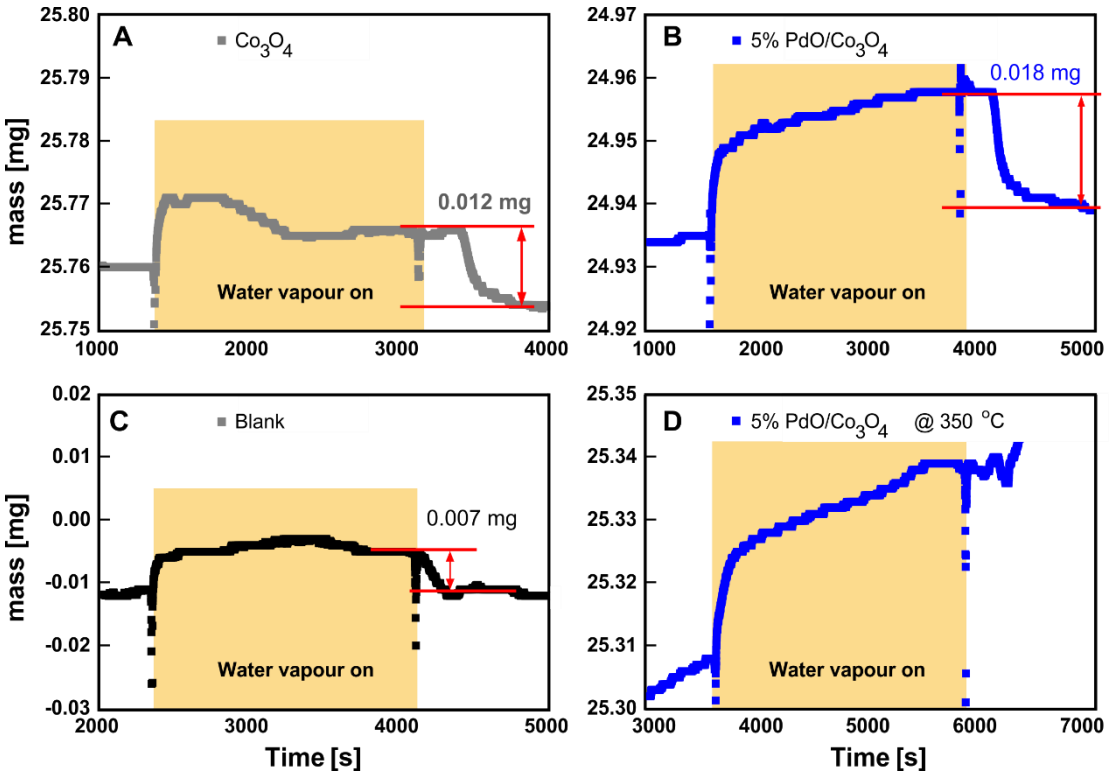


**Figure 55.** Thermogravimetric profiles of equilibrium water adsorption experiments for undoped and 5 wt.% Pd-doped $Co_3O_4$ samples. A) undoped $Co_3O_4$ at 30 °C, B) 5% Pd/$Co_3O_4$ at 30 °C, C) blank test at 30 °C, D) 5% Pd/$Co_3O_4$ at 350 °C.

### 2.4.6 Adhesion test on OCF

#### 2.4.6.1 $PdO/Co_3O_4$ on OCF

In this part of the research (**Paper IV**), the adhesion properties of the $PdO/Co_3O_4$ catalyst on OCF foam were evaluated using a sonication treatment. For this purpose, approximately the same amount of catalyst was deposited on ceramic OCFs made of Zir, Alu and SiC of 30 ppi. According to the results obtained, the three catalytic structures showed an adherence percentage of 98.3 to 98.8 %, showing a strong interaction between the catalytic layer and the wall of the structures. These results confirm an excellent adhesion of the catalyst, independently of the nature of ceramic OCF.

Catalyst adhesion was also evaluated by increasing the catalyst content ($C_{load}^{100}$, $C_{load}^{150}$ and $C_{load}^{250}$) on Zir-OCF of 30 ppi (**Paper V**). After sonication treatment, the weight loss of the catalysts was found to be between 1 and 2 %, indicating excellent adherence of $PdO/Co_3O_4$ catalyst on Zir-OCF. These results were in agreement with those found in the literature [121,167]. It is worth mentioning that the adhesion values decreased with increasing catalyst thickness as follows: 98.6 % for $C_{load}^{100}$, 98.4 % for $C_{load}^{150}$ and 98.1 % for $C_{load}^{250}$. Nevertheless, no dramatic weight loss occurred with increasing catalyst content on the OCF, suggesting a high catalyst compactness.

#### 2.4.6.2 $Rh/CeO_2$ on OCF

Here, the adhesion of $Rh/CeO_2$ catalyst layer on alumina OCFs of different pore density (20, 30 and 40 ppi) was studied via ultrasonic treatment in isopropyl alcohol solution. The

weight loss in each structure (F20, F30 and F40) after each stability cycle (explained in detail in **Paper III**) are shown in **Figure 56**.

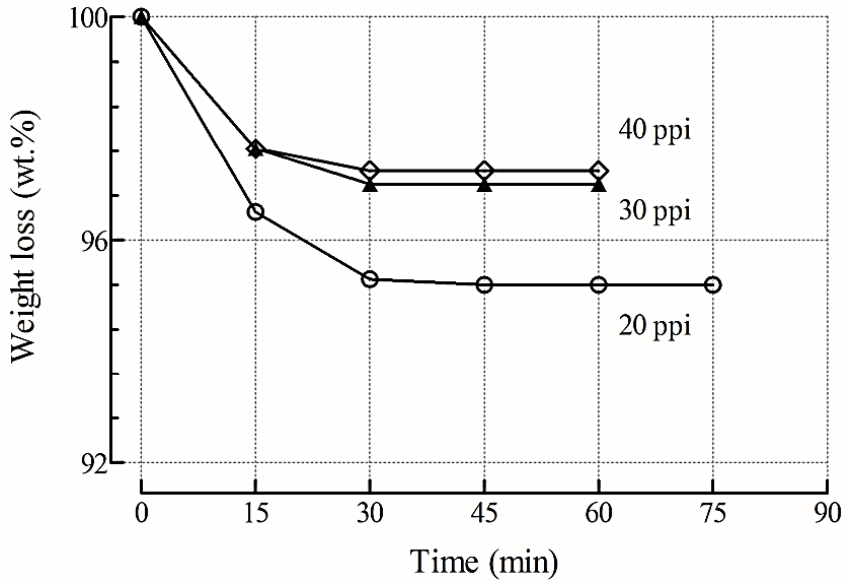


**Figure 56**. Weight loss as a function of time during the ultrasonic treatment of the coated alumina OCF (**Paper III**).

As observed, all three coated OCFs (F20, F30 and F40) showed optimal adhesion of the catalyst layer with weight losses lower than 5%. Therefore, SCS allowed to overcome the coating exfoliation that usually occurs in conventional dip coating techniques [120,262,263]. Different authors suggest that the increased catalytic thickness hinders the adhesion of the coating due to the convex surface of the OCF structures [112]. This explains the increased weight loss as the pore density of OCF decreases.

## 2.4.7 Pressure drops on OCF

Low pressure drop is a fundamental property in reactor design, especially for short contact time reactors. In this research, the effect of pore density (**Paper III, Paper VI**) and foam material (**Paper VI**) on the pressure drop of OCFs was investigated at different superficial gas velocities. In **Paper III**, alumina foams with pore densities of 20, 30 and 40 ppi were used. **Figure 57** shows the pressure drops of all foam structures. By fitting the experimental values to a quadratic function of gas velocity using the Forchheimer-Extended Darcy equation model (**Figure 57a**), it was possible to determine the hydraulic properties of the porous medium: permeability and form drag coefficient. In particular, the permeability decreased with increasing pore density from $6.7\times10^{-8}$ (F20, alumina OCF of 20 ppi) to $2.9\times10^{-8}$ $m^2$ (F40, alumina OCF of 40 ppi). On the other hand, the form coefficient increased with increasing pore density from 122.1 to 300.6 $m^{-1}$ for 20 ppi and 40 ppi OCFs, respectively. These values were in line with those obtained by Wang and Guo [264]. On the other hand, the Ergun model was also used to fit the experimental data (**Figure 57c**), resulting in good agreement for all the OCFs studied. As expected, the pressure drop increases with increasing pore density and voidage of the foams.

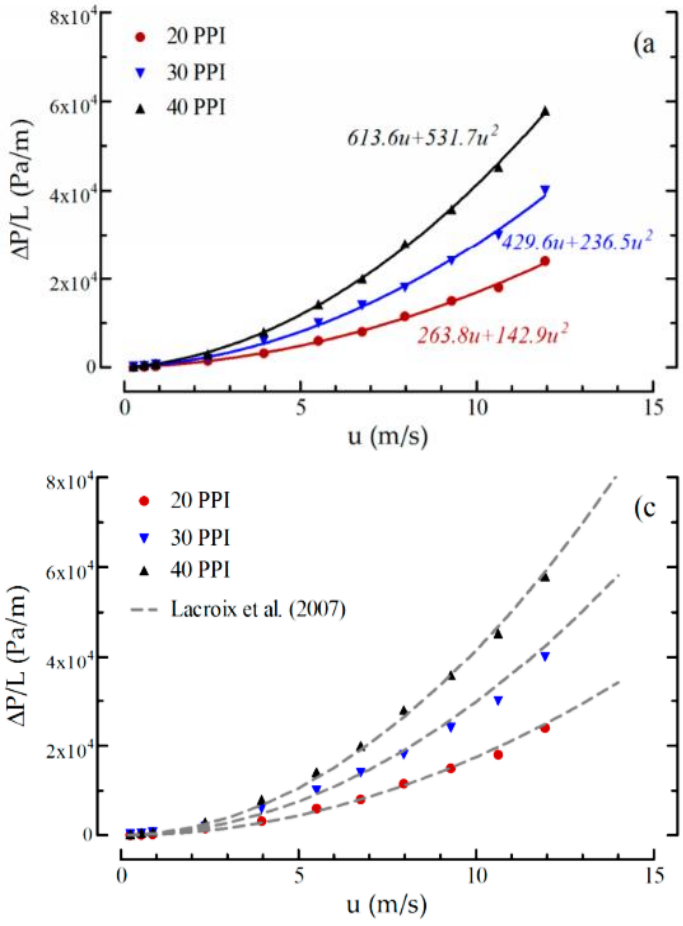


**Figure 57.** Pressure drop measurements for different foam density: Forchheimer-extended Darcy theoretical estimation (a) and Lacroix-extended Ergun theoretical estimation (c) (**Paper III**).

## 2.4.8 X-ray micro-computed tomography

This part of the study focused on the characterization of ceramic OCFs made of zirconia, silicon carbide and alumina of different pore density (30 and 45 ppi) using the computed X-ray microtomography technique (**Paper VI**). This technique allowed the exhaustive and quantitative extraction of morphological and geometrical characteristics of the foams such

as pore density, strut diameter and length, open porosity and specific geometrical surface area. **Figure 58** shows the 2D image slices extracted from the CT reconstruction and the mean and standard deviation of strut diameter, strut length, and pore diameter measured for all OCFs studied. The increase of pore density leads to a much more compact structure due to the higher number of cells and thus of struts per unit volume of foam, regardless of the ceramic material type. Therefore the increase in ppi led to a decrease of morphological properties, since the higher the number of pores per linear inch, the smaller the cell size. In particular, Zir-OCF showed the largest dimensions of morphological properties compared to SiC and Alu foams at the same pore density. On the contrary, the smallest sizes were found for SiC-OCFs.

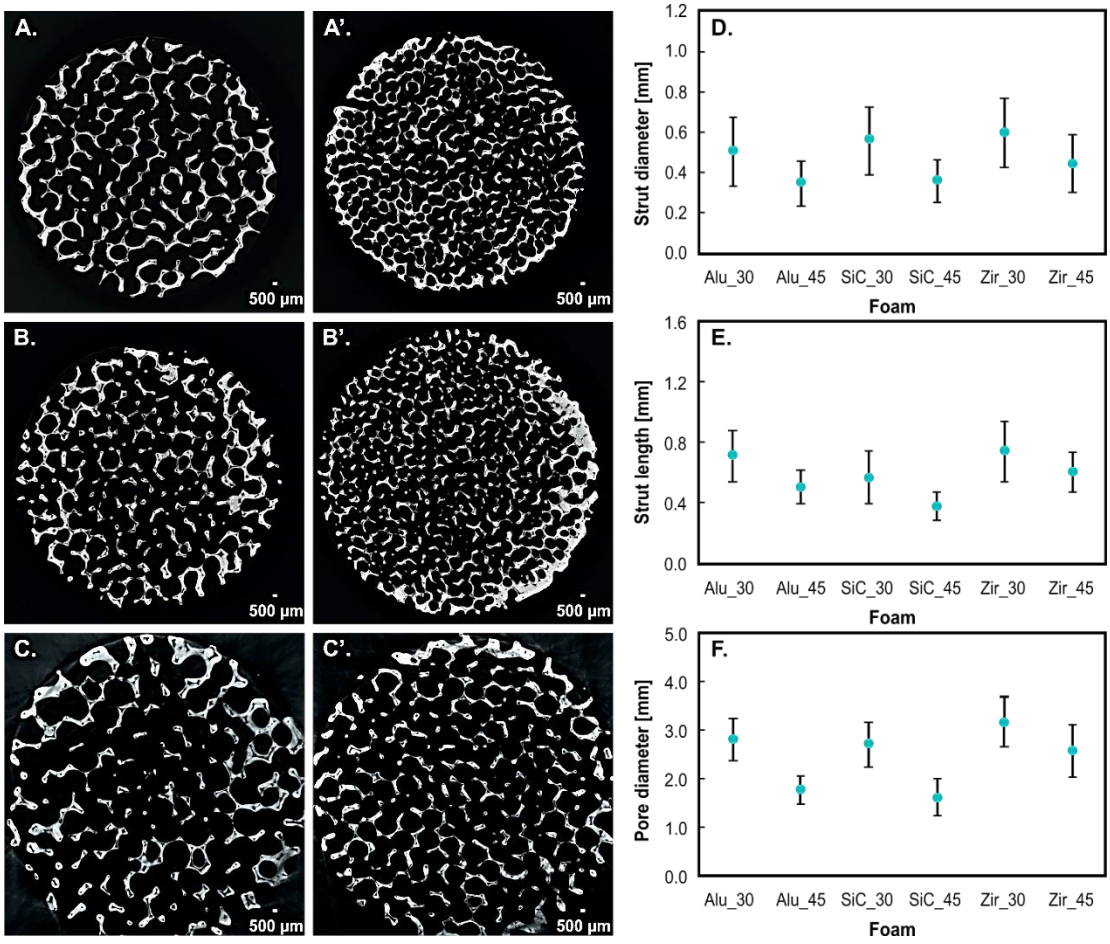


**Figure 58.** 2D reconstructed CT slices (pixel size of 22 µm) for Alu_30/Alu_45 (A/A'), SiC_30/SiC_45 (B/B'), Zir_30/Zir_45 (C/C') and the mean and standard deviation of strut diameter(D), strut length (E), and pore diameter (F) measured for all OCFs studied (**Paper VI**).

A further interesting point to highlight from the results obtained by micro X-CT is the presence of microporosity in the walls of foam skeleton [140,146,149,195,265,266], as observed in **Figure 59a**. This microporosity is also called strut porosity and is attributed to the manufacturing process of ceramic foams (replication technique), which gives rise to

hollow struts with internal volume. Furthermore, the foams were characterized by the presence of dense grains along the microporous walls, caused during the foam preparation stage (see **Figure 59c**) [267–269]. Moreover, it is important to point out that all the foams showed a circular cross-sectional shape (**Figure 59b**). Different authors suggest that ceramic foams with porosity lower than 90% are characterized by a circular shape of struts while metallic foams can vary from triangular to concave depending on the degree of foam porosity [95,105,270–273].

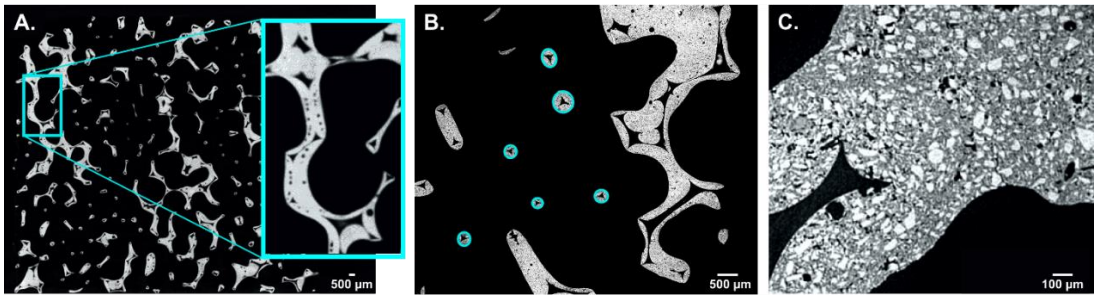


**Figure 59.** Foam micro-porosity (A: Alu_30), circular strut cross section (B: Alu_30) and dense grains along the micro-porous walls (C: SiC_30) (**Paper VI**)

Once the 3D images were reconstructed, it was possible to extract the macroporosity and specific surface area of the ceramic OCFs. **Figure 60** shows preliminary steps prior to the image reconstruction. The open porosity values were very similar to those reported by the manufacturer with a difference lower than 5%. Expectedly, the higher the pore density, the lower was the open porosity of the OCFs, independently of the material nature. In particular, the open porosity values increased in the following order (at the same pore

density): SiC < Alu < Zir. Moreover, it is important to note that the open porosity values were lower than 90%, which is consistent with the porosity values reported for ceramic foam structures.

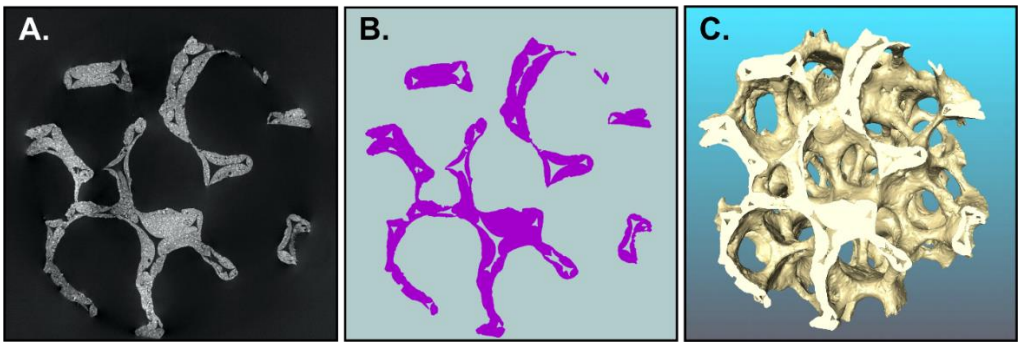


**Figure 60.** (A) Raw gray scale micro-CT data of SiC_30, (B) after grayscale-based thresholding according to the method of Otsu [274], (C) 3D reconstruction of the OCF (**Paper VI**).

Regarding the specific surface area, the increase in pore density led to higher specific areas. At 30 ppi, higher specific surface area values were found for Zir-OCF followed by Alumina-OCF, while SiC-OCF showed the lowest value. However, as the pore density increased to 45 ppi, higher specific surface areas were found in the following order: Zir < Alu < SiC.

Now, the validity and suitability of state-of-the-art correlations on ceramic foams of different material, pore density and open porosity developed mainly for circular strut cross-sectional area shapes will be examined. Although, some models developed for foams with triangular strut cross-section will also be compared. For this purpose, the theoretical [104,140,197,237,265] (based on predictions from correlations reported in literature) and

experimental [149,236,265,266,275,276] (presented both in literature and this dissertation) dimensionless surface area were plotted in **Figure 61** as a function of foam open porosity. From the experimental results, a wide variability of the dimensionless values of specific surface area is observed when varying the open porosity. Particularly, the values reported in this work presented an increase of up to 75 % with respect to those reported in literature in foams of the same material. In fact, when analyzing the experimental values reported by Garrido et al.[149], Grosse et al.[265] and Dietrich et al.[266] on alumina foams with pore density of 30 ppi and nominal open porosity of 0.80, a difference of 44.4, 48.0 and 40.8 %, respectively is observed with respect to the values obtained in this research. Nevertheless, this discrepancy between the experimental values is reduced to approximately 27 % when confronting the 45 ppi alumina foams at the same nominal porosity. This difference between experimental values in foams of the same material, pore density and open porosity has been previously reported by different authors [149,275,276] and has been attributed to the variability and random structure of ceramic foams prepared by different manufacturers. Even if, in most cases, the same preparation technique (polymeric sponge replication) is used, the different stages during the structure production play a fundamental role in the final foam skeleton. Thus, foams of the same chemical composition could have quite different morphological parameters from manufacturer to manufacturer. Moreover, it is well known that the term pore density conventionally used by fabricators to define the number of pores per linear inch (ppi) could also vary from manufacturer to manufacturer, since this definition is not univocal, some fabricators or even researchers do not distinguish between the terms pore and cell. Thus, pore density does not provide an accurate measure but simply represents a range of cell or pore sizes. It is also worth noting the importance

of the imaging techniques and method used for the measurement of the morphological properties of the structure as this could significantly influence the estimation of the geometric parameter value. Such is the case of the results obtained by X-ray tomographic image analysis in **Paper V** and **Paper VI** for zirconia foams with a pore density of 30 ppi. In **Paper V**, zirconia foams with slices of approximately 9 mm diameter were analyzed, while in **Paper VI**, in order to obtain a wider range of measurements and a more accurate estimate of the geometrical parameter, slices of 40 mm diameter were evaluated. The mean pore diameter and strut values increased in 52 and 16%, respectively, when considering a larger foam sample, while the open porosity remained practically the same. Therefore, the mass transfer correlation reported in **Paper V** has a validity in the range of $1.24 < d_p < 1.38$ mm with foam void fraction of $0.75 < \varepsilon_o < 0.85$. In future work, the mass transfer correlation presented in *Chapter V* will be generalized to metal and ceramic foams considering a wide range of pore diameter and porosity.

On the other hand, when comparing the various correlations proposed in literature, it can be observed that although they were developed considering different geometrical models, some of them have exhibited similar results in certain porosity ranges. For instance, the Richardson et al.[140] and Ambrosetti et al. [237] correlations developed for circular strut shape show a deviation of less than 30% for the entire porosity range evaluated. On the other hand, the Lucci et al.[197] and Ambrosetti et al.[237] correlations exhibit a difference of less than 10% at porosities below 0.80. All these mentioned correlations have been developed based on a TTKD model with a circular cross section strut. However, when confronted with those derived using the same geometrical model but considering triangular strut shape

(as reported by authors Buciuman et al.[104] and Richardson et al.[140]), the deviations increase with increasing foam porosity. By contrast, the correlation proposed by Grosse et al.[265] using the Weaire-Phelan model deviates significantly from the predictions presented by the aforementioned authors. Although, at porosity greater than 0.85, the Buciuman correlation tends to be closer to the Grosse model (with deviations less than 20%). When confronting the experimental values with the proposed models, the latter seem to suffer from a large deviation. The theoretical models tend to overestimate the specific surface area measured. [The specific surface area values reported in **Paper IV** and **V** were calculated using the TTKD model proposed by Buciuman et al. [104]. Thus, although the pore and strut diameters were measured experimentally, the $S_{ag}$ value was estimated according to the model mentioned above]. The deviation of the theoretical models from experimental data can be attributed to the assumptions made during the derivation of the geometrical model. Most authors assume a solid strut structure with a constant thickness and a cross section without solid accumulation. However, the real foams have hollow struts with a considerable accumulation of solid material in the vortex area (where the struts are joined), generated by the fabrication process. In addition, during the coating stage of the polymeric matrix, bubbles may form in the cells due to the slipping of ceramic material. As a consequence, some pores in real foams could be partially or completely closed. These factors lead to a lower specific surface area in real foams compared to ideal models, where not only specific surface area values are overestimated but also the impact of void fraction.

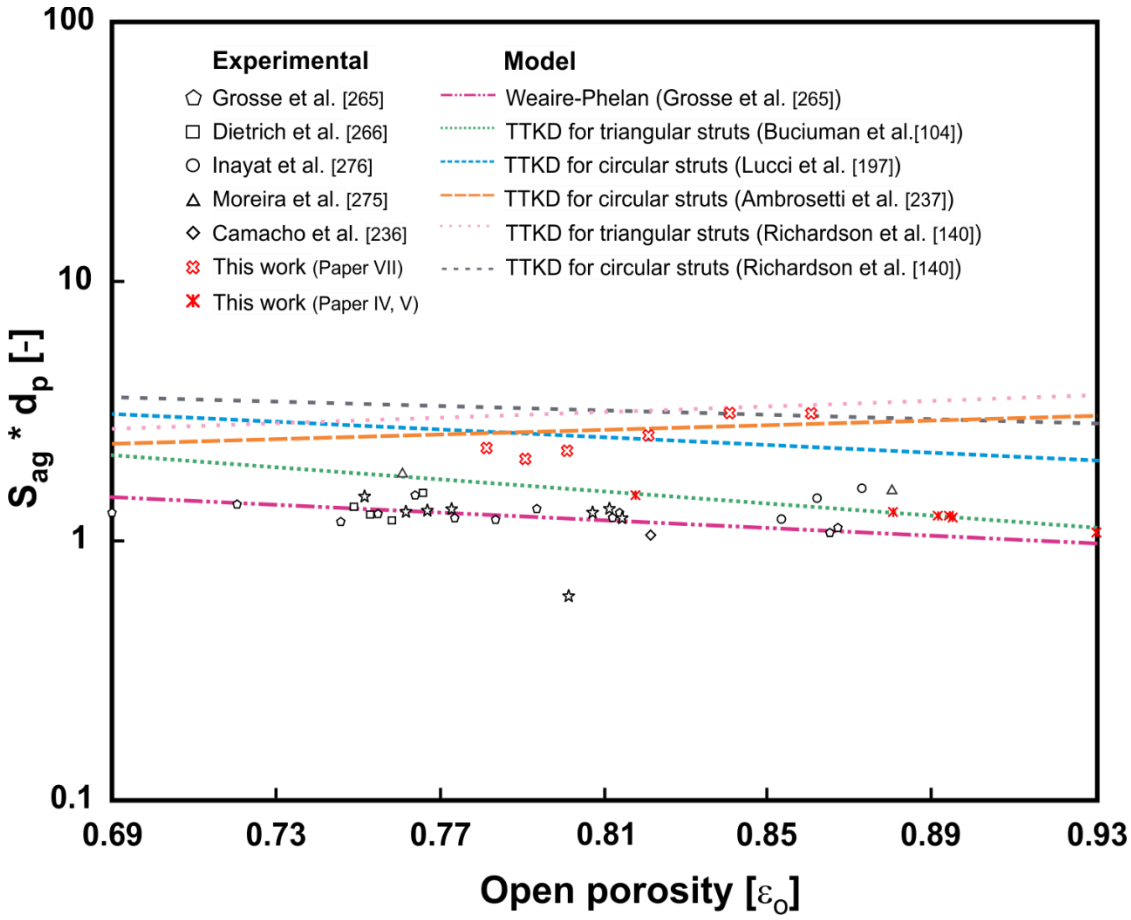


**Figure 61.** Comparison of dimensionless geometric specific surface area versus open porosity of open cell foams: theoretical and experimental values.

In **Paper VII**, the experimental values of specific surface area obtained were confronted with those derived in literature using different theoretical models (**Figure 62A**). It was found that the TTKD model provides an estimate much closer to the experimentally obtained values with a good fit to the data. On the contrary, the cubic cell and Weaire-Phelan based models showed the largest deviations from the experimental values (of about

53%). By fitting the experimental results obtained in this research, an empirical model was presented to determine the specific surface area in ceramic OCFs (see **Figure 62B**).

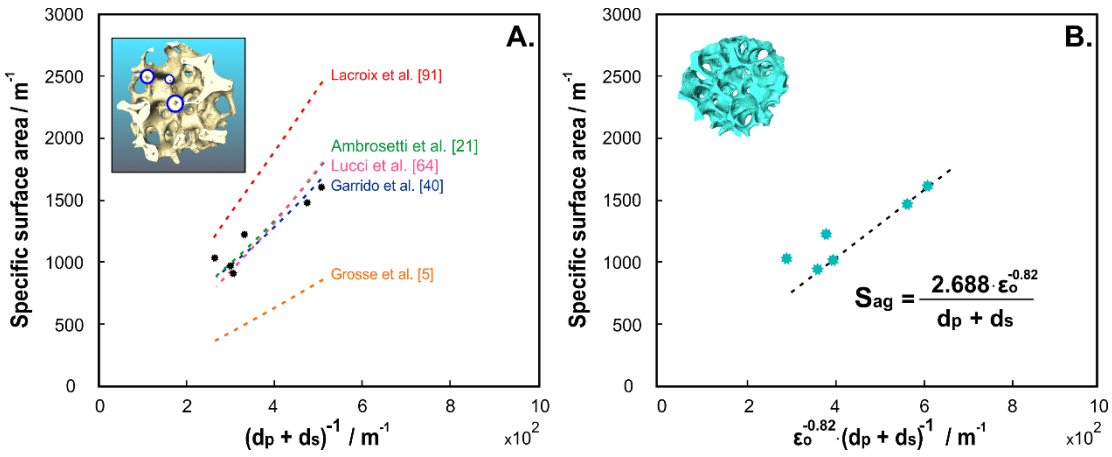


**Figure 62.** (A) correlations available in the literature to estimate the specific surface area $S_{ag}$ with an error ranging from 18 to 53 %; (B) the empirical correlation to estimate the specific surface area $S_{ag}$ of ceramic OCFs. [Remark: The references cited in **Figure 62A** refer to **Paper VI**].

## 2.5 Other work performed

During this research, other studies were also developed which will be published shortly. Among them, the following are listed:

*IFP Energies Nouvelles – collaboration*

- Coated ceramic open cell foams were characterized by micro X-CT, allowing to detect the catalyst thickness, the shape of the catalytic layer and the dispersion of the catalyst along the OCF skeleton.
- Using COMSOL, it was possible to identify the characteristic length scale for open cell foams with circular strut cross-sectional area. In addition, the variations of mass transfer coefficients for different forms of catalytic thickness distribution.
- Based on a Kelvin cell model, it was possible to conduct a mass transport study of the foams and compare it with that obtained using the actual OCF geometry extracted from micro X-CT.

*Universidad del País Vasco – collaboration*

- In order to evaluate the impact on the catalytic performance toward methane combustion, a series of structured catalysts were prepared via washcoating technique. The slurry preparation was a key point to achieve an adequate suspension viscosity. The structures studied were Zir, Alu and SiC foams. In addition, metallic foams made of FeCrAlloy with pore densities of 40 and 60 ppi were also investigated. Thus, the $PdO/Co_3O_4$ catalyst was deposited on the structure. All catalysts were characterized via: XRD, $N_2$ physisorption, chemisorption, laser diffraction, SEM, TPR, viscosity, Z potential.
- Novel catalysts were prepared based on $PdO/NiO_2/Co_3O_4$ supported also on both ceramic and metallic structures.

- Ru/SBA-15 based catalysts were prepared using different metallic and ceramic structures (OCF and monolith) to evaluate the catalytic performance toward methane reforming.

# 3. Conclusions

In this work ceramic open cell foams made of zirconia, alumina and silicon carbide were studied as catalytic supports of 3 wt. % $PdO/Co_3O_4$ toward $CH_4$ combustion in lean conditions. The catalytic performance was evaluated at different flow conditions (WHSV, inlet $CH_4$ concentration and temperature) and design parameters (structure material, pore density, catalyst loading, and foam combination). Focusing on process intensification, the research was dedicated to the analysis of mass transfer effects occurring both in the fluid phase and within the catalyst layer. For this purpose, a careful analysis of the foam geometry was necessary in order to determine the characteristic lengths related to diffusion in the gas phase within the coated layer. Then, using a theoretical model based on the concepts of internal and external mass transfer it was possible to determine the different controlling regimes by varying the operating conditions and design parameters. Furthermore, heat transfer effects occurring during the catalytic reaction were also explored.

As a starting point of the research, the low-dimensional model was applied to both endothermic ($CH_4$ steam reforming) and exothermic ($N_2O$ decomposition) reactions catalyzed with monolithic substrates, since these structures present a much simpler geometry compared to open cell foams. In these studies, a detailed analysis of the geometrical characteristics of bare and coated monolith channels was performed. The influence of catalyst deposition technique, catalyst thickness and flow conditions were also investigated. Subsequently, the theoretical model was adapted to open cell foams, adopting

a Kelvin cell approach and thus taking into account the characteristic geometrical properties of the foams (pore and strut diameter, open porosity, tortuosity, specific surface are, etc.). First, the effect of open cell foam porosity on catalytic performance, mass and heat transfer effects were evaluated. Characteristic times, Weisz-Prater and Carberry numbers were calculated to evaluate the control regime during the biogas steam and oxy-steam reforming reaction.

The intensification of catalytic $CH_4$ combustion process was carried out by supporting the previously optimized $PdO/Co_3O_4$ catalyst on open cell foams. The catalyst was deposited via SCS and WI techniques. The effects of ceramic foam material, catalyst loading and combination of catalytic open cell foams were investigated. Catalytic tests were conducted at different WHSV, temperatures and inlet $CH_4$ concentration, while the $O_2/CH_4$ molar ratio was kept constant at 8 to ensure lean conditions. The stability and adhesion properties of the structured catalyst were also evaluated. A detailed analysis of the foam geometry was first performed before starting the mass and heat transfer calculations in order to establish the gas phase and coated layer transverse diffusion lengths. The pores of the foams were assumed to be circular, although other cases were also analyzed where the pore shape and catalyst thickness varied. A correlation to estimate external mass transfer coefficients in ceramic open cell foams operating at low Reynolds number was derived.

All open cell foams of different porosity and material were characterized by X-ray computed microtomography, which allowed the extraction of characteristic geometrical dimensions such as pore diameter, length and strut diameter as well as open porosity and specific surface area. Moreover, the foam pore density was estimated and contrasted with

the values provided by the manufacturer. Finally, an empirical correlation to determine the specific surface area of ceramic foams was derived.

The following major conclusions can be drawn from this work:

- The increase in open cell foam pore density leads to a much more compact structure because of the higher number of cells and, thus, of struts per unit volume of foam. Thus, a higher specific surface area and lower void space of the macroporous solid.
- The skeletons of all ceramic foams exhibited microporosity and dense grains throughout the structure, as well as circular hollow struts.
- Theoretical models based on the Kelvin cell provided a much closer approximation to the experimental values obtained by X-ray computed microtomography.
- All catalysts showed excellent adhesion to the foams, even with high catalyst contents.
- The catalytic activity of the coated foams increases with increasing pore density, although for foams between 30-45 ppi, similar performances were obtained.
- At the same amount of catalyst deposited, the increase of specific surface area in the foams led to thinner catalyst thicknesses.
- The zirconia foam showed the best catalytic performance toward methane combustion compared to the alumina and silicon carbide structures. However, the light-off temperatures were very similar for all ceramic foam or even lower for the structures with higher thermal conductivity.

- Good stability of the catalytic foam was found after approximately 250 hours of operation.
- At low temperatures and high space velocities, a foam with higher thermal conductivity and higher volumetric heat transfer coefficient (such as SiC-OCF) are useful for retaining the heat of reaction and, consequently, providing the energy needed to drive the ignition of the first reacting molecules on the foam surface.
- The best catalytic performance in terms of $CH_4$ conversion and mass transfer was found for the catalyst loading of 6.1 $mg_{cat}$ $cm^{-2}_{OCF}$.
- The SiC1.5Zir1.5 foam combination showed a promising catalytic performance, achieving complete conversions at much lower temperatures than those obtained with individual coated foams.
- The operating regime (kinetic, internal, external or mixed regimes) of the structured catalyst strongly depends on the operating conditions (temperature, reactant concentration, flow rates) and the catalyst design parameters (catalyst deposition, catalyst content, channel dimensions, pore and strut diameter, specific surface area, open porosity, material type) which fully influence the catalyst performance.
- At low temperatures, all coated foams operated in a kinetic regime independently of the structure material. However, the silicon carbide structure exhibited the lowest temperatures under reaction control.
- No temperature gradients were present within the catalytic layer. Nevertheless, the structures could operate in an unstable zone for external heat transfer

depending on the structure's nature, caused by the strong exothermicity and fast combustion reaction.

- The increased gas velocity led to a higher turbulence of the fluid, thus enhancing the convective heat and consequently shifting the external heat transfer limitations toward higher temperatures.

# 4. References


1. Rahman, S. M. & Miah, M. D. The impact of sources of energy production on globalization: Evidence from panel data analysis. *Renew. Sustain. Energy Rev.* **74**, 110–115 (2017).
2. Metz, B., Meyer, L. & Bosch, P. *Climate change 2007 mitigation of climate change*. *Climate Change 2007 Mitigation of Climate Change* vol. 9780521880 (2007).
3. Zhang, Z., Qu, J. & Zeng, J. A quantitative comparison and analysis on the assessment indicators of greenhouse gases emission. *J. Geogr. Sci.* **18**, 387–399 (2008).
4. Azzi, C. F. & Cox, J. C. *Shadow prices in public program evaluation models*. *Quarterly Journal of Economics* vol. 88 (1974).
5. Intergovernmental Panel on Climate Change. *Climate Change 2014 Mitigation of Climate Change*. *Climate Change 2014 Mitigation of Climate Change* (2014). doi:10.1017/cbo9781107415416.
6. IPCC. *Climate Change 2014 Part A: Global and Sectoral Aspects*. *Climate Change 2014: Impacts, Adaptation, and Vulnerability. Part A: Global and Sectoral Aspects. Contribution of Working Group II to the Fifth Assessment Report of the Intergovernmental Panel on Climate Change* (2014).
7. Dlugokencky, E. J., Nisbet, E. G., Fisher, R. & Lowry, D. Global atmospheric methane: Budget, changes and dangers. *Philos. Trans. R. Soc. A Math. Phys. Eng. Sci.* **369**, 2058–2072 (2011).
8. Saunois, M. *et al.* The global methane budget 2000-2017. *Earth Syst. Sci. Data* **12**, 1561–1623 (2020).
9. Jackson, R. B. *et al.* Increasing anthropogenic methane emissions arise equally from agricultural and fossil fuel sources. *Environ. Res. Lett.* **15**, (2020).
10. Dlugokencky, E. J. Global Monitoring Laboratory - Carbon Cycle Greenhouse Gases. *US Department of Commerce, NOAA, Global Monitoring Laboratory* (2019).
11. Pachauri, R. K. & Meyer, L. *Climate Change 2014: Synthesis Report. Contribution of Working Groups I, II and III to the Fifth Assessment Report of the Intergovernmental Panel on Climate Change*. *Journal of Crystal Growth* vol. 218 (IPCC, 2014).
12. Stolaroff, J. K. *et al.* Review of methane mitigation technologies with application to rapid release of methane from the arctic. *Environ. Sci. Technol.* **46**, 6455–6469 (2012).
13. Global Methane Initiative. Global methane emissions by sector. **2020**, 1–4 (2010).
14. Methane Tracker 2020 – Analysis - IEA. https://www.iea.org/reports/methane-tracker-2020.
15. He, L., Fan, Y., Bellettre, J., Yue, J. & Luo, L. A review on catalytic methane combustion at low temperatures: Catalysts, mechanisms, reaction conditions and reactor designs. *Renew. Sustain. Energy Rev.* **119**, (2020).
16. Clark, N. N. *et al.* Pump-to-wheels methane emissions from the heavy-duty transportation sector. *Environ. Sci. Technol.* **51**, 968–976 (2017).
17. Nam, E. K., Jensen, T. E. & Wallington, T. J. Methane Emissions from Vehicles. *Environ. Sci. Technol.* **38**, 2005–2010 (2004).
18. Wang, W. *et al.* Experimental enrichment of low-concentration ventilation air methane in free diffusion conditions. *Energies* **11**, (2018).
19. Gélin, P. & Primet, M. Complete oxidation of methane at low temperature over noble metal

based catalysts: A review. *Appl. Catal. B Environ.* **39**, 1–37 (2002).

20. Gélin, P., Urfels, L., Primet, M. & Tena, E. Complete oxidation of methane at low temperature over Pt and Pd catalysts for the abatement of lean-burn natural gas fuelled vehicles emissions: Influence of water and sulphur containing compounds. *Catal. Today* **83**, 45–57 (2003).

21. Karakurt, I., Aydin, G. & Aydiner, K. Mine ventilation air methane as a sustainable energy source. *Renew. Sustain. Energy Rev.* **15**, 1042–1049 (2011).

22. Kinnunen, N. M., Hirvi, J. T., Suvanto, M. & Pakkanen, T. A. Methane combustion activity of Pd–PdOx–Pt/Al2O3 catalyst: The role of platinum promoter. *J. Mol. Catal. A Chem.* **356**, 20–28 (2012).

23. Castellazzi, P., Groppi, G., Forzatti, P., Finocchio, E. & Busca, G. Activation process of Pd/Al2O3 catalysts for CH4 combustion by reduction/oxidation cycles in CH4-containing atmosphere. *J. Catal.* **275**, 218–227 (2010).

24. Schwartz, W. R. & Pfefferle, L. D. Combustion of methane over palladium-based catalysts: Support interactions. *J. Phys. Chem. C* **116**, 8571–8578 (2012).

25. Liotta, L. F., Di Carlo, G., Pantaleo, G. & Deganello, G. Catalytic performance of Co3O4/CeO2 and Co3O4/CeO2–ZrO2 composite oxides for methane combustion: Influence of catalyst pretreatment temperature and oxygen concentration in the reaction mixture. *Appl. Catal. B Environ.* **70**, 314–322 (2007).

26. Fiuk, M. M. & Adamski, A. Activity of MnOx–CeO2 catalysts in combustion of low concentrated methane. *Catal. Today* **257**, 131–135 (2015).

27. Ercolino, G., Stelmachowski, P., Kotarba, A. & Specchia, S. Reactivity of Mixed Iron–Cobalt Spinels in the Lean Methane Combustion. *Top. Catal.* **60**, 1370–1379 (2017).

28. Specchia, S., Civera, A., Saracco, G. & Specchia, V. Palladium/perovskite/zirconia catalytic premixed fiber burners for efficient and clean natural gas combustion. *Catal. Today* **117**, 427–432 (2006).

29. Miniajluk, N., Trawczyński, J., Zawadzki, M., Tomaszewski, P. E. & Mišta, W. Solvothermal synthesis and characterization of mixed oxides with perovskite-like structure. *Catal. Today* **257**, 26–34 (2015).

30. Ren, Z. *et al.* Monolithically Integrated Spinel MxCo3−xO4 (M=Co, Ni, Zn) Nanoarray Catalysts: Scalable Synthesis and Cation Manipulation for Tunable Low-Temperature CH4 and CO Oxidation. *Angew. Chemie* **126**, 7351–7355 (2014).

31. Venezia, A. M., La Parola, V. & Liotta, L. F. Structural and surface properties of heterogeneous catalysts: Nature of the oxide carrier and supported particle size effects. *Catal. Today* **285**, 114–124 (2017).

32. Zavyalova, U., Scholz, P. & Ondruschka, B. Influence of cobalt precursor and fuels on the performance of combustion synthesized Co3O4/γ-Al2O3 catalysts for total oxidation of methane. *Appl. Catal. A Gen.* **323**, 226–233 (2007).

33. Choy, J. H. *et al.* New CoO-SiO2-Sol pillared clays as catalysts for NOx conversion. *Chem. Mater.* **14**, 3823–3828 (2002).

34. Ando, M. & Group, M. Optical recognition of CO and H by use of gas-sensitive Au – Co O composite films. 2–6 (2000).

35. Verelst, M. *et al.* Synthesis and Characterization of CoO , Co 3 O 4 , and Mixed Co / CoO Nanoparticules. 2702–2708 (1999).

36. Sc, M. E. & Xiao, B. Development of Advanced Electrode Materials for Lithium Ion Batteries. 1–22 (2013).

37. Dulce, M., De Araújo, M. & Ufrn, D. Q. Brazil mrs meeting. *Powder Metall.* 312–380 (2004).

38. Barrera, E., González, I. & Viveros, T. A new cobalt oxide electrodeposit bath for solar absorbers. *Sol. Energy Mater. Sol. Cells* **51**, 69–82 (1998).

39. Weichel, S. & Møller, P. J. Annealing-induced microfaceting of the CoO(100) surface investigated by LEED and STM. *Surf. Sci.* **399**, 219–224 (1998).

40. Švegl, F., Orel, B., Hutchins, M. G. & Kalcher, K. Structural and Spectroelectrochemical Investigations of Sol-Gel Derived Electrochromic Spinel Co3 O 4 Films. *J. Electrochem. Soc.* **143**, 1532–1539 (1996).

41. Alvarez, A., Ivanova, S., Centeno, M. A. & Odriozola, J. A. Sub-ambient CO oxidation over mesoporous Co3O4: Effect of morphology on its reduction behavior and catalytic performance. *Appl. Catal. A Gen.* **431**–**432**, 9–17 (2012).

42. Ercolino, G. *et al.* Pd/Co3O4-based catalysts prepared by solution combustion synthesis for residual methane oxidation in lean conditions. *Catal. Today* **257**, 66–71 (2015).

43. Wang, Q. *et al.* Synthesis, characterization, and catalytic evaluation of Co3O4/γ-Al2O3 as methane combustion catalysts: Significance of Co species and the redox cycle. *Appl. Catal. B Environ.* **168**–**169**, 42–50 (2015).

44. Ercolino, G., Stelmachowski, P., Grzybek, G., Kotarba, A. & Specchia, S. Optimization of Pd catalysts supported on Co3O4 for low-temperature lean combustion of residual methane. *Appl. Catal. B Environ.* **206**, 712–725 (2017).

45. Shen, J., Hayes, R. E. & Semagina, N. On the contribution of oxygen from Co3O4 to the Pd-catalyzed methane combustion. *Catal. Today* **360**, 435–443 (2019).

46. Wójcik, S. *et al.* Robust Co3O4|α-Al2O3|cordierite structured catalyst for N2O abatement – Validation of the SCS method for active phase synthesis and deposition. *Chem. Eng. J.* **377**, 120088 (2018).

47. Zasada, F., Janas, J., Piskorz, W., Gorczyńska, M. & Sojka, Z. Total Oxidation of Lean Methane over Cobalt Spinel Nanocubes Controlled by the Self-Adjusted Redox State of the Catalyst: Experimental and Theoretical Account for Interplay between the Langmuir-Hinshelwood and Mars-Van Krevelen Mechanisms. *ACS Catal.* **7**, 2853–2867 (2017).

48. Cao, X. *et al.* Co3O4/HZSM-5 catalysts for methane combustion: The effect of preparation methodologies. *Catal. Today* **297**, 219–227 (2017).

49. Roth, W. L. The magnetic structure of Co3O4. *J. Phys. Chem. Solids* **25**, 1–10 (1964).

50. Sousa, O. M., Lima, J. S., Lima, A. F. & Lalic, M. V. Theoretical study of structural, electronic and magnetic properties of the spinel Co 3 O 4 under the pressure from 0 to 30 GPa. *J. Magn. Magn. Mater.* **484**, 21–30 (2019).

51. Seidov, Z., Açıkgöz, M., Kazan, S. & Mikailzade, F. Magnetic properties of Co3O4 polycrystal powder. *Ceram. Int.* **42**, 12928–12931 (2016).

52. Yan, G. & Sautet, P. Surface structure of Co3O4 (111) under reactive gas-phase environments. *ACS Catal.* **9**, 6380–6392 (2019).

53. Bahlawane, N. Kinetics of methane combustion over CVD-made cobalt oxide catalysts. *Appl. Catal. B Environ.* **67**, 168–176 (2006).

54. Zheng, Y. *et al. Enhanced Methane Oxidation over Co 3 O 4 –In 2 O 3 - x Composite Oxide Nanoparticles via Controllable Substitution of Co 3+ /Co 2+ by In 3+ Ions . ACS Applied Nano Materials* (2020). doi:10.1021/acsanm.0c02075.

55. Salavati-Niasari, M., Mir, N. & Davar, F. Synthesis and characterization of Co3O4 nanorods

by thermal decomposition of cobalt oxalate. *J. Phys. Chem. Solids* **70**, 847–852 (2009).

56. Xia, X., Li, M., Liu, T., Liang, P. & Huang, X. Facile synthesis of cobalt oxide as electrocatalyst for the oxygen reduction reaction in microbial fuel cells. *Chem. Eng. J.* **342**, 395–400 (2018).

57. Gunnewiek, R. F. K., Mendes, C. F. & Kiminami, R. H. G. A. Synthesis of spinel cobalt oxide nanoparticles using a modified polymeric precursor method. *Adv. Powder Technol.* **27**, 1056–1061 (2016).

58. Xu, G. L., Li, J. T., Huang, L., Lin, W. & Sun, S. G. Synthesis of Co3O4 nano-octahedra enclosed by {111} facets and their excellent lithium storage properties as anode material of lithium ion batteries. *Nano Energy* **2**, 394–402 (2013).

59. Zhao, Z. W., Konstantinov, K., Yuan, L., Liu, H. K. & Dou, S. X. In-Situ fabrication of nanostructured cobalt oxide powders by spray pyrolysis technique. *J. Nanosci. Nanotechnol.* **4**, 861–866 (2004).

60. Varma, A., Mukasyan, A. S., Rogachev, A. S. & Manukyan, K. V. Solution Combustion Synthesis of Nanoscale Materials. *Chem. Rev.* **116**, 14493–14586 (2016).

61. Specchia, S., Galletti, C. & Specchia, V. *Solution Combustion Synthesis as intriguing technique to quickly produce performing catalysts for specific applications*. *Studies in Surface Science and Catalysis* vol. 175 (Elsevier Masson SAS, 2010).

62. Deganello, F. & Tyagi, A. K. Solution combustion synthesis, energy and environment: Best parameters for better materials. *Prog. Cryst. Growth Charact. Mater.* **64**, 23–61 (2018).

63. Moncada Quintero, C. W., Ercolino, G. & Specchia, S. Effect of the Co3O4 load on the performance of PdO/Co3O4/ZrO2 open cell foam catalysts for the lean combustion of methane: kinetic and mass transfer regimes. *Catal. Today* (2021) doi:10.1016/j.cattod.2021.03.014.

64. Toso, A., Colussi, S., Llorca, J. & Trovarelli, A. The dynamics of PdO-Pd phase transformation in the presence of water over Si-doped Pd/CeO2 methane oxidation catalysts. *Appl. Catal. A Gen.* **574**, 79–86 (2019).

65. Amjad, U. E. S., Vita, A., Galletti, C., Pino, L. & Specchia, S. Comparative study on steam and oxidative steam reforming of methane with noble metal catalysts. *Ind. Eng. Chem. Res.* **52**, 15428–15436 (2013).

66. Italiano, C. *et al.* Rh/CeO2 thin catalytic layer deposition on alumina foams: Catalytic performance and controlling regimes in biogas reforming processes. *Catalysts* **8**, 1–25 (2018).

67. Vita, A. *et al.* Methane oxy-steam reforming reaction: Performances of Ru/γ-Al2O3 catalysts loaded on structured cordierite monoliths. *Int. J. Hydrogen Energy* **39**, 18592–18603 (2014).

68. Ercolino, G. *et al.* The Effect of the Preparation Method of Pd-Doped Cobalt Spinel on the Catalytic Activity in Methane Oxidation Under Lean Fuel Conditions. *Top. Catal.* **60**, 333–341 (2017).

69. Balzarotti, R., Italiano, C., Pino, L., Cristiani, C. & Vita, A. Ni/CeO2-thin ceramic layer depositions on ceramic monoliths for syngas production by Oxy Steam Reforming of biogas. *Fuel Process. Technol.* **149**, 40–48 (2016).

70. Vita, A., Cristiano, G., Italiano, C., Pino, L. & Specchia, S. Syngas production by methane oxy-steam reforming on Me/CeO2 (Me=Rh, Pt, Ni) catalyst lined on cordierite monoliths. *Appl. Catal. B Environ.* **162**, 551–563 (2015).

71. Moncada Quintero, C. W., Ercolino, G., Poozhikunnath, A., Maric, R. & Specchia, S. Analysis of heat and mass transfer limitations for the combustion of methane emissions on PdO/Co3O4

coated on ceramic open cell foams. *Chem. Eng. J.* **405**, 126970 (2021).

72. Ambrosetti, M., Bracconi, M., Maestri, M., Groppi, G. & Tronconi, E. Packed foams for the intensification of catalytic processes : assessment of ξ These authors contributed equally to the work. *Chem. Eng. J.* 122801 (2019) doi:10.1016/j.cej.2019.122801.

73. Tonkovich, A. L. & Daymo, E. *Process intensification*. *Handbook of Thermal Science and Engineering* (2018). doi:10.1007/978-3-319-26695-4_34.

74. Stankiewicz, A. I. & Moulijn, J. A. Process Intensification: Transforming Chemical Engineering. *AIChE - Chem. Eng. Prog.* **96**, 22–33 (2000).

75. Tronconi, E., Groppi, G. & Visconti, C. G. Structured catalysts for non-adiabatic applications. *Curr. Opin. Chem. Eng.* **5**, 55–67 (2014).

76. Huynh, H. L., Tucho, W. M. & Yu, Z. Structured NiFe catalysts derived from in-situ grown layered double hydroxides on ceramic monolith for CO2 methanation. *Green Energy Environ.* **5**, 423–432 (2020).

77. Heck, R. M., Gulati, S. & Farrauto, R. J. The application of monoliths for gas phase catalytic reactions. *Chem. Eng. J.* **82**, 149–156 (2001).

78. Roy, S., Bauer, T., Al-Dahhan, M., Lehner, P. & Turek, T. Monoliths as multiphase reactors: A review. *AIChE J.* **50**, 2918–2938 (2004).

79. Zamaniyan, A., Mortazavi, Y., Khodadadi, A. A. & Manafi, H. Tube fitted bulk monolithic catalyst as novel structured reactor for gas-solid reactions. *Appl. Catal. A Gen.* **385**, 214–223 (2010).

80. Zamaniyan, A., Khodadadi, A. A., Mortazavi, Y. & Manafi, H. Comparative model analysis of the performance of tube fitted bulk monolithic catalyst with conventional pellet shapes for natural gas reforming. *J. Ind. Eng. Chem.* **17**, 767–776 (2011).

81. Rezaei, F. & Webley, P. Structured adsorbents in gas separation processes. *Sep. Purif. Technol.* **70**, 243–256 (2010).

82. Baharudin, L. & Watson, M. J. Monolithic substrate support catalyst design considerations for steam methane reforming operation. *Rev. Chem. Eng.* **34**, 481–501 (2018).

83. Roy, S., K. Heibel, A., Liu, W. & Boger, T. Design of monolithic catalysts for multiphase reactions. *Chem. Eng. Sci.* **59**, 957–966 (2004).

84. Boger, T., Heibel, A. K. & Sorensen, C. M. Monolithic catalysts for the chemical industry. *Ind. Eng. Chem. Res.* **43**, 4602–4611 (2004).

85. Govender, S. & Friedrich, H. B. Monoliths: A review of the basics, preparation methods and their relevance to oxidation. *Catalysts* **7**, (2017).

86. Avila, P., Montes, M. & Miró, E. E. Monolithic reactors for environmental applications: A review on preparation technologies. *Chem. Eng. J.* **109**, 11–36 (2005).

87. Danaci, S. *et al.* Innovative 3D-manufacture of structured copper supports post-coated with catalytic material for CO2 methanation. *Chem. Eng. Process. - Process Intensif.* **127**, 168–177 (2018).

88. Balzarotti, R. *et al.* Periodic open cellular structures (POCS) as enhanced catalyst supports: Optimization of the coating procedure and analysis of mass transport. *Appl. Catal. B Environ.* **283**, 119651 (2021).

89. Aguirre, A., Chandra, V., Peters, E. A. J. F., Kuipers, J. A. M. & Neira D'Angelo, M. F. Open-cell foams as catalysts support: A systematic analysis of the mass transfer limitations. *Chem. Eng. J.* **393**, 124656 (2020).

90. Wan, T., Liu, Y., Zhou, C., Chen, X. & Li, Y. Fabrication, properties, and applications of open-cell aluminum foams: A review. *J. Mater. Sci. Technol.* **62**, 11–24 (2021).

91. Sinn, C., Wentrup, J., Pesch, G. R., Thöming, J. & Kiewidt, L. Structure-heat transport analysis of periodic open-cell foams to be used as catalyst carriers. *Chem. Eng. Res. Des.* **166**, 209–219 (2021).

92. Lu, T. J., Stone, H. A. & Ashby, M. F. Heat transfer in open-cell metal foams. *Acta Mater.* **46**, 3619–3635 (1998).

93. Bianchi, E. *et al.* An appraisal of the heat transfer properties of metallic open-cell foams for strongly exo-/endo-thermic catalytic processes in tubular reactors. *Chem. Eng. J.* **198**–**199**, 512–528 (2012).

94. Wan, T., Liu, Y., Zhou, C., Chen, X. & Li, Y. Fabrication, properties, and applications of open-cell aluminum foams: A review. *J. Mater. Sci. Technol.* **62**, 11–24 (2021).

95. Ghosh, I. How good is open-cell metal foam as heat transfer surface? *J. Heat Transfer* **131**, 1–8 (2009).

96. Jang, W. Y., Kraynik, A. M. & Kyriakides, S. On the microstructure of open-cell foams and its effect on elastic properties. *Int. J. Solids Struct.* **45**, 1845–1875 (2008).

97. Cristiani, C. *et al.* Activation of metallic open-cell foams via washcoat deposition of Ni/MgAl 2O 4 catalysts for steam reforming reaction. *Catal. Today* **197**, 256–264 (2012).

98. Haack, D. P., Butcher, K. R., Kim, T. & Lu, T. J. Novel Lightweight Metal Foam Heat Exchangers. *Am. Soc. Mech. Eng. Process Ind. Div. PID* **6**, 141–147 (2001).

99. Bock, J. A geometric study of liquid retention in open-cell metal foams. 116 (2011).

100. Dashliborun, A. M., Füssel, A. & Larachi, F. Prospect of open-cell solid foams for floating-platform multiphase reactor applications – Maldistribution susceptibility and hydrodynamic behavior. *Chem. Eng. J.* **332**, 596–607 (2018).

101. Skibinski, J. *et al.* The influence of pore size variation on the pressure drop in open-cell foams. *Mater. Des.* **87**, 650–655 (2015).

102. De Schampheleire, S. *et al.* How to study thermal applications of open-cell metal foam: Experiments and computational fluid dynamics. *Materials (Basel).* **9**, 1–27 (2016).

103. Razza, S. *et al.* Heat transfer performance of structured catalytic reactors packed with metal foam supports: Influence of wall coupling. *Catal. Today* **273**, 187–195 (2016).

104. Buciuman, F. C. & Kraushaar-Czarnetzki, B. Ceramic Foam Monoliths as Catalyst Carriers. 1. Adjustment and Description of the Morphology. *Ind. Eng. Chem. Res.* **42**, 1863–1869 (2003).

105. Inayat, A., Freund, H., Zeiser, T. & Schwieger, W. Determining the specific surface area of ceramic foams: The tetrakaidecahedra model revisited. *Chem. Eng. Sci.* **66**, 1179–1188 (2011).

106. Inayat, A., Klumpp, M., Lämmermann, M., Freund, H. & Schwieger, W. Development of a new pressure drop correlation for open-cell foams based completely on theoretical grounds: Taking into account strut shape and geometric tortuosity. *Chem. Eng. J.* **287**, 704–719 (2016).

107. Bracconi, M., Ambrosetti, M., Maestri, M., Groppi, G. & Tronconi, E. A systematic procedure for the virtual reconstruction of open-cell foams. *Chem. Eng. J.* **315**, 608–620 (2017).

108. Große, J. *et al.* Volume image analysis of ceramic sponges. *Chem. Eng. Technol.* **31**, 307–314 (2008).

109. Della Torre, A. *et al.* CFD modeling of catalytic reactions in open-cell foam substrates. *Comput. Chem. Eng.* **92**, 55–63 (2016).

110. De Jaeger, P., T'Joen, C., Huisseune, H., Ameel, B. & De Paepe, M. An experimentally validated and parameterized periodic unit-cell reconstruction of open-cell foams. *J. Appl. Phys.* **109**, (2011).

111. Richardson, J. T., Remue, D. & Hung, J. K. Properties of ceramic foam catalyst supports: Mass and heat transfer. *Appl. Catal. A Gen.* **250**, 319–329 (2003).

112. Sanz, O., Echave, F. J., Sánchez, M., Monzón, A. & Montes, M. Aluminium foams as structured supports for volatile organic compounds (VOCs) oxidation. *Appl. Catal. A Gen.* **340**, 125–132 (2008).

113. Montebelli, A. *et al.* Enabling small-scale methanol synthesis reactors through the adoption of highly conductive structured catalysts. *Catal. Today* **215**, 176–185 (2013).

114. Lacroix, M. *et al.* Silicon carbide foam composite containing cobalt as a highly selective and re-usable Fischer-Tropsch synthesis catalyst. *Appl. Catal. A Gen.* **397**, 62–72 (2011).

115. Park, J. C., Roh, N. S., Chun, D. H., Jung, H. & Yang, J. I. Cobalt catalyst coated metallic foam and heat-exchanger type reactor for Fischer-Tropsch synthesis. *Fuel Process. Technol.* **119**, 60–66 (2014).

116. Egana, A., Sanz, O., Merino, D., Moriones, X. & Montes, M. Fischer-Tropsch Synthesis Intensification in Foam Structures. *Ind. Eng. Chem. Res.* **57**, 10187–10197 (2018).

117. Ou, X. *et al.* Hierarchical Fe-ZSM-5/SiC foam catalyst as the foam bed catalytic reactor (FBCR) for catalytic wet peroxide oxidation (CWPO). *Chem. Eng. J.* **362**, 53–62 (2019).

118. Ou, X. *et al.* On developing ferrisilicate catalysts supported on silicon carbide (SiC) foam catalysts for continuous catalytic wet peroxide oxidation (CWPO) reactions. *Catal. Today* **356**, 631–640 (2020).

119. Pestryakov, A. N. *et al.* Selective oxidation of alcohols over foam-metal catalysts. *Appl. Catal. A Gen.* **227**, 125–130 (2002).

120. Ercolino, G., Karimi, S., Stelmachowski, P. & Specchia, S. Catalytic combustion of residual methane on alumina monoliths and open cell foams coated with Pd/Co3O4. *Chem. Eng. J.* **326**, 339–349 (2017).

121. Ercolino, G., Stelmachowski, P. & Specchia, S. Catalytic Performance of Pd/Co3O4 on SiC and ZrO2 Open Cell Foams for Process Intensification of Methane Combustion in Lean Conditions. *Ind. Eng. Chem. Res.* **56**, 6625–6636 (2017).

122. Meloni, E., Caldera, M., Palma, V., Pignatelli, V. & Gerardi, V. Open cell foams filters for soot abatement from biomass boilers. *Chem. Eng. Trans.* **65**, 799–804 (2018).

123. Correia, N. *et al.* Open cell polyurethane foams for new filters with supported adsorbents. *Mater. Sci. Forum* **514–516**, 892–896 (2006).

124. Ozmat, B., Leyda, B. & Benson, B. Thermal Applications of Open-Cell Metal Foams. *Mater. Manuf. Process.* **19**, 839–862 (2004).

125. Salas, K. I. & Waas, A. M. Convective heat transfer in open cell metal foams. *J. Heat Transfer* **129**, 1217–1229 (2007).

126. De Paepe, M., Huisseune, H., De Jaeger, P. & T'Joen, C. The Use of Open Cell Metal Foams in Heat Exchangers: Possibilities and Limitations. *8th Int. Conf. Heat Transf. Fluid Mech. Thermodyn.* 1–15 (2011).

127. Gauckler, L. J., Waeber, M. M., Conti, C. & Jacob-Duliere, M. Ceramic Foam For Molten metal Filtration. *Jom* **37**, 47–50 (1985).

128. Gauckler, L. J., Waeber, M. M., Conti, C. & Jacob-Duliere, M. Industrial Appl I Cation of

Open Pore Ceramic. *Leight Met.* 251–262 (1985).

129. Kodama, T., Kiyama, A. & Shimizu, K. I. Catalytically activated metal foam absorber for light-to-chemical energy conversion via solar reforming of methane. *Energy and Fuels* **17**, 13–17 (2003).

130. Li, C., Li, C. & Wang, Y. Compressive behavior and energy absorption capacity of unconstrained and constrained open-cell aluminum foams. *Adv. Compos. Lett.* **29**, 1–4 (2020).

131. Banhart, J. Manufacture, characterisation and application of cellular metals and metal foams. *Prog. Mater. Sci.* **46**, 559–632 (2001).

132. Hutter, C., Allemann, C., Kuhn, S. & Rudolf von Rohr, P. Scalar transport in a milli-scale metal foam reactor. *Chem. Eng. Sci.* **65**, 3169–3178 (2010).

133. Hutter, C., Zenklusen, A., Lang, R. & Rudolf von Rohr, P. Axial dispersion in metal foams and streamwise-periodic porous media. *Chem. Eng. Sci.* **66**, 1132–1141 (2011).

134. Hutter, C., Zenklusen, A., Kuhn, S. & Rudolf von Rohr, P. H. Large eddy simulation of flow through a streamwise-periodic structure. *Chem. Eng. Sci.* **66**, 519–529 (2011).

135. Vogt, U. F., Györfy, L., Herzog, A., Graule, T. & Plesch, G. Macroporous silicon carbide foams for porous burner applications and catalyst supports. *J. Phys. Chem. Solids* **68**, 1234–1238 (2007).

136. Ortona, A. *et al.* Aging of reticulated Si-SiC foams in porous burners. *Adv. Appl. Ceram.* **109**, 246–251 (2010).

137. Hasirci, N. & A., B. *Biomaterials: From Molecules to Engineered Tissues*. *Polyurethanes in Biomedical Applications* (2004).

138. Wang, L. *et al.* Delayed diagnosis of intraperitoneal bladder perforation after blunt trauma. *IJU Case Reports* **2**, 83–85 (2019).

139. Open Cell Biomedical Dental Implants | SpotImplant. https://www.spotimplant.com/en/dental-implants/open-cell-biomedical.

140. Richardson, J. T., Peng, Y. & Remue, D. Properties of ceramic foam catalyst supports: Pressure drop. *Appl. Catal. A Gen.* **204**, 19–32 (2000).

141. Twigg, M. V. & Richardson, J. T. Theory and applications of ceramic foam catalysts. *Chem. Eng. Res. Des.* **80**, 183–189 (2002).

142. Pacultová, K. *et al.* Effect of support on the catalytic activity of Co3O4-Cs deposited on open-cell ceramic foams for N2O decomposition. *Mater. Res. Bull.* **129**, (2020).

143. Li, Y., Chen, H. W., Wang, F. Q., Xia, X. L. & Tan, H. P. A development to determine spectral radiative properties of semitransparent struts of open-cell ceramic foams: From macro-scale measurement to pore-scale simulation. *Infrared Phys. Technol.* **113**, 103646 (2021).

144. Scheffler, M. & Colombo, P. *Cellular Ceramics: Structure, Manufacturing, Properties and Applications*. (WILEY-VCH Verlag GmbH & Co. KGaA, Weinheim, 2005).

145. Vita, A. *et al.* High-temperature CO2 methanation over structured Ni/GDC catalysts: Performance and scale-up for Power-to-Gas application. *Fuel Process. Technol.* **202**, 106365 (2020).

146. Twigg, M. V. & Richardson, J. T. Fundamentals and applications of structured ceramic foam catalysts. *Ind. Eng. Chem. Res.* **46**, 4166–4177 (2007).

147. Švecová, I., Tillová, E. & Kuchariková, L. Improving the quality of Al-Si castings by using ceramic filters. *Prod. Eng. Arch.* **26**, 19–24 (2020).

148. Zheng, Y., Luo, X., You, J., Peng, Z. & Zhang, S. Ceramic foams with highly open channel structure from direct foaming method in combination with hollow spheres as pore-former. *J. Asian Ceram. Soc.* 1–11 (2020) doi:10.1080/21870764.2020.1847427.

149. Incera Garrido, G., Patcas, F. C., Lang, S. & Kraushaar-Czarnetzki, B. Mass transfer and pressure drop in ceramic foams: A description for different pore sizes and porosities. *Chem. Eng. Sci.* **63**, 5202–5217 (2008).

150. Zeynep Ilsen Onsan, A. K. A. *Multiphase Catalytic Reactors*. *Multiphase Catalytic Reactors* (John Wiley & Sons, 2016). doi:10.1002/9781119248491.

151. Cybulski, A. & Moulijn, J. A. *Structured Catalysts and Reactors*. (Marcel Dekker, Inc., 1998).

152. Scott Fogler, H. *Elements of chemical reaction engineering*. (Pearson Education, Inc., 2016).

153. Smith, J. M. *Chemical Engineering Kinetics*. (McGraw-Hill, 1970).

154. Kashid, M. N. & Renken, A. Microstructured Reactors for Fluid – Solid Systems. 231–266 (2015).

155. Madhvanand N. Kashid, Albert Renken, L. K.-M. *Microstructured Devices for Chemical Processing*. (Wiley-VCH Verlag GmbH & Co. KGaA, 2013). doi:10.1002/9783527685226.

156. Bracconi, M., Ambrosetti, M., Maestri, M., Groppi, G. & Tronconi, E. A fundamental analysis of the influence of the geometrical properties on the effective thermal conductivity of open-cell foams. *Chem. Eng. Process. - Process Intensif.* **129**, 181–189 (2018).

157. Bhattacharya, M., Harold, M. P. & Balakotaiah, V. Mass-transfer coefficients in washcoated monoliths. *AIChE J.* **50**, 2939–2955 (2004).

158. Incropera, F. P. & DeWitt, D. P. *Fundamentals of Heat and Mass Transfer*. (Prentice Hall, 1996). doi:10.1016/j.applthermaleng.2011.03.022.

159. Cornejo, I., Nikrityuk, P. & Hayes, R. E. Heat and mass transfer inside of a monolith honeycomb: From channel to full size reactor scale. *Catal. Today* (2020) doi:10.1016/j.cattod.2020.10.036.

160. Balakotaiah, V. & West, D. H. Shape normalization and analysis of the mass transfer controlled regime in catalytic monoliths. *Chem. Eng. Sci.* **57**, 1269–1286 (2002).

161. Balakotaiah, V. On the relationship between Aris and Sherwood numbers and friction and effectiveness factors. *Chem. Eng. Sci.* **63**, 5802–5812 (2008).

162. Joshi, S. Y., Harold, M. P. & Balakotaiah, V. Low-Dimensional Models for Real Time Simulations of Catalytic Monoliths. *AIChE J* **55**, 1771–1783 (2009).

163. Joshi, S. Y., Harold, M. P. & Balakotaiah, V. On the use of internal mass transfer coefficients in modeling of diffusion and reaction in catalytic monoliths. *Chem. Eng. Sci.* **64**, 4976–4991 (2009).

164. Joshi, S. Y., Harold, M. P. & Balakotaiah, V. Overall mass transfer coefficients and controlling regimes in catalytic monoliths. *Chem. Eng. Sci.* **65**, 1729–1747 (2010).

165. Joshi, S. Y., Ren, Y., Harold, M. P. & Balakotaiah, V. Determination of kinetics and controlling regimes for H2 oxidation on Pt/Al2O3 monolithic catalyst using high space velocity experiments. *Appl. Catal. B Environ.* **102**, 484–495 (2011).

166. Ashraf, M. A. *et al.* Analysis of Ru/La-Al2O3 catalyst loading on alumina monoliths and controlling regimes in methane steam reforming. *Chem. Eng. J.* **334**, 1792–1807 (2018).

167. Ashraf, M. A., Sanz, O., Montes, M. & Specchia, S. Insights into the effect of catalyst loading on methane steam reforming and controlling regime for metallic catalytic monoliths. *Int. J. Hydrogen Energy* **43**, 11778–11792 (2018).

168. Carberry, J. J. *Chemical and Catalytic Reaction Engineering*. (McGraw-Hill, 1976).

169. Klaewkla, R., Arend, M. & Hoelderich, W. F. A Review of Mass Transfer Controlling the Reaction Rate in Heterogeneous Catalytic Systems. in *Mass Transfer - Advanced Aspects* 667–684 (2011). doi:10.5772/22962.

170. Green, D. W. & Perry, R. H. *Perry's Chemical Engineers' Handbook*. (McGraw-Hill, 2008).

171. Lee, H. H. *Heterogeneous reactor design*. (Butterworths series in chemical engineering., 1985).

172. Froment, G. F., Bischoff, K. B. & De Wilde, J. *Chemical Reactor Analysis and Design*. (John Wiley & Sons, 2011).

173. Balakotaiah, V. & Ratnakar, R. R. On the use of transfer and dispersion coefficient concepts in low-dimensional diffusion-convection-reaction models. *Chem. Eng. Res. Des.* **88**, 342–361 (2010).

174. Hayes, R. E. & Kolaczkowski, S. T. Mass and heat transfer effects in catalytic monolith reactors. *Chem. Eng. Sci.* **49**, 3587–3599 (1994).

175. Shah, R. K. Laminar flow friction and forced convection heat transfer in ducts of arbitrary geometry. *Int. J. Heat Mass Transf.* **18**, 849–862 (1975).

176. Cybulski, A., Van Dalen, M. J., Verkerk, J. W. & Van Den Berg, P. J. Gas-particle heat transfer coefficients in packed beds at low Reynolds numbers. *Chem. Eng. Sci.* **30**, 1015–1018 (1975).

177. Ramanathan, K., Balakotaiah, V. & West, D. H. Light-off criterion and transient analysis of catalytic monoliths. *Chem. Eng. Sci.* **58**, 1381–1405 (2003).

178. Gupta, N. & Balakotaiah, V. Heat and mass transfer coefficients in catalytic monoliths. *Chem. Eng. Sci.* **56**, 4771–4786 (2001).

179. Tronconi, E. & Forzatti, P. Adequacy of lumped parameter models for SCR reactors with monolith structure. *AIChE J.* **38**, 201–210 (1992).

180. Votruba, J., Sinkule, J., Hlaváček, V. & Skřivánek, J. Heat and mass transfer in monolithic honeycomb catalysts-I. *Chem. Eng. Sci.* **30**, 117–123 (1975).

181. Irvine, T. F. & Hartnett, J. P. Advances in Heat Transfer. *Adv. Heat Transf.* **43**, i (2011).

182. Spivey, J. J. & Dooley, K. M. *Catalysis*. (The Royal Society of Chemistry, 2009).

183. Wakao, N. & Smith, J. M. Diffusion in catalyst pellets. *Chem. Eng. Sci.* **17**, 825–834 (1962).

184. Novák, V., Dudák, M., Kočí, P. & Marek, M. Understanding the gas transport in porous catalyst layers by using digital reconstruction techniques. *Curr. Opin. Chem. Eng.* **9**, 16–26 (2015).

185. Dudák, M. *et al.* Prediction of diffusivity and conversion of n-decane and CO in coated Pt/γ-Al2O3 catalyst depending on porous layer morphology. *Appl. Catal. B Environ.* **150–151**, 446–458 (2014).

186. Novák, V. *et al.* Multi-scale modelling and measurements of diffusion through porous catalytic coatings: An application to exhaust gas oxidation. *Catal. Today* **188**, 62–69 (2012).

187. Mears, D. E. Diagnostic criteria for heat transport limitations in fixed bed reactors. *J. Catal.* **20**, 127–131 (1971).

188. Anderson, J. B. A criterion for isothermal behaviour of a catalyst pellet. *Chem. Eng. Sci.* **18**, 147–148 (1963).

189. Maiorov, V. A., Vasil'ev, L. L. & Polyaev, V. M. Porous heat exchangers-classification,

construction, application. *J. Eng. Phys.* **47**, 1110–1123 (1984).

190. Vazifeshenas, Y., Sedighi, K. & Shakeri, M. Open Cell Metal Foam as Extended Coolant Surface – Fuel Cell Application. *Fuel Cells* **20**, 108–115 (2020).

191. Huu, T. T., Lacroix, M., Pham Huu, C., Schweich, D. & Edouard, D. Towards a more realistic modeling of solid foam: Use of the pentagonal dodecahedron geometry. *Chem. Eng. Sci.* **64**, 5131–5142 (2009).

192. Kumar, P. Investigation of Kelvin-like solid foams for potential engineering applications: An attractive set of geometrical and thermo-hydraulic properties. (2014).

193. Weaire, D. & Phelan, R. A counter-example to kelvin's conjecture on minimal surfaces. *Philos. Mag. Lett.* **69**, 107–110 (1994).

194. Groppi, G., Giani, L. & Tronconi, E. Generalized correlation for gas/solid mass-transfer coefficients in metallic and ceramic foams. *Ind. Eng. Chem. Res.* **46**, 3955–3958 (2007).

195. Kumar, P. Investigation of Kelvin-like solid foams for potential engineering applications : An attractive set of geometrical and thermo-hydraulic properties. (Aix-Marseille University, 2015).

196. Kumar, P., Topin, F. & Tadrist, L. Geometrical characterization of Kelvin-like metal foams for different strut shapes and porosity. *J. Porous Media* **18**, 637–652 (2015).

197. Lucci, F. *et al.* Performance of randomized Kelvin cell structures as catalytic substrates: Mass-transfer based analysis. *Chem. Eng. Sci.* **112**, 143–151 (2014).

198. Gibson, L. J. & Ashby, M. F. *Cellular solids: Structure and Properties*. *Journal of Biomechanics* vol. 22 (1988).

199. Specchia, S., Ercolino, G., Karimi, S., Italiano, C. & Vita, A. Solution combustion synthesis for preparation of structured catalysts: A mini-review on process intensification for energy applications and pollution control. *Int. J. Self-Propagating High-Temperature Synth.* **26**, 166–186 (2017).

200. Thommes, M. & Cychosz, K. A. Physical adsorption characterization of nanoporous materials: Progress and challenges. *Adsorption* **20**, 233–250 (2014).

201. Cychosz, K. A. & Thommes, M. Progress in the Physisorption Characterization of Nanoporous Gas Storage Materials. *Engineering* **4**, 559–566 (2018).

202. Sing, K. The use of nitrogen adsorption for the characterisation of porous materials. *Colloids Surfaces A Physicochem. Eng. Asp.* **187**–**188**, 3–9 (2001).

203. Bertier, P. *et al.* On the use and abuse of N2 physisorption for the characterization of the pore structure of shales. 151–161 (2016) doi:10.1346/cms-wls-21.12.

204. Webb, P. Introduction to Chemical Adsorption Analytical Techniques and their Applications to Catalysis. *MIC Tech. Publ.* **13**, 1–4 (2003).

205. Králik, M. Adsorption, chemisorption, and catalysis. *Chem. Pap.* **68**, 1625–1638 (2014).

206. Epp, J. *X-Ray Diffraction (XRD) Techniques for Materials Characterization*. *Materials Characterization Using Nondestructive Evaluation (NDE) Methods* (Elsevier Ltd, 2016). doi:10.1016/B978-0-08-100040-3.00004-3.

207. Prevéy, P. S. X-ray diffraction characterization of crystallinity and phase composition in plasma-sprayed hydroxyapatite coatings. *J. Therm. Spray Technol.* **9**, 369–376 (2000).

208. Giannini, C. *et al.* X-ray Diffraction: A powerful technique for the multiple-length-scale structural analysis of nanomaterials. *Crystals* **6**, 1–22 (2016).

209. Jauncey, G. E. . The Scattering of X-Rays and Bragg'S Law. *Natl. Acad. Sci.* **21**, 675–676 (1905).

210. Azad, M. & Avin, A. Scanning Electron Microscopy (SEM): A Review. *Proc. 2018 Int. Conf. Hydraul. Pneum. - HERVEX* 1–9 (2019).

211. Zhou, W., Apkarian, R., Wang, Z. L. & Joy, D. Fundamentals of scanning electron microscopy (SEM). *Scanning Microsc. Nanotechnol. Tech. Appl.* 1–40 (2007) doi:10.1007/978-0-387-39620-0_1.

212. Tang, C. Y. & Yang, Z. *Transmission Electron Microscopy (TEM)*. *Membrane Characterization* (Elsevier B.V., 2017). doi:10.1016/B978-0-444-63776-5.00008-5.

213. Inkson, B. J. *Scanning Electron Microscopy (SEM) and Transmission Electron Microscopy (TEM) for Materials Characterization*. *Materials Characterization Using Nondestructive Evaluation (NDE) Methods* (Elsevier Ltd, 2016). doi:10.1016/B978-0-08-100040-3.00002-X.

214. Vašková, H. A powerful tool for material identification : Raman spectroscopy.

215. Bumbrah, G. S. & Sharma, R. M. Raman spectroscopy – Basic principle, instrumentation and selected applications for the characterization of drugs of abuse. *Egypt. J. Forensic Sci.* **6**, 209–215 (2016).

216. Stelmachowski, P., Ciura, K. & Grzybek, G. Morphology-dependent reactivity of cobalt oxide nanoparticles in N2O decomposition. *Catal. Sci. Technol.* **6**, 5554–5560 (2016).

217. Jodłowski, P. J., Jędrzejczyk, R. J., Chlebda, D., Gierada, M. & Łojewska, J. In situ spectroscopic studies of methane catalytic combustion over Co, Ce, and Pd mixed oxides deposited on a steel surface. *J. Catal.* **350**, 1–12 (2017).

218. Holbrook, R. D., Galyean, A. A., Gorham, J. M., Herzing, A. & Pettibone, J. *Overview of Nanomaterial Characterization and Metrology*. *Frontiers of Nanoscience* vol. 8 (Elsevier, 2015).

219. Scimeca, M., Bischetti, S., Lamsira, H. K., Bonfiglio, R. & Bonanno, E. Energy dispersive X-ray (EDX) microanalysis: A powerful tool in biomedical research and diagnosis. *Eur. J. Histochem.* **62**, 89–99 (2018).

220. Kumar, C. G., Pombala, S., Poornachandra, Y. & Agarwal, S. V. *Synthesis, characterization, and applications of nanobiomaterials for antimicrobial therapy*. *Nanobiomaterials in Antimicrobial Therapy: Applications of Nanobiomaterials* (Elsevier Inc., 2016). doi:10.1016/B978-0-323-42864-4.00004-X.

221. Besselmann, S., Freitag, C., Hinrichsen, O. & Muhler, M. Temperature-programmed reduction and oxidation experiments with V2O5/TiO2 catalysts. *Phys. Chem. Chem. Phys.* **3**, 4633–4638 (2001).

222. Pirola, C., Galli, F. & Patience, G. S. Experimental methods in chemical engineering: Temperature programmed reduction—TPR. *Can. J. Chem. Eng.* **96**, 2317–2320 (2018).

223. Micromeritics. Temperature-Programmed Reduction Using the AutoChem. *One Micromeritics Drive* 2–3.

224. Agrawal, Y. C., McCave, I. N. & Riley, J. B. Laser diffraction size analysis. *Princ. Methods Appl. Part. Size Anal.* 119–128 (2010) doi:10.1017/cbo9780511626142.012.

225. Storti, F. & Balsamo, F. Particle size distributions by laser diffraction: Sensitivity of granular matter strength to analytical operating procedures. *Solid Earth* **1**, 25–48 (2010).

226. Joseph, E. & Singhvi, G. *Multifunctional nanocrystals for cancer therapy: A potential nanocarrier*. *Nanomaterials for Drug Delivery and Therapy* (Elsevier Inc., 2019). doi:10.1016/B978-0-12-816505-8.00007-2.

227. Williams, P. M. Zeta Potential. *Encycl. Membr.* 1–2 (2015) doi:10.1007/978-3-642-40872-4_612-1.

228. Almeida, L. C. *et al.* Washcoating of metallic monoliths and microchannel reactors. in *Studies in Surface Science and Catalysis* vol. 175 25–33 (2010).

229. Gholami, R., Alyani, M. & Smith, K. J. *Deactivation of Pd catalysts by water during low temperature methane oxidation relevant to natural gas vehicle converters*. *Catalysts* vol. 5 (2015).

230. Vita, A., Italiano, C., Pino, L., Laganà, M. & Recupero, V. Hydrogen-rich gas production by steam reforming of n-dodecane. Part II: Stability, regenerability and sulfur poisoning of low loading Rh-based catalyst. *Appl. Catal. B Environ.* **218**, 317–326 (2017).

231. Kikuchi, E., Uemiya, S., Koyama, A., Machino, A. & Matsuda, T. Steam Reforming of Hydrocarbons on Noble Metal Catalysts (Part 8) Steam Reforming of Methane on Supported Ruthenium Catalysts. *J. Japan Pet. Inst.* **33**, 152–157 (1990).

232. Arai, H. & Machida, M. Thermal stabilization of catalyst supports and their application to high-temperature catalytic combustion. *Appl. Catal. A Gen.* **138**, 161–176 (1996).

233. Moncada Quintero, C. W., Babar, R. Z. & Specchia, S. Performance and Controlling Regimes Analysis of Methane Steam Reforming on Ru/γ-Al2O3 Cordierite Monoliths. *Green Energy Technol.* 91–131 (2021) doi:10.1007/978-981-15-5667-8_5.

234. Toso, A., Colussi, S., Padigapaty, S., de Leitenburg, C. & Trovarelli, A. High stability and activity of solution combustion synthesized Pd-based catalysts for methane combustion in presence of water. *Appl. Catal. B Environ.* **230**, 237–245 (2018).

235. Lacroix, M. *et al.* Pressure drop measurements and modeling on SiC foams. *Chem. Eng. Sci.* **62**, 3259–3267 (2007).

236. Hernandez Camacho, J. N., Lecrivain, G., Schubert, M. & Hampel, U. Droplet Retention Time and Pressure Drop in SiSiC Open-Cell Foams Used as Droplet Separation Devices: A Numerical Approach. *Ind. Eng. Chem. Res.* (2019) doi:10.1021/acs.iecr.9b04247.

237. Ambrosetti, M., Bracconi, M., Groppi, G. & Tronconi, E. Analytical Geometrical Model of Open Cell Foams with Detailed Description of Strut-Node Intersection. *Chemie-Ingenieur-Technik* **89**, 915–925 (2017).

238. Santos, L. & Talaia, M. Experiment and theorisation: An application of the hydrostatic equation and Archimedes Theorem. 1–5 (1996).

239. Baran, I., Straumit, I., Shishkina, O. & Lomov, S. V. X-ray computed tomography characterization of manufacturing induced defects in a glass/polyester pultruded profile. *Compos. Struct.* **195**, 74–82 (2018).

240. Poryles, R. *et al.* Foam trapping in a 3D porous medium:: In situ observations by ultra-fast X-ray microtomography. *Soft Matter* **16**, 6354–6361 (2020).

241. Ou, X. *et al.* X-ray micro computed tomography characterization of cellular SiC foams for their applications in chemical engineering. *Mater. Charact.* **123**, 20–28 (2017).

242. Larachi, F. *et al.* X-ray micro-tomography and pore network modeling of single-phase fixed-bed reactors. *Chem. Eng. J.* **240**, 290–306 (2014).

243. Neethirajan, S., Karunakaran, C., Jayas, D. S. & White, N. D. G. X-ray Computed Tomography Image Analysis to explain the Airflow Resistance Differences in Grain Bulks. *Biosyst. Eng.* **94**, 545–555 (2006).

244. Simplício, L. M. T., Brandão, S. T., Domingos, D., Bozon-Verduraz, F. & Sales, E. A. Catalytic combustion of methane at high temperatures: Cerium effect on PdO/Al2O3 catalysts.

*Appl. Catal. A Gen.* **360**, 2–7 (2009).

245. Colussi, S. *et al.* Structure and morphology of Pd/Al2O3 and Pd/CeO 2/Al2O3 combustion catalysts in Pd-PdO transformation hysteresis. *Appl. Catal. A Gen.* **390**, 1–10 (2010).

246. Nasr, S., Semagina, N. & Hayes, R. E. Kinetic Modelling of Co3O4- and Pd/Co3O4-Catalyzed Wet Lean Methane Combustion. *Emiss. Control Sci. Technol.* **6**, 269–278 (2020).

247. Ciuparu, D., Altman, E. & Pfefferle, L. Contributions of lattice oxygen in methane combustion over PdO-based catalysts. *J. Catal.* **203**, 64–74 (2001).

248. Chin, Y. H. C., García-Diéguez, M. & Iglesia, E. Dynamics and thermodynamics of Pd-PdO phase transitions: Effects of pd cluster size and kinetic implications for catalytic methane combustion. *J. Phys. Chem. C* **120**, 1446–1460 (2016).

249. Italiano, C. *et al.* Preparation of structured catalysts with Ni and Ni–Rh/CeO2 catalytic layers for syngas production by biogas reforming processes. *Catal. Today* **273**, 3–11 (2016).

250. Vita, A. *et al.* Activity and stability of powder and monolith-coated Ni/GDC catalysts for CO2 methanation. *Appl. Catal. B Environ.* **226**, 384–395 (2018).

251. Vita, A., Italiano, C., Ashraf, M. A., Pino, L. & Specchia, S. Syngas production by steam and oxy-steam reforming of biogas on monolith-supported CeO2-based catalysts. *Int. J. Hydrogen Energy* 1–14 (2017) doi:10.1016/j.ijhydene.2017.11.140.

252. Giani, L., Groppi, G. & Tronconi, E. Mass-transfer characterization of metallic foams as supports for structured catalysts. *Ind. Eng. Chem. Res.* **44**, 4993–5002 (2005).

253. Wen, C. Y. & Yu, Y. H. A generalized method for predicting the minimum fluidization velocity. *AIChE J.* **12**, 610–612 (1966).

254. Xu, A., Zhao, T. S., Shi, L. & Xu, J. B. Lattice Boltzmann Simulation of Mass Transfer Coefficients for Chemically Reactive Flows in Porous Media. *J. Heat Transfer* **140**, 1–8 (2018).

255. Hayes, R. E., Kolaczkowskib, S. T., Li, P. K. C. & Awdry, S. Evaluating the effective diffusivity of methane in the washcoat of a honeycomb monolith. *Appl. Catal. B Environ.* **25**, 93–104 (2000).

256. Hadjiev, V. G., Iliev, M. N. & Vergilov, I. V. The Raman spectra of Co3O4. *J. Phys. C Solid State Phys.* **21**, L199–L201 (1988).

257. Zhang, M. *et al.* Effect of Al2O3-SiO2 substrate on gas-sensing properties of TiO2 based lambda sensor at high temperature. *Ceram. Int.* **44**, 3000–3004 (2018).

258. Shi, R. *et al.* Synthesis of ultrafine α-Al2O3 powder by two-step hydrolysis. *Ceram. Int.* **44**, 3741–3750 (2018).

259. Italiano, C., Vita, A., Fabiano, C., Laganà, M. & Pino, L. Bio-hydrogen production by oxidative steam reforming of biogas over nanocrystalline Ni/CeO2 catalysts. *Int. J. Hydrogen Energy* **40**, 11823–11830 (2015).

260. Palma, V., Pisano, D., Martino, M. & Ciambelli, P. Structured catalysts with high thermoconductive properties for the intensification of Water Gas Shift process. *Chem. Eng. J.* **304**, 544–551 (2016).

261. Zasada, F. *et al.* Periodic density functional theory and atomistic thermodynamic studies of cobalt spinel nanocrystals in wet environment: Molecular interpretation of water adsorption equilibria. *J. Phys. Chem. C* **114**, 22245–22253 (2010).

262. Zhao, G., Liu, Y. & Lu, Y. Foam/fiber-structured catalysts: non-dip-coating fabrication strategy and applications in heterogeneous catalysis. *Sci. Bull.* **61**, 745–748 (2016).

263. Palma, V., Pisano, D. & Martino, M. The influence of the textural properties of aluminum foams as catalyst carriers for water gas shift process. *Int. J. Hydrogen Energy* **42**, 23517–23525 (2017).

264. Wang, H. & Guo, L. Experimental investigation on pressure drop and heat transfer in metal foam filled tubes under convective boundary condition. *Chem. Eng. Sci.* **155**, 438–448 (2016).

265. Grosse, J. *et al.* Morphological characterization of ceramic sponges for applications in chemical engineering. *Ind. Eng. Chem. Res.* **48**, 10395–10401 (2009).

266. Dietrich, B., Schabel, W., Kind, M. & Martin, H. Pressure drop measurements of ceramic sponges-Determining the hydraulic diameter. *Chem. Eng. Sci.* **64**, 3633–3640 (2009).

267. Mao, X. Processing of Ceramic Foams. in *Recent Advances in Porous Ceramics* (ed. Uday M. Basheer Al-Naib) (IntechOpen Limited, 2018). doi:10.5772/intechopen.71006.

268. Ahmad, R., Ha, J.-H. & Song, I.-H. Processing Methods for the Preparation of Porous Ceramics. *J. Korean Powder Metall. Inst.* **21**, 389–398 (2014).

269. Liang, X. *et al.* Design of three-layered struts in SiC reticulated porous ceramics for porous burner. *Ceram. Int.* **45**, 8571–8576 (2019).

270. Bhattacharya, A., Calmidi, V. V. & Mahajan, R. L. Thermophysical properties of high porosity metal foams. *Int. J. Heat Mass Transf.* **45**, 1017–1031 (2002).

271. Roberts, A. P. & Garboczi, E. J. Elastic moduli of model random three-dimensional closed-cell cellular solids. *Acta Mater.* **49**, 189–197 (2001).

272. Schmierer, E. N., Razani, A., Keating, S. & Melton, T. Characterization of high porosity open-celled metal foam using computed tomography. *ASME Int. Mech. Eng. Congr. Expo.* 1–10 (2016).

273. Ghosh, I. Deterioration in heat transfer due to axial conduction of heat in open cell metal foam. *AIP Conf. Proc.* **1254**, 254–259 (2010).

274. Otsu, N. A Threshold Selection Method from Gray-Level Histograms. *IEEE Trans. Syst. Man Cybern. Syst.* **smc-9**, 62–66 (1979).

275. Moreira, E. A., Innocentini, M. D. M. & Coury, J. R. Permeability of ceramic foams to compressible and incompressible flow. *J. Eur. Ceram. Soc.* **24**, 3209–3218 (2004).

276. Inayat, A., Freund, H., Schwab, A., Zeiser, T. & Schwieger, W. Predicting the specific surface area and pressure drop of reticulated ceramic foams used as catalyst support. *Adv. Eng. Mater.* **13**, 990–995 (2011).

# CHAPTER I

(*PAPER I*)

Robust $Co_3O_4|\alpha–Al_2O_3|$cordierite structured catalyst for $N_2O$ abatement – validation of the SCS method for active phase synthesis and deposition

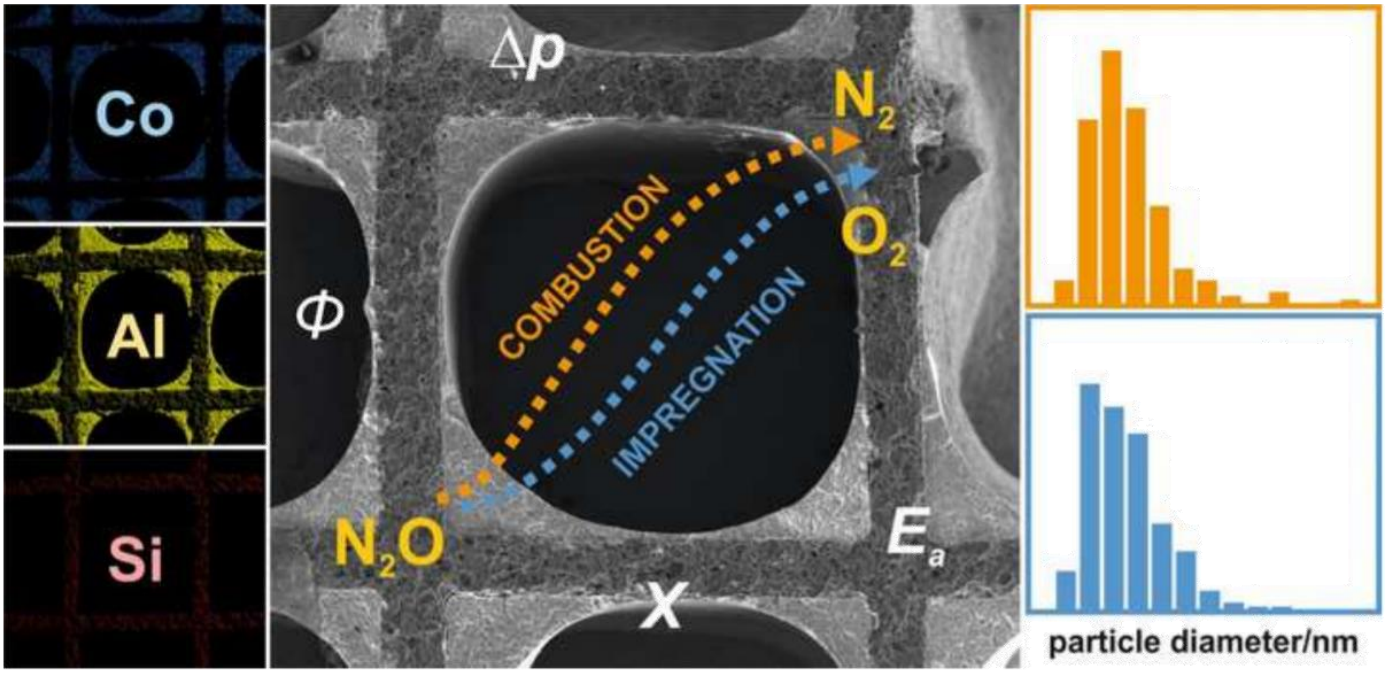


*Chemical Engineering Journal*. Elsevier B.V., 377, p. 120088.

DOI: 10.1016/j.cej.2018.10.025.

Chemical Engineering Journal 377 (2019) 120088

Contents lists available at ScienceDirect

Chemical Engineering Journal

journal homepage: www.elsevier.com/locate/cej

# Robust $Co_3O_4$|α-$Al_2O_3$|cordierite structured catalyst for $N_2O$ abatement – Validation of the SCS method for active phase synthesis and deposition

Sylwia Wójcik[a,*], Giuliana Ercolino[b], Marta Gajewska[c], Carmen W. Moncada Quintero[b], Stefania Specchia[b,*], Andrzej Kotarba[a]

[a] Faculty of Chemistry, Jagiellonian University, Gronostajowa 2, 30-387 Krakow, Poland
[b] Department of Applied Science and Technology, Politecnico di Torino, Corso Duca degli Abruzzi 24, 10129 Torino, Italy
[c] Academic Centre for Materials and Nanotechnology AGH, Mickiewicza 30, 30-059 Krakow, Poland

## HIGHLIGHTS

- One-step dispersion of $Co_3O_4$ on α-$Al_2O_3$|cordierite catalyst for de$N_2O$ by SCS method.
- Optimization of structured catalyst composition and synthesis conditions.
- Evaluation of the catalyst performance, engineering parameters, and robustness.
- Application capability in hospital ventilation system indicated.

## GRAPHICAL ABSTRACT

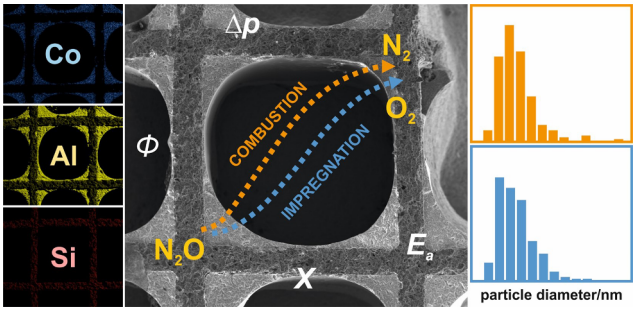


## ARTICLE INFO

*Keywords:*
Monolith
$Co_3O_4$ active phase
Solution Combustion Synthesis
$N_2O$ decomposition
Kinetic regime
Effectiveness factor

## ABSTRACT

$Co_3O_4$|α-$Al_2O_3$|cordierite structured catalysts were developed, optimizing washcoating procedure, active phase loading, and its deposition method via impregnation and solution combustion synthesis (SCS). The catalysts were thoroughly characterized by XRD, μRS, SEM/EDS, and BET, revealing that the catalyst layer deposited over cordierite carrier, consists of a washcoated micrometric α-$Al_2O_3$ (0.1–0.3 μm grains), where spinel nanocrystals (30–50 nm) were uniformly dispersed. It was found out that the SCS method to synthesize and finely disperse spinel nanoparticles results in significant better catalytic performance in low-temperature $N_2O$ decomposition than the classic impregnation method. The effectiveness factor evaluated, based on catalyst morphological features and de$N_2O$ catalytic results, was found to be ≈1. The determined mass transfer coefficients and type of the catalyst working regime (purely kinetic in the whole temperature range) provide the useful platform for rational design of a real de$N_2O$ catalyst.

## 1. Introduction

Increasing human impact on natural environment caused by dynamic industry development and increasing urbanization results in emission of hazardous substances into the atmosphere. Nitrous oxide ($N_2O$), recognized as a one of the most dangerous greenhouse gases [1], is emitted annually in large quantities. Only in European Union (2016) its emission reaches over 758.73 kilotons, which equals to 226 101.08 kilotons of $CO_2$ equivalent [2]. Due to high dispersion, agriculture sources dominating $N_2O$ emission are difficult to control. However,

* Corresponding authors at: Faculty of Chemistry, Jagiellonian University in Krakow, ul. Gronostajowa 2, 30-387 Krakow, Poland; Department of Applied Science and Technology, Politecnico di Torino, Corso Duca degli Abruzzi 24, 10129 Torino, Italy.
*E-mail addresses:* gudyka@chemia.uj.edu.pl (S. Wójcik), stefania.specchia@polito.it (S. Specchia).

https://doi.org/10.1016/j.cej.2018.10.025

Available online 05 October 2018

localized emitters such as incineration (i.e., hospitals [3]) or chemical industrial installations (i.e., nitric acid plant) are taken into the stage of environmental restrictions [4]. Whereas the results for de$N_2O$ catalysts tested in the nitric acid plants installations have been several times published elsewhere [5,6], there is no well documented investigations reported for such tests in the conditions of hospital ventilation systems.

Although there are several, like epidural, uterine and pelvic anesthesia, $N_2O$ is still used as anesthetic in several countries (Sweden, Finland, Norway, England, Australia, Canada and New Zealand) as the best and cheap method in normal birth, since it can be easily handled by the patients themselves. Among several possible ways of $N_2O$ abatement from hospital ventilation air, such as separation purification and reuse, oxidation or reduction, catalytic decomposition seems to be the most effective solution. The working conditions for the catalyst are as follow: 0–2% $N_2O$, 40–60% humidity, air flow, temperature window 400–600 °C with the optimal ($N_2O$ conversion > 95%) destruction temperature of 450 °C [7].

So far, a huge number of catalysts with various chemical composition, types of system (bulk, supported), and forms (pellets, tablets, extrudes, rings) have been reported as active in $N_2O$ abatement [8,9]. Cobalt spinel ($Co_3O_4$)-based catalysts were found to be active and stable in de$N_2O$ reaction conditions [10]. The problem of a relatively high price of bulk $Co_3O_4$ can be easily solved by dispersing its nanoparticles over typical oxide supports, such as alumina [11], ceria [12,13], cordierite [14]. Moreover, structured catalysts based on cordierite ($2MgO\text{-}Al_2O_3\text{-}5SiO_2$) monoliths with parallel, square channels, seems to be a promising solution for $N_2O$ abatement not only from nitric acid plants but also from hospital installations. The commonly used structured supports provide good dispersion and contact between the active phase nanoparticles and gas reactants as well as exhibit suitable thermal conductivity, high mechanical resistance, dust tolerance, and low-pressure drops. In practice, a thin $\alpha\text{-}Al_2O_3$ washcoat layer covering the body of cordierite monolith is required for improving stabilization of the crystalline active phase ($Co_3O_4$) over the structured support and blocking undesired transport of cations ($Mg^{2+}$, $Al^{3+}$) [15] from cordierite into cobalt spinel phase.

Nowadays, various methods of supported catalyst synthesis have been proposed [16–19]. Many of the preparation protocols consist in complex multistep operations, in which sophisticated chemicals and additives are used. Thus, a strong emphasis is placed on process intensification of catalysts preparation via reducing the number of operation units and chemical wastes, while assuring reproducible products. One of the alternative approaches involve the application of Solution Combustion Synthesis (SCS) [20]. An increasing interest in this method is generated by low energy requirements, very short time of synthesis, and minimalized precursor usage. SCS is based on an exothermic and self-sustaining redox reaction between two or more reactants (a combustible precursor and a redox mixture in water solution), initiated at low temperature (typically < 500 °C) [21]. The flameless combustion causes the evolution of gases, which results in formation of voluminous, nanometric oxide particles. It is worth to underline, that the active oxide phase can be synthesized *in situ* the structured body (either a monolith, foam, tissue, or any other shape) leading directly to a structured catalyst [22,23]. Furthermore, by adjusting synthesis conditions, the size and morphology of the obtained nanoparticles can be easily tuned. Due to all these advantages, SCS, as a catalyst preparation method, is directly scalable for industrial applications.

This study aimed to evaluate the possibility of preparing $Co_3O_4|\alpha\text{-}Al_2O_3|$cordierite structured catalysts for $N_2O$ decomposition using SCS method for spinel synthesis and dispersion as an alternative for the classic impregnation method. Various operative parameters of the preparation procedure (such as kind and amount of fuel, cobalt spinel loading) were investigated to optimize the catalyst performance. The morphological features of the fabricated structured catalyst, together with de$N_2O$ kinetic data, allowed for internal and external mass transfer evaluation. The de$N_2O$ performance of the optimal robust catalyst, obtained via SCS method, were benchmarked against a catalyst obtained by standard impregnation method.

## 2. Materials and methods

### 2.1. Chemicals

Cobalt(II) nitrate hexahydrate ($Co(NO_3)_3{\cdot}6H_2O$, ≥99% purity), glycerol ($C_3H_8O_3$, ≥99% purity), glycine ($NH_2CH_2COOH$, ≥99% purity), and urea ($CH_4N_2O$, ≥99% purity), nitric acid ($HNO_3$, 70%), and isopropyl alcohol ($C_3H_8O$, > 98% purity) were purchased from Sigma–Aldrich. $\alpha\text{-}Al_2O_3$ powder (AlO(OH) V700 type, calcined at 1300 °C) was purchased from Sasol. All aqueous solutions were prepared using deionized water purified by a Millipore Milli-Q system with a resistivity > 18 MΩ cm. Gas mixture 5% $N_2O$/He (purity 99.999%), used in catalytic measurements, was supplied in cylinder provided by Air Products company. Cordierite monoliths used in experiments as structured supports for catalysts were produced by Corning company.

### 2.2. Catalysts preparation

Cylindrical cordierite monoliths (length $L_m$ = 10 mm, diameter $d_m$ = 12 mm) with square channels (400 cpsi) were used as catalyst supports (for all other geometrical properties of the monoliths, see Table S1, in the Supporting Information). First, monolith supports were coated with a micrometric $\alpha\text{-}Al_2O_3$ layer using dip-coating method. This step of synthesis was applied to prevent ion migration ($Mg^{2+}$, $Al^{3+}$) from cordierite to the cobalt spinel active phase, as well as to improve surface and structural parameters for the following cobalt spinel deposition. The washcoating procedure consists of slowly dipping (1 mm $min^{-1}$) cordierite monolith into a $\alpha\text{-}Al_2O_3$ slurry, rotational drying, and high-temperature calcination. The washcoating slurry was prepared by mixing $\alpha\text{-}Al_2O_3$ powder with glycerol and demineralized water in concentrations of 55, 10, and 45 wt%, respectively. The pH of the slurry was fixed to 6.5 by 1 M nitric acid addition, viscosity of slurry was 27.4 mPa s. After cordierite dip-coating, the excess of $\alpha\text{-}Al_2O_3$ suspension in the channels was removed with a flow of air. Then, monoliths were dried under rotation (12 rpm) at 120 °C for 2 h. Finally, washcoated monoliths were slowly heated in calm air to 1000 °C at a rate of 2 °C $min^{-1}$, and calcined for 4 h, to avoid cracks.

Cobalt spinel active phase was deposited on $\alpha\text{-}Al_2O_3|$cordierite supports via SCS or impregnation method, the latter described elsewhere [24] as a reference. As-prepared structured supports (contained around 25% wt. $\alpha\text{-}Al_2O_3$) were immersed in a cobalt nitrate-based solution for 5 min. After this time, the excess of impregnation solution was removed and the impregnated $\alpha\text{-}Al_2O_3|$cordierite supports were further treated, depending on the preparation method. In case of SCS method, the samples were immersed in a cobalt nitrate/organic fuel solution and then placed in a hot furnace to ignite the combustion. Once the process ended up, the $Co_3O_4|\alpha\text{-}Al_2O_3|$cordierite SCS samples were calcined in static air at 600 °C for 4 h [25,26]. The SCS method included optimization of the following parameters: kind of fuel (glycine or urea) and its concentration (12–150% of stoichiometric amount), active phase loading, and temperature of ignition. The precursor solutions for the SCS method contained cobalt nitrate solution and urea or glycine. Various loading of active cobalt phase were obtained by subsequent impregnation combustion cycles (up to 6 cycles). As a result, in the series of SCS_$Co_3O_4|\alpha\text{-}Al_2O_3|$cordierite catalysts the cobalt spinel loading ranged from 4 to 17.8 wt%.

The applied SCS synthesis of the catalyst follows the reaction:

$$3Co(NO_3)_2 + \frac{28}{9}\Phi C_2H_5O_2N + 14(\Phi{-}1)O_2 \rightarrow Co_3O_4 + \frac{56}{9}\Phi CO_2 + \frac{70}{9}\Phi H_2O + \left(\frac{14}{9}\Phi + 3\right)N_2$$

where Φ is the fuel-to-oxidizer ratio [27]. The Φ value varied within the range 0.12–1.5 (being Φ = 1 the stoichiometric value of the SCS reaction).

For comparison, a reference benchmark structured catalyst sample was prepared via classic impregnation method [24]. In this case, the washcoated cordierite monolith was impregnated with the corresponding cobalt nitrate solution, dried (120 °C for 2 h) and calcined in the same conditions as for the SCS method.

### 2.3. Catalysts characterization

Phase composition of the structured catalysts was investigated by X-ray diffraction (XRD) analysis as well as micro Raman Spectroscopy (μRS). Loading of $Co_3O_4$ in the obtained series of catalysts was monitored by mass increase. The XRD measurements were carried out using a Bruker D8-advance instrument with CuKα radiation (λ = 1.540598 Å), in the 2 $\Theta$ range between 10° and 90° with the step of 0.2°. The cobalt spinel structure was confirmed by μRS. Spectra were recorded at room temperature (100–1000 $cm^{-1}$, 1 $cm^{-1}$ resolution) using Renishaw InVia spectrometer and confocal microscope Leica DMLM with CCD detector and a wavelength excitation of 785 nm. The signal-to-noise ratio was optimized by accumulating 12 scans for each measurement.

The morphological characterization and chemical analysis of as coated layers were performed using a field emission scanning electron microscope (FESEM FEI Versa 3D) equipped with an energy dispersive spectrometer (EDAX system), at an accelerating voltage of 20 kV. All of the samples were carbon-coated (~20 nm layer) before FESEM imaging.

The specific surface area and pore distributions of the coated catalysts were determined with the BET and NLDFT methods, respectively, using an Autosorb-1 Quantachrome apparatus with nitrogen as the adsorbate at –196 °C. The samples were degassed before measurement at 100 °C for 18 h.

The robustness of the as-prepared structured catalysts was verified via ultrasounds exposure in an aqueous solution of isopropyl alcohol (50 wt%), according to a standardized procedure, and measuring the dried weight before/after the treatment [28,29]. The sonication of monoliths was carried out at 45 kHz and 130 W for 1 h (S3M 2200 device by Sonica).

### 2.4. $N_2O$ decomposition tests

The catalytic activity tests of $N_2O$ decomposition were carried out in a temperature programmed surface reaction (TPSR) and steady-state modes placing structured catalysts in a straight quartz flow reactor. In the TPSR measurements the heating rate was 5 °C $min^{-1}$, whereas in the case of isothermal measurements, the temperature was change stepwise by 25 °C and kept at each step for 30 min. It should be noted however, that the steady-state was reached very fast (after ~1 min the observed QMS signals were stable) in the applied experimental conditions. The reaction was performed in the atmospheric pressure for a model gas 5% $N_2O$/He, flow 30 ml $min^{-1}$, GHSV = 1600 $h^{-1}$. The reaction products were monitored by a quadrupole mass spectrometer (RGA200, SRS, lines m/z = 44 for $N_2O$, 32 for $O_2$, 30 for NO, 28 for $N_2$). For the comparison of the catalysts performance, the reaction rate (expressed as $\mu mol_{N_2O} s^{-1} g^{-1}_{Co_3O_4}$) at 450 °C was calculated from the experimental data as a convenient measure for comparison of the tested catalysts activity. Additionally, as discussed below, the 450 °C is the highest temperature where the investigated catalysts operate in the kinetic regime.

### 2.5. Analysis of overall mass transfer coefficients and controlling regimes

Mass transfer limitations can strongly affect catalytic performance, which is constrained by two limits: the kinetic regime (at low temperatures) and the mass transfer controlled regime (at sufficiently high temperatures). Thus, evaluating mass transfer coefficients and differentiate among kinetic, internal (catalyst diffusion), or external mass transfer control regimes helps in structured catalysts design. In fact, regime transitions depend on catalyst design (channel dimensions and shape, catalyst loading/dispersion, washcoat properties) and the process operating parameters (flow conditions, temperature, inlet concentration). The characteristic time analysis is commonly used to this purpose, with the use of the three characteristic dimensionless Damköhler numbers:

$$Da_I = \frac{t_c}{t_r} > 1 \quad (1)$$

$$Da_{II} = \frac{t_{ext}}{t_r} < 0.1 \quad (2)$$

$$Da_{III} = \frac{t_{int}}{t_r} < 1 \quad (3)$$

where $t_c$ is the characteristic contact, or residence, time [ms], $t_r$ the characteristic reaction time [ms], $t_{ext}$ the characteristic external mass transfer time [ms], and $t_{int}$ the characteristic internal mass transfer time [ms] [30–33].

As a countercheck, the existence of any possible mass transfer limitation, also Carberry number and Weisz-Prater criterion can be evaluated:

$$Ca = \frac{r_{N_2O}}{k_G \bullet a_{gs,c} \bullet C_{N_2O,in}} < 0.05 \quad \text{(for a first−order reaction)} \quad (4)$$

$$WP = \frac{r_{N_2O} \bullet \delta_c^2}{D_{N_2O,e} \bullet C_{N_2O,s}} < 1 \quad (5)$$

where $r_{N_2O}$ is the observed volumetric reaction rate for $N_2O$ (kmol $m^{-3}$ $s^{-1}$), $k_G$ the extra-particle mass transfer coefficient (m $s^{-1}$), $a_{gs,c}$ the geometric surface area of the structured catalyst ($m^{-2}$ $m^{-3}$), $C_{N_2O,in}$ the inlet concentration of $N_2O$ in bulk phase (kmol $m^{-3}$), $\delta_c$ the thickness of coated catalyst (m), $D_{N_2O,e}$ the effective diffusivity of $N_2O$ ($m^2$ $s^{-1}$), and $C_{N_2O,s}$ the concentration of $N_2O$ at surface catalyst (kmol $m^{-3}$ $s^{-1}$). All the correlation and physical parameters used for the calculation of the dimensionless Damköhler, Carberry, and Weisz-Prater numbers are available in the Supporting Information.

## 3. Results and discussion

### 3.1. Physicochemical and catalytic characterization of structured catalysts

The crystalline structure of the prepared catalysts was investigated by XRD and μRS techniques. Fig. 1a shows the XRD patterns for the washcoat structured washcoated support as well as the developed $Co_3O_4$|α-$Al_2O_3$|cordierite structured catalysts (blue and orange lines represent catalysts prepared via impregnation and SCS methods, respectively). The diffraction lines (marked by ○) at 2$\Theta$ = 27.4, 35.1, 37.7, 43.4, 52.5, 57.5, 66.5, and 68.2 correspond to the (1 0 4), (1 1 0), (1 1 3), (0 2 4), (1 1 6), (2 1 1), (1 2 2), (2 1 4), and (3 0 0) reflection planes, respectively, indexed within the trigonal structure space group (*R*-3c) of α-$Al_2O_3$ (ICSD – 9771). Formation of the cobalt spinel in both synthesis methods is clearly evidenced by the presence of the characteristic lower intensity lines (marked by * in Fig. 1) located at 2$\Theta$ = 31.3, 36.9, 44.9, 59.5, 65.4, and 77.3, corresponding to the (2 2 0), (3 1 1), (4 0 0), (5 1 1), (4 4 0), and (6 2 2) reflection planes of $Co_3O_4$ (ICSD – 69378). Typically, diffractograms of the structured catalysts were dominated by cordierite high-intense reflexes, because of the relatively thin catalytic layer coated. However, the presence of both the alumina washcoat layer and cobalt spinel active phase were noticed easily, indicating the development of their crystals structure.

Fig. 1b shows the measured Raman spectra of the catalysts obtained by SCS method (with urea and glycine as fuels: yellow and orange

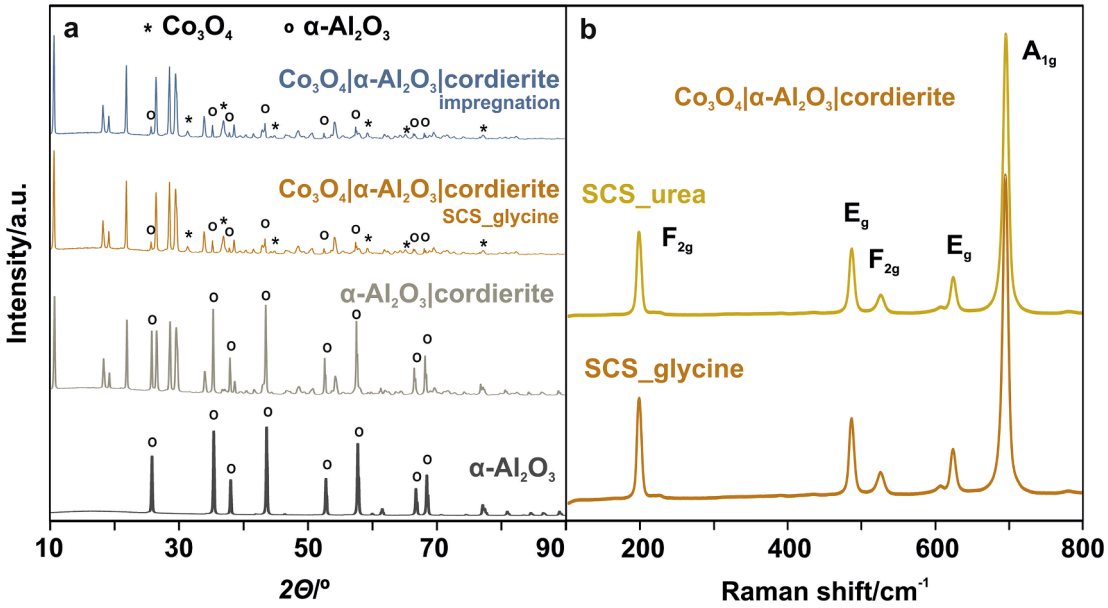


**Fig. 1.** (a) XRD patterns of structured $Co_3O_4|\alpha\text{-}Al_2O_3|$cordierite catalyst prepared by impregnation method (blue) and SCS method with glycine (orange) and the reference systems of washcoat slurry ($\alpha\text{-}Al_2O_3$) and washcoat|monolith ($\alpha\text{-}Al_2O_3|$cordierite). (b) Raman spectra of $Co_3O_4|\alpha\text{-}Al_2O_3|$cordierite catalyst obtained by SCS method with urea (yellow) and glycine (orange). (For interpretation of the references to colour in this figure legend, the reader is referred to the web version of this article.)

curves, respectively), with the characteristic lines located at 195, 487, 526, 624, and 694 $cm^{-1}$, corresponding to the five vibrational modes $F_{2g}$, $E_g$, $F_{2g}$, $F_{2g}$, and $A_{1g}$, respectively [33], of the cobalt spinel. Thus, the presence of cobalt spinel active phase on the surface of the investigated catalysts is confirmed. It is worth to notice, that the $F_{2g}$ (195 $cm^{-1}$) and $A_{1g}$ bands exhibit narrow symmetrical shapes, indicating that the tetrahedral and octahedral positions in the spinel structure are occupied by cobalt ions only. As shown elsewhere [34], the blocking function of the washcoat layer is essential for the effective catalyst [35]. In fact, migration of $Mg^{2+}$ and $Al^{3+}$ (cordierite constituents) into the spinel structure is detrimental for $deN_2O$ catalytic activity.

One of the important factors, that should always be evaluated [36] while preparing catalysts via SCS method, besides the type of fuel used, is the $\Phi$ value of the SCS reaction (see Eq. (1)). It rules the mechanism of the combustion process, influencing the final catalyst morphology [37]. This problem was addressed in this work comparing two types of suitable fuels (glycine or urea) for the synthesis of oxide nanomaterials, and varying $\Phi$ in the range of 0.12–1.5 (corresponding to 12–150% stoichiometric amount of fuel, Fig. 2). The series of $Co_3O_4|\alpha\text{-}Al_2O_3|$cordierite catalysts obtained via SCS method was then screened towards $deN_2O$ reaction in TPSR test-rig. To evaluate the performance of the investigated catalysts, the reaction rate, normalized to the mass of cobalt spinel active phase, was calculated for a selected temperature of interest (450 °C). Fig. 2 compares the results for the two series (SCS_glycine, SCS_urea) of catalysts obtained by SCS method as a function of the $\Phi$ ratio. The data clearly show non-monotonous dependence of the catalyst performance on the fuel stoichiometry. In general, the samples prepared using glycine exhibit higher activity than urea-assisted SCS, in the whole range of the investigated fuel content. Thus, the results allowed for the selection of glycine (orange bars) as significantly better, with the optimal 50% fuel stoichiometry. Based on these results, for further optimization the structured catalyst obtained via SCS with glycine as fuel and $\Phi = 0.5$ was selected.

To optimize the loading of the active phase in the selected structured catalyst (SCS_glycine), a series of samples with different content of $Co_3O_4$ (4–17.8 wt%) was examined in $deN_2O$ catalytic tests. Comparison of 50% conversion temperature ($T_{50\%}$) as a function of the spinel loading clearly indicates the optimal active phase content

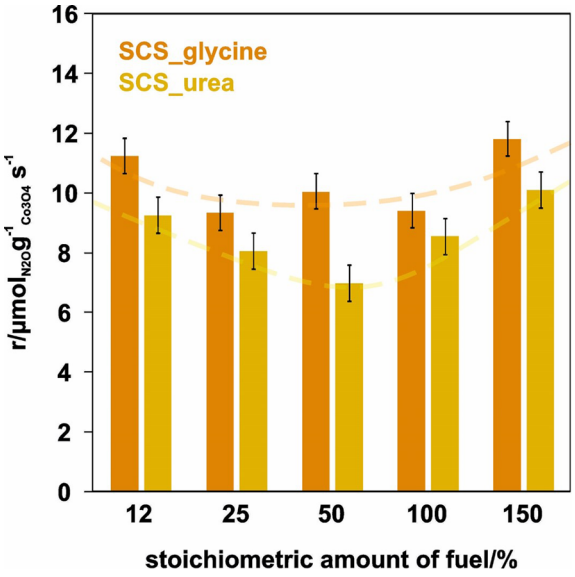


**Fig. 2.** The comparison of $deN_2O$ reaction rates ($N_2O$ μmol per 1 g of $Co_3O_4$ per 1 s) for series of catalysts $Co_3O_4|\alpha\text{-}Al_2O_3|$cordierite obtained via SCS method with various kind of fuel (glycine and urea – orange and yellow bars, respectively) for various amounts of fuel 12–150% (100% corresponds to stoichiometric fuel-oxidizer ratio, $\Phi = 1$). (For interpretation of the references to colour in this figure legend, the reader is referred to the web version of this article.)

(Fig. 3). As can be inferred from the profile of $T_{50\%}$, the increase in the spinel loading over the 7.4 wt% (corresponding 3 succeeding combustion cycles) does not lead to any improvement of the catalytic activity (plateau in the range 7.4 – 17.8 wt%, the highest loading corresponds to 6 combustion cycles). Taking into account all the data mentioned above, the optimal 7.4 wt% $Co_3O_4|\alpha\text{-}Al_2O_3|$cordierite structured catalyst was selected as the most promising structured catalyst and its performance benchmarked to that of a structured catalyst prepared via impregnation method with the similar active phase loading (7.8 wt% of $Co_3O_4$).

The mechanical stability of the selected $Co_3O_4|\alpha\text{-}Al_2O_3|$cordierite

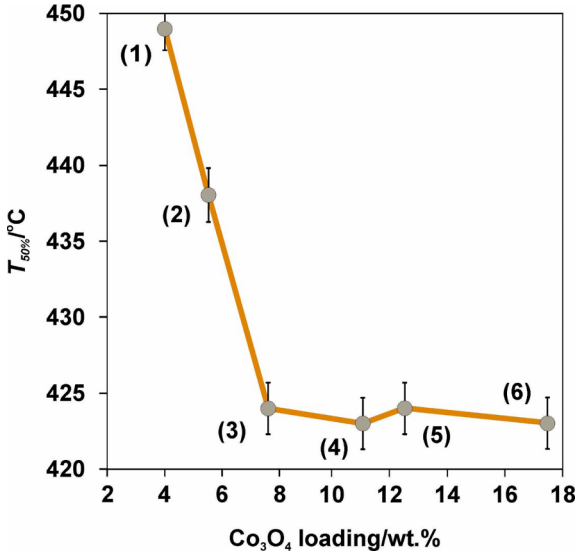


**Fig. 3.** $T_{50\%}$ parameter in $deN_2O$ reaction as a function of $Co_3O_4$ wt.% loading for series of $Co_3O_4|\alpha\text{-}Al_2O_3|$cordierite catalysts obtained via SCS method (50% stoichiometric amount of glycine). The numbers in parentheses indicate combustion cycles used to synthesize the structured catalysts.

structured catalyst, assessed in ultrasonic bath, indicates a highly compact and robust of the catalytic layer, being the weight loss limited to less than 5%, in line with data of coated monoliths available in the literature [28,29].

As can be seen in Fig. 4a, both structured catalysts display a high catalytic activity towards $deN_2O$, sign that both spinel deposition methods, used to coat alumina washcoated cordierite (grey line) were effective. The temperature window of $deN_2O$ catalytic activity covers well the requirements for catalytic process for cleaning gases emitted from hospital ventilation system (400–600 °C). As a matter of fact, the final $Co_3O_4|\alpha\text{-}Al_2O_3|$cordierite structured catalysts exhibit the active phase loading of 8.9 and 9.3 mg $cm^{-2}$ for the SCS_glycine and impregnation samples, respectively. The comparison of the conversion profiles indicates, however, the SCS_glycine as a more effective structured catalyst over the catalyst prepared via impregnation. This is also reflected in the lower value of activation energy for $N_2O$ decomposition, which was determined by fitting first-order kinetics to the experimental data (see Fig. 4b). Since the experimental data match the first-order kinetics very well, the activation barrier can be reliably determined from the Arrhenius dependence with the small error (0.2 kJ $mol^{-1}$). In fact, the apparent activation energy ($E_a$) for SCS_glycine structured catalyst was determined to be 83.4 ± 0.2 kJ $mol^{-1}$, while for the catalyst prepared via impregnation the $E_a$ value increased to 87.7 ± 0.2 kJ $mol^{-1}$. Such apparent activation energies are typical for the $N_2O$ decomposition over supported catalyst where the dispersed cobalt spinel plays the role of the active phase [14,38]. It is worth to underline that these results have serious practical implications, since SCS method is much faster and advantageous from the economical point of view [20,23,39]. The catalytic performance of both structured catalysts resulted unchanged after $deN_2O$ laboratory testing at 600 °C for 10 h.

To explain this founding, the two structured catalysts were evaluated regarding their morphological features, taking into account cobalt spinel nanocrystals distribution, the porosity of the coated layer and the corresponding effectiveness factors.

The surface morphology of the SCS_glycine coatings observed by SEM (Fig. 5) consists of rather loosely packed mainly globular alumina grains of an average size of about 200 nm [40]. The fabricated $Co_3O_4|\alpha\text{-}Al_2O_3$ coatings featured non-uniform thickness (20–200 μm), with coating accumulation in the corners of each square channel of the monolith. Such a feature is commonly observed for catalyst obtained by washcoating deposition procedure [41,42]. EDS analysis (see Fig. 6) of cross-sections of both types of supported catalysts indicated a uniform distribution of $Co_3O_4$ over the whole $\alpha\text{-}Al_2O_3$ coatings. The observed surface morphology of the coatings, produced via impregnation method, was more compact and slightly less rough, with similar shape and the average size of grains, as compared with SCS – prepared coatings. Table 1 lists values related to the spinel active phase loading as well as the specific surface area and pore volumes of the two structured catalysts, resulted from BET and NLDFT methods. While the total pore volume for both catalysts is almost the same, the SCS_glycine

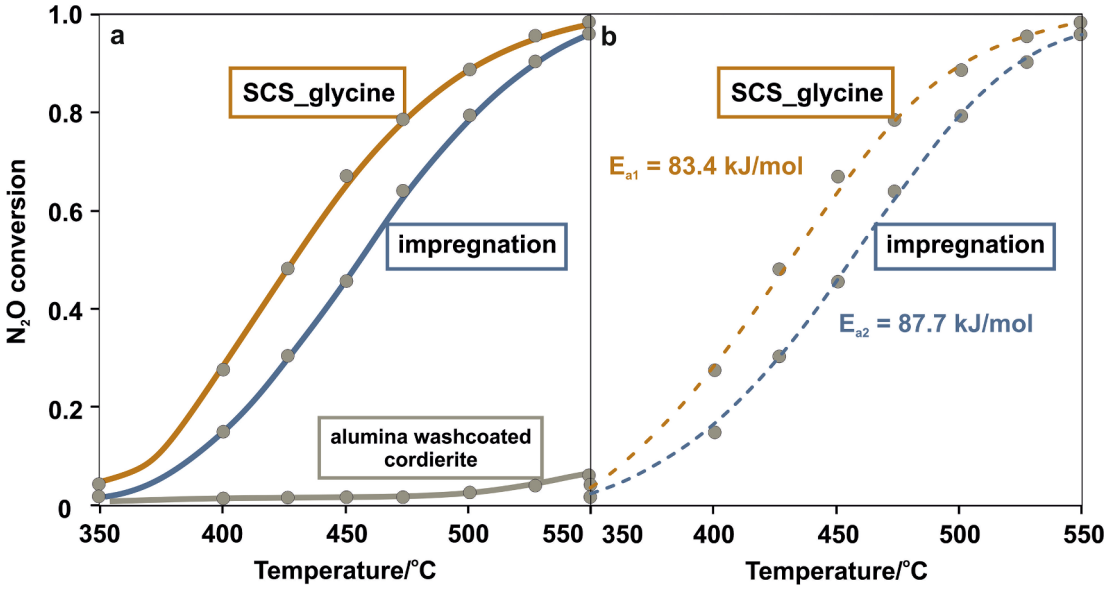


**Fig. 4.** (a) Results of isothermal (dots) and temperature-programed (line) tests of catalytic $deN_2O$ reaction shown as conversion vs temperature for the $Co_3O_4|\alpha\text{-}Al_2O_3|$cordierite structured catalysts obtained via SCS (orange) and impregnation (blue) methods as well as for washcoated-only $\alpha\text{-}Al_2O_3|$cordierite support (grey). (b) First-order kinetic fits to the experimental data of the steady state catalytic measurements for the $Co_3O_4|\alpha\text{-}Al_2O_3|$cordierite structured catalysts obtained via SCS (orange) and impregnation (blue) methods used for activation energy evaluation. (For interpretation of the references to colour in this figure legend, the reader is referred to the web version of this article.)

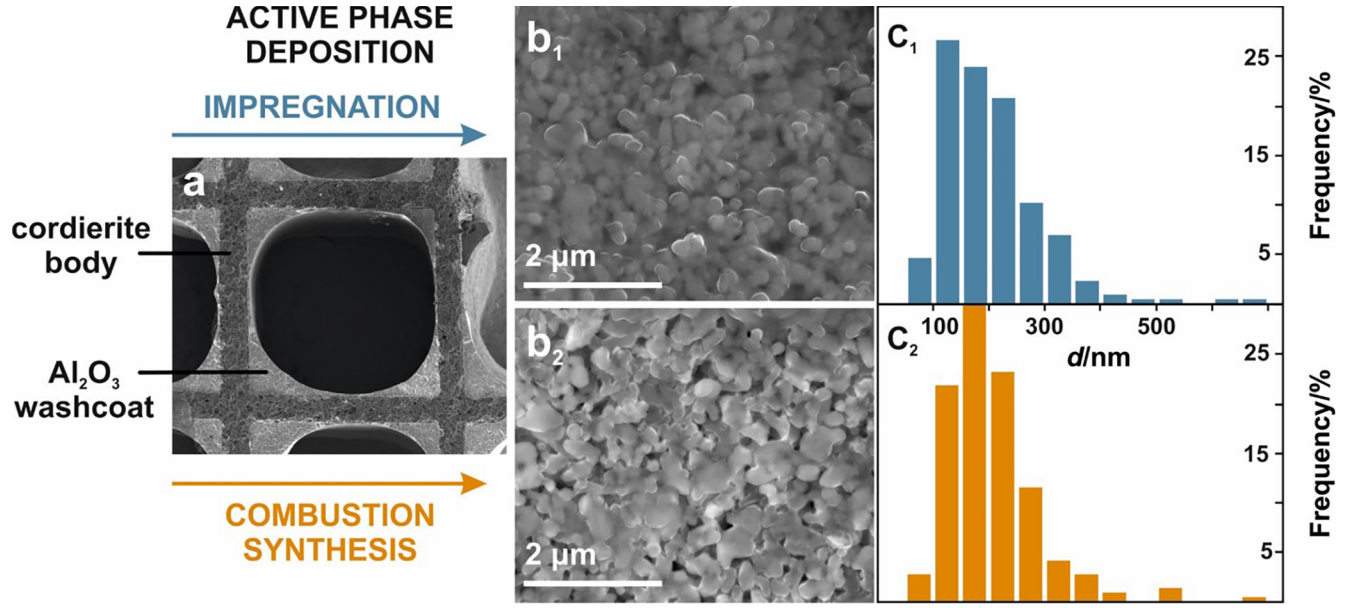


**Fig. 5.** FESEM images of the $|\alpha\text{-}Al_2O_3|$cordierite (a) and $Co_3O_4|\alpha\text{-}Al_2O_3|$cordierite structured catalysts obtained via SCS ($b_1$) and impregnation ($b_2$) methods highlighting the coated catalytic layer, and the size distribution of grains ($c_1$, $c_2$, respectively).

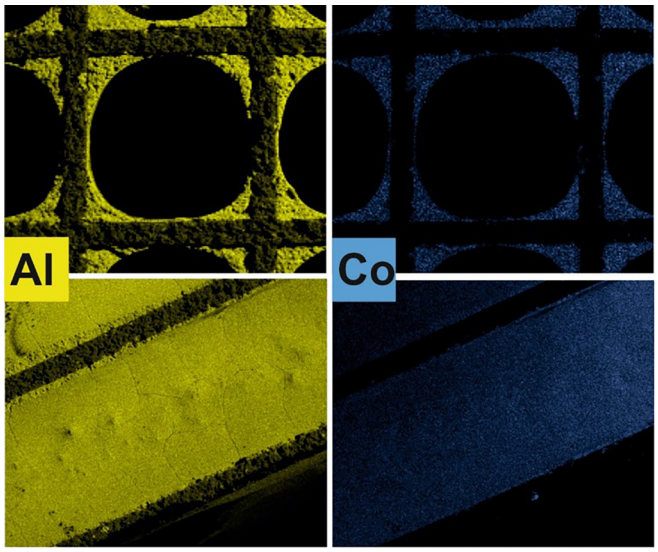


**Fig. 6.** FESEM/EDS analysis of cross- (top panel) and longitudinal (bottom panel) section of $Co_3O_4|\alpha\text{-}Al_2O_3|$cordierite catalyst obtained via SCS glycine-assisted method.

**Table 1**
Basic experimental characterization of the investigated structured catalysts (active phase loading, specific surface area, micropore an total pore volume, and average pore dimension).

| | $Co_3O_4\|\alpha\text{-}Al_2O_3\|$cordierite SCS_glycine | $Co_3O_4\|\alpha\text{-}Al_2O_3\|$cordierite impregnation |
|---|---|---|
| Active phase ($Co_3O_4$) loading [wt%] | 7.4 | 7.8 |
| BET s.s.a. [$m^2\,g^{-1}$] | 1.4 | 2.6 |
| Micropore volume, $V_{mp}$ [$cm^3\,g^{-1}$] | $2.6{\cdot}10^{-4}$ | $3.1{\cdot}10^{-4}$ |
| NLDFT total pore volume, $V_{pt}$ [$cm^3\,g^{-1}$] | $1.6{\cdot}10^{-2}$ | $1.5{\cdot}10^{-2}$ |
| Average pore diameter, $d_p$ [Å] | 460 | 560 |

structured catalyst exhibits a less microporous characteristic, with smaller pores compared to the impregnated sample.

### 3.2. Analysis of overall mass transfer coefficients and controlling regimes

First of all, the presence of any entrance effect on mass transfer was considered negligible. In fact, the length of the entrance zone, $L_{entrance}$ eq. (6), is less than 0.05% of monolith length (10 mm) in all cases, well below the technical limit of 1.63 mm. This condition was verified for all tested conditions and both $Co_3O_4|\alpha\text{-}Al_2O_3|$cordierite structured catalysts [32,43,44].

$$L_{entrance} = 0.05{\cdot}Re{\cdot}Sc{\cdot}d_h \cdot\delta_c = \frac{A_{ch}-A_c}{P_c} \tag{6}$$

From Fig. 4, the $deN_2O$ blank test performed on the $\alpha\text{-}Al_2O_3|$cordierite structured catalyst confirmed the absence of any gas phase reaction in the experimental conditions used. Thus, it is possible to use $Da_I$ to evaluate the relationship between the residence time ($t_c$) and the reaction time ($t_r$), as shown in Fig. 7a. In fact, when $Da_I$ is greater than 1, the reactant mixture has sufficient time to react over the coated catalytic layer of the structured catalyst. Except at low temperature for both samples, this condition is always verified. Moreover, the SCS_glycine performs better compared to the monolith prepared by impregnation, considering the slightly higher $Da_I$ values. This result can be explained considering that $deN_2O$ is a slow reaction at low temperature, especially on structured catalyst prepared by impregnation (values of $t_r$ in Fig. S1, Supporting Information).

The presence of internal/external mass transfer can be verified with $Da_{II}$ and $Da_{III}$. When $Da_{II}$ is lower than 0.1, there is no external mass diffusion limitation. This is always the case for both structured catalysts (Fig. 7b), sign that there is no formation of concentration gradients between the bulk gas phase and the catalyst surface exposed to the bulk gas phase [45,46]. The absence of external mass transfer limitation is confirmed also considering the Carberry number, which in all conditions tested, and for both structured catalysts resulted always lower than 0.005, well below the limit of $Ca < 0.05$.

When $Da_{III}$ is lower than 1, there is no internal mass transfer limitation, while for values greater than 1, the formation of concentration gradients along the coated catalyst thickness, starting from the surface exposed to the bulk gas phase, causes internal mass transfer limitations.

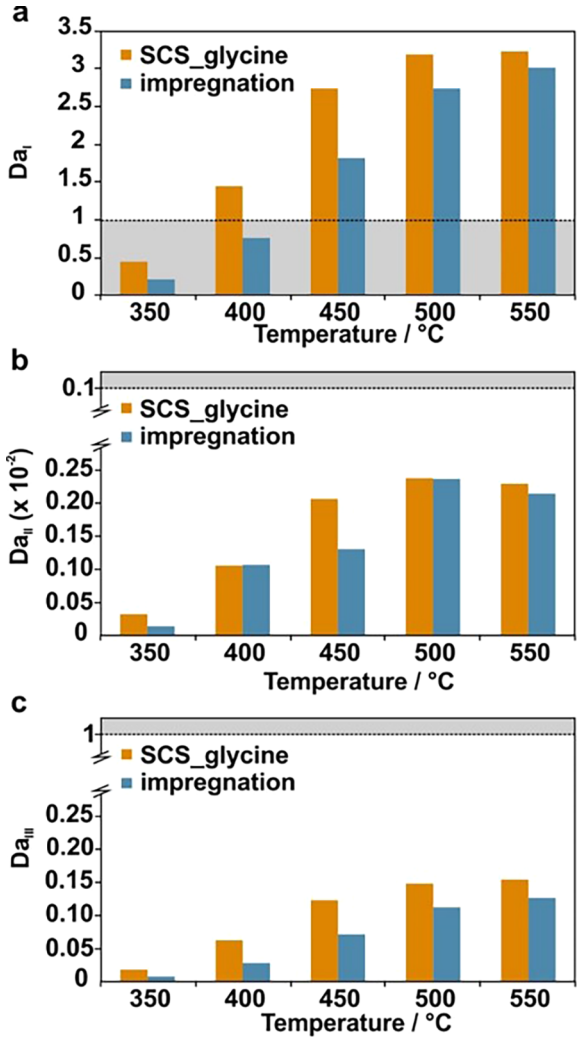


**Fig. 7.** Influence of temperature on $Da_I$, $Da_{II}$, and $Da_{III}$ for $Co_3O_4$|α-$Al_2O_3$|cordierite structured catalysts obtained via SCS (orange) and impregnation (blue) methods. Gray areas denote operative conditions in which Damkhöler numbers indicate the presence of limitations. (For interpretation of the references to colour in this figure legend, the reader is referred to the web version of this article.)

In this specific case, due to the catalyst accumulation in the corners of each channel of the monolith, the definition of average coating thickness cannot be directly applied here. Thus, $Da_{III}$ is determined considering an equivalent catalyst thickness, $\delta_c$, calculated as:

$$\delta_c = \frac{A_{ch} - A_c}{P_c} \tag{7}$$

where $A_{ch}$ ($m^2$) is the area of a single bare channel, $A_c$ ($m^2$) the area remaining available in the channel for the flow of reactants after catalyst deposition, and $P_c$ (m) the circumference of $A_c$ [45]. Fig. 8a highlights the geometry of a coated channel, with the characteristic geometric dimensions used to calculate $\delta_c$. Being $A_c$ far from a perfect circle, the corresponding diameter $d_f$ (μm) has been estimated by SEM (Fig. 5) as an average value derived by several measurements in different channels, considering that the minimum and maximum catalyst thickness values are $\delta_{min}$ = 20 μm and $\delta_{max}$ = 200 μm for both monoliths. In this way, we accounted for $\delta_{eq}$ = 80 μm using Eq. (7). Interestingly, $\delta_c$ is slightly smaller than the average arithmetic value between $\delta_{min}$ and $\delta_{max}$. According to this distinction, both structured monoliths do not suffer internal mass transfer, $Da_{III}$ values are always lower than 0.15, well below the limit of 1 for internal mass transfer limitations (Fig. 7c). The difference in $Da_{III}$ values between the two samples is linked to the different pore distribution values ($V_{pt}$, Table 1), with the SCS_glycine having the smaller average diameter ($d_p$, Table 1), which influences the effective diffusivity of $N_2O$ ($D_{N_2O,e}$) into the coated catalytic layer. In fact, $D_{N_2O,e}$ for SCS_glycine sample is always slightly lower, at all operative temperatures, than the corresponding values of the sample prepared by impregnation (values of $D_{N_2O,e}$ Fig. S2, Supporting Information). It must be underlined that de$N_2O$ reaction, being a surface reaction (i.e., the reaction is complete in a thin boundary catalytic layer near the fluid-catalyst interface), is almost independent from the surface properties of the catalyst, such as a high specific surface area and, even more, a pore volume. The countercheck by calculating the WP numbers, using $\delta_c$, confirms the outcomes of Fig. 7c.

To gain insight the catalyst activity of the two samples, we evaluated the Thiele modulus ($\phi$) for the two $Co_3O_4$|α-$Al_2O_3$|cordierite structured catalysts, the corresponding effectiveness factors ($\eta$), and all the individual/overall resistances to mass transport into a monolith for a first-order kinetics reaction, according to Fig. 8, using the following Eqs. (8,9) [45,47].

$$\phi = \sqrt{\frac{k_{obs} \cdot R_{\Omega i}^2}{D_{N_2O,e}}} \tag{8}$$

$$\eta = \frac{1}{1 + \frac{\phi^2}{Sh_i}} \tag{9}$$

where $k_{obs}$ is the observed first-order reaction rate constant ($s^{-1}$), $R_{\Omega i}$ the effective transverse diffusion length in the coated catalyst layer for the internal resistance (m), $D_{N_2O,e}$ the effective diffusivity of $N_2O$ ($m^2\,s^{-1}$), and $Sh_i$ the internal Sherwood number. All the correlations and physical parameters used for the calculations of $\phi$ and $\eta$ are available in the Supporting Information. For both samples, $\phi$ is very low, below 1, and $\eta$ as well, ranging from 0.6 to 1 (Fig. S3, Supporting Information), sign that the coated catalyst is fully used during the reaction, which indicates the de$N_2O$ process is rate-limited and not diffusion-limited, and the reaction rate is controlled by the intrinsic kinetics. The reaction thus operates in the typical asymptotical situation for which $\eta \rightarrow 1$ *for* $\phi \ll 1$ (as also confirmed by high $t_r$ values (Fig. S1, Supporting Information).

Thus, we calculated the overall resistance to mass transfer $R_t$ ($s\,m^{-1}$) as the sum of three resistances in series, using Eq. (10): the gas phase film resistance $R_e$, the internal mass transfer resistance $R_i$, and the reaction resistance $R_r$, according to a simplified low-dimensional model, specifically developed for the $Al_2O_3$|cordierite washcoated monoliths [45,47]. The model can be used when, as in this specific case for both coated monoliths, the flow is laminar and fully developed. Transverse Peclet number is ≪1. $N_2O$ concentration is low enough to consider small the adiabatic temperature rise (isothermal conditions).

$$R_t = R_e + R_i + R_r = \frac{1}{k_{m,app}} = \frac{1}{k_{m,e}} + \frac{1}{k_{m,i}} + \frac{1}{k_{obs} \cdot R_{\Omega i}} \tag{10}$$

where $k_{m,app}$, $k_{m,e}$, $k_{m,i}$, and $k_{obs} \cdot R_{\Omega i}$ are the experimentally observable apparent mass transfer coefficient, the external/internal mass transfer coefficients, and the reaction coefficient depending on the first-order reaction rate constant, respectively [45,47]. All the correlations and physical parameters used for the calculation of $R_t$ are available in the Supporting Information.

Fig. 9a shows the calculated resistances for both samples. In both cases, $R_t$ is coincident with $R_r$, that is, the overall mass transfer is dominated by the reaction resistance over the entire range of temperature. While both $R_e$ and $R_i$ are negligible (no external and internal mass transfer limitations, as already evidenced with $Da_{II}$ and $Da_{III}$), with $R_i$ bigger than $R_e$. As a practical criterion $R_t \geq 0.9\ R_r$ for kinetic regime [47], as in our case. Only for temperatures higher than 450 °C $R_r$ is slightly lower than $R_t$, but not significantly. Therefore, both coated

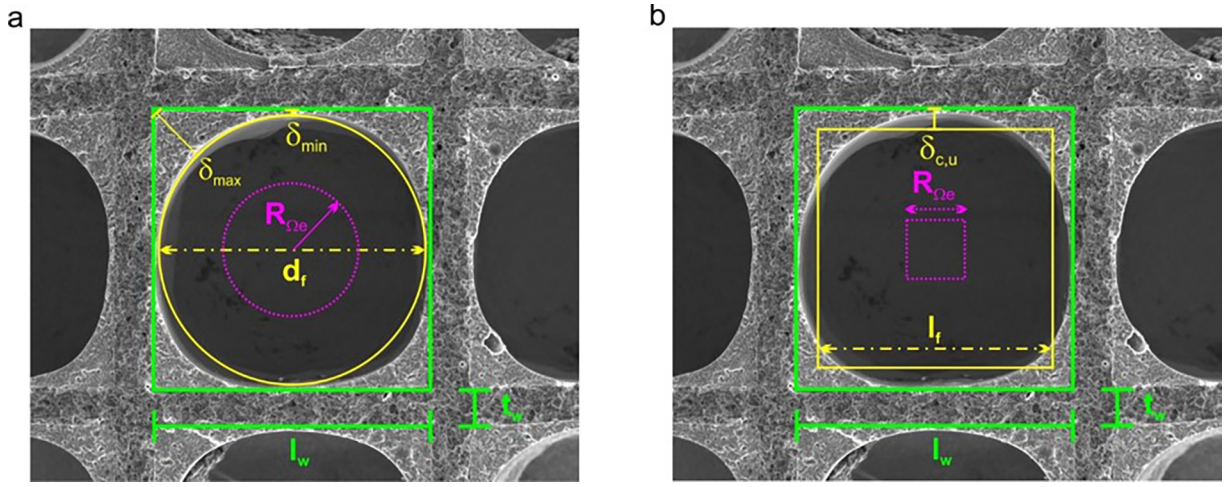


**Fig. 8.** Characteristic geometric dimensions of a single channel of the monolith: channel width ($l_w$) and wall thickness ($t_w$) (referred to bare monolith). (a) Real case: highlighted in green $A_{ch}$ ($l_w \times l_w$, the area of a single bare channel), in yellow $A_c$ ($^{\pi}/_4 \times d_f^2$, the area remaining available in the channel for the flow of reactants after catalyst deposition). The values of $\delta_{min}$, $\delta_{max}$, and $d_f$ estimated from several SEM measurements (Fig. 5). (b) Hypothetical case (uniform catalyst deposition): highlighted in green $A_{ch}$ ($l_w \times l_w$, the area of a single bare channel), in yellow $A_f$ ($l_f \times l_f$, the area remaining available in the channel for the flow of reactants after hypothetical uniform catalyst deposition). $R_{\Omega e}$ represents the effective transverse diffusion length for gas phase for external mass transfer. (For interpretation of the references to colour in this figure legend, the reader is referred to the web version of this article.)

monoliths work in kinetic regime, with $R_t = R_r$ decreasing with the raise of temperature. This result means that also at high temperature the rate of reaction becomes constant, without any significant increase (Fig. 9b). At high temperature, the two samples reach almost the same reaction rate values, with SCS_glycine sample slightly better, in line also with the estimated lower value of $E_a$. Consequently, $R_r$ and $R_t$ for

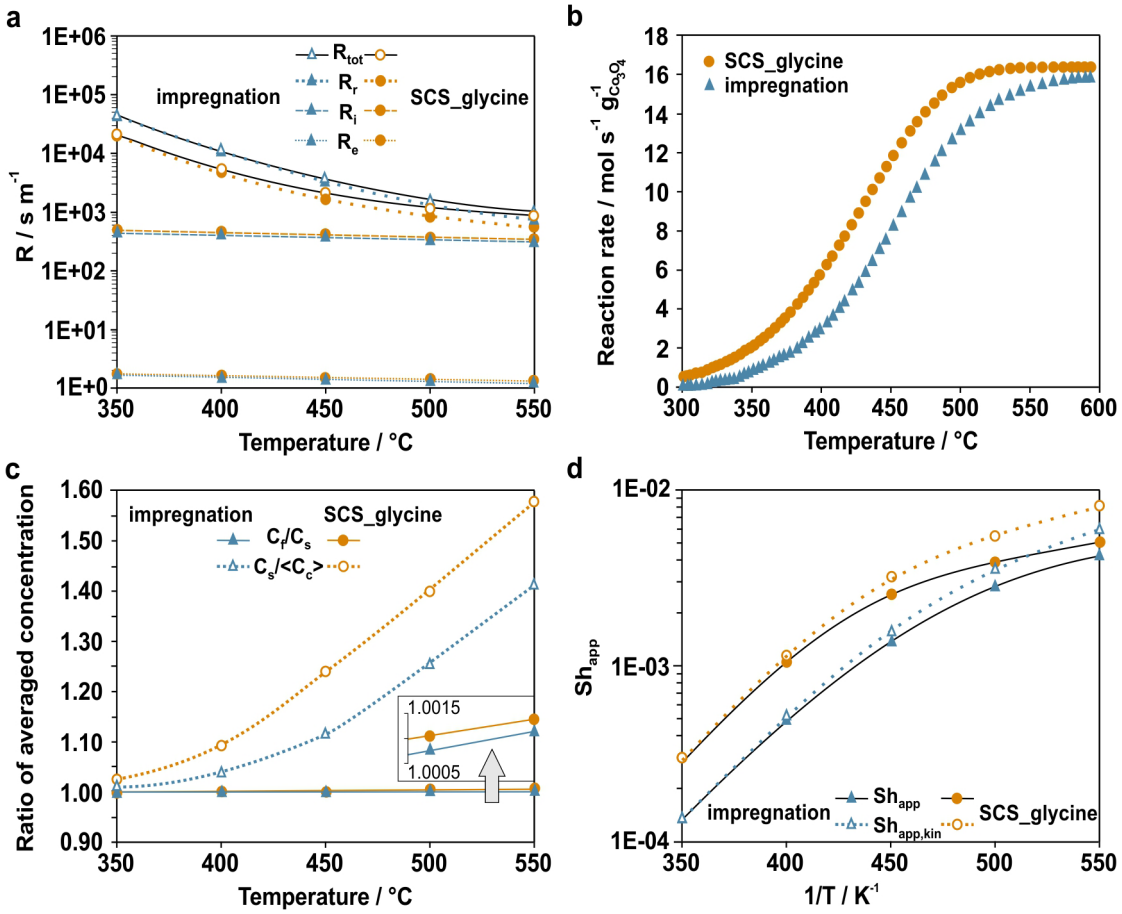


**Fig. 9.** For $Co_3O_4$|α-$Al_2O_3$|cordierite structured catalysts obtained via SCS (orange) and impregnation (blue) methods: (a) Calculated resistances for the mass transfer process from de$N_2O$ tests; (b) Experimental reactions rates; (c) Calculated ratios of transverse average concentrations profiles, showing kinetic regime over the entire operating temperature range; (d) Calculated experimentally observable Sherwood numbers. (For interpretation of the references to colour in this figure legend, the reader is referred to the web version of this article.)

SCS_glycine monolith are slightly lower, especially at low temperature (Fig. 9a): this structured catalyst, offering a lower overall resistance value, is performing better. Since both coated monoliths are working in kinetic regime, the reaction rate is much smaller than the rate of external mass transfer and internal diffusion into the catalyst layer. Therefore, the reaction occurs throughout the whole coated catalyst layer and the concentration profile of $N_2O$ in the transversal direction of the monolith (in each channel) is nearly uniform, especially at temperatures below 450 °C. This result is evident by plotting the ratio of averaged concentrations $C_f/C_s$ and $C_s/ < C_c >$, considering $C_f$ the concentration of $N_2O$ in the bulk gas phase, $C_s$ the concentration of $N_2O$ at gas/catalyst interface boundary, and $< C_c >$ the average concentration of $N_2O$ into the catalyst layer, weighted with respect to activity (Fig. 9c). At all temperatures, $C_f$ and $C_s$ are almost the same (no appreciable differences). Instead, the $C_s/ < C_c >$ ratio remains below the value of 1.1 (limit considered as a trade-off for the kinetic regime) for temperature lower than 400 °C for SCS_glycine and 450 °C for the impregnated monolith. This is a further confirmation that our coated monoliths work in kinetic regime for temperature below 400/450 °C. Fig. S4 in the Supporting Information shows the trends of calculated concentration profiles at low and high temperature. Consequently, writing Eq. (10) in dimensionless form Eq. (11), it is possible to obtain the overall experimentally observable mass transfer coefficient ($Sh_{app}$), Eq. (12); where for SCS_glycine is slightly higher than that of the impregnation sample (Fig. 9d). In both cases, $Sh_{app}$ has very low values, much lower that the theoretical limit of $Sh_{e\infty} = 3.656$ (asymptotic external Sherwood number, [45]) for square channels with circular flow area (as in our case). Notably, $Sh_{app}$ is coincident with $Sh_{app,kin}$, Eq. (13), representing the limiting case of a slow reaction [45], for temperatures below 400/450 °C, whereas for higher temperatures the difference between $Sh_{app}$ and $Sh_{app,kin}$ is rather limited.

$$\frac{1}{Sh_{app}} = \left(\frac{1}{Sh_e} + \frac{\mu \bullet \lambda}{4} \bullet \frac{1}{Sh_i} + \frac{\mu \bullet \lambda}{4 \bullet \phi^2}\right) \tag{11}$$

$$Sh_{app} = \frac{4 \bullet k_{m,app} \bullet R_{\Omega e}}{D_{N_2O,mix}} \tag{12}$$

$$Sh_{app,kin} = \frac{4 \bullet \phi^2}{\mu \bullet \lambda} \tag{13}$$

where $\lambda = \frac{R_{\Omega e}}{R_{\Omega i}}$ and $\mu = \frac{D_{N_2O,mix}}{D_{N_2O,e}}$. As a matter of fact, the $E_a$ previously determined can be considered not as apparent activation energy, but intrinsic kinetic activation energy. Both catalysts operate in kinetic regime in the investigated low-temperature deN$_2$O conditions.

As evident from Fig. 10, looking at the $R_r/R_t$ and $R_i/R_t$ ratios, it emerges that the reaction resistance is independent of $D_{N_2O,e}$, while the internal resistance increases with $D_{N_2O,e}$, which in turns increases with temperature.

Actually, we can imagine a better distribution of the catalytic layer during deposition, leading to a constant catalyst thickness, to exploit better the active phase distribution along the channels. This catalyst shaping, having a square catalyst distribution in square channel monoliths, as hypothetically represented in Fig. 5b, is typical of many coated monoliths used in the literature [32,42,48,49]: with catalyst loadings ranging from 4 to 15 mg cm$^{-2}$, the average uniform catalyst layer ranges from 20 to 100 μm, without huge accumulation in the corners of each channel. Based on this hypothesis, we estimated an average $\delta_{c,u}$ for our structured catalysts, by imposing the same $A_c$ (the area remaining available in the channel for the flow of reactants after catalyst deposition), which means maintaining constant the space velocity into the channels. Thus, we calculated $\delta_{c,u} = 60$ μm, a lower value respect to the previously considered $\delta_q = 80$ μm. Under this hypothesis, we estimated the new $R_t$, $R_e$, $R_i$, and $R_r$, maintaining constant all parameters previously used because of the same space velocity. Fig. 11 shows the results for the two structured catalyst by using the catalyst thickness as fitting parameter: in the whole temperature range,

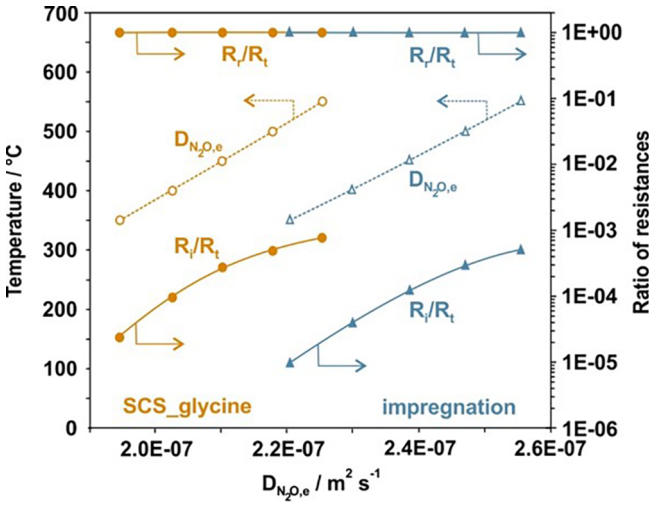


**Fig. 10.** For $Co_3O_4$|α-$Al_2O_3$|cordierite structured catalysts obtained via SCS (orange) and impregnation (blue) methods: increasing trends of $D_{N_2O,e}$ with temperature; calculated ratios of resistances with $D_{N_2O,e}$. (For interpretation of the references to colour in this figure legend, the reader is referred to the web version of this article.)

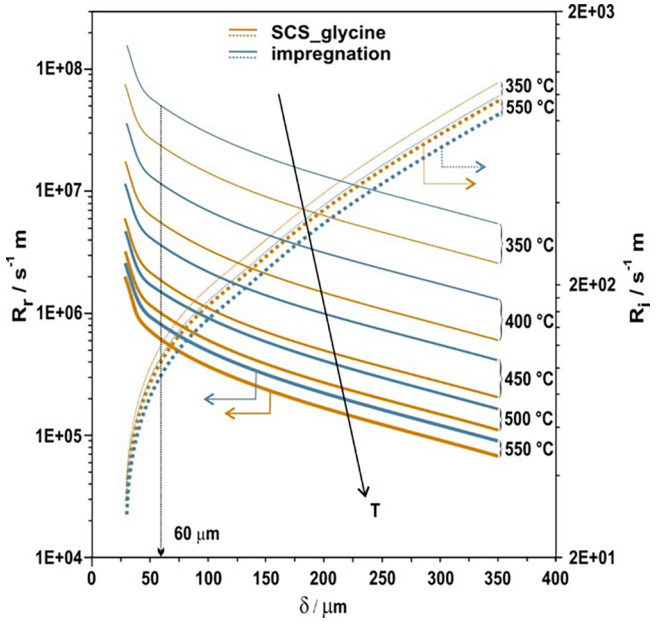


**Fig. 11.** Resistances for the mass transfer process in deN$_2$O tests for $Co_3O_4$|α-$Al_2O_3$|cordierite structured catalysts obtained via SCS (orange) and impregnation (blue) methods, calculated for an hypothetical uniform distribution of the catalyst layer (square catalyst shape in square channel, Fig. 5b). $R_r$ scale (on the left) different from $R_i$ scale (on the right). (For interpretation of the references to colour in this figure legend, the reader is referred to the web version of this article.)

the samples are in kinetic regime, as in the real case, with $R_t = R_r$, with and their trends decreasing with both the temperature and catalyst thickness. Interestingly, when $\delta$ increases (evaluated up to 350 μm), $R_i$ starts rising significantly, becoming more important, but being its contribution always ≪ compared to $R_r$ (three orders of magnitude difference, and $R_r/R_t \approx 1$). The samples operate always in kinetic regime. Again, $Sh_{app}$, almost coincident with $Sh_{app,kin}$, has very low values, much lower that the theoretical limit of $Sh_e = 3.088$ ([45]) for square channels with square catalyst distribution. With $\delta_{c,u} = 60$ μm, the calculated resistances are lower compared to the case of not uniform catalyst shaping ($\delta_{eq} = 80$ μm).

## 4. Conclusions

$Co_3O_4$|α-$Al_2O_3$|cordierite structured catalysts for low-temperature $N_2O$ decomposition were developed, optimizing washcoating procedure, active phase loading, and deposition method. The most appropriate preparation protocol consists of washcoating micrometric α-$Al_2O_3$ onto cordierite monoliths and dispersing uniformly $Co_3O_4$ nanocrystals via solution combustion synthesis (SCS). The results of de$N_2O$ tests showed that the structured catalyst work in kinetic regime in the whole temperature range (following the first-order kinetics model), with an effectiveness factor approaching 1, allowing the determination of the intrinsic kinetic parameters. The control of washcoat thickness allows the evaluation of the impact of internal diffusion limitations, absent in the case of the low rate of de$N_2O$ reaction within the applied conditions. It is demonstrated that the developed catalyst can be considered as a practical solution for low-temperature $N_2O$ abatement, pointing out at the SCS method as a particularly effective for spinel active phase dispersion. As a result, the whole volume of the alumina washcoat (20–200 μm) was exploited in the reaction.

## Acknowledgments

Authors would like to acknowledge National Science Centre in Poland funding awarded by the decision number 2016/23/N/ST8/01512. Sylwia Wójcik gratefully acknowledges the Erasmus+ Programme for her Visiting Scholarship at the Politecnico di Torino (Italy).

## Appendix A. Supplementary data

Supplementary data to this article can be found online at https://doi.org/10.1016/j.cej.2018.10.025.

## References

[1] J. Pérez-Ramírez, F. Kapteijn, K. Schöffel, J.A. Moulijn, Formation and control of $N_2O$ in nitric acid production where do we stand today? Appl. Catal. B Environ. 44 (2003) 117–151, https://doi.org/10.1016/S0926-3373(03)00026-2.
[2] No Title. < http://appsso.eurostat.ec.europa.eu/ > , 2018.
[3] P.J. Armstrong, A.A. Spence, Toxicity of inhalational anaesthesia: long-term exposure of anaesthetic personnel-environmental pollution, Baillieres. Clin. Anaesthesiol. 7 (1993) 915–935, https://doi.org/10.1016/S0950-3501(05)80155-2.
[4] DIRECTIVE OF THE EUROPEAN PARLIAMENT AND OF THE COUNCIL 2009/28/EC, < http://www.lubelskie.pl/file/2017/02/Dyrektywa-w-sprawie-promowania-OZE.pdf/ > , 2009 (accessed June 8, 2018).
[5] M. Inger, M. Wilk, M. Saramok, G. Grzybek, A. Grodzka, P. Stelmachowski, W. Makowski, A. Kotarba, Z. Sojka, Ind. Eng. Chem. Res. 53 (2014) 10335–10342, https://doi.org/10.1021/ie5014579.
[6] J. Pérez-Ramírez, F. Kapteijn, G. Mul, J.A. Moulijn, Chem. Commun. (2001) 693–694, https://doi.org/10.1039/b100953m.
[7] K. Tjus, 8 Destruction of Medical $N_2O$ in Sweden, < http://www.intechopen.com/ > , (n.d.) (accessed August 24, 2018).
[8] M. Konsolakis, Recent Advances on Nitrous Oxide ($N_2O$) Decomposition over Non-Noble-Metal Oxide Catalysts: Catalytic Performance, Mechanistic Considerations, and Surface Chemistry Aspects, (n.d.), doi:10.1021/acscatal.5b01605.
[9] W.-Y. Chen, T. Suzuki, M. Lackner, Handbook of Climate Change Mitigation and Adaptation, Springer New York, New York, NY, 2017, , https://doi.org/10.1007/978-1-4614-6431-0.
[10] J. Kaczmarczyk, F. Zasada, J. Janas, P. Indyka, W. Piskorz, A. Kotarba, Z. Sojka, Thermodynamic Stability, Redox Properties, and Reactivity of $Mn_3O_4$, $Fe_3O_4$ , and $Co_3O_4$ Model Catalysts for $N_2O$ Decomposition: Resolving the Origins of Steady Turnover, (n.d.), doi:10.1021/acscatal.5b02642.
[11] S. Gudyka, G. Grzybek, J. Gryboś, P. Indyka, B. Leszczyński, A. Kotarba, Z. Sojka, Enhancing the de$N_2O$ activity of the supported $Co_3O_4$|α-$Al_2O_3$ catalyst by glycerol-assisted shape engineering of the active phase at the nanoscale, Appl. Catal. B Environ. 201 (2017), https://doi.org/10.1016/j.apcatb.2016.08.034.
[12] L. Xue, C. Zhang, H. He, Y. Teraoka, Catalytic decomposition of $N_2O$ over $CeO_2$ promoted $Co_3O_4$ spinel catalyst 2007 doi:10.1016/j.apcatb.2007.04.013.
[13] G. Grzybek, P. Stelmachowski, S. Gudyka, P. Indyka, Z. Sojka, N. Guillén-Hurtado, V. Rico-Pérez, A. Bueno-López, A. Kotarba, Strong dispersion effect of cobalt spinel active phase spread over ceria for catalytic $N_2O$ decomposition: the role of the interface periphery, Appl. Catal. B Environ. 180 (2016), https://doi.org/10.1016/j.apcatb.2015.07.027.
[14] S. Wójcik, G. Grzybek, J. Gryboś, A. Kotarba, Z. Sojka, Designing, optimization and performance evaluation of the K-$Zn_{0.4}Co_{2.6}O_4$|α-$Al_2O_3$|cordierite catalyst for low-temperature $N_2O$ decomposition, Catal. Commun. 110 (2018) 64–67, https://doi.org/10.1016/j.catcom.2018.03.019.
[15] P. Stelmachowski, G. Maniak, J. Kaczmarczyk, F. Zasada, W. Piskorz, A. Kotarba, Z. Sojka, Mg and Al substituted cobalt spinels as catalysts for low temperature de$N_2O$—evidence for octahedral cobalt active sites, Appl. Catal B, Environ. 146 (2014) 105–111, https://doi.org/10.1016/j.apcatb.2013.05.027.
[16] S.P. Ramnani, S. Sabharwal, J. Vinod Kumar, K. Hari Prasad, Reddy, K.S. Rama Rao, P.S. Sai Prasad, Advantage of radiolysis over impregnation method for the synthesis of $SiO_2$ supported nano-Ag catalyst for direct decomposition of $N_2O$, Catal. Commun. 9 (2008) 756–761, https://doi.org/10.1016/J.CATCOM.2007.08.017.
[17] S. Eriksson, U. Nylén, S. Rojas, M. Boutonnet, Preparation of catalysts from microemulsions and their applications in heterogeneous catalysis, Appl. Catal. A Gen. 265 (2004) 207–219, https://doi.org/10.1016/J.APCATA.2004.01.014.
[18] N. Bahlawane, Kinetics of methane combustion over CVD-made cobalt oxide catalysts (2006). doi:10.1016/j.apcatb.2006.03.024.
[19] W.-C. Li, M. Comotti, F. Schüth, Highly reproducible syntheses of active Au/$TiO_2$ catalysts for CO oxidation by deposition–precipitation or impregnation, J. Catal. 237 (2006) 190–196, https://doi.org/10.1016/j.jcat.2005.11.006.
[20] A. Varma, A.S. Mukasyan, A.S. Rogachev, K.V. Manukyan, Solution combustion synthesis of nanoscale materials, Chem. Rev. 116 (2016) 14493–14586, https://doi.org/10.1021/acs.chemrev.6b00279.
[21] S. Specchia, E. Finocchio, G. Busca, V. Specchia, Combustion synthesis, Handb. Combust. Wiley-VCH Verlag GmbH & Co. KGaA, Weinheim, Germany, 2010, pp. 439–472, , https://doi.org/10.1002/9783527628148.hoc088.
[22] S. Specchia, C. Galletti, V. Specchia, Solution combustion synthesis as intriguing technique to quickly produce performing catalysts for specific applications, Stud. Surf. Sci. Catal. (2010) 59–67, https://doi.org/10.1016/S0167-2991(10)75008-4.
[23] S. Specchia, G. Ercolino, S. Karimi, C. Italiano, A. Vita, Solution combustion synthesis for preparation of structured catalysts: a mini-review on process intensification for energy applications and pollution control, Int. J. Self-Propagating High-Temperature Synth. 26 (2017) 166–186, https://doi.org/10.3103/S1061386217030062.
[24] G. Grzybek, S. Wójcik, K. Ciura, J. Gryboś, P. Indyka, M. Oszajca, P. Stelmachowski, S. Witkowski, M. Inger, M. Wilk, A. Kotarba, Z. Sojka, Influence of preparation method on dispersion of cobalt spinel over alumina extrudates and the catalyst de$N_2O$ activity, Appl. Catal. B Environ. 210 (2017) 34–44, https://doi.org/10.1016/J.APCATB.2017.03.053.
[25] G. Ercolino, S. Karimi, P. Stelmachowski, S. Specchia, Catalytic combustion of residual methane on alumina monoliths and open cell foams coated with Pd/$Co_3O_4$, Chem. Eng. J. 326 (2017) 339–349, https://doi.org/10.1016/j.cej.2017.05.149.
[26] G. Ercolino, P. Stelmachowski, S. Specchia, Catalytic performance of Pd/$Co_3O_4$ on SiC and $ZrO_2$ open cell foams for process intensification of methane combustion in lean conditions, Ind. Eng. Chem. Res. 56 (2017) 6625–6636, https://doi.org/10.1021/acs.iecr.7b01087.
[27] S. Specchia, E. Finocchio, G. Busca, V. Specchia, Combustion Synthesis, Wiley-VCH Verlag GmbH & Co. KGaA, Weinheim, Germany, 2010, , https://doi.org/10.1002/9783527628148.hoc088.
[28] A. Vita, G. Cristiano, C. Italiano, L. Pino, S. Specchia, Syngas production by methane oxy-steam reforming on Me/$CeO_2$ (Me = Rh, Pt, Ni) catalyst lined on cordierite monoliths, Appl. Catal. B Environ. 162 (2015) 551–563, https://doi.org/10.1016/j.apcatb.2014.07.028.
[29] O. Sanz, I. Velasco, I. Reyero, I. Legorburu, G. Arzamendi, L.M. Gandía, M. Montes, Effect of the thermal conductivity of metallic monoliths on methanol steam reforming, Catal. Today 273 (2016) 131–139, https://doi.org/10.1016/j.cattod.2016.03.008.
[30] D. Bhatia, R.W. McCabe, M.P. Harold, V. Balakotaiah, Experimental and kinetic study of NO oxidation on model Pt catalysts, J. Catal. 266 (2009) 106–119, https://doi.org/10.1016/j.jcat.2009.05.020.
[31] P.S. Metkar, N. Salazar, R. Muncrief, V. Balakotaiah, M.P. Harold, Selective catalytic reduction of NO with $NH_3$ on iron zeolite monolithic catalysts: steady-state and transient kinetics, Appl. Catal. B Environ. 104 (2011) 110–126, https://doi.org/10.1016/j.apcatb.2011.02.022.
[32] M.A. Ashraf, O. Sanz, C. Italiano, A. Vita, M. Montes, S. Specchia, Analysis of Ru/La-$Al_2O_3$ catalyst loading on alumina monoliths and controlling regimes in methane steam reforming, Chem. Eng. J. 334 (2018) 1792–1807, https://doi.org/10.1016/j.cej.2017.11.154.
[33] V.G. Hadjievl, M.N. Ilievl, I.V. Vergilovs, The Raman spectra of $Co_3O_4$ The Raman spectra of CoO, J. Phys. C Solid State Phys. J. Phys. J. Phys. C Solid State Phys. 21 (1988), https://doi.org/10.1088/0022-3719/21/7/007/pdf (accessed June 8, 2018).
[34] A.F. Pérez-Cadenas, F. Kapteijn, J.A. Moulijn, Tuning the morphology of monolith coatings (2006). doi:10.1016/j.apcata.2006.11.011.
[35] P. Stelmachowski, G. Maniak, J. Kaczmarczyk, F. Zasada, W. Piskorz, A. Kotarba, Z. Sojka, Mg and Al substituted cobalt spinels as catalysts for low temperature de$N_2O$-Evidence for octahedral cobalt active sites, Appl. Catal. B Environ. 146 (2014) 105–111, https://doi.org/10.1016/j.apcatb.2013.05.027.
[36] K.C. Patil, Advanced ceramics: combustion synthesis and properties, Bull. Mater. Sci. 16 (1993) 533–541 (accessed June 8, 2018), https://link.springer.com/content/pdf/10.1007%2FBF02757654.pdf.
[37] S. Specchia, G. Ercolino, S. Karimi, C. Italiano, A. Vita, Solution combustion synthesis for preparation of structured catalysts: a mini-review on process intensification for energy applications and pollution control, Int. J. Self-Propagating High-Temperature Synth. 26 (2017) 1061–3862, https://doi.org/10.3103/S1061386217030062.
[38] L. Yan, X. Zhang, T. Ren, H. Zhang, X. Wang, J. Suo, Superior performance of nano-

Au supported over $Co_3O_4$ catalyst in direct $N_2O$ decomposition, Chem. Commun. (2002) 860–861, https://doi.org/10.1039/b201237e.
[39] F. Deganello, A.K. Tyagi, Solution combustion synthesis, energy and environment: best parameters for better materials, Prog. Cryst. Growth Charact. Mater. 64 (2018) 23–61, https://doi.org/10.1016/j.pcrysgrow.2018.03.001.
[40] G. Grzybek, K. Ciura, S. Wójcik, J. Gryboś, P. Indyka, M. Inger, K. Antoniak-Jurak, P. Kowalik, A. Kotarba, Z. Sojka, On the selection of the best polymorph of $Al_2O_3$ carriers for supported cobalt nano-spinel catalysts for $N_2O$ abatement: an interplay between preferable surface spreading and damaging active phase-support interaction, Catal. Sci. Technol. (2017), https://doi.org/10.1039/c7cy01575e.
[41] A. Boyano, M.J. Lázaro, C. Cristiani, F.J. Maldonado-Hodar, P. Forzatti, R. Moliner, A comparative study of $V_2O_5$/AC and $V_2O_5/Al_2O_3$ catalysts for the selective catalytic reduction of NO by $NH_3$, Chem. Eng. J. 149 (2009) 173–182, https://doi.org/10.1016/j.cej.2008.10.022.
[42] C. Italiano, R. Balzarotti, A. Vita, S. Latorrata, C. Fabiano, L. Pino, C. Cristiani, Preparation of structured catalysts with Ni and Ni-Rh/$CeO_2$ catalytic layers for syngas production by biogas reforming processes, Catal. Today 273 (2016) 3–11, https://doi.org/10.1016/j.cattod.2016.01.037.
[43] A. Cybulski, J.A. Moulijn, Structured Catalysts and Reactors, second ed., CRC Press, 2005.
[44] N. Kockmann, Transport Phenomena in Micro Process Engineering, Springer-Verlag, Berlin Heidelberg, 2008.
[45] S.Y. Joshi, M.P. Harold, V. Balakotaiah, Overall mass transfer coefficients and controlling regimes in catalytic monoliths, Chem. Eng. Sci. 65 (2010) 1729–1747, https://doi.org/10.1016/j.ces.2009.11.021.
[46] V. Balakotaiah, D.H. West, Shape normalization and analysis of the mass transfer controlled regime in catalytic monoliths, Chem. Eng. Sci. 57 (2002) 1269–1286, https://doi.org/10.1016/S0009-2509(02)00059-3.
[47] S.Y. Joshi, Y. Ren, M.P. Harold, V. Balakotaiah, Determination of kinetics and controlling regimes for $H_2$ oxidation on Pt/Al2O3 monolithic catalyst using high space velocity experiments, Appl. Catal. B Environ. 102 (2011) 484–495, https://doi.org/10.1016/j.apcatb.2010.12.030.
[48] A. Vita, C. Italiano, L. Pino, P. Frontera, M. Ferraro, V. Antonucci, Activity and stability of powder and monolith-coated Ni/GDC catalysts for $CO_2$ methanation, Appl. Catal. B Environ. 226 (2018) 384–395, https://doi.org/10.1016/j.apcatb.2017.12.078.
[49] A. Vita, C. Italiano, M.A. Ashraf, L. Pino, S. Specchia, Syngas production by steam and oxy-steam reforming of biogas on monolith-supported $CeO_2$-based catalysts, Int. J. Hydrogen Energy 43 (2018) 11731–11744, https://doi.org/10.1016/j.ijhydene.2017.11.140.

# Supplementary Information

# Robust $Co_3O_4$|α-$Al_2O_3$|cordierite structured catalyst for $N_2O$ abatement – validation of the SCS method for active phase synthesis and deposition

*Sylwia Wójcik[a] *, Giuliana Ercolino[b], Marta Gajewska[c], Carmen W. Moncada Quintero[b], Stefania Specchia[b]*, Andrzej Kotarba[a]*

[a] Faculty of Chemistry, Jagiellonian University, Gronostajowa 2, 30-387 Krakow, Poland

[b] Department of Applied Science and Technology, Politecnico di Torino, Corso Duca degli Abruzzi 24, 10129 Torino, Italy

[c] Academic Centre for Materials and Nanotechnology AGH, Mickiewicza 30, 30-059 Krakow, Poland

*Corresponding authors: Faculty of Chemistry, Jagiellonian University in Krakow, ul. Gronostajowa 2, 30-387 Krakow, Poland, Fax No. +48 12 6340515, Phone No. +48 12 6632295, e-mail: gudyka@chemia.uj.edu.pl (Sylwia Wójcik); stefania.specchia@polito.it (Stefania Specchia)

In the following, a detailed explanation of fluid properties determination, characteristic time analysis and dimensionless numbers calculation is reported.

## S.1. Geometric properties of the monolith

The geometrical properties of monolith are calculated starting from the monolith diameter ($d_m$, m), the monolith length ($L_m$, cm) and the *cpsi* (**Table S1**).

The monolith channel density ($n_m$, $mm^{-2}$), the bare monolith voidage ($\varepsilon_m$), the bare monolith geometric surface area ($a_{gs,m}$, $m^{-2}$ $m^{-3}$) and is the hydraulic diameter ($d_h$, m) of the bare monolith are calculated as [1]:

$$n_m = \frac{1}{(l_w + t_w)} \quad \text{S.1}$$

$$\varepsilon_m = l_w^2 \cdot n_m \quad \text{S.2}$$

$$a_{gs,m} = 4 \cdot l_w \cdot n_m \quad \text{S.4}$$

$$d_h = \frac{4 \cdot \varepsilon_m}{a_{gs,m}} \quad \text{S.5}$$

where $l_w$ (mm) is the channel width and $t_w$ (mm) is the wall thickness estimated from SEM.

The geometrical properties are re-calculated after catalyst deposition. The coated monolith voidage $\varepsilon_c$, and the coated monolith geometric surface area ($a_{gs,c}$, $mm^{-2}$ $mm^{-3}$) are calculated as:

$$\varepsilon_c = d_f^2 \cdot \pi \cdot n_m \quad \text{S.6}$$

$$a_{gs,c} = a_{gs,m} \cdot \varepsilon_c \quad \text{S.7}$$

where $d_f$ (m) is the average channel dimension estimated by SEM.

## S.2. Estimation of fluid properties

Molecular weight ($M_{mix}$, g $mol^{-1}$), density ($\rho_{mix}$, kg $m^{-3}$) and viscosity ($\mu_{mix}$, kg $m^{-1}$ $s^{-1}$) of gas mixture are calculated as:

$$M_{mix} = \sum_{i=1}^{n} y_i M_i \quad \text{S.8}$$

$$\rho_{mix} = \frac{P M_{mix}}{R T} \quad \text{S.9}$$

$$\mu_{mix} = \frac{\sum_{i=1}^{n} \mu_i y_i M_i^{1/2}}{\sum_{i=1}^{n} y_i M_i^{1/2}} \quad \text{S.10}$$

where gas viscosity of a single component ($\mu_i$, in micropoise (μP), is calculated as:

$$\mu_i = A + BT + CT^2 \quad \text{S.11}$$

using the tabulated values of A, B, and C [2].

| | $N_2O$ | $O_2$ | $N_2$ | He |
|---|---|---|---|---|
| *A* | –5.68 | 44.224 | 42.606 | 71,094 |
| B | 0.556 | 0.526 | 0.475 | 0.433 |
| C | –1.52 | –1.13 | –9.88 | –5.18 |

The diffusivity of $N_2O$ in gas phase ($D_{N_2O,mix}$ , $cm^2\ s^{-1}$) is calculated from the binary diffusion of $N_2O$ and *i* gas species ($D_{N_2O-i}$) by:

$$D_{N_2O,mix} = \frac{1-y_{N_2O}}{\sum_{i=1;i\neq N_2O}^{n} \frac{y_i}{D_{N_2O-i}}} \quad \text{S.12}$$

where $D_{N_2O-i}$ is determined by Fuller equation (eq. S.13) [3]:

$$D_{N_2O-i} = \frac{1.013\cdot10^{-7}\cdot T^{1.75}\cdot\left(\frac{1}{M_{N_2O}}+\frac{1}{M_i}\right)^{0.5}}{P\cdot\left(v_{N_2O}^{1/3}+v_i^{1/3}\right)^2} \quad \text{S.13}$$

With T in (K) and P in (bar), using tabulated values of $v_i$ [4].

| | $N_2O$ | $O_2$ | $N_2$ | He |
|---|---|---|---|---|
| $v_i$ | 35.9 | 16.6 | 17.9 | 2.88 |

The mass transfer coefficient of $N_2O$ ($k_G$, $m\ s^{-1}$) is determined from the Sherwood number ($Sh$) by:

$$k_G = \frac{Sh\cdot D_{N_2O,mix}}{d_h} \quad \text{S.14}$$

where *Sh* is calculated from Reynold ($Re$) and Schmidt ($Sc$) numbers by Eqs. S.8, S.9 and S.10 [5–7].

$$Sh = 2.976\left(1+0.095\cdot Re\cdot Sc\cdot\frac{d_h}{L_m}\right)^{0.45} \quad \text{S.15}$$

$$Re = \frac{d_h\cdot u_0\cdot\rho_{mix}}{\mu_{mix}} \quad \text{S.16}$$

$$Sc = \frac{\mu_{mix}}{\rho_{mix}\cdot D_{N_2O,mix}} \quad \text{S.17}$$

where $d_h$ (m) is the hydraulic diameter of the bare monolith, $Lm$ is the monolith length, $u_0$ ($m\ s^{-1}$) is the inlet gas velocity at operative conditions, $\rho_{mix}$ ($kg\ m^{-3}$) is the density of gas mixture, $\mu_{mix}$ ($kg\ m^{-1}\ s^{-}1$) is the viscosity of gas mixture and $D_{N_2O,mix}$ ($m^2\ s^{-1}$) is the diffusivity of $N_2O$ in gas phase.

The inlet gas velocity at operative conditions $u_0$ ($m\ s^{-1}$) is calculated as:

$$u_o = \frac{F_{ch}}{A_{ch}\cdot\varepsilon_c}\cdot\frac{T}{T_S}\cdot\frac{P}{P_S} \quad \text{S.18}$$

where $F_{ch}$ ($m^3\ s^{-1}$) is the total flow of $N_2O$/He for channel, $\varepsilon_c$ is the coated monolith voidage, $A_{ch}$ ($m^2$) is the frontal area of the bare monolith for square channel, $T_S$ (K) and $P_S$ (Pa) are the standard temperature and pressure, $T$ (K) and $P$ (Pa) are the operative temperature and pressure.

The effective diffusivity of $N_2O$ in coated layer ($D_{N_2O,e}$) is calculated from the Knudsen diffusion ($D_k$ cm$^2$ s$^{-1}$) using equation A.19 [8,9]:

$$D_{N_2O,e} = \frac{\varepsilon_p}{\tau}\left(\frac{1}{D_{N_2O,mix}} + \frac{1}{D_k}\right)^{-1} \quad \text{S.19}$$

where $\varepsilon_p$ is the porosity of the coated catalytic layer, $\tau$ is the tortuosity factor for infinite cylinder [10] and $D_k$ (cm$^2$ s$^{-1}$) is the Knudsen diffusion [11] calculated as:

$$\varepsilon_p = \rho_c\, V_{pt} \quad \text{S.20}$$

$$\tau = 2 - \varepsilon_p \quad \text{S.21}$$

$$D_k = 9.7 \cdot 10^{-5}\, r_p \left(\frac{T}{M_{N_2O}}\right)^{-1/2} \quad \text{S.22}$$

where $\rho_c$ (kg m$^{-3}$) is the bulk density of the catalyst (3,170 kg m$^{-3}$), $V_{pt}$ (cm$^3$ g$^{-1}$) is the NLDFT total pore volume, $r_p$ (Å) is the pore diameter and $M_{N_2O}$ is the molecular weight of $N_2O$.

## S.3. Characteristic time analysis

The characteristic contact time, or residence time ($t_c$, s) is determined by [1]:

$$t_c = \frac{L_m}{u_o} \quad \text{S.23}$$

where $L_m$ (m) is the monolith length and $u_o$ (m s$^{-1}$) is the inlet gas velocity at operative conditions.

The characteristic external mass transfer time ($t_{ext}$ s) is determined by [1]:

$$t_{ext} = \frac{d_h^2}{4 \cdot D_{N_2O,mix} \cdot Sh} \quad \text{S.24}$$

where $d_h$ (m) is the hydraulic diameter, $D_{N_2O,mix}$ (m$^2$ s$^{-1}$) is the diffusivity of $N_2O$ in gas phase and $Sh$ is the Sherwood number.

The characteristic coated layer diffusion time ($t_{int}$, s) is determined by [1]:

$$t_{int} = \frac{{\delta_c}^2}{D_{N_2O,e}} \quad \text{S.25}$$

where $D_{N_2O,e}$ (m$^2$ s$^{-1}$) is the effective diffusivity of $N_2O$ in the coated layer and $\delta c$ (m) is the coated layer thickness calculated as [12]:

$$\delta_c = \frac{l_w^2 - \frac{\pi}{4} \cdot d_f^2}{\pi \cdot d_f} \quad \text{S.26}$$

where $l_w$ (m) is the channel width and $d_f$(m) is the average channel dimension estimated by SEM.

The characteristic reaction time $t_r$ (s) is determined by [1]:

$$t_r = \frac{C_{N_2O,in}}{r_{N_2O} \cdot \rho_c} \quad \text{S.27}$$

where $C_{N_2O,in}$ (kmol m$^{-3}$) is the concentration of $N_2O$ in the feed mixture, $r_{N_2O}$ (kmol m$^{-3}$ s$^{-1}$) is the observed reaction rate for $N_2O$, and $\rho_c$ (kg m$^{-3}$) is the density of the catalytic layer.

The longitudinal diffusion time $t_z$ (s) is determined by [13]:

$$t_z = \frac{{L_m}^2}{D_{N_2O,mix}} \quad \text{S.28}$$

where $L_m$ (m) is the monolith length and $D_{N_2O,mix}$ (m$^2$ s$^{-1}$) is the diffusivity of $N_2O$ in gas phase.

The transverse diffusion time $t_\Omega$ (s) is determined by [13]:

$$t_\Omega = \frac{{R_{\Omega e}}^2}{D_{N_2O,mix}} \quad \text{S.29}$$

where $R_{\Omega e}$ (m) is the characteristic length scale for the fluid phase and $D_{N_2O,mix}$ (m$^2$ s$^{-1}$) is the diffusivity of $N_2O$ in gas phase.

## S.4. External and internal mass transfer analysis

### S.4.1 Characteristic dimensions for the external and internal mass transfer analysis

In order to study the external and internal mass transfer resistances, two different characteristic cross-sectional areas for a single channel of the monolith are defined: the cross-sectional area of gas phase or circular flow area $A_{\Omega e}$ (m$^2$) and the cross-sectional area of coated catalyst layer $A_{\Omega i}$ (m$^2$).

The cross-sectional area of fluid phase $A_{\Omega e}$ (m$^2$) is calculated as:

$$A_{\Omega e} = \frac{\pi \cdot {d_f}^2}{4} \quad \text{S.30}$$

where $d_f$ (m) is the average channel dimension estimated by SEM.

The cross-sectional area of coated catalyst layer $A_{\Omega i}$ (m$^2$) is calculated as:

$$A_{\Omega i} = A_{ch} - A_c \quad \text{S.31}$$

where $A_{ch}$ (m$^2$) is the area of a single bare channel and $A_c$ (m$^2$) is the area remaining available in the channel for the flow of reactants after catalyst deposition. For the channel shape under consideration (square channel with circular flow area), $A_c$ (m$^2$) corresponds with the circular flow area $A_{\Omega e}$ (m$^2$).

The area of a single bare channel $A_{ch}$ (m$^2$) is calculated as:

$$A_{ch} = {l_w}^2 \quad \text{S.32}$$

where $l_w$ (m) is the channel width.

Thus, it is possible to define the characteristic length scales for the fluid phase $R_{\Omega e}$ (m) and for the coated catalyst layer $R_{\Omega i}$ (m).

The characteristic length scale for the fluid phase $R_{\Omega e}$ (m) is defined as [12]:

$$R_{\Omega e} = \frac{A_{\Omega e}}{P_c} \quad \text{S.33}$$

where $A_{\Omega e}$ ($m^2$) is the flow area (or cross-sectional area of fluid phase) and $P_c$ (m) is the fluid-coated catalyst layer interfacial perimeter.

The fluid-coated catalyst layer interfacial perimeter is calculated as:

$$P_c = \pi \cdot d_f \quad \text{S.34}$$

Thus, the characteristic length scale for the fluid phase $R_{\Omega e}$ (m) can be expressed as:

$$R_{\Omega e} = \frac{\frac{\pi \cdot {d_f}^2}{4}}{\pi \cdot d_f} = \frac{d_f}{4} \quad \text{S.35}$$

The characteristic length scale for the coated catalyst layer $R_{\Omega i}$ (m) is defined as [12]:

$$R_{\Omega i} = \frac{A_{\Omega i}}{P_c} \quad \text{S.36}$$

where $A_{\Omega i}$ ($m^2$) is the cross-sectional area of coated catalyst layer and $P_c$ (m) is the fluid-coated catalyst layer interfacial perimeter.

Thus, the characteristic length scale for the coated catalyst layer $R_{\Omega i}$ (m) can be expressed as:

$$R_{\Omega i} = \frac{{l_w}^2 - \frac{\pi \cdot {d_f}^2}{4}}{\pi \cdot d_f} \quad \text{S.37}$$

### S.4.2 External and internal mass transfer coefficients

The external mass transfer coefficient $k_{m,e}$ (m $s^{-1}$) between the bulk of fluid phase and the fluid-coated catalyst layer interface is calculated as [12]:

$$k_{m,e} = \frac{Sh_e \cdot D_{N_2O,mix}}{4 \cdot R_{\Omega e}} \quad \text{S.38}$$

where $Sh_e$ is the external Sherwood number, $D_{N_2O,mix}$ ($m^2$ $s^{-1}$) is the diffusivity of $N_2O$ in gas phase and $R_{\Omega e}$ (m) is the characteristic length scale for the fluid phase.

The internal mass transfer coefficient $k_{m,i}$ (m $s^{-1}$) between the interior of the coated catalyst layer and fluid-coated catalyst layer interface is calculated as[12]:

$$k_{m,i} = \frac{Sh_i \cdot D_{N_2O,e}}{R_{\Omega i}}$$ S.39

where $Sh_i$ is the internal Sherwood number, $D_{N_2O,e}$ ($m^2\ s^{-1}$) is the effective diffusivity of $N_2O$ in the coated layer and $R_{\Omega i}$ (m) is the characteristic length scale for the coated catalyst.

The external Sherwood number $Sh_e$ is calculated by [12]:

$$Sh_e = Sh_{e\infty} + \frac{2.8}{Sc^{1/6}} \cdot \sqrt{P}$$ S.40

where $Sh_{e\infty}$ is the asymptotic external Sherwood number, $Sc$ is the Schmidt ($Sc$) number and $P$ is the transverse Peclet number. For square channel with circular flow, $Sh_{e\infty} = 3.656$.

The transverse Peclet number is calculated as [12]:

$$P = \frac{{R_{\Omega e}}^2 \cdot u_o}{L_m \cdot D_{N_2O,mix}}$$ S.41

where $R_{\Omega e}$ (m) is the characteristic length scale for the fluid phase, $u_o$ ($m\ s^{-1}$) is the inlet gas velocity at operative conditions, $L_m$ (m) is the monolith length and $D_{N_2O,mix}$ ($m^2\ s^{-1}$) is the diffusivity of $N_2O$ in gas phase.

The internal Sherwood number $Sh_i$ is calculated by[12]:

$$Sh_i = Sh_{i\infty} + \frac{\Lambda \cdot ø^2}{1+\Lambda \cdot ø}$$ S.42

where $Sh_{i\infty}$ is the asymptotic internal Sherwood number, $\Lambda$ is a constant that depends on the coated catalyst layer shape and kinetic parameters and ø is the Thiele modulus. For the case of first order kinetics and square channel with circular flow, $Sh_{i\infty} = 0.826$ and $\Lambda = 0.67$.

The Thiele modulus ø for a first order reaction is defined as:

$$ø = \sqrt{\frac{k_{obs} \cdot {R_{\Omega i}}^2}{D_{N_2O,e}}}$$ S.43

where $k_{obs}$ ($s^{-1}$) is the observed first-order reaction rate constant, $R_{\Omega i}$ (m) is the effective transverse diffusion length in the coated catalyst layer and $D_{N_2O,e}$ is the effective diffusivity of $N_2O$ ($m^2\ s^{-1}$).

The effectiveness factor η for a first order reaction can be expressed as [12]:

$$\eta = \frac{1}{1+\frac{ø^2}{Sh_i}}$$ S.44

where ø is the Thiele modulus for a first order reaction and $Sh_i$ is the internal Sherwood number.

### S.4.3 Multiple resistances in series approach

The overall resistance for mass transfer $R_t$($s\ m^{-1}$) is defined as [12]:

$$R_t = R_e + R_i + R_r \quad \text{S.45}$$

where $R_e$ (s m$^{-1}$) is the resistance for the external mass transfer, $R_i$ (s m$^{-1}$) is the resistance for the internal mass transfer and $R_r$ (s m$^{-1}$) is the reaction resistance.

The resistance for the external mass transfer $R_e$ (s m$^{-1}$) can be calculated as:

$$R_e = \frac{1}{k_{m,e}} \quad \text{S.46}$$

where $k_{m,e}$ (m s$^{-1}$) is the external mass transfer coefficient between the bulk of fluid phase and the fluid-coated catalyst layer interface.

The resistance for the internal mass transfer $R_i$ (s m$^{-1}$) can be calculated as:

$$R_i = \frac{1}{k_{m,i}} \quad \text{S.47}$$

where $k_{m,i}$ (m s$^{-1}$) is the internal mass transfer coefficient between the interior of the coated catalyst layer and fluid-coated catalyst layer interface.

The reaction resistance $R_r$ (s m$^{-1}$) can be calculated as:

$$R_t = \frac{1}{k_{obs} \cdot R_{\Omega i}} \quad \text{S.48}$$

where $R_{\Omega i}$ (m) is the characteristic length scale for the coated catalyst layer and $k_{obs}$ (s$^{-1}$) is the observed first-order reaction rate constant.

Thus, the apparent (or overall experimentally observable) mass transfer coefficient $k_{m,app}$ (m s$^{-1}$) can be calculated as [12]:

$$\frac{1}{k_{m,app}} = \frac{1}{k_{m,e}} + \frac{1}{k_{m,i}} + \frac{1}{k_{obs} \cdot R_{\Omega i}} \quad \text{S.49}$$

where $k_{m,e}$ (m s$^{-1}$) is the external mass transfer coefficient between the bulk of fluid phase and the fluid-coated catalyst layer interface, $k_{m,i}$ (m s$^{-1}$) is the internal mass transfer coefficient between the interior of the coated catalyst layer and fluid-coated catalyst layer interface, $k_{obs}$ (s$^{-1}$) is the observed first-order reaction rate constant and $R_{\Omega i}$ (m) is the characteristic length scale for the coated catalyst layer.

Writing S.49 in dimensionless form gives:

$$\frac{1}{k_{m,app}} \cdot \frac{D_{N_2O,mix}}{4 \cdot R_{\Omega e}} = \left( \frac{1}{Sh_e} + \frac{R_{\Omega i} \cdot D_{N_2O,mix}}{4 \cdot R_{\Omega e} \cdot D_{N_2O,e} \cdot Sh_i} + \frac{D_{N_2O,mix}}{4 \cdot R_{\Omega e}\, k_{obs} \cdot R_{\Omega i}} \right) \quad \text{S.50.1}$$

$$\frac{1}{Sh_{app}} = \left( \frac{1}{Sh_e} + \frac{\mu \cdot \lambda}{4} \cdot \frac{1}{Sh_i} + \frac{\mu \cdot \lambda}{4 \cdot \phi^2} \right) \quad \text{S.50.2}$$

where the various dimensionless groups appearing in S.50 are defined as:

$$\lambda = \frac{R_{\Omega i}}{R_{\Omega e}}, \quad \mu = \frac{D_{N_2O,mix}}{D_{N_2O,e}}, \quad \emptyset^2 = \frac{k_{obs} \cdot {R_{\Omega i}}^2}{D_{N_2O,e}}, \quad Sh_{app} = \frac{4 \cdot k_{m,app} \cdot R_{\Omega e}}{D_{N_2O,mix}}$$ S.51

where $k_{m,app}$ (m s$^{-1}$) is the apparent (or overall experimentally observable) mass transfer coefficient, $D_{N_2O,e}$ is the effective diffusivity of $N_2O$ (m$^2$ s$^{-1}$), $D_{N_2O,mix}$ (m$^2$ s$^{-1}$) is the diffusivity of $N_2O$ in gas phase, $R_{\Omega i}$ (m) is the characteristic length scale for the coated catalyst layer, $R_{\Omega e}$ (m) is the characteristic length scale for the fluid phase, $Sh_i$ is the internal Sherwood number, $Sh_e$ is the external Sherwood number, $k_{obs}$ (s$^{-1}$) is the observed first-order reaction rate constant, ø is the Thiele modulus for a first order reaction and $Sh_{app}$ is the apparent (or experimentally observed) mass transfer coefficient.

In kinetic regime, the apparent mass transfer coefficient can be written as:

$$Sh_{app,kin} = \frac{4 * \emptyset^2}{\mu \cdot \lambda}$$ S.52

### S.4.4 Carberry number and Weisz-Prater criterion

The Carberry number is calculated as [1]:

$$Ca = \frac{r_{N_2O}}{k_G \cdot a_{gs,c} \cdot C_{N_2O,in}} < 0.05 \quad \text{(for a first-order reaction)}$$ S.53

The Weisz-Prater criterion can be evaluated as:

$$WP = \frac{r_{N_2O} \cdot \delta_c^2}{D_{N_2O,e} \cdot C_{N_2O,s}} < 1$$ S.54

where $r_{N_2O}$ the observed volumetric reaction rate for $N_2O$ (kmol m$^{-3}$ s$^{-1}$), $k_G$ the extra-particle mass transfer coefficient (m s$^{-1}$), $a_{gs,c}$ the geometric surface area of the structured catalyst (m$^{-2}$ m$^{-3}$), $C_{N_2O,in}$ the inlet concentration of $N_2O$ in bulk phase (kmol m$^{-3}$), $\delta_c$ the thickness of coated catalyst [m], $D_{N_2O,e}$ the effective diffusivity of $N_2O$ (m$^2$ s$^{-1}$), and $C_{N_2O,s}$ the concentration of $N_2O$ at surface catalyst (kmol m$^{-3}$ s$^{-1}$).

The observed volumetric reaction rate for $N_2O$ $r_{N_2O}$ (kmol m$^{-3}$ s$^{-1}$) is calculated as:

$$r_{N_2O} = \frac{F_{N2O} \cdot X_{N2O} \cdot \rho_c}{W}$$ S.55

where $F_{N2O}$ (m$^3$ s$^{-1}$) is the total flow of $N_2O$ per channel, $\rho_c$ (kg m$^{-3}$) is the bulk density of the catalyst (3.170 kg m$^{-3}$) and $W$ (kg) is the mass of the catalyst.

## S.5. Concentration ratios

$$\frac{C_s}{<Cc>} = 1 + \frac{R_i}{R_r}$$ S.56

$$\frac{C_f}{<Cc>} = \frac{R_t}{R_i + R_r}$$ S.57

where $C_f$ (kmol m$^{-3}$) is the concentration of $N_2O$ in the bulk gas phase, $C_s$ (kmol m$^{-3}$) is the concentration of $N_2O$ at gas/catalyst interface boundary, $< Cc >$ (kmol m$^{-3}$) is the average concentration of $N_2O$ into the catalyst layer, $R_t$ (s m$^{-1}$) is the overall resistance for mass transfer, $R_i$ (s m$^{-1}$) is the resistance for the internal mass transfer and $R_r$ (s m$^{-1}$) is the reaction resistance [12,14].

**Table S1.** Geometric properties of the monolith and catalytic layer.

| **Geometric properties of the monolith** | | |
|---|---|---|
| Cell density | $(cpsi)$ | 400 |
| Monolith diameter | $d_m$ (mm) | 12 |
| Monolith length | $L_m$(mm) | 10 |
| Channel density | $n_m$ (mm$^{-2}$) | 0.62 |
| Bare monolith voidage | $\varepsilon_m$ (-) | 0.78 |
| Bare monolith geometric surface area | $a_{gs,m}$ (m$^{-2}$ m$^{-3}$) | 2777.61 |
| Hydraulic diameter | $d_h$ (mm) | 1.12 |
| Channel width (by SEM) | $l_w$ (mm) | 1.12 |
| Wall thickness (by SEM) | $t_w$ (mm) | 0.15 |
| Coated monolith voidage | $\varepsilon_c$ (-) | 0.60 |
| Coated monolith geometric surface area | $a_{gs,c}$, (m$^{-2}$ m$^{-3}$) | 1679.46 |
| Average channel dimension | $d_f$ (m) | 1.11 |

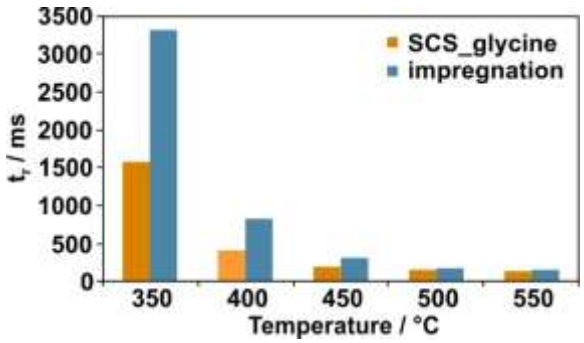


**Fig. S1**. Characteristic reaction time in de$N_2O$ tests for $Co_3O_4$|α-$Al_2O_3$|cordierite structured catalysts obtained via SCS (orange) and impregnation (blue) methods.

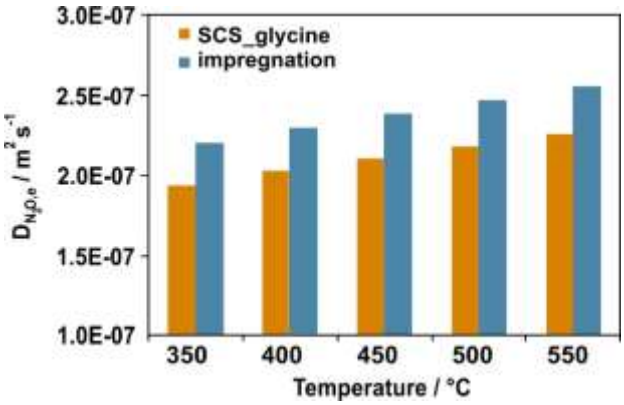


**Fig. S2**. $D_{N_2O,e}$ values in de$N_2O$ tests for $Co_3O_4$|α-$Al_2O_3$|cordierite structured catalysts obtained via SCS (orange) and impregnation (blue) methods.

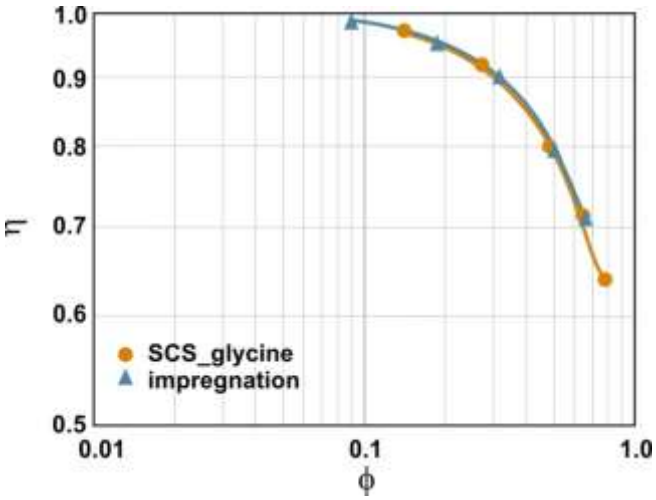


**Fig. S3**. $\phi$ values versus $\eta$ in de$N_2O$ tests for $Co_3O_4$|α-$Al_2O_3$|cordierite structured catalysts obtained via SCS (orange) and impregnation (blue) methods.

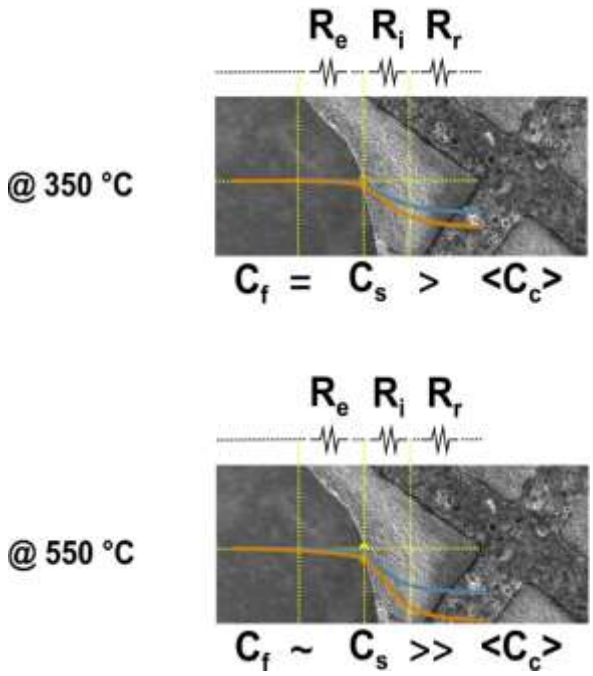


**Fig. S4**. Graphical representation of the multiple resistances in series and of the trends of calculated transverse average concentrations profiles, as per Figure 9c, at low and high temperatures (being $C_f$ the concentration of $N_2O$ in the bulk gas phase, $C_s$ the concentration of $N_2O$ at gas/catalyst interface boundary, and $<C_c>$ the average concentration of $N_2O$ into the catalyst layer, weighted with respect to activity.

**References**

[1] M.A. Ashraf, O. Sanz, C. Italiano, A. Vita, M. Montes, S. Specchia, Analysis of Ru/La-$Al_2O_3$ catalyst loading on alumina monoliths and controlling regimes in methane steam reforming, Chem. Eng. J. 334 (2018) 1792–1807. doi:10.1016/j.cej.2017.11.154.

[2] C.L. Yaws, Chemical Properties Handbook, McGraw-Hill Education, 1999.

[3] E.N. Fuller, P.D. Schettler, J.C. Giddings, New method for prediction of binary gas-phase diffusion coefficients, Ind. Eng. Chem. 58 (1966) 18–27.

[4] J.H. Perry, Chemical engineers' handbook, J. Chem. Educ. 27 (1950) 533.

[5] G. Ertl, H. Knözinger, J. Weitkamp, Handbook of heterogeneous catalysis, VCH, Weinheim (Germany), 1997.

[6] R.K. Shah, Laminar flow friction and forced convection heat transfer in ducts of arbitrary geometry, Int. J. Heat Mass Transf. 18 (1975) 849–862.

[7] G. Incera Garrido, F.C. Patcas, S. Lang, B. Kraushaar-Czarnetzki, Mass transfer and pressure drop in ceramic foams: A description for different pore sizes and porosities, Chem. Eng. Sci. 63 (2008) 5202–5217. doi:10.1016/j.ces.2008.06.015.

[8] R.E. Hayes, S.T. Kolaczkowski, P.K.C. Li, S. Awdry, Evaluating the effective diffusivity of methane in the washcoat of a honeycomb monolith, Appl Catal B Env. 25 (2000) 93–104.

[9] C. Cao, N. Zhang, Y. Cheng, Numerical analysis on steam methane reforming in a plate microchannel reactor: Effect of washcoat properties, Int. J. Hydrog. Energy. 41 (2016) 18921–18941.

[10] S. Kolitcheff, E. Jolimaitre, A. Hugon, J. Verstraete, P.-L. Carrette, M. Tayakout-Fayolle, Tortuosity of mesoporous alumina catalyst supports: Influence of the pore network organization, Microporous Mesoporous Mater. 248 (2017) 91–98.

[11] C.N. Satterfield, Mass transfer in heterogeneous catalysis, MIT Press, Cambridge, 1970.

[12] S.Y. Joshi, M.P. Harold, V. Balakotaiah, Overall mass transfer coefficients and controlling regimes in catalytic monoliths, Chem. Eng. Sci. 65 (2010) 1729–1747. doi:10.1016/j.ces.2009.11.021.

[13] V. Balakotaiah, D.H. West, Shape normalization and analysis of the mass transfer controlled regime in catalytic monoliths, Chem. Eng. Sci. 57 (2002) 1269–1286. doi:10.1016/S0009-2509(02)00059-3.

[14] S.Y. Joshi, Y. Ren, M.P. Harold, V. Balakotaiah, Determination of kinetics and controlling regimes for $H_2$ oxidation on $Pt/Al_2O_3$ monolithic catalyst using high space velocity experiments, Appl. Catal. B Environ. 102 (2011) 484–495. doi:10.1016/j.apcatb.2010.12.030.

# CHAPTER II

(*PAPER II*)

Performance and controlling regimes analysis of methane steam reforming on Ru/γ-$Al_2O_3$ cordierite monoliths

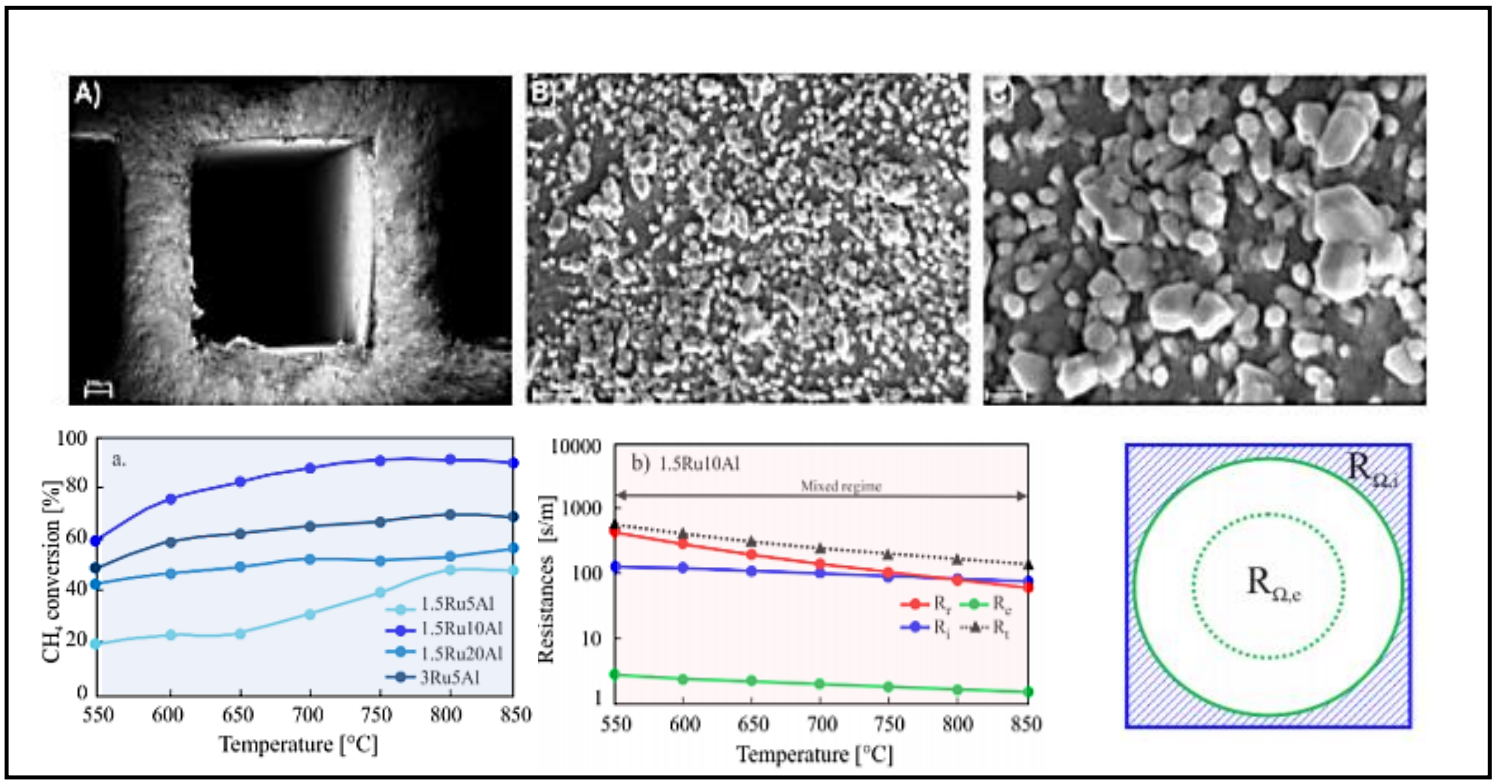


*Green Energy and Technology*, pp. 91–131.

DOI: 10.1007/978-981-15-5667-8_5

# Performance and controlling regimes analysis of methane steam reforming on Ru/γ-$Al_2O_3$ cordierite monoliths

**Carmen W. Moncada Quintero (0000-0002-9058-3646), Roman Z. Babar, Stefania Specchia (0000-0003-3882-3240) ***

Affiliation
*Corresponding Author: Tel.: +39 011 0904608 Fax: +39 011 0904699
E-mail address: stefania.specchia@polito.it

## Abstract

In the frame of methane steam reforming (MSR) process intensification for $H_2$ production, catalysts based on Ruthenium (Ru) supported on Alumina ($Al_2O_3$) on cordierite monolith have been studied in terms of catalytic performance, mass and heat transfer effects. Firstly, we compared the catalytic activity of Ru and Rh supported catalysts. Secondly, we study the effect of catalyst loading by varying the amount of carrier and active metal phase corresponding to 3.20, 6.45 and 12.89 mg $cm^{-2}$. Then, we evaluated the mass/heat transfer effects and controlling regimes for the best-selected catalyst. Finally, the best-selected catalyst was characterized by means of Brunauer-Emmet-Teller (BET), X-Ray diffraction analysis (XRD) and Field-emission scanning electron microscopy (FESEM). The experiments were carried out in the temperature range of 550 to 850 °C, steam to carbon molar ratio (S/C) of 3.0 and different weight hourly space velocity (WHSV= 750, 1500 and 3000 Nl $h^{-1}$ $g_{cat}^{-1}$). The catalyst with 1.5% Ru on 10% Al (1.5Ru10Al) was found to be the most promising toward the MSR reaction in terms of $CH_4$ conversion and $H_2$ production.

This catalyst operates in a mixed regime for all temperature range studied, in which both the kinetic and the intraparticle diffusion co-exist. For the 1.5Ru10Al catalyst, the external thermal effects are important a temperature below 725°C, while that intraparticle heat effects are absent for all the range of temperature studied. An excellent stability of the 1.5Ru10Al catalyst was observed over 70 h of time on stream (TOS) for MSR process.

***Keywords:*** mass transfer; heat transfer; hydrogen production; methane steam reforming

## Nomenclature

*Fluid properties*

| | |
|---|---|
| $C_{CH_4,in}$; $C_b$ | Methane concentration in feed mixture (bulk) (mol·m$^{-3}$) |
| $Cp_f$ | Heat capacity of the gas mixture (J mol$^{-1}$ K$^{-1}$) |
| $Cp_i$ | Heat capacity of i component (J mol$^{-1}$ K$^{-1}$) |
| $C_s$ | Methane concentration at catalyst surface (mol·m$^{-3}$) |
| $D_{CH_4-mix}$ | Diffusivity of $CH_4$ in gas phase (m$^2$·s$^{-1}$) |
| $D_{CH_4,e}$ | Effective diffusivity of $CH_4$ in coated layer (m$^2$·s$^{-1}$) |
| $D_{CH_4-i}$ | Binary diffusion of $CH_4$ and i gas species (m$^2$·s$^{-1}$) |
| $D_k$ | Knudsen diffusion (m$^2$·s$^{-1}$) |
| $h_e$ | Heat transfer coefficient of gas mixture (W m$^{-2}$ K$^{-1}$) |
| $k_{m,e}$;$k_G$ | Mass transfer coefficient of $CH_4$ (m·s$^{-1}$) |
| $k_{m,app}$ | Apparent mass transfer coefficient (m·s$^{-1}$) |
| $M_{CH_4}$ | Molecular weight of $CH_4$ (kg·kmol$^{-1}$) |
| $M_i$ | Molecular weight of *i* compound (kg·kmol$^{-1}$) |
| $M_{mix}$ | Molecular weight of gas mixture (kg·kmol$^{-1}$) |
| $P$ | Transverse Peclet number (m) |
| $R_g$ | Universal gas constant (J·mol$^{-1}$·K$^{-1}$) |
| $u_o$ | Inlet gas velocity (m·s$^{-1}$) |
| $v_{CH_4}$ | Molar volume of $CH_4$ (cm$^3$·mol$^{-1}$) |
| $v_i$ | Molar volume of *i* compound (cm$^3$·mol$^{-1}$) |
| $y_{CH4}$ | Mole fraction of $CH_4$ |
| $y_i$ | Viscosity of *i* compound (kg·m$^{-1}$·s$^{-1}$) |
| $\mu_i$ | Viscosity of *i* compound (kg·m$^{-1}$·s$^{-1}$) |
| $\mu_f$ | Viscosity of gas mixture (kg·m$^{-1}$·s$^{-1}$) |
| $\lambda_i$ | Thermal conductivity of i component (W m$^{-1}$ K$^{-1}$) |

| | |
|---|---|
| $\lambda_{mix}$ | Thermal conductivity of gas mixture (W $m^{-1}$ $K^{-1}$) |
| $\rho_f$ | Density of gas mixture (kg·$m^{-3}$) |

*Reaction data*

| | |
|---|---|
| $F_{tot}$ | Total gas flow rate ($m^3 \cdot s^{-1}$) |
| $k_{obs}$ | Observed 1st order reaction rate constant ($s^{-1}$) |
| $k_s$ | Surface reaction rate constant |
| $P$ | Reaction pressure (kPa) |
| $r_{CH_4}$ | Reaction rate for $CH_4$ (kmol·$kg^{-1}$·$s^{-1}$) |
| $R_{CH_4}$ | Volumetric reaction rate for $CH_4$ (kmol·$m^{-3}$·$s^{-1}$) |
| $T$ | Reaction temperature (K) |
| $T_b, T_s$ | Temperature in the bulk of the gas phase and surface of the catalyst layer (K) |
| $T_{b,c}$ | Temperature in the bulk of the catalyst layer (K) |
| $\phi$ | Thiele modulus |
| $H$ | Effectiveness factor |
| $\Delta H_r$ | Heat of MSR reaction (J $mol^{-1}$) |
| $\lambda_{cat}$ | Catalyst thermal conductivity (W $m^{-1}$ $K^{-1}$) |
| $\lambda_e$ | Effective thermal conductivity (W $m^{-1}$ $K^{-1}$) |

*Monolith properties*

| | |
|---|---|
| $A_{ch}$ | Area of a single bare channel ($m^2$) |
| $A_m$ | Monolith area ($m^2$) |
| $A_{\Omega e}$ | Cross-sectional area of fluid phase ($m^2$) |
| $A_{\Omega i}$ | Cross-sectional area of catalyst layer ($m^2$) |
| $d_h$ | Hydraulic diameter (m) |
| $d_f$ | Average channel dimension (m) |
| $D$ | Inner length of the channel (m |
| $D_m$ | Monolith diameter (m) |
| $GSA$ | Geometric surface area ($m^2 \cdot m^{-3}$) |
| $l_w$ | Channel width (m) |
| $L_m$ | Monolith length and diameter (m) |
| $n$ | Cell density (Nº cell·$m^{-2}$) |
| $P_c$ | Interfacial perimeter (m |
| $R_{\Omega e}$ | Characteristic length for gas phase (m) |
| $R_{\Omega i}$ | Characteristic length for coated layer (m) |
| $\varepsilon$ | Voidage of square channel |
| $\delta_w$ | Wall thickness (m) |
| $\varsigma$ | Cell density (cpsi) |

*Coated layer properties*

| | |
|---|---|
| $k_{m,I}$ | Internal mass transfer coefficient (m) |

| | |
|---|---|
| $r_p$ | Pore radius (m) |
| $S_{BET}$ | Specific surface area ($m^2\ g^{-1}$) |
| $V_{BJH}$ | Total pore volume ($cm^3\ g^{-1}$) |
| $\delta_c$ | Coated layer thickness (m) |
| $\varepsilon_c$ | Coated layer porosity |
| $\rho_c$ | Coated layer density ($kg \cdot m^{-3}$) |
| $\tau_c$ | Tortuosity factor |

*Resistances*

| | |
|---|---|
| $R_e$ | External mass transfer resistance ($s\ m^{-1}$) |
| $R_i$ | Internal mass transfer resistance ($s\ m^{-1}$) |
| $R_r$ | Reaction resistance ($s\ m^{-1}$) |
| $R_t$ | Overall resistance ($s\ m^{-1}$) |

*Characteristic times*

| | |
|---|---|
| $t_c$ | Characteristic contact time (s) |
| $t_d^e$ | Transverse diffusion time for the flow area (s) |
| $t_d^i$ | Transverse diffusion time for the coated area (s) |
| $t_r$ | Characteristic reaction time (s) |
| $t_z$ | Longitudinal diffusion time (s |

*Dimensionless numbers*

| | |
|---|---|
| $A$ | $D_{CH4\text{-}mix}/D_{CH4,e}$ ratio |
| $B$ | $R_{\Omega i}/\ R_{\Omega e}\ ratio$ |
| $Ca$ | Carberry number |
| $Le$ | Lewis number |
| $Pr$ | Prandtl number |
| $Re$ | Reynold number |
| $Sc$ | Schmidt number |
| $Sh_i, Sh_e$ | Internal/external Sherwood number |
| $Sh_{i\infty}, Sh_{e\infty}$ | Asymptotic internal/external Sherwood number |
| $Sh_{app}$ | Apparent Sherwood number |
| $\beta_{in;}\ \beta_{ext}$ | Dimensionless internal/external Prater number |
| $\gamma_b;\ \gamma_s$ | Arrhenuis number at the bulk and surface of the gas phase |
| $\chi$ | Damkholer for interphase heat transport |
| $\psi$ | Damkholer for intraparticle heat |
| $x$ | Radial coordinate |

## Abbreviations

| | |
|---|---|
| BET | Brunauer-Emmet-Teller |

| | |
|---|---|
| EDX | energy dispersive X-ray |
| FESEM | field emission scanning electron microscopy |
| ID | internal diameter |
| MSR | methane steam reforming |
| NDIR | near D infra red |
| $S_{BET}$ | specific surface area calculated by BET method |
| SCS | solution combustion synthesis |
| S/C | steam to carbon ration |
| TOS | time on stream |
| WGS | water gas shift |
| WHSV | weight hourly space velocity |
| XRD | X-ray diffraction |

# 1. INTRODUCTION

Hydrogen ($H_2$) is one of the most abundant elements in the Earth's crust and due to its capability to drive the generation of electricity without emitting harmful pollutants, $H_2$ is considered as a prominent clean, environmentally benign and safe-to-handle major energy carrier of the future [1, 2]. Nowadays, $H_2$ is used in several industrial processes such as refining, treating metals, and food processing. In addition, $H_2$ is an essential building block for the production of ammonia, and thus fertilizers, and of methanol, utilized as a part of the production of many polymers [3–7]. The most important source of $H_2$ today is natural gas (~97 % of $CH_4$) with approximately 80% efficiency. In fact, more than 90% of the world's $H_2$ is produced by steam reforming (SR), being the most viable option for supporting a future hydrogen economy [8, 9]. Methane steam reforming (MSR) is a highly endothermic reaction (Reaction 1) accompanied mainly by the side reaction of the water gas shift (WGS), which is slightly exothermic (Reaction 2):

$$CH_4 + H_2O \rightarrow CO + 3H_2 \qquad \Delta H^0_{298} = +206.3\ kJ\ mol^{-1} \qquad (1)$$

$$CO + H_2O \rightarrow CO_2 + H_2 \qquad \Delta H^0_{298} = -41.1\ kJ\ mol^{-1} \qquad (2)$$

To be feasible at relatively low pressure and temperature (T < 1000 °C, P < 5 bars), these reactions are carried out in the presence of a catalyst. Nickel-based catalysts are actually the most widely used for industrial reforming processes because of their high availability and low cost [8–10]. However, the catalytic activity gradually decreases because of carbon deposition and sintering of Ni. Catalyst systems based on noble metals have been extensively studied by many researchers, giving rise to excellent catalytic performances towards MSR processes [11, 12]. Noble metals such as Ru, Rh, Pd, Pt, and Ir have a higher barrier for carbon formation during operation than Ni. Particularly, whiskers carbon formation (caused by carbon deposition) can s be problematic at severe condition for an effective performance of the catalyst [13]. Moreover, the catalyst may eventually break down [14]. Among

the noble metals, Ru and Rh are the most active metals with comparable performance, while Ru is the most promising candidate due to its lower price [11–15]. On the other hand, the nature of the support in MSR may also have a significant impact on the catalytic activity. Carrier materials for MRS catalysts require high specific surface area, wider pore structure easily accessible for gaseous transport, and thermal stability at high temperature (< 1000 °C), even in the presence of steam [16]. Alumina ($Al_2O_3$) is widely used as catalyst carrier because it is inexpensive, reasonably thermally stable and can provide a wide range of specific surface area and porosity through its different phases [17, 18]. Ferreira-Aparicio et al. [19] investigated the role of $Al_2O_3$ support on the catalytic activity of Ru catalysts during MSR. They found that surface hydroxyl groups play a main role in the catalyst's resistance to deactivation. In the same way, Berman et al. [20] reported that during 10 days of operation of 1 wt.% Ru/γ-$Al_2O_3$ catalyst in the temperature range of 600-900 °C, the activity was stable without carbon depositions and change of mechanical properties of the catalyst.

Nowadays, research on MSR reaction is mainly devoted to improve the catalyst performance by producing as much $H_2$ as possible. Recently, the attention is focused on structured systems with active components supported on different configurations such as monoliths, foams, and honeycombs [16, 21–24]. In particular, monolith catalysts have been widely used in many applications due to for their excellent mechanical and chemical durability, high geometric surface area, rapid response to transient operation, low pressure drop and smaller sizes than reactors with traditional catalyst pellet materials. Furthermore, monolith reactors offer other advantages such as reduced capital cost, smaller footprints, and potentially easier transportation compared to fixed-bed reactors [25–27].

Several studies have shown that structured catalysts improve heat and mass transfer mechanisms between the fluid and solid phases. Especially, for endothermic process, high thermal conductive supports allow optimal thermal management in the catalytic volume maximizing heat transfer from the heating medium to the catalytic volume and reducing the temperature gradient due to the endothermicity of the reaction [28]. According to Tronconi et al. [28, 29], the effective thermal conductivity of a structured catalysts depends fundamentally on the conductivity of the substrate and that of the solid carrier deposited on the substrate. On the other hand, it is well known that in many heterogeneous catalytic reactions, the overall rate of reaction is often limited by mass transfer processes, which include both the internal diffusion (at intermediate temperatures) and external diffusion (at sufficiently high temperatures) of components into and out of the catalyst, especially for highly exothermic or endothermic reactions such as combustion or steam reforming [23, 24, 30, 31].

In the present work, we investigated the catalytic performance towards MSR of Ru and Rh on γ-$Al_2O_3$ catalysts supported on ceramic cordierite monoliths of square channel. Firstly, we compared the catalytic performance in terms of $CH_4$ conversion, $H_2$ production, CO selectivity and $H_2$/CO molar ratio of Rh and Ru supported on γ-$Al_2O_3$. Secondly, we study the influence of the catalyst loading by varying the amount of carrier and active metal phase. Then, we evaluated the different controlling regimes (kinetic, intraparticle, or interphase diffusion control)

and heat transfer effects for the best catalyst. All cordierite monoliths were coated by solution combustion synthesis. Finally, we evaluated the stability of the catalyst on the best-selected one.

## 2. METHODS

### 2.1. Chemicals and monoliths

Aluminium (III) nitrate nonahydrate, $Al(NO)_3\ 9H_2O$ (≥ 98% purity), ruthenium (III) nitrosyl nitrate, $6Ru(NO)(NO_3)_3$ (≥ 98% purity), rhodium(III) chloride, $RuCl_3$ (≥ 98% purity), urea, $CH_4N_2O$ (≥ 99% purity) were purchased from Sigma–Aldrich. All aqueous solutions were prepared using ultrapure water (Millipore Milli-Q system with resistivity > 18 MΩ cm). For catalytic activity tests, pure $CH_4$, $H_2$, and $N_2$ gasses (purity 99.999%) were supplied in cylinders provided by SIAD S.p.A. (Italy) and used as received.
Ceramic monoliths of square channel (100 cell per $in^2$) made of cordierite in dimensions of 40 mm diameter by 30 mm were provided by Chauger Honeycomb Ceramics Co. (Taiwan).

### 2.2. Catalysts preparation

Before the catalyst deposition, cordierite monoliths were cleaned in an ultrasonic bath with a water/acetone solution (50/50 vol.%) for 30 min and dried at 120 °C for 2 h. The catalytic layer based on Ru supported on γ-$Al_2O_3$ was coated by *in-situ* solution combustion synthesis (SCS) following the detailed procedure discussed in our previous work [32]. Briefly, the necessary amounts of aluminum nitrate, ruthenium nitrosyl nitrate as precursors and urea as fuel were dissolved in aqueous solution (3 M) under vigorous stirring. The ratio between the amount of urea used and the stoichiometric amount (Φ) was equal to 1 [33, 34]. Then, each monoliths was dipped in the aqueous solution for 2-3 min and then introduced into a muffle furnace preheated at 600 °C for 10 min, where the combustion reaction occurred, letting the formation of the catalytic layer, and rapidly cooled down to room temperature in few minutes. The operation was repeated until the design weight of Ru/γ-$Al_2O_3$ was reached. Finally, the coated monoliths were calcined at 600 °C for 2 h in static air.
For comparison of the catalytic performance, Rh-based catalysts were also prepared with the same procedure by using the corresponding nitrate of the active metal. A set of X wt.% (X = 1.5 and 3) of metal active phase (Ru, Rh) supported on γ-$Al_2O_3$ (with varying carrier loadings equal to 5, 10 and 20 wt.% compared to the weight of the monolith) were prepared, according to Table 1.

| Metal | Carrier | Catalyst | Abbreviation |
|---|---|---|---|
| 1.5% Ru | 5% $Al_2O_3$ | 1.5% Ru / 5% $Al_2O_3$ | 1.5Ru5Al |
| 3.0% Ru | 5% $Al_2O_3$ | 3.0% Ru / 5% $Al_2O_3$ | 3Ru5Al |
| 1.5% Ru | 10% $Al_2O_3$ | 1.5% Ru / 10% $Al_2O_3$ | 1.5Ru10Al |
| 1.5% Ru | 20% $Al_2O_3$ | 1.5% Ru / 20% $Al_2O_3$ | 1.5Ru20Al |
| 1.5% Rh | 10% $Al_2O_3$ | 1.5% Ru / 10% $Al_2O_3$ | 1.5Rh10Al |

**Table 1.** List of catalyst prepared by varying metal and carrier load.

### 2.3. Catalytic tests

The catalytic activity of coated monoliths was evaluated towards MSR in a tubular reactor of AISI 310 (40 mm ID) placed in an electric oven, which provided sufficient heat to vaporize water. The entire plant was set to provide 3 kW of energy. The micro-reactor temperatures were measured by two K-type thermocouples located, respectively, at the inlet and outlet of the coated monolith. Before starting catalytic tests, the structured catalysts were reduced *in situ* sending a flow of 100 Nml $min^{-1}$ of $H_2$ at 200 °C for 1 h. The catalytic tests were performed over a temperature range of 550-850 °C, at different steam-to-carbon molar ratios (S/C: 3-3.2) and weight hourly space velocities (WHSV 750-3000 Nl $h^{-1}$ $g_{cat}^{-1}$). Mass flow controllers (Brooks Instrument Smart Mass Flow) were used to measure and control the flow of gaseous reactants. The gas stream composition at the reactor outlet is monitored by an ABB gas analyzer (NDIR module Uras 14 for $CO/CO_2/CH_4$, paramagnetic module Magnos 106 for $O_2$ and $H_2$; water removed prior to entering the analyzer in a condenser at 3 °C). For all catalytic tests, measurements were repeated at least three times to assure their reproducibility and to check any possible aging phenomena on the structured catalysts.
The investigated catalysts were compared on the basis of $CH_4$ conversion, $H_2$ production, CO selectivity and $H_2$/CO molar ratio. The $CH_4$ conversion is calculated to determine the amount of inlet $CH_4$ that has reacted and converted to products (Equation 3).This value is based on the total dry outlet flow rate ($F_{out,dry}$), the inlet $CH_4$ flow rate ($CH_{4,inlet}$) and the $CH_4$ concentration in the product mixture ($CH_{4,conc}$).

$$CH_4\ conversion = \left[1 - \frac{\left(\frac{CH_{4_{conc}} \times Fout_{dry}}{100}\right)}{CH_{4_{inlet}}}\right] \times 100 \qquad (3)$$

The $H_2$ production is the $H_2$ concentration in the product mixture ($H_{2,conc}$). The $H_2$ selectivity (Equation 4) is based on the molar volume of gas mixture (assuming it is an ideal gas mixture) and the $CH_4$ and $H_2$ outlet flowrates ($CH_{4,outlet}$ and $H_{2,outlet}$, respectively).

$$H_2\ Selectivity = \left[\frac{H_{2_{outlet}}}{\left(\left(\frac{CH_{4_{inlet}}}{Molecular\ Volume}\right) - CH_{4_{outlet}}\right)}\right] \times 100 \quad (4)$$

The CO selectivity (**Errore. L'origine riferimento non è stata trovata.**) is based on the molar volume of gas mixture (assuming it is an ideal gas mixture) and the $CH_4$ and CO outlet flowrates ($CH_{4,\ outlet}$ and $CO_{outlet}$, respectively).

$$CO\ Selectivity = \left[\frac{CO_{outlet}}{\left(\left(\frac{CH_{4_{inlet}}}{Molecular\ Volume}\right) - CH_{4_{outlet}}\right)}\right] \times 100 \quad (5)$$

Finally, the molar ratio of $H_2$/CO (Equation 6) is monitored to analyze the product in syngas concentration.

$$H_2/_{CO}\ Ratio = \frac{H_{2_{outlet}}}{CO_{outlet}} \quad (6)$$

### 2.4. Characterization on the best-selected catalyst

The specific surface area, textural properties of powder and structured samples were determined by $N_2$ physisorption at −196 °C using an ASAP 2020 instrument from Micromeritics. Prior to analysis, about 100 mg of each sample was outgassed overnight at 150 °C under high vacuum. The specific surface areas ($S_{BET}$) were determined by Brunauer-Emmet-Teller (BET) method in the relative pressure range of 0.05 and 0.30.

By using the same apparatus, the chemisorption analysis was carried out, in order to evaluate the active metals dispersion on supports. $H_2$ saturation was first performed by flowing 20 $Ncm^3\ min^{-1}$ of $H_2$ for 2 h at 350 °C, and at the end, a He flow rate of 20 $Ncm^3\ min^{-1}$ for 1.5 h was fed to the apparatus increasing the temperature to 370 °C. Then, at room temperature, a mixture of 10% CO in He was injected in pulses of 500 NμL each, until the fulfillment of constant outlet peaks. The amount of adsorbed gas was determined as the difference between the total injected volume and the residual escaped one. The metal dispersion on the carrier surface was determined as follows:

$$D_{\%} = 100 \cdot S_f \cdot \frac{V_{ads} \cdot M_{me}}{V_g \cdot F_{me}} \quad (7)$$

considering the stoichiometric factor $S_f$ is equal to 1 (i.e., each Ru atom adsorbed one CO molecule), the total volume of CO chemisorbed refers to the mass of the carrier used for the analysis in $Ncm^3\ g^{-1}$ ($V_{ads}$), the metal atomic weight $M_{me}$ (101.07

g $mol^{-1}$ for Ru) and the total mass fraction of the metal on the catalyst (expressed as $g_{me}$ $g^{-1}$ of carrier), and that one gas $g_{mole}$, $V_g$, occupies 22,414 $cm^3$ at normal conditions.
X-ray diffraction (XRD) patterns were collected using a Philips X-Pert MPD X-ray diffractometer equipped with Copper Kα radiation at 40 kV and 30 mA to verify the effective composition of the samples and derive qualitative indications of the presence of comparatively large noble metals crystallite from its eventually visible peaks. All powder samples were scanned in the 2θ range of 20-70° over 1h. The peaks were assigned according to the PCPFWIN database.
The surface morphology of the catalyst was examined by using Field-emission scanning electron microscopy FESEM (FESEM JEOL-JSM-6700F instrument). The elemental composition analysis was carried out by energy dispersive X-ray spectroscopy EDX (Oxford Instruments Inca EDX apparatus).
The geometrical properties of monoliths for square channel are calculated by [35–39]:

$$n = \frac{1}{(D+\delta_W)^2} \tag{8}$$

$$\varepsilon = D^2 \cdot n \tag{9}$$

$$GSA = \frac{4(\sqrt{\varepsilon}-\varepsilon)}{\delta_w} \tag{10}$$

$$d_h = \frac{4\cdot\varepsilon}{GSA} \tag{11}$$

where $n$ is the cell density (N° cell·$m^{-2}$), $D$ inner length of the channel (m), $\delta_w$ is the wall thickness (m), $\varepsilon$ is the voidage for square channels, $GSA$ is the geometric surface area ($m^2$ $m^{-3}$) and $d_h$ is the hydraulic diameter (m).

### 2.5. Stability measurements

Stability tests were performed over 70 h of time on stream (TOS) at 800 °C for the best-selected catalyst. The reactor was fed with a reactive mixture containing $CH_4$ and $H_2O$ with a S/C equal to 3 and WHSV equal to 750 Nl $h^{-1}$ $g_{cat}^{-1}$. At 30 h of TOS the WHSV was increased up to 1500 Nl $h^{-1}$ $g_{cat}^{-1}$. At 50 h of TOS the WHSV was reported to 750 Nl h $h^{-1}$ $g_{cat}^{-1}$ till the end of the experiment (70 h of TOS), according to the thermal cycling shown in Figure 1.

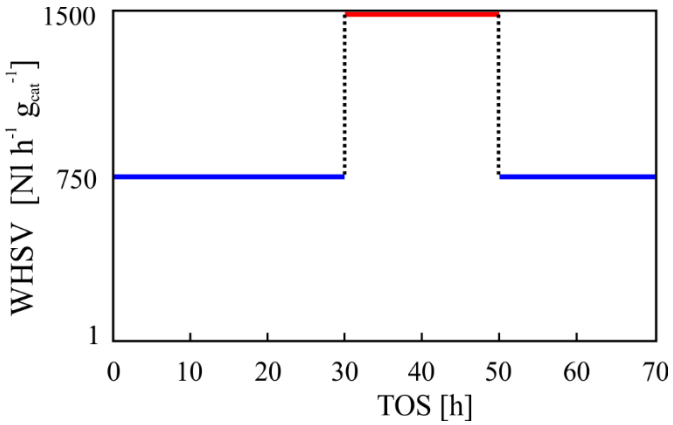


**Fig. 1.** Thermal cycling for stability tests: WHSV vs WHSV at 800 °C and S/C of 3.

## 3. RESULTS AND DISCUSSION

### 3.1. Ru/Rh metal on y-$Al_2O_3$ carrier: metal-base catalysts comparison

In order to compare the catalytic performance of noble metals coated on monolith supports, Ru and Rh (active metal loading equal to 1.5 wt.%) on γ-$Al_2O_3$ (10 wt.% on the bare cordierite monolith) were tested toward the MSR reaction. The experiments were carried out in the temperature range of 550 to 850 °C, S/C equal to 3.0, and WHSV of 750 Nl $h^{-1}$ $g_{cat}^{-1}$.

As can be seen from Figure 2.a., both noble-metal-based catalysts do not reach complete methane conversion. However, the catalytic activity of the Ru-based one was found to be the most promising toward the MSR reaction in terms of $CH_4$ conversion, $H_2$ production, and CO selectivity. At temperatures higher than 750 °C, $CH_4$ conversion for 1.5Ru10Al catalyst remained slightly stable at 88.2 %, reaching the maximum conversion (91.0 %) at 800 °C, while for 1.5Rh10Al catalyst, $CH_4$ conversion increased for the entire temperature range studied achieving the maximum value of 87 % at 850 °C. On the other hand, $H_2$ produced for both catalysts was nearly the same, except at temperatures between 600-700 °C, where $H_2$ production was slightly higher for 1.5Ru10Al catalyst (Fig.2.a). As far as the selectivity of CO is concerned, both catalysts showed an increase in CO selectivity at temperatures between 550-700 °C. At temperatures above 700 °C, CO selectivity for 1.5Rh10Al catalyst remained stable at approximately 42 %, while for 1.5Ru10Al catalyst it continued to increase up to 750 °C, where it reached the maximum selectivity value of 50.25 % and then decreased due probably to the WGS reaction, which converts CO into $CO_2$ (Fig. 2.b). In fact, as shown in Figure 2.c, at temperatures between 725-850 °C, the $H_2$/CO molar ratio was slightly higher for the Rh-based catalyst because of CO consumption (WGS reaction), which leaded

to a higher $CO_2$ selectivity compared to that obtained for the 1.5Ru10Al catalyst (Fig. 2.d). It is important to point out that the Ru-based catalyst produced a syngas richer in $H_2$ and selective to CO compared to the Rh-based catalyst one. For this reason, Ru was selected as the active metal phase for further investigations.

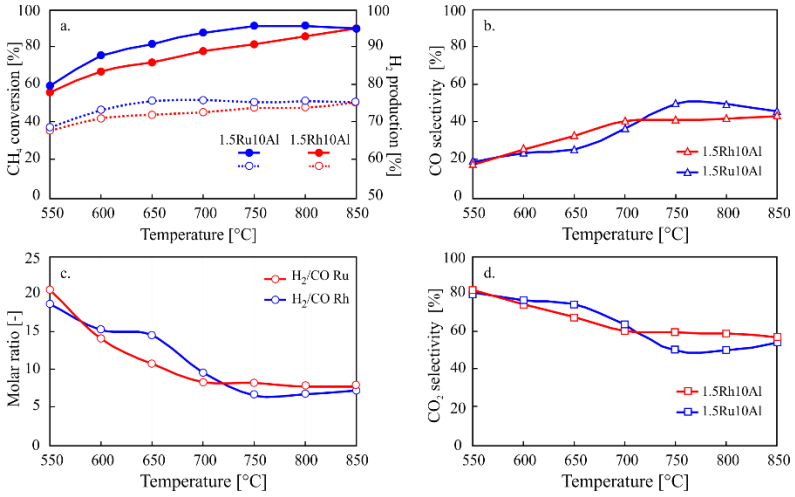


**Fig. 2.** MSR tests, performance comparison of monoliths 1.5% Ru and 1.5% Rh on 10% γ-$Al_2O_3$ at WHSV = 750 and S/C = 3. a) $CH_4$ conversion and $H_2$ production; b) CO selectivity; c) $H_2$/CO molar ratio, and d) $CO_2$ selectivity.

### 3.2. Ru/γ-$Al_2O_3$ catalyst: loading comparison

The effect of catalyst loading on catalytic performance of Ru/γ-$Al_2O_3$ for MSR was studied by varying the amount of both the carrier and the active metal phase. Three different loads of γ-$Al_2O_3$ (5, 10, and 20 wt.%), corresponding to 3.20, 6.45, and 12.89 mg $cm^{-2}$, respectively, were studied. Ru, as the noble metal phase, was loaded on γ-$Al_2O_3$ with two different percentages of active phase (1.5 and 3.0 wt.%, respectively) corresponding to a catalyst mass loading of 3.20 mg $cm^{-2}$. All experiments were carried out in the temperature range of 550 to 850 °C, with fixed S/C molar ratio of 3.0 and volumetric flow equal to 32.65 NL $h^{-1}$.

Fig. 3 (a-d) shows the effect of the carrier and active phase loading on the catalytic performance of the various catalytic monoliths. The results pointed out that the best catalytic performance was obtained with a load of 6.45 mg $cm^{-2}$ (corresponding to 10 wt.% of γ-$Al_2O_3$ and 1.5 wt.% of Ru, sample 1.5Ru10Al), where the maximum $CH_4$ conversion achieved was 91 % at 800 °C (Fig. 3.a). On the other hand, $H_2$ concentration was quite stable for all catalyst at temperatures from 650 to 850 °C, with a $H_2$ production higher than 60 %, except for 1.5Ru5Al catalyst (Fig. 3.b), where the highest concentration of $H_2$ reached was 43.22 %. Analyzing the selectivity of CO and the $H_2$/CO molar ratio (Fig. 3.c and 3.d), the highest concentration in dry reformate of CO was obtained for 1.5Ru10Al catalyst over the

entire temperature range studied. Interestingly, for the catalysts with mass loading of 3.2 mg $cm^{-2}$ (corresponding to 5 wt. % of $Al_2O_3$ on the bare monolith), the catalytic performance was significantly improved with increasing metal loading (from 1.5 to 3 wt.%). In fact, the maximum $CH_4$ conversions reached at 800 °C for 1.5Ru5Al and 3Ru5Al catalysts were 48.19 % and 69.24 %, respectively. Thus, the 3Ru5Al catalyst showed the second highest production of $H_2$ and CO selectivity after the 1.5Ru10Al one. It is also important to note that all catalysts studied showed similar CO selectivity (23.37-27.08 %) at 650 °C. Comparing with the results obtained by Amjad et al. [21] for $Ru/Al_2O_3$ catalyst powder, similar results were reached in terms of $CH_4$ conversion, $H_2$ production, and CO selectivity in the temperature range of 550 to 650 °C. Thus, according to our previous work [39], it is possible to conclude that by increasing catalyst loading by more than 10 mg $cm^{-2}$, the catalytic performance towards the MSR reaction decreases. This result can be explained considering that an excess of $Al_2O_3$ carrier, which leads to a thicker layer covering the monolith walls, could not participate in the catalytic reaction and may even decrease both the dispersion of the noble metal and the number of active sites. Besides, it is well known that higher catalyst loadings lead to higher coating thickness and, therefore, a higher intraparticle mass transfer resistance, worsening the overall catalyst performance [40–42]. In the following section, we highlight in depth the mass transfer effects on structured monolith catalyst.

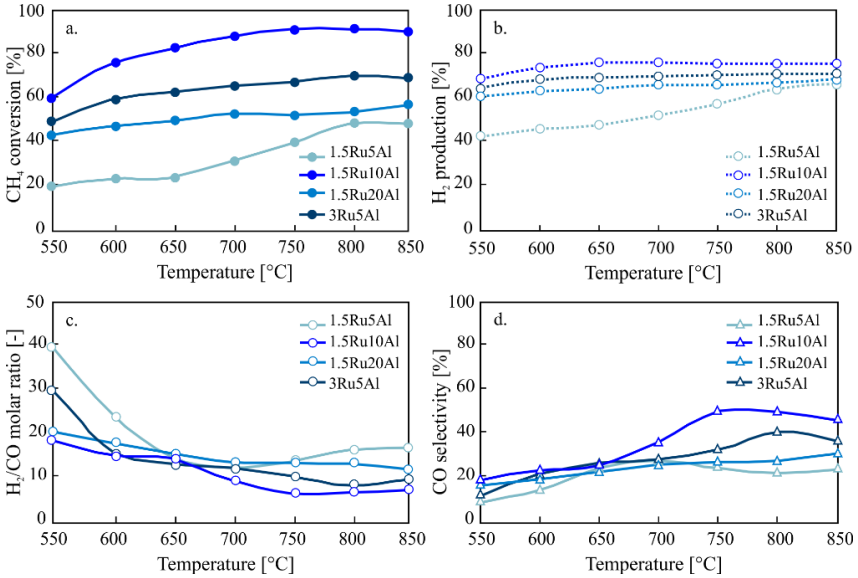


**Fig. 3.** MSR tests, performance comparison at WHSV = 750 and 3 S/C = 3 of $Ru/\gamma$-$Al_2O_3$ monoliths with different catalyst loadings: a) $CH_4$ conversion; b) $H_2$ production; c) $H_2$/CO molar ratio; d) CO selectivity.

### 3.4. Mass transfer effects on Ru/y-$Al_2O_3$ structured monolith catalyst

It is well known that the performance of a catalytic monolith involves a combination of reaction and transport processes, where the reactants and products undergo a series of steps over the catalyst, including: 1. diffusion of the reactants from the bulk gas phase to the external surface of the structured catalyst (external or inter-phase diffusion); 2. diffusion of the reactants into the catalyst pores to the active sites (internal or intra-phase diffusion); 3. adsorption of the reactants onto active sites; 4. reaction at specific active sites on the catalyst surface; 5. desorption of products from catalyst sites; 6. diffusion of the products through the catalyst pores (internal or intra-phase diffusion) and 7. diffusion of the products across the boundary layer surrounding the structured catalyst (external or inter-phase diffusion) [43–45].
According to the literature, three main regimes of catalytic rate control can exist in a coated monolith: (i) external/inter-phase diffusion regime (steps 1 and 7); (ii) internal/intra-phase diffusion regime (steps 2 and 6); and kinetic regime (steps 2 and 6) of the catalyst performance. Joshi et al. [46] developed a low-dimensional (LD) model to analyze catalytic reactions in washcoated monolith with channels of arbitrary shape. The LD model was derived directly by averaging the governing equations and using the concept of internal and external mass transfer coefficients, which were expressed in terms of three concentrations and two temperature modes and include washcoat diffusional effects without using the concept of effectiveness factor. Moreover, a practical criterion was developed to determine the transition between various controlling regimes in terms of resistances or concentration ratios [47]. We used this criterion to quantify the relative importance of reaction, pore diffusion, and external mass transfer processes in a coated monolith by SCS. Firstly, we defined the characteristic length scales for transverse diffusion associated within gas phase ($R_{\Omega,e}$) and catalytic layer ($R_{\Omega,i}$) in a monolith of square channel and circular diameter with a coated layer for the case of first order reaction. Then, we determined the external mass transfer coefficient ($k_{m,e}$) between the bulk of gas phase and the fluid-catalytic layer interface as [48]:

$$k_{m,e} = \frac{Sh_e \cdot D_{CH_4-mix}}{4 \cdot R_{\Omega,e}} \tag{12}$$

and the internal mass transfer coefficient ($k_{m,i}$) between the gas-catalytic layer interface and bulk of catalytic layer as:

$$k_{m,i} = \frac{Sh_i \cdot D_e}{R_{\Omega,i}} \tag{13}$$

where $D_f$ is the molecular diffusivity of the reactant in gas phase ($m^2\ s^{-1}$), $D_e$ is the effective diffusivity of $CH_4$ within coated layer ($m^2\ s^{-1}$), $Sh_e$ and $Sh_i$ are the external and internal Sherwood numbers, respectively. To determine $Sh_e$ we considered the approximation proposed by Balakotaiah and West [49] used for any arbitrary geometry:

$$Sh_e = Sh_{e,\infty} + \frac{2.8}{Sc^{\frac{1}{6}}}\sqrt{P} \quad (14)$$

where $Sh_{e,\infty}$ is the asymptotic external Sherwood number ($Sh_{e,\infty}$ = 2.98 for square channel), $Sc$ is the Schmidt number, and $P$ is the transverse Peclet number calculated as [50, 51]:

$$P = \frac{{R_{\Omega,e}}^2 \cdot u}{L \cdot D_{CH_4-mix}} \quad (15)$$

To estimate $Sh_i$ we used the correlation proposed by Balakotaiah et al. [52]:

$$Sh_i = Sh_{i,\infty} + \frac{\Lambda\phi^2}{1+\Lambda\phi} \quad (16)$$

where $Sh_{i,\infty}$ is the asymptotic internal Sherwood number, $\phi$ is the Thiele modulus and $\Lambda$ is a constant that depends on the coated layer geometric and kinetic parameter [48]. Table 2 shows the effective diffusion lengths, asymptotic external and internal Sherwood numbers and $\Lambda$ for the channel shape and flow area under consideration. Thus, considering the following assumptions: 1. laminar and fully developed flow, 2. the hydraulic diameter of the channel much smaller than the length of cordierite monolith 3. isothermal conditions, and 4. first order kinetic; we expressed the overall resistance for mass transfer in a coated monolith by SCS according to Balakotaiah et al. [47] as:

$$R_t = R_e + R_i + R_r \quad (17)$$

$$\textbf{a}.\quad R_e = \frac{4 \cdot R_{\Omega,e}}{Sh_e \cdot D_{CH_4-mix}} \qquad \textbf{b}.\quad R_i = \frac{R_{\Omega,i}}{Sh_i \cdot D_e} \qquad \textbf{c}.\quad R_r = \frac{1}{k_r \cdot R_{\Omega,i}} \quad (18)$$

with $R_e$ resistance for external mass transfer (s m$^{-1}$), $R_i$ resistance for internal mass transfer (s m$^{-1}$), $R_r$ resistance for MSR reaction (s m$^{-1}$), and $R_t$ overall resistance for MSR process (s m$^{-1}$).

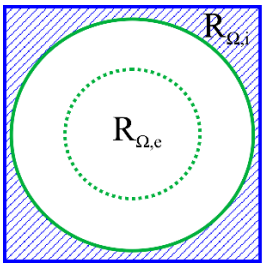


**Fig. 4.** Definition of the characteristic length scales for transverse diffusion associated within gas phase ($R_{\Omega,e}$) and catalytic layer ($R_{\Omega,i}$) in a monolith of square channel and circular diameter with a coated layer.

To characterize the flow and the reactions the following five characteristic times are used [49, 53, 54]:

$$t_c = \frac{L}{u} \quad t_z = \frac{L_m^2}{D_{CH_4-mix}} \quad t_d^e = \frac{R_{\Omega,e}^2}{D_{CH_4-mix}} \quad t_d^i = \frac{\delta_c^2}{D_e} \quad t_r = \frac{C_{CH_4,in}}{r_{CH_4} \cdot \rho_c} \qquad (19)$$

where $t_c$ is the convection (or residence) time, $t_z$ is the longitudinal diffusion time for the flow area, $t_d^e$ is the transverse diffusion time for the flow area, $t_d^i$ is the transverse diffusion time for the coated area, and $t^r$ is the reaction time.

| Catalyst | $R_{\Omega,e}$ [mm] | $R_{\Omega,i}$ [mm] | $Sh_{e,\infty}$ | $Sh_{i,\infty}$ | $\Lambda$ |
|---|---|---|---|---|---|
| 1.5Ru5Al | 0.45 | 0.188 | 2.98 | 1.836 | 1.2 |
| 3Ru5Al | 0.4508 | 0.1865 | 2.98 | 1.836 | 1.2 |
| 1.5Ru10Al | 0.435 | 0.225 | 2.98 | 1.836 | 1.2 |
| 1.5Ru20Al | 0.4 | 0.3182 | 2.98 | 2.533 | 0.73 |

**Table 2.** Effective diffusion lengths, asymptotic external and internal Sherwood numbers and $\Lambda$ for square channel shape and circular flow area for the different catalyst studied.

In fig. 5 (a-d) we show the effect of γ-$Al_2O_3$ amount on the controlling regimes towards MSR reaction on the prepared coated monolith catalysts. For all the catalysts studied, the resistances to mass transfer (inter/intra-phase diffusion) are much less temperature sensitive, since the diffusivities of reacting species in the gas phase ($D_{CH4-mix}$) and in the coated layer ($D_e$) are much weaker functions of temperature in comparison to the reaction resistance, which is strongly dependent on Arrhenius equation. Thus, the interphase and intraparticle mass transfer rates increase only slightly with temperature. Therefore, as the catalyst temperature is

increased, the reaction rate increases exponentially, the reaction resistance becomes less dominant and the mass transfer resistances become important.

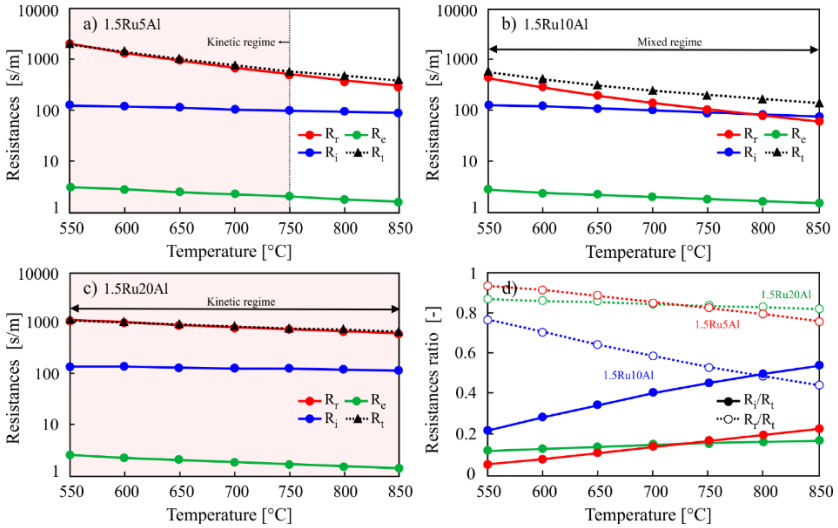


**Fig. 5.** Definition of the characteristic length scales for transverse diffusion associated within gas phase ($R_{\Omega,e}$) and catalytic layer ($R_{\Omega,i}$) in a monolith of square channel and circular diameter with different coating: a) 1.5Ru5Al; b) 1.5Ru10Al; c) 1.5Ru20Al; d) resistance ratios for all catalysts loading.

When comparing the effect of γ-$Al_2O_3$ amount on the controlling regimes in catalytic monoliths, the 1.5Ru5Al monolith operates in a kinetic regime at temperatures lower than 750 °C (Fig.5.a). By increasing the γ-$Al_2O_3$ loading to 20 wt.% (1.5Ru20Al catalyst), the process is completely controlled by the reaction for the entire temperature range studied (Fig.5.c). As a result, a nearly uniform concentration profile prevails in the transverse direction of the structure (fig 6). Thus, when the catalytic performance of MSR reaction is solely governed by the reaction kinetics, the total resistance ($R_t$) is practically equal to the reaction resistance and the $R_r/R_t$ ratio is greater than 0.8 (Fig 5.d). Besides, as expected, when the monolith operates in a kinetic regime, the characteristic times for the MSR reaction are much larger than that for the external and internal mass transfer diffusion (see Table S.I X). On the other hand, for the 1.5Ru10Al catalyst (10 wt.% of alumina, 6.45 mg $cm^{-2}$), the monolith operates in a mixed regime for all temperature range studied, in which both the kinetic and the intraparticle diffusion co-exist (fig.5.a), with both $R_r/R_t$ and $R_i/R_t$ lower than 0.8. By observing the catalytic performance for the different loading of γ-$Al_2O_3$ (Fig. 3), it is worth noting that for the 1.5Ru20Al catalyst, the conversion of $CH_4$ increases slightly with temperature, being practically steady for the temperature range under consideration. This effect explains why the reaction resistance is practically independent with temperature.

On the contrary, for the 1.5Ru10Al catalyst, $CH_4$ conversion increases more rapidly with temperature up to 750 °C, and then remains slightly stable.

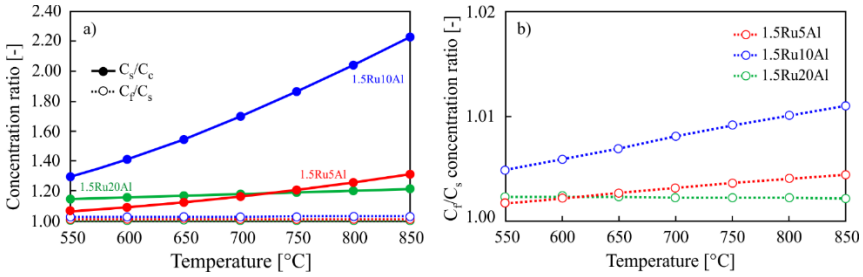


**Fig. 6.** Concentration ratios for the various catalysts tested.

To gain insight into the catalyst activity by varying the γ-$Al_2O_3$ content, we evaluated the Thiele modulus ($\phi$) and the effectiveness factor ($\eta$) for a first-order kinetics reaction, according to the following equations [47, 48]:

$$ø = \sqrt{\frac{k_r \cdot R_{\Omega i}^2}{D_e}} \qquad \eta = \frac{1}{1+\frac{ø^2}{Sh_i}} \qquad (20)$$

where $k_r$ is the observed first-order reaction rate constant ($s^{-1}$), $R_{\Omega,i}$ the effective transverse diffusion length in the coated catalyst layer for the internal resistance (m), $D_e$ is the effective diffusivity of $CH_4$ ($m^2\ s^{-1}$), and $Sh_i$ is the internal Sherwood number. All the correlations and physical parameters used for the calculations of $\phi$ and $\eta$ are available in the Appendix. Fig.7 shows the effectiveness factor as a function of Thiele modulus for the different catalyst loadings. As expected, the effectiveness factor for the case of slow reaction $\phi << 1$ tends to unit. In particular, the 1.5Ru20Al catalyst showed a variation of $\phi$ much less sensitive to temperature ($0.82 < \phi < 0.87$) than the other catalyst loadings, indicating that the process is rate-limited and the reaction rate is controlled by the intrinsic kinetics.

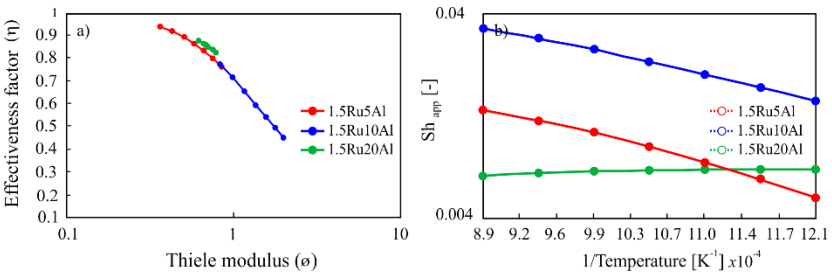


**Fig. 7.** Effectiveness factor (a) and apparent Sherwood number (b) for the various coated monoliths.

Additionally, we plot the experimentally observable overall Sherwood number ($Sh_{app}$) calculated using Eqn. 21 as a function of reciprocal of temperature on a logarithmic scale (Fig.7b). The theoretical upper limit for $Sh_{app}$ ($Sh_{e,\infty}$) is 2.98 for the channel shape under consideration (square channel with circular flow area) [50, 51].

$$\frac{1}{Sh_{app}} = \frac{1}{Sh_e} + \frac{\mu\cdot\lambda}{4}\cdot\frac{1}{Sh_i} + \frac{\mu\cdot\lambda}{4\cdot\phi^2} \tag{21}$$

$$\mu = \frac{R_{\Omega,i}}{R_{\Omega,e}} \qquad \lambda = \frac{D_f}{D_e} \tag{22}$$

It is evident from the results that the experimental conditions used lead to rather low values of *Sh*. Bennett et al. [55] reported a value of $Sh_{app}$ as small as 0.05, which was attributed to the low activation energies and pre-exponential factors obtained for the catalytic oxidation of propane. Similar results were obtained by Joshi et al. [56] for the case of hydrogen oxidation on Pt, which presents a very low intrinsic activation energy (~ 9 kJ mol$^{-1}$), obtaining experimental Sherwood numbers ($Sh_{app}$) less than 0.55. In our study, the apparent activation energies obtained for the MSR reaction were determined from the conversion data ($X_{CH4}$ < 5 %) for the different catalyst loads ($Ea_{app} \approx 50\ kJ\ mol^{-1}$). These values are low compared to other activation energies on supported Ru catalyst for MSR reaction [57, 58]. As shown in Fig.7b, low $Sh_{app}$ values (below 0.035) are obtained for the three catalysts studied, especially for 1.5Ru20Al catalyst.

On the other hand, it is interesting to note that the ratios of reactant diffusivities in the gas phase and the coated layer ($\mu$) obtained in our study are greater than 225. Joshi et al. [48] studied the variation of $Sh_{app}$ for the different controlling regimes by varying the values of $\mu$ for circular channel with circular flow area. They obtained that for values of diffusivity ratios higher than 200, the $Sh_{app}$ for $\phi \ll 1$ (slow reaction) are much lower than 0.1 (~ $10^{-2}$-$10^{-3}$), as obtained in this study.

To study the effect of WHSV and S/C molar ratio on the controlling regimes in a coated monolith by SCS, we selected the 1.5Ru10Al catalyst according to the best results obtained in terms of $CH_4$ conversion, $H_2$ production, and CO selectivity. The 1.5Ru10Al catalyst was studied at space velocities of 750, 1,500, and 3,000 NL h$^{-1}$ $g_{cat}^{-1}$, calculated on metal basis, and S/C molar ratio of 3 and 3.2 respectively. As visible in Fig.8, as the S/C molar ratio increases, both the mass transfer resistances and the reaction resistance increase. In particular, $R_r$ for the S/C molar ratio of 3.2 is about 1.5 times higher than that obtained at S/C 3 for the entire temperature range studied. Since the catalytic performance decreased as the S/C molar ratio increased (Fig.A1), lower rate constants ($k_r^{obs}$) were obtained for S/C equal to 3.2, thus increasing the reaction resistance. Since a higher bulk reaction controlling is obtained either by increasing the S/C molar ratio as the WHSV, a concentration profile closer to the unit exists in the transverse direction of the monolith (Fig. 8b).

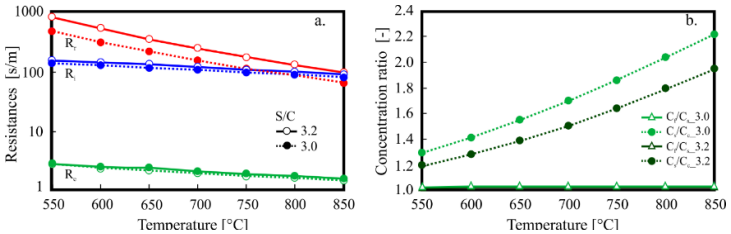


**Fig. 8.** Resistances (a) and concentration ratios for different S/C values for the 1.5Ru10Al coated monolith.

### 3.5. Heat transfer effects on Ru/γ-$Al_2O_3$ structured monolith catalyst

For heterogeneous catalytic processes, heat management in chemical reactions is a very important aspect for both reactor design and overall performance of the process. In addition to mass transfer effects, heat transfer effects can also occur in heterogeneous catalysis for reactions with a significant heat of reaction, either exothermal or endothermal such as combustion or steam reforming [45, 59, 60]. External temperature gradients between the bulk of the fluid phase and the surface of the catalytic layer are originated from the reaction enthalpy associated with surface reaction. The external temperature difference can be large even when mass transfer limitations are negligible, which disguises the actual reaction kinetics occurring at surface temperature ($T_s$) and not at the bulk of the fluid phase temperature ($T_b$). The surface temperature can be determined by the heat balance at steady state conditions, assuming that the outer surface of the catalyst layer is uniformly available for the reactants. In this way, each section of the outer surface behaves kinetically in the same way as all other parts, thus the steady-state analysis of that system is essentially one-dimensional [45, 59]. For more details of the heat balance go to the supplementary information section. We report the final expression of the heat balance using the Chilton-Colburn analogies between mass and heat transfer:

$$(T_b - T_s) = \left(\frac{\Delta H_r \cdot C_b}{\rho_f \cdot c_{p,f}}\right) \cdot Le^{-2/3} \cdot Ca \tag{23}$$

$$Le = \frac{Sc}{Pr} \;\; ; \;\; Ca = \frac{C_b - C_s}{C_b} \tag{24}$$

where $T_b, T_s$ is the temperature in the bulk of the gas phase and surface of the catalyst layer (K) respectively, $\Delta H_r$ is the heat of MSR reaction (J $mol^{-1}$), $C_b$ is the concentration in the bulk of the gas phase (mol $m^{-3}$), $\rho_f$ is the density of the gas phase (Kg $m^{-3}$), $c_{p,f}$ is the heat capacity of the gas phase (J $Kg^{-1}$ $K^{-1}$), $Le$ is the fluid Lewis number, $Pr$ is the Prandtl number and $Ca$ is the Carberry number. Thus, by dividing Equation 23 by $T_b$, it is possible to obtain the dimensionless external Prater

number which represents the ratio of the maximum heat consumption and heat transfer rates:

$$\beta_{ext} = \frac{\Delta T_{ad}}{T_b} \cdot Le^{-2/3} = \left(\frac{\Delta H_r \cdot C_b}{\rho_f \cdot c_{p,f}}\right) \cdot \frac{1}{T_b} \cdot Le^{-2/3} \quad (25)$$

The interphase heat transfer limitations can be evaluated using the criterion derived by Mears [61] (Eq. 26) with the perturbation approach, in which the heat transfer resistance of the fluid phase is assumed to be lumped at the surface. We use this criterion to estimate the external heat transfer effects by varying the alumina content in the monolithic catalyst:

$$\chi = \frac{(\Delta H \cdot R^{obs} \cdot R_{\Omega e})}{h_e \cdot T_b} < \frac{0.15}{\gamma_b}; \qquad \gamma_b = \frac{E_{act}}{R_g \cdot T_b} \quad (26)$$

where $R^{obs}$ is the observed reaction rate (mol m$^3$ s$^{-1}$), $h_e$ is the heat transfer coefficient associated for the gas phase (W m$^{-2}$ K$^{-1}$), $R_g$ is the gas constant (J mol$^{-1}$ K$^{-1}$), $E_{act}$ is the apparent activation energy of the reaction (J mol$^{-1}$), $\chi$ is the Damkholer for interphase heat transport and $\gamma_b$ is the Arrhenuis number evaluated at the bulk of the gas phase.

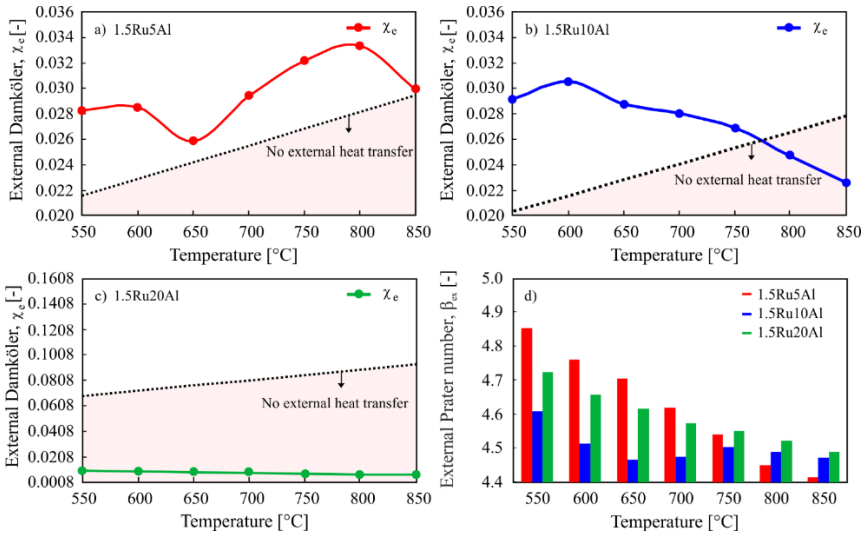


**Fig. 9.** External Damköhler numbers in a monolith of square channel and circular diameter with different coating: a) 1.5Ru5Al; b) 1.5Ru10Al; c) 1.5Ru20Al. External Prater number for the various catalysts loading (d).

As observed in Fig. 9, for the 1.5Ru5Al2O3 catalyst, external heat transfer limitations are presented for the complete temperature range studied, while for the 1.5Ru10Al catalyst the thermal effects are important a temperature below 725°C. On the other hand, not interphase heat transfer limitations are observed for the higher catalyst loading. It is important to note that for the lower alumina content the temperature difference between the bulk of the gas phase and the surface of the catalytic layer increases considerably as the inlet gas temperature increases from 650-800 °C, and then start to decrease probably as mentioned above, in this temperature range initiates the WGS reaction which is exothermic and leads to an increase in the $T_s$. For catalysts with 10 and 20 wt.% of alumina, the $\Delta T$ is practically constant as the temperature of the reactant gas increases, approximately 70 and 25 K respectively. It is also important to point out that the temperature difference between bulk and outer catalytic layer surface is directly proportional to the heat of MSR reaction per mol of diffusing reactant and the fractional drop in concentration between the bulk of the gas phase and the surface of the catalyst layer (see eq. 23). Thus, the quotient of the heat consumed by complete reaction of unit volume of reacting gas mixture ($\Delta H_r \cdot C_b$) and the volumetric heat capacity of the reacting mixture ($\rho_f \cdot c_{p,f}$) gives the temperature rise equivalent to complete adiabatic conversion of the reacting mixture when $C_s$ is zero. The eq. 23 also shows that heat transfer limitation and $\Delta T$ may be significant if $\Delta H_r$ values are large, even when concentration gradients are small as those obtained in section 3.4 for all the alumina loading studied. Since the MSR reaction is highly endothermic, the temperature of the catalyst surface will be less than in the bulk fluid phase, and the observed rate will be less than that corresponding to the bulk-fluid temperature.

In addition to the interphase heat transfer limitations, a large number of highly exothermic and endothermic catalytic reactions are accompanied by internal thermal effects, particularly for relatively fast intrinsic kinetics. Anderson in 1963 [62] applied the perturbation approach to derive a criterion for the lack of importance of temperature gradients in catalyst particles. The reaction is assumed to follow Arrhenius temperature dependence and this criterion is valid regardless of whether there are diffusion limitations in the particle or not. Thus, we use this criterion to evaluate the intraparticle heat transfer effects by varying the alumina content in the structured catalyst:

$$\frac{(\Delta H \cdot R^{obs} \cdot R_{\Omega i}^2)}{\lambda_{cat} \cdot T_s} < \frac{0.75}{\gamma_s} \qquad (27)$$

$$\psi = \frac{(\Delta H \cdot R^{obs} \cdot R_{\Omega i}^2)}{\lambda_{cat} \cdot T_s}; \qquad \gamma_s = \frac{E_{act}}{R_g \cdot T_s} \qquad (28)$$

where $\lambda_{cat}$ is the thermal conductivity of the $Ru/Al_2O_3$ catalyst (W $m^{-1}$ $K^{-1}$), $\psi$ is the Damkohler for intraparticle heat transport and $\gamma_s$ is the Arrhenuis number evaluated at the surface of the gas phase. As observed from the Fig. 10 (a-c), for all the catalyst loading studied $\psi << \frac{0.75}{\gamma_s}$ indicating that the absence of intraparticle

heat transfer. This can also be observed by studying the temperature gradients within the catalytic layer using the relationship originally derived by Damköhler in 1943 [63], which is valid for all the kinetics and applies to all the particle geometries assuming that $T_s$ and $C_s$ are uniform over the entire boundary surface [45]:

$$(T_s - T_{b,c}) = (\Delta H_r) \cdot \frac{D_e}{\lambda_e} \cdot (C_s - C_{b,c}) \qquad (29)$$

where $T_{b,c}$ is the temperature in the bulk of the catalyst layer (K), $C_{b,c}$ is the concentration within the catalyst layer and $\lambda_e$ is the effective thermal conductivity. It is worth noting the largest possible temperature difference into the catalyst layer is attained when the concentrations within the bulk of the catalyst layer becomes zero, hence we can refer the maximum temperature difference ($\Delta T_{max}$) to the surface temperature using the dimensionless internal Prater number ($\beta_{in}$) by [45, 59]:

$$\beta_{in} = \frac{\Delta T max}{T_s} = \frac{(\Delta H_r) \cdot C_s}{T_s} \cdot \frac{D_e}{\lambda_e} \qquad (30)$$

As shown in Fig. 10 d, all $\beta_{in}$ values are much smaller than one, indicating the absence of temperature gradients within the catalytic layer, confirming in this way the results obtained by using the Anderson criterion.

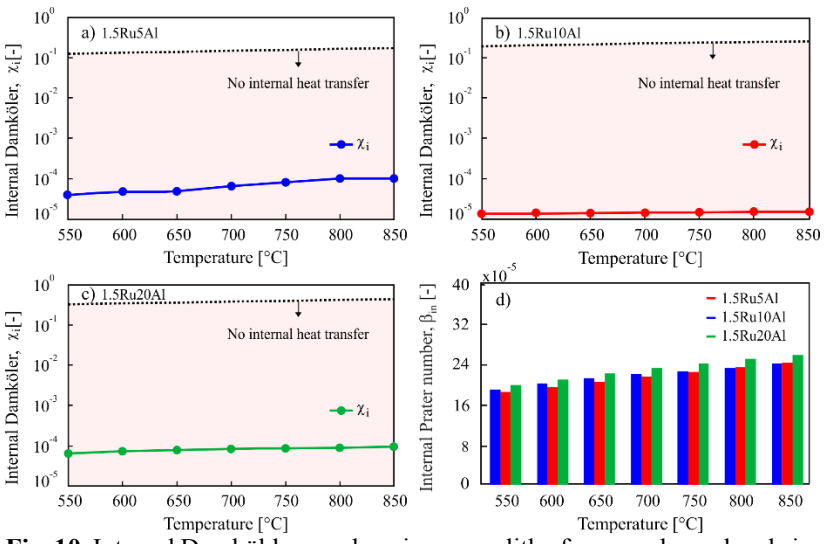


**Fig. 10.** Internal Damköhler numbers in a monolith of square channel and circular diameter with different coating: a) 1.5Ru5Al; b) 1.5Ru10Al; c) 1.5Ru20Al. Internal Prater number for the various catalysts loading (d).

In the following section, we will discuss the results obtained of the physico-chemical caracterization on the best catalyst-selected.

### 3.6 Characterization of powdered catalyst and coated structured supports.

Table 3 shows the specific surface area ($S_{BET}$) of powder samples, bare and coated monoliths. Comparing with the pure powder of γ-$Al_2O_3$, the $S_{BET}$ of 1.5 wt.% Ru/γ-$Al_2O_3$ powder catalyst was decreased by 82.6%, to 191.5 $m^2$ $g^{-1}$. Instead, considering the practically zero $S_{BET}$ of the bare monolith, As expected, the deposition of γ-$Al_2O_3$ on the monolith, as carrier of Ru (the active metal) notably increased the $S_{BET}$ of the bare monolith.

| Catalyst | $S_{BET}$ [$m^2$ $g^{-1}$] |
|---|---|
| γ-$Al_2O_3$ powder | 231.7 [39] |
| Ru/γ-$Al_2O_3$ powder | 191.5 [21] |
| 1.5 wt. % Ru/γ-$Al_2O_3$ on cordierite monolith | 23.8 |
| Bare cordierite monolith | 0.009 |

**Table 3.** Specific surface area values of different types of catalysts.

Ru metal dispersion and crystallite size obtained from $H_2$ chemisorption were 5.3% and 25 nm, respectively. Similar results were obtained in our previous work in terms of crystal size [33], while a greater dispersion of Ru is obtained when the catalyst is prepared in a single step by SCS.
Fig. 11 shows the XRD diffraction patterns of the 1.5 wt.% Ru/γ-$Al_2O_3$ catalyst , compared with the reference patterns of γ-$Al_2O_3$ and $RuO_2$. The diffractogram shows the peaks related to the Ru in its oxidized form ($RuO_2$ JCPDS database, ref. 00-002-1365) and the γ-$Al_2O_3$ in its amorphous structure (JCPDS database, ref. 00-001-1243).

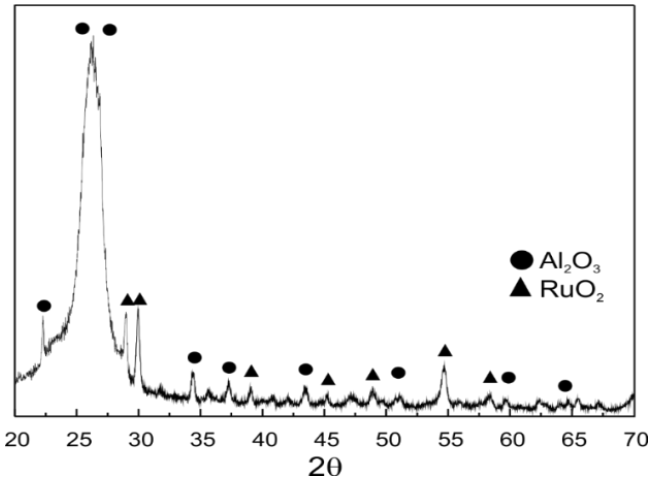

**Fig. 11.** XRD patterns of 1.5 wt.% Ru/γ-$Al_2O$ catalyst, with the reference peaks of $RuO_2$ (JCPDS database, ref. 00-002-1365) and γ-$Al_2O_3$ (JCPDS database, ref. 00-001-1243).

Figure 12 shows FESEM images of the coated monolith. There is a good dispersion of the catalytic particles on the surface of the monolith. In particular, alumina particles on the surface of the monolith are well dispersed by providing sufficient specific surface area to host Ru. Furthermore, Ru particle size distribution on $Al_2O_3$ particles seems to be wider. Table 4 shows the EDX analysis coupled with FESEM, giving evidence of the presence of Ru particles and alumina.

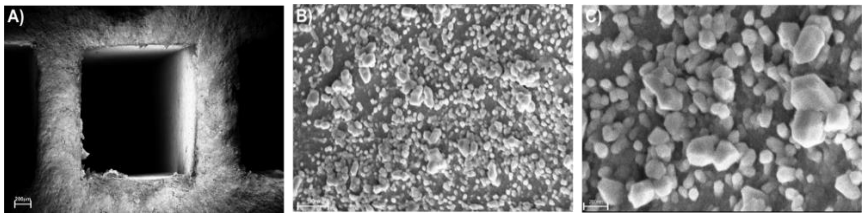


**Fig. 12.** FESEM images of 1.5% Ru on 10% alumina on 100 cpsi monolith at different magnifications. **A)** 100X, **B)** 50000 kX, **C)** 150000 kX.

| Element | Weight % | Atomic % |
|---|---|---|
| O | 53.45 | 68.56 |
| Mg | 1.09 | 0.92 |
| Al | 34.88 | 26.50 |
| Si | 5.54 | 2.58 |
| Ru | 7.04 | 1.44 |
| Tot | 100.00 | 100.00 |

**Table 4.** EDX analysis of the 100 cpsi monolith coated with 1.5% Ru on 10% alumina.

### 3.7 Ageing test on the best performing coated monolith.

After performing various experiments, the catalyst 1.5Ru10Al performed best in all types of test. The conversion remained higher than the others and it showed high productivity and higher CO selectivity at low WHSV for temperatures between 600-750°C and S/C 3. The most competitive catalyst with the same experimental conditions was Rh, but it was clearly seen that the difference in performance was almost more than 8%.
Furthermore, a new cordierite monolith was coated with the best catalyst, 1.5%Ru/10%$Al_2O_3$, and its catalytic performance was evaluated with respect to

time. Figure 13 shows methane conversion versus the time on stream (TOS), at two different WHSV. In the first 30 hrs, reaction conditions were fixed at 800 °C, WHSV = 750 and S/C = 3. Then, for the next 20 hrs, WHSV was increased to 1500, and finally reduced again to 750 (being T and S/C always constant at 800 °C and 3, respectively). Clearly, the coated monolith kept methane conversion almost constant at its starting value, independent of the variation of WHSV.
Thus, this test confirms that overall at the temperature of 800 °C, even when varying the WHSV, no significant difference is recorded in methane conversion, which remained stable throughout the time period.

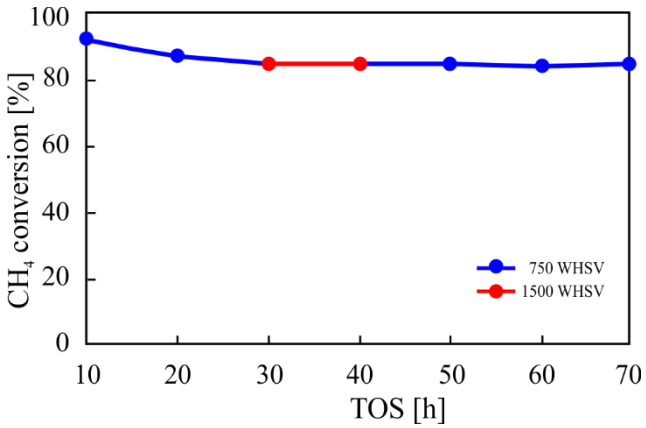


**Fig. 13.** Stability test of the cordierite monolith coated with 1.5%Ru/10%$Al_2O_3$ catalyst at 800 °C and S/C =3. WHSV variable between 750 and 1500 Nl $h^{-1}$ $g_{cat}^{-1}$.

## 4. CONCLUSION

In this study, the catalytic performance and mass/heat transfer effects were evaluated for Ru/γ-$Al_2O_3$ catalyst supported on ceramic cordierite monolith towards MSR reaction. All the catalysts were prepared in a single step by solution combustion synthesis coated on over monolith of square channel with 100 cpsi. By comparing the catalytic performance of Ru and Rh as active metal phase, the Ru-based catalyst was found to be more active towards MSR reaction, showing a syngas richer in $H_2$ for the entire temperature range studied. The best catalyst loading of Ru/γ-$Al_2O_3$ catalyst was 6.45 mg $cm^{-2}$, where the excess of $Al_2O_3$ carrier could only lead to a thicker layer and not participate in the catalytic reaction, leading to the catalyst working in an entirely kinetic regime. The temperature dependence on the external and internal diffusion regimes is much weaker compared to the reaction resistance, which is strongly dependent of the Arrhenius equation. External heat transfer limitations were presented at lower carrier content, while that low values of internal Prater numbers confirmed the absence of internal heat limitation. An

excellent stability of the 1.5% Ru on 10% $Al_2O_3$ catalyst (1.5Ru10Al sample) was observed over 70 h of TOS for MSR process.

# 5. APPENDIX

In the following, a detailed explanation of fluid and catalyst layer properties determination, characteristic time analysis, external and internal mass transfer calculations and heat transfer investigation is reported.

### A.1 Estimation of fluid properties

Molecular weight ($M_{mix}$), density ($\rho_f$) and viscosity ($\mu_f$) of gas mixture were calculated as:

$$M_{mix} = \sum_{i=1}^{n} y_i \, M_i \tag{S1}$$

$$\rho_f = \frac{P \, M_{mix}}{R_g \, T} \tag{S2}$$

$$\mu_f = \frac{\sum_{i=1}^{n} \mu_i \, y_i \, M_i^{1/2}}{\sum_{i=1}^{n} y_i \, M_i^{1/2}} \tag{S3}$$

where $y_i$ is the mole fraction of the compound, $M_i$ is the molecular weight of the compound (kg kmol$^{-1}$), $P$ is the pressure (kPa), $T$ is the absolute temperature (K), $R$ is the universal gas constant (J mol$^{-1}$ K$^{-1}$) and $\mu_i$ is the viscosity of a single component (kg m$^{-1}$ s$^{-1}$).
Gas viscosity ($\mu_i$ , μP) of a single component was calculated as:

$$\mu_i = A + BT + CT^2 \tag{S4}$$

using the tabulated values of A, B, and C [64].

| | **$CH_4$** | **$H_2O$** | **$H_2$** | **CO** | **$CO_2$** |
|---|---|---|---|---|---|
| **A** | 3.844 | –36.826 | 27.758 | 23.811 | 11.811 |
| **B** | 0.40112 | 0.429 | 0.212 | 0.53944 | 0.49838 |
| **C** | –0.00014303 | –0.0000162 | –0.0000328 | –0.00015411 | –0.0001085 |

**Table A1.** Values of A, B, and C used in eq. S.4.

The diffusivity of $CH_4$ in gas mixture ($D_{CH_4-mix}$ , cm$^2$ s$^{-1}$) was calculated from the binary diffusion of $CH_4$ and $i$ gas species ($D_{CH_4-i}$) by:

$$D_{CH_4-mix} = \frac{1-y_{CH_4}}{\sum_{i=1;i\neq CH_4}^{n} \frac{y_i}{D_{CH_4-i}}} \tag{S5}$$

where $D_{CH_4-i}$ was determined by Fuller equation (eq. S.6) [65], using tabulated values of $v_i$ [66].

$$D_{CH_4-i} = \frac{10^{-3}\, T^{1.75} \left(\frac{1}{M_{CH_4}} + \frac{1}{M_i}\right)}{P\left(v_{CH_4}^{1/2} + v_i^{1/3}\right)^2} \qquad \text{(S6)}$$

where $v_i$ are tabulate in Table A2.

| | $CH_4$ | $H_2O$ | $H_2$ | CO | $CO_2$ |
|---|---|---|---|---|---|
| $v_i$ ($cm^3 \cdot mol^{-1}$) | 24.4 | 12.7 | 7.1 | 18.9 | 26.9 |

**Table A2.** Values of $v_i$ used in eq. S.6.

The effective diffusivity of methane ($D_{CH_4,e}$) in the catalytic layer was calculated using the following equation [67, 68]:

$$D_{CH_4,e} = \frac{\varepsilon_c}{\tau_c} \cdot \left(\frac{1}{D_{CH_4-mix}} + \frac{1}{D_k}\right)^{-1} \qquad \text{(S7)}$$

where $\varepsilon_c$ is the coated layer porosity ($\varepsilon_c = \rho_c \cdot V_{BJH}$) [69], $\tau$ is the tortuosity factor ($\tau = 2 - \varepsilon_c$) [70] and the Knudsen diffusion ($D_k$) was determined by eq. S.8 [71]:

$$D_k = 9700 \cdot r_p \cdot \sqrt{\frac{T}{M_{CH_4}}} \qquad \text{(S8)}$$

where $\rho_c$ (kg $m^{-3}$) is the bulk density of the catalyst (3500 kg $m^{-3}$), $V_{BJH}$ is the total pore volume ($cm^3$ $g^{-1}$), $r_p$ is the pore diameter (cm) and $M_{CH_4}$ is the molecular weight of $CH_4$.
The mass transfer coefficient of $CH_4$ ($k_G$, m $s^{-1}$) was determined from the Sherwood number ($Sh$) by:

$$k_G = \frac{Sh \cdot D_{CH_4-mix}}{d_h} \qquad \text{(S9)}$$

where $Sh$ is calculated from Reynold ($Re$) and Schmidt ($Sc$) numbers by Eqs. S.10, S.11 and S.12 [60, 72, 73].

$$Sh = 2.976 \cdot \left(1 + 0.095 \cdot Re \cdot Sc \cdot \frac{d_h}{L_m}\right)^{0.45} \qquad \text{(S10)}$$

$$Re = \frac{d_h \cdot u_0 \cdot \rho_f}{\mu_f} \qquad \text{(S11)}$$

$$Sc = \frac{\mu_f}{\rho_f \cdot D_{CH_4-mix}} \quad \text{(S12)}$$

where $d_h$ is the hydraulic diameter of the bare monolith (m), $L_m$ is the monolith length (m), $u_0$is the inlet gas velocity at operative conditions (m $s^{-1}$), $\rho_f$ is the density of gas mixture (kg $m^{-3}$), $\mu_f$ is the viscosity of gas mixture (kg $m^{-1}$ $s^{-}1$) and $D_{CH_4-mix}$ is the diffusivity of $CH_4$ in gas phase ($m^2$ $s^{-1}$).
The inlet gas velocity at operative conditions $u_0$ (m $s^{-1}$) was calculated as:

$$u_o = \frac{F_{ch}}{A_{ch} \cdot \varepsilon} \cdot \frac{T}{T_{St}} \cdot \frac{P}{P_{St}} \quad \text{(S13)}$$

where $F_{ch}$ is the total flow of the gas mixture for channel ($m^3$ $s^{-1}$), $\varepsilon$ is the coated monolith voidage, $A_{ch}$ is the frontal area of the bare monolith for square channel ($m^2$), $T_{St}$ (K) and $P_{St}$ (Pa) are the standard temperature and pressure, $T$ (K) and $P$ (Pa) are the operative temperature and pressure.
The thermal conductivity of gas mixture ($\lambda_{mix}$, W $m^{-1}$ $K^{-1}$) was calculated as:

$$\lambda_{mix} = \frac{\sum_{i=1}^{n} \lambda_i \, y_i \, M_i^{1/2}}{\sum_{i=1}^{n} y_i \, M_i^{1/2}} \quad \text{(S14)}$$

where $\lambda_i$ is the thermal conductivity of a single component (W $m^{-1}$ $K^{-1}$) calculated as:

$$\lambda_i = A + BT + CT^2 \quad \text{(S15)}$$

using the tabulated values of A, B, and C [64].

| | $CH_4$ | $H_2O$ | $H_2$ | CO | $CO_2$ |
|---|---|---|---|---|---|
| **A** | –0.00935 | 0.00053 | 0.03951 | 0.00158 | –0.01200 |
| **B** | 1.4028E–04 | 4.7093E–05 | 4.5918E–04 | 8.2511E–05 | 1.0208E–04 |
| **C** | 3.3180E–08 | 4.9551E–08 | –6.4933E–08 | –1.9081E–08 | –2.2403E–081 |

**Table A3.** Values of A, B, and C used in eq. S.15.

The heat capacity of the gas mixture ($Cp_f$ J $mol^{-1}$ $K^{-1}$) was calculated as:

$$Cp_f = \frac{\sum_{i=1}^{n} Cp_i \, y_i \, M_i^{1/2}}{\sum_{i=1}^{n} y_i \, M_i^{1/2}} \quad \text{(S16)}$$

where $Cp_i$ is the heat capacity of a single component (J $mol^{-1}$ $K^{-1}$) calculated as [64]:

$$Cp_i = A + BT + CT^2 + DT^3 + ET^4 \quad \text{(S17)}$$

| | $CH_4$ | $H_2O$ | $H_2$ | CO | $CO_2$ |
|---|---|---|---|---|---|
| **A** | 34.942 | 33.933 | 25.399 | 29.556 | 27.437 |
| **B** | –3.9957E–02 | –8.4186E–03 | 2.0178E–02 | –6.5807E–03 | 4.2315E–02 |
| **C** | 1.9184E–04 | 2.9906E–08 | –3.8549E–05 | 2.0130E–05 | –1.9555E–05 |
| **D** | –1.5303E–07 | –1.7825E–08 | 3.188E–08 | –1.2227E–08 | 3.9968E–09 |
| **E** | 3.9321E–11 | 3.6942E–12 | –8.758E–12 | 2.2617E–12 | –2.9872E–13 |

**Table A4.** Values of A, B, C, D, and E used in eq. S.17.

### A.2 Estimation of coated layer properties

Specific surface area ($SA_{BET}$ = 23.79 $m^2 \cdot g^{-1}$) was determined from Brunauer-Emmett-Teller (BET) and Barrett-Joyner-Halenda (BJH) analytic methods for $N_2$ adsorption-desorption isotherms. Pore radius ($r_p$ = 100 Å) was given by $2PV_{BJH}/SA_{BET}$ equation.

### A.3 Characteristic time analysis

The characteristic contact time, or residence time ($t_c$, s) is determined by [73]:

$$t_c = \frac{L_m}{u_o} \quad \text{(S18)}$$

where $L_m$ is the monolith length (m) and $u_o$ is the inlet gas velocity at operative conditions (m $s^{-1}$).
The transverse diffusion time for the flow area ($t_d^e$, s) is determined by [73]:

$$t_d^e = \frac{R_{\Omega e}^2}{D_{CH_4-mix}} \quad \text{(S19)}$$

where $R_{\Omega e}$ is the characteristic length scale for the fluid phase (m) and $D_{CH_4-mix}$ is the diffusivity of $CH_4$ in gas phase ($m^2$ $s^{-1}$).
The transverse diffusion time for the coated area ($t_d^i$, s) is determined by [73]:

$$t_d^i = \frac{{\delta_c}^2}{D_{CH_4,e}} \quad \text{(S20)}$$

where $D_{CH_4,e}$ is the effective diffusivity of $CH_4$ in the coated layer ($m^2$ $s^{-1}$) and $\delta c$ is the coated layer thickness (m) calculated as [47]:

$$\delta_c = \frac{l_w^2 - \frac{\pi}{4} d_f^2}{\pi \cdot d_f} \quad \text{(S21)}$$

where $l_w$ (m) is the channel width and $d_f$(m) is the average channel dimension estimated by SEM.
The characteristic reaction time $t_r$ (s) is determined by [73]:

$$t_r = \frac{C_{CH_4,in}}{r_{CH_4} \cdot \rho_c} \qquad \text{(S22)}$$

where $C_{CH_4,in}$ is the concentration of $CH_4$ in the feed mixture (kmol $m^{-3}$), $r_{CH_4}$ is the observed reaction rate for $CH_4$ (kmol $m^{-3}$ $s^{-1}$), and $\rho_c$ is the density of the catalytic layer (kg $m^{-3}$).
The longitudinal diffusion time $t_z$ (s) is determined by [49]:

$$t_z = \frac{{L_m}^2}{D_{CH_4-mix}} \qquad \text{(S23)}$$

where $L_m$ is the monolith length (m) and $D_{CH_4-mix}$ is the diffusivity of $CH_4$ in gas phase ($m^2$ $s^{-1}$).

## A.4 External and internal mass transfer analysis

### A.4.1 Characteristic dimensions for the external and internal mass transfer analysis

In order to study the external and internal mass transfer resistances, two different characteristic cross-sectional areas for a single channel of the monolith are defined: the cross-sectional area of gas phase or circular flow area $A_{\Omega e}$ ($m^2$) and the cross-sectional area of coated catalyst layer $A_{\Omega i}$ ($m^2$).
The cross-sectional area of fluid phase $A_{\Omega e}$ ($m^2$) is calculated as:

$$A_{\Omega e} = \frac{\pi \cdot {d_f}^2}{4} \qquad \text{(S24)}$$

where $d_f$ (m) is the average channel dimension estimated by SEM.
The cross-sectional area of coated catalyst layer $A_{\Omega i}$ ($m^2$) is calculated as:

$$A_{\Omega i} = A_{ch} - A_c \qquad \text{(S25)}$$

where $A_{ch}$ is the area of a single bare channel ($m^2$) and $A_c$ is the area remaining available in the channel for the flow of reactants after catalyst deposition ($m^2$). For the channel shape under consideration (square channel with circular flow area), $A_c$ ($m^2$) corresponds with the circular flow area $A_{\Omega e}$ ($m^2$).
The area of a single bare channel $A_{ch}$ ($m^2$) is calculated as:

$$A_{ch} = {l_w}^2 \qquad \text{(S26)}$$

where $l_w$ (m) is the channel width.
Thus, it is possible to define the characteristic length scales for the fluid phase $R_{\Omega e}$ (m) and for the coated catalyst layer $R_{\Omega i}$ (m).
The characteristic length scale for the fluid phase $R_{\Omega e}$ (m) is defined as [47]:

$$R_{\Omega e} = \frac{A_{\Omega e}}{P_c} \quad \text{(S27)}$$

where $A_{\Omega e}$ ($m^2$) is the flow area (or cross-sectional area of fluid phase) and $P_c$ (m) is the fluid-coated catalyst layer interfacial perimeter.
The fluid-coated catalyst layer interfacial perimeter is calculated as:

$$P_c = \pi \cdot d_f \quad \text{(S28)}$$

Thus, the characteristic length scale for the fluid phase $R_{\Omega e}$ (m) can be expressed as:

$$R_{\Omega e} = \frac{\frac{\pi \cdot {d_f}^2}{4}}{\pi \cdot d_f} = \frac{d_f}{4} \quad \text{(S29)}$$

The characteristic length scale for the coated catalyst layer $R_{\Omega i}$ (m) is defined as [47]:

$$R_{\Omega i} = \frac{A_{\Omega i}}{P_c} \quad \text{(S30)}$$

where $A_{\Omega i}$ ($m^2$) is the cross-sectional area of coated catalyst layer and $P_c$ (m) is the fluid-coated catalyst layer interfacial perimeter.
Thus, the characteristic length scale for the coated catalyst layer $R_{\Omega i}$ (m) can be expressed as:

$$R_{\Omega i} = \frac{{l_w}^2 - \frac{\pi \cdot {d_f}^2}{4}}{\pi \cdot d_f} \quad \text{(S31)}$$

### A.4.2 External and internal mass transfer coefficients

The external mass transfer coefficient $k_{m,e}$ (m $s^{-1}$) between the bulk of fluid phase and the fluid-coated catalyst layer interface is calculated as [47]:

$$k_{m,e} = \frac{Sh_e \cdot D_{CH_4-mix}}{4 \cdot R_{\Omega e}} \quad \text{(S32)}$$

where $Sh_e$ is the external Sherwood number, $D_{CH_4-mix}$ is the diffusivity of $CH_4$ in gas phase ($m^2$ $s^{-1}$) and $R_{\Omega e}$ is the characteristic length scale for the fluid phase (m).
The internal mass transfer coefficient $k_{m,i}$ (m $s^{-1}$) between the interior of the coated catalyst layer and fluid-coated catalyst layer interface is calculated as [47]:

$$k_{m,i} = \frac{Sh_i \cdot D_{CH_4,e}}{R_{\Omega i}} \quad \text{(S33)}$$

where $Sh_i$ is the internal Sherwood number, $D_{CH_4,e}$ is the effective diffusivity of $CH_4$ in the coated layer ($m^2\ s^{-1}$) and $R_{\Omega i}$ is the characteristic length scale for the coated catalyst (m).
The external Sherwood number $Sh_e$ is calculated by [47]:

$$Sh_e = Sh_{e\infty} + \frac{2.8}{Sc^{1/6}} \cdot \sqrt{P} \quad \text{(S34)}$$

where $Sh_{e\infty}$ is the asymptotic external Sherwood number, $Sc$ is the Schmidt ($Sc$) number and $P$ is the transverse Peclet number. For square channel, $Sh_{e\infty} = 2.98$.
The transverse Peclet number is calculated as [47]:

$$P = \frac{{R_{\Omega e}}^2 \cdot u_o}{L_m \cdot D_{CH_4-mix}} \quad \text{(S35)}$$

where $R_{\Omega e}$ is the characteristic length scale for the fluid phase (m), $u_o$ is the inlet gas velocity at operative conditions ($m\ s^{-1}$), $L_m$ is the monolith length (m) and $D_{CH_4-mix}$ is the diffusivity of $CH_4$ in gas phase ($m^2\ s^{-1}$).
The internal Sherwood number $Sh_i$ is calculated by [47]:

$$Sh_i = Sh_{i\infty} + \frac{\Lambda \cdot \phi^2}{1 + \Lambda \cdot \phi} \quad \text{(S36)}$$

where $Sh_{i\infty}$ is the asymptotic internal Sherwood number, $\Lambda$ is a constant that depends on the coated catalyst layer shape and kinetic parameters and ø is the Thiele modulus.
The Thiele modulus ø for a first order reaction is defined as:

$$\phi = \sqrt{\frac{k_{obs} \cdot {R_{\Omega i}}^2}{D_{CH_4,e}}} \quad \text{(S37)}$$

where $k_{obs}$ is the observed first-order reaction rate constant ($s^{-1}$), $R_{\Omega i}$ is the effective transverse diffusion length in the coated catalyst layer (m) and $D_{CH_4,e}$ is the effective diffusivity of $CH_4$ ($m^2\ s^{-1}$).
The effectiveness factor η for a first order reaction can be expressed as [47]:

$$\eta = \frac{1}{1 + \frac{\phi^2}{Sh_i}} \quad \text{(S38)}$$

where ø is the Thiele modulus for a first order reaction and $Sh_i$ is the internal Sherwood number.

### A.4.3 Multiple resistances in series approach

The overall resistance for mass transfer $R_t$(s m$^{-1}$) is defined as [47]:

$$R_t = R_e + R_i + R_r \tag{S39}$$

where $R_e$ is the resistance for the external mass transfer (s m$^{-1}$), $R_i$ is the resistance for the internal mass transfer (s m$^{-1}$) and $R_r$ is the reaction resistance (s m$^{-1}$).
The resistance for the external mass transfer $R_e$ (s m$^{-1}$) can be calculated as:

$$R_e = \frac{1}{k_{m,e}} \tag{S40}$$

where $k_{m,e}$ is the external mass transfer coefficient between the bulk of fluid phase and the fluid-coated catalyst layer interface (m s$^{-1}$).
The resistance for the internal mass transfer $R_i$ (s m$^{-1}$) can be calculated as:

$$R_i = \frac{1}{k_{m,i}} \tag{S41}$$

where $k_{m,i}$ is the internal mass transfer coefficient between the interior of the coated catalyst layer and fluid-coated catalyst layer interface (m s$^{-1}$).
The reaction resistance $R_r$ (s m$^{-1}$) can be calculated as:

$$R_t = \frac{1}{k_{obs} \cdot R_{\Omega i}} \tag{S42}$$

where $R_{\Omega i}$ (m) is the characteristic length scale for the coated catalyst layer and $k_{obs}$ (s$^{-1}$) is the observed first-order reaction rate constant.
Thus, the apparent (or overall experimentally observable) mass transfer coefficient $k_{m,app}$ (m s$^{-1}$) can be calculated as [47]:

$$\frac{1}{k_{m,app}} = \frac{1}{k_{m,e}} + \frac{1}{k_{m,i}} + \frac{1}{k_{obs} \cdot R_{\Omega i}} \tag{S43}$$

where $k_{m,e}$ is the external mass transfer coefficient between the bulk of fluid phase and the fluid-coated catalyst layer interface (m s$^{-1}$), $k_{m,i}$ is the internal mass transfer coefficient between the interior of the coated catalyst layer and fluid-coated catalyst layer interface (m s$^{-1}$), $k_{obs}$ is the observed first-order reaction rate constant (s$^{-1}$) and $R_{\Omega i}$ is the characteristic length scale for the coated catalyst layer (m).
Writing S.43 in dimensionless form gives:

$$\frac{1}{k_{m,app}} \cdot \frac{D_{CH_4-mix}}{4 \cdot R_{\Omega e}} = \left( \frac{1}{Sh_e} + \frac{R_{\Omega i} \cdot D_{CH_4-mix}}{4 \cdot R_{\Omega e} \cdot D_{CH_4,e} \cdot Sh_i} + \frac{D_{CH_4-mix}}{4 \cdot R_{\Omega e}\, k_{obs} \cdot R_{\Omega i}} \right) \tag{S44}$$

$$\frac{1}{Sh_{app}} = \left(\frac{1}{Sh_e} + \frac{\alpha\cdot\beta}{4}\cdot\frac{1}{Sh_i} + \frac{\alpha\cdot\beta}{4\cdot\phi^2}\right) \quad \text{(S45)}$$

where the various dimensionless groups appearing in S.45 are defined as:

$$\beta = \frac{R_{\Omega i}}{R_{\Omega e}} \qquad \alpha = \frac{D_{CH_4-mix}}{D_{CH_4,e}}, \quad \phi^2 = \frac{k_{obs}\cdot {R_{\Omega i}}^2}{D_{CH_4,e}}, \quad Sh_{app} = \frac{4\cdot k_{m,app}\cdot R_{\Omega e}}{D_{CH_4-mix}} \quad \text{(S46)}$$

where $k_{m,app}$ (m $s^{-1}$) is the apparent (or overall experimentally observable) mass transfer coefficient, $D_{CH_4,e}$ is the effective diffusivity of $CH_4$ ($m^2$ $s^{-1}$), $D_{CH_4-mix}$ is the diffusivity of $CH_4$ in gas phase mixture($m^2$ $s^{-1}$), $R_{\Omega i}$ is the characteristic length scale for the coated catalyst layer (m), $R_{\Omega e}$ is the characteristic length scale for the fluid phase (m), $Sh_i$ is the internal Sherwood number, $Sh_e$ is the external Sherwood number, $k_{obs}$ is the observed first-order reaction rate constant ($s^{-1}$), ø is the Thiele modulus for a first order reaction and $Sh_{app}$ is the apparent (or experimentally observed) mass transfer coefficient.
In kinetic regime, the apparent mass transfer coefficient can be written as:

$$Sh_{app,kin} = \frac{4*\phi^2}{\alpha\cdot\beta} \quad \text{(S47)}$$

### A.5 Heat transfer effects

For highly endothermic reactions such as methane steam reforming, temperature gradients between the gas phase and catalyst surface cannot be neglected. Under steady-state conditions, the rate of mass transfer of methane reactant from the gas phase mixture to the solid surface must be equal to the rate of methane reactant conversion by surface reaction:

$$k_{m,e}\cdot A_{\Omega e}\cdot(C_b - C_s) = k_s\cdot A_{\Omega e}\cdot {C_s}^n \quad \text{(S48)}$$

where $k_s$ is the surface reaction rate constant, $C_b$ is the concentration in the bulk of the gas phase (mol $m^{-3}$), $C_s$ is the concentration in the surface of the catalyst layer (mol $m^{-}$).
Assuming that the outer surface of the catalyst particle is uniformly accessible to the reagents, that is, the thickness of the concentration and thermal boundary layers over the particle surface has constant values. Since each section of the outer surface behaves kinetically the same as all other parts, steady-state analysis of such a system is essentially one-dimensional [45, 59]. Thus, the heat generated by the surface reaction can be calculated by multiplying the mass transfer rate with the heat of reaction per mol of reactant. At steady state, we can obtain:

$$k_{m,e}\cdot A_{\Omega e}\cdot(C_b - C_s)\cdot(\Delta H_r) = h_e\cdot A_{\Omega e}\cdot(T_b - T_s) \quad \text{(S49)}$$

Solving the temperature difference, the final expression is given by:

$$\frac{k_{m,e}}{h_e} \cdot (C_b - C_s) \cdot (\Delta H_r) = (T_b - T_s) \qquad \text{(S50)}$$

where $T_b, T_s$ is the temperature in the bulk of the gas phase and surface of the catalyst layer (K) respectively, $\Delta H_r$ is the heat of MSR reaction (J mol$^{-1}$) and $h_e$ is the heat transfer coefficient associated for the gas phase (W m$^{-2}$ K$^{-1}$).
Hence, using the Chilton–Colburn analogy between heat and mass transfer ($j_H \approx j_M$) for simple gas mixture, we can replace the ratio $\frac{k_{m,e}}{h_e}$ and obtain the following expression [45, 59]:

$$k_{m,e} = \frac{j_M \cdot G}{\rho_f \cdot Sc^{\frac{2}{3}}} \qquad h_e = \frac{j_H \cdot G \cdot Cp_f}{Pr^{\frac{2}{3}}} \qquad \text{(S51)}$$

$$(T_b - T_s) = \frac{\Delta H_r}{\rho_f \cdot Cp_f} \cdot \left(\frac{Pr}{Sc}\right)^{\frac{2}{3}} \cdot (C_b - C_s) \qquad \text{(S52)}$$

Considering the Lewis ($Le$) and Carberry ($Ca$) number, we can obtain the final expression as [45, 59]:

$$Le = \frac{Sc}{Pr} \qquad Ca = \frac{C_b - C_s}{C_b} \qquad \text{(S53)}$$

$$(T_b - T_s) = \left(\frac{\Delta H_r \cdot C_b}{\rho_f \cdot c_{p,f}}\right) \cdot Le^{-2/3} \cdot Ca \qquad \text{(S54)}$$

where $\rho_f$ is the density of the gas phase (Kg m$^{-3}$), $c_{p,f}$ is the heat capacity of the gas phase ( J Kg$^{-1}$ K$^{-1}$) and $Pr$ is the Prandtl number.
Thus, by dividing Eq. S.53 by $T_b$, it is possible to obtain the dimensionless external Prater number ($\beta_{ext}$) which represents the ratio of the maximum heat consumption and heat transfer rates:

$$\frac{T_s}{T_b} = 1 - \left(\frac{\Delta H_r \cdot C_b}{\rho_f \cdot c_{p,f}}\right) \cdot \frac{1}{T_b} \cdot Le^{-2/3} \cdot Ca \qquad \text{(S55)}$$

$$\frac{T_s}{T_b} = 1 - \frac{\Delta T_{ad}}{T_b} \cdot Le^{-2/3} \cdot Ca \qquad \text{(S56)}$$

$$\frac{T_s}{T_b} = 1 - \beta_{ext} \cdot Ca \qquad \text{(S57)}$$

where $\Delta T_{ad}$ is the adiabatic temperature rise ($\Delta T_{ad} = \frac{\Delta H_r \cdot C_b}{\rho_f \cdot c_{p,f}}\ ; K$) and $\beta_{ext}$ is the dimensionless external Prater number ($\beta_{ext} = \frac{\Delta T_{ad}}{T_b} \cdot Le^{-2/3}$).

The interphase heat transfer limitations can be evaluated using the criterion derived by Mears [61] (Eq. S.58) with the perturbation approach, in which the heat transfer resistance of the fluid phase is assumed to be lumped at the surface:

$$\chi = \frac{(\Delta H \cdot R^{obs} \cdot R_{\Omega e})}{h_e \cdot T_b} < \frac{0.15}{\gamma_b}; \qquad \gamma_b = \frac{E_{act}}{R_g \cdot T_b} \quad \text{(S58)}$$

where $R^{obs}$ is the observed reaction rate (mol m$^3$ s$^{-1}$), $h_e$ is the heat transfer coefficient associated for the gas phase (W m$^{-2}$ K$^{-1}$), $R_g$ is the gas constant (J mol$^{-1}$ K$^{-1}$), $E_{act}$ is the apparent activation energy of the reaction (J mol$^{-1}$), $\chi$ is the Damkholer for interphase heat transport and $\gamma_b$ is the Arrhenuis number evaluated at the bulk of the gas phase.

Anderson in 1963 [62] applied the perturbation approach to derive a criterion for the lack of importance of temperature gradients in catalyst particles. The reaction is assumed to follow Arrhenius temperature dependence and this criterion is valid regardless of whether there are diffusion limitations in the particle or not:

$$\frac{(\Delta H \cdot R^{obs} \cdot R_{\Omega i}^2)}{\lambda_{cat} \cdot T_s} < \frac{0.75}{\gamma_s} \quad \text{(S59)}$$

$$\psi = \frac{(\Delta H \cdot R^{obs} \cdot R_{\Omega i}^2)}{\lambda_{cat} \cdot T_s}; \qquad \gamma_s = \frac{E_{act}}{R_g \cdot T_s} \quad \text{(S60)}$$

where $\lambda_{cat}$ is the thermal conductivity of the Ru/$Al_2O_3$ catalyst (W m$^{-1}$ K$^{-1}$), $\psi$ is the Damkohler for intraparticle heat transport and $\gamma_s$ is the Arrhenuis number evaluated at the surface of the gas phase.

In order to study the effects of mass and heat transfer, both balances must be solved simultaneously to estimate the concentration and temperature profile. From the mass balance, we can write the following expression:

$$D_e \cdot \frac{d^2c}{dx^2} - (-R) = 0 \quad \text{(S61)}$$

The heat balance can be written as:

$$\lambda_e \frac{d^2T}{dx^2} - (-R) \cdot (\Delta H_r) = 0 \quad \text{(S62)}$$

where $\lambda_e$ is the effective thermal conductivity (W m$^{-1}$ K$^{-1}$). Considering that the reaction rate (R) is the same in both balances, we can obtain the following expression:

$$\frac{D_e \cdot (\Delta H_r)}{\lambda_e} \cdot \frac{d^2c}{dx^2} = \frac{d^2T}{dx^2} \quad \text{(S63)}$$

By integrating the Equation S.63 and considering the surface concentration and temperature ($C_s, T_s$), we can obtain the following linear expression between internal temperature and reactant concentration [15,16]:

$$(T_s - T_{b,c}) = (\Delta H_r) \cdot \frac{D_e}{\lambda_e} \cdot (C_s - C_{b,c}) \qquad \text{(S64)}$$

where $T_{b,c}$ is the temperature in the bulk of the catalyst layer (K) and $C_{b,c}$ is the concentration within the catalyst layer (mol m$^{-3}$). It is worth noting the largest possible temperature difference into the catalyst layer is attained when the concentrations within the bulk of the catalyst layer becomes zero, hence we can refer the maximum temperature difference ($\Delta T_{max}$) to the surface temperature using the dimensionless internal Prater number ($\beta_{in}$) by [15,16]:

$$\beta_{in} = \frac{\Delta T_{max}}{T_s} = \frac{(\Delta H_r) \cdot C_s}{T_s} \cdot \frac{D_e}{\lambda_e} \qquad \text{(S65)}$$

| **Σ** | [cpsi] | 100 |
|---|---|---|
| $D_m$ | [m] | 0.030 |
| $L_m$ | [m] | 0.0019 |
| $\delta_w$ | [m] | 0.00063 |
| N | [m] | 0.1563 |
| E | [-] | 0.564 |
| GSA | [m$^2$ m$^{-3}$] | 1187,333 |
| $d_h$ | [m] | 0.0019 |
| $A_m$ | [m] | 0.00126 |

**Table A5.** Properties of the bare monolith.

| **T [°C]** | $t_c$ **[s]** | $t_d^i$ **[s]** | $t_d^e$ **[s]** | $t_r$ **[s]** | $t_z$ **[s]** |
|---|---|---|---|---|---|
| 550 | 0.3091 | 0.0456 | 0.0012 | 0.2238 | 5.1500 |
| 600 | 0.2914 | 0.0441 | 0.0010 | 0.1928 | 4.5926 |
| 650 | 0.2756 | 0.0428 | 0.0009 | 0.1883 | 4.1264 |
| 700 | 0.2615 | 0.0405 | 0.0008 | 0.1441 | 3.6903 |
| 750 | 0.2487 | 0.0394 | 0.0007 | 0.1151 | 3.3138 |
| 800 | 0.2371 | 0.0384 | 0.0007 | 0.0943 | 2.9217 |
| 850 | 0.2266 | 0.0384 | 0.0006 | 0.0939 | 2.6402 |

**Table A6.** Characteristic times for the 1.5Ru5Al catalyst.

| T [°C] | $t_c$ [s] | $t_d^i$ [s] | $t_d^e$ [s] | $t_r$ [s] | $t_z$ [s] |
|---|---|---|---|---|---|
| 550 | 0.3091 | 0.0714 | 0.0010 | 0.1521 | 4.5226 |
| 600 | 0.2914 | 0.0691 | 0.0008 | 0.1212 | 3.9330 |
| 650 | 0.2756 | 0.0670 | 0.0007 | 0.1113 | 3.4816 |
| 700 | 0.2614 | 0.0651 | 0.0007 | 0.1040 | 3.1674 |
| 750 | 0.2487 | 0.0634 | 0.0006 | 0.1001 | 2.9079 |
| 800 | 0.2371 | 0.0618 | 0.0006 | 0.1001 | 2.6688 |
| 850 | 0.2266 | 0.0604 | 0.0005 | 0.1014 | 2.4751 |

**Table A7.** Characteristic times for the 1.5Ru10Al catalyst.

| T [°C] | $t_c$ [s] | $t_d^i$ [s] | $t_d^e$ [s] | $t_r$ [s] | $t_z$ [s] |
|---|---|---|---|---|---|
| 550 | 0.3091 | 0.1319 | 0.0008 | 0.4222 | 4.7509 |
| 600 | 0.2914 | 0.1277 | 0.0008 | 0.3860 | 4.2279 |
| 650 | 0.2756 | 0.1239 | 0.0007 | 0.3713 | 3.8065 |
| 700 | 0.2614 | 0.1204 | 0.0006 | 0.3459 | 3.4299 |
| 750 | 0.2487 | 0.1172 | 0.0006 | 0.3495 | 3.1437 |
| 800 | 0.2371 | 0.1142 | 0.0005 | 0.3401 | 2.8716 |
| 850 | 0.2266 | 0.1115 | 0.0005 | 0.3195 | 2.6049 |

**Table A8.** Characteristic times for the 1.5Ru20Al catalyst.

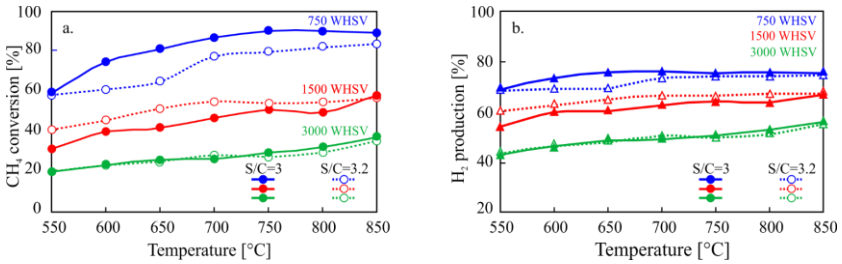


**Fig. A1.** MSR tests, performance comparison of monoliths 1.5% Ru on 10% γ-$Al_2O_3$ at various WHSV and S/C a) $CH_4$ conversion; b) $H_2$ production.

## 6. REFERENCES

[1] Hosseini, S.E., Wahid, M.A. Hydrogen production from renewable and sustainable energy resources: Promising green energy carrier for clean development. Renew. Sustain. Energy Rev. 57 (2016)850–866.

[2] IAEA (1999) IAEA-TECDOC-1085: Hydrogen as an energy carrier and its production by nuclear power. Iaea-Tecdoc-1085

[3] Alves, J.J., Towler, G.P. Analysis of refinery hydrogen distribution systems. Ind. Eng. Chem. Res. 41 (2002) 5759–5769.

[4] Meyers, R.A. Handbook of petroleum Refining Processes, Second. McGraw-Hill, New York (1996).

[5] Yamaguchi, D., Tang, L., Burke, N., et al. Small Scale Hydrogen Production from Metal-Metal Oxide Redox Cycles. Hydrog Energy - Challenges Perspect. 2 (2012) 31-54.

[6] Karadag, D., Köroğlu, O.E., Ozkaya, B., et al. A review on fermentative hydrogen production from dairy industry wastewater. J. Chem. Technol. Biotechnol. 89 (2014) 1627–1636.

[7] Holladay, J.D., Hu, J., King, D.L., Wang, Y. An overview of hydrogen production technologies. Catal. Today 139 (2009) 244–260.

[8] Barreto, L., Makihira, A., Riahi, K. The hydrogen economy in the 21st century: A sustainable development scenario. Int. J. Hydrogen Energy 28 (2003) 267–284.

[9] Hansen, K., Ingerslev, M., Felby, C., et al. Bioenergy in the Nordic-baltic-NW Russian Region. 66 (2006).

[10] Abbas, S.Z., Dupont, V., Mahmud, T. Kinetics study and modelling of steam methane reforming process over a NiO/Al2O3 catalyst in an adiabatic packed bed reactor. Int. J. Hydrogen Energy 42 (2017) 2889–2903.

[11] De, S., Zhan,g J., Luque, R., Yan, N. Ni-based bimetallic heterogeneous catalysts for energy and environmental applications. Energy Environ. Sci. 9 (2016) 3314–3347.

[12] Omoregbe, O., Danh, H.T., Abidin, S.Z., et al. Influence of Lanthanide Promoters on Ni/SBA-15 Catalysts for Syngas Production by Methane Dry Reforming. Procedia Eng. 148 (2016) 1388–1395.

[13] Tsyganok, A.I., Inaba, M., Tsunoda, T., et al. Dry reforming of methane over supported noble metals: A novel approach to preparing catalysts. Catal Commun 4 (2003) 493–498.

[14] Rass-Hansen, J., Christensen, C.H., Sehested, J., et al. Renewable hydrogen: Carbon formation on Ni and Ru catalysts during ethanol steam-reforming. Green Chem. 9 (2007) 1016–1021.

[15] Rostrup-Nielsen, J.R., Bak Hansen, J.H. $CO_2$-reforming of methane over transition metals. J. Catal. 144 (1993) 38–49.

[16] Ashraf, M.A., Sanz, O., Italiano, C., et al. Analysis of Ru/La-$Al_2O_3$ catalyst loading on alumina monoliths and controlling regimes in methane steam reforming. Chem. Eng. J. 334 (2018) 1792–1807.

[17] Tijburg, I.I.M., Geus, J.W., Zandbergen, H.W. Application of lanthanum to pseudo-boehmite and $\gamma$-$Al_2O_3$. J. Mater. Sci. 26 (1991) 6479–6486.

[18] Arai, H., Machida, M. Thermal stabilization of catalyst supports and their application to high-temperature catalytic combustion. Appl. Catal. A Gen. 138 (1996) 161–176

[19] Ferreira-Aparicio, P., Rodríguez-Ramos, I., Anderson, J.A., Guerrero-Ruiz, A. Mechanistic aspects of the dry reforming of methane over ruthenium

catalysts. Appl. Catal. A Gen. 202 (2000) 183–196.
[20] Berman, A., Karn, R.K., Epstein, M. Steam reforming of methane on a $Ru/Al_2O_3$ catalyst promoted with Mn oxides for solar hydrogen production. Green Chem. 9 (2007) 626–631.
[21] Amjad, U., Vita, A., Galletti, C., et al. Comparative study on steam and oxidative steam reforming of methane with noble metal catalysts. Ind. Eng. Chem. Res. 52 (2013) 15428–15436.
[22] Amjad, U., Moncada Quintero, C.W., Ercolino, G., et al. Methane Steam Reforming on the $Pt/CeO_2$ Catalyst: Effect of Daily Start-Up and Shut-Down on Long-Term Stability of the Catalyst. Ind. Eng. Chem. Res. 58 (2019) 16395–16406.
[23] Italiano, C., Ashraf, M.A., Pino, L., et al. $Rh/CeO_2$ thin catalytic layer deposition on alumina foams: Catalytic performance and controlling regimes in biogas reforming processes. Catalysts 8 (2018) 1–25.
[24] Vita, A., Italiano, C., Ashraf, M.A., et al. Syngas production by steam and oxy-steam reforming of biogas on monolith-supported $CeO_2$-based catalysts. Int. J. Hydrogen Energy 43 (2018) 11731–11744.
[25] Govender, S., Friedrich, H.B. Monoliths: A review of the basics, preparation methods and their relevance to oxidation. Catalysts 7 (2017).
[26] Roy, S., Bauer, T., Al-Dahhan, M., et al. Monoliths as multiphase reactors: A review. AIChE J. 50 (2004) 2918–2938.
[27] Boger, T., Heibel, A.K., Sorensen, C.M. Monolithic catalysts for the chemical industry. Ind. Eng. Chem. Res. 43 (2004) 4602–4611.
[28] Visconti, C.G., Tronconi, E., Groppi, G., et al. Monolithic catalysts with high thermal conductivity for the Fischer-Tropsch synthesis in tubular reactors. Chem. Eng. J. 171 (2011) 1294–1307.
[29] Tronconi, E., Groppi, G., Visconti, C.G. Structured catalysts for non-adiabatic applications. Curr. Opin. Chem. Eng. 5 (2014) 55–67.
[30] Ercolino, G., Karimi, S., Stelmachowski, P., Specchia, S. Catalytic combustion of residual methane on alumina monoliths and open cell foams coated with $Pd/Co_3O_4$. Chem. Eng. J. 326 (2017) 339–349.
[31] Ercolino, G., Stelmachowski, P., Specchia, S. Catalytic Performance of $Pd/Co_3O_4$ on SiC and $ZrO_2$ Open Cell Foams for Process Intensification of Methane Combustion in Lean Conditions. Ind. Eng. Chem. Res. 56 (2017) 6625–6636.
[32] Ercolino, G., Grzybek, G., Stelmachowski, P., et al. $Pd/Co_3O_4$-based catalysts prepared by solution combustion synthesis for residual methane oxidation in lean conditions. Catal. Today 257 (2015) 66–71.
[33] Vita, A., Cristiano, G., Italiano, C., et al. Methane oxy-steam reforming reaction: Performances of $Ru/\gamma\text{-}Al_2O_3$ catalysts loaded on structured cordierite monoliths. Int. J. Hydrogen Energy 39 (2014) 18592–18603.
[34] Specchia, S., Galletti, C., Specchia, V. Solution Combustion Synthesis as intriguing technique to quickly produce performing catalysts for specific applications. Stud. Surf. Sci. Catal. 175 (2010) 59–67.
[35] Nijhuis, T.A., Beers, A.E.W., Vergunst, T., et al. Preparation of monolithic catalysts. Catal. Rev. - Sci. Eng. 43 (2001) 345–380.

[36] Williams, J.L. Monolith Structures, Materials, Properties and Uses. Catal. Today 69 (2001) 3–9.

[37] Plummer, H.K., Baird, R.J., Hammerle, R.H., et al. Measurement of automotive catalyst washcoat loading parameters by microscopy techniques. Microsc. Microanal. 5 (1999) 267–281.

[38] Cybulski, A., Moulijn, J.A. Structured Catalysts and Reactors. Marcel Dekker, Inc., New York (1998).

[39] Wójcik, S., Ercolino, G., Gajewska, M., et al. Robust $Co_3O_4$|α-$Al_2O_3$|cordierite structured catalyst for $N_2O$ abatement – Validation of the SCS method for active phase synthesis and deposition. Chem. Eng. J. (2018) in press.

[40] Millington, B., Whipple, V., Pollet, B.G. A novel method for preparing proton exchange membrane fuel cell electrodes by the ultrasonic-spray technique. J. Power Sources 196 (2011) 8500–8508.

[41] Arzamendi, G., Die, P.M., Gandia, L.M. Renewable hydrogen technologies: Renewable hydrogenenergy - An overview (2013).

[42] Spivey, J.J., Dooley, K.M. Catalysis. The Royal Society of Chemistry (2009).

[43] Dumesic, J.A., Huber, G.W., Boudart, M. Principles of Heterogeneous Catalysis. In: Handbook of Heterogeneous Catalysis. Wiley-VCH Verlag GmbH & Co. KGaA (2008).

[44] Klaewkla, R., Arend, M., Hoelderich, W.F. A Review of Mass Transfer Controlling the Reaction Rate in Heterogeneous Catalytic Systems. In: Mass Transfer - Advanced Aspects. pp 667–684 (2011).

[45] Kashid, M.N., Renken, A. Microstructured Devices for Chemical Microreactors. Wiley-VCH Verlag Gmbh & Co. (2013)

[46] Joshi, S.Y., Harold, M.P., Balakotaiah, V. Low-Dimensional Models for Real Time Simulations of Catalytic Monoliths. AIChE J. 55 (2009) 1771–1783.

[47] Joshi, S.Y., Harold, M.P., Balakotaiah, V. Overall mass transfer coefficients and controlling regimes in catalytic monoliths. Chem. Eng. Sci. 65 (2010) 1729–1747.

[48] Joshi, S.Y., Harold, M.P., Balakotaiah, V. On the use of internal mass transfer coefficients in modeling of diffusion and reaction in catalytic monoliths. Chem. Eng. Sci. 64 (2009) 4976–4991.

[49] Balakotaiah, V., West, D.H. Shape normalization and analysis of the mass transfer controlled regime in catalytic monoliths. Chem. Eng. Sci. 57 (2002) 1269–1286.

[50] Young, L.C., Finlayson, B.A. Mathematical models of the monolith catalytic converter: Part II. Application to automobile exhaust. AIChE J. 22 (1976) 343–353.

[51] Bhattacharya, M., Harold, M.P., Balakotaiah, V. Mass-transfer coefficients in washcoated monoliths. AIChE J. 50 (2004) 2939–2955.

[52] Balakotaiah, V. On the relationship between Aris and Sherwood numbers and friction and effectiveness factors. Chem. Eng. Sci. 63 (2008) 5802–5812.

[53] Laguna, O.H., Domínguez, M.I., Centeno, M.A., Odriozola, J.A. Catalysts on Metallic Surfaces: Monoliths and Microreactors. New Materials for Catalytic Applications. Elsevier B.V. (2016).
[54] Kockmann, N. Transport Phenomena in Micro Process Engineering. Norbert Kockmann, Springer (2008).
[55] Bennett, C.J., Hayes, R.E., Kolaczkowski, S.T., Thomas, W.J. An experimental and theoretical study of a catalytic monolith to control automobile exhaust emissions. Proc. R. Soc. Lond. A 439 (1992) 465–483.
[56] Joshi, S.Y., Ren, Y., Harold, M.P., Balakotaiah, V. Determination of kinetics and controlling regimes for $H_2$ oxidation on $Pt/Al_2O_3$ monolithic catalyst using high space velocity experiments. Appl. Catal. B Environ. 102 (2011) 484–495.
[57] Berman, A., Karn, R.K., Epstein, M. Kinetics of steam reforming of methane on $Ru/Al_2O_3$ catalyst promoted with Mn oxides. Appl. Catal. A Gen. 282 (2005) 73–83.
[58] Choudhary, T.V., Goodman, D.W. Methane activation on Ni and Ru model catalysts. J. Mol. Catal. A Chem. 163 (2000) 9–18.
[59] Onsan, Z.I., Avci, A.K. Multiphase Catalytic Reactors. John Wiley & Sons, Hoboken, N.J. (2016).
[60] Shah, R.K., London, A.L. Laminar Flow Forced Convection in Ducts: A Source Book for Compact Heat Exchanger Analytical Data. Academic Press, New York (1978)
[61] Mears, D.E. Diagnostic criteria for heat transport limitations in fixed bed reactors. J. Catal 20 (1971) 127–131.
[62] Anderson, J.E. A criterion for isothermal behaviour of a catalyst pellet. Chem. Eng. Sci. 18 (1963) 147–148.
[63] Damköhler, G. The Excess Temperature in Contact Grains. Z Phys Chemie 193 (1943) 16–28.
[64] Yaws, .CL. Chemical properties Handbook. McGraw-Hill, New York (1999).
[65] Fuller, E.N., Schettler, P.D., Giddings, J.C. A new method for prediction of binary gas-phase diffusion coefficients. Ind. Eng. Chem. 58 (1966) 18–27.
[66] Green, D.W., Perry, R.H. Perry's Chemical Engineers' Handbook, 8th ed. McGraw-Hill (2008).
[67] Cao, C., Zhang, N., Cheng, Y. Numerical analysis on steam methane reforming in a plate microchannel reactor: Effect of washcoat properties. Int. J. Hydrogen Energy 41 (2016) 18921–18941.
[68] Hayes, R.E., Kolaczkowski, S.T., Li, P.K.C., Awdry, S. Evaluating the effective diffusivity of methane in the washcoat of a honeycomb monolith. Appl. Catal. B Environ. 25 (2000) 93–104.
[69] Talebian-Kiakalaieh, A., Amin, N.A.S. Theoretical and experimental evaluation of mass transfer limitation in gas phase dehydration of glycerol to acrolein over supported HSiW catalyst. J. Taiwan Inst. Chem. Eng. 59 (2016) 11–17.
[70] Kolitcheff, S., Jolimaitre, E., Hugon, A., et al. Tortuosity of mesoporous alumina catalyst supports: Influence of the pore network organization.

Microporous Mesoporous Mater 248 (2017) 91–98.
[71] Satterfield, C.N. Mass Transfer in Heterogeneous Catalysis. Massachusetts Institute of Technology Press, Cambridge (1970).
[72] Ertl, G., Knözinger, H., Weitkamp, J. Handbook of heterogeneous catalysis. VCH, Weinheim (1997).
[73] Incera Garrido, G., Patcas, F.C., Lang, S., Kraushaar-Czarnetzki, B. Mass transfer and pressure drop in ceramic foams: A description for different pore sizes and porosities. Chem. Eng. Sci. 63 (2008) 5202–5217.

# CHAPTER III

(*PAPER III*)

Rh/$CeO_2$ Thin Catalytic Layer Deposition on Alumina Foams:

Catalytic Performance and Controlling Regimes in Biogas

Reforming Processes

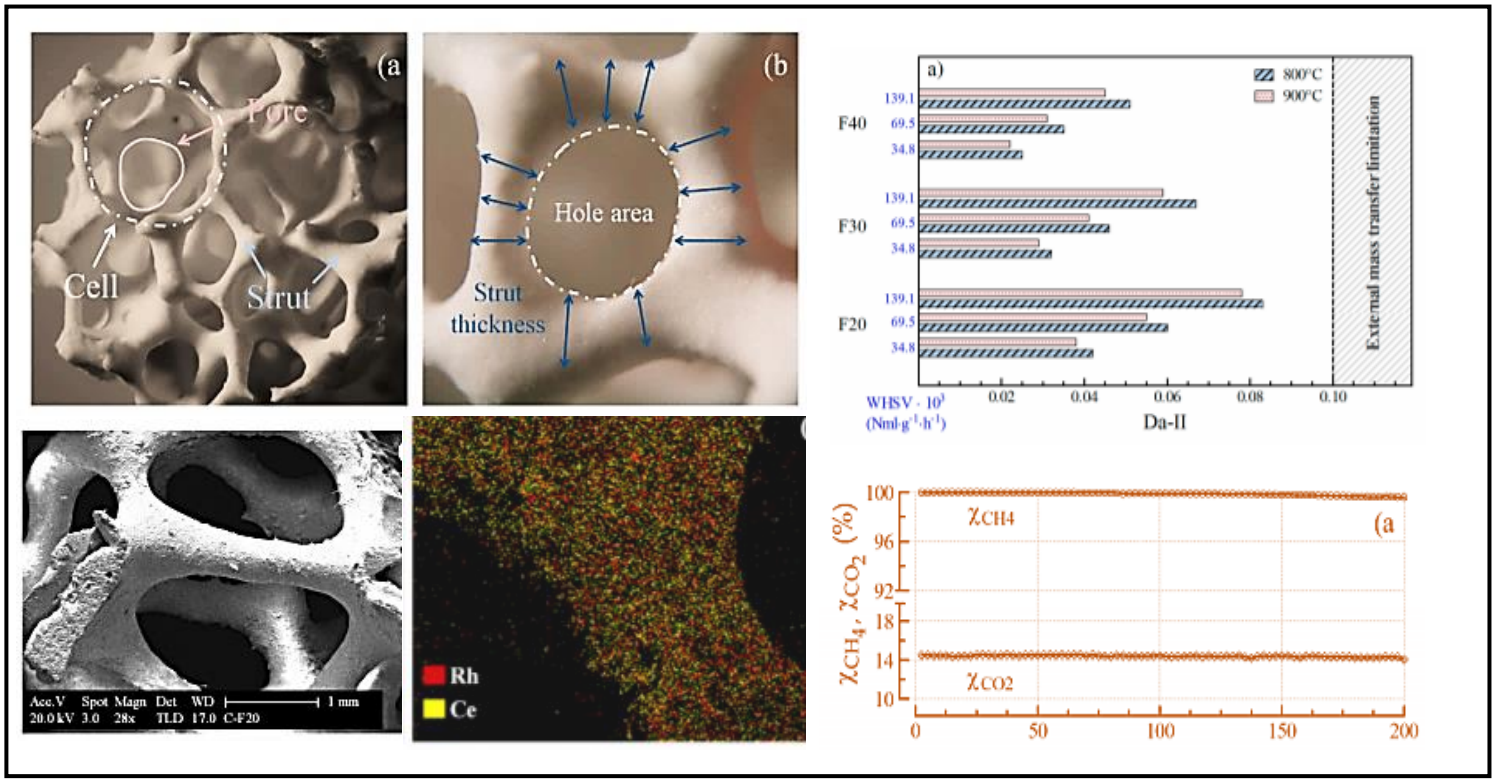


*Catalysts*, 8(10), pp. 1–25.

DOI: 10.3390/catal8100448

catalysts

MDPI

Article

# $Rh/CeO_2$ Thin Catalytic Layer Deposition on Alumina Foams: Catalytic Performance and Controlling Regimes in Biogas Reforming Processes

**Cristina Italiano [1,*], Muhammad Arsalan Ashraf [2], Lidia Pino [1], Carmen Williana Moncada Quintero [3], Stefania Specchia [1,3] and Antonio Vita [1]**

1 CNR-ITAE, Institute for Advanced Energy Technologies "Nicola Giordano", Via S. Lucia sopra Contesse 5, 98126 Messina, Italy; lidia.pino@itae.cnr.it (L.P.); stefania.specchia@polito.it (S.S.); antonio.vita@itae.cnr.it (A.V.)

2 Department of Chemical Engineering, University of Bath, Claverton Down Rd., Bath BA2 7AY, UK; m.a.ashraf@bath.ac.uk

3 Department of Applied Science and Technology, Politecnico di Torino, Corso Duca degli Abruzzi 24, 10129 Torino, Italy; carmen.moncada@polito.it

* Correspondence: cristina.italiano@itae.cnr.it; Tel.: +39-090-624-927

Received: 10 September 2018; Accepted: 8 October 2018; Published: 11 October 2018


**Abstract:** The application of ceramic foams as structured catalyst supports is clearly expanding due to faster mass/heat transfer and higher contact efficiency than honeycomb monoliths and, mainly, packed beds. In this paper, alumina open-cell foams (OCFs) with different pore density (20, 30 and 40 ppi) were coated with $Rh/CeO_2$ catalyst via a two steps synthesis method involving: (i) the solution combustion synthesis (SCS) to in-situ deposit the $CeO_2$ carrier and (ii) the wet impregnation (WI) of the Rh active phase. The catalytic coatings were characterized in terms of morphology and adhesion properties by SEM/EDX analysis and ultrasounds test. Permeability and form coefficient were derived from pressure drop data. Catalytic performance was evaluated towards biogas Steam Reforming (SR) and Oxy-Steam Reforming (OSR) processes at atmospheric pressure by varying temperature (800–900 °C) and space velocity (35,000–140,000 $NmL \cdot g^{-1} \cdot h^{-1}$). Characteristics time analysis and dimensionless numbers were calculated to identify the controlling regime. Stability tests were performed for both SR and OSR over 200 h of time-on-stream (TOS) through consecutive start-up and shut-down cycles. As a result, homogenous, thin and high-resistance catalytic layers were in situ deposited on foam struts. All structured catalysts showed high activity, following the order 20 ppi < 30 ppi ≈ 40 ppi. External interphase (gas-solid) and external diffusion can be improved by reducing the pore diameter of the OCF structures. Anderson criterion revealed the absence of internal heat transfer resistances, as well as Damköhler and Weisz-Prater numbers excluded any internal mass transfer controlling regime, mainly due to thin coating thickness provided by the SCS method. Good stability was observed over 200 h of TOS for both SR and OSR processes.

**Keywords:** open-cell foam; structured catalyst; solution combustion synthesis; steam and oxy-steam reforming; process intensification

## 1. Introduction

Bio-economy is a sustainable solution to meet the challenges of food security, resource scarcity, energy demand and climate change by efficient production of bio-resources and their conversion into food, bio-energy and biomaterials [1]. Process intensification (PI) is a promising strategy to develop more competitive and sustainable processes in a transition towards a bio-based economy. The innovative methodologies of PI are exploited to overcome limitations of conventional

processes and develop novel processes by implementing efficient technologies that is, novel reactors, materials, separation processes, bio-materials and bio-based process routes [2,3]. The most interesting technological approach in heterogeneous catalysis is the application of structured catalysts (e.g., monoliths and foams) which paves a way for more energy and resources through efficient chemical transformations [4,5]. Monolith- and foam-structured catalysts are widely used in environmental applications for controlling both automotive and stationary emissions [6]. Moreover, they are increasingly under development for many reaction applications, such as highly endothermic and exothermic reactions (hydrogenation, combustion or reforming processes) especially at low contact time [7,8].

Biogas plays a major role as a renewable energy source in the bio-economy domain according to the European Union policy [9,10]. Biogas is produced by anaerobic digestion of biomasses coming from different sources such as sewage, sludge, landfill, or industry [11]. Basically, it consists of 50–75% $CH_4$, 25–45% $CO_2$, 2–7% $H_2O$ (at 20–40 °C), 2% $N_2$, <1% $H_2$ with traces of $H_2S$, $O_2$, $NH_3$, halides and siloxanes [12,13]. The high levels of $CO_2$ and $CH_4$ enable the conversion of biogas to syngas (CO and $H_2$) by methane dry reforming (DR) reaction [14–16]:

$$CH_4 + CO_2 \rightarrow 2H_2 + 2CO \quad \Delta H^0_{298K} = +247\ \text{kJ·mol}^{-1} \tag{1}$$

The high operating temperatures needed to perform the endothermic DR reaction lead to active species sintering and coke formation [17]. Besides, DR is accompanied by several side reactions, among which the methane cracking reaction ($CH_4 \rightarrow C + 2H_2$, $\Delta H^0_{298K}$ = +75 kJ·mol$^{-1}$) and the Boudouard reaction ($2CO \rightarrow C + CO_2$, $\Delta H^0_{298K} = -173$ kJ·mol$^{-1}$) appear to be the most important [17,18]. The steam reforming (SR) of biogas is a combination of DR (Equation (1)) and methane SR (Equation (2)). The presence of steam reduces carbon formation by coke reforming reaction ($C + H_2O \rightarrow CO + H_2$, $\Delta H^0_{298K}$ = +131 kJ·mol$^{-1}$) and increases $H_2$ concentration in the product mixture by favouring the water gas shift (WGS) reaction ($CO + H_2O \rightarrow CO_2 + H_2$, $\Delta H^0_{298K} = -41$ kJ·mol$^{-1}$) [19].

$$CH_4 + H_2O \rightarrow 3H_2 + CO \quad \Delta H^0_{298K} = +206\ \text{kJ·mol}^{-1} \tag{2}$$

Moreover, in the oxy-steam reforming (OSR) of biogas, the presence of oxygen improves the energy efficiency of the process by exothermic methane partial/total oxidation reactions (Equations (3) and (4)), as well as favours coke oxidation ($C + O_2 \rightarrow CO_2$, $\Delta H^0_{298K} = -394$ kJ·mol$^{-1}$) [20,21].

$$CH_4 + O_2 \rightarrow 2H_2 + CO \quad \Delta H^0_{298K} = -36\ \text{kJ·mol}^{-1} \tag{3}$$

$$CH_4 + 2O_2 \rightarrow 2H_2O + CO_2 \quad \Delta H^0_{298K} = -802\ \text{kJ·mol}^{-1} \tag{4}$$

Biogas can be effectively transformed to syngas by reforming processes, with the aim to further upgrade it into bio-hydrogen, bio-fuels or chemicals. SR is a well-established conventional process for syngas production at industrial scale, which is usually carried out over Ni- and Ru-based pellet catalysts in tubular reactors [22,23], with severe heat and mass transport limitations [24]. As a toolbox of PI, structured catalysts provide a promising way to overcome these limitations thanks to enhanced heat and mass transfer coefficients, higher surface-to-volume ratio and lower pressure drop [25,26]. These characteristics enhance the catalytic performance of reforming reactions, allowing operation at high space velocity simultaneously reducing the amount of catalytic material [27,28]. Thus, the research interest in structured catalysts development is constantly growing [4,27,29–36].

Monolith-based catalysts have been tested successfully for reforming reactions with improved catalytic performance but limitations still exist due to the absence of radial mass and convective heat transfer in straight channels. On the other hand, the tortuous structure of ceramic open-cell foam (OCF) provides a fast radial heat and mass transport with higher contact efficiency [37,38]. Indeed, OCFs are macroporous reticulated three-dimensional (3D) structures in which the cells are connected by open windows, providing high porosity with 80–90% void space [39]. As an alternative

to conventional systems (pellets made of magnesium aluminate or calcium aluminate spinels), alumina OCFs are potential structured supports for reforming processes with proven mechanical, chemical and hydrothermal suitability for severe working conditions: high temperature (600–900 °C), high pressure (20–30 bar) and steam rich environment ($S/CH_4$ = 1.5–3.0) [40,41]. However, the catalytic functionalization of the foam structures still remains one of the main critical issues. In fact, the catalytic coated layer needs to be highly active and stable, as well as resistant to thermal and mechanical stresses occurring during reforming reactions [4,29,42]. The conventional washcoating technique suffers from non-uniformity and exfoliation of coatings, as well as binder contamination. Moreover, a proper use of the washcoating method implies the optimization of many parameters, such as pH, viscosity of the slurry, primers' and binders' utilization, speed of dipping and so forth. [7,30,43]. Recently, we proved that solution combustion synthesis (SCS) is a suitable procedure to in-situ deposit uniform, thin and high-strength catalytic layers on the surface of both ceramic monoliths [7,25,30–32] and foams [7,44]. The SCS method takes the advantage of an exothermic, very quick and self-sustaining chemical reaction between metal precursors and an organic fuel (i.e., urea), resulting in the synthesis of nanocrystalline oxide powders over the surface of structured supports [4,45–47].

In this paper, alumina OCFs with different pore density (20, 30 and 40 pore per square inch, ppi) were coated with $Rh/CeO_2$ catalyst by SCS. The coated structures were physically characterized by scanning electron microscopy with energy dispersive X-ray spectroscopy (SEM/EDX) and transmission electron microscopy (TEM) to analyse their morphological characteristics. The mechanical stability of the coating was analysed using ultrasound tests. The permeability and form coefficients were derived from pressure drop data. The catalytic performance was investigated towards biogas SR and OSR reactions, evaluating the effects of temperature and space velocity. Characteristics time analysis and dimensionless numbers were calculated to identify the reaction controlling regime. Stability tests were also performed as a function of time-on-stream (TOS).

## 2. Results

### *2.1. Characterization of Samples*

#### 2.1.1. Geometrical Properties of OCFs Structures

Figure 1 shows one of the three structures used in this work (30 ppi OCF), with the characteristic geometric parameters and pore diameter distribution. OCFs are composed of cell units which are repeated in all space dimensions; cells are the void part enclosed by struts and interconnected pores (Figure 1a). The measured hole area ($A$) and strut thickness ($t_s$) (Figure 1b) were averaged among at least 250 images of 15 different bare supports. Pore diameter ($d_p = \sqrt{\frac{4A}{\pi}}$) was calculated by considering the hole as an equivalent circle [48]. A broad pore diameter distribution ranging from 1.0 to 2.0 mm was evaluated, as shown in Figure 1c.

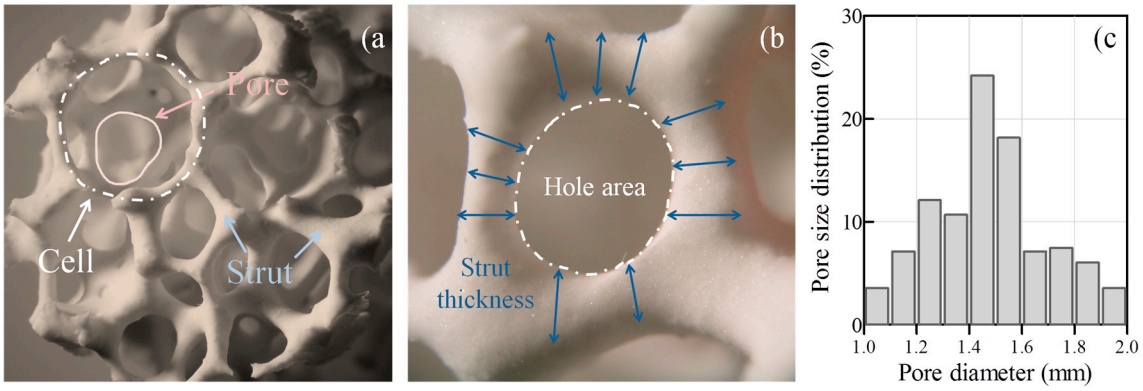


**Figure 1.** Geometric parameters (**a**,**b**) and pore diameter distribution (**c**) of 30 ppi alumina OCF structure.

Table 1 lists the geometrical properties of OCFs structures (20, 30 and 40 ppi) and the related equations. The voidage ($\varepsilon$) was calculated from the relative density ($\rho_r$) by the equation $\varepsilon = 1 - \left[2.59\left(\frac{t_s}{t_s+d_p}\right)^2\right]$ [49]. Bed porosity ($V_p$) was determined by helium pycnometry. The geometric surface area ($GSA$) was calculated according to the tetrakaidecahedron model reported by of Buciuman and Kraushaar-Czarnetzki [50].

**Table 1.** Geometrical characteristics of the investigated open cell foam (OCF) structures.

| **Structured Substrate** | **F20** | **F30** | **F40** |
|---|---|---|---|
| | 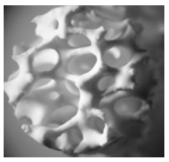 | 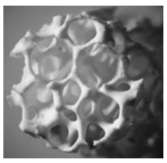 | 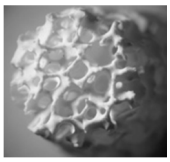 |
| Pore per inch, *ppi* | 20 | 30 | 40 |
| Diameter, $\phi$—Length, $L$ (mm) | 10–15 | 10–15 | 10–15 |
| Hole area, $A$ (mm$^2$) | 2.88 | 1.55 | 0.92 |
| Average pore diameter, $d_p$ (mm) $d_p = \sqrt{\frac{4A}{\pi}}$ | 1.92 | 1.40 | 1.08 |
| Average strut thickness, $t_s$ (mm) | 0.51 | 0.41 | 0.33 |
| Face diameter, $d_f$ (mm) $d_f = d_p + t_s$ | 2.42 | 1.81 | 1.41 |
| Relative density, $\rho_r$ $\rho_r = 2.59\left(\frac{t_s}{d_f}\right)^2$ | 0.11 | 0.13 | 0.14 |
| Voidage, $\varepsilon$ $\varepsilon = 1 - \rho_r$ | 0.89 | 0.87 | 0.86 |
| Bed porosity, $V_p$ (%) | 88.3 | 85.1 | 83.6 |
| Geometric surface area, $GSA$ (m$^2$·m$^{-3}$) $GSA = \frac{4.82}{d_f} \cdot \sqrt{\rho_r}$ | 669 | 967 | 1273 |
| Exposed surface area, $SA_{OCF}$ (mm$^2$) $SA_{OCF} = V_{OCF} \cdot GSA$ | 788 | 1138 | 1500 |
| Catalyst loading, $C_{load}$ (mg·cm$^{-2}$) $C_{load} = \frac{W_{cat}}{SA_{OCF}}$ | 22.2 | 15.2 | 12.0 |
| Catalytic layer thickness, $\delta_c$ (µm) | 25–40 | 15–30 | 5–20 |

### 2.1.2. Pressure Drop Measurements

Figure 2 shows the pressure drops of all OCFs structures measured at different superficial velocities, together with the theoretical estimations. As reported by several Authors [51–53], Forchheimer-extended Darcy equation is a valid model for describing the pressure drop in OCFs at fluid velocity higher than 0.1 m·s$^{-1}$. In the proposed model, the pressure drop per unit length ($\Delta P/L$) is expressed as a quadratic function of the inlet gas velocity ($u$) by the following equation:

$$\frac{\Delta P}{L} = au + bu^2 \quad (5)$$

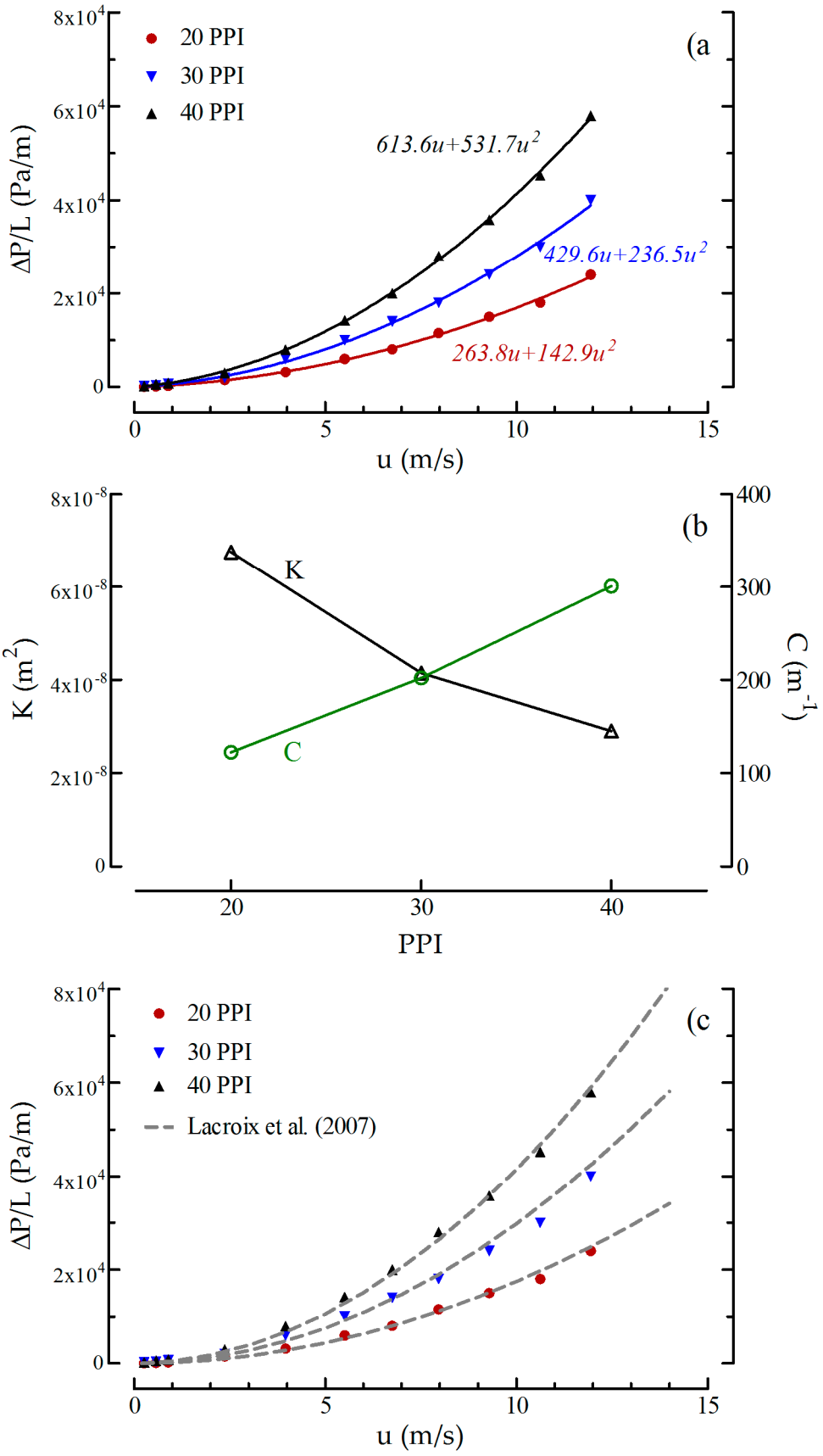


**Figure 2.** Pressure drop measurements for different foam density: Forchheimer-extended Darcy theoretical estimation (**a**); effect of pore density on the permeability and form coefficient (**b**); Lacroix-extended Ergun theoretical estimation (**c**).

The terms a and b represent the viscous drag and the inertial drag, respectively [48,54,55]. The first term ($a = \mu/K$) represents the linear dependence of pressure drop on flow velocity. It can be expressed as the ratio between the dynamic viscosity of the fluid ($\mu$) and the permeability of the foam ($K$). The second term ($b = \rho \cdot C$), representing the quadratic dependence of the pressure drop on flow velocity, can be determined from the product of fluid density ($\rho$) and the form coefficient of the foam ($C$) [53,54,56].

By fitting the measured pressure drop values as a quadratic function of the fluid velocity (Figure 2a), the two hydraulic properties of a porous medium, permeability ($K$) and form coefficient ($C$), were determined from a and b constants of the curve-fit, known the dynamic viscosity ($\mu_{N_2}$) = 1.78 × $10^{-5}$ Pa·s) and density ($\rho_{N_2}$) = 1.17 kg·$m^{-3}$) of $N_2$. Indeed, the permeability decreased by increasing the pore density from 6.7 × $10^{-8}$ (20 ppi OCF) to 2.9 × $10^{-8}$ $m^2$ (40 ppi OCF). An opposite trend was observed for the form coefficient, which increased from 122.1 to 300.6 $m^{-1}$ for 20 ppi and 40 ppi OCFs, respectively (Figure 2b). Similar results were reported by Wang and Guo [54], measuring the pressure drop of different foams as a function of the material porosity.

In the literature, several researchers adopted Ergun model to explain and fit the experimental data [57–59]:

$$\frac{\Delta P}{L} = E_1 \frac{\mu_{N_2}(1-\varepsilon)^2}{\varepsilon^3 d_p^2} u + E_2 \frac{\rho_{N_2}(1-\varepsilon)}{\varepsilon^3 d_p} u^2 \quad (6)$$

where the Ergun constants $E_1$ and $E_2$, depending on the nature of the porous media, ranged between 100 to 865 and 0.65 to 2.65, respectively [59]. In the work of Lacroix et al. [60], a simple analogy between the traditional spherical particle bed and the foam was proposed. Thus, the values of 150 and 1.75 for $E_1$ and $E_2$, respectively, were used for the estimation of the pressure drop in OCFs with different porosity. As shown in Figure 2c, the Ergun model is in good agreement with our experimental data. As expected, the measured pressure drop increased by decreasing the pore diameter and voidage (Table 1), following the order F20 < F30 < F40 structures.

#### 2.1.3. SEM/EDX Measurements

A homogeneous catalytic coating fully covering the OCFs was observed, without clogging of cells or pores (as highlighted in Figure 3a,b,d,e,g,h). The EDX mapping of the coated structured samples evidenced that ceria is well deposited on the alumina surface. Furthermore, rhodium seemed to be in turn well dispersed on the surface of ceria (Figure 3c,f,i). A homogeneous morphology of the catalytic layer was further evidenced in the cross-section view of the F40 system, highlighting a good interconnection between the foam and coated layer (Figure 4). Moreover, the catalyst particles penetrated into the porosity of the alumina foam, thus ensuring an optimal adhesion of the catalytic layer [61]. Indeed, a reduction of the macro-porosity of the alumina surface was observed after depositing the catalytic layer (see Figure S1 in Supplementary Materials).

In order to compare the catalytic behaviour of OCFs with different pore density, the same amount of catalyst (1.5 wt.% Rh immobilized over ~170 mg of ceria carrier) was deposited on each foam. The catalyst loading decreased from 22.2 to 12.0 mg·$cm^{-2}$ due to the increase of *GSA* from 669 (F20) to 1273 $m^2 \cdot m^{-3}$ (F40), as reported in Table 1. The higher the *GSA*, the thinner catalytic coated layer. Therefore, thickness values between 5–20 μm, 15–30 μm and 25–40 μm were determined for F40, F30 and F20 structures, respectively (Figure 5).

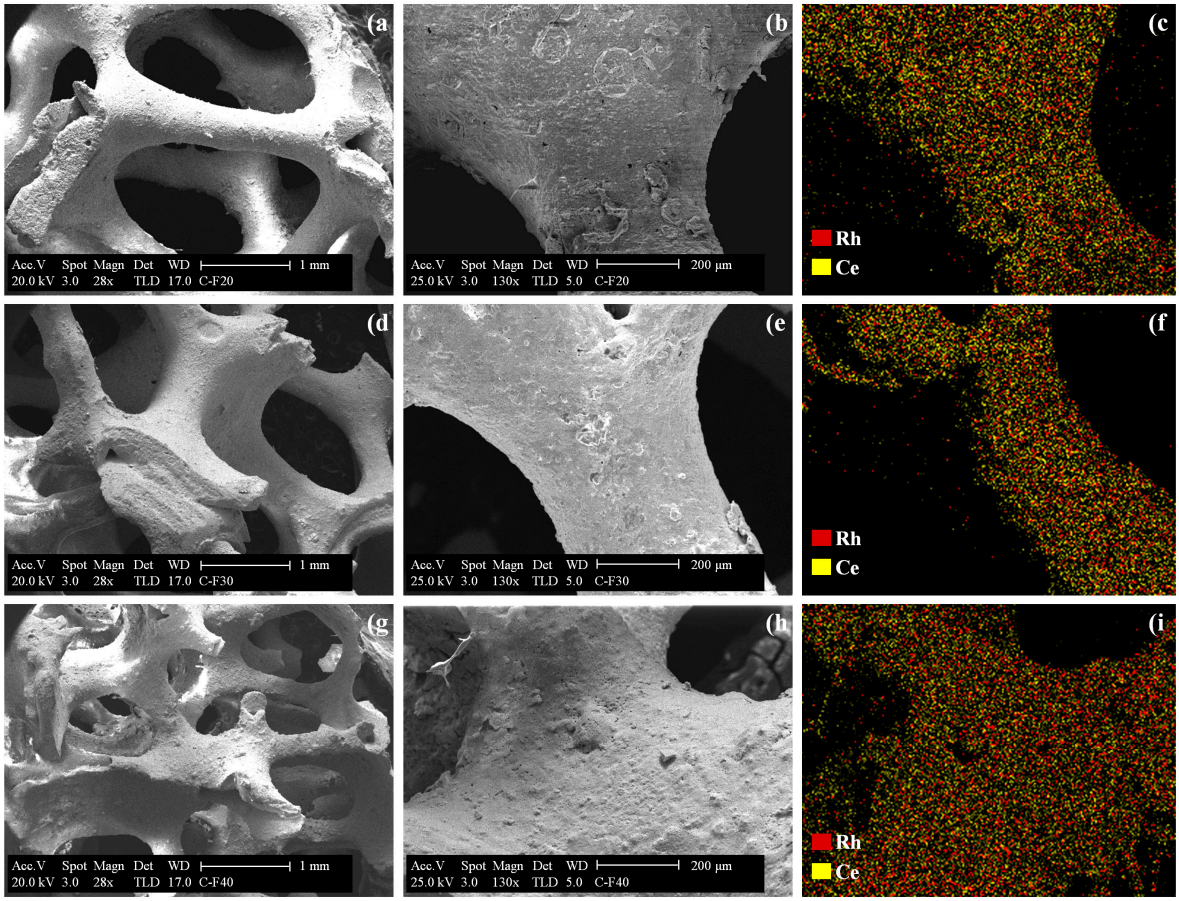


**Figure 3.** Scanning electron microscopy (SEM) micrographs at different magnification of the Rh/$CeO_2$-coated F20 (**a**,**b**), F30 (**d**,**e**) and F40 (**g**,**h**) structures and corresponding EDX mapping (**c**,**f**,**i**).

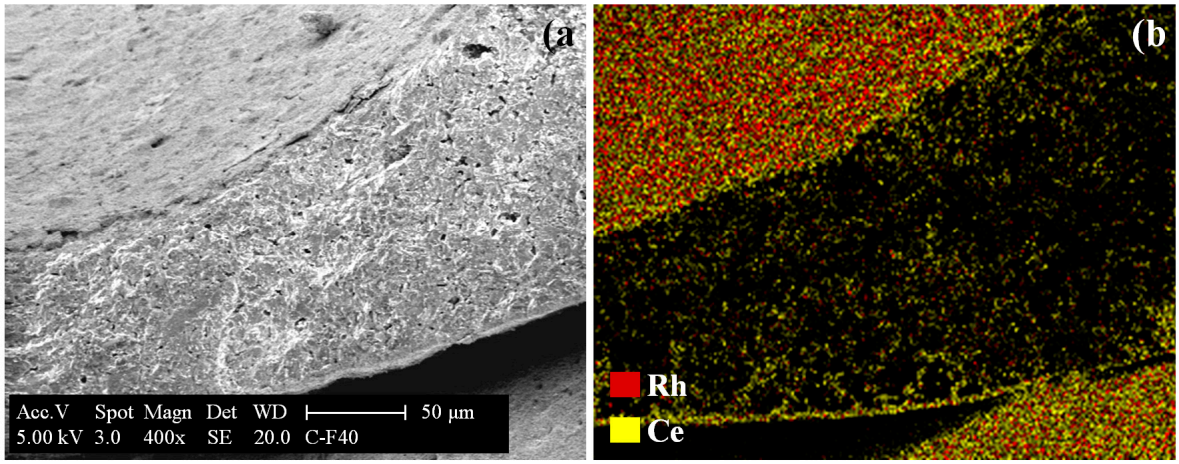


**Figure 4.** SEM micrographs of the Rh/$CeO_2$-coated F40 catalyst: cross section (**a**) and relative EDX mapping (**b**).

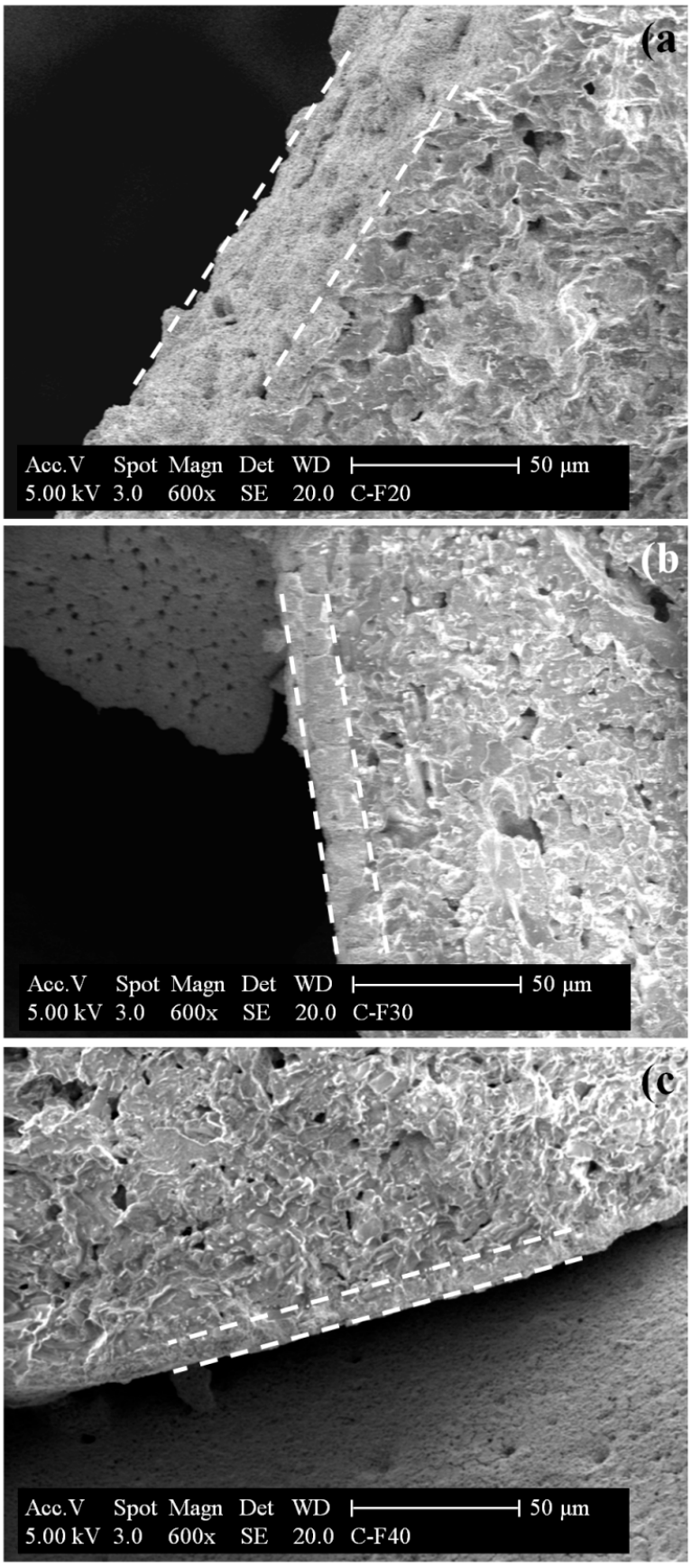


**Figure 5.** SEM images of 20 ppi (**a**), 30 ppi (**b**) and 40 ppi (**c**) coated layers.

### 2.1.4. Adhesion Measurements

The mechanical resistance of the coated layers onto the foam structures was evaluated by ultrasonic treatment in isopropyl alcohol solution. Figure 6 shows the weight loss of the coated F20, F30 and F40 structures after each stability cycle. In all cases, the adherence of the catalytic layer to the alumina support was very good, with weight losses lower than 5%, in agreement with the literature [7,30–32,44]. Therefore, SCS allowed overcoming the exfoliation of coatings usually encountered in conventional dip-coating techniques [7,39,62]. The good resistance of the coated layer to mechanical stress can be ascribed to the irregular porous surface of the support, which is beneficial to anchoring or interlocking the catalytic precursors (see Figure S1 in Supplementary Materials) [63]. The worst (but even good) stability was observed for the F20 OCF, probably due to the thicker catalyst layer compared to that of F30 and F40 structures (Figure 5). Similar results were previously reported by other Authors, suggesting that the pore density of the substrate influenced the adherence properties of the resulting systems [64,65]. An increase in pore density led to a decreased *GSA* and, in turn, increased thickness of the catalytic layer, hindering the adhesion of the coating due to the convex surface of the foam structures [65].

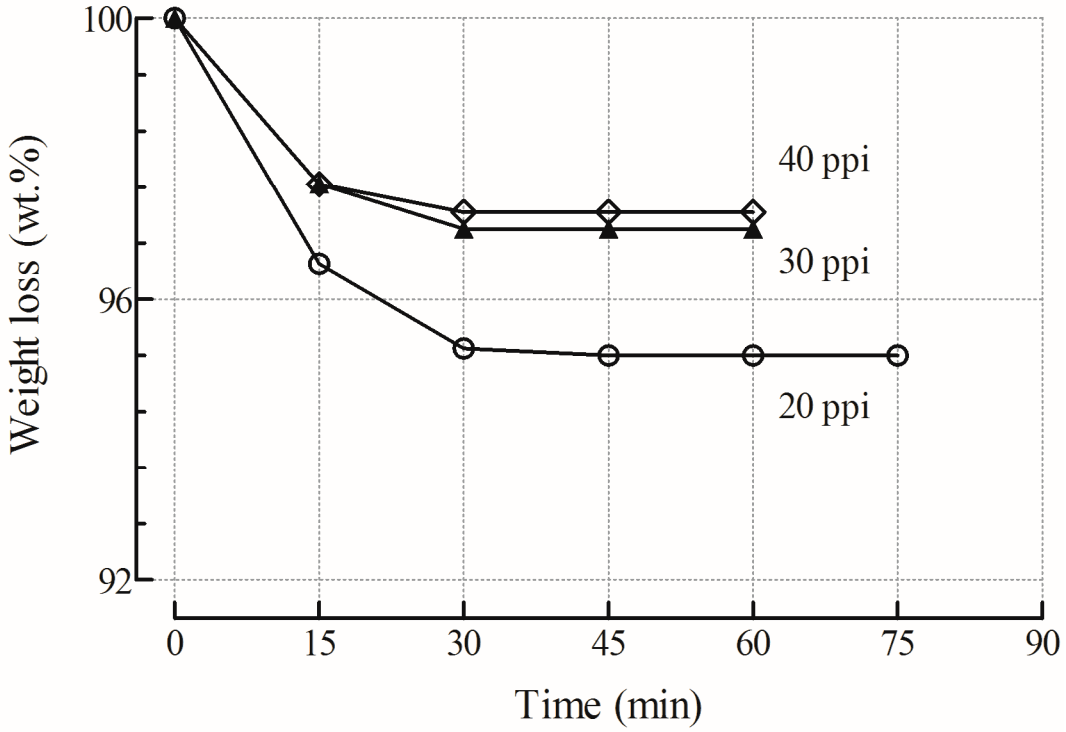


**Figure 6.** Weight loss as a function of time during the ultrasonic treatment of the coated foams.

### 2.1.5. TEM Measurements

The morphology of the $Rh/CeO_2$ catalytic layer was investigated by TEM analysis on the powder mechanically scraped from F40 alumina walls. TEM image in Figure 7 showed 40–70 nm $CeO_2$ particles in agglomerate form, with well distributed Rh particles, ranging between 2 and 7 nm. A similar morphology was previously observed for $Rh/CeO_2$ catalytic phase deposited on the inner walls of cordierite monoliths [30].

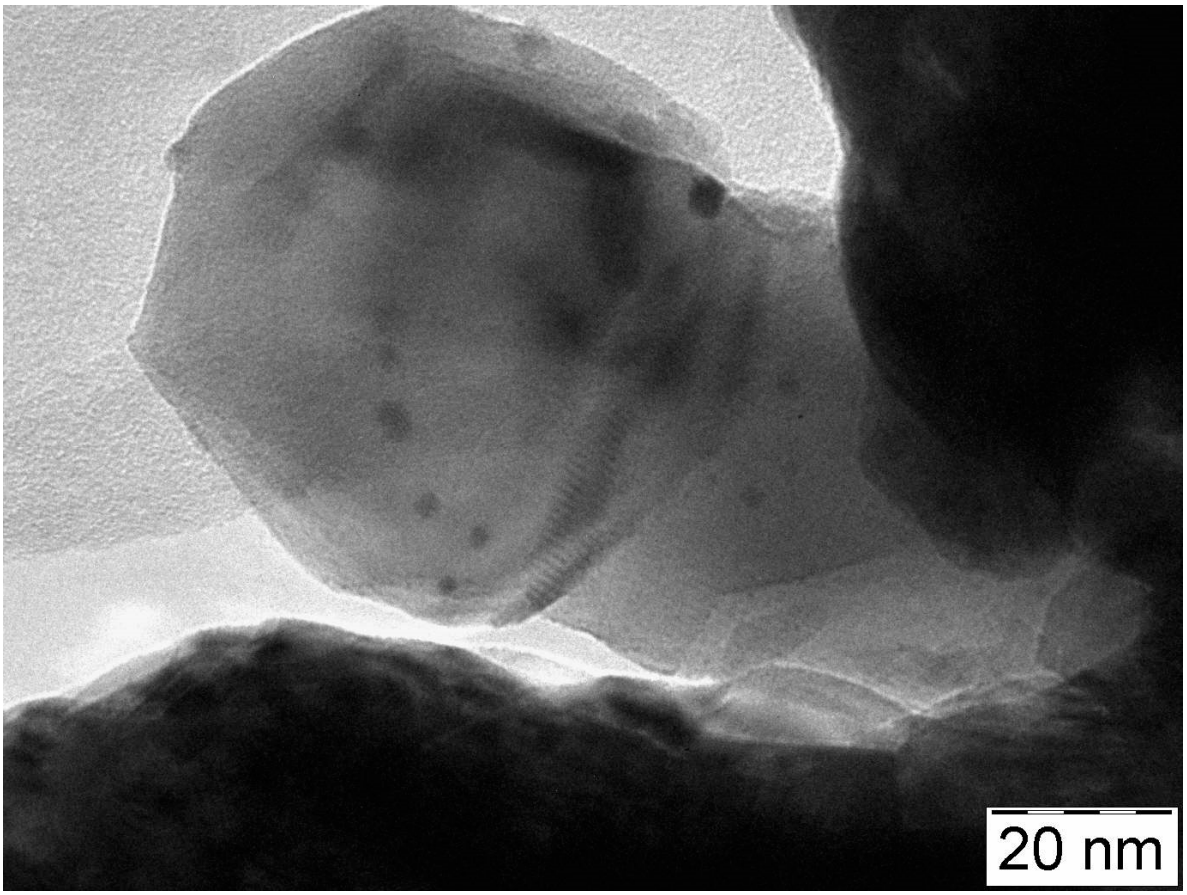


**Figure 7.** TEM images of the $Rh/CeO_2$ catalyst reduced at 300 °C under hydrogen flow and scraped from the foam walls.

### *2.2. Catalytic Tests towards Biogas Steam and Oxy-Steam Reforming*

#### 2.2.1. Evaluation of External Interphase (Gas-Solid) and Internal Heat Transfer Limitations

Due to the consumption of reactants and the production or consumption of heat, temperature profiles can develop around the catalytic coating and inside the catalyst particles [66]. The criterion proposed by Mears [67] was used to check the significance of external interphase (gas-solid) heat transport limitations:

$$\frac{E_a\ (-\Delta H_r^0)\ R_{CH_4}}{h\ GSA\ R\ T_b^2} < 0.15 \tag{7}$$

Tee values calculated ranged between 0.037–0.133 (F20), 0.022–0.079 (F30) and 0.013–0.050 (F40). Indeed, the criterion was satisfied and therefore interphase heat transport limitations can be ignored. However, it could be noticed that the gas-solid heat transfer resistance increased by the decreasing of *GSA*, following the order F20 > F30 > F40.

The temperature gradients inside the catalytic coating can be neglected since the Anderson criterion (Equation (8)) was satisfied [67,68]:

$$\frac{E_a\ (-\Delta H_r^0)\ r_{CH_4}\ \rho_c\ \delta_c^2}{\lambda_c\ R\ T^2} < 0.75 \tag{8}$$

The values calculated (0.0001–000067) were found to be much lower than 0.75, mainly due to the extremely thin coating layer, as evidenced in SEM images (Figures 4 and 5). A detailed explanation of the Mears and Anderson criteria is provided in the Supplementary Materials.

2.2.2. Evaluation of External and Internal Mass Transfer Limitations

The tortuous nature of the OCFs structures allows high contact efficiency between reactants and catalyst. However, mass transfer limitations can still occur with strong impact on the catalytic performance [69]. The catalytic reaction between reactant molecules and active sites, generally located inside the catalyst pores, takes place after the reactant molecules diffuse from gas phase to the catalyst surface (external diffusion) and through the pores of the coated layer (internal diffusion). Thus, three operating regimes, namely kinetic, external mass transfer and internal diffusion, can control the reforming processes. In addition, it is important to exclude any type of mass transfer limitation in order to improve the mixing and optimize the geometry of the reforming reactor [69,70].

As previously reported [31], the characteristic time analysis is widely used to investigate physical and chemical processes involved in structured catalysts. A detailed explanation of the calculations is provided in the Supplementary Materials. To describe the trade-off between reaction kinetic (reaction time scale) and convective transport flux (diffusion time scale) the first Damkohler (*Da-I*) number was introduced as the ratio between the residence time ($t_c$) and the characteristic reaction time ($t_r$):

$$Da - I = \frac{t_c}{t_r} > 1 \quad (9)$$

The *Da-I* numbers calculated (2.8–3.2) were found to be greater than 1 due to high voidage of alumina OCFs (0.86–0.89, as shown in Table 1), confirming that the reactant mixture had sufficient time to react over the catalyst within OCFs pores. High *Da-I* values showed the potential to increase space velocity even at values higher than 140,000 $NmL \cdot g^{-1} \cdot h^{-1}$. This condition is necessary to ensure high reforming performances of the catalysts under investigation, while the influence of the external and internal mass transfer limitations was investigated by calculating the second Damköhler (*Da-II*) and the third Damköhler (*Da-III*) numbers, respectively [42,71–73].

The dimensionless *Da-II* number relates the reaction rate to the external transport phenomena in the system. It can be calculated from a relation between the characteristic external mass transfer time ($t_{ext}$) and the characteristic reaction time ($t_r$):

$$Da - II = \frac{t_{ext}}{t_r} < 0.1 \quad (10)$$

If *Da-II* number is greater than 0.1, external mass transfer limitations become important in the system, allowing for a concentration gradient between the bulk gas and the outside surface of the coated layer [74,75]. Figures 8a and 9a show the calculated values for biogas SR and OSR experiments, respectively. In both cases, *Da-II* increased by increasing the space velocity or by decreasing the pore density, whereas it was not much affected by the temperature [75]. Moreover, *Da-II* number lower than 0.1 (0.02–0.08) revealed the absence of external diffusion limitations at all the investigated conditions. However, F20 catalyst showed *Da-II* numbers close to 0.1 (0.08) at 140,000 $NmL \cdot g^{-1} \cdot h^{-1}$, indicating that the reactants could not have enough time for mass transfer and reaction. The effect of external diffusion on the reforming activity was also estimated by the Carberry criterion for a first-order reaction with respect to methane [76,77]:

$$Ca = \frac{R_{CH_4}}{k_G \, GSA \, C_{CH_4}} < 0.05 \quad (11)$$

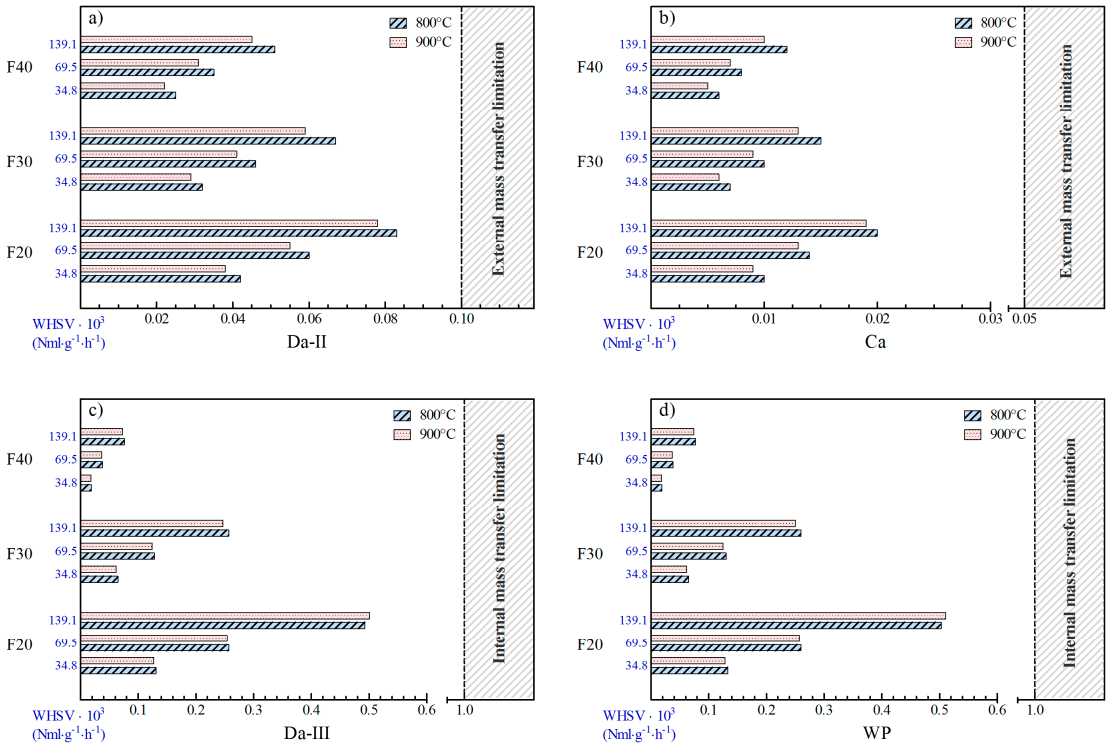


**Figure 8.** Influence of temperature and space velocity on (**a**) *Da-II*, (**b**) *Ca*, (**c**) *Da-III* and (**d**) *WP* dimensionless numbers on biogas SR experiments over F20, F30 and F40 catalysts.

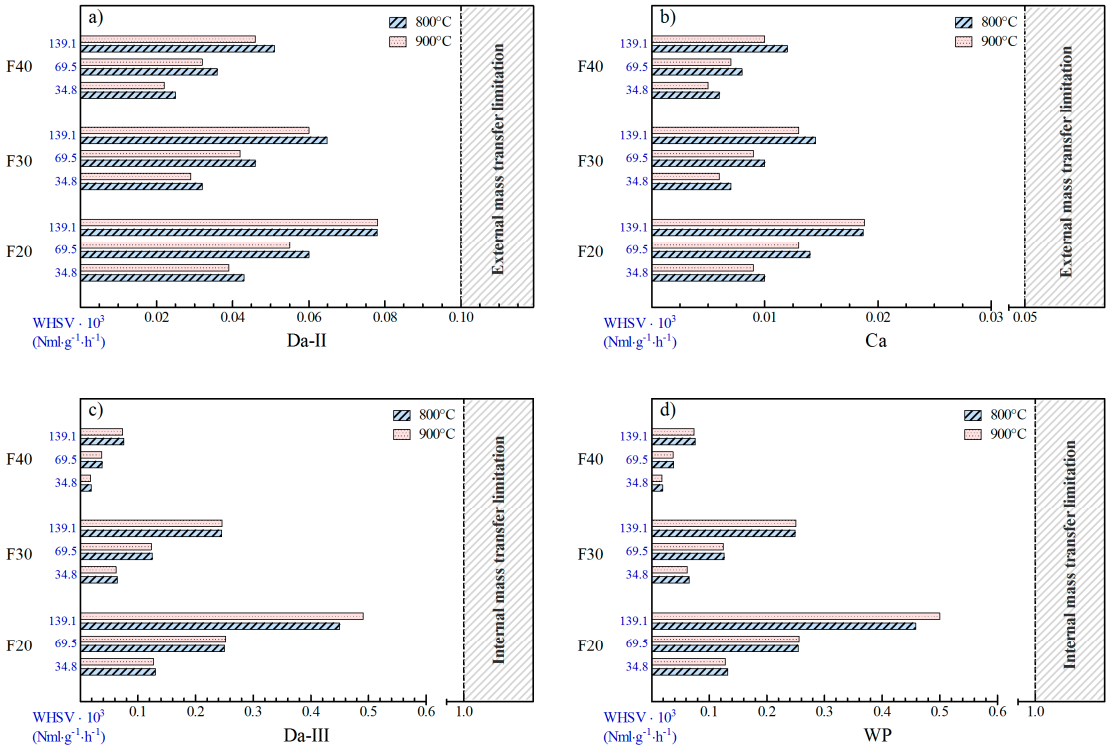


**Figure 9.** Influence of temperature and space velocity on (**a**) *Da-II*, (**b**) *Ca*, (**c**) *Da-III* and (**d**) *WP* dimensionless numbers on biogas OSR experiments over F20, F30 and F40 catalysts.

According to *Ca* numbers, the results showed that biogas SR (Figure 8b) and OSR (Figure 9b) experiments were not affected by external diffusion limitations, confirming the results obtained by

calculating *Da-II*. However, high pore density OCF (F40) with smaller pore diameter and higher geometric surface area (Table 1) emerged as the more adequate configuration.

The internal mass transfer limitations were investigated by calculating the third Damköhler number (*Da-III*) as the ratio between the characteristic coated layer diffusion time ($t_{int}$) and the characteristic reaction time ($t_r$):

$$Da - III = \frac{t_{int}}{t_r} < 1 \quad (12)$$

*Da-III* values (0.02–0.50) lower than 1 excluded any internal mass transfer controlling regime at all the investigated conditions (Figures 8c and 9c). Thus, reactants rapidly diffused through the pores of the coated layer, avoiding the formation of concentration gradients between the catalyst surface and active sites [78,79]. These results were also confirmed by using the Weisz-Prater criterion [25,31], as reported in Figure 8d (biogas SR) and Figure 9d (biogas OSR).

$$WP = \frac{r_{CH_4}\,\rho_c\,{\delta_c}^2}{D_{CH_4,e}\,C_{CH_4,s}} < 1 \quad (13)$$

The *WP* values calculated (0.02–0.50) highlighted the absence of any internal mass transfer limitation, mainly due to thin coating thickness provided by the SCS method (Figure 5).

#### 2.2.3. Influence of the Pore Density on Biogas SR and OSR Activity

Figure 10 shows the influence of temperature ($T_{SET}$ = 800–900 °C) and space velocity (WHSV = 35,000–140,000 NmL·g$^{-1}$·h$^{-1}$) on biogas SR activity in terms of $CH_4$ and $CO_2$ conversion and $H_2$/CO molar ratio. Thermodynamic data are also reported for comparison. The F20 structured catalyst showed almost total $CH_4$ conversion at 900 °C and 35,000 NmL·g$^{-1}$·h$^{-1}$ (Figure 10a), slightly decreasing afterwards to ca. 98% by increasing the space velocity up to 140,000 NmL·g$^{-1}$·h$^{-1}$. The same trend was observed for $CO_2$ conversion, which decreased from 16 to 10%, remaining slightly higher than the equilibrium value, due to the effect of the reverse WGS reaction [30,32,33]. This result led to $H_2$/CO ratios (2.60–2.73) slightly lower than the thermodynamic values (2.74). Both $CH_4$ and $CO_2$ conversions decreased by decreasing the temperature and increasing the space velocity (Figure 10a). Indeed, the F20 sample showed ca. 98% of $CH_4$ conversion at 800 °C and 35,000 NmL·g$^{-1}$·h$^{-1}$, which lowered to ca. 92% at 140,000 NmL·g$^{-1}$·h$^{-1}$, due to the decreased contact time between reactants and catalyst. Moreover, negative values of $CO_2$ conversion were revealed as the result of the competition between DR (Equation (1)), SR (Equation (2)) and WGS reactions [19,33,80]. Indeed, at high steam content (S/$CH_4$ = 3), $CH_4$ reacted preferentially with steam due to the more stable nature of $CO_2$, leading to a lower contribution of the DR reaction. Simultaneously, the greater contribution of the $CO_2$-producing WGS reaction led to a negative $CO_2$ conversion at 800 °C and 140,000 NmL·g$^{-1}$·h$^{-1}$ (Figure 10a). Similar trends were reported by Ashrafi et al. [81]; $CO_2$ conversion data ranged from ca. −27% to 10% were shown at S/$CH_4$ ratio of 2.71 in the temperature range of 600–900 °C [81]. The decrease in catalytic activity by increasing the space velocity was less pronounced as the pore density increased to 30 ppi (Figure 10b, F30) and 40 ppi (Figure 10c, F40). In fact, F30 and F40 catalysts showed almost total (<99%) and stable $CH_4$ conversion at all the investigated conditions.

Similarly, the pore density of OFCs affected the OSR activity. Figure 11 shows the influence of temperature ($T_{SET}$ = 800–900 °C) and space velocity (WHSV = 35,000–140,000 NmL·g$^{-1}$·h$^{-1}$) on biogas OSR activity for the three OCFs catalysts, along with the thermodynamic data, reported as dotted lines. At WHSV of 35,000 NmL·g$^{-1}$·h$^{-1}$, the experimental results were very close to the equilibrium calculations for all the structured catalysts. However, both $CH_4$ and $CO_2$ conversion decreased by increasing space velocity over the F20 system (Figure 11a), leading to an increase of the $H_2$/CO ratio [82,83]. As expected, a higher activity was observed by increasing the pore density to 30 and 40 ppi. At high temperature (900 °C), the F30 and F40 catalysts showed $CH_4$ (99.6%) and $CO_2$ (50.6%) conversion very close to the equilibrium at all the investigated space velocities. Instead, a slight

decrease of $CH_4$ conversion from ca. 99 to 95% was observed at 800 °C by increasing the space velocity up to 140,000 NmL·g$^{-1}$·h$^{-1}$ over the F30 system (Figure 11b). In these conditions, the F40 catalyst still showed high $CH_4$ conversion (ca. 98–99%), which slightly decreased to ca. 96% by further increasing the space velocity up to 140,000 NmL·g$^{-1}$·h$^{-1}$.

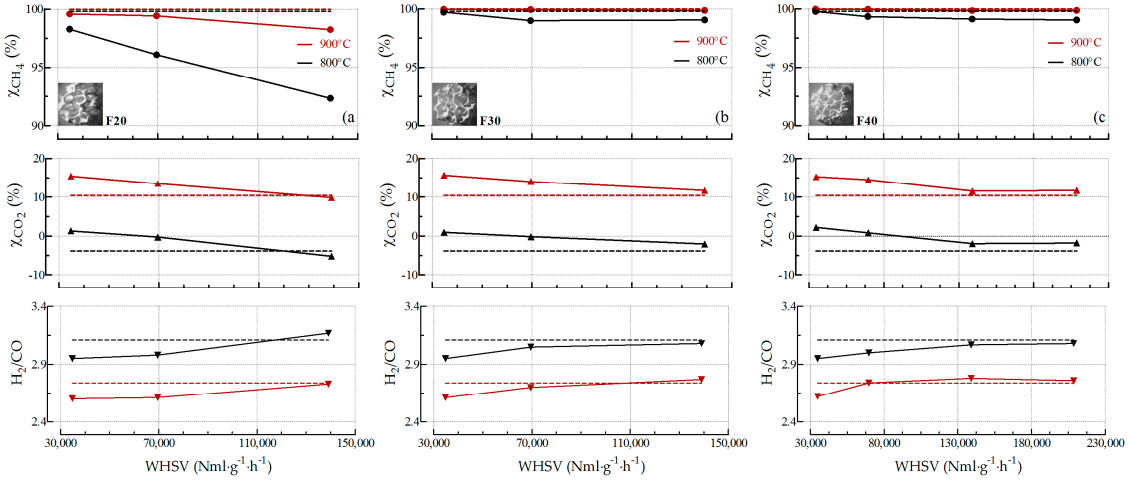


**Figure 10.** Biogas SR activity (S/$CH_4$ = 3) over F20 (**a**), F30 (**b**) and F40 (**c**) catalysts. Influence of temperature ($T_{SET}$ = 800–900 °C) and space velocity (WHSV = 35,000–140,000 NmL·g$^{-1}$·h$^{-1}$) on $CH_4$ conversion and $H_2$/CO molar ratio (thermodynamic data reported as dotted lines).

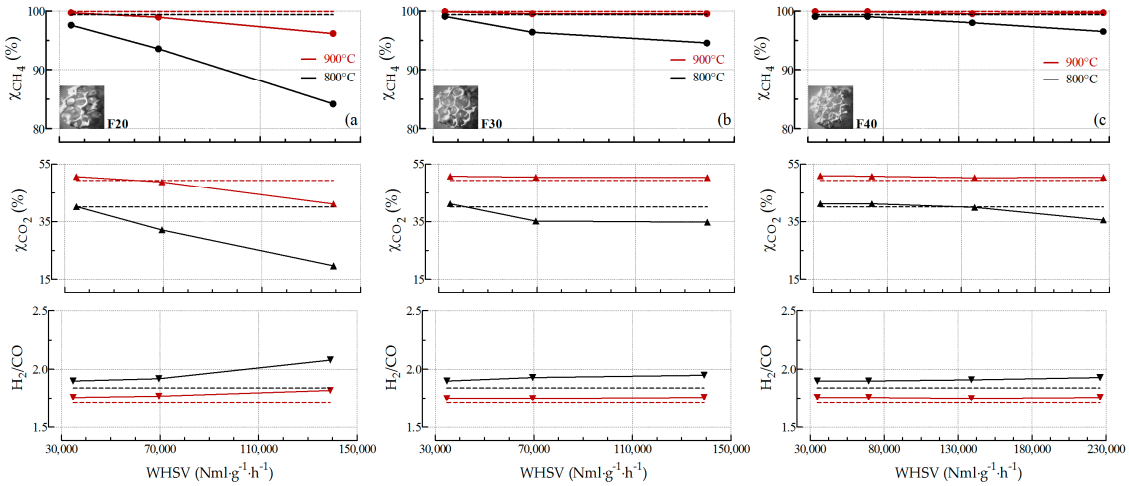


**Figure 11.** Biogas OSR activity (S/$CH_4$ = 1; $O_2$/$CH_4$ = 0.2) over F20 (**a**), F30 (**b**) and F40 (**c**) catalysts. Influence of temperature ($T_{SET}$ = 800–900 °C) and space velocity (WHSV = 35,000–140,000 NmL·g$^{-1}$·h$^{-1}$) on $CH_4$ conversion, $CO_2$ conversion and $H_2$/CO molar ratio (thermodynamic data reported as dotted lines).

### 2.2.4. Stability towards SR and OSR Processes

The stability evaluation is a noticeable issue in commercial application of heterogeneous structured catalysts [33,84]. Long-term tests were carried out over F40 catalyst at extreme operative conditions, such as $T_{SET}$ = 900 °C and GHSV = 70,000 NmL·g$^{-1}$·h$^{-1}$, with consecutive start-up and shut-down cycles. Figure 12 shows the results as $CH_4$ and $CO_2$ conversion and effluent composition over 200 h TOS for both SR (Figure 12a) and OSR (Figure 12b) experiments. Clearly, the F40 catalyst showed a steady performance, with negligible changes during the stability tests, indicating that the Rh/$CeO_2$ catalytic phase did not deactivate during TOS. Only a slight deactivation was observed for biogas SR

test after 150 h, probably due to a slight sintering of Rh active phase induced by the high reaction temperature, as previously reported [30].

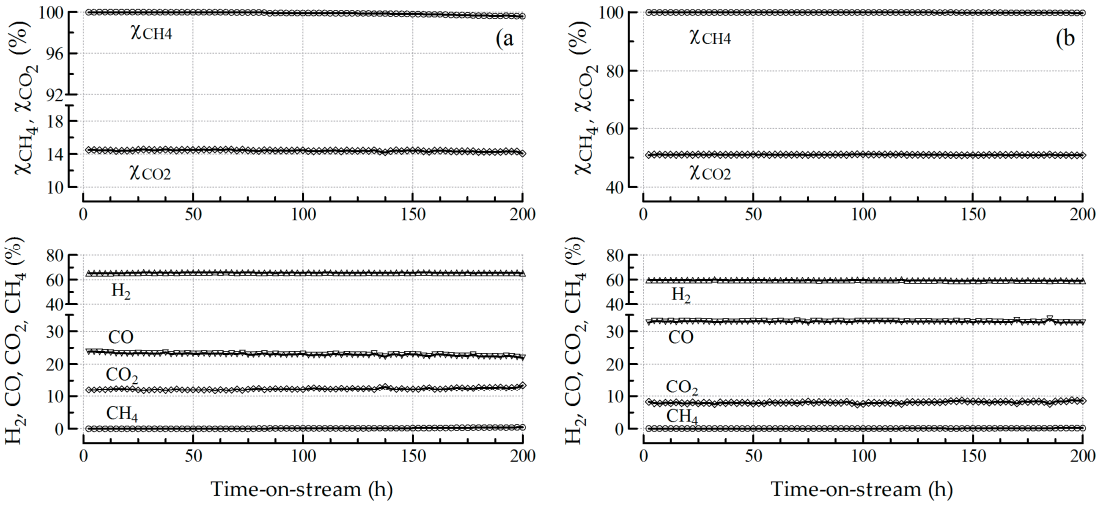


**Figure 12.** Biogas SR (**a**) and OSR (**b**) stability over F40 catalyst. $CH_4$ conversion, $CO_2$ conversion and effluent composition as a function of time-on-stream ($T_{SET}$ = 900 °C; WHSV = 70,000 NmL·g$^{-1}$·h$^{-1}$).

## 3. Discussion

The SR and OSR activity of OCFs coated with Rh/$CeO_2$ catalyst increased with pore density of the structures under investigation (Figures 10 and 11). As the number of catalyst active sites were fixed per unit volume of alumina foam by using the same catalyst loading (1.5 wt.% Rh immobilized over ~170 mg of ceria carrier), the observed catalytic performances indicated the importance of catalyst layer thickness and geometric characteristics. Indeed, activity results could be attributed first to the exposed surface area of the catalysts. In fact, the increase of *GSA* from 669 (F20) to 1273 m$^2$·m$^{-3}$ (F40) (Table 1) led to an increase in both SR and OSR activity following the order F20 < F30 ≈ F40. Moreover, a decrease in pore diameter resulted in improved heat and mass transport properties, as evidenced by the results of the previously discussed criteria.

Although the Mears criterion revealed the absence of external interphase (gas-solid) heat transport limitations, as well as Damköhler (*Da-II*) and Carberry numbers revealed the absence of external mass transfer limitations, the observed transport properties can play an important role in determining the catalytic performances. The values of these criteria decreased with increasing pore density, which indicated the enhancement in heat and mass transfer characteristics. It is well known that the fluid turbulence caused by tortuous flow path and radial convective flows is a major cause of gas-solid heat transfer improvement. Therefore, the increase in pressure drop values with pore density (Figure 3) led to higher turbulence and improved transport characteristics with potential reduction of reactor size. The higher values on the F20 catalyst estimated by Mears criterion were indicative of lower gas-solid heat transfer efficiency, contributing to the lower catalytic activity of F20 catalyst as compared to F30 and F40 systems. Similarly, the high external mass transfer resistance (Figures 8 and 9) of F20 catalyst allowed for a concentration gradient between the bulk gas and catalyst surface, leading to a drop in reactants conversion (Figures 10a and 11a) while almost stable activity was observed for F30 and F40 catalysts, due to their improved transport properties, as confirmed by *Da-II* and Carberry numbers. Mbodji et al. [85] reported comparable results on methane SR in a millistructured reactor. In their study, external mass transfer limitations appeared on a highly active catalyst at high temperature and large hydraulic diameter (< 1 mm). Arzamendi et al. [86] showed that in the case of Rh-based catalyst, it was needed to decrease the hydraulic diameter below 0.4 mm to eliminate external mass transfer limitations for process intensification. In addition, the lower porosity and pores size of the 40 ppi

system led to higher pressure drop (Figure 2) and increased residence time of reactants, thus resulting as the more adequate configuration for hydrogen production [87].

As reported by several Authors [88–91], the thickness of the coated layer strongly affects both the heat and reactants diffusion through the catalyst pores. Indeed, the resistance to internal diffusion increased with increasing the coating thickness, leading to higher Anderson criterion values (heat transfer limitations), as well as higher *Da-III* and W-P numbers (mass transfer limitations) [31,38,69,79]. In this regard, a thicker catalyst layer (such as > 100–150 μm) still remains a major issue of the systems prepared by conventional washcoating technique [62,92,93]. If the washcoat is thin and well anchored, all the active sites are accessible to reagents but the amount of catalyst could be not sufficient to process the inflowing reactants, decreasing $CH_4$ and $CO_2$ conversions. On the other side, the greater the amount of catalyst, the thicker washcoated layer, resulting in internal transfer limitations. Thus, high reactor throughput requires an excellent control of the catalyst layer thickness, that need to be sufficient (to ensure high $H_2$ yield) and sufficiently thin (to guarantee the absence of internal limitation) [91,94], as demonstrated also for other catalytic reactions [95]. As most interesting conclusion, the SCS method allowed the in-situ deposition of very thin (5–40 μm) catalytic layers (Table 1), avoiding internal heat and mass transfer limitations and positively affecting the performance towards biogas reforming processes. Moreover, this resulted in increased volumetric catalyst productivity for high reactor throughput with increasing in pore density while operating in kinetic control regime.

## 4. Experimental Section

### *4.1. Chemicals and Foams*

Technical grade cerium nitrate ($Ce(NO_3)_3{\cdot}3H_2O$), rhodium nitrate ($Rh(NO_3)_3{\cdot}nH_2O$), urea ($CH_4N_2O$), isopropyl alcohol ($C_3H_8O$) and acetone ($C_3H_6O$) were purchased from Sigma-Aldrich (St. Louis, MO, USA). All aqueous solutions were prepared using ultrapure water (Millipore Milli-Q system with resistivity > 18 MΩ cm). High purity (99.999 vol%) $CH_4$, $CO_2$, $H_2$, $N_2$ and $O_2$ gases were supplied in cylinders by Rivoira S.p.A. (Milan, Italy). Alumina-based ceramic OCFs with pore density of 20, 30 and 40 ppi were purchased from Lanik S.r.o. (Czech Republic).

### *4.2. Catalysts Preparation*

Cylindrical OCFs (10 mm diameter, 15 mm length) were sonicated in water/acetone (50/50 vol.%) mixture for 30 min and dried at 120 °C for 2 h. The structured catalysts were prepared in two subsequent steps: (i) SCS procedure to in-situ deposit the $CeO_2$ carrier and (ii) WI of the Rh active phase.

Briefly, the OCFs were dipped in an aqueous solution containing cerium nitrate as precursor and urea as fuel, then introduced into a muffle furnace preheated at 600 °C for ca. 10 min to initiate the combustion reaction and rapidly cooled down to room temperature in few minutes. The process was repeated for 4–6 times to deposit ca. 170 mg of $CeO_2$ carrier [25,30,32,46,47]. Figure 13 shows the loaded $CeO_2$ carrier versus the number of immersion cycles for different substrates. 4 cycles were needed for 40 ppi OCF due to its relatively high *GSA* (Table 1), while 6 cycles were required to deposit approximately the same $CeO_2$ loading (170 mg) on 20 ppi OCF.

Then, the 1.5 wt.% Rh active phase was deposited by WI technique. The coated structures were dipped in an aqueous solution of rhodium precursor, calculated based on the deposited $CeO_2$ carrier. After each immersion, the structures were dried at 120 °C for ca. 10 min. Afterwards, the coated OCFs were calcined at 800 °C in static air for 2 h.

The analysis of the diffraction pattern of coated OCF showed the characteristic peaks of both cubic $CeO_2$ fluorite and α-$Al_2O_3$ phase, while no diffraction peaks of Rh oxides were detected, due to the low loading and high dispersion of the noble metal (see Figure S2 in Supplementary Materials) [96–99].

The calculated catalyst loading, as amount of $Rh/CeO_2$ catalyst per exposed surface area of the foam structure, followed the order 40 ppi OCF (12.0 $mg{\cdot}cm^{-2}$) < 30 ppi OCF (15.2 $mg{\cdot}cm^{-2}$) < 20 ppi OCF (22.2 $mg{\cdot}cm^{-2}$) (Table 1).

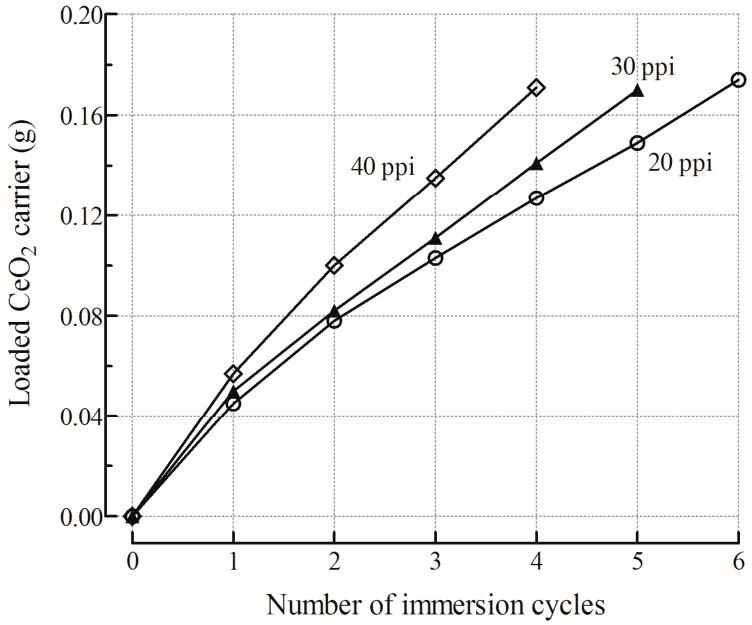


**Figure 13.** Evolution of the loaded $CeO_2$ carrier after sequential immersion cycles of the different OCFs.

### *4.3. Physicochemical Characterization*

All OCFs were scanned with Nikon SMZ1500 Stereoscope (Nikon Cooperation, Tokyo, Japan) and the images processed by ImageJ software (NIH, Bethesda, MD, USA) to measure characteristic geometric dimensions.

OCFs porosity was determined by helium pycnometry using a Micromeritics 1305 Multivolume Pycnometer (Norcross, GA, USA).

X-ray diffraction (XRD) patterns were recorded by a Philips X-Pert 3710 diffractometer (Almelo, the Netherlands) with a scanning speed of $1.50° \cdot min^{-1}$ over the range $2\theta = 20°–75°$. The diffractometer was equipped with a Cu Kα radiation source, operating at 40 kV and 20 mA. The coated OCF was finely ground before the measurements. The peaks were assigned according to the PCPFWIN database. The $CeO_2$ crystallite size was calculated by the Scherrer equation based on the $CeO_2$ (111) reflection peak.

$N_2$ adsorption-desorption was carried out at liquid nitrogen temperature (196 °C) with a Micromeritics ASAP 2020 instrument (Micrometrics Inc., Norcross, GA, USA) to measure the Brunauer-Emmett-Teller (BET) specific surface area Barrett-Joyner-Halenda (BJH) pore volume. The samples were degassed by heating at 300 °C under vacuum for 6 h before the measurement.

A U-tube manometer connected to the reactor containing the OCFs was used to measure the pressure drop at different superficial velocities. $N_2$ flow was supplied at ambient temperature by a mass flow-meter (Brooks Instrument, Hatfield, PA, USA) and measured by a digital flow-meter (Agilent ADM 2000, Santa Clara, CA, USA). The height difference between the two columns of water in the two branches of the U-tube manometer was converted into pressure drop via the Stevin's law $\left(\Delta z = \frac{\Delta P}{g \cdot \rho_{H_2O}}\right)$ [7].

The coating procedure was evaluated in terms of homogeneity of the coating, amount of catalyst deposited and adhesion force. SEM/EDX images were collected by using a Philips XL-30 FEG ESEM (FEI-Phillips, Hillsboro, OR, USA) in order to analyse the morphological characteristics of the coatings deposited onto the structures. The structured samples were cut longitudinally to evaluate the thickness of the catalytic layer. At least 30 images for each OCF were collected. The adherence of the coating layer was evaluated in terms of weight loss after ultrasonic treatment in 50 vol.% isopropyl alcohol solution. The coated OCFs were treated for 15 min at 45 kHz and 130 W using the USC 900D ultrasonic

bath and dried for 1 h at 120 °C. The sequence was repeated several times until the weight loss stayed stable. The weight loss percentage was referred to the catalytic layer deposited.

TEM micrographs were obtained using a Philips CM12 instrument (FEI-Phillips, Hillsboro, OR, USA). The reduced coating layer was scraped from the OCF walls, dispersed in isopropyl alcohol by ultrasonic treatment and placed on holey copper grids.

### *4.4. Catalytic Tests*

A detailed description of the experimental setup is provided in our previous publications [25,30,32,46,47]. Biogas SR and OSR experiments were carried out at atmospheric pressure in a quartz fixed-bed reactor. The structured catalysts were placed at the centre of the reactor and inserted into a furnace equipped with a PID temperature controller. A simulated biogas ($CH_4$:$CO_2$ = 60:40 *v*/*v*) was used for the investigations. SR experiments were carried out at fixed steam-to-methane molar ratio ($S/CH_4$ = 3), varying temperature ($T_{SET}$ = 800–900 °C) and space velocity (WHSV = 35,000–140,000 $NmL \cdot g^{-1} \cdot h^{-1}$, defined as hourly volume of the gaseous feed per gram of catalytic layer). Similarly, OSR experiments were carried out at fixed $S/CH_4$ = 1 and oxygen-to-methane molar ratio ($O_2/CH_4$ = 0.2). Activity tests were conducted for 6 h and repeated three times to verify the repeatability. Catalyst stability was investigated over 200 h of TOS through consecutive start-up and shut-down cycles as accelerated stress test. Before the catalytic tests, the structured catalysts were reduced in-situ with a flow of $H_2/N_2$ (50/50 vol.%, 30 $Nml \cdot min^{-1}$) at 300 °C for 1 h. Mass flow controllers (Brooks Instrument Smart Mass Flow, Hatfield, PA, USA) were used to measure and control the flow of gaseous reactants. Steam was fed using an isocratic pump (Agilent 1100 Series) and an evaporator. The composition of reagents and products was determined using an on-line gas chromatograph (Agilent 6890 Plus) equipped with thermal conductivity (TCD) and flame ionization (FID) detectors. The results are reported in terms of $CH_4$ conversion ($\chi_{CH_4}$), $CO_2$ conversion ($\chi_{CO_2}$) and hydrogen-to-carbon monoxide ratio ($H_2/CO$) in reaction products. Chemical composition in thermochemical equilibrium was calculated with HSC Chemistry 7.1® calculation software (Outotec Oyj Technologies, Espoo, Finland), using the Gibbs free-energy minimization method.

## 5. Conclusions

As potential structured catalytic supports, alumina open-cell foams (OCFs) with different pore density (20, 30 and 40 ppi) were investigated towards biogas steam reforming (SR) and oxidative steam reforming (OSR) processes for syngas production. Catalytic alumina OCFs were synthesized with a thin and uniform $Rh/CeO_2$ catalyst layer by coupling: (i) solution combustion synthesis (SCS) to in-situ deposit the $CeO_2$ carrier and (ii) wet impregnation (WI) of the Rh active phase. Various physico-chemical characterization techniques were utilized to determine geometric and catalytic characteristics of bare and coated foams. Then, the catalytic performance of coated foams was evaluated at atmospheric pressure by varying temperature (800–900 °C) and space velocity (35,000–140,000 $NmL \cdot g^{-1} \cdot h^{-1}$). Characteristic time analysis and dimensionless numbers were calculated to assess the prevalence of the kinetic regime on mass and heat transfer limitations. OCFs showed a variation in pore size with increasing pore density which further influenced the other geometric and catalytic characteristics. The results of characterization techniques (XRD, SEM/EDX and TEM) highlighted the non-dependence of physico-chemical characteristics of coated catalysts on the geometry of the OCFs, with the exception of the catalyst layer thickness. Ultrasound adherence tests confirmed the excellent mechanical resistance of the coated layers, with weight losses lower than 5%. The structured catalysts showed outstanding results in biogas SR and OSR, following the activity order 20 ppi < 30 ppi ≈ 40 ppi, mainly due to the increased geometric surface area, heat and mass transfer properties. No internal and external heat and mass transport limitations were observed as evaluated by different criteria. A very homogeneous and thin (ranging from 5 to 40 μm with increasing the pore density) catalytic coated layer was successfully deposited by using the SCS technique which resulted in negligible internal heat

and mass transport limitations and excellent catalytic performance. The decrease in pore size of the alumina OCF resulted in higher pressure drop and fluid turbulence, leading to improved gas-solid transport characteristics and catalytic performances with potential reduction of reactor size. A stable catalytic activity of F40 structured catalyst was observed over 200 h of TOS for both biogas SR and OSR processes.

**Supplementary Materials:** The following are available online at http://www.mdpi.com/2073-4344/8/10/448/s1, Figure S1. SEM micrographs of bare (a,c,e) and Rh/$CeO_2$-coated (b,d,f) OCFs: F20 (a,b), F30 (c,d) and F40 (e,f) structures (inset: images of the macroscopic bare OFCs), Figure S2. XRD pattern of Rh/$CeO_2$ as a powder, bare and Rh/$CeO_2$-coated F30 (included also reference peaks of $CeO_2$: JPDS 4-593 and reference peaks of $Al_2O_3$: JPDS 10-0173).

**Author Contributions:** All Authors have written the manuscript. C.I. has prepared the samples and performed the catalytic tests. C.I. and A.V. performed XRD, BET and SEM analysis. M.A.A. and S.S. determined geometric properties and pressure drops. M.A.A., C.I. and C.W.M.Q. performed the calculations. A.V., L.P. and S.S. coordinated the research activities.

**Funding:** This research was funded by the Italian Ministry of Education, University and Research (MIUR).

**Acknowledgments:** This work was financially supported by the Italian Ministry of Education, University and Research (MIUR, Progetti di Ricerca Scientifica di Rilevante Interesse Nazionale 2010–2011) within the project: "Intensification of catalytic processes for clean energy, low-emission transport and sustainable chemistry using open-cell FOAMS as novel advanced structured materials" (IFOAMS, protocol no. 2010XFT2BB).

**Conflicts of Interest:** The authors declare no conflict of interest.

## Nomenclature

| | | |
|---|---|---|
| ***OCFs properties*** | $d_p$ | Average pore diameter (m) |
| | $d_f$ | Average face diameter (m) |
| | $GSA$ | Geometric surface area ($m^2 \cdot m^{-3}$) |
| | $L$ | Length (m) |
| | OFA | Open frontal area ($m^2$) |
| | $\varepsilon$ | Voidage |
| | $\phi$ | Diameter (m) |
| ***Coated layer properties*** | $d_{p,c}$ | Average coated pore diameter (m) |
| | $d_{f,c}$ | Average coated face diameter (m) |
| | $r_p$ | Pore radius (m) |
| | $\delta_c$ | Coated layer thickness (m) |
| | $\varepsilon_c$ | Coated layer porosity |
| | $\lambda_c$ | Coated layer effective thermal conductivity ($kW \cdot m^{-1} \cdot K^{-1}$) |
| | $\rho_c$ | Coated layer density ($kg \cdot m^{-3}$) |
| | $\tau$ | Tortuosity factor |
| ***Reaction data*** | $E_a$ | Apparent activation energy ($J \cdot mol^{-1}$) |
| | $F_{tot}$ | Total gas flow rate ($m^3 \cdot s^{-1}$) |
| | $P$ | Reaction pressure (kPa) |
| | $T$ | Reaction temperature (K) |
| | $T_b$ | Bulk fluid temperature (K) |
| | $T_{IN}$ | Inlet bed temperature (K) |
| | $T_{OUT}$ | Outlet bed temperature (K) |
| | $\boldsymbol{r_{CH_4}}$ | Reaction rate for $CH_4$ ($kmol \cdot kg^{-1} \cdot s^{-1}$) |
| | $\boldsymbol{R_{CH_4}}$ | Volumetric reaction rate for $CH_4$ ($kmol \cdot m^{-3} \cdot s^{-1}$) |
| | $\Delta \boldsymbol{H_r^0}$ | Standard reaction enthalpy ($J \cdot mol^{-1}$) |

| | | |
|---|---|---|
| ***Dimensionless Numbers*** | $Ca$ | Carberry number |
| | $E_1$ | Ergun Constant |
| | $E_2$ | Ergun Constant |
| | $Nu$ | Nusselt number |
| | $Re$ | Reynold number |
| | $Sc$ | Schmidt number |
| | $Sh$ | Sherwood number |
| | $WP$ | Weisz-Prater number |
| ***Fluid Properties*** | $\boldsymbol{C_{CH_4}}$ | Methane concentration in feed mixture (kmol·m$^{-3}$) |
| | $\boldsymbol{C_{CH_{4,s}}}$ | Methane concentration at catalyst surface (kmol·m$^{-3}$) |
| | $\boldsymbol{D_{CH_4}}$ | Diffusivity of $CH_4$ in gas phase (m$^2$·s$^{-1}$) |
| | $\boldsymbol{D_{CH_{4,e}}}$ | Effective diffusivity of $CH_4$ in coated layer (m$^2$·s$^{-1}$) |
| | $\boldsymbol{D_{CH_4-i}}$ | Binary diffusion of $CH_4$ and $i$ gas species (m$^2$·s$^{-1}$) |
| | $D_k$ | Knudsen diffusion (m$^2$·s$^{-1}$) |
| | $h$ | Gas-solid heat transfer coefficient (kW·m$^{-2}$·K$^{-1}$) |
| | $k_G$ | Mass transfer coefficient of $CH_4$ (m·s$^{-1}$) |
| | $\boldsymbol{M_{CH_4}}$ | Molecular weight of $CH_4$ (kg·kmol$^{-1}$) |
| | $M_i$ | Molecular weight of $i$ compound (kg·kmol$^{-1}$) |
| | $M_j$ | Molecular weight of $j$ compound (kg·kmol$^{-1}$) |
| | $M_{mix}$ | Molecular weight of gas mixture (kg·kmol$^{-1}$) |
| | $P_{c,i}$ | Critical pressure of $i$ compound (kPa) |
| | $R$ | Universal gas constant (J·mol$^{-1}$·K$^{-1}$) |
| | $T_{c,i}$ | Critical temperature of $i$ compound (K) |
| | $u$ | Inlet gas velocity (m·s$^{-1}$) |
| | $\boldsymbol{y_i}$ | Mole fraction of $i$ compound |
| | $\lambda_i$ | Thermal conductivity of $i$ compound (kW·m$^{-1}$·K$^{-1}$) |
| | $\lambda_{mix}$ | Thermal conductivity of gas mixture (kW·m$^{-1}$·K$^{-1}$) |
| | $\boldsymbol{\mu_{H_2}}$ | Viscosity of $H_2$ (kg·m$^{-1}$·s$^{-1}$) |
| | $\boldsymbol{\mu_{H_2O}}$ | Viscosity of $H_2O$ (kg·m$^{-1}$·s$^{-1}$) |
| | $\mu_i$ | Viscosity of $i$ compound (kg·m$^{-1}$·s$^{-1}$) |
| | $\mu_j$ | Viscosity of $j$ compound (kg·m$^{-1}$·s$^{-1}$) |
| | $\mu_{mix}$ | Viscosity of gas mixture (kg·m$^{-1}$·s$^{-1}$) |
| | $\boldsymbol{\mu_{N_2}}$ | Viscosity of $N_2$ (kg·m$^{-1}$·s$^{-1}$) |
| | $\rho_{mix}$ | Density of gas mixture (kg·m$^{-3}$) |
| | $\boldsymbol{\rho_{N_2}}$ | Density of $N_2$ (kg·m$^{-3}$) |
| | $\boldsymbol{v_{CH_4}}$ | Molar volume of $CH_4$ (cm$^3$·mol$^{-1}$) |
| | $v_i$ | Molar volume of $i$ compound (cm$^3$·mol$^{-1}$) |
| ***Characteristic Times*** | $t_c$ | Characteristic contact time (s) |
| | $t_{ext}$ | Characteristic external mass transfer time (s) |
| | $t_{int}$ | Characteristic coated layer diffusion time (s) |
| | $t_r$ | Characteristic reaction time (s) |

## References


1. Lewandowski, I. *Bioeconomy. Shaping the Transition to a Sustainable, Biobased Economy*; Springer: Berlin, Germany, 2018; pp. 5–74. ISBN 978-3-319-68152-8.
2. Piemonte, V.; De Falco, M.; Basile, A. *Sustainable Development in Chemical Engineering: Innovative Technologies*; John Wiley & Sons Ltd.: Chichester, UK, 2013; pp. 95–118. ISBN 978-1-118-62984-0.
3. Balzarotti, R.; Ciurlia, M.; Cristiani, C.; Paparella, F. Washcoat deposition of Ni- and Co-$ZrO_2$ low surface area powders onto ceramic open-cell foams: Influence of slurry formulation and rheology. *Catalysts* **2015**, *5*, 2271–2286. [CrossRef]

4. Specchia, S.; Ercolino, G.; Karimi, S.; Italiano, C.; Vita, A. Solution combustion synthesis for preparation of structured catalysts: A mini-review on process intensification for energy applications and pollution control. *J. Self-Propag. High-Temp. Synth.* **2017**, *26*, 166–186. [CrossRef]
5. Moulin, J.A.; Stankewicz, A.; Kapteijn, F. The pontential of structured reactors in process intensification. *Chem. Sustainable Dev.* **2003**, *11*, 3–9.
6. Williams, J.L. Monolith structures, materials, properties and uses. *Catal. Today* **2001**, *69*, 3–9. [CrossRef]
7. Ercolino, G.; Karimi, S.; Stelmachowski, P.; Specchia, S. Catalytic combustion of residual methane on alumina monoliths and open cell foams coated with $Pd/Co_3O_4$. *Chem. Eng. J.* **2017**, *326*, 339–349. [CrossRef]
8. Cybulski, A.; Moulijn, J.A. *Structured Catalysts and Reactors*, 2nd ed.; CRC Press, Taylor & Francis Group: Boca Raton, FL, USA, 2005; pp. 1–18. ISBN 978-1-4200-2800-3.
9. Pfau, S.F.; Hagens, J.E.; Dankbaar, B. Biogas between renewable energy and bio-economy policies—Opportunities and constraints resulting from a dual role. *Energy. Sustain. Soc.* **2017**, *7*, 1–15. [CrossRef]
10. Nahar, G.; Mote, D.; Dupont, V. Hydrogen production from reforming of biogas: Review of technological advances and an Indian perspective. *Renew. Sust. Energy Rev.* **2017**, *76*, 1032–1052. [CrossRef]
11. Lo Faro, M.; Vita, A.; Pino, L.; Aricò, A.S. Performance evaluation of a solid oxide fuel cell coupled to an external biogas tri-reforming process. *Fuel Process. Technol.* **2013**, *115*, 238–245. [CrossRef]
12. Farhad, S.; Yoo, Y.; Hamdullahpur, F. Effects of fuel processing methods on industrial scale biogas-fuelled solid oxide fuel cell system for operating in wastewater treatment plants. *J. Power Sources* **2010**, *195*, 1446–1453. [CrossRef]
13. Rasi, S.; Veijanen, A.; Rintala, J. Trace compounds of biogas from different biogas production plants. *Energy* **2007**, *32*, 1375–1380. [CrossRef]
14. Rathod, V.; Bhale, P.V. Experimental investigation on biogas reforming for syngas production over an alumina based nickel catalyst. *Energy Procedia* **2014**, *54*, 236–245. [CrossRef]
15. Lino, A.V.P.; Assaf, E.M.; Assaf, J.M. Hydrotalcites derived catalysts for syngas production from biogas reforming: Effect of nickel and cerium load. *Catal. Today* **2017**, *289*, 78–88. [CrossRef]
16. Eltejaei, H.; Reza Bozorgzadeh, H.; Towfighi, J.; Reza Omidkhah, M.; Rezaei, M.; Zanganeh, R.; Zamaniyan, A.; Zarrin Ghalam, A. Methane dry reforming on $Ni/Ce_{0.75}Zr_{0.25}O_2$–$MgAl_2O_4$ and $Ni/Ce_{0.75}Zr_{0.25}O_2$-$\gamma$–alumina: Effects of support composition and water addition. *Int. J. Hydrogen Energy* **2012**, *37*, 4107–4118. [CrossRef]
17. Löfberg, A.; Kane, T.; Guerrero-Caballero, J.; Jalowiecki-Duhamel, L. Chemical looping dry reforming of methane: Toward shale-gas and biogas valorization. *Chem. Eng. Process. Process Intensif.* **2017**, *122*, 523–529. [CrossRef]
18. Lahijani, P.; Zainal, Z.A.; Mohammadi, M.; Mohamed, A.R. Conversion of the greenhouse gas $CO_2$ to the fuel gas CO via the boudouard reaction: A review. *Renew. Sustain. Energy Rev.* **2015**, *41*, 615–632. [CrossRef]
19. Vita, A.; Italiano, C.; Previtali, D.; Fabiano, C.; Palella, A.; Freni, F.; Bozzano, G.; Pino, L.; Manenti, F. Methanol synthesis from biogas: A thermodynamic analysis. *Renew. Energy* **2018**, *118*, 673–684. [CrossRef]
20. Song, C.; Pan, W. Tri-reforming of methane: A novel concept for catalytic production of industrially useful synthesis gas with desired $H_2/CO$ ratios. *Catal. Today* **2004**, *98*, 463–484. [CrossRef]
21. Cipitì, F.; Pino, L.; Vita, A.; Laganà, M.; Recupero, V. Model-based investigation of a CO preferential oxidation reactor for polymer electrolyte fuel cell systems. *Int. J. Hydrogen Energy* **2007**, *32*, 4040–4051. [CrossRef]
22. Holladay, J.D.; Hu, J.; King, D.L.; Wang, Y. An overview of hydrogen production technologies. *Catal. Today* **2009**, *139*, 244–260. [CrossRef]
23. Joensen, F.; Rostrup-Nielsen, J.R. Conversion of hydrocarbons and alcohols for fuel cells. *J. Power Sources* **2002**, *105*, 195–201. [CrossRef]
24. Karakaya, M.; Keskin, S.; Avci, A.K. Parametric study of methane steam reforming to syngas in a catalytic microchannel reactor. *Appl. Catal. A Gen.* **2012**, *411–412*, 114–122. [CrossRef]
25. Vita, A.; Italiano, C.; Pino, L.; Frontera, P.; Ferraro, M.; Antonucci, V. Activity and stability of powder and monolith-coated Ni/GDC catalysts for $CO_2$ methanation. *Appl. Catal. B Environ.* **2018**, *226*, 384–395. [CrossRef]
26. Frey, M.; Édouard, D.; Roger, A.-C. Optimization of structured cellular foam-based catalysts for low-temperature carbon dioxide methanation in a platelet milli-reactor. *C. R. Chim.* **2015**, *18*, 283–292. [CrossRef]

27. Ricca, A.; Palma, V.; Martino, M.; Meloni, E. Innovative catalyst design for methane steam reforming intensification. *Fuel* **2017**, *198*, 175–182. [CrossRef]
28. Tomašić, V.; Jović, F. State-of-the-art in the monolithic catalysts/reactors. *Appl. Catal. A gen.* **2006**, *311*, 112–121. [CrossRef]
29. Weng, J.; Lu, X.; Gao, P.-X. Nano-array integrated structured catalysts: A new paradigm upon conventional wash-coated monolithic catalysts? *Catalysts* **2017**, *7*, 253. [CrossRef]
30. Vita, A.; Cristiano, G.; Italiano, C.; Pino, L.; Specchia, S. Syngas production by methane oxy-steam reforming on Me/$CeO_2$ (Me = Rh, Pt, Ni) catalyst lined on cordierite monoliths. *Appl. Catal. B Environ.* **2015**, *162*, 551–563. [CrossRef]
31. Ashraf, M.A.; Sanz, O.; Italiano, C.; Vita, A.; Montes, M.; Specchia, S. Analysis of Ru/La-$Al_2O_3$ catalyst loading on alumina monoliths and controlling regimes in methane steam reforming. *Chem. Eng. J.* **2018**, *334*, 1792–1807. [CrossRef]
32. Vita, A.; Cristiano, G.; Italiano, C.; Specchia, S.; Cipitì, F.; Specchia, V. Methane oxy-steam reforming reaction: Performances of Ru/$\gamma$-$Al_2O_3$ catalysts loaded on structured cordierite monoliths. *Int. J. Hydrogen Energy* **2014**, *39*, 18592–18603. [CrossRef]
33. Roy, P.S.; Song, J.; Kim, K.; Kim, J.-M.; Park, C.S.; Raju, A.S.K. Effects of $CeZrO_2$–$Al_2O_3$ support composition of metal-foam-coated Pd–Rh catalysts for the steam-biogas reforming reaction. *J. Ind. Eng. Chem.* **2018**, *62*, 120–129. [CrossRef]
34. Zapf, R.; Thiele, R.; Wichert, M.; O'Connell, M.; Ziogas, A.; Kolb, G. Application of rhodium nanoparticles for steam reforming of propane in microchannels. *Catal. Commun.* **2013**, *41*, 140–145. [CrossRef]
35. Sadykov, V.; Mezentseva, N.; Fedorova, Y.; Lukashevich, A.; Pelipenko, V.; Kuzmin, V.; Simonov, M.; Ishchenko, A.; Vostrikov, Z.; Bobrova, L.; et al. Structured catalysts for steam/autothermal reforming of biofuels on heat-conducting substrates: Design and performance. *Catal. Today* **2015**, *251*, 19–27. [CrossRef]
36. Govender, S.; Friedrich, H.B. Monoliths: A review of the basics, preparation methods and their relevance to oxidation. *Catalysts* **2017**, *7*, 62. [CrossRef]
37. Carty, M.W.; Lednor, P.W. Monolithic ceramics and heterogeneous catalysts: Honeycombs and foams. *Curr. Opin. Solid State Mater. Sci.* **1996**, *1*, 88–95. [CrossRef]
38. Voltolina, S.; Marín, P.; Díez, F.V.; Ordóñez, S. Open-cell foams as beds in multiphase reactors: Residence time distribution and mass transfer. *Chem. Eng. J.* **2017**, *316*, 323–331. [CrossRef]
39. Zhao, G.; Liu, Y.; Lu, Y. Foam/fiber-structured catalysts: Non-dip-coating fabrication strategy and applications in heterogeneous catalysis. *Sci. Bull.* **2016**, *61*, 745–748. [CrossRef]
40. Faure, R.; Rossignol, F.; Chartier, T.; Bonhomme, C.; Maître, A.; Etchegoyen, G.; Del Gallo, P.; Gary, D. Alumina foam catalyst supports for industrial steam reforming processes. *J. Eur. Ceram. Soc.* **2011**, *31*, 303–312. [CrossRef]
41. Faure, R.; Basile, F.; Bersani, I.; Chartier, T.; Cuni, A.; Cornillac, M.; Gallo, P.D.; Etchegoyen, G.; Gary, D.; Rossignol, F.; et al. Foam-supported catalysts tailored for industrial steam reforming processes. In *Studies in Surface Science and Catalysis*; Gaigneaux, E.M., Devillers, M., Eds.; Elsevier: Amsterdam, The Netherlands, 2010; pp. 241–244. ISBN 978-0-444-53601-3.
42. Laguna, O.H.; Domínguez, M.I.; Centeno, M.A.; Odriozola, J.A. Catalysts on metallic surfaces: Monoliths and microreactors. In *New Materials for Catalytic Applications*; Parvulescu, V.I., Kemnitz, E., Eds.; Elsevier: Amsterdam, The Netherlands, 2016; pp. 81–120. ISBN 978-0-444-63587-7.
43. Balzarotti, R.; Italiano, C.; Pino, L.; Cristiani, C.; Vita, A. Ni/$CeO_2$-thin ceramic layer depositions on ceramic monoliths for syngas production by oxy steam reforming of biogas. *Fuel Process. Technol.* **2016**, *149*, 40–48. [CrossRef]
44. Ercolino, G.; Stelmachowski, P.; Specchia, S. Catalytic performance of Pd/$Co_3O_4$ on SiC and $ZrO_2$ open cell foams for process intensification of methane combustion in lean conditions. *Ind. Eng. Chem. Res.* **2017**, *56*, 6625–6636. [CrossRef]
45. Rivero-Mendoza, D.E.; Stanley, J.N.G.; Scott, J.; Aguey-Zinsou, K.-F. An alumina-supported Ni-La-based catalyst for producing synthetic natural gas. *Catalysts* **2016**, *6*, 170–184. [CrossRef]
46. Italiano, C.; Vita, A.; Fabiano, C.; Laganà, M.; Pino, L. Bio-hydrogen production by oxidative steam reforming of biogas over nanocrystalline Ni/$CeO_2$ catalysts. *Int. J. Hydrogen Energy* **2015**, *40*, 11823–11830. [CrossRef]

47. Vita, A.; Italiano, C.; Fabiano, C.; Laganà, M.; Pino, L. Influence of Ce-precursor and fuel on structure and catalytic activity of combustion synthesized Ni/$CeO_2$ catalysts for biogas oxidative steam reforming. *Mater. Chem. Phys.* **2015**, *163*, 337–347. [CrossRef]
48. Patcas, F.C.; Garrido, G.I.; Kraushaar-Czarnetzki, B. CO oxidation over structured carriers: A comparison of ceramic foams, honeycombs and beads. *Chem. Eng. Sci.* **2007**, *62*, 3984–3990. [CrossRef]
49. Gibson, L.J.; Ashby, M.F. *Cellular Solids Structure and Properties*, 2nd ed.; Cambridge University Press: Cambridge, UK, 1999; pp. 15–51. ISBN 0521499119.
50. Buciuman, F.C.; Kraushaar-Czarnetzki, B. Ceramic foam monoliths as catalyst carriers. 1. Adjustment and Description of the Morphology. *Ind. Eng. Chem. Res.* **2003**, *42*, 1863–1869. [CrossRef]
51. Bhattacharya, A.; Calmidi, V.V.; Mahajan, R.L. Thermophysical properties of high porosity metal foams. *Int. J. Heat. Mass Transf.* **2002**, *45*, 1017–1031. [CrossRef]
52. Boomsma, K.; Poulikakos, D.; Ventikos, Y. Simulations of flow through open cell metal foams using an idealized periodic cell structure. *Int. J. Heat Fluid Flow* **2003**, *24*, 825–834. [CrossRef]
53. Hamadouche, A.; Nebbali, R.; Benahmed, H.; Kouidri, A.; Bousri, A. Experimental investigation of convective heat transfer in an open-cell aluminum foams. *Exp. Therm. Fluid Sci.* **2016**, *71*, 86–94. [CrossRef]
54. Wang, H.; Guo, L. Experimental investigation on pressure drop and heat transfer in metal foam filled tubes under convective boundary condition. *Chem. Eng. Sci.* **2016**, *155*, 438–448. [CrossRef]
55. Richardson, J.; Remue, D.; Hung, J.-K. Properties of ceramic foam catalyst supports: Mass and heat transfer. *Appl. Catal. A Gen.* **2003**, *250*, 319–329. [CrossRef]
56. Richardson, J.; Peng, Y.; Remue, D. Properties of ceramic foam catalyst supports: Pressure drop. *Appl. Catal. A Gen.* **2000**, *204*, 19–32. [CrossRef]
57. Nie, Z.; Lin, Y.; Tong, Q. Numerical investigation of pressure drop and heat transfer through open cell foams with 3D Laguerre-Voronoi model. *Int. J. Heat Mass Transfer* **2017**, *113*, 819–839. [CrossRef]
58. Ergun, S.; Orning, A.A. Fluid flow through randomly packed columns and fluidized beds. *Ind. Eng. Chem.* **1949**, *41*, 1179–1184. [CrossRef]
59. Edouard, D.; Lacroix, M.; Huu, C.P.; Luck, F. Pressure drop modeling on SOLID foam: State-of-the art correlation. *Chem. Eng. J.* **2008**, *144*, 299–311. [CrossRef]
60. Lacroix, M.; Nguyen, P.; Schweich, D.; Huu, C.P.; Savin-Poncet, S.; Edouard, D. Pressure drop measurements and modeling on SiC foams. *Chem. Eng. Sci.* **2007**, *62*, 3259–3267. [CrossRef]
61. Sollier, B.M.; Gómez, L.E.; Boix, A.V.; Miró, E.E. Oxidative coupling of methane on Sr/$La_2O_3$ catalysts: Improving the catalytic performance using cordierite monoliths and ceramic foams as structured substrates. *Appl. Catal. A Gen.* **2017**, *532*, 65–76. [CrossRef]
62. Palma, V.; Pisano, D.; Martino, M. The influence of the textural properties of aluminum foams as catalyst carriers for water gas shift process. *Int. J. Hydrogen Energy* **2017**, *42*, 23517–23525. [CrossRef]
63. Chai, R.; Zhang, Z.; Chen, P.; Zhao, G.; Liu, Y.; Lu, Y. Ni-foam-structured NiO-$MO_x$-$Al_2O_3$ (M = Ce or Mg) nanocomposite catalyst for high throughput catalytic partial oxidation of methane to syngas. *Microporous Mesoporous Mater.* **2017**, *253*, 123–128. [CrossRef]
64. Méndez, F.J.; Sanz, O.; Montes, M.; Guerra, J.; Olivera-Fuentes, C.; Curbelo, S.; Brito, J.L. Selective hydrogenation of 1,3-butadiene in the presence of 1-butene under liquid phase conditions using structured catalysts. *Catal. Today* **2016**, 151–161. [CrossRef]
65. Sanz, O.; Javier Echave, F.; Sánchez, M.; Monzón, A.; Montes, M. Aluminium foams as structured supports for volatile organic compounds (VOCs) oxidation. *Appl. Catal. A Gen.* **2008**, *340*, 125–132. [CrossRef]
66. Ertl, G.; Knözinger, H.; Schüth, F.; Weitkamp, J. *Handbook of Heterogeneous Catalysis*, 2nd ed.; Wiley-VCH: Weinheim, Germany, 2008; ISBN 978-3-527-31241-2.
67. Mears, D.E. Diagnostic criteria for heat transport limitations in fixed bed reactors. *J. Catal.* **1971**, *20*, 127–131. [CrossRef]
68. Anderson, J.B. A criterion for isothermal behaviour of a catalyst pellet. *Chem. Eng. Sci.* **1963**, *18*, 147–148.
69. Daele, T.V.; del Pozo, D.F.; Hauwermeiren, D.V.; Gernaey, K.V.; Wohlgemuth, R.; Nopens, I. A generic model-based methodology for quantification of mass transfer limitations in microreactors. *Chem. Eng. J.* **2016**, *300*, 193–208. [CrossRef]
70. Wijaya, W.Y.; Kawasaki, S.; Watanabe, H.; Okazaki, K. Damköhler number as a descriptive parameter in methanol steam reforming and its integration with absorption heat pump system. *Appl. Energy* **2012**, *94*, 141–147. [CrossRef]

71. Liao, C.; Erickson, P.A. Characteristic time as a descriptive parameter in steam reformation hydrogen production processes. *Int. J. Hydrogen Energy* **2008**, *33*, 1652–1660. [CrossRef]
72. Talebian-Kiakalaieh, A.; Amin, N.A.S. Theoretical and experimental evaluation of mass transfer limitation in gas phase dehydration of glycerol to acrolein over supported hsiw catalyst. *J. Taiwan Inst. Chem. Eng.* **2016**, *59*, 11–17. [CrossRef]
73. Bandopadhyay, A.; Borgne, T.L.; Méheust, Y.; Dentz, M. Enhanced reaction kinetics and reactive mixing scale dynamics in mixing fronts under shear flow for arbitrary Damköhler numbers. *Adv. Water Resour.* **2017**, *100*, 78–95. [CrossRef]
74. Metkar, P.S.; Salazar, N.; Muncrief, R.; Balakotaiah, V.; Harold, M.P. Selective catalytic reduction of NO with $NH_3$ on iron zeolite monolithic catalysts: Steady-state and transient kinetics. *Appl. Catal. B Environ.* **2011**, *104*, 110–126. [CrossRef]
75. Groppi, G.; Tronconi, E. Design of novel monolith catalyst supports for gas/solid reactions with heat exchange. *Chem. Eng. Sci.* **2000**, *55*, 2161–2171. [CrossRef]
76. Boldrini, D.E.; Sánchez, M.J.F.; Tonetto, G.M.; Damiani, D.E. Monolithic stirrer reactor: Performance in the partial hydrogenation of sunflower oil. *Ind. Eng. Chem. Res.* **2012**, *51*, 12222–12232. [CrossRef]
77. Dekker, F.H.M.; Bliek, A.; Kapteijn, F.; Moulijn, J.A. Analysis of mass and heat transfer in transient experiments over heterogeneous catalysts. *Chem. Eng. Sci.* **1995**, *50*, 3573–3580. [CrossRef]
78. Hayes, R.E.; Kolaczkowskib, S.T.; Li, P.K.C.; Awdry, S. Evaluating the effective diffusivity of methane in the washcoat of a honeycomb monolith. *Appl. Catal. B Environ.* **2000**, *25*, 93–104. [CrossRef]
79. Joshi, S.Y.; Harold, M.P.; Balakotaiah, V. Overall mass transfer coefficients and controlling regimes in catalytic monoliths. *Chem. Eng. Sci.* **2010**, *65*, 1729–1747. [CrossRef]
80. Roy, P.S.; Raju, A.S.K.; Kim, K. Influence of S/C ratio and temperature on steam reforming of model biogas over a metal-foam-coated Pd–Rh/($CeZrO_2$–$Al_2O_3$) catalyst. *Fuel* **2015**, *139*, 314–320. [CrossRef]
81. Ashrafi, M.; Pröll, T.; Pfeifer, C.; Hofbauer, H. Experimental study of model biogas catalytic steam reforming: 1. Thermodynamic optimization. *Energy Fuels* **2008**, *22*, 4182–4189. [CrossRef]
82. Zeppieri, M.; Villa, P.L.; Verdone, N.; Scarsella, M.; De Filippis, P. Kinetic of methane steam reforming reaction over nickel- and rhodium-based catalysts. *Appl. Catal. A Gen.* **2010**, *387*, 147–154. [CrossRef]
83. Roh, H. Methane-reforming reactions over Ni/Ce-$ZrO_2$/θ-$Al_2O_3$ catalysts. *Appl. Catal. A Gen.* **2003**, *251*, 275–283. [CrossRef]
84. Zhang, Z.; Ding, J.; Chai, R.; Zhao, G.; Liu, Y.; Lu, Y. Oxidative dehydrogenation of ethane to ethylene: A promising $CeO_2$-$ZrO_2$-modified NiO-$Al_2O_3$/Ni-foam catalyst. *Appl. Catal. A Gen.* **2018**, *550*, 151–159. [CrossRef]
85. Mbodji, M.; Commenge, J.M.; Falk, L.; Di Marco, D.; Rossignol, F.; Prost, L.; Valentin, S.; Joly, R.; Del-Gallo, P. Steam methane reforming reaction process intensification by using a millistructured reactor: Experimental setup and model validation for global kinetic reaction rate estimation. *Chem. Eng. J.* **2012**, *207–208*, 871–884. [CrossRef]
86. Arzamendi, G.; Diéguez, P.M.; Montes, M.; Odriozola, J.A.; Sousa-Aguiar, E.F.; Gandía, L.M. Methane steam reforming in a microchannel reactor for GTL intensification: A computational fluid dynamics simulation study. *Chem. Eng. J.* **2009**, *154*, 168–173. [CrossRef]
87. Zhou, W.; Ke, Y.; Wang, Q.; Wan, S.; Lin, J.; Zhang, J.; Hui, K.S. Development of cylindrical laminated methanol steam reforming microreactor with cascading metal foams as catalyst support. *Fuel* **2017**, *191*, 46–53. [CrossRef]
88. Mbodji, M.; Commenge, J.-M.; Falk, L. Preliminary design and simulation of a microstructured reactor for production of synthesis gas by steam methane reforming. *Chem. Eng. Res. Des.* **2014**, *92*, 1728–1739. [CrossRef]
89. González-Castaño, M.; Ivanova, S.; Laguna, O.H.; Martínez, T.L.M.; Centeno, M.A.; Odriozola, J.A. Structuring Pt/$CeO_2$/$Al_2O_3$ WGS catalyst: Introduction of buffer layer. *Appl. Catal. B Environ.* **2017**, *200*, 420–427.
90. Deutschmann, O.; Schwiedemoch, R.; Maier, L.I.; Chatterjee, D. Natural gas conversion in monolithic catalysts: Interaction of chemical reactions and transport phenomena. *Stud. Surf. Sci. Catal.* **2001**, 251–258.
91. Stutz, M.J.; Poulikakos, D. Optimum washcoat thickness of a monolith reactor for syngas production by partial oxidation of methane. *Chem. Eng. Sci.* **2008**, *63*, 1761–1770. [CrossRef]

92. Montebelli, A.; Visconti, C.G.; Groppi, G.; Tronconi, E.; Kohler, S.; Venvik, H.J.; Myrstad, R. Washcoating and chemical testing of a commercial $Cu/ZnO/Al_2O_3$ catalyst for the methanol synthesis over copper open-cell foams. *Appl. Catal. A Gen.* **2014**, *481*, 96–103. [CrossRef]
93. Italiano, C.; Balzarotti, R.; Vita, A.; Latorrata, S.; Fabiano, C.; Pino, L.; Cristiani, C. Preparation of structured catalysts with Ni and $Ni–Rh/CeO_2$ catalytic layers for syngas production by biogas reforming processes. *Catal. Today* **2016**, *273*, 3–11. [CrossRef]
94. Cao, C.; Zhang, N.; Cheng, Y. Numerical analysis on steam methane reforming in a plate microchannel reactor: Effect of washcoat properties. *Int. J. Hydrog. Energy* **2016**, *41*, 18921–18941. [CrossRef]
95. Wójcik, S.; Ercolino, G.; Gajewska, M.; Moncada Quintero, C.M.; Specchia, S.; Kotarba, A. Robust $Co_3O_4$ | $\alpha–Al_2O_3$ | cordierite structured catalyst for $N_2O$ abatement—Validation of the SCS method for active phase synthesis and deposition. *Chem. Eng. J.* **2018**, in press.
96. Palma, V.; Pisano, D.; Martino, M.; Ciambelli, P. Structured catalysts with high thermoconductive properties for the intensification of water gas shift process. *Chem. Eng. J.* **2016**, *304*, 544–551. [CrossRef]
97. Vita, A.; Italiano, C.; Pino, L.; Laganà, M.; Recupero, V. Hydrogen-rich gas production by steam reforming of n-dodecane. Part II: Stability, regenerability and sulfur poisoning of low loading Rh-based catalyst. *Appl. Catal. B Environ.* **2017**, *218*, 317–326. [CrossRef]
98. Zhang, M.; Ning, T.; Sun, P.; Yan, Y.; Zhang, D.; Li, Z. Effect of $Al_2O_3$-$SiO_2$ substrate on gas-sensing properties of $TiO_2$ based lambda sensor at high temperature. *Ceram. Int.* **2018**, *44*, 3000–3004. [CrossRef]
99. Shi, R.; Shang, Y.; Zhang, Y.; Wang, P.; Zhang, A.; Yang, P. Synthesis of ultrafine $\alpha$-$Al_2O_3$ powder by two-step hydrolysis. *Ceram. Int.* **2018**, *44*, 3741–3750. [CrossRef]


# Supplementary Materials: Rh/$CeO_2$ thin catalytic layer deposition on alumina foams: catalytic performance and controlling regimes in biogas reforming processes

**Cristina Italiano *, Muhammad Arsalan Ashraf, Lidia Pino, Carmen Williana Moncada Quintero, Stefania Specchia and Antonio Vita**

## S.1. SEM images

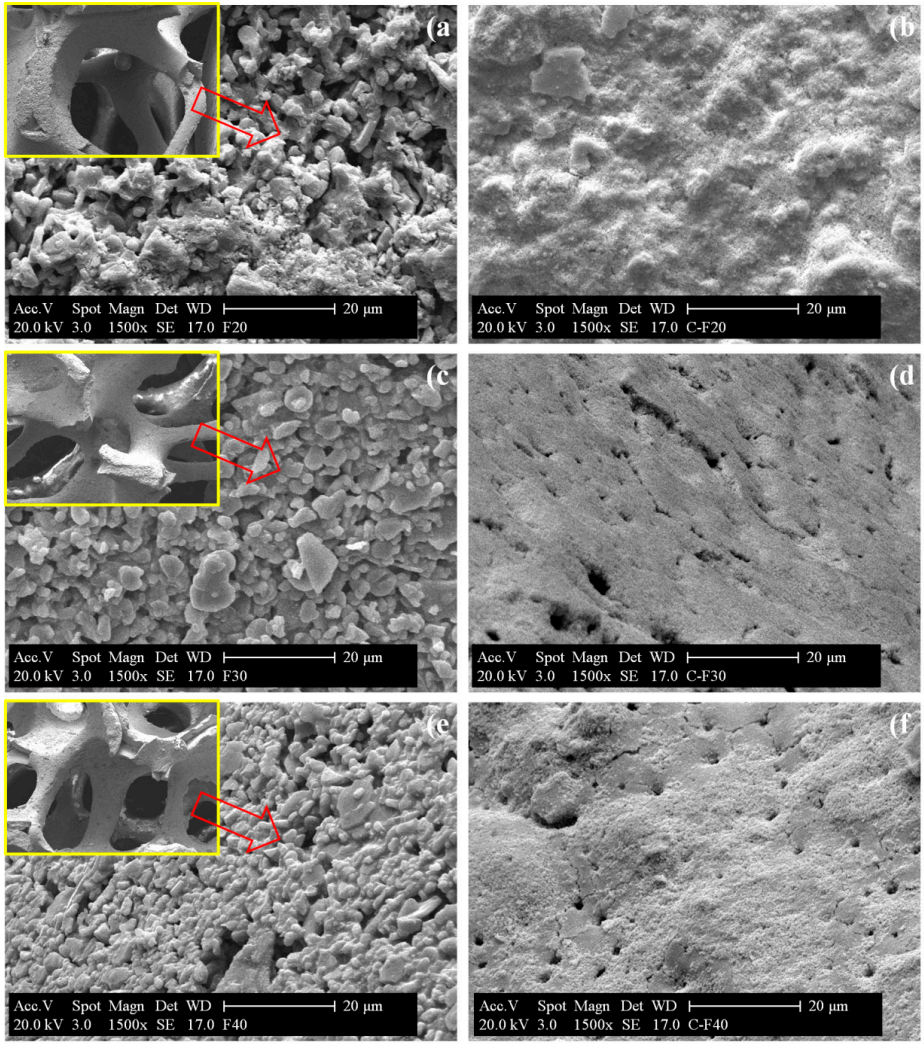


**Figure S1.** SEM micrographs of bare (**a**, **c**, **e**) and Rh/$CeO_2$-coated (**b**, **d**, **f**) OCFs: F20 (**a**, **b**), F30 (**c**, **d**) and F40 (**e**, **f**) structures (inset: images of the macroscopic bare OFCs).

An irregular porous surface was evidenced in SEM images of bare OCFs (Figure S.1 a, c, e) while a reduction of the macro-porosity of the alumina surface was revealed after depositing the catalytic layer (Figure S1b, d, f).

## S.2. XRD measurements

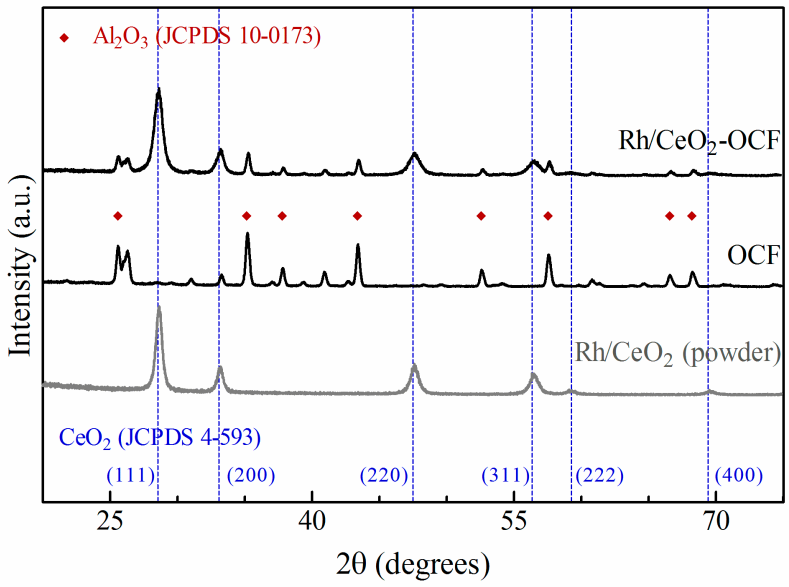


**Figure S2.** XRD pattern of Rh/$CeO_2$ as a powder, bare and Rh/$CeO_2$-coated F30 (included also reference peaks of $CeO_2$: JPDS 4-593 and reference peaks of $Al_2O_3$: JPDS 10-0173).

**Figure S2** shows X-ray diffraction patterns of bare and Rh/$CeO_2$-coated 30 ppi OCF, and Rh/$CeO_2$ in powder form. In the Rh/$CeO_2$ powder, the diffraction peaks can be assigned to the crystal planes of face-centered cubic $CeO_2$ (JCPDS 4-593) with typical diffraction peaks at 28.55° (111), 33.08° (200), 47.50° (220), 56.33° (311), 59.26° (222), and 69.41° (400) [1]. No diffraction peaks of Rh oxides were detected, due to the low loading and high dispersion of the noble metal [2]. The analysis of the diffraction pattern of bare 30 ppi OCF allowed the identification of $\alpha$-$Al_2O_3$ phase (JCPDS 10-0173), with peaks located at 25.59° (012), 35.16° (104) 37.81° (110), 43.38° (113) 52.58° (024), 57.52° (116), 66.57° (214) and 68.27° (306) [3,4]. As expected, both cubic $CeO_2$ fluorite type and $\alpha$-$Al_2O_3$ phase were identified after depositing the Rh/$CeO_2$ catalytic layer on the 30 ppi OCF [5]. The average crystallite size, calculated by the Scherrer equation from the main $CeO_2$ (111) reflection, was found to be 14.8 nm for Rh/$CeO_2$ powder catalyst and 11.2 nm for Rh/$CeO_2$ deposited on the foam. Almost equal results (not shown) were obtained for F20 and F40 structured catalysts.

## S.3. Mass and heat transport limitations

In the following, a detailed explanation of fluid properties determination, characteristic time analysis and dimensionless numbers calculation is provided.

### Gas, gas-solid and solid properties

Molecular weight ($M_{mix}$), density ($\rho_{mix}$) and, viscosity ($\mu_{mix}$) of gas mixture were calculated as:

$$M_{mix} = \sum_{i=1}^{n} y_i \, M_i \tag{S1}$$

$$\rho_{mix} = \frac{P \, M_{mix}}{R \, T} \tag{S2}$$

$$\mu_{mix} = \frac{\sum_{i=1}^{n} \mu_i \, y_i \, M_i^{1/2}}{\sum_{i=1}^{n} y_i \, M_i^{1/2}} \tag{S3}$$

where gas viscosity of a single component ($\mu_i$) was calculated from a corresponding state method [6].

For $CH_4$, $CO_2$, CO, and $N_2$ it was calculated by Equation S4, using the tabulated values of $T_{c,i}$ and $P_{c,i}$ [7].

$$\mu_i = \frac{64.008 \cdot 10^{-5} \left(4.5 \frac{T}{T_{c,i}} - 1.67\right)^{0.625}}{0.176\, T_{c,i}^{1/6}\, M_i^{-1/2}\, P_{c,i}^{-2/3}} \quad \text{(S4)}$$

| | $CH_4$ | $CO_2$ | CO | $N_2$ |
|---|---|---|---|---|
| $T_{c,i}$ **(K)** | 190.7 | 304.1 | 133.0 | 126.2 |
| $P_{c,i}$ **(kPa)** | 46.4 | 73.7 | 35.0 | 33.9 |

For $H_2$ and $H_2O$ it was calculated by Equations S5 and S6, respectively.

$$\mu_{H_2} = 326.55 \cdot 10^{-5} \,(0.1375\, T - 1.167)^{0.625} \quad \text{(S5)}$$

$$\mu_{H_2O} = 1170.828 \cdot 10^{-5} \,(0.011662\, T - 0.551) \quad \text{(S6)}$$

Diffusivity of $CH_4$ in gas phase ($D_{CH_4}$) was calculated from the binary diffusion of $CH_4$ and i gas species ($D_{CH_4-i}$) by:

$$D_{CH_4} = \frac{1 - y_{CH_4}}{\sum_{i=1;i\neq CH_4}^{n} \frac{y_i}{D_{CH_4-i}}} \quad \text{(S7)}$$

where $D_{CH_4-i}$ was determined by Fuller equation (Equation S8) [8], using tabulated values of $v_i$ [7].

$$D_{CH_4-i} = \frac{10^{-3}\, T^{1.75} \left(\frac{1}{M_{CH_4}} + \frac{1}{M_i}\right)^{1/2}}{\frac{P}{101.325}\left(v_{CH_4}^{1/3} + v_i^{1/3}\right)^2} \quad \text{(S8)}$$

| | $CH_4$ | $CO_2$ | CO | $N_2$ | $H_2$ | $H_2O$ |
|---|---|---|---|---|---|---|
| $v_i$ **(cm³·mol⁻¹)** | 24.4 | 26.9 | 18.9 | 17.9 | 7.1 | 12.7 |

Mass transfer coefficient of $CH_4$ ($k_G$) was determined from the Sherwood number (*Sh*) by:

$$k_G = \frac{Sh\, D_{CH_4}}{d_{p,c}} \quad \text{(S9)}$$

*Sh* was calculated from Reynold (*Re*) and Schmidt (*Sc*) numbers by Equations S10, S11 and S12 [9–12].

$$Sh = 1.00\, Re^{0.47}\, Sc^{0.33} \left(\frac{d_{f,c}}{0.001m}\right)^{0.58} \varepsilon^{0.44} \quad \text{(S10)}$$

$$Re = \frac{d_{p,c}\, u\, \rho_{mix}}{\mu_{mix}} \quad \text{(S11)}$$

$$Sc = \frac{\mu_{mix}}{\rho_{mix}\, D_{CH_4}} \quad \text{(S12)}$$

where the average coated face diameter ($d_{f,c}$) and the average coated pore diameter ($d_{p,c}$) were determined according to Equations S13 and S14, respectively:

$$d_{f,c} = d_f + 2\,\delta_c \tag{S13}$$

$$d_{p,c} = d_p - 2\,\delta_c \tag{S14}$$

while the inlet gas velocity ($u$) at standard temperature ($T_S$) and pressure ($P_S$) was calculated from Equation S15:

$$u = \frac{F_{tot}}{OFA\;\varepsilon}\,\frac{T}{T_S}\,\frac{P}{P_S} \quad \text{with} \quad OFA = \frac{\pi\,\phi^2}{4} \tag{S15}$$

Effective diffusivity of $CH_4$ in coated layer ($D_{CH_4,e}$) was calculated from the Knudsen diffusion ($D_k$) by the Equation [13–15]:

$$D_{CH_4,e} = \frac{\varepsilon_c}{\tau}\left(\frac{1}{D_{CH_4}} + \frac{1}{D_k}\right)^{-1} \tag{S16}$$

where $\varepsilon_c$ is the coated layer porosity ($\varepsilon_c = \rho_c\,PV_{BJH} = 0.12$) [16], $\tau$ is the tortuosity factor ($\tau = 1 - ln\varepsilon_c = 3.12$) [17] and $D_k$ was determined by equation S17 [18]:

$$D_k = 9.7 \cdot 10^{-5}\,r_p\left(\frac{T}{M_{CH_4}}\right)^{-1/2} \tag{S17}$$

Average values of specific surface area ($SA_{BET} = 24$ $m^2 \cdot g^{-1}$) and pore volume ($PV_{BJH} = 0.06$ $cm^3 \cdot g^{-1}$) were determined from Brunauer-Emmett-Teller (BET) and Barrett-Joyner-Halenda (BJH) analytic methods for $N_2$ adsorption-desorption isotherms of the structured catalysts. Pore radius ($r_p = 50$ Å) was given by $2PV_{BJH}/SA_{BET}$ equation.

The thermal conductivity of the gas mixture ($\lambda_{mix}$) was calculated by [19]:

$$\lambda_{mix} = \sum_{i=1}^{n}\frac{y_i\,\lambda_i}{\sum_{j=1}^{n} y_j\,\Phi_{ij}} \quad \text{with} \quad \Phi_{ij} = \frac{1}{\sqrt{8}}\left(1 + \frac{M_i}{M_j}\right)^{-1/2}\left[1 + \left(\frac{\mu_i}{\mu_j}\right)^{1/2}\left(\frac{M_j}{M_i}\right)^{1/4}\right]^2 \tag{S18}$$

where the thermal conductivity of a single gas component ($\lambda_i$) was found from the correlation $\lambda_i = A + B \cdot T + C \cdot T^2 + D \cdot T^3$, using tabulated values of *A*, *B*, *C* and *D* constants.

| | ***A*** | ***B*** | ***C*** | ***D*** |
|---|---|---|---|---|
| ***CH₄*** | −1.869·10⁻³ | 8.727·10⁻⁵ | 1.179·10⁻⁷ | −3.614·10⁻¹¹ |
| ***H₂*** | 8.099·10⁻³ | 6.689·10⁻⁴ | −4.158·10⁻⁷ | 1.562·10⁻¹⁰ |
| ***H₂O*** | 7.341·10⁻³ | -1.013·10⁻⁵ | 1.801·10⁻⁷ | −9.100·10⁻¹¹ |
| ***N₂*** | 3.919·10⁻⁴ | 9.816·10⁻⁵ | −5.067·10⁻⁸ | 1.504·10⁻¹¹ |
| ***CO*** | 5.0678·10⁻⁴ | 9.125·10⁻⁵ | −3.524·10⁻⁸ | 8.199·10⁻¹² |
| ***CO₂*** | −7.215·10⁻³ | 8.015·10⁻⁵ | 5.477·10⁻⁹ | −1.053·10⁻¹¹ |

The gas-solid heat transfer coefficient ($h$) was calculated from Nusselt number ($Nu$) by the equation [20]:

$$Nu = \frac{h\,d_{p,c}}{\lambda_{mix}} \tag{S19}$$

where $Nu$ was determined by Equation S20 [21]:

$$Nu = 2.49 \cdot 10^{-8}\, \varepsilon\, T_b + 12.6\, Re \text{ with } T_b = \frac{T_{IN} + T_{OUT}}{2} \quad \text{(S20)}$$

The temperatures registered at the inlet ($T_{IN}$) and outlet ($T_{OUT}$) of the catalytic bed during SR and OSR experiments are summarized below. However, experimental errors due to the positioning of thermocouples cannot be excluded.

| | **WHSV·10³** | **SR tests at T=900 °C** | | **SR tests at T=800 °C** | | **OSR tests at T=900 °C** | | **OSR tests at T=800 °C** | |
|---|---|---|---|---|---|---|---|---|---|
| | **(Nml g⁻¹·h⁻¹)** | $T_{IN}$ **(°C)** | $T_{OUT}$ **(°C)** | $T_{IN}$ **(°C)** | $T_{OUT}$ **(°C)** | $T_{IN}$ **(°C)** | $T_{OUT}$ **(°C)** | $T_{IN}$ **(°C)** | $T_{OUT}$ **(°C)** |
| **20 ppi** | 34.8 | 882 | 912 | 788 | 812 | 910 | 921 | 805 | 820 |
| | 69.5 | 883 | 922 | 795 | 821 | 915 | 927 | 804 | 822 |
| | 139.1 | 902 | 925 | 800 | 829 | 900 | 940 | 828 | 820 |
| **30 ppi** | 34.8 | 895 | 917 | 801 | 821 | 932 | 948 | 857 | 840 |
| | 69.5 | 897 | 924 | 809 | 827 | 926 | 931 | 831 | 833 |
| | 139.1 | 906 | 934 | 822 | 834 | 892 | 922 | 801 | 823 |
| **40 ppi** | 34.8 | 906 | 927 | 827 | 809 | 923 | 931 | 830 | 832 |
| | 69.5 | 914 | 941 | 829 | 843 | 925 | 939 | 831 | 840 |
| | 139.1 | 915 | 955 | 828 | 850 | 925 | 942 | 834 | 845 |

Absence of external interphase (gas-solid) heat transfer limitations.

Mears criterion [22] was applied to determine the effect of external interphase (gas-solid) heat transfer limitations by Equation S21:

$$\frac{E_a\, (-\Delta H_r^0)\, R_{CH_4}}{h\, GSA\, R\, T_b^2} < 0.15 \quad \text{(S21)}$$

where $E_a$ and $\Delta H_r^0$ are the apparent activation energy (92 kJ·mol⁻¹) and the standard reaction enthalpy (206.2 kJ·mol⁻¹) [23,24], $R_{CH_4}$ is the observed reaction rate for $CH_4$ based on foam volume, $h$ is the gas-solid heat transfer coefficient, $GSA$ is the geometric surface area of the OCF, $R$ is the universal gas constant (8.314 J·mol⁻¹ K⁻¹), and $T_b$ is the bulk fluid temperature estimated as in the Equation S20.

**Absence of internal heat transfer limitations**

Anderson criterion [22,25] was applied to determine the effect of internal heat transfer limitations by Equation S22:

$$\frac{E_a\, (-\Delta H_r^0)\, r_{CH_4}\, \rho_c\, \delta_c^2}{\lambda_c\, R\, T^2} < 0.75 \quad \text{(S22)}$$

where $r_{CH_4}$ is the observed reaction rate for $CH_4$, $\rho_c$ is the coated layer density, $\delta_c$ is the coated layer thickness, $\lambda_c$ is the effective thermal conductivity of porous materials (assumed equal to 0.3 W·m⁻¹·K⁻¹) [9,20], and $T$ is the reaction temperature.

**Characteristic time analysis**

The characteristic contact time, or residence time ($t_c$) describes the flow time of reactants through the OCFs catalysts at feed inlet conditions [26,27]. It was determined by:

$$t_c = \frac{L}{u} \quad \text{(S23)}$$

where $L$ is the OCF length and $u$ is the inlet gas velocity.

The characteristic external mass transfer time ($t_{ext}$) involves the diffusion of methane from bulk gas to the catalyst surface [28,29]. It was determined by:

$$t_{ext} = \frac{d_{p,c}^2}{4\, D_{CH_4}\, Sh} \tag{S24}$$

where $d_{p,c}$ is the average coated pore diameter, $D_{CH_4}$ is the diffusivity of $CH_4$ in gas phase and *Sh* is the Sherwood number.

The characteristic coated layer diffusion time ($t_{int}$) involves the transport of reactants inside the pores of the catalytic layer [30]. It was determined by:

$$t_{int} = \frac{\delta_c^2}{D_{CH_{4,e}}} \tag{S25}$$

where $\delta_c$ is the coated layer thickness and $D_{CH_{4,e}}$ is the effective diffusivity of $CH_4$ in the coated layer.

The characteristic reaction time ($t_r$) describes the rate of methane conversion [31–33]. It was determined by:

$$t_r = \frac{C_{CH_4}}{r_{CH_4}\, \rho_c} \tag{S26}$$

where $C_{CH_4}$ is the concentration of $CH_4$ in the feed mixture, $r_{CH_4}$ is the observed reaction rate for $CH_4$ and $\rho_c$ is the density (2 g·cm$^{-3}$) of the catalytic layer.

***Absence of external and internal mass transfer limitations***

Damköhler numbers were determined to describe the trade-off between reaction kinetic and diffusion limitations by Equations S27 (first Damkohler number, *Da-I*), S28 (second Damkohler number, *Da-II*), and S29 (third Damkohler number, *Da-III*) [34–38].

$$Da\text{-}I = \frac{t_c}{t_r} > 1 \tag{S27}$$

$$Da\text{-}II = \frac{t_{ext}}{t_r} < 0.1 \tag{S28}$$

$$Da\text{-}III = \frac{t_{int}}{t_r} < 1 \tag{S29}$$

Carberry [39,40] and Weisz-Prater [30,41,42] numbers were calculated to determine the effect of external and/or internal mass transfer limitation by Equations S30 and S31, respectively.

$$Ca = \frac{R_{CH_4}}{k_G\, GSA\, C_{CH_4}} < 0.05 \tag{S30}$$

$$WP = \frac{r_{CH_4}\, \rho_c\, {\delta_c}^2}{D_{CH_{4,e}}\, C_{CH_{4,s}}} < 1 \tag{S31}$$

where $R_{CH_4}$ is the observed reaction rate for $CH_4$ based on foam volume and $C_{CH_{4,s}}$ is the concentration of $CH_4$ at catalyst surface, assumed equal to $CH_4$ concentration in the feed mixture ($C_{CH_4}$) in absence of external diffusion controlling regime, otherwise calculated by Equation S32:

$$C_{CH_4,s} = C_{CH_4}(1 - Ca) \quad \text{(S32)}$$

## References


1. Italiano, C.; Vita, A.; Fabiano, C.; Laganà, M.; Pino, L. Bio-hydrogen production by oxidative steam reforming of biogas over nanocrystalline Ni/$CeO_2$ catalysts. *Int. J. Hydrogen Energy* **2015**, *40*, 11823–11830.
2. Palma, V.; Pisano, D.; Martino, M.; Ciambelli, P. Structured catalysts with high thermoconductive properties for the intensification of water gas shift process. *Chem. Eng. J.* **2016**, *304*, 544–551.
3. Zhang, M.; Ning, T.; Sun, P.; Yan, Y.; Zhang, D.; Li, Z. Effect of $Al_2O_3$-$SiO_2$ substrate on gas-sensing properties of TiO2 based lambda sensor at high temperature. *Ceram. Int.* **2018**, *44*, 3000–3004.
4. Shi, R.; Shang, Y.; Zhang, Y.; Wang, P.; Zhang, A.; Yang, P. Synthesis of ultrafine $\alpha$-$Al_2O_3$ powder by two-step hydrolysis. *Ceram. Int.* **2018**, *44*, 3741–3750.
5. Gómez, L.E.; Tiscornia, I.S.; Boix, A.V.; Miró, E.E. Co preferential oxidation on cordierite monoliths coated with CO/$CeO_2$ catalysts. *Int. J. Hydrogen Energy* **2012**, *37*, 14812–14819.
6. Bahadori, A. *Natural gas processing: Technology and engineering design*, 1st ed.; Gulf Professional Publishing: Waltham, MA, USA, 2014; pp. 23-58; ISBN 978-0-08-099971-5.
7. Perry, R.H.; Green, D.W.; Maloney, J.O. *Perry's chemical engineers' handbook*, 7th ed.; McGraw-Hill: New York City, NY, USA, 1999; ISBN 0-07-049841-5.
8. Fuller, E.N.; Schettler, P.D.; Giddings, J.C. New method for prediction of binary gas-phase diffusion coefficients. *Ind. Eng. Chem.* **1966**, *58*, 18–27.
9. Ertl, G.; Knözinger, H.; Schüth, F.; Weitkamp, J. Handbook of heterogeneous catalysis, 2nd ed.; Wiley-VCH: Weinheim, Germany, 2008; ISBN 978-3-527-31241-2.
10. Incera Garrido, G.; Patcas, F.C.; Lang, S.; Kraushaar-Czarnetzki, B. Mass transfer and pressure drop in ceramic foams: A description for different pore sizes and porosities. *Chem. Eng. Sci.* **2008**, *63*, 5202–5217.
11. Lucci, F.; Della Torre, A.; von Rickenbach, J.; Montenegro, G.; Poulikakos, D.; Dimopoulos Eggenschwiler, P. Performance of randomized kelvin cell structures as catalytic substrates: Mass-transfer based analysis. *Chem. Eng. Sci.* **2014**, *112*, 143–151.
12. Shah, R.K. Laminar flow friction and forced convection heat transfer in ducts of arbitrary geometry. *Int. J. Heat Mass Transf.* **1975**, *18*, 849–862.
13. von Rickenbach, J.; Lucci, F.; Narayanan, C.; Eggenschwiler, P.D.; Poulikakos, D. Effect of washcoat diffusion resistance in foam based catalytic reactors. *Chem. Eng. J.* **2015**, 276, 388–397.
14. Cao, C.; Zhang, N.; Cheng, Y. Numerical analysis on steam methane reforming in a plate microchannel reactor: Effect of washcoat properties. *Int. J. Hydrog. Energy* **2016**, *41*, 18921–18941.
15. Hayes, R.E.; Kolaczkowskib, S.T.; Li, P.K.C.; Awdry, S. Evaluating the effective diffusivity of methane in the washcoat of a honeycomb monolith. *Appl. Catal. B: Environ.* **2000**, *25*, 93–104.
16. Talebian-Kiakalaieh, A.; Amin, N.A.S. Theoretical and experimental evaluation of mass transfer limitation in gas phase dehydration of glycerol to acrolein over supported HSiW catalyst. *J. Taiwan Inst. Chem. Eng.* **2016**, *59*, 11–17.
17. Kolitcheff, S.; Jolimaitre, E.; Hugon, A.; Verstraete, J.; Carrette, P.-L.; Tayakout-Fayolle, M. Tortuosity of mesoporous alumina catalyst supports: Influence of the pore network organization. *Microporous Mesoporous Mater.* **2017**, *248*, 91–98.
18. Satterfield, C.N. *Mass transfer in heterogeneous catalysis*; MIT Press: Cambridge, MA, USA, 1970; ISBN 0-26-219062-1.
19. Demirel, Y. *Nonequilibrium thermodynamics: Transport and rate processes in physical, chemical and biological systems*, 3rd ed; Elsevier: Amsterdam, 2014; ISBN 978-0-444-59557-7.
20. Fratalocchi, L.; Visconti, C.G.; Groppi, G.; Lietti, L.; Tronconi, E. Intensifying heat transfer in Fischer-Tropsch tubular reactors through the adoption of conductive packed foams. *Chem. Eng. J.* **2018**, 349, 829–837.
21. Richardson, J..; Remue, D.; Hung, J.-K. Properties of ceramic foam catalyst supports: mass and heat transfer. *Appl. Catal. A Gen.* **2003**, *250*, 319–329.

22. Mears, D.E. Diagnostic criteria for heat transport limitations in fixed bed reactors. *J. Catal.* **1971**, *20*, 127–131.
23. Halabi, M.H.; de Croon, M.H.J.M.; van der Schaaf, J.; Cobden, P.D.; Schouten, J.C. Intrinsic kinetics of low temperature catalytic methane–steam reforming and water–gas shift over Rh/$Ce_{\alpha}Zr_{1-\alpha}O_2$ catalyst. *Appl. Catal. A Gen.* **2010**, *389*, 80–91.
24. Hennings, U.; Reimert, R. Stability of rhodium catalysts supported on gadolinium doped ceria under steam reforming conditions. *Appl. Catal. A Gen.* **2008**, *337*, 1–9.
25. Anderson, J.B. A criterion for isothermal behaviour of a catalyst pellet. *Chem Eng. Sci.* **1963**, *18, 147–148*.
26. Laguna, O.H.; Domínguez, M.I.; Centeno, M.A.; Odriozola, J.A. Catalysts on metallic surfaces: Monoliths and microreactors. In *New Materials for Catalytic Applications*; Parvulescu, V.I., Kemnitz, E., Eds.; Elsevier: Amsterdam, Netherlands, 2016; pp. 81–120; ISBN: 978-0-444-63587-7.
27. Kockmann, N. *Transport phenomena in micro process engineering*; Springer: New York City, NY, USA, 2008; ISBN 978-3-540-74616-4.
28. Matlosz, M.; Falk, L.; Commenge, J.-M. Process intensification. In *Microchemical engineering in practice*; Dietrich, T.R., Ed.; Wiley & Sons, Inc: Hoboken, NJ, USA, 2009; pp. 325–348; ISBN 978-0-470-23956-8.
29. Cybulski, A.; Moulijn J.A. *Structured Catalysts and Reactors*, 2nd ed.; CRC Press, Taylor & Francis Group: Boca Raton, FL, USA, 2005; pp. 1–18; ISBN: 978-1-4200-2800-3.
30. Mbodji, M.; Commenge, J.-M.; Falk, L. Preliminary design and simulation of a microstructured reactor for production of synthesis gas by steam methane reforming. *Chem. Eng. Res. Des.* **2014**, *92*, 1728–1739.
31. Metkar, P.S.; Salazar, N.; Muncrief, R.; Balakotaiah, V.; Harold, M.P. Selective catalytic reduction of NO with $NH_3$ on iron zeolite monolithic catalysts: Steady-state and transient kinetics. *Appl. Catal. B: Environ.* **2011**, *104*, 110–126.
32. Bhatia, D.; McCabe, R.W.; Harold, M.P.; Balakotaiah, V. Experimental and kinetic study of NO oxidation on model Pt catalysts. *J. Catal.* **2009**, *266*, 106–119.
33. Liao, C.; Erickson, P.A. Characteristic time as a descriptive parameter in steam reformation hydrogen production processes. *Int. J. Hydrogen Energy* **2008**, *33*, 1652–1660.
34. Beguin, B.; Garbowski, E.; Primet, M. Stabilization of alumina by addition of lanthanum. *Appl. Catal.* **1991**, *75*, 119–132.
35. Wijaya, W.Y.; Kawasaki, S.; Watanabe, H.; Okazaki, K. Damköhler number as a descriptive parameter in methanol steam reforming and its integration with absorption heat pump system. *Appl. Energy* **2012**, *94*, 141–147.
36. Stutz, M.J.; Poulikakos, D. Optimum washcoat thickness of a monolith reactor for syngas production by partial oxidation of methane. *Chem. Eng. Sci.* **2008**, *63*, 1761–1770.
37. Arzamendi, G.; Uriz, I.; Navajas, A.; Diéguez, P.M.; Gandía, L.M.; Montes, M.; Centeno, M.A.; Odriozola, J.A. A CFD study on the effect of the characteristic dimension of catalytic wall microreactors. *AIChE J.* **2011**, *58*, 2785–2797.
38. Arzamendi, G.; Diéguez, P.M.; Montes, M.; Odriozola, J.A.; Sousa-Aguiar, E.F.; Gandía, L.M. Methane steam reforming in a microchannel reactor for GTL intensification: A computational fluid dynamics simulation study. *Chem. Eng. J.* **2009**, *154*, 168–173.
39. Boldrini, D.E.; Sánchez M., J.F.; Tonetto, G.M.; Damiani, D.E. Monolithic stirrer reactor: Performance in the partial hydrogenation of sunflower oil. *Ind. Eng. Chem. Res.* **2012**, *51*, 12222–12232.
40. Dekker, F.H.M.; Bliek, A.; Kapteijn, F.; Moulijn, J.A. Analysis of mass and heat transfer in transient experiments over heterogeneous catalysts. *Chem. Eng. Sci.* **1995**, *50*, 3573–3580.
41. González-Castaño, M.; Ivanova, S.; Laguna, O.H.; Martínez T., L.M.; Centeno, M.A.; Odriozola, J.A. Structuring Pt/$CeO_2$/$Al_2O_3$ WGS catalyst: Introduction of buffer layer. *Appl. Catal. B Environ.* **2017**, *200*, 420–427.
42. Deutschmann, O.; Schwiedemoch, R.; Maier, L.I.; Chatterjee, D. Natural gas conversion in monolithic catalysts: Interaction of chemical reactions and transport phenomena. *Studies in Surface Science and Catalysis* **2001**, 251–258.

# CHAPTER IV

(*PAPER IV*)

Analysis of heat and mass transfer limitations for the combustion of methane emissions on $PdO/Co_3O_4$ coated on ceramic open cell foams

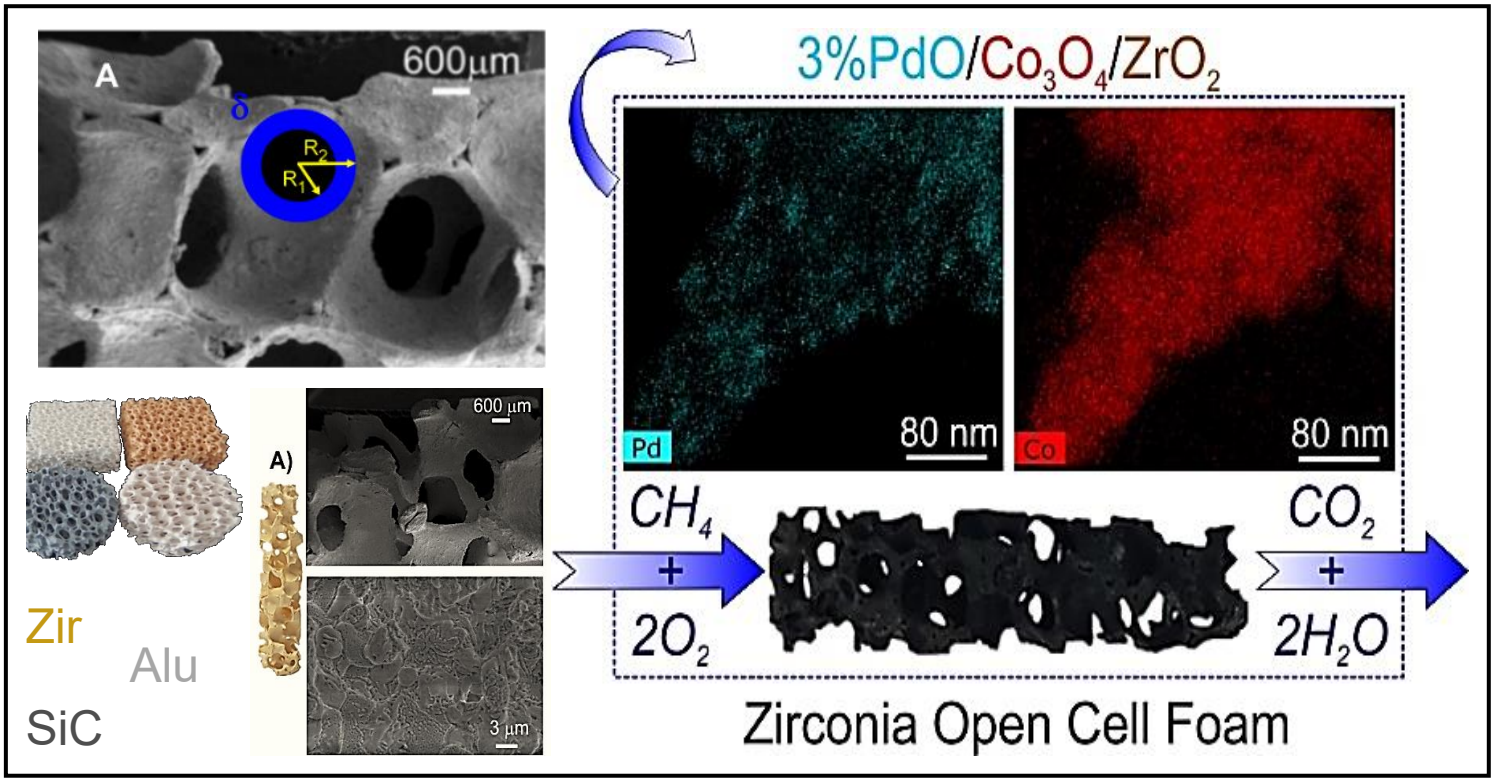


*Chemical Engineering Journal*. Elsevier, 405, p. 126970.

DOI: 10.1016/j.cej.2020.126970

Chemical Engineering Journal 405 (2021) 126970

Contents lists available at ScienceDirect

Chemical Engineering Journal

journal homepage: www.elsevier.com/locate/cej

# Analysis of heat and mass transfer limitations for the combustion of methane emissions on $PdO/Co_3O_4$ coated on ceramic open cell foams

Carmen W. Moncada Quintero[a,*], Giuliana Ercolino[a], Abhinav Poozhikunnath[b,c], Radenka Maric[b,c], Stefania Specchia[a,*]

[a] Politecnico di Torino, Department of Applied Science and Technology, Corso Duca degli Abruzzi 24, 10129 Torino, Italy
[b] University of Connecticut, Department of Materials Science and Engineering, 97 North Eagleville Road, Storrs, CT 06269, USA
[c] University of Connecticut, Center for Clean Energy Engineering, 44 Weaver Road, Storrs, CT 06269-5233, USA

## HIGHLIGHTS

- 3% $PdO/Co_3O_4$ coated on alumina, silicon carbide, and zirconia open cell foams.
- Best catalytic activity belongs to zirconia open cell foam coated with 200 mg on $Co_3O_4$.
- Importance of the low thermal conductivity of the foam to favor the catalytic reaction.
- Catalytic activity decreases slightly after 250 h of time on stream.
- STEM analysis for PdO dispersion on fresh/aged zirconia open cell foams.

## GRAPHICAL ABSTRACT

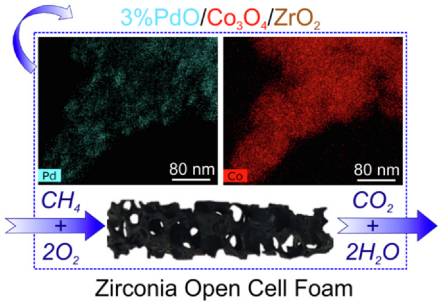


## ARTICLE INFO

*Keywords:*
Structured catalysts
Ceramic open cell foams
Mass/heat transfer effects
Thermal conductivity
Stability
PdO dispersion

## ABSTRACT

Coated ceramic open cells foams (OCFs) with catalysts offer an attractive alternative to packed bed reactors for process intensification. Here, the effect of 3 wt% PdO on $Co_3O_4$ coated on three different OCFs (alumina, silicon carbide and zirconia) was investigated toward the reaction of $CH_4$ combustion in lean conditions. The OCFs were characterized by Raman spectroscopy and FESEM analysis. The operating regime of each OCF catalyst was investigated using a series of mass transfer resistances assuming pseudo first order reaction (large excess of oxygen). The thermal conductivity of OCFs plays an important role on the overall performance of the combustion reaction in terms of heat and mass transfer. The best OCF structured catalyst was tested up to 250 h of time-on-stream, demonstrating good stability. PdO dispersion over the structured catalyst at the fresh and aged status was assessed by STEM analysis.

## 1. Introduction

Global warming is one of the most serious environmental threats facing the world today. Greenhouse gases (GHGs) such as carbon dioxide ($CO_2$), methane ($CH_4$), and nitrous oxide ($N_2O$) are the main factors responsible for greatly warming the surface of the Earth [1]. Transportation sector is one of the largest sources of GHG emissions [2]. Globally, about 27% of man-made $CO_2$ emissions come from burning fossil fuels in motor vehicles (mainly internal combustion engines) [3]. Natural gas (primarily composed of $CH_4$) is the most attractive and clean burning alternative transportation fuel to reduce environmental pollution since it emits the lowest $CO_2$ emissions, less $NO_x$, and particulates in the exhaust compared to gasoline and diesel engines [4]. In addition, natural gas engines can operate at lean-burn conditions,

* Corresponding authors.
*E-mail addresses:* carmen.moncada@polito.it (C.W. Moncada Quintero), stefania.specchia@polito.it (S. Specchia).

https://doi.org/10.1016/j.cej.2020.126970
Received 18 May 2020; Received in revised form 4 September 2020; Accepted 5 September 2020
Available online 10 September 2020
1385-8947/ 

minimizing the typical products of incomplete combustion in comparison to stoichiometric conditions [3]. However, these advantages are in part offset by the emissions of unburned $CH_4$ in the exhaust gases.

Catalytic converters are an efficient technology to reduce $CH_4$ emissions, via a catalytic oxidation at low temperature [5]. Pd-based catalysts have been reported to be the most active catalytic systems for the total oxidation of $CH_4$, due to their high activity at low temperature [6–9]. However, due to the relatively high cost associated with palladium, researchers have paid much attention to the study of different alternative systems such as oxides or mixed oxides [10–12] and perovskites [13–15] supporting Pd. In all cases, catalytic properties of supported Pd catalysts depend on the nature of catalyst carrier as well as active phase-support interaction [6,9,16,17].

Today, scientists focus the attention on structured catalysts for process intensification [18–23]. In particular, monolith- and foam-based catalysts offer a series of advantages compared to classical fixed beds with pellets [24], such as higher superficial geometric area (surface/volume ratio, $m^2\ m^{-3}$), higher thermal stability, higher porosity, and tortuosity, an homogeneous structure able to guarantee constant characteristics over a wide range of operative conditions. Thus, monolith- and foam-based structured catalysts offer lower pressure drop and higher space velocity while in operation, allowing for a reduction of the catalyst loading [18–23].

In particular, OCFs are already available on the market and represent a valid and economic alternative to ceramic monoliths [25–30]. To our knowledge, OCFs are commercially used in many different applications, such as filters for foundry industry and aluminum production, filters for hot gases or liquids in petrochemical and food industry, thermal insulators or heat exchangers in mechanical and construction sectors, and bone substitute for implants in biomedical applications [25–30]. No commercial applications are yet implemented in the catalysis sector. Indeed, there are many research groups, our included, which are focusing their research efforts on ceramic and metallic OCFs as supports for catalysts in many different chemical reactions, such as reforming of methane and biogas [31,32], partial and total oxidation of methane [33,34], CO and VOC oxidation [35,36], and many other applications in chemical reactor engineering [19,37–39]. Thus, OCFs represent a viable and potential substitute of commercially available monoliths, and the research in this field is growing fast.

The reduction of Pd content in supported Pd-based catalysts while maintaining or improving the catalytic activity is another important research target for a more economical process. On this purpose, transition metal oxides constitute probably one of the most interesting supports in many catalytic reactions such as oxidation of CO [40,41], activation of hydrocarbons [42,43], and reduction of $NO_x$ [44,45]. Among all the transition metal oxides, spinel cobalt oxide ($Co_3O_4$) represents a promising transition oxide catalyst for the total oxidation of methane in combination with Pd [10,46,47], mainly due to its high surface oxide mobility [48,49].

The main objective of this work is to evaluate the impact of the different ceramic OCF materials coated with a 3 wt% $PdO/Co_3O_4$ on mass and heat transport for the complete methane combustion in lean conditions. Possible applications can be envisaged in the removal of unburnt $CH_4$ in the automotive sector, or process intensification for environmental cleaning. This specific catalyst composition was selected from our previous optimization works performed on $PdO/Co_3O_4$ at powder level, in terms of PdO amount and best conditions of synthesis [46,47,50]. The $PdO/Co_3O_4$ catalyst was deposited on ceramic OCFs of various compositions (alumina, silicon, carbide, and zirconia) via a two-steps synthesis: first, solution combustion synthesis (SCS) of the $Co_3O_4$ spinel on the OCFs, and second, wetness impregnation (WI) of 3 wt% PdO on the $Co_3O_4$ spinel, according to our previous optimizations [46,47,50]. The SCS is a well-known and user-friendly method for preparing structured catalysts in a fast and cheap way by mixing metal nitrate precursors with an organic fuel [34,51–54]. Moreover, SCS is an easily scalable technique in the case of possible large-scale production for process intensification [55,56]. The catalytic activity of all the OCF catalysts was tested towards the lean combustion of $CH_4$ by varying the inlet $CH_4$ concentration (0.5 and 1.0 vol%), maintaining constant the $CH_4/O_2$ molar ratio, equal to 8, and at WHSV of 30 NL $h^{-1}$ $g_{cat}^{-1}$. Mass and heat transfer effects were evaluated at the inlet $CH_4$ concentration of 0.5 vol% for all the OCF catalysts. The most promising support for $PdO/Co_3O_4$ catalyst toward $CH_4$ combustion was selected to investigate the stability of the catalyst after approximately 250 h of operative time of stream [57]. All coated structures were characterized from the chemical point of view via Raman spectroscopy. The morphology of the catalysts was analyzed by field emission scanning electron microscopy (FESEM) and scanning transmission electron microscopy (STEM) techniques.

## 2. Materials and methods

### 2.1. Open cell foams and chemicals

Zirconia OCF (Vukopor® HT30, labelled Zir-OCF), alumina OCF (Vukopor® A30, labelled Alu-OCF), and silicon carbide OCF (Vukopor® S30, labelled SiC-OCF) of 30 ppi (pore per inch) were purchased from Lanik s.r.o. (Czech Republic, [26]). The OCFs were of 30 mm length and 9 mm diameter.

All the reagents were purchased from Sigma–Aldrich: cobalt(II) nitrate hexahydrate $Co(NO_3)_2{\cdot}6H_2O$ (≥98% purity), palladium(II) nitrate hydrate $Pd(NO_3)_2{\cdot}xH_2O$ (≥99% purity), glycine $NH_2CH_2COOH$ (≥99% purity), ethanol $CH_3CH_2OH$ (≥99.8% purity), isopropyl alcohol $(CH_3)_2CHOH$ (≥98% purity), and propanone $CH_3COCH_3$ (≥99.8% purity). Aqueous solutions were prepared using ultrapure water obtained from a Millipore Milli-Q system with a resistivity ≈ 18 MΩ cm. For catalytic activity tests, pure methane, oxygen, and nitrogen (purity 99.999%) were supplied in cylinders provided by SIAD S.p.A.

### 2.2. Preparation of the structured catalysts

Before use, all OCFs were cleaned in water/propanone (50/50 vol %) ultrasonic bath for 30 min at room temperature and dried at 250 °C for 60 min. Then, according to our previous optimization described in Ercolino et al. [33,34,46], 200 mg of $Co_3O_4$ catalyst was deposited on all OCFs by the SCS method. The coating procedure, which was repeated till the desired spinel loading was achieved, consisted of immersion of each OCF in a solution of cobalt nitrate and glycine (cobalt nitrate/glycine stoichiometric ratio of 0.25), removal of the excess of solution with a flow of compressed air, and SCS reaction step in a furnace at 250 °C for 15 min. As the last step, all OCFs were calcined for 4 h at 600 °C in calm air.

Then, 3 wt% PdO was deposited by WI, from a 3 M solution of Pd nitrate, by repeating the impregnation several times till reaching the desired amount, followed by a further calcination of 4 h at 600 °C in calm air, as described in our previous works [33,34,46].

### 2.3. Adherence tests

Sonication was used to mechanically stress the coated OCFs and verify the adhesion of the coated catalyst to the ceramic structures, according to our previous works and the literature [47,58,59]. The coated foams were immersed in a 50/50 solution of water/isopropanol and sonicated at 40 kHz, 130 W, for 2 h (S3M 2200 device by Sonica). The OCFs were weighted before and after sonication treatment (after 30 min drying in a static oven at 120 °C), to evaluate the loss of weight after sonication.

### 2.4. Catalytic tests toward $CH_4$ combustion

A series of catalytic tests was performed by evaluating the activity of the three different OCF materials (3 wt% PdO on 200 mg $Co_3O_4$ on Alu-

OCF, SiC-OCF, and Zir-OCF, respectively) toward $CH_4$ combustion, feeding 0.5 vol% $CH_4$ and 4 vol% $O_2$ in $N_2$, or 1.0 vol% $CH_4$, and 8 vol% $O_2$ in $N_2$, as inlet concentration ($O_2/CH_4$ molar ratio of 8, lean conditions, in both series of tests). A fixed bed reactor consisting of a straight quartz tube, 10 mm ID, placed into a PID-regulated electrical oven, was used to this purpose. To avoid channeling phenomena, all OCFs were wrapped with a vermiculite foil to perfectly fit the cross section of the reactor. The WHSV was set at 30 NL $h^{-1}$ $g_{cat}{}^{-1}$.

All catalytic tests were performed according to the procedure described in detail in Ercolino et al. [33,34]. After heating the reactor up to 700 °C at 10 °C $min^{-1}$ while feeding the reactive gas mixture, and reached steady state conditions (that is, full conversion of $CH_4$), the reactor was cooled to room temperature (5 °C $min^{-1}$) while monitoring the reactor outlet dry gas concentrations as a function of temperature (measured by a K-type thermocouple placed few mm inside the inlet side of the OCF). An online analyzer (ABB Company) equipped with an NDIR module Uras 14 for $CO/CO_2/CH_4$, and a paramagnetic module Magnos 106 for $O_2$, was used on purpose. The data collected from the online analyzer were elaborated and analyzed to draw $CH_4$ conversion as a function of the temperature. Each catalytic test was repeated at least three times, and the average values among the three tests are reported (standard deviation below 3%).

### 2.5. Stability measurements

A catalytic test was performed on the best-selected OCF catalyst, while maintaining constant inlet $CH_4$ concentration of 0.5 vol% ($O_2/CH_4$ molar ratio equal to 8) and WHSV of 30 NL $h^{-1}$ $g_{cat}{}^{-1}$, with the main purpose of verifying the stability of the best catalyst [57]. The reaction was initially run for five consecutive days at 400 °C, and again for another five consecutive days at 400 °C after two days resting at room temperature. The catalytic activity of the best-performing OCF catalyst was evaluated as described previously, at the beginning and at the end of the stability test (fresh/aged conditions), after approximately 250 h of operative time of stream.

### 2.6. External and internal mass transfer limitations

In order to study the internal (inside the pore of the catalyst layer) and external (gas film surrounding the structured catalyst) mass transfer effects, a series of resistances have been considered to evaluate the operating regime of each OCF catalyst. The total resistance to mass transfer ($R_m{}^t$) can be expressed as the sum of two diffusive resistance contributions (using a series approach) [60–63]:

$$R_m{}^t = R_m{}^e + R_m{}^i \tag{1}$$

$$R_m{}^t = \frac{1}{k_m{}^t};\ \ R_m{}^e = \frac{1}{k_m{}^e};\ \ R_m{}^i = \frac{1}{k_m{}^i} \tag{2}$$

where $R_m{}^e$ is the resistance due to the external mass transfer between the bulk of the gas phase and the outer surface of the $PdO/Co_3O_4$ catalyst layer (m); $R_m{}^i$ is the resistance due to mass transfer within the $PdO/Co_3O_4$ catalyst layer (m); $k_m{}^t$, $k_m{}^e$, and $k_m{}^i$ are the total, external and internal mass transfer coefficients (m $s^{-1}$), respectively.

For solid OCF, the external mass transfer coefficient ($k_m{}^e$) can be estimated according to Garrido et. al. [64] as:

$$Sh_{OCF} = 1.0 \cdot Re^{0.47} \cdot Sc^{\frac{1}{3}} \cdot F_g \tag{3}$$

$$k_m{}^e = \frac{Sh_{OCF} \cdot D_f}{4 \cdot R_{\Omega e}} \tag{4}$$

$$Re_{OCF} = \frac{d_{p,c} \cdot u \cdot \rho_f}{\mu_f};\ \ Sc = \frac{\mu_f}{\rho_f \cdot D_f};\ \ F_g = \left(\frac{d_{p,c}}{0.001}\right)^{0.58} \cdot \varepsilon_{ocf}^{0.44} \tag{5}$$

where $Sh_{OCF}$ is the external Sherwood number for solid OCF, $Re$ is the Reynold number, $Sc$ is the Smith number, $F_g$ is the geometrical factor which depends on the pore diameter ($d_{p,c}$) and the voidage ($\varepsilon_{ocf}$) of the OCF, $D_f$ is the molecular diffusivity of $CH_4$ in gas mixture ($m^2$ $s^{-1}$), $R_{\Omega e}$ is the characteristic length scale for transverse diffusion associated within gas phase (m) calculated as the ratio of the flow area $A_{\Omega,e}$ to the gas–coated layer interfacial perimeter ($P_\Omega$), $u$ is the inlet gas velocity at operative conditions (m $s^{-1}$), $\rho_f$ is the density of gas mixture (kg $m^{-3}$), and $\mu_f$ is the viscosity of gas mixture (kg $m^{-1}$ $s^{-1}$). The correlation for the estimation of the dimensionless mass transfer coefficient $Sh_{OCF}$ (Eq. 3) is valid for the range of OCF voidage of $0.75 \le \varepsilon_{ocf} \le 0.85$ and cell diameter of $0.87 \le d_{p,c} \le 3.13mm$.

The internal mass transfer coefficient ($k_m{}^i$) can be estimated according to the correlation proposed by Joshi et al. [61]:

$$Sh_c = Sh_{c,\infty} + \frac{\Lambda \cdot \phi^2}{1 + \Lambda \cdot \phi} \tag{6}$$

$$k_m{}^i = \frac{Sh_c \cdot D_e}{R_{\Omega,i}} \tag{7}$$

where $Sh_c$ is the internal Sherwood number, $Sh_{c,\infty}$ is the asymptotic internal Sherwood number ($Sh_{c,\infty} = 3.013$ for circular pore diameter and coated layer shape) [65,66], ϕ is the Thiele modulus, Λ is a constant that depends on the coated layer geometric and kinetic parameter for a first order reaction (Λ = 0.38 for a circular coated layer shape with circular crown ratio of 1.01) [60,61], $D_e$ is the effective diffusivity of $CH_4$ in the coated layer ($m^2$ $s^{-1}$), and $R_{\Omega,i}$ is the characteristic length scale for the coated catalyst layer (m) [60–63,66] calculated as the ratio of coated cross-sectional area ($A_{\Omega,i}$) to the gas-coated layer interfacial perimeter ($P_\Omega$). Since the reaction under consideration (complete combustion of methane) is carried out in a large excess of oxygen $C_{O2} \gg C_{CH4}$(lean conditions), the kinetic can be approximated as a pseudo-first order reaction:

$$CH_4 + 2O_2 \rightarrow CO_2 + 2H_2O \tag{8}$$

$$R^{obs} = k \cdot C_{CH_4} \tag{9}$$

where $R^{obs}$ is the observed reaction rate expressed with respect to methane (mol $m^{-3}$ $s^{-1}$) and $k$ is the apparent first order reaction rate constant ($s^{-1}$) which was determined by the Arrhenius equation (see Eq. 10) using the experimental data points with methane conversion lower than 10%:

$$k = A_o \cdot e^{-\frac{E_{app}}{R_g \cdot T}} \tag{10}$$

where $A_o$ is the pre-exponential factor ($s^{-1}$), $E_{app}$ is the apparent activation energy of the combustion reaction (J $mol^{-1}$), $R_g$ is the universal gas constant (J $mol^{-1}$ $K^{-1}$) and $T$ is the absolute temperature (K).

To describe the relationship between diffusion and reaction rate in porous catalyst with no mass transfer limitations, the Thiele modulus ($\phi$) for a first order reaction was determined by the following expression [60–62,65–68]:

$$ø = \sqrt{\frac{k \cdot {R_{\Omega i}}^2}{D_e}} \tag{11}$$

If the Thiele modulus is large ($\gg 1$, fast reaction), the conversion of the combustion process is controlled by diffusion, while if the Thiele modulus is small ($\ll 1$, slow reaction), the conversion is controlled by chemical reaction.

The effectiveness factor ($\eta$) was calculated using the analytical solution for cylindrical geometry for first order reaction as [60–62,65,67]:

$$\eta = \frac{1}{\phi} \cdot \frac{I_1(2\phi)}{I_0(2\phi)} \tag{12}$$

where $I_0$, $I_1$ are the zero and first order modified Bessel functions of the first kind, respectively. For slow reaction the effectiveness factor $\eta \rightarrow 1$ and fast reaction $\eta \rightarrow \frac{1}{\phi}$.

### 2.7. External and internal heat transfer limitations

In addition to mass transfer effects, heat transfer limitations can also occur in heterogeneous catalysis, in particular for strongly exothermic reactions such as the complete combustion of methane. Temperature gradients can be originated within the catalytic layer (internal heat transfer) or more frequently, between the bulk of the gas phase and the surface of the catalyst (external heat transfer) which lead to the catalyst deactivation due to the thermal sintering. For that, heat management in chemical reactions is of vital importance for both reactor design and control of the overall process.

The interphase heat transfer limitations can be evaluated using the criterion derived by Mears in 1971 [69] using the perturbation approach, in which the heat transfer resistance of the fluid phase is assumed to be lumped at the surface:

$$\chi = \left| \frac{(-\Delta H_r)\cdot R^{obs}\cdot R_{\Omega e}}{h_e\cdot T_b} \right| < \frac{0.15}{\gamma_b}; \tag{13}$$

$$\gamma_b = \frac{E_{app}}{R_g\cdot T_b} \tag{14}$$

where $\Delta H_r$ is the heat of methane combustion reaction (J mol$^{-1}$), $h_e$ is the heat transfer coefficient associated for the gas phase (W m$^{-2}$ K$^{-1}$), $T_b$ is the temperature in the bulk of the gas phase (K); $\gamma_b$ is the Arrhenuis number evaluated at the bulk of the gas phase, $R_g$ is the universal gas constant (J mol$^{-1}$ K$^{-1}$), and $\chi$ is the Damkholer for interphase heat transport [65,67–71].

Concerning the intraparticle heat transfer effects, the thermal gradients inside the catalyst layer can be assumed absent according to the Anderson's criterion proposed in 1963 as [72]:

$$\psi = \left| \frac{(-\Delta H_r\cdot R^{obs}\cdot R_{\Omega i}^2)}{\lambda_e\cdot T_s} \right| < \frac{0.75}{\gamma_s}; \tag{15}$$

$$\gamma_s = \frac{E_{app}}{R_g\cdot T_s} \tag{16}$$

where $\lambda_e$ is the effective thermal conductivity (W m$^{-1}$ K$^{-1}$), $T_s$ is the temperature at the surface of the catalyst layer (K), $\gamma_s$ is the Arrhenuis number evaluated at the surface of the gas phase, and $\psi$ is the Damkohler for intraparticle heat transport [65,67,68,70–72].

Under steady state conditions, the heat released by the methane combustion reaction ($Q_r$) on any element of the outer PdO/$Co_3O_4$ catalyst surface must be transported from the solid catalytic thickness to the bulk fluid. Assuming pseudo-first order reaction the steady state analysis is given as [67]:

$$Q_r = Q \tag{17}$$

$$Q_r = (R_{CH4}^{'})\cdot(-\Delta H_r) = A_o^{'}\cdot e^{\left(\frac{\gamma_b}{\theta+1}\right)}\cdot C_{CH4}\cdot(-\Delta H_r) \tag{18}$$

$$Q = h_e\cdot a_m\cdot(T_s - T_b) = h_e\cdot a_m\cdot T_b\cdot\theta \tag{19}$$

where $Q_r$ is the rate of heat generation per unit mass of catalyst (J Kg$^{-1}$ s$^{-1}$), $Q$ is the rate of heat removal per unit mass of catalyst (J Kg$^{-1}$ s$^{-1}$), $R_{CH4}^{'}$ is the reaction rate expressed with respect to methane per unit mass of catalyst (mol Kg$^{-1}$ s$^{-1}$), $A_o^{'}$ is the pre-exponential factor per unit of the catalyst bulk density (m$^3$ Kg$^{-1}$ s$^{-1}$), $a_m$ is the external surface area per unit mass of catalyst (m$^2$ Kg$^{-1}$), and $\theta$ is the dimensionless temperature defined by Eq. 20:

$$\theta = \frac{T_s - T_b}{T_b} \tag{20}$$

### 2.8. Physical-chemical characterization

The chemical composition of the 3% PdO/$Co_3O_4$ catalyst coated on all OCFs was analyzed via Raman spectroscopy with a Micro-Raman instrument (Renishaw plc, Wottonunder-Edge, UK, equipped with a cooled CCD camera with an excitation wavelength of 514 nm). The Raman scattered light was collected in the spectral range 200–1000 cm$^{-1}$. Twelve scans per measurements were accumulated to ensure a sufficient signal-to-noise ratio.

The morphology and homogeneity of the catalytic coating was investigated on Zir-OCF via field-emission scanning electron microscopy (FESEM, JEOL-JSM-6700F).

The specific surface areas ($S_{BET}$) of the coated OCFs were measured by nitrogen physisorption at –196 °C using a Micromeritics ASAP 2020 instrument. The measurements were performed by inserting small pieces of the foams into the burette, and outgassing overnight at 150 °C in low vacuum (10 Pa). The $S_{BET}$ were evaluated by the Brunauer–Emmett–Teller method between 0.05 and 0.30p/p∘.

PdO dispersion on $Co_3O_4$ coated on Zir-OCF was evaluated before and after the stability test on the fresh and aged structured catalyst by scanning transmission electron microscopy (STEM, 200 kV Talos F200X FEG S/TEM) coupled with energy dispersive X-ray spectroscopy (EDXS) mapping. The specimens for STEM analysis were prepared by cutting a few pieces of catalyst coated material from the Zir-OCF and dispersing it in ethanol by sonication and adding one drop of the dispersed mixture on to a 3 mm Cu grid with holey carbon film (Pacific Grid-Tech). The specimens were covered and allowed to dry overnight at room temperature before they were analyzed.

## 3. Results and discussion

### 3.1. Physical-chemical characterization

Table 1 summarizes the textural and geometrical properties of the three bare 30 ppi OCFs, evaluated according to Buciuman and Kraushaar-Czarnetzki [73]. Section S.1 of the *Supporting Info* (*S.1. Estimation of the textural and geometrical properties of the OCF*) explains all the equations used to obtain the values listed in Table 1, as reported in our previous works [33,34]. Notwithstanding the same pore per inch values of the three types of OCFs, the textural properties are very different. For example, the average pore dimension increases in the order Zir-OCF < Alu-OCF < SiC-OCF, while the geometric surface area and surface area decreases in the order Zir-OCF > Alu-OCF > SiC-OCF. Instead, in terms of voidage, Zir-OCF has the lowest value, whereas the Alu-OCF and SiC-OCF have very similar, slightly higher values. In addition, the thermal conductivity is very different, increasing in the order Zir-OCF < Alu-OCF < SiC-OCF. The $S_a$ values are very low, equivalent to a specific surface area of approx. 0.002 m$^2$ g$^{-1}$. The $S_a$ values listed in Table 1 have been calculated by applying the formula of Buciuman and Kraushaar-Czarnetzki [73], considering the strut of the foam as a dense package of single tetrakaidekahedron (all the formula employed are listed in the section S.1 of the *Supporting Info*). Because of these low values of $S_a$, and considering that OCFs can be porous with additional internal void volume due to the fabrication process,

**Table 1**
Textural and geometrical properties of the three 30 ppi OCFs.

| Bare OCF | Zir-OCF | Alu-OCF | SiC-OCF |
|---|---|---|---|
| Average pore dimension, $d_p$ [mm] | 1.30 ± 0.73 | 1.34 ± 0.55 | 1.63 ± 0.65 |
| Average strut thickness, $t_s$ [mm] | 0.47 ± 0.16 | 0.34 ± 0.10 | 0.42 ± 0.16 |
| Face diameter, $d_f$ [mm] | 1.77 | 1.68 | 2.05 |
| Foam relative density, $\rho_r$ [-] | 0.183 | 0.106 | 0.109 |
| Voidage, $\varepsilon$ [-] | 0.817 | 0.894 | 0.891 |
| Geometric surface area, $S_{ga}$ [mm$^{-1}$] | 1.164 | 0.934 | 0.776 |
| Surface area, $S_a$ [mm$^2$] | 2221 | 1783 | 1480 |
| Thermal condictivity, $\lambda_f$ [W m$^{-1}$ K$^{-1}$] | 0.027 [75] | 0.16 [76] | 0.40 [77] |

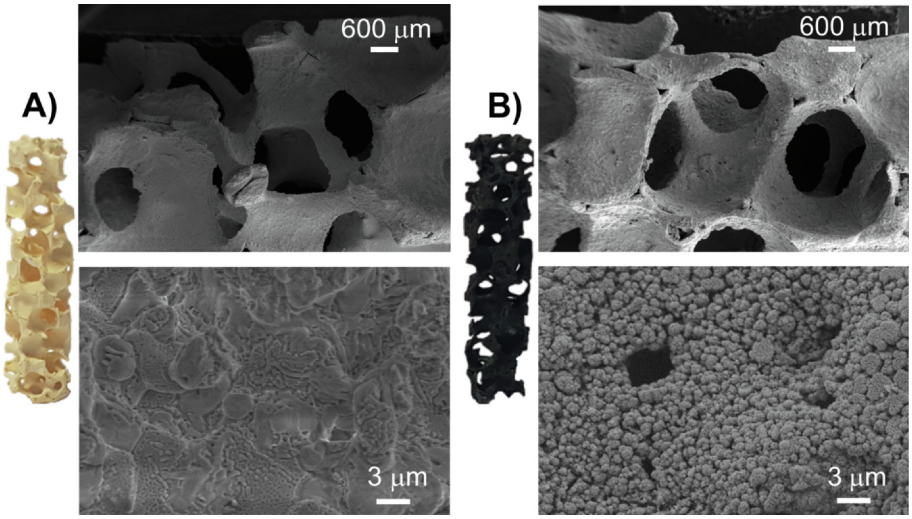


**Fig. 1.** 30 ppi Zir-OCF used in this work: A) bare structure, and B) coated structure with 3 wt,% $PdO/Co_3O_4$. FESEM images at 40X and 10,000X magnification.

measuring the $S_{BET}$ on bare OCFs via conventional physisorption methods has no practical meaning [64,74].

From the adherence tests performed by sonication, the adherence values span from 98.3 to 98.8 wt%, showing a strong interaction of the catalytic layer with the walls of the structures, independently of the nature of the ceramic foams. These values, with an overall loss of catalyst slightly higher than 1 wt%, are matching very well with our previous adherence results on ceramic and metallic foams [23,34,58] and also with literature values on ceramic and metallic foams [22,78]

Fig. 1 shows pictures and FESEM images at low and high magnification of Zir-OCF, in the bare and coated status (3% PdO on 200 mg $Co_3O_4$). The surface of the bare OCF is flat, confirming the low $S_a$ values calculated, while the surface of the coated OCF is rather rough, thanks to the gasses released during the SCS reaction [54,55]. The catalytic layer results homogeneously distributed all along the structure, and very well anchored, with an average thickness of about 55 ± 15 µm. This value is in line with the values reported in the open literature for similar structures, both monoliths and foams [55,58,79,80]. Very similar morphology and thicknesses were observed also for Alu-OCF and SiC-OCF (not shown here). The $S_{BET}$ values measured on the three coated foams (adsorption/desorption curves not reported here) were very similar among them ranging from 4.6 to 5.0 $m^2\ g^{-1}$, various orders of magnitude higher than the specific surface area values of the bare OCFs. These values are typical of the $PdO/Co_3O_4$ $S_{BET}$ values in powder, which is equal to 5.1 $m^2\ g^{-1}$, for 3% PdO deposited over $Co_3O_4$, as we evaluated experimentally in one of our previous works [47]. Thus, even if the starting ceramic materials are different, and with very low specific area (see $S_a$ values in Table 1), we can affirm that their low and almost equal $S_a$ values do not influence the nature and morphology of the catalyst lined on the bare OCFs when we move from powder to structured ones, being the morphological characteristic of the coated $PdO/Co_3O_4$ deposited over the foams the same of the powder $PdO/Co_3O_4$. We got similar results by lining a different catalyst ($Ru/La\text{-}Al_2O_3$) either on ceramic and metallic monoliths [23,81]. Thus, we can conclude that the coating process allows us obtaining ceramic OCFs with a high specific surface area, which depends exclusively on the nature of the catalyst coated over.

Fig. 2 shows Raman spectra of the three coated 30 ppi OCFs. All recorded spectra are almost identical, sign that the SCS method allowed coating the catalyst maintaining its chemical characteristics on the three different structures, independently of their nature (zirconia, alumina, or silicon carbide). The lines located at 487, 526, 624, and 694 $cm^{-1}$, respectively, correspond to the $E_g$, $2xF_{2g}$, and $A_{1g}$ vibrational modes of crystalline $Co_3O_4$ spinel [82,83], confirming definitely its

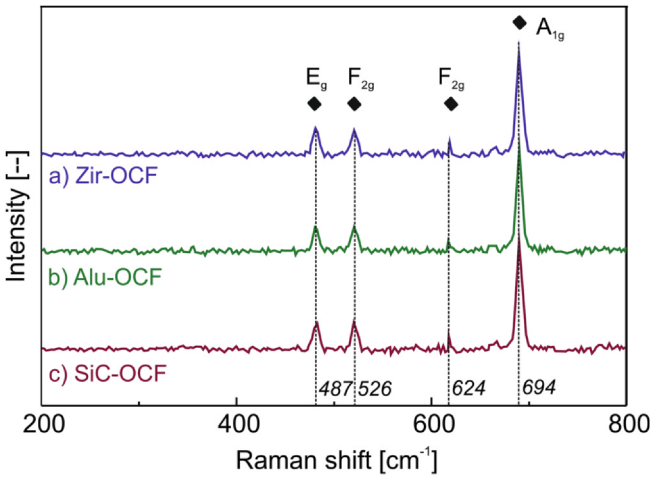


**Fig. 2.** Raman spectra of the three OCFs coated with 3% PdO on 200 mg $Co_3O_4$.

presence in all structured catalysts. The spectra of the structured catalysts are almost coincident with the Raman spectra obtained for $PdO/Co_3O_4$ synthesized as a powder in our previous studies [46]. Raman spectra of PdO, expected at around 467, 640, and 680 $cm^{-1}$ ($E_g$ and $B_{1g}$ vibrational modes) [46,84], cannot be distinguished clearly because of the relatively low concentration of PdO [46].

### 3.2. Catalytic tests toward $CH_4$ combustion

The three OCFs coated with 3 wt% PdO on 200 mg of $Co_3O_4$ were tested toward $CH_4$ combustion in lean conditions at 30 WHSV, feeding two different inlet $CH_4$ concentrations in the reactor (0.5 and 1.0 vol%, respectively), as shown in Fig. 3. All the three types of coated OCFs reach full $CH_4$ conversion at a temperature below 460 °C, independently on the inlet $CH_4$ concentration. A higher inlet $CH_4$ concentration shifts the curves toward slightly higher values of temperature. In all examined cases, Zir-OCF behaves better than Alu-OCF and SiC-OCF, respectively, reaching complete conversion at a temperature below 380 °C. The light-off temperatures ($T_{10}$, temperature at which the catalyst reached 10% of $CH_4$ conversion) are very similar for all OCFs, from a minimum of 235 °C for Zir-OCF (0.5% $CH_4$ inlet) to a maximum of 270 °C for SiC-OCF (1.0% $CH_4$ inlet). Interestingly, the difference is more evident on light-on temperatures ($T_{90}$, temperature at which the catalyst reached 90% of $CH_4$ conversion), which range from a minimum of 323 °C for Zir-OCF (0.5% $CH_4$ inlet) to a maximum of 392 °C for SiC-

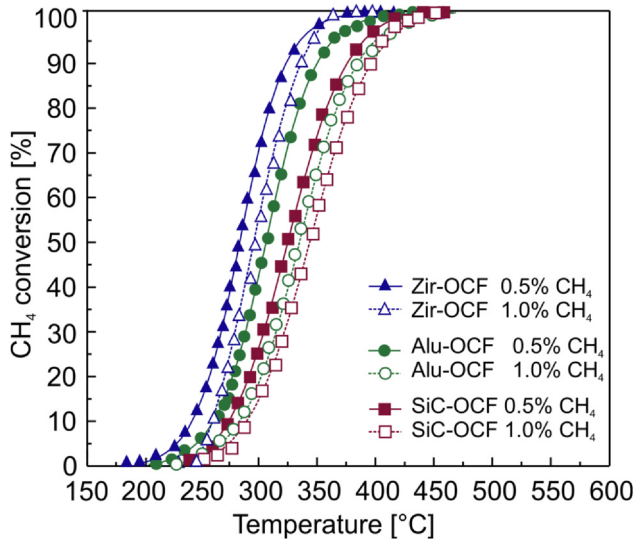


**Fig. 3.** $CH_4$ conversion versus temperature of the three OCFs coated with 3% PdO on 200 mg $Co_3O_4$, tested at 30 NL $h^{-1}$ $g_{cat}^{-1}$ with two different $CH_4$ inlet concentrations.

OCF (1.0% $CH_4$ inlet). Both Zir-OCF reach full conversion at a temperature of ≈ 360 °C, while the other two supports at temperatures higher than 410 °C. These results can be explained considering the different values of the thermal conductivity of the three OCFs (listed in Table 1). In fact, the lowest thermal conductivity value of Zir-OCF allows reaching complete $CH_4$ conversion at lower temperature compared to the other supports. As we estimated in our previous works by measuring either in inlet and outlet temperatures during the reaction in different reactive conditions [33,34], the volumetric heat transfer coefficients are increasing with WHSV and decreasing with temperature, following the order Zir-OCF ($2{\cdot}10^4$–$0.5{\cdot}10^5$ W $m^{-3}$ $K^{-1}$) < Alu-OCF ($1.5{\cdot}10^5$–$9{\cdot}10^5$ W $m^{-3}$ $K^{-1}$) < SiC-OCF ($2{\cdot}10^5$–$1{\cdot}10^6$ W $m^{-3}$ $K^{-1}$). These values are in logic agreement with the thermal conductivities values of different monoliths, ceramic and metallic available in the literature [20,85–87]. Moreover, these results are in fully agreement with the results obtained by Sanz et al. [78] and Santos et al. [59], studying the catalytic endo- or exo-thermic reactions on ceramic and metallic monoliths coated with catalysts: the most active structured catalysts are the ceramic ones, which have the lowest values of thermal conductivity, as in our case. Thus, these results confirm the important role of the thermal conductivity in favoring the catalytic reaction.

### 3.3. External and internal mass transfer limitations

Table 2 provides the catalyst layer thickness of each OCF structure, calculated by assuming that the PdO/$Co_3O_4$ catalyst is uniformly distributed inside the pores of the OCF and the shape of the catalyst coated layer is circular (see Fig. 4). As observed, the catalyst thickness increases in the order of Zir-OCF < Alu-OCF < SiC-OCF, maintaining the $R_2/R_1$ ratio of the coated circular crown approximately equal to 1.1, as proposed by Joshi et al. [60,61] for washcoated monolith.

The evolution of the individual and overall resistances as a function of the temperature is shown in Fig. 5. As can be noted, the mass transfer resistances ($R_m^e$, $R_m^i$) are much less temperature sensitive in

**Table 2**
Average catalyst thickness of the OCF catalyst.

| OCF material | Zir | Alu | SiC |
|---|---|---|---|
| δ (μm) | 46.3 | 57.7 | 69.6 |
| $R_2/R_1$ | 1.080 | 1.093 | 1.094 |

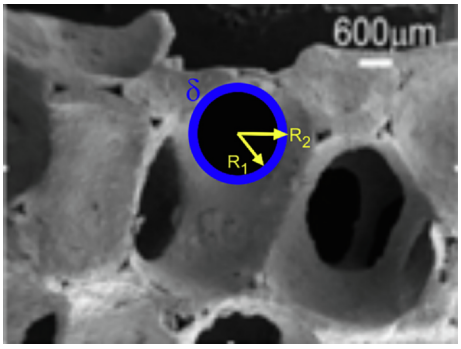


**Fig. 4.** Distribution of the PdO/$Co_3O_4$ catalyst inside the pore of the OCF with circular coated layer shape.

comparison to the reaction resistance ($R_r$), which is strongly dependent on Arrhenius equation. In fact, for the three OCFs studied, the $R_m^e$ is nearly independent of temperature. As far as the $R_m^i$ is concerned, $R_m^i$ is practically invariant at temperatures below 350 and 300 °C for Al- and SiC-OCF catalyst, respectively; while for Zir-OCF catalyst, the $R_m^i$ is roughly independent for the entire temperature range studied. Besides, it is also worth noting that the $R_m^i$ becomes more important at lower temperatures for the coated OCFs with higher thermal conductivity and thicker catalytic thickness (Alu- and SiC-OCF, respectively). In particular, the $R_m^i$ is more significant for Al-OCF catalyst at temperatures above 400 °C, while for SiC-OCF in the temperature range of 350 to 400 °C, decreasing further as the temperature increases and the $R_m^e$ becoming dominant at temperatures above 550 °C . On the other hand, since the external resistance to mass transfer is strongly dependent on flow conditions (e.g., temperature, pressure, and superficial gas velocity [88], the three OCF catalysts showed similar values of $R_m^e$ (all the catalytic tests were carried out under the same flow conditions). The small difference between the values could be due to the geometrical properties of each OCF such as voidage, pore, and face diameter.

Regarding the kinectic regime, the reaction resistance ($R_r$) decreases faster for the supports as greater is the thermal conductivity (Alu- and SiC-OCF, respectively). Expectedly, at low temperature the reaction resistance is the largest resistance for all the OCF catalysts. In particular, the $R_r$ becomes more important for Zir-OCF at temperatures below 300 °C, while for Alu- and SiC-OCF at temperature lower than 250 °C. Furthermore, comparing the values of Thiele modulus (ø) and effectiveness factors ($\eta$) for all the OCFs studied (see Fig. 6B), it can be noticed that the Zir-OCF obtained the lowest values of Thiele modulus ($ø_{max,@600^\circ C}$=3. 5), leading therefore to effectiveness factor values very close to 1, operating the catalytic process in a combination between kinetic ($T < 300^\circ C$; $ø \ll 1$) and transition regime ($T > 300^\circ C$). On the other hand, for Alu- and SiC-OCF, the reaction rate tends to be faster, thus obtaining higher Thiele modulus values, especially for SiC-OCF with $ø > 100$ at temperatures above 550 °C, becoming the diffusion the dominant process at $T > 350^\circ C$. It is also necessary to point out that the $R_r$ is directly dependent on the kinetics of the reaction. Thus, we first calculate the apparent rate constant per unit of the catalyst bulk density ($k^{'}$) for a first-order reaction as :

$$k^{'}(T) = \frac{1}{\tau}\cdot\ln\left(\frac{1}{1 - X_{CH4}(T)}\right) \quad (21)$$

$$\tau = \frac{W_{cat}\cdot C_{CH4}^{in}}{F_{CH4}^{in}} \quad (22)$$

where $\tau$ is the contact time ($g_{cat}$ s $m^{-3}$), $X_{CH4}$ is the conversion of methane, $W_{cat}$ is the weight of PdO/$Co_3O_4$ catalyst (0.2 $g_{cat}$) and $C_{CH4}^{in}$, $F_{CH4}^{in}$ are the inlet concentration (mol $m^{-3}$), and molar flow of methane (mol $s^{-1}$), respectively.

Then, the $k^{'}$ was plotted as a function of inverse temperature for methane conversions below 10% using the logarithmic form of the

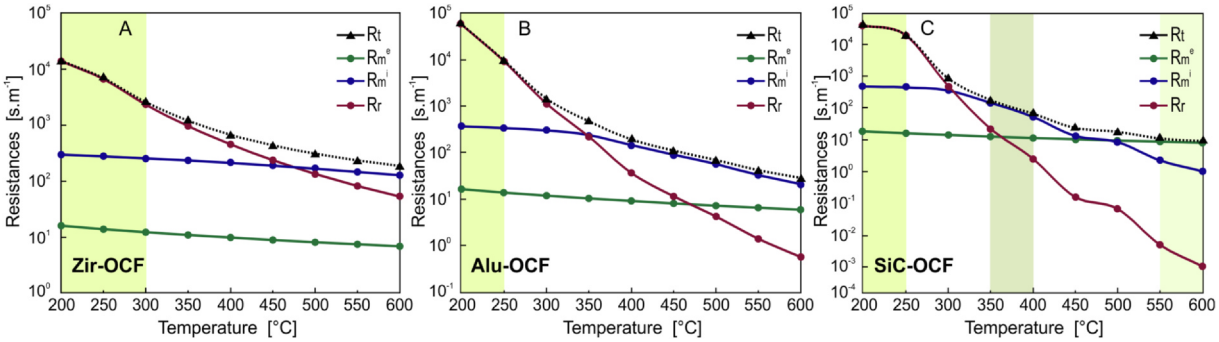


**Fig. 5.** Various resistances for the three OCF catalysts in the process of mass transfer with chemical reaction: A. Zir-OCF, B. Alu-OCF and C. SiC-OCF.

Arrhenius equation (see Fig. 6.A). The activation energy for the three OCF catalyst were found to be 85.95, 107.2 and 191.6 kJ $mol^{-1}$ for Zir-, Alu-, and SiC-OCF, respectively. The kinetic rate constants were given by the following expressions:

$$k_{Zir-OCF} = 2.78 \cdot 10^{-1} \cdot e^{-\frac{10338}{T}} \quad (23)$$

$$k_{Al-OCF} = 3.74 \cdot 10^{4} \cdot e^{-\frac{12897}{T}} \quad (24)$$

$$k_{SiC-OCF} = 2.83 \cdot 10^{12} \cdot e^{-\frac{23052}{T}} \quad (25)$$

As can be observed, lower activation energy values were obtained for Alu- and Zir-OCF. These activation energy values could correspond to the activation energies for the transition and internal diffusive regime (inside the $PdO/Co_3O_4$ catalyst). In fact, for the entire temperature range studied, the slope of the line corresponding to $-E_a/R$ (obtained by plotting the Arrhenius equation on a logarithmic scale) was practically the same for both OCF structures. On the contrary, for SiC-OCF catalyst, three zones can be distinguished: kinetic regime (at low temperatures with $CH_4$ conversions lower than 10%), internal diffusion regime (at medium temperatures), where the slope $(-E_a/R)$ corresponds to approximately half of the slope obtained for the kinetic regime ($E_a^{id} = E_a/2$), and external diffusion regime (at high temperatures) with $E_a^{ed} \approx 0$. Also, as expected, the internal diffusion activation energies ($E_a^{id}$) for the three coated OCFs showed similar values ($E_{a\,Zir-OCF}^{id} = 85.95\ kJ\ mol^{-1}$; $E_{a\,Al-OCF}^{id} = 92.4\ kJ\ mol^{-1}$; $E_{a\,SiC-OCF}^{id}$). $= 86.1\ kJ\ mol^{-1}$

### 3.4. External and internal heat transfer limitations

According to the criteria developed by Mears (Eq. 13), external heat transfer limitations are present at temperatures approximately above 215, 250, and 242 °C for Zir-, Alu- and SiC-OCF, respectively (see Fig. 7A). These heat effects could be due to the fact that the reaction starts to develop conversions higher than 10% producing more heat due to the exothermicity of the combustion process than the heat removed by the flue gases. Furthermore, analyzing the heat reaction and removal rates as a function of bulk temperature (Fig. 8), it can be noted that the heat removal ($Q$) for Zir-OCF is higher than the heat produced by the combustion reaction ($Q_r$) at bulk temperatures below 400 °C (Fig. 8A), reaching the temperature at the catalyst surface $T_s$ ($T_{s,Zir-OCF} = 453$ °C; at the steady state condition) in the metastable zone of the heat of reaction curve, for which $Q_r$ is greater than Q (Fig. 8B). On the other side, for Alu- and SiC-OCF supports, heat removal is higher than heat production at temperatures lower than 304 and 278 °C, respectively (see Fig. 8C and Fig. 8E), thus the process is operated in a stable zone reaching the $T_s$ (obtained from the intersection of the Q and $Q_r$ curves, which correspond to the steady state condition) of 317 and 286 °C for Alu- and SiC-OCF, respectively (see Fig. 8D and Fig. 8F). At higher temperatures, the process performance is in an unstable zone as the heat produced by combustion is greater than the heat removed.

On the contrary, as observed in Fig. 7B, no internal heat transfer limitations are observed according to the criterion developed by Anderson (Eq.15), thus confirming the absence of temperature gradients inside the catalytic layer.

It is important to remark that the analysis of heat and mass transfer above presented has been conducted by assuming that all pores of the foam are of circular shape, as well as circular is also the shape of the coated layer of catalyst (that is a coated catalyst of constant thickness, Fig. 4). However, as evident from FESEM images (Fig. 1), most of the foam pores are not perfectly circular, but they have an oval tendency. Thus, the characteristic lengths, both internal and external, vary. To study the effect of the pore shape and catalyst thickness on mass and heat transfer analysis, we performed a comparative analysis of mass and heat transfer for the best structured catalyst that is Zir-OCF, tested in the conditions of inlet $CH_4$ concentration of 0.5 vol% and WHSV of 30 NL $h^{-1}$ $g_{cat}{}^{-1}$.

We performed a new set of calculations for case-studies assuming the zirconia foam with pores of oval shape instead of circular. More

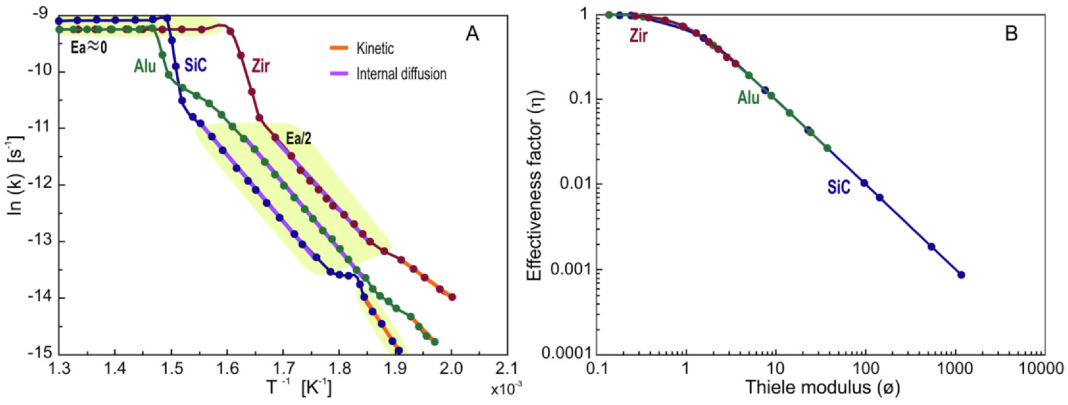


**Fig. 6.** Estimation of rate constant from the experimental data (A) and effectiveness factor vs Thiele modulus for cylindrical geometry (B) for all the OCF catalyst.

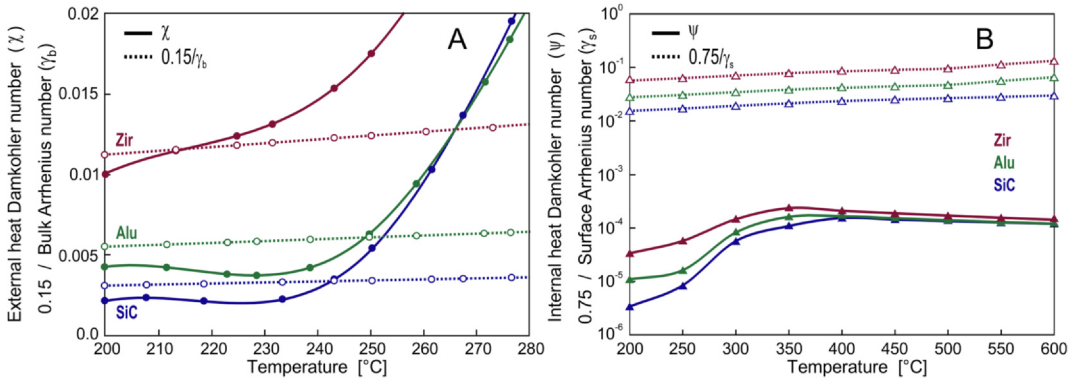


**Fig. 7.** Criteria for evaluating the effects of external heat transfer (A) and internal heat transfer (B) for all the OCF catalysts.

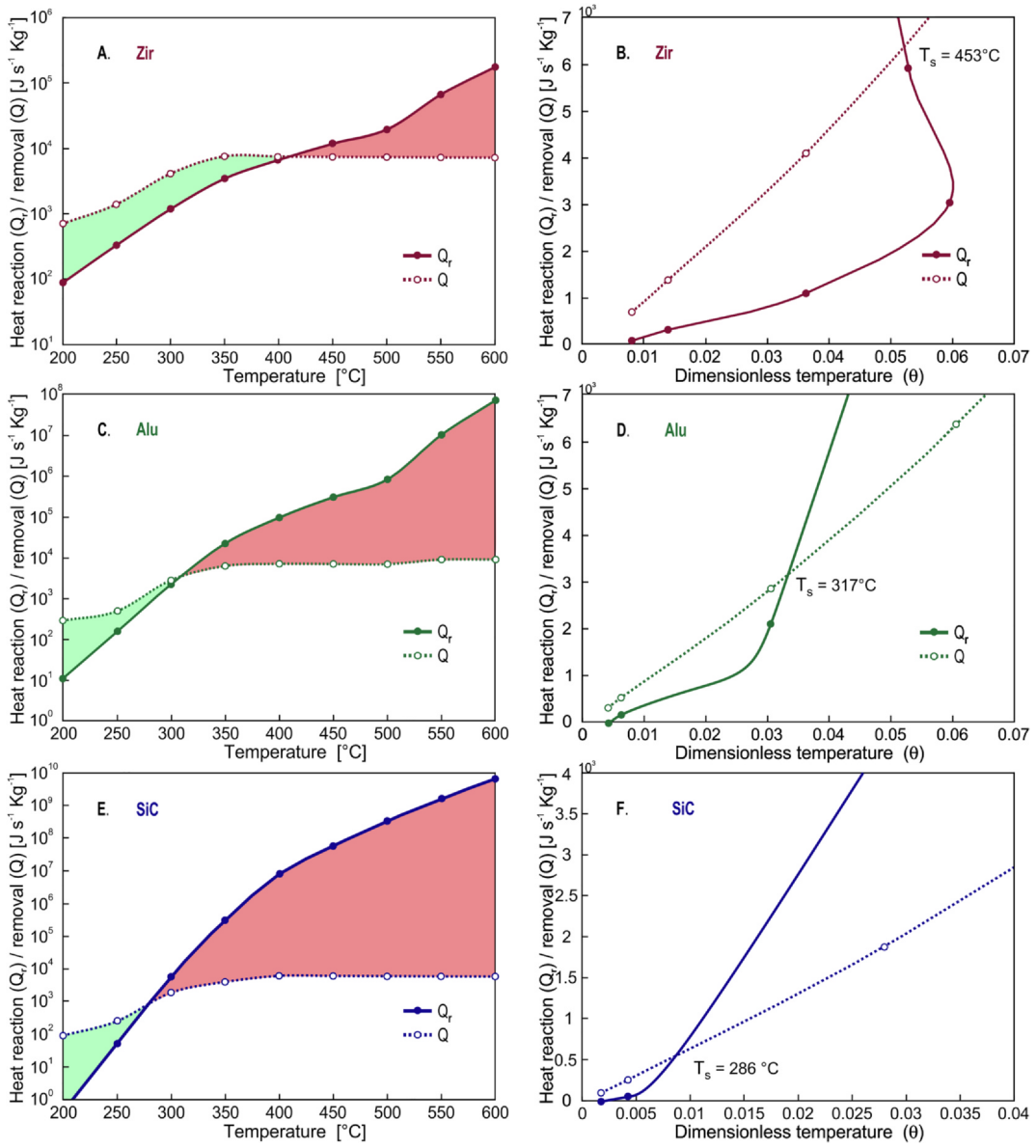


**Fig. 8.** Heat reaction and removal rates as a function of bulk and dimensionless temperatures for Zir-OCF (A/B), Alu-OCF (C/D) and SiC-OCF (E/F).

than 50 measurements were performed on FESEM images to determine the average length of the major and minor axis of the pore. For the coated catalyst layer, we considered two alternative cases, shown in Fig. 9B/C: oval (B) and circular (C) shape of the coated layer (thus, constant or variable thickness for the coated catalyst), while considering the foam pores always oval. These figures are available in an enlarged view in the *Supporting Info S.3* (FESEM Images), Figs. S3.1, S3.2, and S3.3.

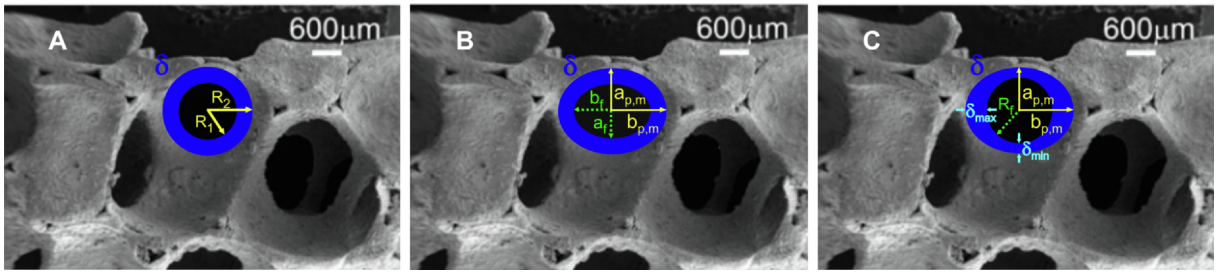


**Fig. 9.** The three different hypothesis considered to evaluate heat and mass transfer on Zir-OCF: case A) circular pore with circular deposition of the catalyst layer; case B) oval pore with oval deposition of the catalyst layer; case C): oval pore with circular deposition of the catalyst layer.

**Table 3**
Comparative heat and mass transfer analysis considering different case studies for the coated Zir-OCF (Fig. 9): case A) circular pore with circular deposition of the catalyst layer; case B) oval pore with oval deposition of the catalyst layer; case C): oval pore with circular deposition of the catalyst layer. See *Supporting Info S.4* (Diffusion and kinetic resistances of the cases A, B, and C and related Figs. S4.1, S4.2, and S4.3). Reaction conditions: inlet $CH_4$ concentration of 0.5 vol% and WHSV of 30 NL $h^{-1}$ $g_{cat}{}^{-1}$.

| | Pore-coated layer shape (Fig. 9) | | |
|---|---|---|---|
| | Circular-Circular A (Fig. S4.1) | Oval-Oval B (Fig. S4.2) | Oval-Circular C (Fig. S4.3) |
| | Temperature [°C] | | |
| Kinetic control | 300 < | 300 < | – |
| Transition I : *Kinetic predomination* | 300–474 | 300–476 | 200–283 |
| Transition II: *Internal diffusion predomination* | 474 > | 476 > | 283–550 |
| Internal mass transfer control (IMTC) | – | – | 550 > |
| $\chi = \left\lvert \frac{(-\Delta H_r)\cdot R^{obs}\cdot R_{\Omega e}}{h_e \cdot T_b} \right\rvert < \frac{0.15}{\gamma_b}$ | 215 > | 233 > | 261 > |
| $\psi = \left\lvert \frac{(-\Delta H_r \cdot R^{obs}\cdot R^2_{\Omega i})}{\lambda_e \cdot T_s} \right\rvert < \frac{0.75}{\gamma_s}$ | No internal heat transfer | | |

Table 3 shows a comparison of the effect of pore shape and catalyst thickness in terms of predominant resistances (kinetic, internal, and external diffusive) and heat transfer limitations (for 3 wt% PdO/$Co_3O_4$ catalyst on Zir-OCF, inlet $CH_4$ vol.% = 0.5, WHSV 30, temperature range 200–600 °C). As observed, when considering oval both the pore shape and catalyst thickness, the kinetic control prevails at temperatures below 300 °C (see Fig. S4.2). As the temperature increases, the reaction rate increases as well, giving rise to a Transition I regime in which the reaction kinetics predominates ($R_r^o \gg R_m^{i,o}$, $R_m^{e,o}$). At temperatures above 476 °C, the reaction rate continues to increase and the concentration in the catalyst thickness decreases. Thus, since the reaction occurs in the catalyst layer, the diffusion limitations begin to appear, and the process moves to a second Transition II regime in which internal diffusion predominates in the combustion process. These results are practically similar to those obtained previously considering of circular shape both the pore and catalyst thickness, with a negligible difference (less than 1%, comparison of Fig. S4.1 and S4.2). Regarding the heat transfer, according to Mears criterion, external heat limitations are observed at temperatures above 233 °C, showing a difference of around 18 °C with respect to the result obtained for circular pore and catalyst layer. On the other hand, the case C), with oval pore and circular catalyst thickness shape, describes the general situation in which the catalyst is deposited preferentially in some areas of the pore, exhibiting a maximum thickness ($\delta_{max}$), while in other areas only a thin layer of catalyst is present in the pore ($\delta_{min}$). As expected, with a greater accumulation of catalyst in some areas of the pore, the performance of the process in terms of predominant resistance is affected, even if not in a considerable and significant way. In this case, the internal diffusive resistance becomes predominant at a temperature above 283 °C, reaching control with respect to $R_m^{e,oc}$, and $R_r^{oc}$ at a temperature above 550 °C (see Fig. S4.3). Concerning the heat transfer, external heat limitations are observed at a temperature above 261 °C, differing from the circular pore-catalyst layer case of approximately 46 °C. No internal heat transfer limitations were found for any of the cases studied.

### 3.5. Stability measurements

Lastly, on the best selected Zir-OCF with an amount of 200 mg of $Co_3O_4$ and 3% PdO, we conducted a stability test running the reaction of $CH_4$ combustion in lean conditions for approximately 250 h of time on stream (reaction conditions: WHSV 30 NL $h^{-1}$ $g_{cat}{}^{-1}$ and 0.5 vol% $CH_4$ inlet concentration). Fig. 10 shows the comparison of the catalytic activity of the selected Zir-OCF before and after the stability test, that is in the fresh and aged status. The catalytic activity suffers of a slight worsening, with a shift of the temperature of full $CH_4$ conversion from 380 to 420 °C. The stability of such a structured catalyst can be considered good. According to the literature, the deactivation of Pd-based catalysts in $CH_4$ combustion at temperatures below 450 °C, in a fuel lean environment, can be linked with hydroxyl accumulation on the oxide supports [9,47].

Fig. 11.A/E show the high angle annular dark field (HAADF) images of the fresh and aged PdO/$Co_3O_4$ catalyst material extracted from the Zir-OCF before and after the stability test. Due to the inadequate difference in contrast between PdO and $Co_3O_4$, it was difficult to identify distinct particles of PdO or distinguish between PdO and $Co_3O_4$ using only Z-contrast in the HAADF images. Therefore, EDXS mapping was

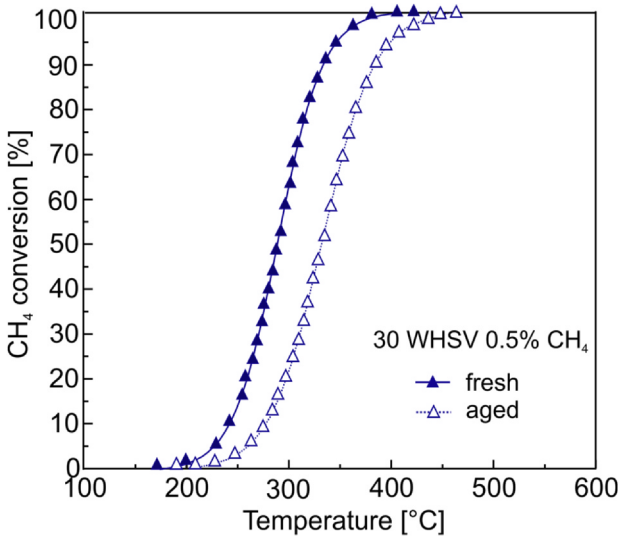


**Fig. 10.** Stability performance: $CH_4$ conversion versus temperature of the Zir-OCF coated with 3 wt% PdO on 200 mg $Co_3O_4$ (tested at 30 NL $h^{-1}$ $g_{cat}{}^{-1}$ and 0.5 vol% $CH_4$ inlet concentration) in the fresh and aged status (after 250 h of time on stream).

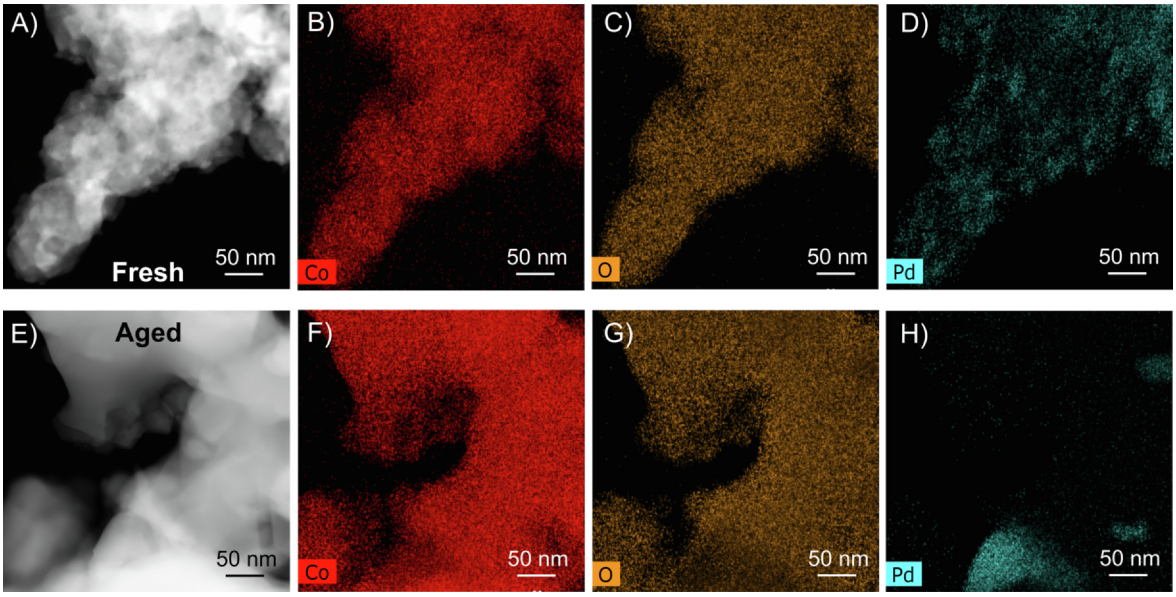


**Fig. 11.** HAADF STEM images and EDXS mappings showing Co, O, and Pd distribution in (A/B/C/D) freshly prepared PdO/$Co_3O_4$ and, (E/F/G/H) 250 h aged PdO/$Co_3O_4$, collected from Zir-OCF tested in Fig. 10.

used to identify Pd-rich regions. The Pd map of the fresh Zir-OCF in Fig. 11D shows that Pd-rich regions are distributed across the analyzed region, covering in a large and homogeneous extent the surface of the $Co_3O_4$ spinel (Fig. 11B/C). We do not have specific PdO dispersion data on this structured catalyst, but from our previous studies on 3% PdO/$Co_3O_4$ at powder level, the dispersion of PdO was around 30%, which means a high degree of coverage of PdO on the $Co_3O_4$ spinel [47], which is a result in good agreement this these EXDS mapping of PdO/$Co_3O_4$ coated on Zir-OCF. From Fig. 11, EDXS maps of Co and O overlap well with each other in the case of both fresh and aged samples, indicating an absence of Co segregation. However, morphological differences in $Co_3O_4$ between the fresh and aged samples are evident from the HAADF images. In the case of the fresh sample (Fig. 11A), the $Co_3O_4$ has a rough morphology, as confirmed also by STEM imaging (Fig. 11B), while in the aged sample (Fig. 11E) it appears to be denser. From EDXS mapping, Co and O distribution in the fresh and aged status remain apparently the same, indicating that $Co_3O_4$ crystals are preserved, while Pd distribution appears different, not anymore homogeneously distributed after use (Fig. 11H), but concentrated in some specific areas. Specifically, Fig. 11H indicates local segregation of Pd, with an expected slight reduction of PdO dispersion in the aged catalyst. This also suggests the possibility of particle coarsening, although it is difficult to confirm this directly using these HAADF images due to inadequate contrast. The mobility of Pd, in particular its segregation in areas at high and low Pd concentration could be responsible for the slightly lower performance of the aged catalyst.

## 4. Conclusions

The main contribution of this work was to analyze the performance of the 3 wt% PdO/$Co_3O_4$ catalyst supported on open cell foams of different ceramic materials (zirconia, alumina, and silicon carbide) with 30 ppi for the complete combustion of methane in lean conditions. The $Co_3O_4$ spinel was deposited by solution combustion synthesis, while PdO by wetness impregnation. External and internal mass/heat transfer effects were investigated using corroborating theory to determine the apparent kinetics and control regimes of each structured catalyst. The structured catalyst with the wider operative condition is the Zir-OCF, which always displayed temperatures of $CH_4$ combustion below 380 °C at 30 WHSV. The lowest thermal conductivity value of Zir-OCF allows reaching complete $CH_4$ conversion at lower temperature compared to the other supports, favoring this highly exothermic reaction. The diffusion inside catalytic layer (internal mass transfer) becomes more important at lower temperatures for the coated OCF with higher thermal conductivity and thicker catalytic thickness (Alu-OCF and SiC-OCF). Because the bulk diffusion (external mass transfer) is strongly dependent on flow conditions, the three OCF catalysts showed similar diffusive values (all tests were carried out at the same flow conditions).

The catalysts investigated, PdO/$Co_3O_4$, resulted highly stable after approximately 250 h of operation toward $CH_4$ combustion in lean conditions. The main suggestion from these results is that for a process intensification requiring high flowrates (that is high WHSV), the use of zirconia OCF with higher values of pore per inches is recommended to avoid external mass-transfer limitations. These results confirm the important role of the thermal conductivity in favoring the catalytic reaction.

## Declaration of Competing Interest

The authors declare that they have no known competing financial interests or personal relationships that could have appeared to influence the work reported in this paper.

## Acknowledgements

This work was performed under the SOL-CARE project (ENERG-065 funded by the Italian Ministry of Education, University and Research – MIUR – through the support of the ERANETMED network). The authors gratefully acknowledge the Global Affairs Office and Office of Vice President for Research of the University of Connecticut (UCONN) for the financial contribution. The STEM studies were performed using the facilities in the UCONN/Thermo Fisher Scientific Center for Advanced Microscopy and Materials Analysis (CAMMA). The FESEM studies were performed using the facilities in the POLITO laboratories (Mr Mauro Raimondo warmly acknowledged). G.E. gratefully acknowledges the financial support of the SOL-CARE project for her stay at UCONN.

## Appendix A. Supplementary data

Supplementary data to this article can be found online at https://doi.org/10.1016/j.cej.2020.126970.

## References


[1] S.M. Rahman, M.D. Miah, The impact of sources of energy production on globalization: evidence from panel data analysis, Renew. Sustain. Energy Rev. 74 (2017) 110–115, https://doi.org/10.1016/j.rser.2017.02.037.

[2] A. Burnham, J. Han, C.E. Clark, M. Wang, J.B. Dunn, I. Palou-Rivera, Life-cycle greenhouse gas emissions of shale gas, natural gas, coal, and petroleum, Environ. Sci. Technol. 46 (2012) 619–627, https://doi.org/10.1021/es201942m.

[3] E.K. Nam, T.E. Jensen, T.J. Wallington, Methane emissions from vehicles, Environ. Sci. Technol. 38 (2004) 2005–2010, https://doi.org/10.1021/ES034837G.

[4] N.N. Clark, D.L. McKain, D.R. Johnson, W.S. Wayne, H. Li, V. Akkerman, C. Sandoval, A.N. Covington, R.A. Mongold, J.T. Hailer, O.J. Ugarte, Pump-to-wheels methane emissions from the heavy-duty transportation sector, Environ. Sci. Technol. 51 (2017) 968–976, https://doi.org/10.1021/acs.est.5b06059.

[5] A. Raj, Methane emission control, Johnson Matthey Technol. Rev. 60 (2016) 228–235, https://doi.org/10.1595/205651316X692554.

[6] P. Gélin, L. Urfels, M. Primet, E. Tena, Complete oxidation of methane at low temperature over Pt and Pd catalysts for the abatement of lean-burn natural gas fuelled vehicles emissions: influence of water and sulphur containing compounds, Catal. Today 83 (2003) 45–57, https://doi.org/10.1016/S0920-5861(03)00215-3.

[7] N.M. Kinnunen, J.T. Hirvi, M. Suvanto, T.A. Pakkanen, Methane combustion activity of Pd–$PdO_x$–Pt/$Al_2O_3$ catalyst: the role of platinum promoter, J. Mol. Catal. A Chem. 356 (2012) 20–28, https://doi.org/10.1016/j.molcata.2011.12.023.

[8] P. Castellazzi, G. Groppi, P. Forzatti, E. Finocchio, G. Busca, Activation process of Pd/$Al_2O_3$ catalysts for $CH_4$ combustion by reduction/oxidation cycles in $CH_4$-containing atmosphere, J. Catal. 275 (2010) 218–227, https://doi.org/10.1016/j.jcat.2010.07.028.

[9] W.R. Schwartz, L.D. Pfefferle, Combustion of methane over palladium-based catalysts: Support interactions, J. Phys. Chem. C 116 (2012) 8571–8578, https://doi.org/10.1021/jp2119668.

[10] L.F. Liotta, G. Di Carlo, G. Pantaleo, G. Deganello, Catalytic performance of $Co_3O_4$/$CeO_2$ and $Co_3O_4$/$CeO_2$–$ZrO_2$ composite oxides for methane combustion: Influence of catalyst pretreatment temperature and oxygen concentration in the reaction mixture, Appl. Catal. B Environ. 70 (2007) 314–322, https://doi.org/10.1016/j.apcatb.2005.12.023.

[11] G. Ercolino, P. Stelmachowski, A. Kotarba, S. Specchia, Reactivity of mixed iron–cobalt spinels in the lean methane combustion, Top. Catal. 60 (2017) 1370–1379, https://doi.org/10.1007/s11244-017-0826-9.

[12] M.M. Fiuk, A. Adamski, Activity of $MnO_x$–$CeO_2$ catalysts in combustion of low concentrated methane, Catal. Today. 257 (2015) 131–135, https://doi.org/10.1016/j.cattod.2015.01.029.

[13] S. Specchia, A. Civera, G. Saracco, V. Specchia, Palladium/perovskite/zirconia catalytic premixed fiber burners for efficient and clean natural gas combustion, Catal. Today 117 (2006) 427–432, https://doi.org/10.1016/j.cattod.2006.06.041.

[14] N. Miniajluk, J. Trawczyński, M. Zawadzki, P.E. Tomaszewski, W. Mišta, Solvothermal synthesis and characterization of mixed oxides with perovskite-like structure, Catal. Today 257 (2015) 26–34, https://doi.org/10.1016/j.cattod.2015.03.029.

[15] Y. Wang, H. Arandiyan, J. Scott, M. Akia, H. Dai, J. Deng, K.-F. Aguey-Zinsou, R. Amal, High performance Au–Pd supported on 3D hybrid strontium-substituted lanthanum manganite perovskite catalyst for methane combustion, ACS Catal. 6 (2016) 6935–6947, https://doi.org/10.1021/acscatal.6b01685.

[16] A.M. Venezia, V. La Parola, L.F. Liotta, Structural and surface properties of heterogeneous catalysts: Nature of the oxide carrier and supported particle size effects, Catal. Today 285 (2017) 114–124, https://doi.org/10.1016/j.cattod.2016.11.004.

[17] U. Zavyalova, P. Scholz, B. Ondruschka, Influence of cobalt precursor and fuels on the performance of combustion synthesized $Co_3O_4$/γ-$Al_2O_3$ catalysts for total oxidation of methane, Appl. Catal. A Gen. 323 (2007) 226–233, https://doi.org/10.1016/j.apcata.2007.02.021.

[18] P. Avila, M. Montes, E.E. Miró, Monolithic reactors for environmental applications: a review on preparation technologies, Chem. Eng. J. 109 (2005) 11–36, https://doi.org/10.1016/j.cej.2005.02.025.

[19] M.V. Twigg, J.T. Richardson, Fundamentals and applications of structured ceramic foam catalysts, Ind. Eng. Chem. Res. 46 (2007) 4166–4177, https://doi.org/10.1021/ie061122o.

[20] E. Tronconi, G. Groppi, C.G. Visconti, Structured catalysts for non-adiabatic applications, Curr. Opin. Chem. Eng. 5 (2014) 55–67, https://doi.org/10.1016/j.coche.2014.04.003.

[21] S. Voltolina, P. Marín, F.V. Díez, S. Ordóñez, Open-cell foams as beds in multiphase reactors: residence time distribution and mass transfer, Chem. Eng. J. 316 (2017) 323–331, https://doi.org/10.1016/j.cej.2017.01.113.

[22] R. Balzarotti, C. Italiano, L. Pino, C. Cristiani, A. Vita, Ni/$CeO_2$-thin ceramic layer depositions on ceramic monoliths for syngas production by Oxy Steam Reforming of biogas, Fuel Process. Technol. 149 (2016) 40–48, https://doi.org/10.1016/j.fuproc.2016.04.002.

[23] M.A. Ashraf, O. Sanz, C. Italiano, A. Vita, M. Montes, S. Specchia, Analysis of Ru/La-$Al_2O_3$ catalyst loading on alumina monoliths and controlling regimes in methane steam reforming, Chem. Eng. J. 334 (2018) 1792–1807, https://doi.org/10.1016/j.cej.2017.11.154.

[24] K. Pangarkar, T.J. Schildhauer, J.R. Van Ommen, J. Nijenhuis, F. Kapteijn, J.A. Moulijn, Structured packings for multiphase catalytic reactors, Ind. Eng. Chem. Res. 47 (2008) 3720–3751, https://doi.org/10.1021/ie800067r.

[25] F. García-Moreno, Commercial applications of metal foams: Their properties and production, Materials 9 (2016) 20–24, https://doi.org/10.3390/ma9020085.

[26] Lanik Foam Ceramics, https://www.lanik.eu/en/.

[27] ERG materials & aerospace, http://ergaerospace.com/.

[28] Fraunhofer IFAM, https://www.ifam.fraunhofer.de/content/dam/ifam/en/documents/dd/Infoblätter/open_cell_metal_foams_fraunhofer_ifam_dresden.pdf.

[29] T. Wan, Y. Liu, C. Zhou, X. Chen, Y. Li, Fabrication, properties, and applications of open-cell aluminum foams: a review, J. Mater. Sci. Technol. 62 (2021) 11–24, https://doi.org/10.1016/j.jmst.2020.05.039.

[30] I. Švecová, E. Tillová, L. Kuchariková, Improving the quality of Al-Si castings by using ceramic filters, Prod. Eng. Arch. 26 (2020) 19–24, https://doi.org/10.30657/pea.2020.26.05.

[31] C. Italiano, M.A. Ashraf, L. Pino, C.W. Moncada Quintero, S. Specchia, A. Vita, Rh/$CeO_2$ thin catalytic layer deposition on alumina foams: Catalytic performance and controlling regimes in biogas reforming processes, Catalysts 8 (2018) 1–25, https://doi.org/10.3390/catal8100448.

[32] M. Luneau, E. Gianotti, N. Guilhaume, E. Landrivon, F.C. Meunier, C. Mirodatos, Y. Schuurman, Experiments and modeling of methane autothermal reforming over structured Ni–Rh-based Si-SiC foam catalysts, Ind. Eng. Chem. Res. 56 (2017) 13165–13174.

[33] G. Ercolino, P. Stelmachowski, S. Specchia, Catalytic Performance of Pd/$Co_3O_4$ on SiC and $ZrO_2$ Open Cell Foams for Process Intensification of Methane Combustion in Lean Conditions, Ind. Eng. Chem. Res. 56 (2017) 6625–6636, https://doi.org/10.1021/acs.iecr.7b01087.

[34] G. Ercolino, S. Karimi, P. Stelmachowski, S. Specchia, Catalytic combustion of residual methane on alumina monoliths and open cell foams coated with Pd/$Co_3O_4$, Chem. Eng. J. 326 (2017) 339–349, https://doi.org/10.1016/j.cej.2017.05.149.

[35] O. Sanz, F.J. Echave, M. Sánchez, A. Monzón, M. Montes, Aluminium foams as structured supports for volatile organic compounds (VOCs) oxidation, Appl. Catal. A Gen. 340 (2008) 125–132, https://doi.org/10.1016/j.apcata.2008.02.007.

[36] F.C. Patcas, G.I. Garrido, B. Kraushaar-Czarnetzk, CO oxidation over structured carriers: a comparison of ceramic foams, honeycombs and beads, Chem. Eng. Sci. 62 (2007) 3984–3990, https://doi.org/10.1016/j.ces.2007.04.039.

[37] L. Giani, G. Groppi, E. Tronconi, Mass-transfer characterization of metallic foams as supports for structured catalysts, Ind. Eng. Chem. Res. 44 (2005) 4993–5002, https://doi.org/10.1021/ie0490886.

[38] A. Aguirre, V. Chandra, E.A.J.F. Peters, J.A.M. Kuipers, M.F. Neira D'Angelo, Open-cell foams as catalysts support: a systematic analysis of the mass transfer limitations, Chem. Eng. J. 393 (2020) 124656, , https://doi.org/10.1016/j.cej.2020.124656.

[39] G. Pauletto, A. Vaccari, G. Groppi, L. Bricaud, P. Benito, D.C. Boffito, J.A. Lercher, G.S. Patience, FeCrAl as a catalyst support, Chem. Rev. 120 (2020) 7516–7550.

[40] Z. Ren, V. Botu, S. Wang, Y. Meng, W. Song, Y. Guo, R. Ramprasad, S.L. Suib, P.-X. Gao, Monolithically integrated spinel $M_xCo_{3-x}O_4$ (M = Co, Ni, Zn) nanoarray catalysts: scalable synthesis and cation manipulation for tunable low-temperature $CH_4$ and CO oxidation, Angew. Chemie. 126 (2014) 7351–7355, https://doi.org/10.1002/ange.201403461.

[41] I.V. Lukiyanchuk, V.S. Rudnev, I.V. Chernykh, I.V. Malyshev, L.M. Tyrina, M.V. Adigamova, Composites with transition metal oxides on aluminum and titanium and their activity in CO oxidation, Surf. Coatings Technol. 231 (2013) 433–438, https://doi.org/10.1016/j.surfcoat.2012.10.031.

[42] J.C. Védrine, I. Fechete, Heterogeneous partial oxidation catalysis on metal oxides, Comptes Rendus Chim. 19 (2016) 1203–1225, https://doi.org/10.1016/j.crci.2015.09.021.

[43] B. Farin, A.H.A. Monteverde Videla, S. Specchia, E.M. Gaigneaux, Bismuth molybdates prepared by solution combustion synthesis for the partial oxidation of propene, Catal. Today (2015) 11–17, https://doi.org/10.1016/j.cattod.2015.03.045.

[44] P. Stelmachowski, G. Maniak, J. Kaczmarczyk, F. Zasada, W. Piskorz, A. Kotarba, Z. Sojka, Mg and Al substituted cobalt spinels as catalysts for low temperature de$N_2O$-evidence for octahedral cobalt active sites, Appl. Catal. B Environ. 146 (2014) 105–111, https://doi.org/10.1016/j.apcatb.2013.05.027.

[45] P. Stelmachowski, K. Ciura, G. Grzybek, Morphology-dependent reactivity of cobalt oxide nanoparticles in $N_2O$ decomposition, Catal. Sci. Technol. 6 (2016) 5554–5560, https://doi.org/10.1039/c6cy00365f.

[46] G. Ercolino, G. Grzybek, P. Stelmachowski, S. Specchia, A. Kotarba, V. Specchia, Pd/$Co_3O_4$-based catalysts prepared by solution combustion synthesis for residual methane oxidation in lean conditions, Catal. Today 257 (2015) 66–71, https://doi.org/10.1016/j.cattod.2015.03.006.

[47] G. Ercolino, P. Stelmachowski, G. Grzybek, A. Kotarba, S. Specchia, Optimization of Pd catalysts supported on $Co_3O_4$ for low-temperature lean combustion of residual methane, Appl. Catal. B Environ. 206 (2017) 712–725, https://doi.org/10.1016/j.apcatb.2017.01.055.

[48] F. Zasada, W. Piskorz, S. Cristol, J.F. Paul, A. Kotarba, Z. Sojka, Periodic density functional theory and atomistic thermodynamic studies of cobalt spinel nanocrystals in wet environment: molecular interpretation of water adsorption equilibria, J. Phys. Chem. C 114 (2010) 22245–22253, https://doi.org/10.1021/jp109264b.

[49] F. Zasada, W. Piskorz, Z. Sojka, Cobalt spinel at various redox conditions: DFT + U investigations into the structure and surface thermodynamics of the (100) facet, J. Phys. Chem. C 119 (2015) 19180–19191, https://doi.org/10.1021/acs.jpcc.5b05136.

[50] G. Ercolino, A. Grodzka, G. Grzybek, P. Stelmachowski, S. Specchia, A. Kotarba, The Effect of the preparation method of pd-doped cobalt spinel on the catalytic activity in methane oxidation under lean fuel conditions, Top. Catal. 60 (2017) 333–341, https://doi.org/10.1007/s11244-016-0620-0.

[51] A. Varma, A.S. Rogachev, A.S. Mukasyan, S. Hwang, Combustion synthesis of advanced materials: principles and applications, Adv. Chem. Eng. 24 (1998) 79–226, https://doi.org/10.1016/S0065-2377(08)60093-9.

[52] S. Specchia, E. Finocchio, G. Busca, V. Specchia, Combustion Synthesis, Wiley-VCH

Verlag GmbH & Co. KGaA, 2010. doi: 10.1002/9783527628148.hoc088.
[53] S. Specchia, C. Galletti, V. Specchia, Solution combustion synthesis as intriguing technique to quickly produce performing catalysts for specific applications, Elsevier Masson SAS (2010), https://doi.org/10.1016/S0167-2991(10)75008-4.
[54] A. Varma, A.S. Mukasyan, A.S. Rogachev, K.V. Manukyan, Solution Combustion synthesis of nanoscale materials, Chem. Rev. 116 (2016) 14493–14586, https://doi.org/10.1021/acs.chemrev.6b00279.
[55] S. Specchia, G. Ercolino, S. Karimi, C. Italiano, A. Vita, Solution combustion synthesis for preparation of structured catalysts: a mini-review on process intensification for energy applications and pollution control, Int. J. Self-Propagating High-Temperature Synth. 26 (2017) 166–186, https://doi.org/10.3103/S1061386217030062.
[56] F. Deganello, A.K. Tyagi, Solution combustion synthesis, energy and environment: best parameters for better materials, Prog. Cryst. Growth Charact. Mater. 64 (2018) 23–61, https://doi.org/10.1016/j.pcrysgrow.2018.03.001.
[57] U.-S. Amjad, C.W. Moncada Quintero, G. Ercolino, C. Italiano, A. Vita, S. Specchia, Methane steam reforming on the Pt/$CeO_2$ catalyst: effect of daily start-up and shut-down on long-term stability of the catalyst, Ind. Eng. Chem. Res. 58 (2019) 16395–16406, https://doi.org/10.1021/acs.iecr.9b02436.
[58] A. Vita, G. Cristiano, C. Italiano, L. Pino, S. Specchia, Syngas production by methane oxy-steam reforming on Me/$CeO_2$ (Me = Rh, Pt, Ni) catalyst lined on cordierite monoliths, Appl. Catal. B Environ. 162 (2015) 551–563, https://doi.org/10.1016/j.apcatb.2014.07.028.
[59] D.F.M. Santos, O.S.G.P. Soares, J.L. Figueiredo, O. Sanz, M. Montes, M.F.R. Pereira, Preparation of ceramic and metallic monoliths coated with cryptomelane as catalysts for VOC abatement, Chem. Eng. J. 382 (2020) 122923, , https://doi.org/10.1016/j.cej.2019.122923.
[60] S.Y. Joshi, M.P. Harold, V. Balakotaiah, Overall mass transfer coefficients and controlling regimes in catalytic monoliths, Chem. Eng. Sci. 65 (2010) 1729–1747, https://doi.org/10.1016/j.ces.2009.11.021.
[61] S.Y. Joshi, M.P. Harold, V. Balakotaiah, On the use of internal mass transfer coefficients in modeling of diffusion and reaction in catalytic monoliths, Chem. Eng. Sci. 64 (2009) 4976–4991, https://doi.org/10.1016/j.ces.2009.08.008.
[62] S.Y. Joshi, Y. Ren, M.P. Harold, V. Balakotaiah, Determination of kinetics and controlling regimes for $H_2$ oxidation on Pt/$Al_2O_3$ monolithic catalyst using high space velocity experiments, Appl. Catal. B Environ. 102 (2011) 484–495, https://doi.org/10.1016/j.apcatb.2010.12.030.
[63] V. Balakotaiah, R.R. Ratnakar, On the use of transfer and dispersion coefficient concepts in low-dimensional diffusion-convection-reaction models, Chem. Eng. Res. Des. 88 (2010) 342–361, https://doi.org/10.1016/j.cherd.2009.10.008.
[64] G. Incera Garrido, F.C. Patcas, S. Lang, B. Kraushaar-Czarnetzki, Mass transfer and pressure drop in ceramic foams: A description for different pore sizes and porosities, Chem. Eng. Sci. 63 (2008) 5202–5217, https://doi.org/10.1016/j.ces.2008.06.015.
[65] L.K.-M. Madhvanand N. Kashid, Albert Renken, Microstructured Devices for Chemical Processing, Wiley-VCH Verlag GmbH & Co. KGaA, 2013. doi: 10.1002/9783527685226.
[66] M. Bhattacharya, M.P. Harold, V. Balakotaiah, Mass-transfer coefficients in wash-coated monoliths, AIChE J. 50 (2004) 2939–2955, https://doi.org/10.1002/aic.10212.
[67] A.K.A. Zeynep Ilsen Onsan, Multiphase Catalytic Reactors, John Wiley & Sons, Hoboker, New Jersey, 2016. doi: 10.1002/9781119248491.
[68] J.J. Carberry, Chemical and Catalytic Reaction Engineering, McGraw-Hill, New York, 1976.
[69] D.E. Mears, Diagnostic criteria for heat transport limitations in fixed bed reactors, J. Catal. 20 (1971) 127–131, https://doi.org/10.1016/0021-9517(71)90073-X.
[70] R.P. Chhabra, Fluid Flow and Heat Transfer from Circular and Noncircular Cylinders Submerged in Non-Newtonian Liquids, in: Y.I. Cho, G.A. Greene (Eds.), Adv. Heat Transf. Vol. 43, Elsevier Ltd, 2011: pp. 289–417. doi:10.1016/B978-0-12-381529-3.00004-9.
[71] F.P. Incropera, D.P. DeWitt, Fundamentals of Heat and Mass Transfer, IV, Prentice Hall, Mexico, 1996. doi:10.1016/j.applthermaleng.2011.03.022.
[72] J.B. Anderson, A criterion for isothermal behaviour of a catalyst pellet, Chem. Eng. Sci. 1 (1963) 147–148.
[73] F.C. Buciuman, B. Kraushaar-Czarnetzki, Ceramic Foam monoliths as catalyst carriers. 1. Adjustment and description of the morphology, Ind. Eng. Chem. Res. 42 (2003) 1863–1869, https://doi.org/10.1021/ie0204134.
[74] A. Inayat, H. Freund, T. Zeiser, W. Schwieger, Determining the specific surface area of ceramic foams: The tetrakaidecahedra model revisited, Chem. Eng. Sci. 66 (2011) 1179–1188, https://doi.org/10.1016/j.ces.2010.12.031.
[75] W.-L. Huo, X.-Y. Zhang, Y.-G. Chen, Y.-J. Lu, W.-T. Liu, X.-Q. Xi, Y.-L. Wang, J. Xu, J.-L. Yang, Highly porous zirconia ceramic foams with low thermal conductivity from particle-stabilized foams, J. Am. Ceram. Soc. 99 (2016) 3512–3515, https://doi.org/10.1111/jace.14555.
[76] T. Shimizu, K. Matsuura, H. Furue, K. Matsuzak, Thermal conductivity of high porosity alumina refractory bricks made by a slurry gelation and foaming method, J. Eur. Ceram. Soc. 33 (2013) 3429–3435, https://doi.org/10.1016/j.jeurceramsoc.2013.07.001.
[77] T. Fend, B. Hoffschmidt, R. Pitz-Paal, O. Reutter, P. Rietbrock, Porous materials as open volumetric solar receivers: Experimental determination of thermophysical and heat transfer properties, Energy 29 (2004) 823–833, https://doi.org/10.1016/S0360-5442(03)00188-9.
[78] O. Sanz, I. Velasco, I. Reyero, I. Legorburu, G. Arzamendi, L.M. Gandía, M. Montes, Effect of the thermal conductivity of metallic monoliths on methanolsteam reforming, Catal. Today 273 (2016) 131–139, https://doi.org/10.1016/j.cattod.2016.03.008.
[79] D. Ugues, S. Specchia, G. Saracco, Optimal microstructural design of a catalytic premixed FeCrAlloy fiber burner for methane combustion, Ind. Eng. Chem. Res. 43 (2004) 1990–1998, https://doi.org/10.1021/ie034202q.
[80] L.C. Almeida, F.J. Echave, O. Sanz, M.A. Centeno, J.A. Odriozola, M. Montes, Washcoating of metallic monoliths and microchannel reactors, in, Stud. Surf. Sci. Catal. (2010) 25–33, https://doi.org/10.1016/S0167-2991(10)75004-7.
[81] M.A. Ashraf, O. Sanz, M. Montes, S. Specchia, Insights into the effect of catalyst loading on methane steam reforming and controlling regime for metallic catalytic monoliths, Int. J. Hydrogen Energy 43 (2018) 11778–11792, https://doi.org/10.1016/j.ijhydene.2018.04.126.
[82] V.G. Hadjiev, M.N. Iliev, I.V. Vergilov, The Raman spectra of $Co_3O_4$, J. Phys. C Solid State Phys. 21 (1988) L199–L201, https://doi.org/10.1088/0022-3719/21/7/007.
[83] A. Alvarez, S. Ivanova, M.A. Centeno, J.A. Odriozola, Sub-ambient CO oxidation over mesoporous $Co_3O_4$: effect of morphology on its reduction behavior and catalytic performance, Appl. Catal. A Gen. 431–432 (2012) 9–17, https://doi.org/10.1016/j.apcata.2012.04.006.
[84] P.J. Jodłowski, R.J. Jędrzejczyk, D. Chlebda, M. Gierada, J. Łojewska, In situ spectroscopic studies of methane catalytic combustion over Co, Ce, and Pd mixed oxides deposited on a steel surface, J. Catal. 350 (2017) 1–12, https://doi.org/10.1016/j.jcat.2017.03.022.
[85] C.G. Visconti, E. Tronconi, G. Groppi, L. Lietti, M. Iovane, S. Rossini, R. Zennaro, Monolithic catalysts with high thermal conductivity for the Fischer-Tropsch synthesis in tubular reactors, Chem. Eng. J. 171 (2011) 1294–1307, https://doi.org/10.1016/j.cej.2011.05.014.
[86] C.G. Visconti, G. Groppi, E. Tronconi, Accurate prediction of the effective radial conductivity of highly conductive honeycomb monoliths with square channels, Chem. Eng. J. 223 (2013) 224–230, https://doi.org/10.1016/j.cej.2013.02.095.
[87] M. Bracconi, M. Ambrosetti, M. Maestri, G. Groppi, E. Tronconi, A fundamental analysis of the influence of the geometrical properties on the effective thermal conductivity of open-cell foams, Chem. Eng. Process. – Process Intensif. 129 (2018) 181–189, https://doi.org/10.1016/j.cep.2018.04.018.
[88] H. Scott Fogler, Elements of Chemical Reaction Engineering, 5th ed., Pearson Education Inc., Kendallville, Indiana (USA), 2016.

# Supporting Information

# of

# Analysis of heat and mass transfer limitations for the combustion of methane emissions on $PdO/Co_3O_4$ coated on ceramic open cell foams

*Carmen W. Moncada Quintero[1]*, Giuliana Ercolino[1], Abhinav Poozhikunnath[2,3], Radenka Maric[2,3], Stefania Specchia[1]**

[1] *Politecnico di Torino, Department of Applied Science and Technology, Corso Duca degli Abruzzi 24, 10129 Torino, Italy*

[2] *University of Connecticut, Department of Materials Science and Engineering, 97 North Eagleville Road, Storrs, CT 06269, USA*

[3] *University of Connecticut, Center for Clean Energy Engineering, 44 Weaver Road, Storrs, CT, 06269-5233, USA*

* Corresponding authors: carmen.moncada@polito.it, stefania.specchia@polito.it

In the following, a detailed explanation of the calculations of textural and geometrical properties of the OCF and the characteristic length scales for transverse diffusion is reported.

## S.1. Estimation of the textural and geometrical properties of the OCF

The volume of the OCF was calculated as:

$$V_{OCF} = \frac{\pi \cdot d_{OCF}^2}{4} \cdot L_{OCF} \quad \text{A.1}$$

where $V_{OCF}$ is the volume of the OCF ($m^3$), $d_{OCF}$ is the diameter of the OCF ($d_{OCF} = 9 \cdot 10^{-3}\ m$) and $L_{OCF}$ is the length of the OCF ($L_{OCF} = 30 \cdot 10^{-3}\ m$).

The face diameter of the OCF was determined by [1]:

$$d_f = d_p + t_s \quad \text{A.2}$$

where $d_f$ is the face diameter of the OCF (m), $d_p$ is the average pore diameter of the OCF (measured by SEM : Zir-OCF = 1.30 ± 0.73 mm; Alu-OCF = 1.34 ± 0.55 mm and SiC-OCF = 1.63 ± 0.65 mm) and $t_s$ is the average strut thickness of the OCF (measured by SEM: Zir-OCF = 0.47 ± 0.16 mm; Alu-OCF = 0.34 ± 0.10 mm and SiC-OCF = 0.42 ± 0.16 mm) [2]

The foam relative density of the OCF was calculated by:

$$\rho_r = 2.59 \cdot \left(\frac{t_s}{d_f}\right)^2 \quad \text{A.3}$$

where $t_s$ is the average strut thickness of the OCF and $d_f$ is the face diameter of the OCF (m).

The voidage of the OCF was determined as:

$$\varepsilon = 1 - \rho_r \quad \text{A.4}$$

where $\varepsilon$ is the voidage of the OCF (-).

The geometrical surface area of the OCF was calculated as:

$$S_{ga} = \frac{4.82}{d_f} \cdot \sqrt{\rho_r} \quad \text{A.5}$$

where $S_{ga}$ is the geometrical surface area of the OCF ($m^{-1}$).

The surface area of the OCF was determined by:

$$S_a = V_{OCF} \cdot S_{ga} \quad \text{A.6}$$

where $S_a$ is the surface area of the OCF ($m^2$).

The catalyst loading was calculated as:

$$C_{load} = \frac{m_{cat}}{S_a} \quad \text{A.7}$$

where $C_{load}$ is the catalyst loading on the OCF (g $m^{-2}$) and $m_{cat}$ is the catalyst mass deposited on the OCF (g).

The catalyst thickness on the OCF was calculated as:

$$\delta = \frac{C_{load}}{\rho_{cat}} \quad \text{A.8}$$

where $\delta$ is the catalyst thickness on the OCF (m) and $\rho_{cat}$ is the catalyst density ($\rho_{cat} = 2 \cdot 10^6\ g \cdot m^3\ for\ 3\ wt.\%\ Pd/Co_3O_4$).

## S.2. Estimation of the characteristic length scale for transverse diffusion

### S.2.1 Characteristic length scale for the gas phase

The characteristic length scale for the gas phase ($R_{\Omega,e}$) is defined as the ratio of the flow area ($A_{\Omega,e}$) to the gas-coated layer interfacial perimeter ($P_\Omega$).

Assuming that the $Pd/Co_3O_4$ catalyst is uniformly distributed inside the pores of the OCF and considering that the shape of both the pore and the catalytic layer is circular (**Fig. S3.1** Case A.), the $R_{\Omega,e}$ (m) was determined as [3–5]:

$$R_{\Omega,e} = \frac{A^c_{\Omega,e}}{P^c_\Omega} \quad \text{A.9}$$

$$A^c_{\Omega,e} = \frac{\pi \cdot d^2_{p_c}}{4} \quad \text{A.10}$$

$$P^c_\Omega = \pi \cdot d_{p_c} \quad \text{A.11}$$

where $A^c_{\Omega,e}$ is the cross-sectional area of fluid phase for circular shape of the pore and catalyst layer ($m^2$), $d_{p_c}$ is the catalyst-coated pore diameter of the OCF (where $d_{p_c}(m) = 2 \cdot R_1$), $P^c_\Omega$ is the gas-coated catalyst layer circular interfacial perimeter (m).

Similarly, assuming oval shape of the pore and catalyst coated layer (**Fig. S3.2** Case B.), the $R_{\Omega,\mathrm{e}}$ (m) was determined considering the properties of an oval as:

$$R_{\Omega,\mathrm{e}} = \frac{A^{o}_{\Omega,\mathrm{e}}}{P^{o}_{\Omega}} \quad \text{A.12}$$

$$A^{o}_{\Omega,\mathrm{e}} = \pi \cdot a_f \cdot b_f \quad \text{A.13}$$

$$P^{o,*}_{\Omega} = 2 \cdot \pi \sqrt{\frac{{a_f}^2 + {b_f}^2}{2}}; \text{ for } b_f < 3 \cdot a_f \quad \text{A.14}$$

$$P^{o,**}_{\Omega} = \pi \cdot \left[3 \cdot \left(a_f + b_f\right) - \sqrt{(3 \cdot a_f + b_f) \cdot (a_f + 3 \cdot b_f)}\right] \quad \text{A.15}$$

where $A^{o}_{\Omega,\mathrm{e}}$ is the cross-sectional area of fluid phase for oval shape of the pore and catalyst layer (m$^2$), $a_f$ is the semi-minor axe of the oval coated pore (m), $b_f$ is the semi-major axe of the oval coated pore (m), $P^{o,*}_{\Omega}$ (m) is the gas-coated catalyst layer oval interfacial perimeter (Eq. A.14 valid when $b_f < 3 \cdot a_f$), $P^{o,**}_{\Omega}$ (m) is the gas-coated catalyst layer oval interfacial perimeter derived by Ramanujan.

To study the general situation in which the catalyst is deposited preferentially in some areas of the pore, accumulating a thicker layer of catalyst ($\delta_{max}$), while in other zones of the pore only a thin catalytic layer is deposited ($\delta_{min}$), we consider the case of an OCF with oval pore shape where the catalyst is deposited inside the inner wall of the pore with a circular shape of catalytic layer (**Fig. S3.3** Case C.). Thus, the $R_{\Omega,\mathrm{e}}$ (m) was calculated as:

$$R_{\Omega,\mathrm{e}} = \frac{A^{cc}_{\Omega,\mathrm{e}}}{P^{cc}_{\Omega}} \quad \text{A.16}$$

$$A^{oc}_{\Omega,\mathrm{e}} = \frac{\pi \cdot {d^2_p}_{cc}}{4} \quad \text{A.17}$$

$$P^{oc}_{\Omega} = \pi \cdot {d_p}_{cc} \quad \text{A.18}$$

where $A^{cc}_{\Omega,\mathrm{e}}$ is the cross-sectional area of fluid phase for circular shape of the catalyst layer (m$^2$), ${d_p}_{cc}$ is the catalyst-coated pore diameter of the OCF (m), $P^{cc}_{\Omega}$ (m) is the gas-coated catalyst layer circular interfacial perimeter (considering oval bare pore of OCF and circular coated layer shape).

### S.2.2 Characteristic length scale for the coated layer

The characteristic length scale for the catalyst layer ($R_{\Omega,\mathrm{i}}$) is defined as the ratio of coated catalyst layer cross-sectional area ($A_{\Omega,\mathrm{i}}$) to the interfacial perimeter ($P_{\Omega}$).

For the case A (pore and coated catalyst layer with circular shape), the $R_{\Omega,\mathrm{i}}$ (m) was determined as [3–5]:

$$R_{\Omega,\mathrm{i}} = \frac{A^{c}_{\Omega,\mathrm{i}}}{P^{c}_{\Omega}} \quad \text{A.19}$$

$$A^{c}_{\Omega,\mathrm{i}} = \frac{\pi}{4} \cdot ({d^2_p}_b - {d^2_p}_c) \quad \text{A. 20}$$

where $A^{c}_{\Omega,i}$ is the cross-sectional area of the coated catalyst layer for circular shape of the bare pore and coated catalyst ($m^2$), $d_{p_b}$ (m) is the pore diameter of the bare OCF (where $d_{p_b} = 2 \cdot R_2$).

For the case B (oval shape of the pore and coated catalyst layer), the $R_{\Omega,i}$ (m) was determined as:

$$R_{\Omega,i} = \frac{A^{o}_{\Omega,i}}{P^{o}_{\Omega}} \quad \text{A.21}$$

$$A^{o}_{\Omega,i} = \pi \cdot (a_{p,m} \cdot b_{p,m} - a_f \cdot b_f) \quad \text{A.22}$$

where $A^{o}_{\Omega,i}$ is the cross-sectional area of the coated catalyst layer for oval shape of the bare pore and coated catalyst ($m^2$), $a_{p,m}$ is the average of semi-minor axe of the oval bare pore (m), $b_{p,m}$ is the average of semi-major axe of the oval coated pore (m), $P^{o}_{\Omega}$ (m) is the gas-coated catalyst layer oval interfacial perimeter (calculated using Equation A.14 or A.15)

For the case C (oval pore shape and circular shape of the coated catalyst layer), the $R_{\Omega,i}$ (m) was calculated as:

$$R_{\Omega,i} = \frac{A^{oc}_{\Omega,i}}{P^{oc}_{\Omega}} \quad \text{A.23}$$

$$A^{oc}_{\Omega,i} = \frac{\pi \cdot d^2_{p_{oc}}}{4} \quad \text{A.24}$$

where $A^{oc}_{\Omega,i}$ is the cross-sectional area of the coated catalyst layer for oval shape of the bare pore and circular shape of the coated catalyst layer ($m^2$), $d_{p_{oc}}$ (m) is the catalyst-coated pore diameter (where $d_{p_{oc}} = 2 \cdot R_f$).

**S.3. FESEM images**

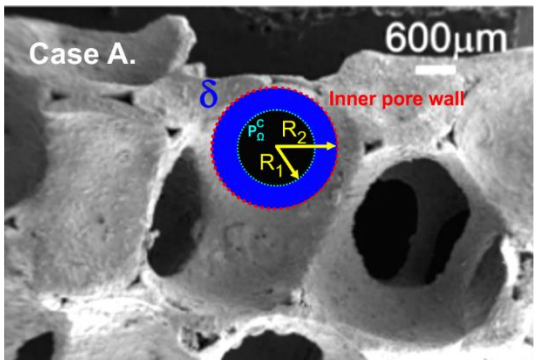


**Fig. S3.**1 SEM micrographs of Zir-OCF with 30 ppi considering case A: Circular shape of the pore and coated catalyst layer.

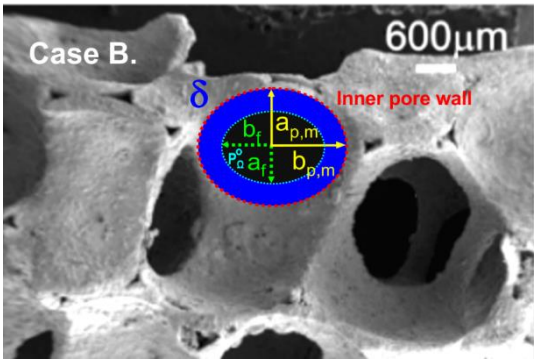


**Fig. S3.2** SEM micrographs of Zir-OCF with 30 ppi considering case B: Oval shape of the pore and coated catalyst layer.

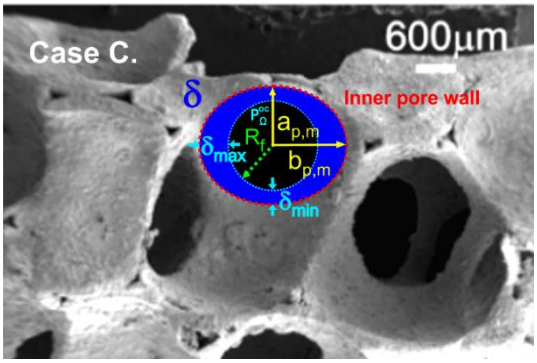


**Fig. S3.3** SEM micrographs of Zir-OCF with 30 ppi considering case C: Oval shape of the pore and circular shape of the coated catalyst layer.

**S.4. Diffusion and kinetic resistances of the cases A, B, and C.**

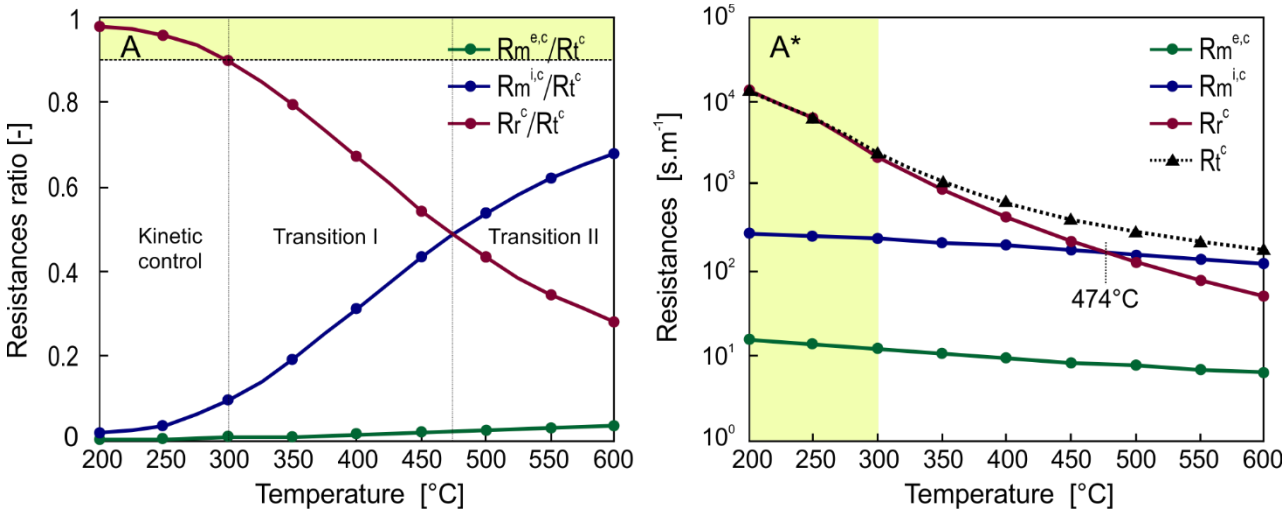


**Fig. S4.1** Resistances ratio (A) and resistances (A*) as a function of temperature for the case A: Circular shape of the pore and coated catalyst layer.

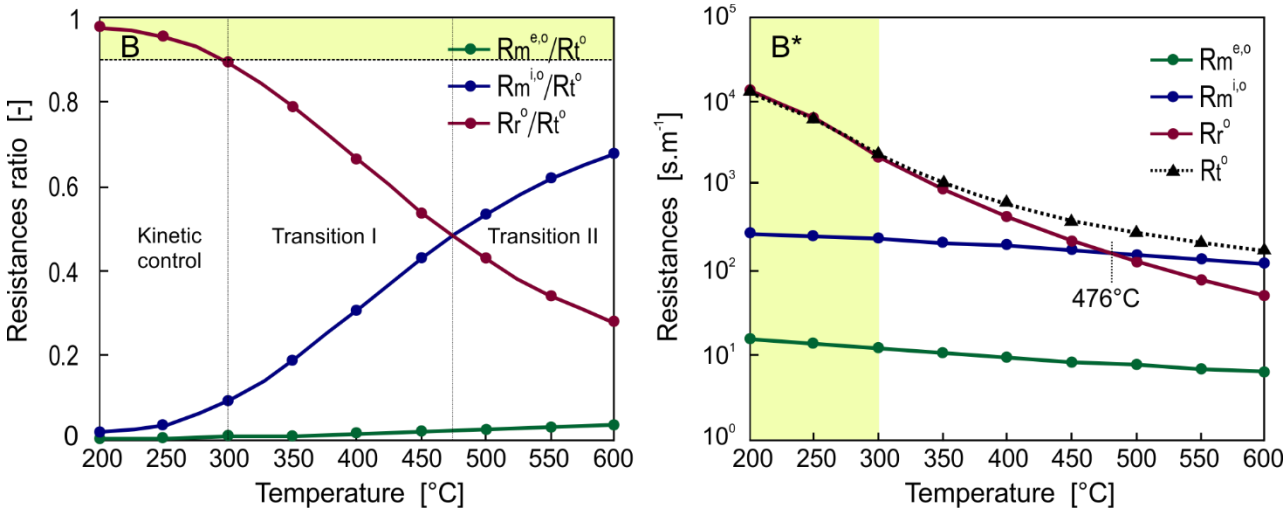


**Fig. S4.2** Resistances ratio (B) and resistances (B*) as a function of temperature for the case B: Oval shape of the pore and coated catalyst layer.

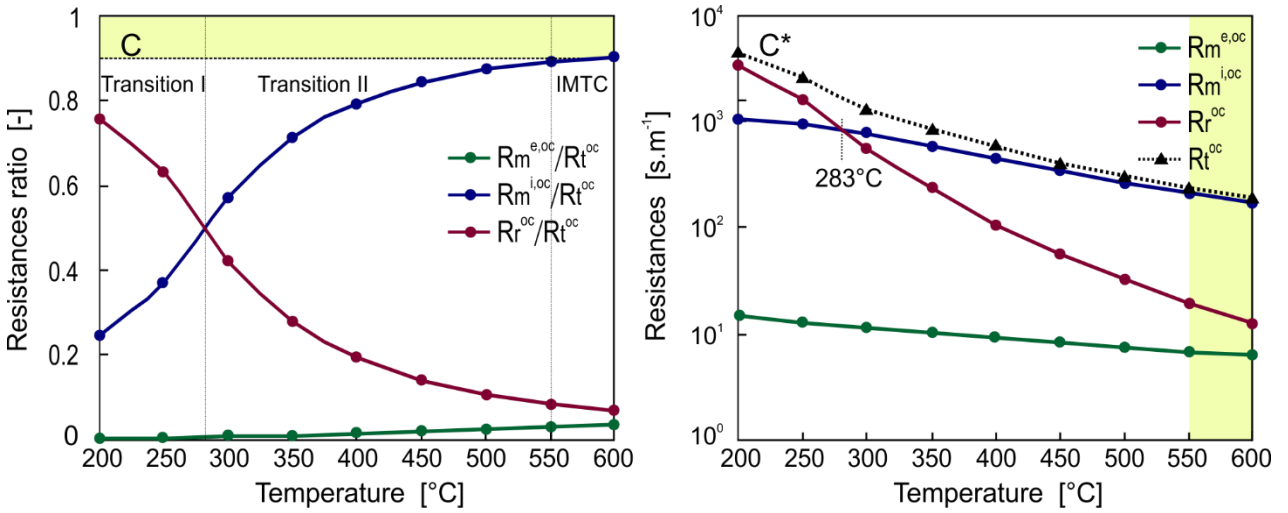


**Fig. S4.3** Resistances ratio (C) and resistances (C*) as a function of temperature for the case C: Oval shape of the pore and circular shape of the coated catalyst layer.

**S.4 Comparison of the effects of external and internal heat transfer of the cases A, B and C.**

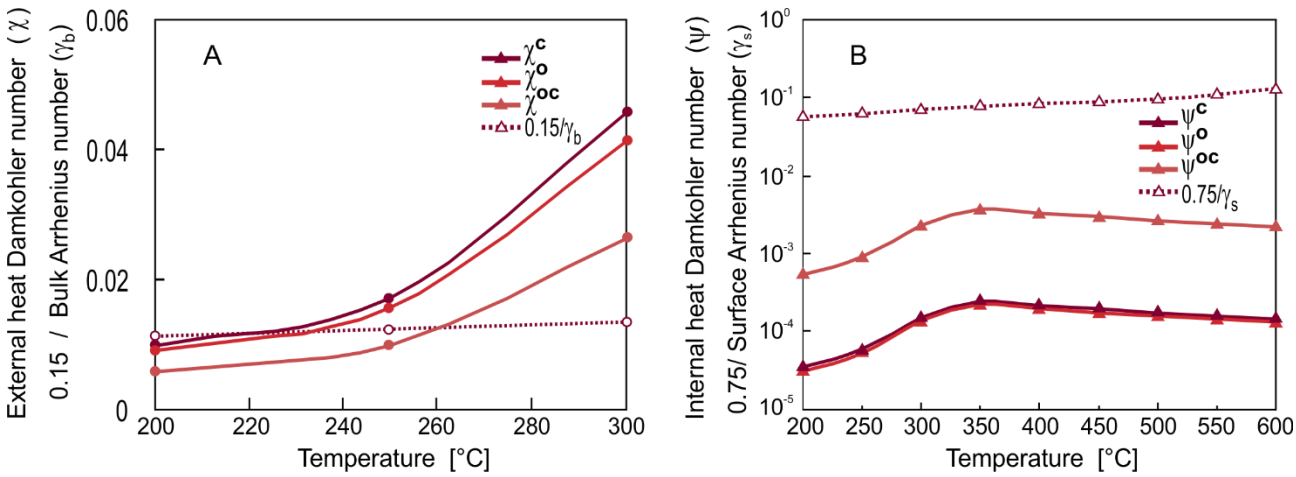


**Fig. S.4.1** Criteria for evaluating the effects of external heat transfer (A) and internal heat transfer (B) for the case A, B and C.

**References**


[1] F.C. Buciuman, B. Kraushaar-Czarnetzki, Ceramic foam monoliths as catalyst carriers. 1. Adjustment and description of the morphology, Ind. Eng. Chem. Res. 42 (2003) 1863–1869. doi:10.1021/ie0204134.

[2] G. Ercolino, P. Stelmachowski, S. Specchia, Catalytic performance of $Pd/Co_3O_4$ on SiC and $ZrO_2$ open cell foams for process intensification of methane combustion in lean conditions, Ind. Eng. Chem. Res. 56 (2017) 6625–6636. doi:10.1021/acs.iecr.7b01087.

[3] S.Y. Joshi, M.P. Harold, V. Balakotaiah, On the use of internal mass transfer coefficients in modeling of diffusion and reaction in catalytic monoliths, Chem. Eng. Sci. 64 (2009) 4976–4991. doi:10.1016/j.ces.2009.08.008.

[4] S.Y. Joshi, M.P. Harold, V. Balakotaiah, Overall mass transfer coefficients and controlling regimes in catalytic monoliths, Chem. Eng. Sci. 65 (2010) 1729–1747. doi:10.1016/j.ces.2009.11.021.

[5] S.Y. Joshi, Y. Ren, M.P. Harold, V. Balakotaiah, Determination of kinetics and controlling regimes for $H_2$ oxidation on $Pt/Al_2O_3$ monolithic catalyst using high space velocity experiments, Appl. Catal. B Environ. 102 (2011) 484–495. doi:10.1016/j.apcatb.2010.12.030.

# CHAPTER V

(*PAPER V*)

Effect of the $Co_3O_4$ load on the performance of $PdO/Co_3O_4/ZrO_2$ open cell foam catalysts for the lean combustion of methane: Kinetic and mass transfer regimes

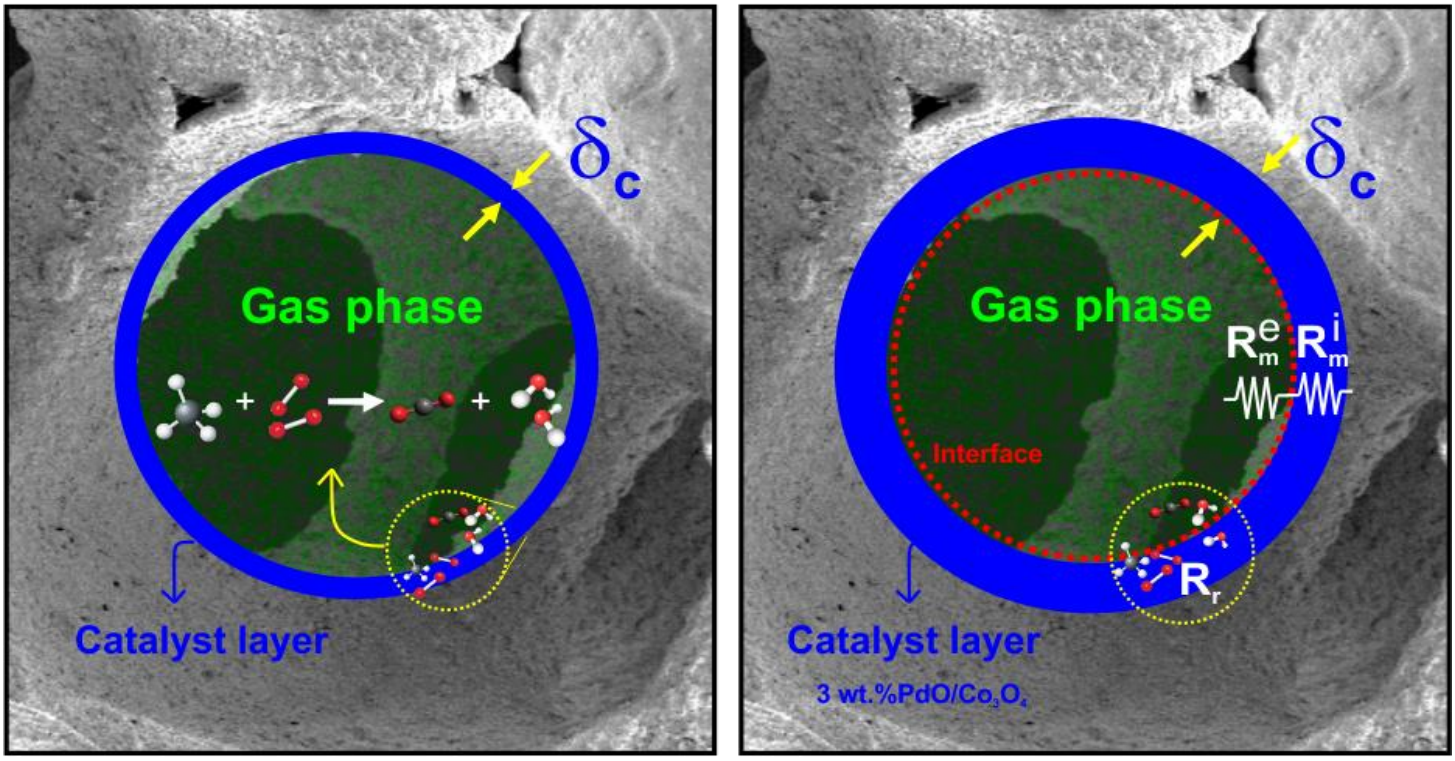


*Catalysis Today*. Elsevier B.V.

DOI: 10.1016/j.cattod.2021.03.014.

Catalysis Today xxx (xxxx) xxx

Contents lists available at ScienceDirect

Catalysis Today

journal homepage: www.elsevier.com/locate/cattod

# Effect of the $Co_3O_4$ load on the performance of $PdO/Co_3O_4/ZrO_2$ open cell foam catalysts for the lean combustion of methane: Kinetic and mass transfer regimes☆

Carmen W. Moncada Quintero *, Giuliana Ercolino, Stefania Specchia *

*Politecnico di Torino, Department of Applied Science and Technology, Corso Duca degli Abruzzi 24, 10129, Torino, Italy*

ARTICLE INFO

*Keywords:*
Controlling resistances
Catalyst loading
Catalyst thickness
Mass transfer
Pd-PdO transformation
Methane combustion

ABSTRACT

In this study, kinetic and mass transfer resistances (pore and interphase diffusion) were evaluated by varying the $Co_3O_4$ amount in the catalyst ($PdO/Co_3O_4$) supported on the zirconia open cell foam (Zir-OCF) of 30 ppi. The catalytic performance was examined toward the methane combustion in lean conditions (0.5 and 1.0 vol.% $CH_4$ inlet concentration, $O_2/CH_4$ molar ratio 8, WHSV 30, 60 and 90 NL $h^{-1}$ $g_{cat}^{-1}$). Pore and strut geometry of the bare foam were evaluated by SEM images and X-CT data analysis. Solution combustion synthesis was employed to line the $Co_3O_4$ spinel on the foam, while the wetness impregnation for the PdO on the spinel. The various resistances were evaluated and compared at different WHSV by varying the $Co_3O_4$ amount. Finally, we derived a correlation that describes the mass transfer in OCFs at low Reynolds numbers.

## 1. Introduction

Open cell foams (OCFs) have become an excellent candidate for a multiplicity of industrial applications, thanks to the combination of their attractive features such as high porosity, large specific surface area and mechanical strength as well as high fluid flow permeability and lightness [1–3]. In chemical engineering, OCFs are used as attractive catalytic supports since they offer a lower pressure drop compared to conventional fixed bed reactors [4–8]. In addition, their particular structural geometry produces a tortuous flow path that improves mixing and thus mass transfer compared to other catalytic supports such as monolith and honeycombs, resulting in high catalyst activity per unit volume [7, 9–14]. In recent years, several research groups have made efforts to study and quantify mass transfer in OCFs both experimentally and computational simulations [4,15–21]. Richardson et al. [15] studied the mass transfer during the CO oxidation on $Pt/\gamma\text{-}Al_2O_3$-coated alumina ceramic foam of 30 ppi. They demonstrated that the flow through the foam follows exactly the same convective fluid mechanics principles as in packed beds of equivalent diameter (volume/surface ratio). Later, Giani et al. [4] measured the mass transfer coefficients for the CO combustion over $Pd/\gamma\text{-}Al_2O_3$ washcoated metallic foams with different nominal cell size. The authors found that the mass transfer values obtained during their experiments resembled those estimated from semi-theoretical literature correlations for heat transfer in flow across series of tubes at low Reynolds numbers. They further expanded their work by deriving a generalized correlation valid for both ceramic and metallic foams [17]. On the other hand, Incera Garrido et al. [5] estimated the mass transfer coefficients over $Pt/SnO_2$-coated ceramic foams by monitoring the CO oxidation for foams with porosities between 75 % and 85 %, and pore counts between 10–45 ppi. A geometric factor was implemented to obtain a single descriptor in terms of pore density and void fraction.

Recently, Aguirre et al. [21] analyzed the mass transfer with a series of experiments and numerical simulations using the oxidation of CO on $Pt/\gamma\text{-}Al_2O_3$/metallic foam as reaction model. They derived a correlation with an asymptotic value of Sherwood number of 1.94, assuming the foam with a structure described by the Kelvin cell model. This correlation obtained a slightly higher dependence between the Sherwood number and Reynolds numbers when compared to the above mentioned studies. However, most of these correlations have been derived for Reynolds much larger than 10, making them inaccurate for the description of catalytic processes at low flow rates. Besides, most of

☆ The Authors dedicate this paper to Professors José Antonio Odriozola (University of Sevilla, Spain) and Mario Montes (University of the Basque Country, Spain), on the occasion of their 65th birthday.

* Corresponding authors.
*E-mail addresses:* carmen.moncada@polito.it (C.W. Moncada Quintero), stefania.specchia@polito.it (S. Specchia).

https://doi.org/10.1016/j.cattod.2021.03.014
Received 25 September 2020; Received in revised form 8 February 2021; Accepted 15 March 2021
Available online 18 March 2021

these studies were focused only on the external mass transfer effects, ignoring the relative importance of pore diffusion effects (inside the catalyst layer). In fact, in such studies it was assumed that conversion in foam-based reactors changes from kinetically limited to external mass transfer limited directly, without taking into account the effect of the catalyst thickness and its influence on the measurement of the mass transfer coefficients. Von Rickenbach et al. [22] demonstrated that the diffusion within the catalyst layer in OCFs is considerable even at high values of mass transfer coefficient. Thus, a careful evaluation of each controlling regime (kinetic, internal, and external diffusion) should be checked to effectively determine external mass transfer coefficients.

In our previous work, the catalytic performance of 3 wt.% PdO/$Co_3O_4$ catalyst in lean conditions was studied, either in powder [23] or structured form [7,24,25], at different weight hourly space velocity (WHSV 30, 60, 90 NL $h^{-1}$ $g_{cat}^{-1}$) and inlet methane concentrations (0.5–1 %). In those studies, the structured catalysts were prepared by covering the OCFs with the same amount of catalyst (~ 200 mg), such that the catalytic thickness was kept roughly constant. In addition, we carefully analyzed the heat and mass transfer during the complete methane combustion in lean conditions on three different ceramic OCF materials (zirconia, silicon carbide, and alumina) [25]. We obtained that the best catalytic performance in terms of $CH_4$ conversion, heat transfer, and mass was obtained for the Zirconia-OCF (Zir-OCF) one. In this work, we focused our attention on studying the different control resistances (kinetic, pore, and interphase diffusion) and the effect on the catalytic performance by increasing the $Co_3O_4$ amount in the catalyst (3 wt.% PdO/$Co_3O_4$) coated on the 30 ppi Zir-OCF by performing the $CH_4$ oxidation in lean conditions. First of all, we characterized the pore and strut geometry of the bare foams by a series of accurate SEM and X-CT analyses. Then, the $Co_3O_4$ spinel was deposited on the foams by solution combustion synthesis (SCS), while the PdO via wetness impregnation. The catalytic tests were performed at different WHSV and concentrations of methane (0.5 and 1 vol.%). The various resistances were evaluated and compared at different WHSV by varying the $Co_3O_4$ amount. Finally, we derived a correlation that describes the mass transfer in OCFs at low Reynolds numbers.

## 2. Materials and methods

### 2.1. Open cell foams and chemicals

Cobalt (II) nitrate hexahydrate $Co(NO_3)_2{\cdot}6H_2O$ (purity ≥ 98 %), palladium(II) nitrate hydrate $Pd(NO_3)_2{\cdot}xH_2O$ (≥99 % purity), glycine $NH_2CH_2COOH$ (purity ≥ 99 %), isopropyl alcohol $CH_3CHOHCH_3$ (purity ≥99.7 %), and ethanol $CH_3CH_2OH$ (purity ≥99.8 %) were purchased from Sigma-Aldrich. Ultrapure water (Millipore Milli-Q system with a resistivity ≈ 18 MΩ cm) was used to prepare the aqueous solutions. Methane, oxygen, and nitrogen gases (purity 99.999 %) flowed from cylinders purchased from SIAD Company. Zirconia open cell foams (Zir-OCFs) with pore density of 30 ppi (Vukopor® HT30) were purchased from Lanik S.r.o. (Czech Republic). The overall dimensions of Zir-OCFs were of 30 mm as length and 9 mm as diameter.

### 2.2. Preparation of the structured catalysts

Firstly, the Zir-OCFs were washed for 30 min in a solution of water/acetone (50/50 vol.%) using an ultrasonic bath at room temperature and dried for 60 min at 140 °C. The cleaned OCFs were used as support for three different amounts of $Co_3O_4$ catalyst (100, 150, and 250 mg, respectively), which were deposited on Zir-OCFs via SCS, as described in detailed in our previous works [7,25–27]. Briefly, the Zir-OCFs were dipped for 3 min in a 3 M cobalt nitrate and glycine solution (amount of glycine equal to 0.25 compared to the stoichiometric amount). The excess of the solution was removed with compressed air. The wet OCFs were placed in a furnace at 250 °C for 20 min to allow the ignition of the combustion reaction. The coating process was repeated several times until the desired amount of $Co_3O_4$ carrier was achieved. Finally, the $Co_3O_4$-coated Zir-OCFs were calcined at 600 °C for 4 h in static air. Then, 3 wt.% PdO was deposited on the $Co_3O_4$-coated Zir-OCFs by incipient wetness impregnation using an aqueous solution of palladium nitrate. After each dipping, the wet OCFs were dried at 140 °C for 1 h and then calcined at 600 °C for 4 h in static air. Table 1 shows the overall catalyst loading for the three $Co_3O_4$ amounts employed. Such values account also for the PdO present on each OCF prepared. Table S1 in the *Supplementary Data* lists the exact amounts of $Co_3O_4$ and PdO loaded on the three OCFs prepared ($W_{Co_3O_4}$ and $W_{PdO}$).

As a quick test before testing the reactivity of the prepared OCFs, we tested the adhesive properties of the coated catalytic layers via sonication (S3M 2200 device by Sonica). Briefly, as also described in our previous works [7,11,12,25], we immersed the prepared OCFs in a solution of 50/50 water/isopropyl alcohol and sonicated for 2 h at 40 kHz and 130 W. The difference of weight before and after sonication was taken as an indication of the adhesion of the catalyst coating over the foams.

### 2.3. Catalytic tests toward $CH_4$ combustion

The catalytic activity towards $CH_4$ oxidation of the three OCFs coated with the different amounts of $Co_3O_4$ (100, 150, and 250 mg) was tested in a lab-scale fixed-bed reactor (a straight quartz tube, 10 mm ID), inserted in a PID-regulated electrical oven. Each Zir-OCF, wrapped in a thin vermiculite foil to avoid channeling phenomena and heat dispersion, was placed at the center of the reactor and the oven was heated up to 700 °C flowing 0.1 NL $min^{-1}$ of $N_2$ with a heating rate of 10 °C $min^{-1}$. Once the set temperature has been reached, the reactive $CH_4/O_2/N_2$ gas mixture was fed (various runs performed at 0.5 or 1.0 vol.% of $CH_4$, 4.0 or 8.0 vol.% of $O_2$ in $N_2$, keeping constant the $O_2/CH_4$ molar ratio to 8 to assure lean conditions). When the combustion reaction reached steady state conditions at 700 °C (complete conversion of $CH_4$), the reactor was cooled down up to room temperature with a cooling rate of 5 °C $min^{-1}$, while measuring the outlet dry gas concentrations as a function of the temperature. A K-type thermocouple located few mm inside the inlet side of the OCF monitored the reaction temperature. An ABB analyzer equipped with a NDIR module Uras 14 for $CO/CO_2/CH_4$ and a paramagnetic module Magnos 106 for $O_2$ (water vapor was removed before entering the analyzer in a condenser set at 3 °C) was used to analyze the reactor outlet dry gas composition. The reagents flow rate was varied between 50–400 NmL $min^{-1}$, to perform catalytic tests at three different values of the weight hourly space velocity (WHSV 30, 60, and 90 NL $h^{-1}$ $g_{cat}^{-1}$, respectively). Such WHSV has been maintained considering the amount of effective mass of catalyst, that is, $W_{cat} = W_{PdO} + W_{Co_3O_4}$ (Table S1). The reproducibility of the results was assured by repeating each catalytic run for at least three times.

### 2.4. Characterization of the pore and strut size

Scanning Electron Microscope (SEM) images were acquired by FESEM Leo 50/50 V P equipped with a Gemini-type column to evaluate the textural properties of the bare Zir-OCFs. SEM images were obtained from small pieces of the bare structure with an accelerating voltage of 8 kV and a working distance of 30 mm.

X-ray Computed Tomography (X-CT) was carried out with an Xradia

**Table 1**
Overall catalyst loading (3 wt.% PdO/$Co_3O_4$) for the three OCFs prepared by varying the desired $Co_3O_4$ amount: 100 ($C_{load}^{100}$), 150 ($C_{load}^{150}$) and 250 ($C_{load}^{250}$) mg on Zir-OCF.

| Catalyst loading : $mg_{cat}$ $cm^{-2}_{OCF}$ | | |
|---|---|---|
| $C_{load}^{100}$ | $C_{load}^{150}$ | $C_{load}^{250}$ |
| 6.1 | 8.2 | 13.7 |

MicroXCT 400 scanner in order to determine the geometric structural parameters of the foams. High resolution scans were employed with an objective lens of 1X and voxel size of 22 μm. The sample was placed on a rotating plate between the X-ray source and the detector. X-ray images were collected by rotating 360° each sample, with an angular rotation interval of 0.3 degrees and exposure time of 4 s, resulting in 1233 images per sample. The X-ray power was set to 8 W and 80 kV. The Xradia's filtered back-projection algorithm was used to reconstruct CT slices. The images were then processed using the freeware program FIJI ImageJ. A sub-volume of the CT scan was selected (630 × 630 × 550) to eliminate uninteresting areas from the processing analysis. Then, a Gaussian filter was used to blur and remove noise from images [28]. This filter allows to smooth the region of interest and reduce the smoothening in the vicinity of edges. Lastly, high-signal (void filled with fluid phase) and low-signal (solid ceramic material) regions can be identified by converting the gray-scale CT data into a binary format, with an iterative procedure based on the isodata algorithm to obtain the gray level threshold [29]. The threshold value was checked using the Otsu method on the same gray-scale CT data [30–33]. Single spots of noise remained were removed by tagging the groups of connected voxels, calculating their number of solid voxels and removing all groups below the thresold limit of ten solid voxels, according to Marseille method [28]. Finally, a morphological closing operation followed by filling of the hollow struts. Fig. 1 shows the different steps of image processing by using FIJI ImageJ.

An image analysis was carried out for the characterization of the pore and strut diameters using the same open software. First of all, we assume a circular shape of the foam pore, thus the area of each pore was accurately evaluated by the software and then the diameter of an equivalent circle was determined as shown in Fig. 2A. As reported in our previous work [25], the circular pore shape assumption can be perfectly adopted for the analysis of OCFs as supports for catalysts, even if some pores are oval. This assumption does not invalidate the results on heat and mass transfer, being the difference between assuming pores of oval or circular shape extremely limited [25]. The strut thickness was measured in the middle of the strut length (Fig. 2B). More than 100 pore and strut measurements were analyzed and the average diameter was calculated as an arithmetic mean. Pore and strut size distributions were obtained from X-CT data and SEM images, where the mean pore and strut size of the sample was determined using the Gaussian peak fitting module of OriginPro 8 software.

## 3. Results and discussion

### 3.1. Characterization of pore and strut diameter

Fig. 3 shows a comparison of the strut diameter distribution obtained from the X-CT data and SEM images. As can be seen, the strut diameter distribution plots were deconvoluted into two peaks (using Gaussian distribution) corresponding to two different strut sizes along the strut length for both characterization techniques (Fig. 3A and B from X-CT data and SEM images, respectively). The mean strut size of the first peak was taken as the characteristic thickness (corresponding to the thinnest part of the strut). The second peak showed practically the same mean strut value (approximately 0.50 mm) for both measurements, with a higher frequency for the X-CT measurements. On the other hand, the pore distribution plots showed a narrow Gaussian distribution with a slightly larger mean pore diameter for the data extracted from the X-CT than those obtained from the manual measurements of the SEM images (Fig. 3C/X-CT-data and 3D/SEM images). Table 2 shows a comparison of the nominal geometrical properties provided by the manufacturer and those obtained from the tomography data of the 30 ppi zirconia foam.

From Table 2, it can be seen that the nominal size of pore and strut are higher than those obtained from X-CT images. The difference between such values could be due to manufacturing defects or irregularities of the cellular structure, as well as a possible overestimation of the diameters by the manufacturer [5]. It is also important to mention that the open porosity was estimated by measuring the remaining void volume after the artificial filling of cavities within the solid phase. Because the resolution of the X-CT in this study was lower than the size of certain microscopic pores in the solid phase (strut), only the open porosity of zirconia foam was characterized.

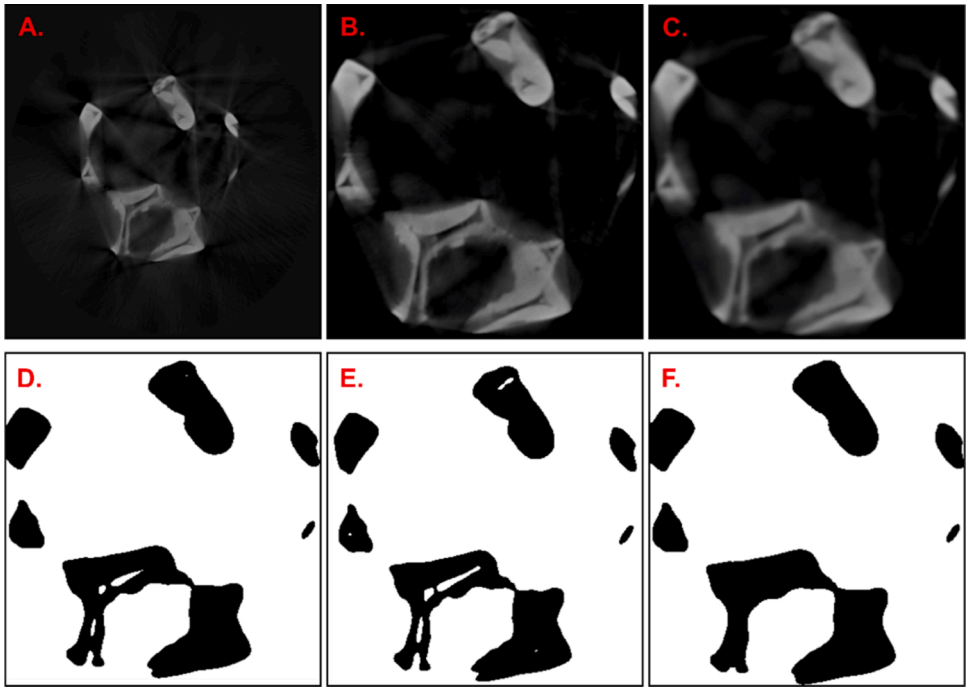


**Fig. 1.** Image processing steps: **(A)** Original image, **(B)** Cut image, **(C)** Gaussian filtered image, **(D)** Setting binary format, **(E)** Threshold checked by Otsu method, **(F)** Noise elimination, closing morphological operation and filling of inner void struts. The images are slices of a 3D matrix.

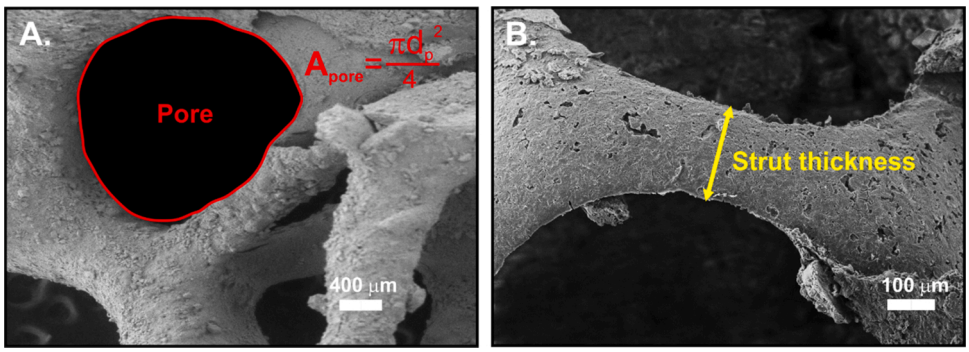


**Fig. 2.** Image analysis: Pore **(A)** and strut **(B)** size evaluation.

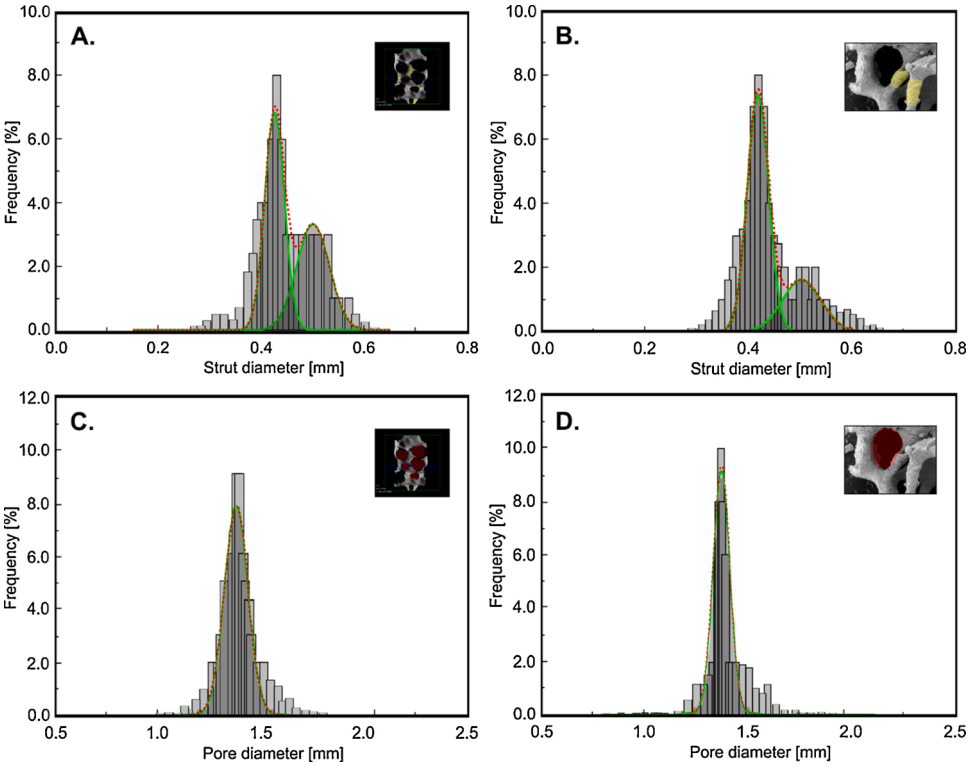


**Fig. 3.** Strut and pore size distribution from X-CT data **(A/C)** and SEM images **(B/D).**

**Table 2**
Nominal and measured (by X-CT images) geometrical properties of the Zir-OCF with 30 ppi.

| | $d_s$ [mm] | $d_p$ [mm] | $\epsilon_o$ | $Sv$ [$mm^{-1}$] |
|---|---|---|---|---|
| **Nominal** | 0.85 | 2.20 | 0.84 | 1.308 |
| **X-CT data** | 0.43 | 1.38 | 0.85 | 1.015 |

### 3.2. Catalytic tests toward $CH_4$ lean combustion

Ahead of the catalytic tests, we checked the adhesive properties of the catalysts' layers coated over the foams via sonication. The adherence values were 98.6 % for the $C_{load}^{100}$, 98.4 % the $C_{load}^{150}$ and 98.1 % the $C_{load}^{200}$, respectively. A weight percentage loss of catalyst layer ranging between 1 and 2% after sonication is a sign of excellent adhesion of the catalyst on the ceramic foam, and perfectly in line with literature results [7,12, 25,34]. Interestingly, an increase of the catalyst loading, corresponding to a thicker layer of catalyst covering the surface of the foam, does not lead to a dramatic loose of the catalyst itself. This result is a clear sign of the compactness of the catalyst and its optimal adhesive properties.

Fig. 4 shows the catalytic performance in lean methane combustion for the three PdO/$Co_3O_4$-coated Zir-OCF catalysts (with 3 wt.% of PdO on $Co_3O_4$ carrier) at different WHSV (30, 60, and 90 NL $h^{-1}$ $g_{cat}^{-1}$) and inlet $CH_4$ concentrations. The curves reported in Fig. 4 are explicative of the best conversion profiles obtained during the cooling phase of the tests. In fact, conversion curves during the cooling phase are more favorable, considering the hysteresis due to either the existence of multiple steady-states [35–37] and the PdO-Pd transition [38–40], which decreases the rate of $CH_4$ combustion. Figs. S.1 and S.2 in the *Supplementary Data* show all the tests performed, with repeatability and standard deviation on the $T_{50}$. As expected, the increase of WHSV leads to worsening of the combustion process, with a shift of $CH_4$ conversion curves toward higher temperatures, because of the reduction of contact time between the catalyst and reactants. In fact, at WHSV of 30, the complete conversion of $CH_4$ is achieved at temperatures between 380 and 630 °C depending on both the catalyst amount and the inlet $CH_4$ volume fraction, while at WHSV of 90, only the catalyst with a loading of 6.1 $mg_{cat}$ $cm^{-2}_{OCF}$ ($C_{load}^{100}$) reached full conversion of $CH_4$ at temperatures

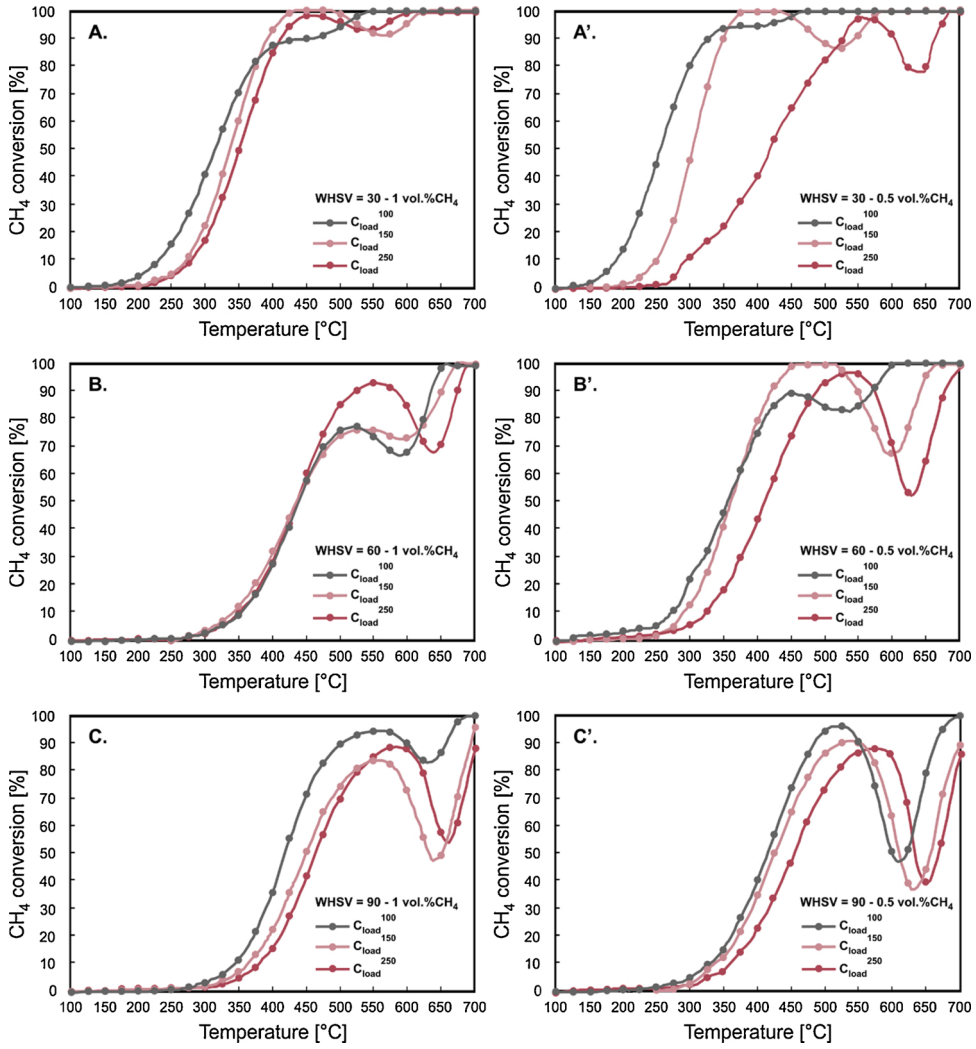


**Fig. 4.** $CH_4$ conversion versus temperature by varying the $Co_3O_4$ load in the $PdO/Co_3O_4$ catalyst coated Zir-OCF at different WHSV and inlet $CH_4$ concentration.

below 700 °C for both the inlet $CH_4$ concentrations. Furthermore, when comparing the catalytic performance at 0.5 and 1 vol.% $CH_4$ as inlet concentration, a slight improvement in terms of conversion is observed at lower concentrations for all WHSV and catalyst loading investigated.

Fig. S3 in the *Supplementary Data* shows the characteristic temperatures $T_{10}$, $T_{50}$, and $T_{90}$ corresponding to 10, 50, and 90 % of $CH_4$ conversion (taken as the lowest temperature value obtained from light-off curves, Fig. 4), by increasing the WHSV for the three different catalyst loading. As general trend, for all WHSV and inlet $CH_4$ concentration, higher light-off temperatures ($T_{10}$) were obtained by increasing the $Co_3O_4$ amount. Similar trends were also obtained by comparing the temperatures at 50 % $CH_4$ conversion ($T_{50}$). On the other hand, it was more difficult to establish a specific trend for the $T_{90}$ values when increasing the catalyst loading and the inlet $CH_4$ volume fraction because of the presence of the PdO-Pd transformation at high temperature. Interestingly, we recorded lower $T_{10}$, $T_{50}$, and $T_{90}$ values at the highest WHSV (90 NL $h^{-1}$ $g_{cat}^{-1}$) compared to those values obtained at 60 as WHSV, for the structured catalyst with the lowest amount of active phase, $C_{load}^{100}$, and when flowing the highest fraction of $CH_4$, 1 wt.%.

On the other hand, it is worth noting that for all catalytic tests, a decrease in $CH_4$ conversion is observed at medium/high temperatures. This drop in catalytic activity has been observed in numerous studies on methane oxidation over Pd-based catalysts, and was attributed to the decomposition of PdO to Pd and consequent Pd re-oxidation during the heating and cooling ramps, affecting negatively the catalytic reaction [38,41–47]. According to the literature, both transformations (PdO ↔ Pd decomposition and Pd ↔ PdO re-oxidation) occur via the formation of intermediate compounds identified as surface or interfacial $PdO_x$, which are the key species in the complete redox decomposition/re-oxidation reaction [38,44,48–51]. As mentioned above, all catalytic tests were carried out by cooling the reactor, that is, when the reactor reached the set temperature of 700 °C (by sending a flow of $N_2$), the reactive gas mixture was fed and once the steady-state conditions were achieved, the reactor was cooled down up to room temperature (cooling ramp of 5 °C $min^{-1}$). Hence, the decrease in $CH_4$ conversion obtained for all structured catalysts could be attributed to Pd re-oxidation. Colussi et al. [44] reported that the complete oxidation of the metal to the oxide that takes place during the cooling process is characterized as a kinetically-controlled process at high temperatures, which could explain the hysteresis observed. Further increase in catalytic activity by progressively decreasing the temperature is associated with the complete formation of the active phase (PdO), that is, the full oxidation of Pd. An additional interesting point is that by maintaining constant WHSV and catalyst loading (Table S2), when the reactor is fed with lower inlet $CH_4$ concentration, the hysteresis of the light-off curve is more accentuated (minor drop in $CH_4$ conversion). This could be explained by the fact that increasing the $CH_4$ inlet volume fraction in the reactor, maintaining the $O_2/CH_4$ molar ratio constant and equal to 8, leads to an increase of $O_2$ concentration and thus its partial pressure (ideal gas). Several authors suggest that increasing the partial pressure

of $O_2$ helps to stabilize the $PdO_x$ system by promoting the formation of PdO (active phase) as the temperature decreases (Pd ↔ PdO transformation) [43,44,46,48,49,52]. Farrauto et al. [41] also demonstrated using the thermogravimetric analysis that increasing oxygen concentration, both PdO decomposition and Pd re-oxidation shift to higher temperatures, where each temperature change corresponds to a different quasi-equilibrium oxygen content. In fact, as shown in Table S2, the $\Delta T$ of Pd-PdO transformation occurs at higher temperatures as the $O_2$ inlet concentration increased. Such an effect could also be due to the increased amount of PdO present on the foams when the overall catalyst load is increased.

Thus, taking into account the results obtained in this work and literature, we can infer that by increasing the $Co_3O_4$ load, the amount of oxygen present in the catalyst increases and hence a greater percentage of oxygen can be supplied during the Pd-PdO transformation, helping to stabilize the $PdO_x$ species and shifting the Pd-PdO hysteresis to higher temperatures. Nevertheless, the strong interactions between metal and support could lead to a synergetic effect which is the key in the $Co_3O_4$ lattice oxygen supply for methane combustion in fuel-lean condition. In fact, recently we proposed a reaction scheme of the lean combustion of $CH_4$ using a catalytic powder of 3 wt.% $PdO/Co_3O_4$. With a series of XRF and XPS measurements we noted that bulk and surface composition of the catalysts is different [53]. Specifically, the surface concentration of Pd is higher than the bulk one, pointing out a strong interaction between Pd as active phase and $Co_3O_4$ as support carrying on oxygen, able to synergistically donate oxygen through an effective energy transfer via lattice vibrations involving surface Pd and oxygen ions [49].

Another interesting point to highlight from Fig. 4 is that as the catalyst loading increases (by maintaining constant flow conditions), the light-off curves tend to shift towards higher temperatures, which could denote internal diffusional limitations. Since gases must diffuse through the catalyst pores to reach the catalytically active sites, an increase in catalyst loading leads to a thicker catalyst thickness, offering greater resistance to internal diffusion. Thus, a thicker catalyst thickness results in concentration gradients of the reactive species inside the catalyst, worsening the overall performance of the catalyst [54–56].

In the following section, we will evaluate the effect of $Co_3O_4$ amount on internal and external mass transfer.

### 3.3. Kinetic and mass transfer resistances analysis

To analyze the mass transfer effects that occur during the combustion reaction on the coated Zir-OCFs, we first determine the observed rate constant ($k^{obs}$), with the assumption of a pseudo-first order reaction because of the large excess of oxygen, according to the following equation:

$$k^{obs}\left(T\right) = \frac{1}{\tau}\cdot\ln\left(\frac{1}{1 - X_{CH4}(T)}\right) \tag{1}$$

$$\tau = \frac{W_{cat}\cdot C^{in}_{CH4}}{F^{in}_{CH4}} \tag{2}$$

where $\tau$ is the contact time ($g_{cat}$ s $m^{-3}$), $X_{CH4}$ is the conversion of methane, $W_{cat}$ is the weight of 3 wt.% $PdO/Co_3O_4$ catalyst ($g_{cat}$) and $C^{in}_{CH4}$, $F^{in}_{CH4}$ are the inlet concentration (mol $m^{-3}$) and molar flow of methane (mol $s^{-1}$), respectively. The logarithm of $k^{obs}$ was plotted as a function of the inverse of the temperature according to the Arrhenius law.

Fig. 5 shows a comparison of Arrhenius plots obtained at different catalyst contents for WHSV of 30 and inlet $CH_4$ concentration of 1 wt.%. By observing Fig. 5, we can distinguish three characteristic zones for all catalyst loadings: I. at low temperatures (with $X_{CH4} < 5$ %), the reaction rate is very slow and the process is governed by the kinetic regime $\left(E_a \approx E_{app}\right)$; II. as the temperature increases, the internal diffusion limitations begin to appear reaching the point where the time for internal

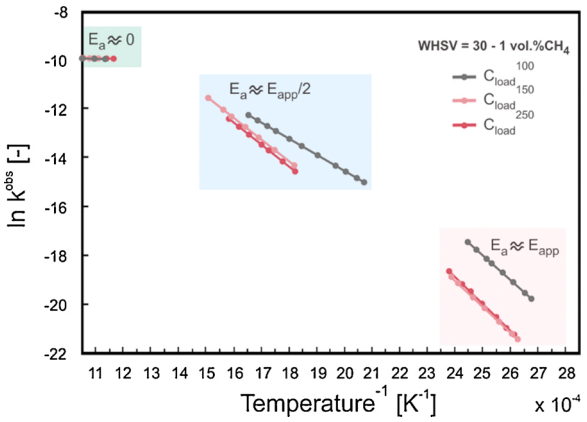


**Fig. 5.** Arrhenius plots for tha various catalyst contents ($C^{100}_{load}$, $C^{150}_{load}$, and $C^{250}_{load}$) at WHSV of 30 and inlet $CH_4$ concentration of 1 wt.%.

diffusion exceeds the reaction and external mass transfer time, thus, $E_a$ drops at almost half of the slope obtained in the kinetic regime $\left(E_a \approx \frac{E_{app}}{2}\right)$ and the process is governed by the internal diffusion; and III. at sufficiently high temperatures, the performance of the catalyst depends solely on the external mass transfer from the bulk gas phase to the gas-catalyst interface, thus, the external diffusion takes control of the process ($E_a \approx 0$). The slopes in Fig. 5, given by $\left(-\frac{E_a}{R}\right)$, are practically parallel, indicating similar apparent activation energy values. The displacement of the $C^{100}_{load}$ slope is due to the experimental points of the curve at low conversions. Table S3 in the *Supplementary Data* lists the values of $E_{app}$ with the related standard deviations. Analoguous plots can be obtained also for the other $Co_3O_4$ loads and WHSV (Fig. S4 in the *Supplementary Data*).

Then, for the study of each controlling resistance during the lean oxidation of $CH_4$, we used the criteria developed in the group of Balakotaiah [57–60] for first order catalytic reactions in washcoated monolith, adapting the model to the OCF geometry. Consequently, it is possible to characterize the operation regimes by increasing the catalyst content on the foam. First of all, the characteristic length scales for transverse diffusion associated within gas phase ($R_{\Omega,e}$) and catalyst layer ($R_{\Omega,i}$) can be defined assuming circular shape of the foam pore and catalyst layer, that is, the catalyst is deposited uniformly within the internal wall of the pore forming a circular ring of thickness $\delta_c$, as reported in our previous work [25] (Fig. 6A and B).

For the gas phase, the characteristic length scale is defined as the ratio of the flow area $\left(A_{\Omega,e} = \frac{\pi\cdot d_p^{c2}}{4}\right)$ to the gas-catalyst layer interface perimeter ($P_\Omega = \pi\cdot d_p^c$), while for the the catalyst layer is defined as the ratio of the catalyst layer cross sectional area $\left(A_{\Omega,i} = \frac{\pi\cdot(d_p^{b2} - d_p^{c2})}{4}\right)$ to the interfacial perimeter ($P_\Omega$). It is important to note that $R_{\Omega,e}$ is related to the hydraulic diameter ($d_h^c$) by the expression $d_h^c = 4\cdot R_{\Omega,e}$ and $R_{\Omega,i}$ corresponds to the effective catalyst thickness ($\delta_c$).

$$R_{\Omega,e} = \frac{A_{\Omega,e}}{P_\Omega} = \frac{d_p^c}{4} = 4\cdot d_h^c \tag{3}$$

$$R_{\Omega,i} = \frac{A_{\Omega,i}}{P_\Omega} = \frac{d_p^{b2} - d_p^{c2}}{4\cdot d_p^c} = \delta_c \tag{4}$$

where $d_p^b$ and $d_p^c$ are the diameter of the bare and catalyst coated OCF pore, respectively.

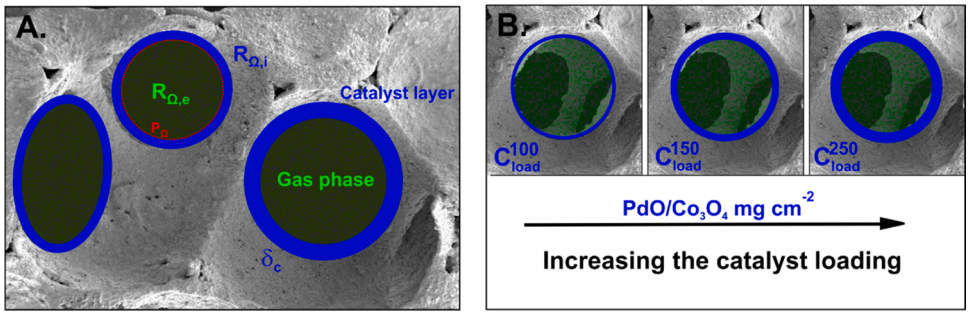


**Fig. 6.** Characteristic length scales for transverse diffusion connected with gas phase and catalyst layer **(A)** and distribution of the $PdO/Co_3O_4$ catalytic layer on the pores' walls of the Zir-OCF with a circular shape by varying the $Co_3O_4$ amount **(B).**

Next, we determined the external mass transfer coefficient ($k^e_m$) between the bulk of gas phase and the gas-catalyst layer interface as [58, 59]:

$$k^e_m = \frac{Sh_e \cdot D_{CH4,mix}}{4 \cdot R_{\Omega,e}} = \frac{Sh_e \cdot D_{CH4,mix}}{d^c_h} \tag{5}$$

and the internal mass transfer coefficient ($k^i_m$) between the gas-catalytic layer interface and bulk of catalytic layer as [58,59]:

$$k^i_m = \frac{Sh_i \cdot D_{CH4,e}}{R_{\Omega,i}} = \frac{Sh_i \cdot D_{CH4,e}}{\delta_c} \tag{6}$$

where $Sh_e$, $Sh_i$ are the external and internal Sherwood number, $D_{CH4,mix}$ and $D_{CH4,e}$ are the molecular and effective diffusivity of the $CH_4$ in the gas phase and within the catalyst layer, respectively.

To determine the $Sh_e$, we used the equation proposed by Balakotaiah and West [61] used for any arbitrary geometry:

$$Sh_e = Sh_{e,\infty} + 2.8 \cdot Sc^{\frac{1}{6}} \cdot P^{\frac{1}{2}} \tag{7}$$

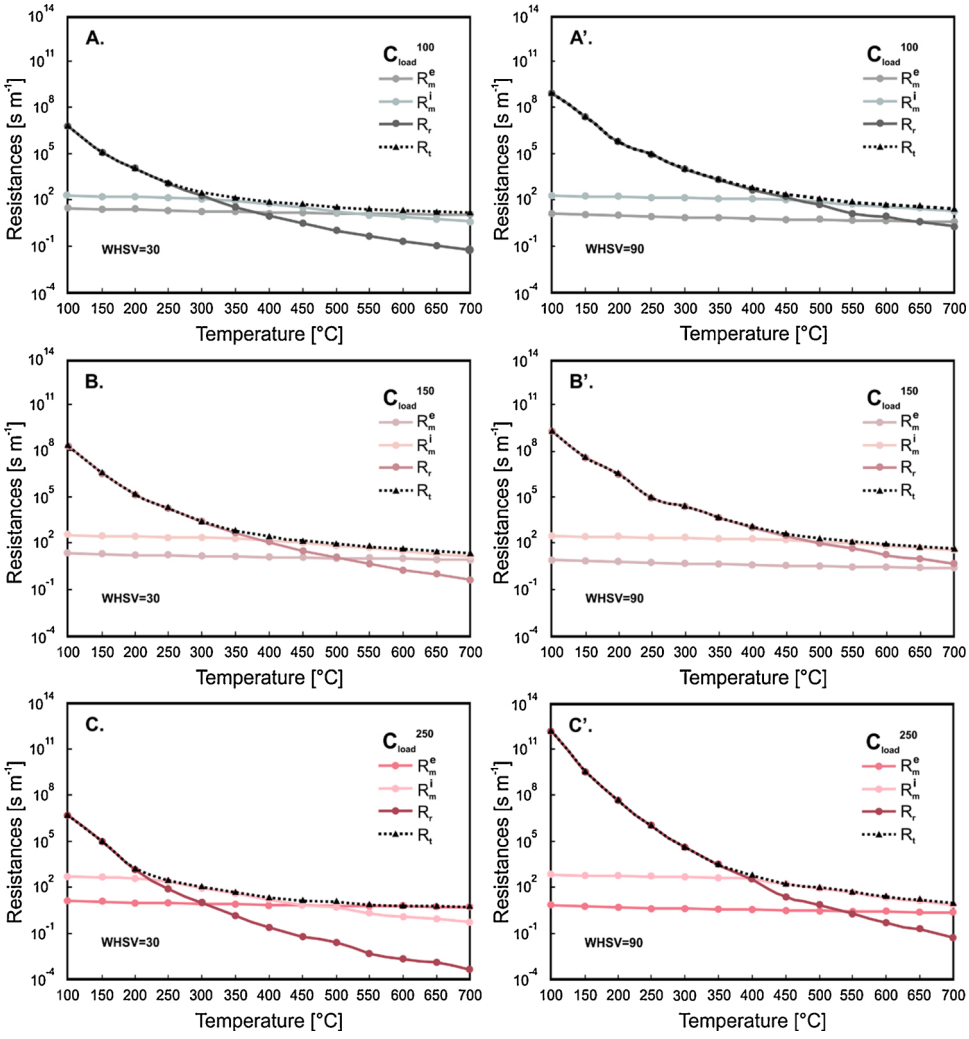


**Fig. 7.** Various resistances versus temperature for the three catalyst contents at WHSV of 30 (**A,B** and **C**) and 90 (**A',B'** and **C'**) for $C^{100}_{load}$, $C^{150}_{load}$ and $C^{250}_{load}$, respectively.

To estimate $Sh_i$, we used the correlation proposed by Joshi et al. [58] for a first order reaction:

$$Sh_i = Sh_{i,\infty} + \frac{\Lambda \cdot \phi^2}{1 + \Lambda \cdot \phi} \tag{8}$$

where $Sh_{e,\infty}$, $Sh_{i,\infty}$ are the asymptotic external ($Sh_{e,\infty} = 3.656$) and internal ($Sh_{i,\infty} = 3.013$ [58]) Sherwood numbers for circular pore diameter and coated layer shape, $Sc$ is the Schmidt number, $P$ is the transverse Peclet number ($P = \frac{R_{\Omega,e}{}^2 \cdot u}{\tau_f \cdot L_f \cdot D_{CH4,mix}}$), $\Lambda$ is a constant that depends on the catalyst layer geometry for first order reactions ($\Lambda = 0.38$ for a circular coated layer shape with circular crown ratio of 1.01 [58]) and $\phi$ is the Thiele modulus.

Hence, by considering the following assumptions: i. laminar and fully developed flow, ii. $d_h^e$ much smaller than the OCF length ($L_f$), iii. isothermal conditions, and iv. first order kinetic; we can evaluate the overall resistance of the process in a coated OCF as:

$$R_t = R_m^e + R_m^i + R_r \tag{9}$$

$$R_m^e = \frac{1}{k_{m,e}} \; ; \; R_m^i = \frac{1}{k_{m,i}} \; ; \; R_r = \frac{1}{k \cdot R_{\Omega,i}} \tag{10}$$

where $R_m^e, R_m^i$ are the resistances for external and internal mass transfer, $R_r$ is the reaction resistance, $R_t$ is the overall resistance of the process and $k$ is the apparent first order reaction rate constant ($s^{-1}$). The latter calculated with the equation of Arrhenius considering only the experimental values with a $CH_4$ conversion lower than 5%.

Fig. 7 shows a comparison of the evolution of the different regimes by varying the catalyst content on the foam at WHSV of 30 and 90 with inlet $CH_4$ concentration of 1 vol.%. As observed, all resistances show a decreasing trend with increasing temperature, although the diffusion resistances ($R_m^e, R_m^i$) are much less temperature sensitive compared to the reaction resistance ($R_r$), which is strongly dependent on the Arrhenius equation. As expected, at low temperatures, the reaction rate is much slower than the internal and external diffusion rate, thus, the reaction resistance is the controlling resistance ($R_r \gg R_m^e, R_m^i$). Particularly, $C_{load}^{150}$ showed a wider temperature range under kinetic control at both WHSV (at $T < 300$ °C for WHSV = 30 and at $T < 388$ °C for WHSV = 90). As the temperature raises, the reaction rate raises and the diffusion effects begin to be significant in the process. The increase of the catalyst loading from 6.1–13.7 $mg_{cat}$ $cm^{-2}{}_{OCF}$ led to a greater dominance of the $R_m^i$ to lower temperatures at both gas velocities studied. These results are consistent with the light-off curves (Fig. 4), where as mentioned above, the increase of the catalyst loading shifted the $CH_4$ conversion curves to higher temperatures. To evaluate whether the combustion reaction was limited by internal diffusion, we used the Weisz-Prater criterion according to the following expression:

$$WP = \frac{r_{CH_4}^{obs} \cdot \delta_c^2}{D_{CH_4,e} \cdot C_{CH_4}^s} < 1 \tag{11}$$

where $r_{CH_4}^{obs}$ is the observed volumetric reaction rate for $CH_4$ (mol $m^{-3}$ $s^{-1}$) and $C_{CH_4}^s$ is the $CH_4$ concentration at surface catalyst (mol $m^{-3}$).

It can be clearly noted from Fig. S5, the complete absence of internal diffusional limitations for $C_{load}^{100}$ (corresponding to 6.1 $mg_{cat}$ $cm^{-2}{}_{OCF}$). However, when increasing the catalyst loading to 8.2 and 13.7 $mg_{cat}$ $cm^{-2}{}_{OCF}$, the WP values exceed unity, indicating diffusional limitations. For $C_{load}^{150}$, the WP number is higher than 1 at temperatures between 500−550 °C, then the value decays as a consequence of the conversion drop during Pd-PdO transformation and subsequently exceeds unity at 700 °C at WHSV of 90. For $C_{load}^{250}$, the WP number exceeds 1 at temperatures above 400° and 450 °C at WHSV of 30 and 90, respectively. With regard to Fig. 4B, the fact that the curves are overlapping does not mean that diffusional problems are not present, but a consequence of the experimental data selected and their repeatability. From the WP criterion, it is evident that also for these data diffusional problems exist when the loading of catalyst is increased.

On the other hand at sufficiently high temperature, the $R_m^e$ becomes dominant at lower WHSV (30) for the $C_{load}^{100}$ and $C_{load}^{250}$. The analysis of the resistances and WP values at WHSV of 60 was characterized by intermediate values between those obtained at 30 and 90 WHSV (Fig. S6 in the *Supplementary Data*). For a more detailed analysis, we plotted the ratio of each resistance to the total resistance as a function of temperature in Fig. 8.

For the $C_{load}^{100}$, the catalyst performance is controlled by the kinetic at temperatures below 240 and 365 °C at WHSV of 30 and 90 respectively, with an $\frac{R_r}{R_t} > 0.9$. At temperatures between 315 and 550 °C (at WHSV = 30) and above 470 °C (at WHSV = 90), the $R_m^i$ is dominant with an $\frac{R_m^i}{R_t} > 0.5$ reaching a $\left[\frac{R_m^i}{R_t}\right]_{max}$ of 0.68 (at WHSV = 30) and 0.81 (at WHSV = 90)

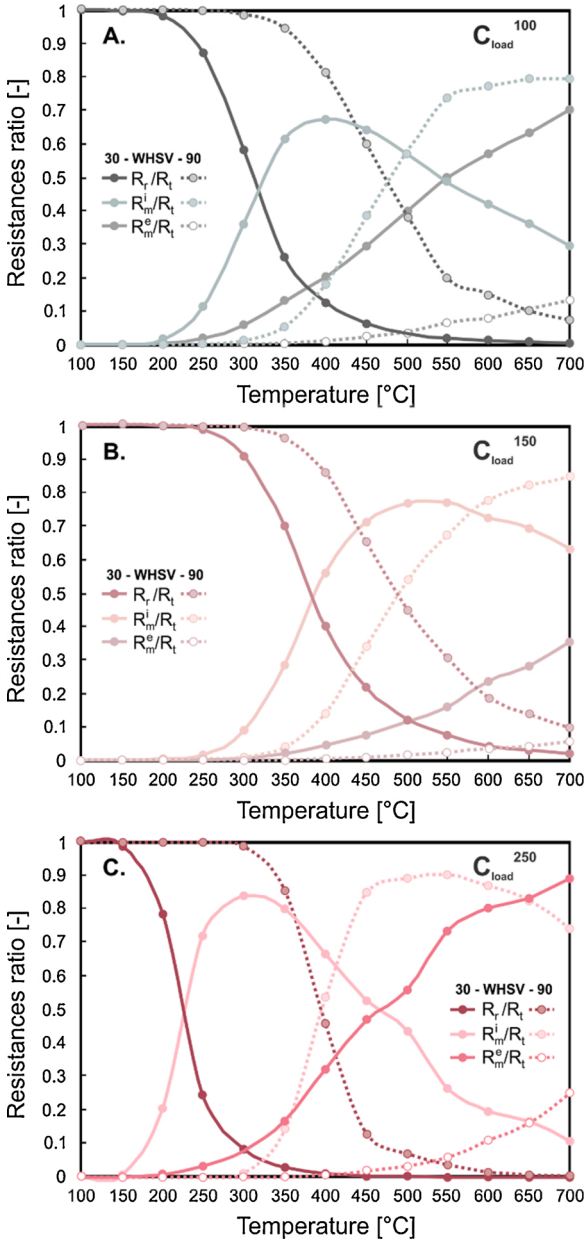


**Fig. 8.** Ratio resistances as a function of temperature at WHSV of 30 and 90 for $C_{load}^{100}$ (**A**), $C_{load}^{150}$ (B) and $C_{load}^{250}$ (C).

at 400 and 680 °C, respectively. Interestingly, the slope for $C_{load}^{100}$ at intermediate temperatures (where the internal mass transfer dominates) was lower than those obtained at higher catalyst loading ($C_{load}^{150}$ and $C_{load}^{250}$), indicating a transitional regime between kinetic and external mass transfer control at WHSV of 30. At temperatures above 550 °C and WHSV of 30, the $R_m^e$ dominates the performance ($\frac{R_m^e}{R_t} > 0.5$), achieving the $\left[\frac{R_m^e}{R_t}\right]_{max}$ of 0.81 at 700 °C. On the other hand, the raise of the gas velocity leads to a remarkable improvement of the external mass transfer where the $\left[\frac{R_m^e}{R_t}\right]_{max}$ reached at WHSV = 90 was of 0.12 at 700 °C.

By increasing the catalyst amount to $C_{load}^{150}$, the combustion is kinetically controlled at temperatures below 300 and 370 °C at WHSV of 30 and 90, respectively. At temperatures above 370 °C (WHSV = 30) and 473 °C (WHSV = 90), $R_m^i$ becomes the dominant resistance ($\frac{R_m^i}{R_t} > 0.5$) reaching the maximum ratio of 0.76 and 0.85 at 550 and 700 °C, respectively. The $\frac{R_m^e}{R_t}$ remained below 0.35 and 0.05 (at $T < 700$ °C) for WHSV of 30 and 90, respectively.

Finally, at the highest catalyst loading ($C_{load}^{250}$), the complete kinetic regime $\frac{R_r}{R_t} > 0.9$ is found at temperatures below 170 °C (at WHSV = 30) and 338 °C (at WHSV = 90). At temperatures between 225 and 463 °C and WHSV of 30, the internal diffusion prevails ($\frac{R_m^i}{R_t} > 0.5$), where it reaches a maximum value of 0.85 at 300 °C. Above 463 °C, the $R_m^e$ dominates the process, reaching the control at 700 °C ($\frac{R_m^e}{R_t} > 0.9$). On the other hand, at WHSV of 90, the combustion is dominated by the internal diffusion at temperatures above 400 °C, reaching a slight stability between 450 and 600 °C with $\frac{R_m^i}{R_t}$ values between 0.87 and 0.92. Thereafter, it starts to decrease reaching the value of 0.73 at 700 °C.

On the basis of the results obtained, we can generalize the discussion by considering the case of a catalyst supported on an open-cell foam, in which the temperature is systematically increased to span all the regimes of the catalytic process. Below, we describe in detail each of the regimes.

At low temperatures the reaction rate is much slower than the diffusion rates. The reaction occurs through the catalytic layer and the reactant concentration profile is nearly uniform. At this point, the reaction is controlled by kinetics that includes the processes of (i) adsorption of reactants on the active sites, (ii) catalytic reaction at the surface and (iii) desorption of products from the active sites. In this regime, the Thiele modulus, $\phi$, (which describes the relationship between the rate of reaction and diffusion in a porous catalyst) is much lower than unity, while the effectiveness factor, $\eta$, (which is defined as the ratio of the observed reaction rate to the hypothetical rate in the absence of mass transfer limitations) is near unity. Thus, using Eq. 9, we can write: $R_t \approx R_r$ since $R_r \gg (R_m^e + R_m^i)$.

As the temperature increases, the reaction rate increases and diffusional limitations become important. If the characteristic time for internal diffusion is much higher than the reaction and external mass transfer time, strong intraparticle diffusional limitations will exist, whereby a concentration gradient will be present within the catalytic layer. A further increase of the temperature leads to an exponential increase of the reaction rate such that the characteristic reaction time is approximately zero and a reactant concentration gradient is formed at the fluid-catalyst layer interface. Strong internal and external concentration gradients will prevail. Finally, at sufficiently high temperatures, the performance of the catalytic foam will depend on mass transport from the bulk gas to the interface. At this point, the Thiele modulus is much larger than one, while the effectiveness factor tends to zero.

It is important to point out that the passage from one regime to another is given by a transition regime during which the catalyst operates. In this regime, the characteristic reaction and diffusion times are comparable. Furthermore, it is noteworthy that for highly fast reactions, the reactants are completely consumed on the external catalyst surface, whereby only the external mass transfer can influence the effective transformation rate. In this case, the internal mass transfer resistance is not considered. It is clear that the presence of each regime will depend on the different design and operating parameters such as catalyst thickness, foam dimensions, catalyst loading, reaction activation energy, effective diffusivity, etc.

Thus, based on $CH_4$ conversion and mass transfer values obtained, the best performance for the full oxidation of methane in lean condition is provided by the structured catalyst with a loading of 6.1 $mg_{cat}\ cm^{-2}{}_{OCF}$ ($C_{load}^{100}$), that is with the structured catalyst hosting the lowest amount of active phase. These results are in agreement with those obtained in our previous works [11,62], where internal mass transfer limitations were observed at catalyst loads greater than 10 mg $cm^{-2}$, leading to a decrease in catalytic performance.

In the following section we will derive a correlation that describes the external mass transfer at low Reynolds number ($Re < 6$) for a catalyst-coated foam.

### 3.4. Mass transfer correlation for OCFs

Several correlations have been derived in the literature to investigate the external diffusion effects in OCFs as structured catalysts [4,5,15,17,19,21,63]. However, most of these correlations have been derived for Reynolds greater than 10, which make them inaccurate for the description of the process at low flow rates. For this purpose, we derived a correlation that allows to estimate the mass transfer coefficient at low Reynolds number, taking into consideration the parameters of the coated-OCF and considering a tetrakaidekahedral (TTKD) cell model, which has been well reported in many studies to be the configuration that best fits the OCF geometry [5,19,21]. For the flow conditions investigated (WHSV = 30, 60, 90; vol.%$_{CH4}$ = 0.5–1; P = 1 atm), the external diffusion control was confirmed by the constancy of the conversion at elevated temperatures (temperatures higher than the temperature range where the Pd-PdO transformation occurs) with $\frac{R_m^e}{R_t} > 0.9$. Under full diffusive regime, the observed reaction rate is equal to the rate of transport of the reactants through the gas phase in steady-state conditions. Thus, the mass transfer coefficients can be estimated according to the steady-state $CH_4$ mass balance, considering isothermal plug flow reactor and negligible axial dispersion ($Pe > 50$) as:

$$k_{m,OCF}^e = -\frac{\ln(1 - X_{CH4})}{Sv_{TTKD} \cdot \left(\frac{V_f}{F^v}\right)} \tag{12}$$

where $X_{CH4}$ is the methane conversion, $Sv_{TTKD}$ is the specific surface area calculated assuming TTKD unit cell ($m^2\ m^{-3}$), $V_f$ is the foam volume ($m^3$) and $F^v$ is the total volumetric flow of the gas mixture ($m^3\ s^{-1}$).

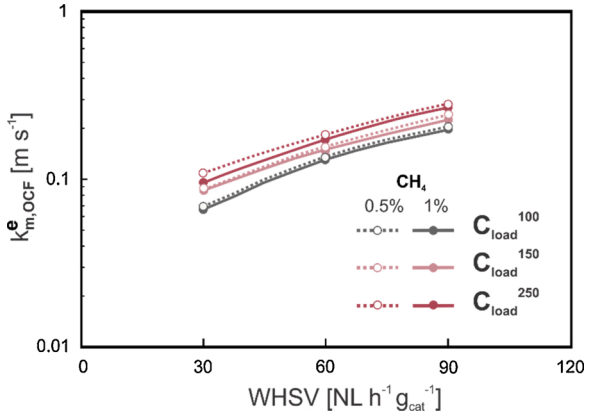


**Fig. 9.** Mass-transfer coefficients versus inlet flow rate estimated for different catalyst loading at 1 and 0.5 vol.% of $CH_4$ concentration.

Fig. 9 shows the mass transfer coefficients by varying the amount of $Co_3O_4$ (with 3 wt.% of PdO) on the OCF with inlet $CH_4$ concentration of 1 vol.% as a function of WHSV. As observed, both the increase of the catalyst thickness on the foam and flow rate lead to an increase of the mass transfer coefficient. As already stated, we considered the properties of the coated OCF and assumed that the catalyst was deposited uniformly on the inner wall of the foam pore with circular shape of the catalytic layer (Fig. 6), thus the thickness of the $PdO/Co_3O_4$ increases and the pore diameter available for the passage of the gas flow decreases. Therefore, as the pore diameter decreases, the higher the mass transfer coefficient is. These results are consistent with those obtained in the literature [4,5,17,64]. For instance, Younis and Viskanta [64] used a single-blow transient technique to determine the volumetric heat transfer coefficient between the ceramic foam and a stream of air. That coefficient was strongly dependent on the average pore diameter, where the volumetric heat transfer coefficient increased with decreasing pore size. Giani and co-workers [4,17] also obtained an increase of the mass transfer coefficient with the decrease of the pore diameter in metallic foams. We attribute this effect to the fact that as the pore diameter decreases, the specific surface of the foam increases ($S_v$, $m^2\ m^{-3}$), leading thus to a high fluid-to-solid mass transfer rate.

Mass transfer coefficients were expressed in dimensionless form $\left(Sh = \frac{k^e_{m,OCF} \cdot d^c_p}{D_{CH4,mix}}\right)$, plotted against the Reynolds number on a logarithmic scale for all flow conditions investigated and fitted by a single correlation of the form $Sh = A \cdot Re^m \cdot Sc^{1/3}$ obtaining:

$$Sh = 1.07 \cdot Re^{0.55} \cdot Sc^{1/3} \quad (13)$$

where $Re$ is the Reynolds number (considering as characteristic length the pore diameter of coated foam) and assuming Sherwood number dependency on the Schmidt number of $^1/_3$, as obtained from the boundary layer theory. This correlation was derived for the range of $0.75 < Re < 6$, foam void fraction of $0.75 < \varepsilon_o < 0.85$ and pore diameter of $1.24 < d_p < 1.38$ mm. Fig. 10 shows the derived correlation for the investigated OCFs (valid thus for zirconia, 30 ppi, covered with different catalyst loadings).

By comparing the correlation obtained with those derived from the literature [4,15–21], it is observed that the parameter $A$ (which is a function of the porosity and geometric properties of the foam) is consistent with the values reported in various studies of foams of different material, both ceramic and metallic, ($Al_2O_3$ and FeCrAlloy), and cell densities (10–45 ppi) [4,5,17]. However, the exponent $m$ that characterizes the dependence of Sherwood number with the magnitude of the velocity is slightly higher than the reported ones at relative high Re ($Re > 10$). Wen and Yu [65] investigated the mass transfer of naphthalene sublimation in a fixed bed where it was then fed into a converter and burned completely to $CO_2$ and $H_2O$. The data showed a nearly linear dependence ($m = 0.95$) of the Sherwood number with Reynolds at low flow velocities ($0.1 < Re < 5$). Later, Cybulski et al. [66] investigated the mass transport at low Reynolds numbers in a bed packed with silicon copper particles and air as a gaseous medium. They confirmed the results obtained by Wen, obtaining a linear correlation for Reynolds range of ($0.24 < Re < 0.63$). Recently, Xu et al. [67] studied theoretically the mass transport from bulk fluid to pore surface in chemically reactive flows for ordered and disordered porous structures. The authors found that for disordered porous structures, the $Sh$ increases linearly with $Re$ at the creeping flow regime, while for $Re > 10$ a one-half power law dependence was exhibited. In a recently published study, Aguirre et al. [21] reported a correlation that describes the mass transfer in aluminum OCF coated with layers of $Pt(1\%)/\gamma\text{-}Al_2O_3$ of thickness from 15 to 50 μm for the CO oxidation at low gas velocities ($2 < Re < 20$). They fitted the model to a correlation of the type: $Sh = Sh_\infty + A \cdot Re^m \cdot Sc^{1/3}$, where the Reynolds number dependency ($m$) was of 0.53, quite similar to the one obtained in this study. All these correlations, including the one reported in Eq. 13, show a strong dependence on the Reynolds number (at low $Re$ numbers), indicating a significant improvement in mass transfer by increasing the flow rate. It is also important to note that the correlation derived in this work, as well as those derived from the literature on both metallic and ceramic OCFs, show a weak dependence on flow velocity compared to unconsolidated systems where the solid phase is a discrete medium [21].

As next steps, we will expand our correlation to other porosities, and type of ceramic foams (alumina, cordierite or others).

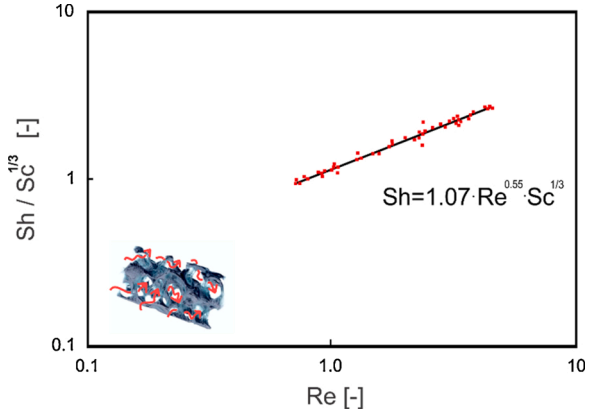


**Fig. 10.** Mass-transfer coefficients versus inlet flow rate estimated for different catalyst loadings.

## 4. Conclusions

This work studied the impact of catalyst loading by varying the $Co_3O_4$ amount (3 wt.% PdO on 100/150/250 mg $Co_3O_4$ spinel) coated on zirconia open cell foams (Zir-OCF) of 30 ppi used for the lean combustion of $CH_4$. The $Co_3O_4$ spinel was coated on the foams by solution combustion synthesis, while the PdO on the $Co_3O_4$ spinel by wetness impregnation. $CH_4$ combustion in lean conditions (0.5/1.0 vol.% $CH_4$ inlet combustion, 8 as $O_2/CH_4$ molar ratio, and 30, 60, and 90 as WHSV) was the investigated reaction model. According to the results obtained in this work, the main conclusions were the following:

- At the highest WHSV (90 NL $h^{-1}$ $g^{-1}_{cat}$), only the catalyst loading of 6.1 $mg_{cat}\ cm^{-2}{}_{OCF}$ ($C^{100}_{load}$) reached full conversion of $CH_4$ at temperatures below 700 °C for both the inlet $CH_4$ concentrations studied.
- As general trend, for all WHSV and inlet $CH_4$ concentration investigated, the increase of the $Co_3O_4$ amount led to an increase of the characteristic temperatures $T_{10}$, $T_{50}$, and $T_{90}$.
- The decrease in $CH_4$ conversion obtained for all structured catalysts could be attributed to Pd re-oxidation.
- The increase of the amount of $Co_3O_4$ led to a shifting of the light-off curve toward higher temperatures maintaining the Pd–PdO hysteresis and exhibiting a greater drop in $CH_4$ conversion.
- The increase of the catalyst loading from 6.1–13.7 $mg_{cat}\ cm^{-2}{}_{OCF}$ led to a greater dominance of the internal mass transfer resistance ($R^i_m$) to lower temperatures at both gas velocities studied.
- The best performance for the complete $CH_4$ oxidation in lean condition was obtained with the catalyst loading of 6.1 $mg_{cat}\ cm^{-2}{}_{OCF}$ ($C^{100}_{load}$).
- The mass transfer correlation derived in this study was found comparable with those derived from the literature, exhibiting a dependence of the Sherwood number with the Reynolds number slightly higher for $Re < 6$.

## CRediT authorship contribution statement

**Carmen W. Moncada Quintero:** Conceptualization, Methodology,

Investigation, Data curation, Formal analysis, Validation, Writing - original draft, Writing - review & editing. **Giuliana Ercolino:** Conceptualization, Investigation, Data curation. **Stefania Specchia:** Conceptualization, Methodology, Validation, Supervision, Writing - review & editing, Funding acquisition, Resources.

## Declaration of Competing Interest

The authors report no declarations of interest.

## Acknowledgements

This work was supported by the Italian Ministry of Education, University and Research (MIUR, Italy), via the ERANETMED network (SOLCARE project, grant number ENERG-065). The invaluable contribution to the electron microscopy observations of Mr Mauro Raimondo from the Politecnico di Torino is highly appreciated. The authors deeply acknowledge Prof. Radenka Maric, Vice President for Research of the University of Connecticut, for sponsoring the X-CT analyses, performed at the UCONN/Thermo Fisher Scientific Center for Advanced Microscopy and Materials Analysis (CAMMA).

## Appendix A. Supplementary data

Supplementary material related to this article can be found, in the online version, at doi:https://doi.org/10.1016/j.cattod.2021.03.014.

## References

[1] F. García-Moreno, Commercial applications of metal foams: their properties and production, Materials (Basel) 9 (2016) 20–24, https://doi.org/10.3390/ma9020085.

[2] V. Papetti, P. Dimopoulos Eggenschwiler, A. Della Torre, F. Lucci, A. Ortona, G. Montenegro, Additive manufactured open cell polyhedral structures as substrates for automotive catalysts, Int. J. Heat Mass Transf. 126 (2018) 1035–1047, https://doi.org/10.1016/j.ijheatmasstransfer.2018.06.061.

[3] I. Švecová, E. Tillová, L. Kuchariková, Improving the quality of Al-Si castings by using ceramic filters, Prod. Eng. Arch. 26 (2020) 19–24, https://doi.org/10.30657/pea.2020.26.05.

[4] L. Giani, G. Groppi, E. Tronconi, Mass-transfer characterization of metallic foams as supports for structured catalysts, Ind. Eng. Chem. Res. 44 (2005) 4993–5002, https://doi.org/10.1021/ie0490886.

[5] G. Incera Garrido, F.C. Patcas, S. Lang, B. Kraushaar-Czarnetzki, Mass transfer and pressure drop in ceramic foams: a description for different pore sizes and porosities, Chem. Eng. Sci. 63 (2008) 5202–5217, https://doi.org/10.1016/j.ces.2008.06.015.

[6] M. Bracconi, M. Ambrosetti, O. Okafor, V. Sans, X. Zhang, X. Ou, C.P. Da Fonte, X. Fan, M. Maestri, G. Groppi, E. Tronconi, Investigation of pressure drop in 3D replicated open-cell foams: Coupling CFD with experimental data on additively manufactured foams, Chem. Eng. J. 377 (2018) 120–123, https://doi.org/10.1016/j.cej.2018.10.060.

[7] G. Ercolino, P. Stelmachowski, S. Specchia, Catalytic performance of $Pd/Co_3O_4$ on SiC and $ZrO_2$ open cell foams for process intensification of methane combustion in lean conditions, Ind. Eng. Chem. Res. 56 (2017) 6625–6636, https://doi.org/10.1021/acs.iecr.7b01087.

[8] E. Reichelt, M. Jahn, Generalized correlations for mass transfer and pressure drop in fiber-based catalyst supports, Chem. Eng. J. 325 (2017) 655–664, https://doi.org/10.1016/j.cej.2017.05.119.

[9] F.C. Buciuman, B. Kraushaar-Czarnetzki, Ceramic foam monoliths as catalyst carriers. 1. Adjustment and description of the morphology, Ind. Eng. Chem. Res. 42 (2003) 1863–1869, https://doi.org/10.1021/ie0204134.

[10] E. Tronconi, G. Groppi, C.G. Visconti, Structured catalysts for non-adiabatic applications, Curr. Opin. Chem. Eng. 5 (2014) 55–67, https://doi.org/10.1016/j.coche.2014.04.003.

[11] M.A. Ashraf, O. Sanz, C. Italiano, A. Vita, M. Montes, S. Specchia, Analysis of $Ru/La\text{-}Al_2O_3$ catalyst loading on alumina monoliths and controlling regimes in methane steam reforming, Chem. Eng. J. 334 (2018) 1792–1807, https://doi.org/10.1016/j.cej.2017.11.154.

[12] C. Italiano, M.A. Ashraf, L. Pino, C.W. Moncada Quintero, S. Specchia, A. Vita, $Rh/CeO_2$ thin catalytic layer deposition on alumina foams: catalytic performance and controlling regimes in biogas reforming processes, Catalysts 8 (2018) 1–25, https://doi.org/10.3390/catal8100448.

[13] S. Voltolina, P. Marín, F.V. Díez, S. Ordóñez, Open-cell foams as beds in multiphase reactors: residence time distribution and mass transfer, Chem. Eng. J. 316 (2017) 323–331, https://doi.org/10.1016/j.cej.2017.01.113.

[14] A. Klegova, A. Inayat, P. Indyka, J. Gryboś, Z. Sojka, K. Pacultová, W. Schwieger, A. Volodarskaja, P. Kuśtrowski, A. Rokicińska, D. Fridrichová, L. Obalová, Cobalt mixed oxides deposited on the SiC open-cell foams for nitrous oxide decomposition, Appl. Catal. B Environ. 255 (2019), https://doi.org/10.1016/j.apcatb.2019.117745.

[15] J.T. Richardson, D. Remue, J.K. Hung, Properties of ceramic foam catalyst supports: mass and heat transfer, Appl. Catal. A Gen. 250 (2003) 319–329, https://doi.org/10.1016/S0926-860X(03)00287-4.

[16] F.C. Patcas, G.I. Garrido, B. Kraushaar-Czarnetzk, CO oxidation over structured carriers: a comparison of ceramic foams, honeycombs and beads, Chem. Eng. Sci. 62 (2007) 3984–3990, https://doi.org/10.1016/j.ces.2007.04.039.

[17] G. Groppi, L. Giani, E. Tronconi, Generalized correlation for gas/solid mass-transfer coefficients in metallic and ceramic foams, Ind. Eng. Chem. Res. 46 (2007) 3955–3958, https://doi.org/10.1021/ie061330g.

[18] F. Lucci, A. Della Torre, J. von Rickenbach, G. Montenegro, D. Poulikakos, P. Dimopoulos Eggenschwiler, Performance of randomized Kelvin cell structures as catalytic substrates: mass-transfer based analysis, Chem. Eng. Sci. 112 (2014) 143–151, https://doi.org/10.1016/j.ces.2014.03.023.

[19] A. Della Torre, F. Lucci, G. Montenegro, A. Onorati, P. Dimopoulos Eggenschwiler, E. Tronconi, G. Groppi, CFD modeling of catalytic reactions in open-cell foam substrates, Comput. Chem. Eng. 92 (2016) 55–63, https://doi.org/10.1016/j.compchemeng.2016.04.031.

[20] S. De Schampheleire, P. De Jaeger, K. De Kerpel, B. Ameel, H. Huisseune, M. De Paepe, How to study thermal applications of open-cell metal foam: experiments and computational fluid dynamics, Materials (Basel) 9 (2016) 1–27, https://doi.org/10.3390/ma9020094.

[21] A. Aguirre, V. Chandra, E.A.J.F. Peters, J.A.M. Kuipers, M.F. Neira D'Angelo, Open-cell foams as catalysts support: a systematic analysis of the mass transfer limitations, Chem. Eng. J. 393 (2020) 124656, https://doi.org/10.1016/j.cej.2020.124656.

[22] J. von Rickenbach, F. Lucci, C. Narayanan, P. Dimopoulos Eggenschwiler, D. Poulikakos, Effect of washcoat diffusion resistance in foam based catalytic reactors, Chem. Eng. J. 276 (2015) 388–397, https://doi.org/10.1016/j.cej.2015.03.132.

[23] G. Ercolino, G. Grzybek, P. Stelmachowski, S. Specchia, A. Kotarba, V. Specchia, $Pd/Co_3O_4$-based catalysts prepared by solution combustion synthesis for residual methane oxidation in lean conditions, Catal. Today 257 (2015) 66–71, https://doi.org/10.1016/j.cattod.2015.03.006.

[24] G. Ercolino, S. Karimi, P. Stelmachowski, S. Specchia, Catalytic combustion of residual methane on alumina monoliths and open cell foams coated with $Pd/Co_3O_4$, Chem. Eng. J. 326 (2017) 339–349, https://doi.org/10.1016/j.cej.2017.05.149.

[25] C.W. Moncada Quintero, G. Ercolino, A. Poozhikunnath, R. Maric, S. Specchia, Analysis of heat and mass transfer limitations for the combustion of methane emissions on $PdO/Co_3O_4$ coated on ceramic open cell foams, Chem. Eng. J. 405 (2021) 126970, https://doi.org/10.1016/j.cej.2020.126970.

[26] S. Specchia, C. Galletti, V. Specchia, Solution Combustion Synthesis as Intriguing Technique to Quickly Produce Performing Catalysts for Specific Applications, Studies in Surface Science and Catalysis, in: Eric M. Gaigneaux (Ed.), Scientific Bases for the Preparation of Heterogeneous Catalysts, 175, Elsevier B.V., 2010, pp. 59–67.

[27] S. Specchia, G. Ercolino, S. Karimi, C. Italiano, A. Vita, Solution combustion synthesis for preparation of structured catalysts: a mini-review on process intensification for energy applications and pollution control, Int. J. Self-Propagating High-Temperature Synth. 26 (2017) 166–186, https://doi.org/10.3103/S1061386217030062.

[28] J. Große, B. Dietrich, H. Martin, M. Kind, J. Vicente, E.H. Hardy, Volume image analysis of ceramic sponges, Chem. Eng. Technol. 31 (2008) 307–314, https://doi.org/10.1002/ceat.200700403.

[29] T.W. Ridler, S. Calvard, Picture Thresholding Using an Iterative Selection Method, IEEE Trans. Syst. Man Cybern. smc-8 (8) (1978) 630–632, doi:0018-9472/78/0800-0632$00.75.

[30] N. Otsu, A tlreshold selection method from gray-level histograms, IEEE Trans. Syst. Man Cybern. smc 9 (1) (1979) 62–66.

[31] S. Neethirajan, C. Karunakaran, D.S. Jayas, N.D.G. White, X-ray computed tomography image analysis to explain the airflow resistance differences in grain bulks, Biosyst. Eng. 94 (2006) 545–555, https://doi.org/10.1016/j.biosystemseng.2006.04.013.

[32] T.B. Kim, S. Yue, Z. Zhang, E. Jones, J.R. Jones, P.D. Lee, Additive manufactured porous titanium structures: through-process quantification of pore and strut networks, J. Mater. Process. Technol. 214 (2014) 2706–2715, https://doi.org/10.1016/j.jmatprotec.2014.05.006.

[33] A. Inayat, H. Freund, T. Zeiser, W. Schwieger, Determining the specific surface area of ceramic foams: the tetrakaidecahedra model revisited, Chem. Eng. Sci. 66 (2011) 1179–1188, https://doi.org/10.1016/j.ces.2010.12.031.

[34] M.A. Ashraf, O. Sanz, M. Montes, S. Specchia, Insights into the effect of catalyst loading on methane steam reforming and controlling regime for metallic catalytic monoliths, Int. J. Hydrogen Energy 43 (2018) 11778–11792, https://doi.org/10.1016/j.ijhydene.2018.04.126.

[35] A.K. Datye, J. Bravo, T.R. Nelson, P. Atanasova, M. Lyubovsky, L. Pfefferle, Catalyst microstructure and methane oxidation reactivity during the Pd↔PdO transformation on alumina supports, Appl. Catal. A Gen. 198 (2000) 179–196, https://doi.org/10.1016/S0926-860X(99)00512-8.

[36] B.A.P.A. Carlsson, M. Skoglundh, E. Fridell, E. Jobson, Induced low temperature catalytic ignition by transient changes in the gas composition, Catal. Today 73 (2002) 307–313, https://doi.org/10.1016/j.cej.2010.10.051.

[37] S. Specchia, S. Tacchino, V. Specchia, Facing the catalytic combustion of $CH_4/H_2$ mixtures into monoliths, Chem. Eng. J. 167 (2011) 622–633, https://doi.org/10.1016/j.cej.2010.10.051.
[38] M. Cargnello, J.J. Delgado Jaén, J.C. Hernández Garrido, K. Bakhmutsky, T. Montini, J.J. Calvino Gámez, R.J. Gorte, P. Fornasiero, Exceptional activity for methane combustion over modular $Pd@CeO_2$ subunits on functionalized $Al_2O_3$, Science (80-.) 337 (2012) 713–717, https://doi.org/10.1126/science.1222887.
[39] S. Colussi, P. Fornasiero, A. Trovarelli, Structure-activity relationship in $Pd/CeO_2$ methane oxidation catalysts, Chinese J. Catal. 41 (6) (2020) 938–950, https://doi.org/10.1016/S1872-2067(19)63510-2.
[40] J. Lin, X. Chen, Y. Zheng, F. Huang, Y. Xiao, Y. Zheng, L. Jiang, Facile construction of ultrastable alumina anchored palladium catalysts: via a designed one pot strategy for enhanced methane oxidation, Catal. Sci. Technol. 10 (2020) 4612–4623, https://doi.org/10.1039/d0cy00727g.
[41] R.J. Farrauto, M.C. Hobson, T. Kennelly, E.M. Waterman, Catalytic chemistry of supported palladium for combustion of methane, Appl. Catal. A Gen. 81 (1992) 227–237, https://doi.org/10.1016/0926-860X(92)80095-T.
[42] G. Groppi, C. Cristiani, L. Lietti, P. Forzatti, Study of PdO/Pd transformation over alumina supported catalysts for natural gas combustion, Stud. Surf. Sci. Catal. 130 (2000) 3801–3806, https://doi.org/10.1016/s0167-2991(00)80615-1. D.
[43] L.M.T. Simplício, S.T. Brandão, D. Domingos, F. Bozon-Verduraz, E.A. Sales, Catalytic combustion of methane at high temperatures: cerium effect on PdO/$Al_2O_3$ catalysts, Appl. Catal. A Gen. 360 (2009) 2–7, https://doi.org/10.1016/j.apcata.2009.03.005.
[44] S. Colussi, A. Trovarelli, E. Vesselli, A. Baraldi, G. Comelli, G. Groppi, J. Llorca, Structure and morphology of $Pd/Al_2O_3$ and $Pd/CeO_2/Al_2O_3$ combustion catalysts in Pd-PdO transformation hysteresis, Appl. Catal. A Gen. 390 (2010) 1–10, https://doi.org/10.1016/j.apcata.2010.09.033.
[45] M. Danielis, S. Colussi, C. De Leitenburg, L. Soler, J. Llorca, A. Trovarelli, The effect of milling parameters on the mechanochemical synthesis of $Pd\text{-}CeO_2$ methane oxidation catalysts, Catal. Sci. Technol. 9 (2019) 4232–4238, https://doi.org/10.1039/c9cy01098j.
[46] S. Nasr, N. Semagina, R.E. Hayes, Kinetic modelling of $Co_3O_4$- and $Pd/Co_3O_4$-Catalyzed wet lean methane combustion, Emiss. Control Sci. Technol. 6 (2020) 269–278, https://doi.org/10.1007/s40825-019-00143-0.
[47] J. Shen, R.E. Hayes, N. Semagina, On the contribution of oxygen from $Co_3O_4$ to the Pd-catalyzed methane combustion, Catal. Today 360 (2019) 435–443, https://doi.org/10.1016/j.cattod.2019.12.041.
[48] D. Ciuparu, E. Altman, L. Pfefferle, Contributions of lattice oxygen in methane combustion over PdO-based catalysts, J. Catal. 203 (2001) 64–74, https://doi.org/10.1006/jcat.2001.3331.
[49] Y.H.C. Chin, M. García-Diéguez, E. Iglesia, Dynamics and thermodynamics of Pd-PdO phase transitions: effects of pd cluster size and kinetic implications for catalytic methane combustion, J. Phys. Chem. C 120 (2016) 1446–1460, https://doi.org/10.1021/acs.jpcc.5b06677.
[50] M. Monai, T. Montini, R.J. Gorte, P. Fornasiero, Catalytic oxidation of methane: Pd and beyond, Eur. J. Inorg. Chem. 2018 (2018) 2884–2893, https://doi.org/10.1002/ejic.201800326.
[51] H. Stotz, L. Maier, A. Boubnov, A.T. Gremminger, J.D. Grunwaldt, O. Deutschmann, Surface reaction kinetics of methane oxidation over PdO, J. Catal. 370 (2019) 152–175, https://doi.org/10.1016/j.jcat.2018.12.007.
[52] R. Gholami, M. Alyani, K.J. Smith, Deactivation of Pd catalysts by water during low temperature methane oxidation relevant to natural gas vehicle converters, Catalysts 5 (2) (2015) 561–594, https://doi.org/10.3390/catal5020561.
[53] G. Ercolino, P. Stelmachowski, G. Grzybek, A. Kotarba, S. Specchia, Optimization of Pd catalysts supported on $Co_3O_4$ for low-temperature lean combustion of residual methane, Appl. Catal. B Environ. 206 (2017) 712–725, https://doi.org/10.1016/j.apcatb.2017.01.055.
[54] B. Millington, V. Whipple, B.G. Pollet, A novel method for preparing proton exchange membrane fuel cell electrodes by the ultrasonic-spray technique, J. Power Sources 196 (2011) 8500–8508, https://doi.org/10.1016/j.jpowsour.2011.06.024.
[55] L.M. Gandía, G. Arzamendi, P.M. Diéguez, Renewable Hydrogen Energy: An Overview. Renewable Hydrogen Technologies: Production, Purification, Storage, Applications and Safety, Elsevier B.V., 2013, pp. 1–17.
[56] J.J. Spivey, K.M. Dooley, Catalysis, Royal Society of Chemistry, 2009.
[57] M. Bhattacharya, M.P. Harold, V. Balakotaiah, Mass-transfer coefficients in washcoated monoliths, AIChE J. 50 (2004) 2939–2955, https://doi.org/10.1002/aic.10212.
[58] S.Y. Joshi, M.P. Harold, V. Balakotaiah, On the use of internal mass transfer coefficients in modeling of diffusion and reaction in catalytic monoliths, Chem. Eng. Sci. 64 (2009) 4976–4991, https://doi.org/10.1016/j.ces.2009.08.008.
[59] S.Y. Joshi, M.P. Harold, V. Balakotaiah, Overall mass transfer coefficients and controlling regimes in catalytic monoliths, Chem. Eng. Sci. 65 (2010) 1729–1747, https://doi.org/10.1016/j.ces.2009.11.021.
[60] S.Y. Joshi, Y. Ren, M.P. Harold, V. Balakotaiah, Determination of kinetics and controlling regimes for H2 oxidation on $Pt/Al_2O_3$ monolithic catalyst using high space velocity experiments, Appl. Catal. B Environ. 102 (2011) 484–495, https://doi.org/10.1016/j.apcatb.2010.12.030.
[61] V. Balakotaiah, D.H. West, Shape normalization and analysis of the mass transfer controlled regime in catalytic monoliths, Chem. Eng. Sci. 57 (2002) 1269–1286, https://doi.org/10.1016/S0009-2509(02)00059-3.
[62] S. Wójcik, G. Ercolino, M. Gajewska, C.W. Moncada Quintero, S. Specchia, A. Kotarba, Robust $Co_3O_4|\alpha\text{-}Al_2O_3|$cordierite structured catalyst for $N_2O$ abatement – validation of the SCS method for active phase synthesis and deposition, Chem. Eng. J. 377 (2018) 120088, https://doi.org/10.1016/j.cej.2018.10.025.
[63] M. Bracconi, M. Ambrosetti, M. Maestri, G. Groppi, E. Tronconi, A fundamental analysis of the influence of the geometrical properties on the effective thermal conductivity of open-cell foams, Chem. Eng. Process. - Process Intensif. 129 (2018) 181–189, https://doi.org/10.1016/j.cep.2018.04.018.
[64] L.B. Younis, R. Viskanta, Experimental determination of the volumetric heat transfer coefficient between stream of air and ceramic foam, Int. J. Heat Mass Transf. 36 (1993) 1425–1434, https://doi.org/10.1016/S0017-9310(05)80053-5.
[65] C.Y. Wen, Y.H. Yu, A generalized method for predicting the minimum fluidization velocity, AIChE J. 12 (1966) 610–612, https://doi.org/10.1002/aic.690120343.
[66] A. Cybulski, M.J. Van Dalen, J.W. Verkerk, P.J. Van Den Berg, Gas-particle heat transfer coefficients in packed beds at low Reynolds numbers, Chem. Eng. Sci. 30 (1975) 1015–1018, https://doi.org/10.1016/0009-2509(75)87002-3.
[67] A. Xu, T.S. Zhao, L. Shi, J.B. Xu, Lattice Boltzmann simulation of mass transfer coefficients for chemically reactive flows in porous media, J. Heat Transfer 140 (2018) 1–8, https://doi.org/10.1115/1.4038555.

*Supplementary Data*

*of*

# Effect of the $Co_3O_4$ load on the performance of $PdO/Co_3O_4/ZrO_2$ open cell foam catalysts for the lean combustion of methane: kinetic and mass transfer regimes

*Carmen W. Moncada Quintero*, Giuliana Ercolino, Stefania Specchia**

---

## Nomenclature

*Latin letters*

| | |
|---|---|
| $A$ | Parameter of the general mass transfer correlation [-] |
| $A_{\Omega,e}$ | Cross-sectional area of fluid phase [$m^2$] |
| $A_{\Omega,i}$ | Cross-sectional area of catalyst layer [$m^2$] |
| $C_{load}^{100}$ | Catalyst loading with 100 mg of $Co_3O_4$ [$mg_{cat}$ $cm^{-2}_{OCF}$] |
| $C_{load}^{150}$ | Catalyst loading with 150 mg of $Co_3O_4$ [$mg_{cat}$ $cm^{-2}_{OCF}$] |
| $C_{load}^{250}$ | Catalyst loading with 250 mg of $Co_3O_4$ [$mg_{cat}$ $cm^{-2}_{OCF}$] |
| $C_{CH4}^{s}$ | Concentration of $CH_4$ at the catalyst surface [mol $m^{-3}$] |
| $C_{CH4}^{in}$ | Inlet $CH_4$ concentration [mol $m^{-3}$] |
| $D_{CH4,mix}$ | Diffusivity of $CH_4$ in the gas mixture [$m^2 \cdot s^{-1}$] |
| $D_{CH4,e}$ | Effective diffusivity of $CH_4$ within coated layer [$m^2 \cdot s^{-1}$] |
| $d_p^b$ | Diameter of the bare OCF pore [m] |
| $d_p^c$ | Diameter of the catalyst coated OCF pore [m] |
| $d_h^c$ | Coated hydraulic diameter [m] |
| $d_s$ | Strut diameter [mm] |
| $d_p$ | Pore diameter [mm] |
| $d_f$ | Face diameter [mm] |
| $E_a$ | Activation energy [kJ $mol^{-1}$] |
| $E_{app}$ | Apparent activation energy [kJ $mol^{-1}$] |
| $F_{CH4}^{in}$ | Inlet $CH_4$ molar flow [mol $s^{-1}$] |
| $F^v$ | Total volumetric flow of the gas mixture [$m^3$ $s^{-1}$] |
| $k^{obs}(T)$ | Observed 1st-order reaction rate constant [$m^3$ $g_{cat}^{-1}$ $s^{-1}$] |
| $k$ | Apparent rate constant [$s^{-1}$] |
| $k_m^e$ | External mass transfer coefficient [m $s^{-1}$] |
| $k_{m,OCF}^e$ | Estimated mass transfer coefficient [m $s^{-1}$] |
| $k_m^i$ | Internal mass transfer coefficient [m $s^{-1}$] |
| $L_f$ | Length of the OCF [m] |

| | |
|---|---|
| $m$ | Exponent of Reynolds number in the general mass transfer correlation [-] |
| $P$ | Transverse Peclet number [-] |
| $P_\Omega$ | Gas-catalyst layer interface perimeter [m] |
| $Re$ | Reynolds number [-] |
| $R_{\Omega,e}$ | Transverse diffusion length for fluid phase [m] |
| $R_{\Omega,i}$ | Transverse diffusion length for fluid phase [m] |
| $R_t$ | Overall resistance [s $m^{-1}$] |
| $R_m^e$ | External mass transfer resistance [s $m^{-1}$] |
| $R_m^i$ | Internal mass transfer resistance [s $m^{-1}$] |
| $R_r$ | Reaction resistance [s $m^{-1}$] |
| $r_{CH_4}^{obs}$ | Observed volumetric reaction rate for $CH_4$ [mol $m^{-3}$ $s^{-1}$] |
| $Sc$ | Schmidt number [-] |
| $Sh$ | Estimated Sherwood number [-] |
| $Sh_e$ | External Sherwood number [-] |
| $Sh_i$ | Internal Sherwood number [-] |
| $Sh_{e,\infty}$ $(Sh_{i,\infty})$ | Asymptotic external (internal) Sherwood number [-] |
| $Sv$ | Specific surface area [$m^2 \cdot m^{-3}$] |
| $Sv_{TTKD}$ | Specific surface area calculated assuming TTKD unit cell [$m^2$ $m^{-3}$] |
| $T_{10}$ / $T_{50}$ / $T_{90}$ | Temperature at 10/50/90 % of $CH_4$ conversion [°C] |
| $\Delta T_{Pd\leftrightarrow PdO}$ | Temperature range for the Pd-PdO transformation [°C] |
| $u$ | Gas velocity [$m \cdot s^{-1}$] |
| $V_f$ | Foam volume [$m^3$] |
| $W_{cat}$ | Weight of 3 wt.% Pd/$Co_3O_4$ catalyst [$g_{cat}$] |
| $W_{Co_3O_4}$ | Weight of $Co_3O_4$ carrier [g] |
| $W_{3\text{wt.\%Pd}}$ | Weight of active metal phase (3 wt.%) [g] |
| $X_{CH4}(T)$ | Conversion of methane [-] |
| $X_{CH_4,Pd\leftrightarrow PdO}^{min}$ | Minimum $CH_4$ conversion for the Pd-PdO transformation [-] |
| $WP$ | Weisz-Prater number [-] |
| | |
| *Greek letters* | |
| $\delta_c$ | Effective catalyst thickness [m] |
| $\varepsilon_o$ | Open porosity of zirconia foam [-] |
| $\phi$ | Thiele modulus $(\frac{k \cdot R_{\Omega,i}^2}{D_{CH4,e}})^{\frac{1}{2}}$ [-] |
| $\Lambda$ | Constant used in the correlation for internal mass transfer coefficient [-] |
| $\tau$ | Contact time [$g_{cat}$ s $m^{-3}$] |
| $\tau_f$ | Foam tortuosity [-] |

**Table S1**. Overall catalyst loading (3 wt.% $PdO/Co_3O_4$) for the three OFCs prepared by varying the $Co_3O_4$ amount: 100 ($C_{load}^{100}$), 150 ($C_{load}^{150}$) and 250 ($C_{load}^{250}$) mg on Zir-OCF.

| | **Zir-OCF$^{bare}$** | $C_{load}^{100}$ [c] | $C_{load}^{150}$ [c] | $C_{load}^{250}$ [c] |
|---|---|---|---|---|
| $W_{Co_3O_4}$ [mg] | -- | 114.12 | 154.50 | 257.50 |
| $W_{3wt.\%\ Pd}$ [mg] | -- | 3.42 | 4.63 | 7.72 |
| $W_{cat}$ [mg] | -- | 117.54 | 159.13 | 265.22 |
| $d_p$ [mm] | 1.38[a] | 1.32 | 1.29 | 1.24 |
| $d_s$ [mm] | 0.43[a] | 0.48 | 0.51 | 0.56 |
| $d_f$ [mm] | 1.80[b] | 1.80 | 1.80 | 1.80 |
| $Sv$ [$mm^{-1}$] | 1.015[a] | 1.16 | 1.21 | 1.34 |
| $\varepsilon_o$ [-] | 0.85[a] | 0.81 | 0.79 | 0.75 |
| $\tau_f$ [-] | 1.346 | 1.37 | 1.39 | 1.42 |
| $\delta_c$ [μm] | -- | 30.33 | 41.07 | 68.45 |
| $C_{load,eff}$ [mg $cm^{-2}_{OCF}$] | -- | 6.07 | 8.20 | 13.7 |

[a] Estimated from X-CT data.

[b] Estimated using the following expression [1]: $d_f = d_p + d_s$

[c] All the properties of the coated foam were calculated according to our previous work [1,2]


[1] G. Ercolino, P. Stelmachowski, S. Specchia, Catalytic performance of $Pd/Co_3O_4$ on SiC and $ZrO_2$ open cell foams for process intensification of methane combustion in lean conditions, Ind. Eng. Chem. Res. 56 (2017) 6625–6636. doi:10.1021/acs.iecr.7b01087.

[2] C.W. Moncada Quintero, G. Ercolino, A. Poozhikunnath, R. Maric, S. Specchia, Analysis of heat and mass transfer limitations for the combustion of methane emissions on $PdO/Co_3O_4$ coated on ceramic open cell foams, Chem. Eng. J. 405 (2020) 126970. doi:10.1016/j.cej.2020.126970.

**Table S2.** *ΔT* of Pd-PdO transformation as a function of $CH_4$ inlet concentration, WHSV, and catalyst load (data extracted from **Fig. 4**).

| | $C_{load}^{100}$ | | $C_{load}^{150}$ | | $C_{load}^{250}$ | |
|---|---|---|---|---|---|---|
| | **WHSV = 30 NL $h^{-1}$ $g_{cat}^{-1}$** | | | | | |
| **vol.% $CH_4$** | **0.5** | **1** | **0.5** | **1** | **0.5** | **1** |
| $X_{CH_4,Pd\leftrightarrow PdO}^{min}$ *[%]* | 94.6 | 90.2 | 87.0 | 90.1 | 75.0 | 93.6 |
| $\Delta T_{Pd\leftrightarrow PdO}$ [°C] | 343-472 | 408-542 | 420-600 | 465-635 | 515-690 | 480-600 |
| | **WHSV = 60 NL $h^{-1}$ $g_{cat}^{-1}$** | | | | | |
| $X_{CH_4,Pd\leftrightarrow PdO}^{min}$ *[%]* | 82.4 | 67.7 | 66.6 | 72.8 | 53.4 | 68.9 |
| $\Delta T_{Pd\leftrightarrow PdO}$ [°C] | 446-630 | 510-610 | 500-670 | 515-670 | 530-700 | 567-700 |
| | **WHSV = 90 NL $h^{-1}$ $g_{cat}^{-1}$** | | | | | |
| $X_{CH_4,Pd\leftrightarrow PdO}^{min}$ *[%]* | 47.8 | 84.0 | 36.8 | 47.5 | 39.5 | 54.6 |
| $\Delta T_{Pd\leftrightarrow PdO}$ [°C] | 497-700 | 554-700 | 540-700 | 584-700 | 562-700 | 578-700 |

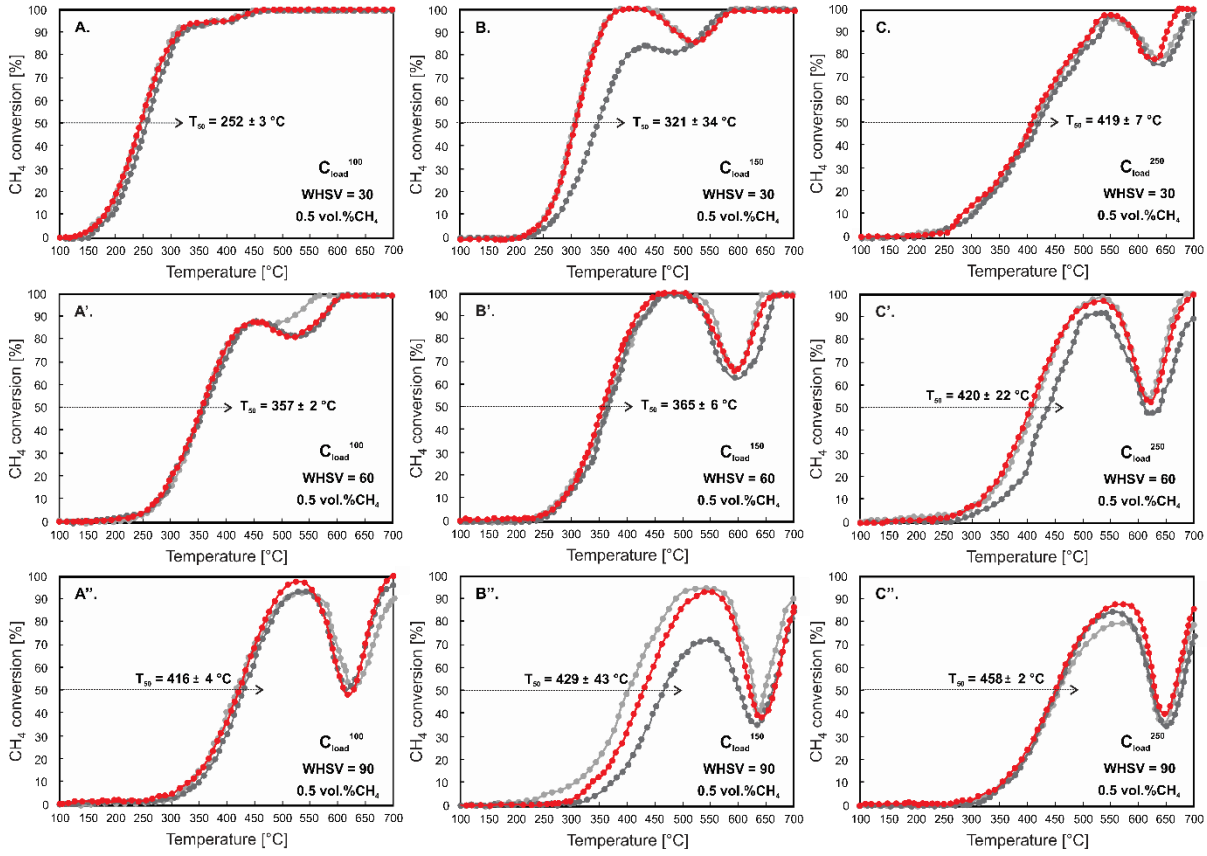


**Figure S1.** Repeatability of light-off curves and average $T_{50}$ with standard deviation by varying the $Co_3O_4$ load in the $PdO/Co_3O_4$ catalyst coated Zir-OCF at different WHSV and inlet $CH_4$ concentration of 0.5 vol.% (A/B/C: WHSV = 30 NL $h^{-1}$ $g_{cat}^{-1}$; A'/B'/C' = 60 NL $h^{-1}$ $g_{cat}^{-1}$; A''/B''/C'' = 90 NL $h^{-1}$ $g_{cat}^{-1}$; A/A'/A'': $C_{load}^{100}$; B/B'/B'': $C_{load}^{150}$; C/C'/C'': $C_{load}^{250}$). Curves taken during the cooling cycle of the tests. The red curves are the ones reported in **Figure 4** of the paper, and used to perform calculations on heat and mass transfer limitations.

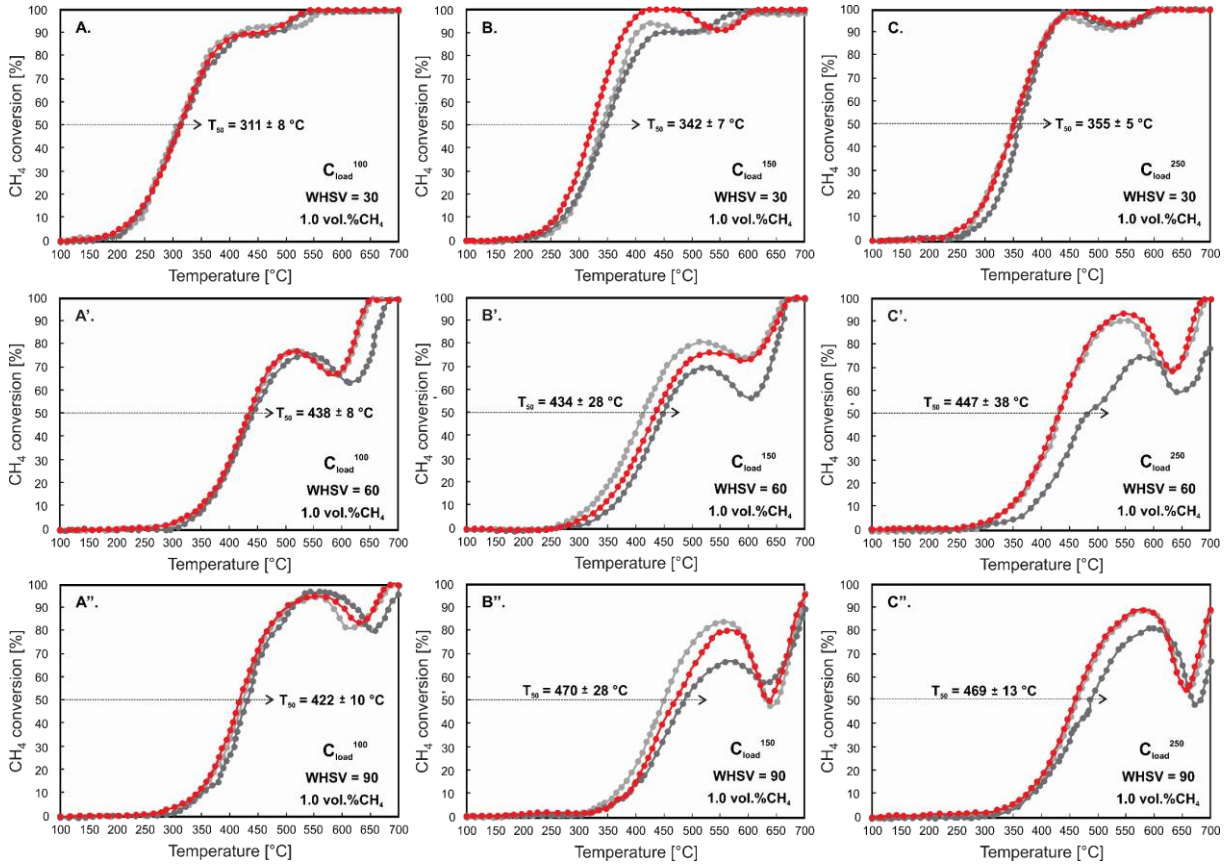


**Figure S2.** Repeatability of light-off curves and average $T_{50}$ with standard deviation by varying the $Co_3O_4$ load in the $PdO/Co_3O_4$ catalyst coated Zir-OCF at different WHSV and inlet $CH_4$ concentration of 1.0 vol.% (A/B/C: WHSV = 30 NL $h^{-1}$ $g_{cat}^{-1}$; A'/B'/C' = 60 NL $h^{-1}$ $g_{cat}^{-1}$; A''/B''/C'' = 90 NL $h^{-1}$ $g_{cat}^{-1}$; A/A'/A'': $C_{load}^{100}$; B/B'/B'': $C_{load}^{150}$; C/C'/C'': $C_{load}^{250}$). Curves taken during the cooling cycle of the tests. The red curves are the ones reported in **Figure 4** of the paper, and used to perform calculations on heat and mass transfer limitations.

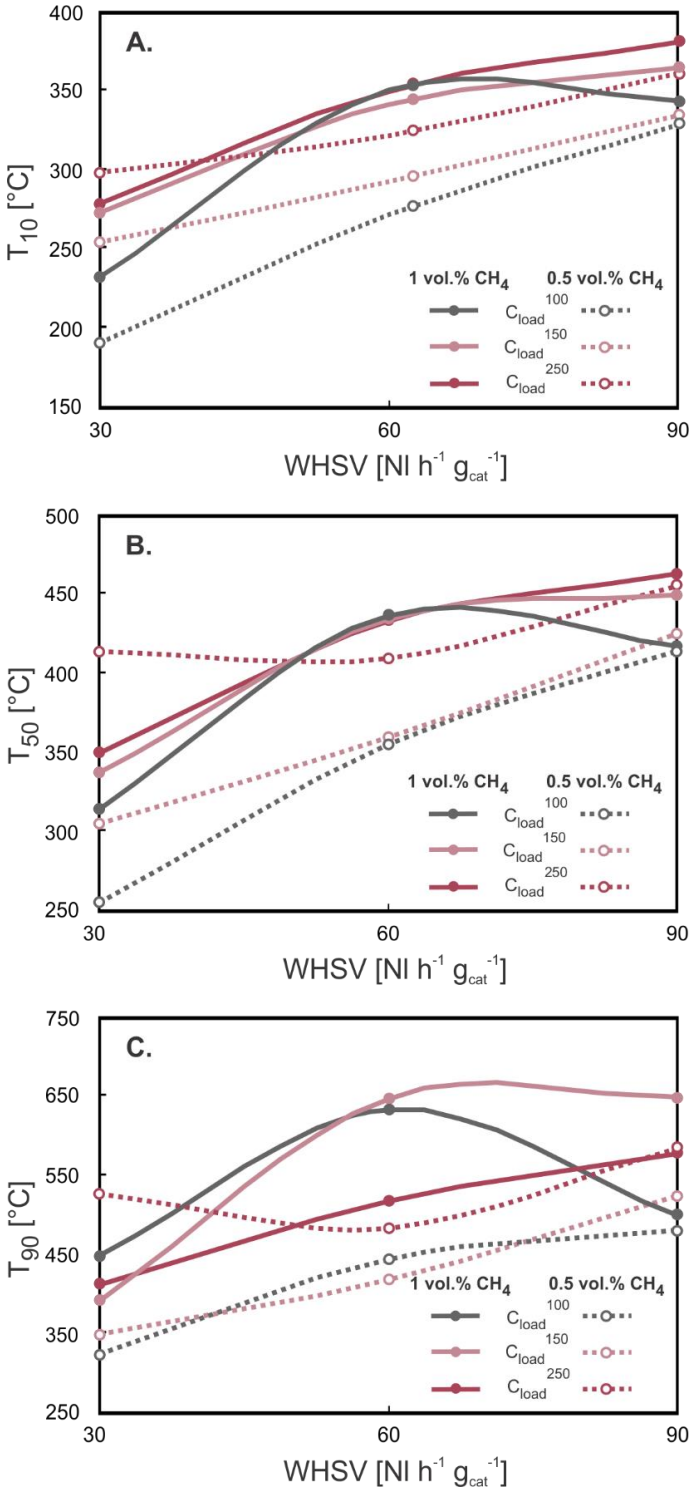


**Figure S3.** Characteristic temperatures $T_{10}$ **(A)**, $T_{50}$ **(B)** and $T_{90}$ **(C)** corresponding to 10, 50 and 90% of $CH_4$ conversion by increasing WHSV for the three different catalyst loading. The $T_{50}$ and $T_{90}$ values were taken as the lowest temperature values obtained from the $CH_4$ combustion light-off curves (**Fig. 4**).

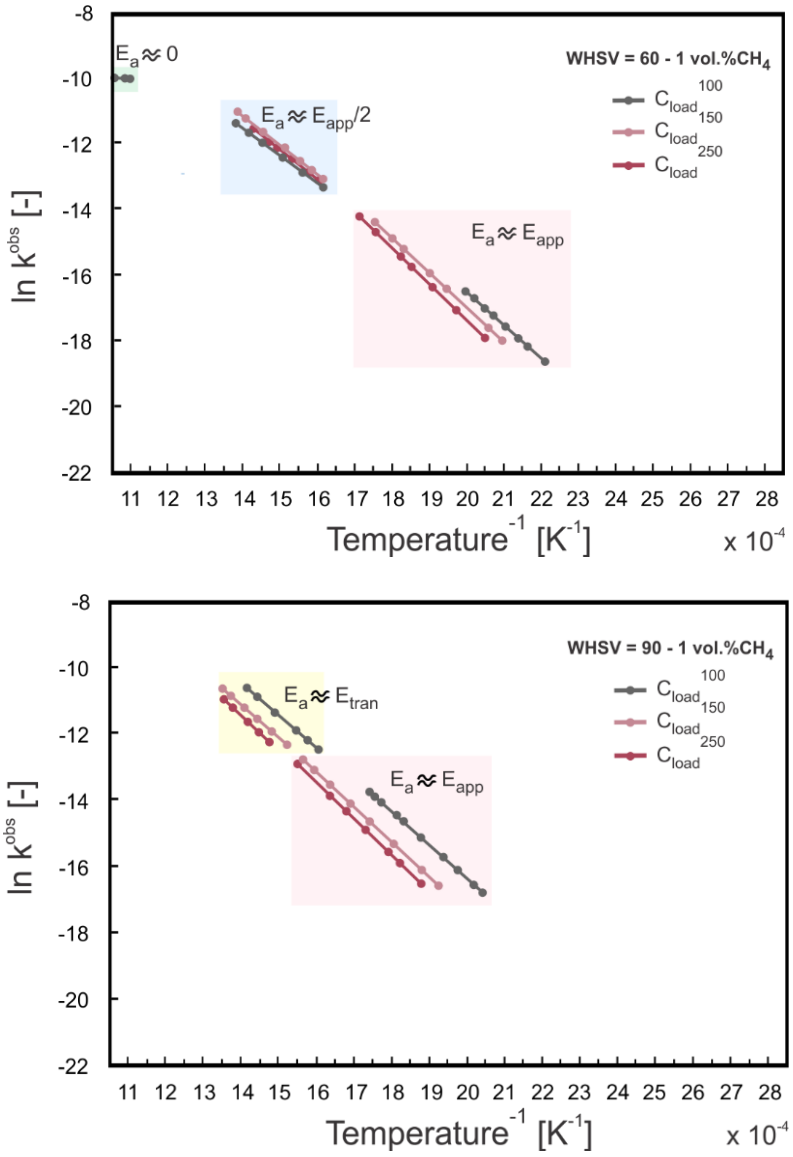


**Figure S4.** Arrhenius plots for the various catalyst contents ($C_{load}^{100}$, $C_{load}^{150}$, and $C_{load}^{250}$) at WHSV of 60 and 90 and inlet $CH_4$ concentration of 1 vol.%.

**Table S3.** Average activation energy and standard deviation calculated for the various catalyst contents ($C_{load}^{100}$, $C_{load}^{150}$, and $C_{load}^{250}$) at WHSV of 30, 60 and 90 NL $h^{-1}$ $g_{cat}^{-1}$ and inlet $CH_4$ concentration of 1 vol.%.

| **WHSV** [NL $h^{-1}$ $g_{cat}^{-1}$] | **$E_{a,average}$** [kJ $mol^{-1}$] | **SD** [kJ $mol^{-1}$] |
|---|---|---|
| *30* | 103.3 | 17.6 |
| *60* | 122.9 | 28.8 |
| *90* | 118.7 | 45.2 |

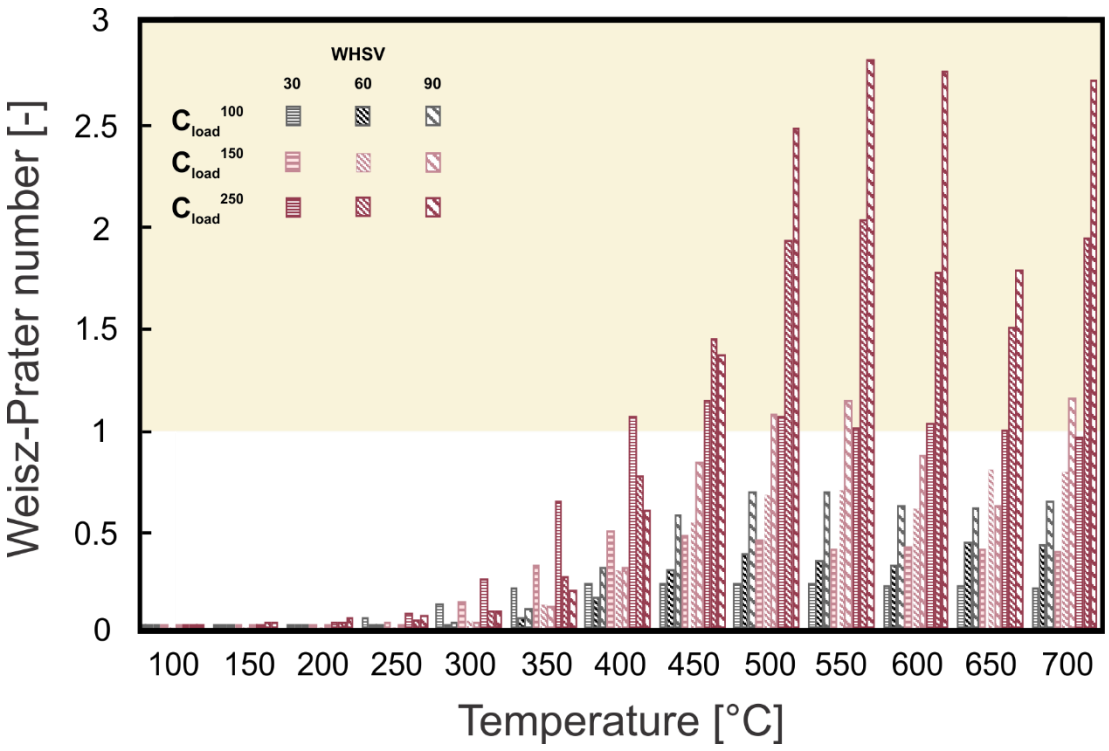


**Figure S5.** Weisz-Prater values for the various catalyst contents ($C_{load}^{100}$, $C_{load}^{150}$, and $C_{load}^{250}$) at WHSV of 30,60 and 90 NL $h^{-1}$ $g_{cat}^{-1}$ and inlet $CH_4$ concentration of 1 vol.%.

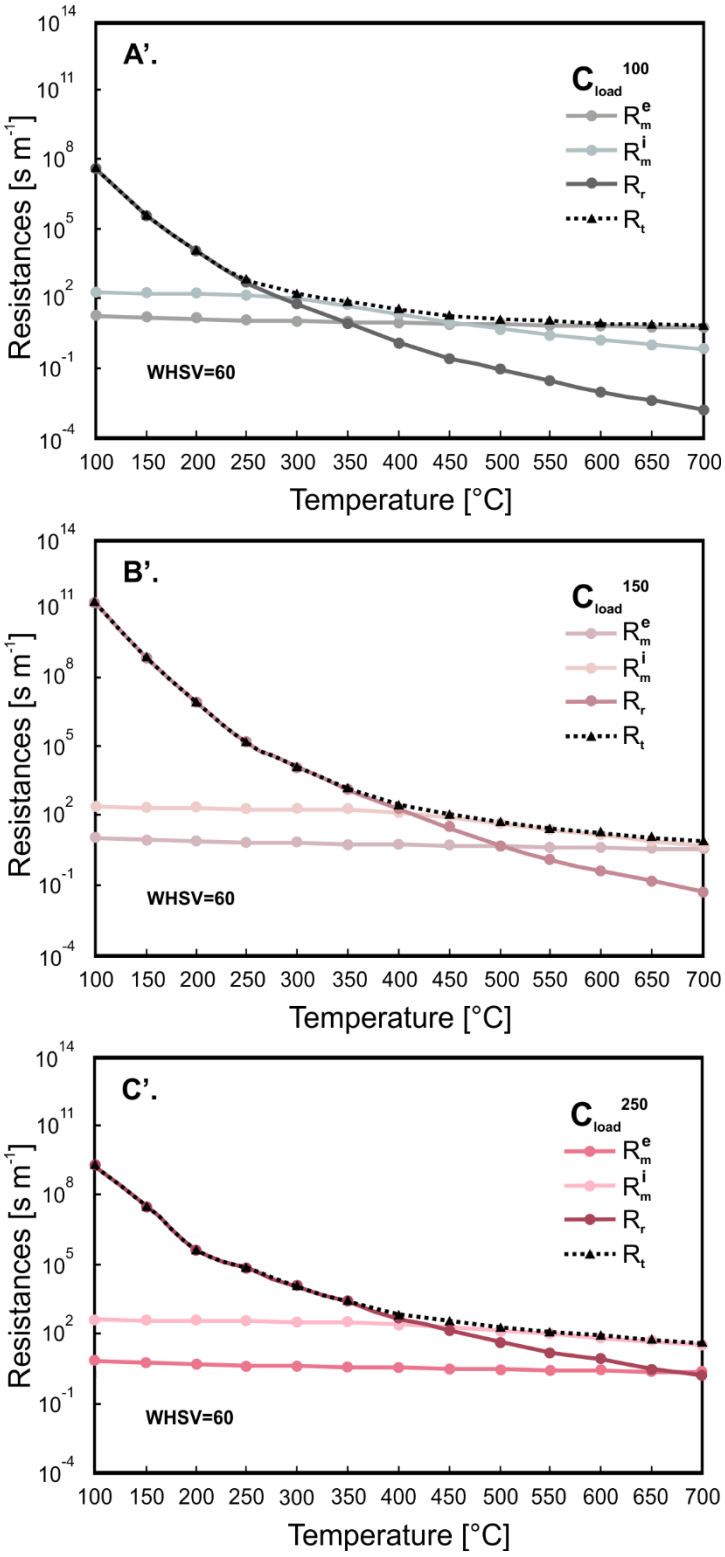


**Figure S6.** Various resistances versus temperature for the three catalyst contents at WHSV of 60 and inlet $CH_4$ concentration of 1 vol.%: $C_{load}^{100}$ (**A'**), $C_{load}^{150}$ (**B'**), and $C_{load}^{250}$ (**C'**).

# CHAPTER VI

(*PAPER VI*)

Imaging ceramic open cell foams by X-ray microcomputed tomography

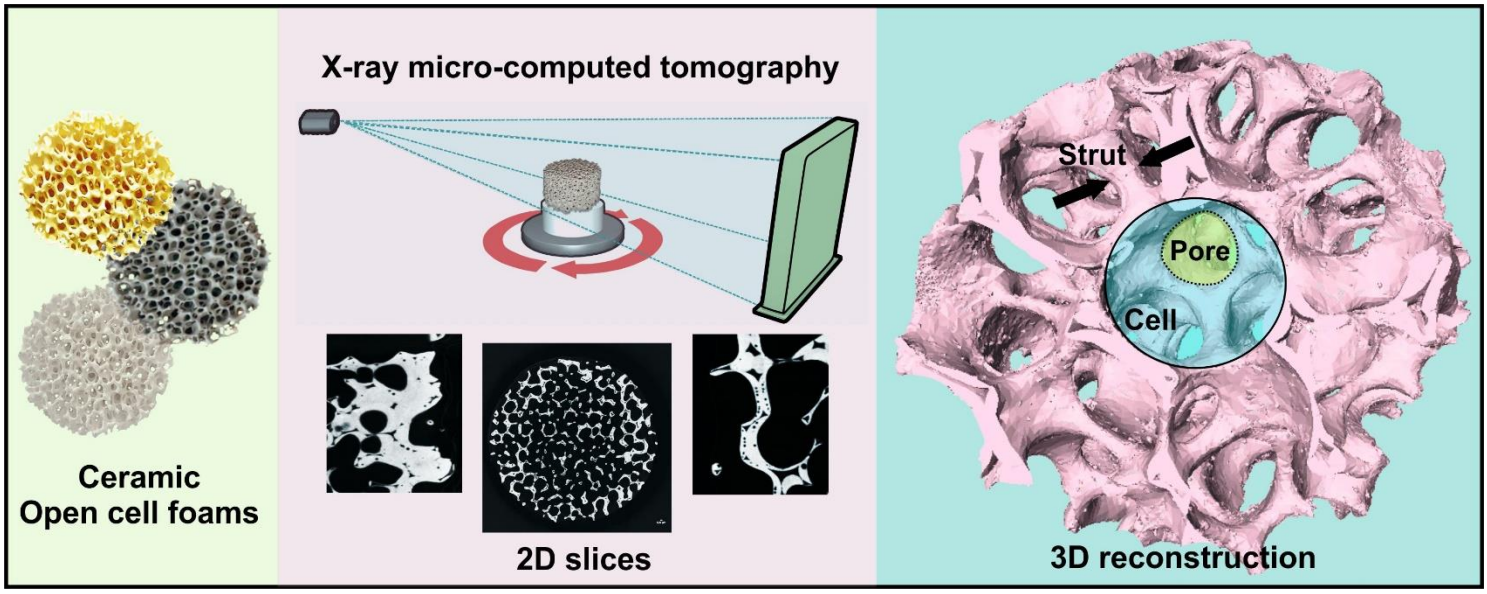


Under preparation

# Imaging ceramic open cell foams by X-ray micro-computed tomography

*Carmen W. Moncada Quintero*[a]*, *Marion Servel*[b], *Frédéric Augier*[b], *Yacine Haroun*[b], *Jean-François Joly*[b], *Stefania Specchia*[a]*

[a] Politecnico di Torino, Department of Applied Science and Technology, Corso Duca degli Abruzzi 24, I-10129 Torino, Italy

[b] IFP Energies Nouvelles, Établissement de Lyon, Rond-point de l'échangeur de Solaize, BP 3, F-69360 Solaize, France

* Corresponding authors: carmen.moncada@polito.it, stefania.specchia@polito.it

**KEYWORDS**

X-ray microcomputed tomography; strut/node/pore diameters; open porosity; specific surface area; pressure drop.

**ABSTRACT**

Ceramic open cell foams (OCFs) have become one of the most attractive structures for a wide variety of industrial applications. Therefore, the morphological and geometrical information on OCFs are an indispensable aspect in order to study the hydrodynamic and fluid flow transport phenomena. In this work, we focused on the characterization of OCFs made of zirconia, silicon carbide and alumina of different nominal pore densities using X-ray micro-tomography. This technique allowed the exhaustive and quantitative extraction of morphological and geometrical characteristics of the structures such as pore size, strut diameter and length, node diameter, open porosity, and specific geometrical surface area. Furthermore,

we evaluated the validity and suitability of different correlations reported in the literature that allow estimating the specific geometric surface area. Finally, we derived an empirical correlation that allows determining the specific surface area of foams at porosities in the range of 78-86 % for this kind of OCFs.

## 1. Introduction

In recent years, open cell foams (OCFs) have become one of the most attractive structures for a wide variety of industrial applications in the field of chemical engineering for process intensification, [1–4] and also in other engineering applications.[5–7] OCFs are irregular cellular materials made of interconnected solid struts that give rise to a continuous three-dimensional network, which enclose empty regions called cells.[8–12] This network leads to a highly porous structure that provides a flow pathway through the open windows that communicates with neighboring cells, as shown in **Figure 1**. OCFs are also characterized by a unique combination of physical properties such as high rigidity, lightweight, high specific surface area, and permeability,[13–17] offering clear advantages over classical fixed or packed bed reactors.[18–21]

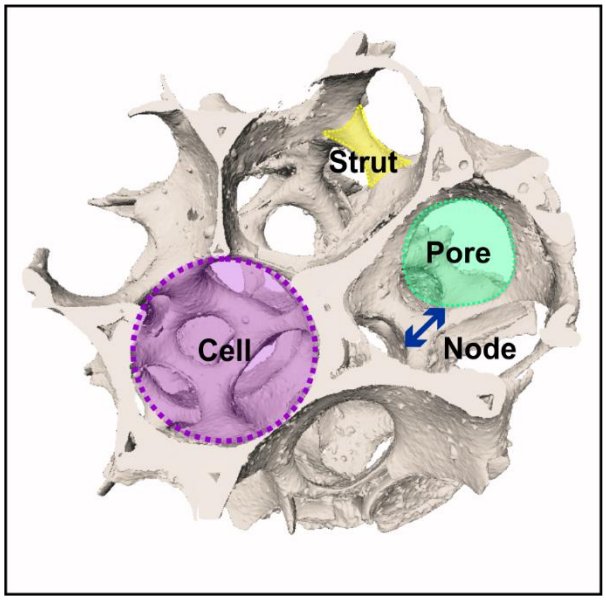


**Figure 1.** Morphological characteristic parameters of OCFs.

Depending on their composition, metallic or ceramic, OCFs have attracted interest in the design of compact heat exchangers[22–24] as well as structured catalysts,[2,3,8] burner heads,[25,26] fuel cell bipolar flow plates[27,28] and ~~as~~ structured packaging for the process intensification of reactors and columns.[29–41] Several authors have reported a remarkable enhancement in the performance when using foams as catalyst supports instead of operating in classical packed bed reactors or even in other types of substrates such as honeycombs and monoliths.[16,33,42–44] This is mainly due to the improved flow mixing (caused by the tortuous paths) and thus enhancement of mass/heat transfer properties, which are accompanied by lower pressure drops when compared to fixed beds. Both metallic and ceramic OCFs can be fabricated using methods as replication or direct foaming, where the choice of one material or the other depends on the structure's application.[6,8,13,17,24,44–51]

Recently, we studied ceramic OCFs and ceramic monoliths of different porosities as catalytic supports for both highly endothermic and exothermic reactions.[36,37,43,52–54] We found that both the foams and monoliths showed excellent catalyst adhesion and a clear enhancement of catalytic activity and mass transfer per unit volume. This advantage leads to a lower amount of noble metal to be loaded on the surface, which determines a cost reduction in the reactor design. Moreover, we also demonstrated that an increase of the catalyst loading (as mg of catalyst per $cm^{-2}$ of OCF or monolith) led to a greater dominance of the internal mass transfer resistance and limited residence time to complete the reactions.[37,54] It is clear that in structures as OCFs the hydrodynamic and transport properties are closely related to their peculiar morphology and geometrical characteristics such as pore size, strut thickness, porosity, specific surface area, etc. Such properties, not only allow to characterize the structure, but also to obtain a detailed analysis of the fluid-dynamic processes occurring within the foam network. Since the unit cell of foams commonly resembles a polyhedron with pentagonal or hexagonal faces that limit an inner space of spherical aspect, various authors have proposed different models to represent the open cell foam structures.[5,8–11,14,40,48–50,55] The first deterministic model was proposed by Lord Kelvin in 1887. This model was based on a tetrakaidecahedron cell (or commonly known as Kelvin's cell) composed of fourteen faces (eight hexagonal and six quadrilaterals) and twenty-four vertices, as shown in **Figure 2**. Lord Kelvin proposed the

tetrakaidecahedron cell as a packing pattern and stated that the cell shape was capable of dividing space into identical units of equal volume with a minimum surface energy.[56–59] Later, Weaire and Phelan[60] proposed an improved model of the Kelvin cell consisting of eight cells, six tetrakaidecahedra and two pentagonal dodecahedra. The structure proposed by the authors showed a surface area reduction of 0.3% with respect to the Kelvin structure. As the adoption of an anisotropic periodic cell structure showed unusual mechanical compatibility due to the lack of randomness present in real foams,[61,62] many researchers have proposed alternative methods that take into account the random disorder of foams. Habisreuther at al.[63] and Lucci et al.[64] varied the vertices positions of the ordered Kelvin multicellular structure using vectors with stochastic directions and values. Other researchers based their study on random models using Voronoi tessellation. This model requires initial seed points, which are generated by randomly packing spheres of cell diameter size through a discrete element method.[11,62,65–68] Once the spheres are settled, the centers are extracted and imported into the Voronoi algorithm, thus generating the foam skeleton. This model has proven to be able to adequately reproduce foams consisting of closed and open cells, allowing the generation of large virtual cellular structures following a predefined cell size distribution, cell arrangement and cross-section strut distribution law.[11,68–70] However, some authors have pointed out that the number of struts per vertex of the structures generated by Voronoi tessellation is higher than that of real foam structures, and the structural parameters of the foams reconstructed by Voronoi tessellation are different from those of real foams.[63,71] **Figure 2** shows the most common theoretical models for representing foams.

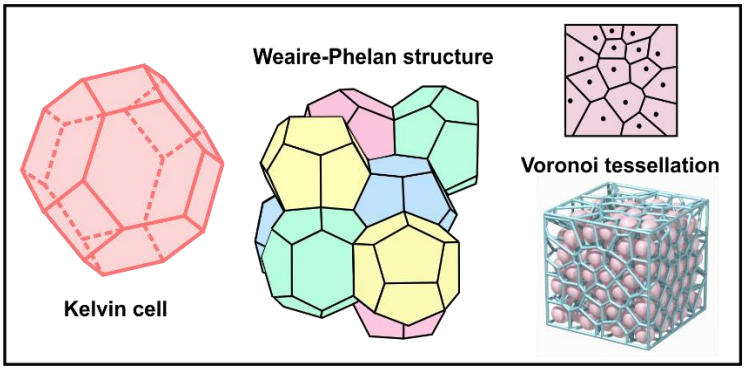


**Figure 2**. Kelvin unit cell, Weaire-Phelan structure and typical Voronoi tessellation used to represent the foam structure.

With the advancement of technology, imaging techniques that allow to recreate the three-dimensional structure of materials have become one of the fundamental tools in the study and inspection of the solids properties. In particular, X-ray computed micro-tomography (micro-CT) has become an indispensable method for the morphological properties characterization of foams.[37,72–78] The technique is based on the non-invasive and non-destructive inspection of the internal structure of a solid with a spatial resolution at the micron level that allows the construction of a three-dimensional model from two-dimensional cross-sectional image slices. It also provides a detailed exploration of the morphological and architectural parameters characteristic of the material, thus leading to a modeling study of the material structure.[9,79–81] The prediction of properties from microstructural information requires an accurate quantitative description of the material.[10]

In the present contribution, we characterized commercial ceramic OCFs made of zirconia (Zir), silicon carbide (SiC), and alumina (Alu) at different nominal pore densities (30 and 45 pore per inch, ppi) using X-ray micro-tomography techniques and image analysis to extract structural information (pore size, strut thickness, porosity, specific surface area, etc.). Furthermore, we evaluated the suitability and validity of several correlations reported in the literature that allow estimating the specific geometrical surface area of ceramic foams by comparing them with the experimental results obtained. Finally, we derived an empirical model based only on our experimental results that allows to determine the specific surface area from parameters easily accessible with standard laboratory equipment. We point out that our methodology is a simplified way to characterize OCFs, compared to what already available in the literature. Our methodology does not require sophisticated algorithms to find out parameters useful to calculate heat and mass transport properties when a catalytic reaction is performed on OCFs used as supports for catalysts.

## 2. Materials and methods

### 2.1. Open cell foams (OCFs)

In this study, different OCFs made of zirconia (Vukopor® HT, labelled as Zir), silicon carbide (Vukopor® S, labelled as SiC), and alumina (Vukopor® A, labelled as Alu) with nominal pore densities of 30 and 45 ppi each were analyzed. The foams were manufactured by Lanik S.r.o.[82] (Czech Republic) and supplied in cylindrical shapes with dimensions of 40 mm or 9 mm in diameter and 30 mm in length. The fabrication process applied by the company is based on the polymeric foam replication technique, where the OCFs are obtained as positive images of the template. Basically, the technique consists of infiltrating the ceramic slurry (containing $Al_2O_3$, SiC, $ZrO_2$, etc.) into the polymeric foam, removing the excess slurry, drying and then burning the polymeric template.[13,48,49,83] Once the plastic is vaporized, the ceramic particles sinter together giving rise to a ceramic replica or positive image ceramic foam. The chemical composition of the OCFs studied in this work are reported in **Table 1**, as provided by the manufacturer.[82]

**Table 1.** Chemical composition (weight percentage) of the studied ceramic OCFs.[82]

| *Chemical composition* | *Vukopor® HT (Zir)* | *Vukopor® S (SiC)* | *Vukopor® A (Alu)* |
|---|---|---|---|
| *SiC* | -- | 65.0 % | -- |
| *$Al_2O_3$* | 1.5 % | 15.0 % | 85.0 % |
| *$SiO_2$* | 0.3 % | 20.0 % | 14.0 % |
| *$ZrO_2$* | 92.3 % | -- | -- |
| *MgO* | 12.7 % | -- | 1.0 % |

### 2.2. X-ray computed tomography analysis

The structural characterization and 3D internal reconstruction of the foams was carried out using the non-destructive X-ray computed micro-tomography technique (micro-CT). Micro-CT scans were performed with an EasyTom (RX Solutions, France) system equipped with a 150/160 kV micro focus X-ray tube and a Varian plat panel detector. The principle of tomographic image acquisition consisted of directing X-rays at an object from multiple orientations and measuring the decrease in intensity along a series of linear trajectories (rotational axis).[84] **Figure 3** shows a schematic representation of the micro-CT device. The scan procedure can be briefly described as follows: i) the foam sample is placed on a rotating stage between the X-ray source and the detector, ii) a source transmits X-rays with a certain intensity, where part of the radiation is absorbed, part is scattered and the rest penetrates through the specimen, iii) the amount of X-rays attenuated by the sample is recorded by the detector, iv) the foam sample is then rotated 360° to transmit the rays from all possible directions with an angular rotation interval of 0.25 degrees and exposure time of 2 s, resulting in 1450 images per sample and lastly, v) a computer algorithm captures the data of each discrete part producing a 2D projection/scanned image and the CT slices are reconstructed by software creating the 3D volumetric rendering of the foams.

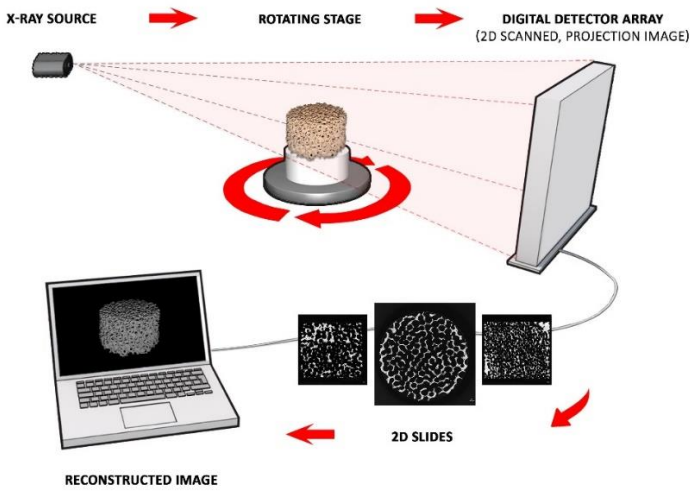


**Figure 3.** Schematic representation of the micro-CT device.

In order to obtain information about internal characteristic dimensions of the foams, all OCF samples with larger dimensions were first analyzed using two X-ray generators: i) for 150 micro focus X-ray tube, the X-ray power was set to 80 kV, current of 142 µA with pixel size of 22 µm and ii) for 160 micro focus X-ray tube, the X-ray source was operated at 100 kV, current of 50 µA with pixel size of 5 µm. Then, smaller foam cylinders (9 mm in diameter and 30 mm in length) were examined to determine the external porosity and geometrical surface area of the macro-porous solid using a micro focus X-ray tube set to 70 kV and 200 µA with pixel size of 5 µm. For all measurements, an aluminum filter was used to selectively attenuate or block out, the lower energy photons during x-ray imaging.

### 2.3. Image processing

Once the images were acquired, they were filtered using an RX-solution post-processing program and processed using Avizo Thermo Fisher Scientific Version 2019.1 software. First of all, a pixel-binning mode was applied to obtain smaller image volumes and reduce the computational time of analysis. This process consisted of combining a group of pixels into a single pixel. Thus, for a 2 x 2 binning process, a group of 4 pixels was converted into a single larger pixel, reducing the overall number of pixels while guaranteeing sufficient image contrast. Then, 2 x 2 x 2 binned sub-volumes (1006 x 1006 x 736 voxels) were selected to remove uninteresting regions from the original micro-CT image. Subsequently, a Gaussian filter (Kernel size factor of 2) was employed to blur and reduce the noise introduced during the image acquisition/transmission step.[12] This filter allowed smoothing the region of interest while preserving edges and corners of the solid structure. Finally, a segmentation process was applied to transform the original image volume into a binary volume. Basically, the ceramic solid phase (low-signal region) and the gas phase contained within the void cells (high-signal region) were distinguished by converting the grayscale micro-CT data into a binary format using the adaptive histogram technique developed by Otsu.[85] This method is based on an automatic global thresholding algorithm focused on maximizing separability in the gray level classes.[9,75,79,85,86] At this point, the internal strut pores were filled due to binning process, thus, only the foam macro-porosity was taken into account. After segmentation operation, the images were ready

for analysis allowing the morphology characterization of OCFs. The image analysis was carried out using both Avizo and the free software FijiImageJ, which allowed the extraction of information such as strut length ($l_s$), pore and strut diameter ($d_p, d_s$), geometric surface area ($S_{ga}$) and open porosity ($\varepsilon_o$).

## 3. Results and discussion

### 3.1 Characteristic dimensions

Pore, strut and node dimensions ($d_p, d_s, l_s, d_n$) were extracted directly from the 2D micro-CT images. In order to estimate the pore diameter, we first accurately evaluated the area of each pore (cross-sectional area of the void space) using the FijiImageJ software, then the diameter of an equivalent circle was determined (**Figure 4.A**). As reported in our previous work,[36] the circular pore shape assumption can be perfectly adopted for the analysis of foams as catalytic supports, even if the structures present mostly oval pores. As for the strut, because during the manufacturing process the ceramic precursor slurry is deposited mostly at the nodes instead of being homogeneously distributed along the length, the strut exhibits a variable cross-section with diameter values that reach a maximum at the intersections (nodes) and a minimum at the center of its length. We measured the diameter of the strut in the middle of the strut length (as shown in **Figure 4.B**) and the node diameter at the junction between the strut and the node (as shown in **Figure 4.C**) using Fiji ImageJ.[40,87] Furthermore, for a further insight into the foam geometry, the strut-to-strut angle of all ceramic structures was also evaluated. More than 550 measurements were taken for each characteristic dimension of the foams analyzed.

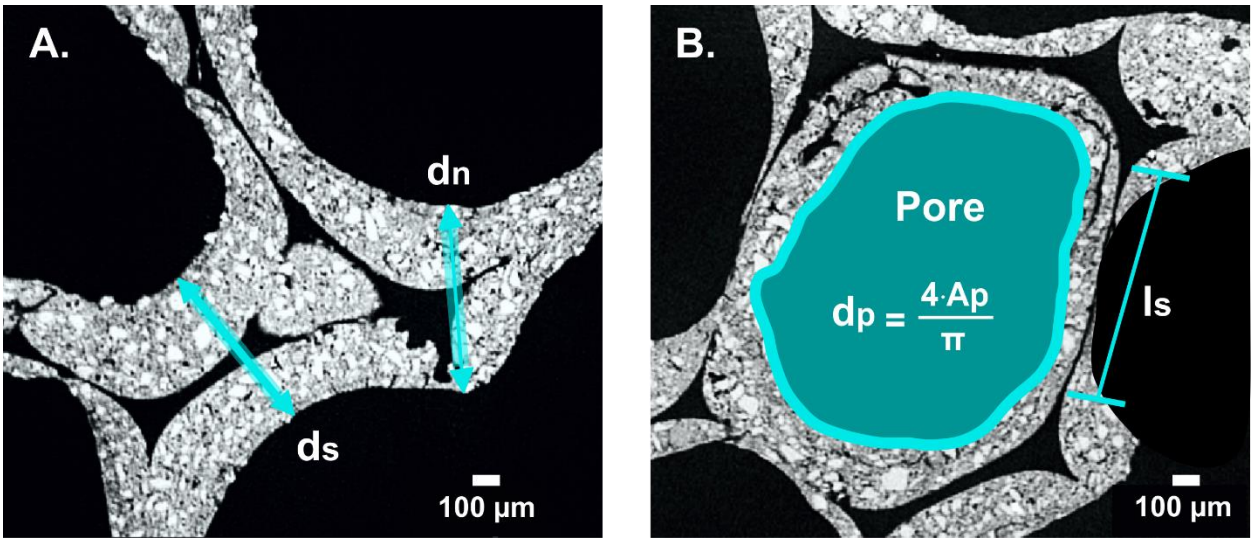


**Figure 4.** Evaluation of node diameter, pore diameter, and strut length / diameter (pixel size of 5 µm).

**Figure 5** (A1/2 for Alu_30/Alu_45; B1/2 for SiC_30/SiC_45; C1/2 for Zir_30/Zir_45) shows the 2D image slices extracted from the CT reconstruction for all the OCFs studied. It can be clearly observed that for all three ceramic materials, the increase in nominal pore density from 30 to 45 ppi leads to a much more compact structure due to the higher number of cells and hence struts per unit volume present in the foam. In fact, the increment of ppi caused a decrease in size of the characteristic morphological properties, since the higher the number of pores per linear inch, the smaller the cell size (as observed in **Figures 5** D/E/F/G/H). Interestingly at both ppi values, the zirconia foam exhibited larger morphological properties compared to the alumina and silicon carbide foams. For example, at 45 ppi, the Zir_45 foam shows an increase in pore size of 593 and 458 % with respect to the SiC_45 and Alu_45 foams, respectively. On the other hand, the SiC foam showed the lowest dimensions in terms of strut length and pore diameter at both ppi studied. **Table 2** lists the min/max, average values and standard deviations of the pore/node/strut diameters, and strut length and strut-to-strut angle for all the OCFs analyzed. The slight deviations could be due to the method of analysis of the tomographic and microscopic images as well as to the method of fabrication of the foams applied by each manufacturer. As far as the strut-to-strut angle is concerned ($\alpha_{ss}$),

the mean values ranged between 115.6 and 118° (see **Figure 5H**), being slightly higher than the theoretical angle reached at thermodynamic equilibrium in liquid foams, according to Plateau's laws.[88] These deviations have also been reported in the literature for polyurethane foams and the difference with respect to the theoretical rule was attributed to the fact that polymeric foams are not perfectly equilibrium structures, since they freeze before they can reach such a state.[72] Besides, the differences can also be attributed to the different shape stresses that can exist in the real foam systems.[72]

**Table 2.** Min/max/verage values and standard deviations of the pore and node dieter, strut diameter and length, strut-to-strut angle for all the OCFs analyzed, as reported in **Figure 5** D/E/F/G/H.

| **Pore diameter** | | | | |
|---|---|---|---|---|
| **Foam** | Min $d_p$ [mm] | Max $d_p$ [mm] | Average $d_p$ [mm] | Standard deviation [mm] |
| **Alu_30** | 0.75 | 3.25 | 2.58 | 0.47 |
| **Alu_45** | 0.54 | 2.14 | 1.52 | 0.26 |
| **SiC_30** | 0.58 | 3.07 | 2.22 | 0.53 |
| **SiC_45** | 0.32 | 2.05 | 1.47 | 0.26 |
| **Zir_30** | 1.81 | 3.87 | 2.87 | 0.44 |
| **Zir_45** | 0.75 | 2.86 | 2.25 | 0.39 |
| **Node diameter** | | | | |
| **Foam** | Min $d_n$ [mm] | Max $d_n$ [mm] | Average $d_n$ [mm] | Standard deviation [mm] |
| **Alu_30** | 0.24 | 1.11 | 0.55 | 0.16 |
| **Alu_45** | 0.17 | 0.87 | 0.46 | 0.12 |
| **SiC_30** | 0.21 | 1.07 | 0.65 | 0.15 |
| **SiC_45** | 0.19 | 0.86 | 0.44 | 0.11 |
| **Zir_30** | 0.31 | 1.24 | 0.65 | 0.18 |
| **Zir_45** | 0.27 | 0.98 | 0.56 | 0.14 |

| Strut diameter | | | | |
|---|---|---|---|---|
| **Foam** | Min $d_s$ [mm] | Max $d_s$ [mm] | Average $d_s$ [mm] | Standard deviation [mm] |
| **Alu_30** | 0.13 | 0.97 | 0.38 | 0.13 |
| **Alu_45** | 0.04 | 0.57 | 0.23 | 0.08 |
| **SiC_30** | 0.13 | 0.76 | 0.35 | 0.12 |
| **SiC_45** | 0.03 | 0.32 | 0.21 | 0.05 |
| **Zir_30** | 0.16 | 1.01 | 0.51 | 0.17 |
| **Zir_45** | 0.10 | 0.74 | 0.33 | 0.12 |
| **Strut length** | | | | |
| **Foam** | Min $L_s$ [mm] | Max $L_s$ [mm] | Average $L_s$ [mm] | Standard deviation [mm] |
| **Alu_30** | 0.27 | 1.06 | 0.64 | 0.14 |
| **Alu_45** | 0.17 | 0.72 | 0.40 | 0.08 |
| **SiC_30** | 0.27 | 1.05 | 0.62 | 0.18 |
| **SiC_45** | 0.12 | 0.70 | 0.37 | 0.08 |
| **Zir_30** | 0.34 | 1.36 | 0.77 | 0.20 |
| **Zir_45** | 0.25 | 0.95 | 0.57 | 0.13 |
| **Strut-to-strut angle** | | | | |
| **Foam** | Min $\alpha_s$ [°] | Max $\alpha_s$ [°] | Average $\alpha_s$ [°] | Standard deviation [°] |
| **Alu_30** | 103.77 | 133.71 | 116.31 | 6.73 |
| **Alu_45** | 100.56 | 151.87 | 116.18 | 7.56 |
| **SiC_30** | 101.68 | 131.28 | 115.60 | 6.69 |
| **SiC_45** | 97.18 | 129.48 | 115.91 | 7.46 |
| **Zir_30** | 95.52 | 126.63 | 116.48 | 7.18 |
| **Zir_45** | 89.33 | 135.52 | 117.99 | 7.88 |

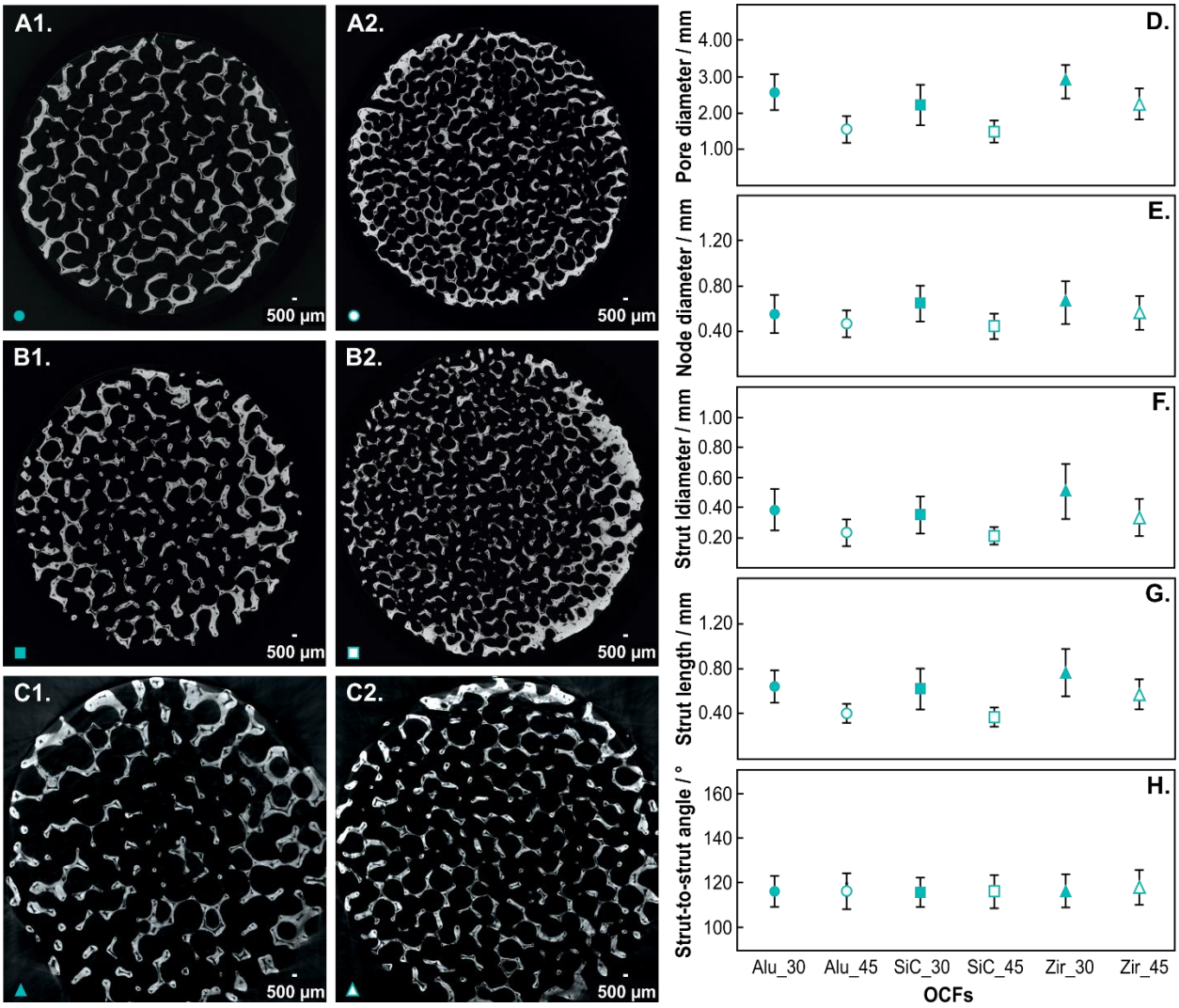


**Figure 5**. 2D reconstructed CT slices (pixel size of 22 µm) for Alu_30/Alu_45 (A1/A2), SiC_30/SiC_45 (B1/B2), Zir_30/Zir_45 (C1/C2) and the mean and standard deviation of pore diameter (D), node diameter (E), strut diameter (F), strut length (G), and strut-to-strut angle (H) measured for all OCFs studied.

For comparison, we plotted in **Figure 6A** the mean values of node diameter vs. strut diameter obtained experimentally in this work with those reported in the literature on ceramic foams. Clearly, there is a linear correlation between $d_n$ and $d_s$ (**Figure 6B**) and the values obtained here are in line with those reported

previously by different authors on foams made of $Al_2O$,[39,40,49] SiC,[80,87] and SiSiC.[89] The literature values used in **Figure 6B** have been estimated according to the calculations available in the *Annex 1*.

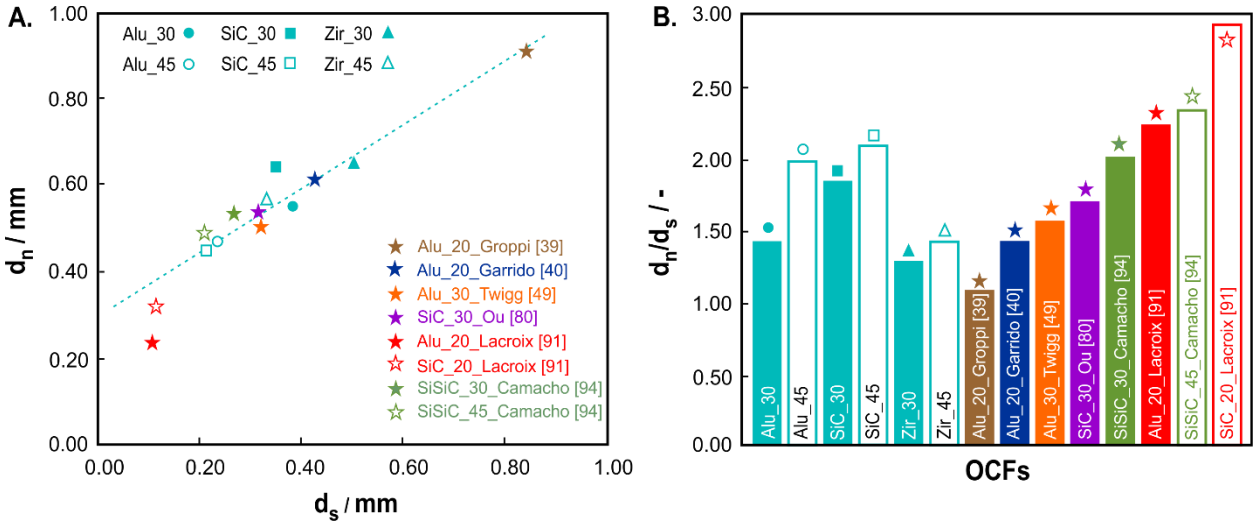


**Figure 6**. Relationship between the node diameter and the strut diameter for Alu_30/Alu_45, SiC_30/SiC_45, Zir_30/Zir_45 and different OCFs from the open literature (A), and $d_n/d_s$ ratio for all the OCFs examined.

Moreover, it is important to highlight that the pore size of OCFs is conventionally estimated by counting the number of pores per linear inch (usually denoted as ppi), referred to this paper as nominal pore density. Nevertheless, such a definition is rather confusing since in some studies the pore is usually the entire section of a cell, while in others it is a window.[5,8–10,21,40,46,48,49,55,77,87] A cell represents a 3D volume, but the ppi reduces this volume to a linear measurement of the non-defined pore. Furthermore, this pore density, commonly used by foam manufacturers, does not provide a precise measurement, but it merely represents a range of cell or pore sizes. Generally, the reference scale of foams changes according to each manufacturer, thus a foam defined as 80 ppi by one manufacturer could be defined as 110 ppi by another.[90]

However, some authors still use the nominal ppi value in the determination of the pore size and as a modeling parameter.[91,92]

Another point worth noting is the presence of microporous walls in the foam skeleton (**Figure 7.A**). This micro-porosity is commonly referred to as "strut porosity". It is originated during the manufacturing process.[5,40,48,83,93,94] Since most commercial foams, including those studied in this work are manufactured using the replication technique, the OCFs are obtained as positive images of the burned polymer templates giving rise to hollow struts with internal void volume. Such porosity can be avoided by using other manufacturing techniques such as direct foaming, which can result in fully dense solid skeletons but with much more closed cells.[17,51,95] A further aspect observed in the foam skeleton is the presence of dense grains along the microporous walls (**Figure 7.C**). These defects could be due to the various steps of the replication process, such as the preparation of ceramic slurry, the grain size of the ceramic particles, the dispersion of stabilizers or wetting agents, the viscosity, etc.[51,95,96] On the other hand, all the foams showed a circular strut cross-section shape (as shown in **Figure 7.B**).

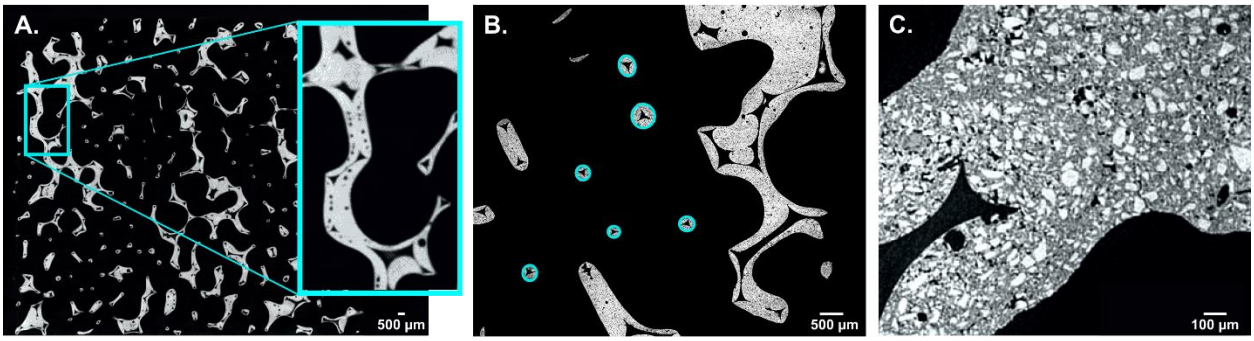


**Figure 7.** Foam micro-porosity (A: Alu_30), circular strut cross section (B: Alu_30) and dense grains along the micro-porous walls (C: SiC_30).

### 3.2 Porosity

Several authors have reported that OCFs manufactured using the replication method are characterized by three types of porosity:[5,9,10,12,97] i) open porosity ($\varepsilon_o$), ii) strut porosity ($\varepsilon_s$), and iii) total porosity ($\varepsilon_t$). The open porosity or also called hydrodynamic porosity refers to the void volume space present between the strut network of the foam, which is fluid-dynamically relevant. The strut porosity, also called internal porosity, is the fraction of void present in the ceramic foam skeleton that originates from the manufacturing process, which is fluid-dynamically irrelevant. The total porosity is the combination of open and strut porosity, which can be expressed as follows:

$$\varepsilon_t = \varepsilon_o + \varepsilon_s \quad (1)$$

**Figure 8** shows a fragment of the strut (**Figure 8.A**) and a zoom of the skeleton (**Figure 8.B**) of the Zir_30 foam. Clearly, **Figure 8** reveals the presence of a micro-porosity within the structure. Since fluid access and even catalyst deposition inside the micro-pores is quite difficult, the hydrodynamic study of OCFs usually neglects the strut porosity. In fact, some authors have characterized the total and open porosity of foams using techniques such as helium pycnometry[52] and mercury intrusion porosimetry.[5,9,97] They have concluded that the difference of such porosity values, due to the presence of eventual internal strut cavities was lower than 5 %.

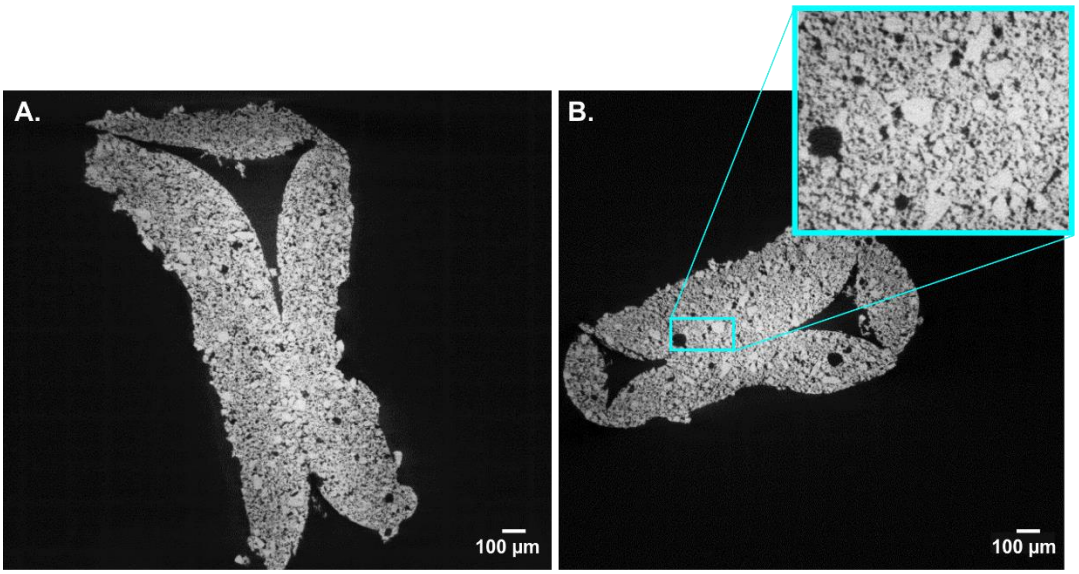


**Figure 8.** Fragment of the strut (A) and a magnification (B) of the Zir_30 foam skeleton (pixel size of 1.7 µm).

Since the micro-CT technique does not allow access to the internal voids of the foam skeleton at an adequate resolution scale, only the macro-porosity of the structure was evaluated in this work. Using the segmentation process, it was possible to fill the hollow strut and the micro-porosity of the solid skeleton,[98] as shown in **Figure 9**. Once the 3D image was reconstructed, a cylinder volume was analyzed and the measured open porosity ($\varepsilon_{o,m}$) was determined as:

$$\varepsilon_{o,m} = 1 - \frac{v_f}{v_c} \quad (2)$$

where $v_f$ is the macro-porous solid volume and $v_c$ is the analyzed cylinder volume.

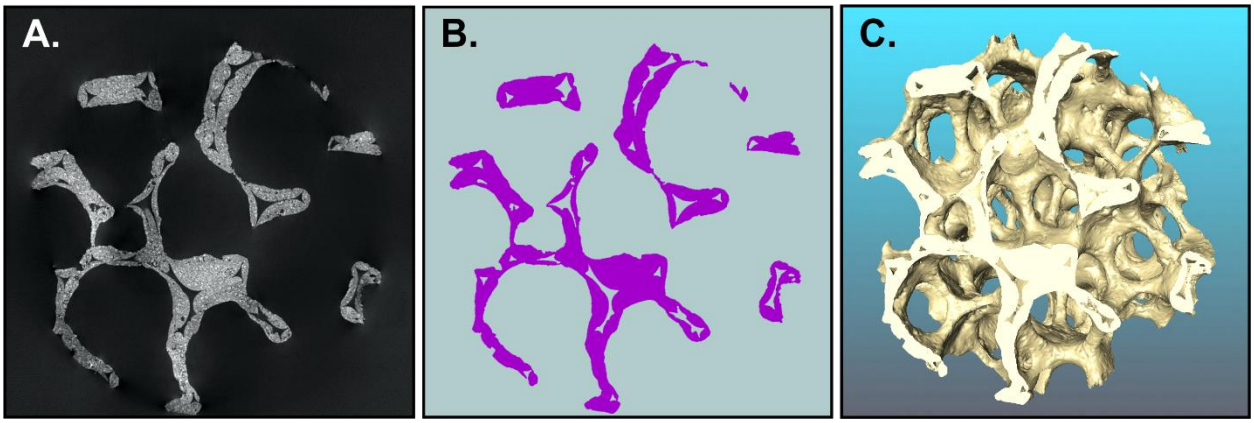


**Figure 9.** (A) Raw gray scale micro-CT data of SiC_30, (B) after grayscale-based thresholding according to the method of Otsu[85], (C) 3D reconstruction of the OCF.

**Table 3** lists the nominal and measured (by micro-CT) porosity values of all ceramic foams studied. As observed, the difference between the value of nominal and estimated open porosities is below 5%. Furthermore, it is clear that the higher pore density the lower the void space of the macro-porous solid, which is in line with the measured open porosity values. However, such aspect cannot be evidenced in the porosity values supplied by the manufacturer, as they report only one open porosity value per ceramic material. On the other hand, it is important to highlight the influence of $\boldsymbol{\varepsilon_o}$ on the strut cross section. As we mentioned in the previous section, the circular cross section was mostly observed in all the ceramic OCFs studied in this work. Several authors have reported that the shape of the strut cross section in the foam skeleton depends directly on the material's open porosity.[9,46,55,77,87,99–101] Bhattacharya et al.[46] studied metal fiber foams made of aluminum alloy with porosities between 0.85 and 0.97. They concluded that the cross section of the strut changes from circular to triangular when the porosity reaches a value of 0.935. At porosities above 0.935, the cross section transforms into a concave triangular shape. Huu et al.[55] reported that the change of cross section from circular to triangular occurs at porosities of about 0.9. The authors concluded that such a phenomenon was valid in both ceramic and metal foams. However, they did not demonstrate experimental evidence of such a statement in ceramic foams. Later, Lacroix et al.[87] investigated

ceramic foams made of β-SiC with porosities between 0.76 and 0.92. They reported the presence of a concave triangular shape at porosities above 0.9. Nevertheless, the porosity boundary where the triangular strut changes to concave has not yet been identified. Recently, Inayat et al.[9] focused their study on the morphological properties of ceramic foams based on sintered silicon carbide with porosities below 0.9. The authors concluded that for open porosities lower than 0.9, the ceramic foams show circular cross section. All these studies mentioned above are in line with those obtained in this work, where the three ceramic OCFs (Zir, Alu, and SiC) at open porosities in the range 0.78-0.86 showed a circular hollow strut cross section.

**Table 3.** Nominal ($\boldsymbol{\varepsilon_{o,n}}$) and measured ($\boldsymbol{\varepsilon_{o,m}}$) open porosities of all ceramic OCFs studied.

| FOAM | $\boldsymbol{\varepsilon_{o,n}}$ | $\boldsymbol{\varepsilon_{o,m}}$ |
|---|---|---|
| **ALU_30** | 0.82 | 0.82 |
| **ALU_45** | | 0.80 |
| **SIC_30** | 0.82 | 0.79 |
| **SIC_45** | | 0.78 |
| **ZIR_30** | 0.84 | 0.86 |
| **ZIR_45** | | 0.84 |

### 3.3 Specific surface area

The specific geometric surface area of OCFs is one of the most relevant properties for mass, heat, and momentum transfer, influencing the reaction rate in heterogeneous catalysis,[102] as well as being a key input parameter for the modeling of pressure drop across the structure.[103] It is defined as the total external surface area of the struts per unit geometric volume, assuming that all struts have a perfectly smooth surface. However, the material may have a rough surface and possess a porosity within the hollow strut, as in the

case of the ceramic foams studied in this work. Therefore, conventional methods such as nitrogen adsorption (BET) cannot be used to experimentally measure the specific surface area, since it leads to an overestimation of the parameter. Because of this fact, volume imaging techniques such as micro-CT play a fundamental role in the determination of the specific geometric surface area. We estimate the surface area of ceramic foams by analyzing micro-CT images of the samples using smaller specimens (9 mm x 30 mm in diameter and length, respectively) in order to reduce the computational efforts during data processing.[104] **Table 4** lists the specific surface area values of all the foams studies. As expected, the increase in pore density leads to a higher specific surface area due to the increase in the number of strut per unit volume. Interestingly, at lower pore density the zirconia foam showed a higher geometric surface area with respect to the alumina and silicon carbide foams. However, as the pore density increased to 45 ppi, the ceramic foams made of alumina and silicon carbide showed a higher compactness (higher number of strut/solid phase per unit volume) in their structure compared to the zirconia foam (see **Figure 5** from **A1** to **C2**), which led to higher specific surface areas for the alumina and silicon carbide foams with respect to the zirconia one.

**Table 4.** Measured specific geometrical surface areas of all ceramic OCFs investigated.

| FOAM | $S_{ga,m}$ [$M^{-1}$] |
|---|---|
| **ALU_30** | 996.02 |
| **ALU_45** | 1480.85 |
| **SIC_30** | 899.90 |
| **SIC_45** | 1504.24 |
| **ZIR_30** | 1092.15 |
| **ZIR_45** | 1397.47 |

In order to compare the experimental values of specific surface area obtained here, we review some literature-derived correlations developed as a function of open porosity, which take into account the cross section of the strut. Since the surface area/volume ratio changes with varying strut cross section, this may have a strong impact on the overall geometrical surface area. Therefore, we evaluate the validity and suitability of different correlations presented in literature for circular strut cross sections (based on both periodic unit cell assembly and empirical formulations) with the experimental specific surface area data obtained in this work. The related equations are reported in **Table 5** and discussed below.

**Table 5.** Correlations for the estimation of $\boldsymbol{S_{ga}}$ derived in literature for circular strut cross-sections.

| REFERENCE | CELL MODEL | $\boldsymbol{S_{ga}}$ |
|---|---|---|
| **Lacroix et al.**[87] | Cubic | $S_{ga} = \frac{4}{d_s} \cdot (1 - \varepsilon_o)$ |
| **Garrido et al.**[40] | Empirical | $S_{ga} = 3.84 \cdot \left(\frac{d_p + d_s}{m}\right)^{-0.85} \cdot {\varepsilon_o}^{-0.82}$ |
| **Grosse et al.**[5] | Weaire-Phelan | $S_{ga} = \frac{4.84\sqrt{1 - \varepsilon_o} - 2.64 \cdot (1 - \varepsilon_o)}{d_p + d_s}$ |
| **Lucci et al.**[64] | TKKD | $S_{ga} = \frac{10.33 \cdot \sqrt{1 - \varepsilon_o} - 5.8 \cdot (1 - \varepsilon_o)}{d_p + d_s}$ |
| **Ambrosetti et al.**[21] | TKKD | $S_{ga} = \frac{-7.377 \cdot d_s^2 + 10.082 \cdot d_s \cdot d_c + 0.3548 \cdot d_c^2}{0.419 \cdot (d_c + d_s)^3}$ |

Lacroix et al.[87] used the cubic cell model originally proposed by Lu et al.[29] to derive a correlation of the specific geometric surface. This model considers the foam struts as cylindrical ligaments that are connected three-dimensionally giving rise to a regular cubic lattice. Later, Garrido et al.[40] proposed an empirical correlation in ceramic foams with porosities lower than 0.82. The authors introduced a dimensionless geometrical parameter ($m$) that allowed them to adjust their experimental values. On the other hand, Grosse

et al.[5] used the Weaire-Phelan structure to model their ceramic foams. Since their experimental results deviated from the theoretical model, they developed a semi-empirical correlation by fitting data while essentially maintaining the Weaire-Phelan model. Later, Lucci et. al.[64] presented a model based on the stacking of regular Kelvin cells (TKKD model). They used the theoretical model to determine the specific surface area, and then compared them with a series of parametric CAD reconstructions of foams at different porosity and cell diameters. Since the theoretical model overestimated the values obtained at low porosities, they derived a correlation that permitted them to adjust the geometrical results. Recently, Ambrosetti et al.[21] developed a geometrical model of OCFs based on a Kelvin cell as a unitary periodic unit. This model was derived under purely analytical considerations assuming that the shape of the strut was circular. The authors compared their results with a wide variety of foams of different porosity obtaining a good fit of the experimental results.

From **Figure 10**, it can be observed that the models based on the Kelvin cell provide a much closer approximation to the experimental values obtained. Particularly, the correlations derived by Lucci et. al.[64] and Ambrosetti et al.[21] showed a deviation lower than 25 %, fitting our experimental data to a good extent. Similarly, the empirical correlation derived by Garrido et al.[40] showed an error of 18 % for foams with porosity lower than 0.82, while increasing the porosity to 0.86, the deviation from our experimental results increased to 22 %. On the other hand, it is observed that the equation derived by Lacroix et al.[87] overestimates the specific surface area values, while the Weaire-Phelan model deviates by approximately 53 % from our experimental values.

Thus, we developed an empirical model based on the geometric surface areas, pore diameters and open porosities estimated using micro-CT by fitting parameters to experimental values, resulting in a good correlation of the geometric characteristics of ceramic foams with circular strut cross-sections (**Figure 10**). The equation we derived can be expressed as:

$$S_{ga} = \frac{2.688 \cdot \varepsilon_o^{-0.82}}{d_p + d_s} \quad (3)$$

We underline that this empirical correlation is valid for OCFs with porosity in the range 78-86 %, derived from OCFs of Alu, SiC and Zir. To our knowlegde, in the literature there are no availability of data related to zirconia foams. As appreciable from **Figure 10**, our correlation estimates the specific surface area of foams with an average error of 12 %. Consequenlyt its validity for OCFs different from these commercial ones, must be verified.

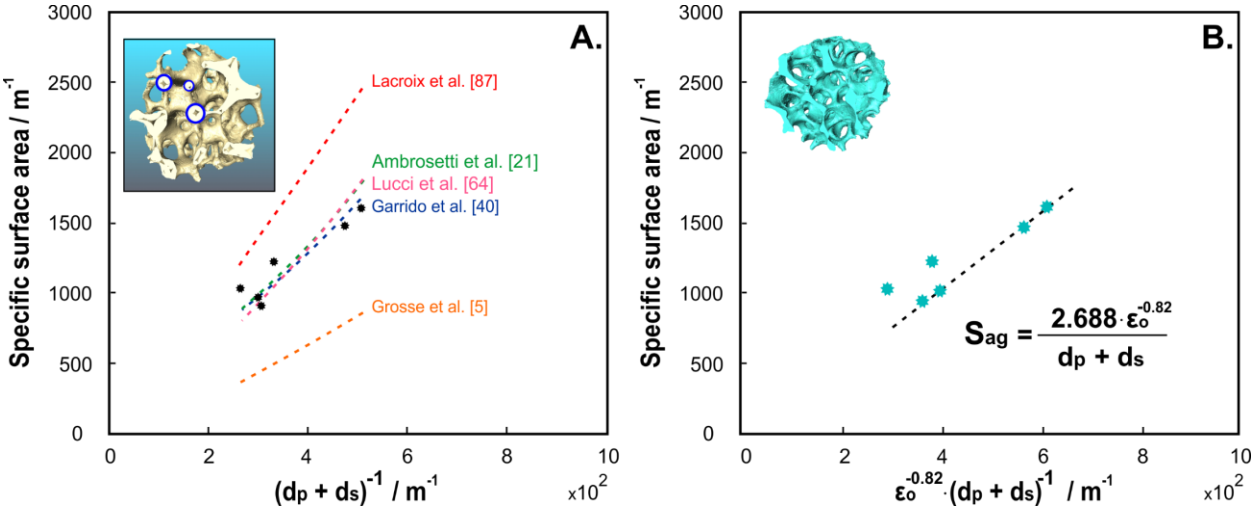


**Figure 10.** (A) correlations available in the literature to estimate the specific surface area $S_{ga}$ with an error ranging from 18 to 53 %; (B) the correlation we derived to estimate the specific surface area $S_{ga}$ from micro-CT measurements, with an average error of 12 %.

## Conclusion

Ceramic open cell foams made of zirconia, silicon carbide and alumina with nominal pore densities of 30 and 45 ppi have been characterized using the micro-CT technique. Characteristic dimensions such as pore size, strut diameter, and strut length as well as open porosity and specific surface geometry have been experimentally measured. For all ceramic structures the increase in nominal pore density led to a much more compact structure due to the higher number of cells and hence of strut per unit volume. The zirconia foam showed larger dimensions in terms of pore diameter, strut length and strut diameter at both nominal

ppi values studied. The estimated experimental pore density was not congruent with the manufacturer's definition of pores per linear inch. Dense grains and microporous walls caused by the replication technique applied by the manufacturer were evidenced in all foam skeletons. Furthermore, all foams showed circular strut cross sections at open porosities below 85 %. On the other hand, the specific surface area of the foams increased with increasing pore density, where theoretical models based on the Kelvin cell provided a much closer approximation to the experimental values obtained. An empirical correlation that allows to determine the specific surface area of ceramic foams at porosities in the range 78-86 % was proposed. The results obtained in this work provide an opportunity for detailed modeling and fluid dynamic studies based on open cell foams.

## ASSOCIATED CONTENT

*Annex I* (file type: EXCEL). **Measurement sheets**: calculations of the characteristic dimensions of Alu, SiC and Zir OCFs (this work) and of OCFs from the literature (Twigg et al., Camacho et al., Garrido et al, Groppi et al, Ou et al).

## AUTHOR INFORMATION

### Corresponding Authors

**Carmen W. Moncada Quintero** – *Department of Applied Science and Tehnology, Politecnico di Torino, Torino 10129, Italy*; orcid.org/0000-0002-9058-3646; Email: carmen.moncada@polito.it

**Stefania Specchia** – *Department of Applied Science and Tehnology, Politecnico di Torino, Torino 10129, Italy*; orcid.org/0000-0003-3882-3240; Email: stefania.specchia@polito.it

### Authors

**Marion Servel** – *IFP Energies Nouvelles, Établissement de Lyon, Rond-point de l'échangeur de Solaize, BP 3, F-69360 Solaize, France*; orcid.org/ 0000-0002-9267-8462; Email: marion.servel@ifpen.fr

**Frédéric Augier** – *IFP Energies Nouvelles, Établissement de Lyon, Rond-point de l'échangeur de Solaize, BP 3, F-69360 Solaize, France*; Email: frederic.augier@ifpen.fr

**Yacine Haroun** – *IFP Energies Nouvelles, Établissement de Lyon, Rond-point de l'échangeur de Solaize, BP 3, F-69360 Solaize, France*; Email: yacine.haroun@ifpen.fr

**Jean-François Joly** – *IFP Energies Nouvelles, Établissement de Lyon, Rond-point de l'échangeur de Solaize, BP 3, F-69360 Solaize, France*; orcid.org/0000-0003-2157-9288; Email: jean-francois.joly@ifpen.fr

## Author Contributions

The manuscript was written through contributions of all authors. All authors have given approval to the final version of the manuscript. C.W. M.Q.: Conceptualization, Methodology, Investigation, Data curation, Formal analysis, Validation, Writing -original draft, Writing - review & editing. S. M.: Data curation, Validation. F. A.: Methodology, Formal analysis, Validation. Y. H.: Investigation, Data curation, Formal analysis, Validation, Writing -original draft. J.-F. J.: Conceptualization, Supervision, Writing - review & editing, Resources. S.S.: Conceptualization, Methodology, Validation, Supervision, Writing - review & editing, Funding acquisition, Resources.

## Funding Sources

This work was supported by the Italian Ministry of University and Research (MUR, Italy), via the ERANETMED network (SOLCARE project, grant number ENERG-065). The stay of C.W.M.Q. at IFP Energies Nouvelles, site of Solaize (France) was funded by the Erasmus+ traineeship from the Politecnico

di Torino (European Charter for Higher Education 28995-LA-1-2014-1-IT-E4AKA1-ECHE, 2014–2020, call 2018/2019).

**Notes**

The authors declare no competing financial interest.

**ACKOWLEDGEMENT**

The authors deeply thank Dr Elisabeth Rosenberg from IFP Energies Nouvelles, site of Rueil-Malmaison (France) for the X-ray micro-CT measurements.

## Table of Content graphic

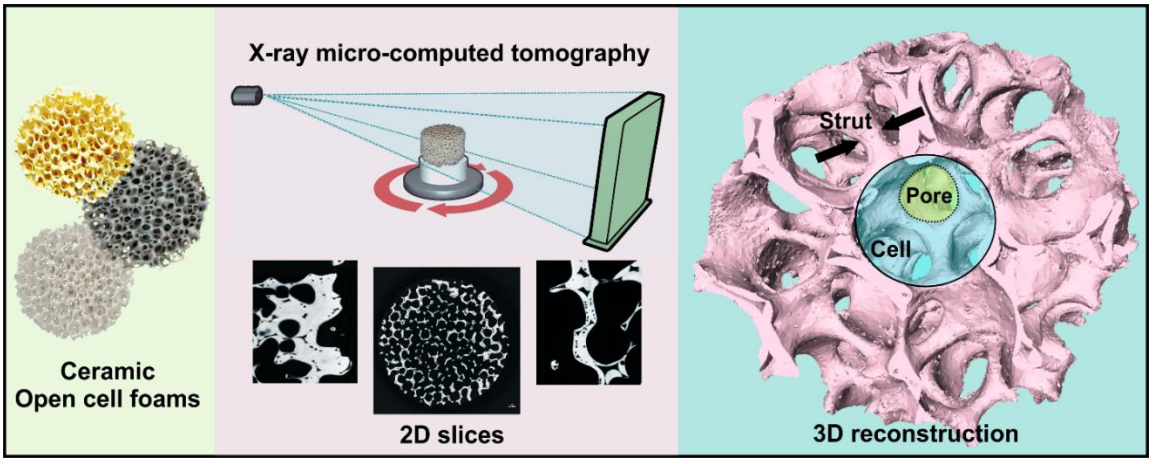


**REFERENCES**

(1) Wan, T.; Liu, Y.; Zhou, C.; Chen, X.; Li, Y. Fabrication, Properties, and Applications of Open-Cell Aluminum Foams: A Review. *J. Mater. Sci. Technol.* **2021**, *62*, 11–24. https://doi.org/10.1016/j.jmst.2020.05.039.

(2) Aguirre, A.; Chandra, V.; Peters, E. A. J. F.; Kuipers, J. A. M.; Neira D'Angelo, M. F. Open-Cell Foams as Catalysts Support: A Systematic Analysis of the Mass Transfer Limitations. *Chem. Eng. J.* **2020**, *393*, 124656. https://doi.org/10.1016/j.cej.2020.124656.

(3) Specchia, S.; Ercolino, G.; Karimi, S.; Italiano, C.; Vita, A. Solution Combustion Synthesis for Preparation of Structured Catalysts: A Mini-Review on Process Intensification for Energy Applications and Pollution Control. *Int. J. Self-Propagating High-Temperature Synth.* **2017**, *26* (3), 166–186. https://doi.org/10.3103/S1061386217030062.

(4) Bracconi, M.; Ambrosetti, M.; Maestri, M.; Groppi, G.; Tronconi, E. Analysis of the Effective Thermal Conductivity of Isotropic and Anisotropic Periodic Open Cellular Structures for the Intensification of Catalytic Processes. *Chem. Eng. Process. - Process Intensif.* **2020**, *158*, 108169. https://doi.org/10.1016/j.cep.2020.108169.

(5) Grosse, J.; Dietrich, B.; Garrido, G. I.; Habisreuther, P.; Zarzalis, N.; Martin, H.; Kind, M.; Bettina, K. C. Morphological Characterization of Ceramic Sponges for Applications in Chemical Engineering. *Ind. Eng. Chem. Res.* **2009**, *48* (23), 10395–10401. https://doi.org/10.1016/j.cej.2012.05.045.

(6) Banhart, J. Manufacture, Characterisation and Application of Cellular Metals and Metal Foams. *Prog. Mater. Sci.* **2001**, *46* (6), 559–632. https://doi.org/10.1016/S0079-6425(00)00002-5.

(7) Banhart, J.; Weaire, D. On the Road Again: Metal Foams Find Favor. **2011**, No. December, 37–42. https://doi.org/10.1063/1.1506749.

(8) Buciuman, F. C.; Kraushaar-Czarnetzki, B. Ceramic Foam Monoliths as Catalyst Carriers. 1. Adjustment and Description of the Morphology. *Ind. Eng. Chem. Res.* **2003**, *42* (9), 1863–1869. https://doi.org/10.1021/ie0204134.

(9) Inayat, A.; Freund, H.; Zeiser, T.; Schwieger, W. Determining the Specific Surface Area of

Ceramic Foams: The Tetrakaidecahedra Model Revisited. *Chem. Eng. Sci.* **2011**, *66* (6), 1179–1188. https://doi.org/10.1016/j.ces.2010.12.031.

(10) Inayat, A.; Klumpp, M.; Lämmermann, M.; Freund, H.; Schwieger, W. Development of a New Pressure Drop Correlation for Open-Cell Foams Based Completely on Theoretical Grounds: Taking into Account Strut Shape and Geometric Tortuosity. *Chem. Eng. J.* **2016**, *287*, 704–719. https://doi.org/10.1016/j.cej.2015.11.050.

(11) Bracconi, M.; Ambrosetti, M.; Maestri, M.; Groppi, G.; Tronconi, E. A Systematic Procedure for the Virtual Reconstruction of Open-Cell Foams. *Chem. Eng. J.* **2017**, *315*, 608–620. https://doi.org/10.1016/j.cej.2017.01.069.

(12) Große, J.; Dietrich, B.; Martin, H.; Kind, M.; Vicente, J.; Hardy, E. H. Volume Image Analysis of Ceramic Sponges. *Chem. Eng. Technol.* **2008**, *31* (2), 307–314. https://doi.org/10.1002/ceat.200700403.

(13) Scheffler, M.; Colombo, P. *Cellular Ceramics: Structure, Manufacturing, Properties and Applications*; WILEY-VCH Verlag GmbH & Co. KGaA, Weinheim, 2005.

(14) Kumar, P.; Topin, F.; Tadrist, L. Geometrical Characterization of Kelvin-like Metal Foams for Different Strut Shapes and Porosity. *J. Porous Media* **2015**, *18* (6), 637–652. https://doi.org/10.1615/JPorMedia.v18.i6.70.

(15) Razza, S.; Heidig, T.; Bianchi, E.; Groppi, G.; Schwieger, W.; Tronconi, E.; Freund, H. Heat Transfer Performance of Structured Catalytic Reactors Packed with Metal Foam Supports: Influence of Wall Coupling. *Catal. Today* **2016**, *273*, 187–195. https://doi.org/10.1016/j.cattod.2016.02.058.

(16) Della Torre, A.; Lucci, F.; Montenegro, G.; Onorati, A.; Dimopoulos Eggenschwiler, P.; Tronconi, E.; Groppi, G. CFD Modeling of Catalytic Reactions in Open-Cell Foam Substrates. *Comput.*

*Chem. Eng.* **2016**, *92*, 55–63. https://doi.org/10.1016/j.compchemeng.2016.04.031.

(17) Zheng, Y.; Luo, X.; You, J.; Peng, Z.; Zhang, S. Ceramic Foams with Highly Open Channel Structure from Direct Foaming Method in Combination with Hollow Spheres as Pore-Former. *J. Asian Ceram. Soc.* **2020**, 1–11. https://doi.org/10.1080/21870764.2020.1847427.

(18) Zalucky, J.; Möller, F.; Schubert, M.; Hampel, U. Flow Regime Transition in Open-Cell Solid Foam Packed Reactors: Adaption of the Relative Permeability Concept and Experimental Validation. *Ind. Eng. Chem. Res.* **2015**, *54* (40), 9708–9721. https://doi.org/10.1021/acs.iecr.5b02233.

(19) Louati, H.; Scheuermann, T.; Maschke, B.; Zanota, M. L.; Vicente, J.; Kotyczka, P.; Pitault, I. Network-Based Modeling of Transport Phenomena in Solid and Fluid Phases of Open-Cell Foams: Construction of Graphs. *Adv. Eng. Mater.* **2020**, *22* (5), 1–11. https://doi.org/10.1002/adem.201901468.

(20) Sinn, C.; Wentrup, J.; Pesch, G. R.; Thöming, J. Heat Transport in Open-Cell Foams: CFD Analysis of Artificial Heat Sources vs Fully Resolved Exothermal Reactions. *Ind. Eng. Chem. Res.* **2021**, *60* (12), 4542–4551. https://doi.org/10.1021/acs.iecr.0c05982.

(21) Ambrosetti, M.; Bracconi, M.; Groppi, G.; Tronconi, E. Analytical Geometrical Model of Open Cell Foams with Detailed Description of Strut-Node Intersection. *Chemie-Ingenieur-Technik* **2017**, *89* (7), 915–925. https://doi.org/10.1002/cite.201600173.

(22) Haack, D. P.; Butcher, K. R.; Kim, T.; Lu, T. J. Novel Lightweight Metal Foam Heat Exchangers. *Am. Soc. Mech. Eng. Process Ind. Div. PID* **2001**, *6* (July), 141–147.

(23) Vazifeshenas, Y.; Sedighi, K.; Shakeri, M. Open Cell Metal Foam as Extended Coolant Surface – Fuel Cell Application. *Fuel Cells* **2020**, *20* (2), 108–115. https://doi.org/10.1002/fuce.201800147.

(24) Ozmat, B.; Leyda, B.; Benson, B. Thermal Applications of Open-Cell Metal Foams. *Mater. Manuf. Process.* **2004**, *19* (5), 839–862. https://doi.org/10.1081/lmmp-200030568.

(25) Ortona, A.; Pusterla, S.; Fino, P.; MacH, F. R. A.; Delgado, A.; Biamino, S. Aging of Reticulated Si-SiC Foams in Porous Burners. *Adv. Appl. Ceram.* **2010**, *109* (4), 246–251. https://doi.org/10.1179/174367510X12663198542586.

(26) Gao, H. B.; Qu, Z. G.; Feng, X. B.; Tao, W. Q. Methane/Air Premixed Combustion in a Two-Layer Porous Burner with Different Foam Materials. *Fuel* **2012**, *115*, 154–161. https://doi.org/10.1016/j.fuel.2013.06.023.

(27) Tseng, C.-J.; Tsai, B. T.; Liu, Z.-S.; Cheng, T.-C.; Chang, W.-C.; Lo, S.-K. A PEM Fuel Cell with Metal Foam as Flow Distributor. *Energy Convers Manag* **2012**, *62*, 14–21. https://doi.org/10.1016/j.enconman.2012.03.018.

(28) Baroutaji, A.; Carton, J. G.; Stokes, J.; Olabi, A. G. Application of Open Pore Cellular Foam for Air Breathing PEM Fuel Cell. *Int. J. Hydrogen Energy* **2017**, *42* (40), 25630–25638. https://doi.org/10.1016/j.ijhydene.2017.05.114.

(29) Lu, T. J.; Stone, H. A.; Ashby, M. F. Heat Transfer in Open-Cell Metal Foams. *Acta Mater.* **1998**, *46* (10), 3619–3635. https://doi.org/10.1016/S1359-6454(98)00031-7.

(30) Ercolino, G.; Stelmachowski, P.; Grzybek, G.; Kotarba, A.; Specchia, S. Optimization of Pd Catalysts Supported on Co3O4 for Low-Temperature Lean Combustion of Residual Methane. *Appl. Catal. B Environ.* **2017**, *206*, 712–725. https://doi.org/10.1016/j.apcatb.2017.01.055.

(31) Cristiani, C.; Finocchio, E.; Latorrata, S.; Visconti, C. G.; Bianchi, E.; Tronconi, E.; Groppi, G.; Pollesel, P. Activation of Metallic Open-Cell Foams via Washcoat Deposition of Ni/MgAl 2O 4 Catalysts for Steam Reforming Reaction. *Catal. Today* **2012**, *197* (1), 256–264. https://doi.org/10.1016/j.cattod.2012.09.003.

(32) Bianchi, E.; Heidig, T.; Visconti, C. G.; Groppi, G.; Freund, H.; Tronconi, E. An Appraisal of the Heat Transfer Properties of Metallic Open-Cell Foams for Strongly Exo-/Endo-Thermic Catalytic Processes in Tubular Reactors. *Chem. Eng. J.* **2012**, *198–199*, 512–528. https://doi.org/10.1016/j.cej.2012.05.045.

(33) Balzarotti, R.; Ambrosetti, M.; Beretta, A.; Groppi, G.; Tronconi, E. Investigation of Packed Conductive Foams as a Novel Reactor Configuration for Methane Steam Reforming. *Chem. Eng. J.* **2020**, *391* (September 2019), 123494. https://doi.org/10.1016/j.cej.2019.123494.

(34) Dashliborun, A. M.; Füssel, A.; Larachi, F. Prospect of Open-Cell Solid Foams for Floating-Platform Multiphase Reactor Applications – Maldistribution Susceptibility and Hydrodynamic Behavior. *Chem. Eng. J.* **2018**, *332*, 596–607. https://doi.org/10.1016/j.cej.2017.09.116.

(35) Ho, P. H.; Nolf, W. de; Ospitali, F.; Beton, D.; Torkuhl, L.; Fornasari, G.; Vaccari, A.; Benito, P. Insights into Coated NiCrAl Open-Cell Foams for the Catalytic Partial Oxidation of CH4. *React. Chem. Eng.* **2019**, *4*, 1768–1778. https://doi.org/10.1039/C9RE00178F.

(36) Moncada Quintero, C. W.; Ercolino, G.; Poozhikunnath, A.; Maric, R.; Specchia, S. Analysis of Heat and Mass Transfer Limitations for the Combustion of Methane Emissions on PdO/Co3O4 Coated on Ceramic Open Cell Foams. *Chem. Eng. J.* **2021**, *405*, 126970. https://doi.org/10.1016/j.cej.2020.126970.

(37) Moncada Quintero, C. W.; Ercolino, G.; Specchia, S. Effect of the Co3O4 Load on the Performance of PdO/Co3O4/ZrO2 Open Cell Foam Catalysts for the Lean Combustion of Methane: Kinetic and Mass Transfer Regimes. *Catal. Today* **2021**. https://doi.org/10.1016/j.cattod.2021.03.014.

(38) Kodama, T.; Kiyama, A.; Shimizu, K. I. Catalytically Activated Metal Foam Absorber for Light-to-Chemical Energy Conversion via Solar Reforming of Methane. *Energy and Fuels* **2003**, *17* (1),

13–17. https://doi.org/10.1021/ef0200525.

(39) Groppi, G.; Giani, L.; Tronconi, E. Generalized Correlation for Gas/Solid Mass-Transfer Coefficients in Metallic and Ceramic Foams. *Ind. Eng. Chem. Res.* **2007**, *46* (12), 3955–3958. https://doi.org/10.1021/ie061330g.

(40) Incera Garrido, G.; Patcas, F. C.; Lang, S.; Kraushaar-Czarnetzki, B. Mass Transfer and Pressure Drop in Ceramic Foams: A Description for Different Pore Sizes and Porosities. *Chem. Eng. Sci.* **2008**, *63* (21), 5202–5217. https://doi.org/10.1016/j.ces.2008.06.015.

(41) *Advances in Bioceramics and Porous Ceramics IV: Ceramic Engineering and Science Proceedings, Volume 32*; Narayan, R., Colombo, P., Widjaja, S., Singh, D., Eds.; Wiley, 2011. https://doi.org/10.1002/9781118095263.

(42) Ciambelli, P.; Palma, V.; Palo, E. Comparison of Ceramic Honeycomb Monolith and Foam as Ni Catalyst Carrier for Methane Autothermal Reforming. *Catal. Today* **2010**, *155* (1–2), 92–100. https://doi.org/10.1016/j.cattod.2009.01.021.

(43) Ercolino, G.; Karimi, S.; Stelmachowski, P.; Specchia, S. Catalytic Combustion of Residual Methane on Alumina Monoliths and Open Cell Foams Coated with Pd/Co3O4. *Chem. Eng. J.* **2017**, *326*, 339–349. https://doi.org/10.1016/j.cej.2017.05.149.

(44) Gancarczyk, A.; Sindera, K.; Iwaniszyn, M.; Piatek, M.; Macek, W.; Jodłowski, P. J.; Wroński, S.; Sitarz, M.; Łojewska, J.; Kołodziej, A. Metal Foams as Novel Catalyst Support in Environmental Processes. *Catalysts* **2019**, *9* (7). https://doi.org/10.3390/catal9070587.

(45) Fend, T.; Hoffschmidt, B.; Pitz-Paal, R.; Reutter, O.; Rietbrock, P. Porous Materials as Open Volumetric Solar Receivers: Experimental Determination of Thermophysical and Heat Transfer Properties. *Energy* **2004**, *29* (5–6), 823–833. https://doi.org/10.1016/S0360-5442(03)00188-9.

(46) Bhattacharya, A.; Calmidi, V. V.; Mahajan, R. L. Thermophysical Properties of High Porosity Metal Foams. *Int. J. Heat Mass Transf.* **2002**, *45* (5), 1017–1031. https://doi.org/10.1016/S0017-9310(01)00220-4.

(47) García-Moreno, F. Commercial Applications of Metal Foams: Their Properties and Production. *Materials (Basel).* **2016**, *9* (2), 20–24. https://doi.org/10.3390/ma9020085.

(48) Richardson, J. T.; Peng, Y.; Remue, D. Properties of Ceramic Foam Catalyst Supports: Pressure Drop. *Appl. Catal. A Gen.* **2000**, *204* (1), 19–32. https://doi.org/10.1016/S0926-860X(00)00508-1.

(49) Twigg, M. V.; Richardson, J. T. Theory and Applications of Ceramic Foam Catalysts. *Chem. Eng. Res. Des.* **2002**, *80* (2), 183–189. https://doi.org/10.1016/S0263-8762(02)72166-7.

(50) Richardson, J. T.; Remue, D.; Hung, J. K. Properties of Ceramic Foam Catalyst Supports: Mass and Heat Transfer. *Appl. Catal. A Gen.* **2003**, *250* (2), 319–329. https://doi.org/10.1016/S0926-860X(03)00287-4.

(51) Mao, X. Processing of Ceramic Foams. In *Recent Advances in Porous Ceramics*; Uday M. Basheer Al-Naib, Ed.; IntechOpen Limited: London, 2018. https://doi.org/10.5772/intechopen.71006.

(52) Italiano, C.; Ashraf, M. A.; Pino, L.; Moncada Quintero, C. W.; Specchia, S.; Vita, A. Rh/CeO2 Thin Catalytic Layer Deposition on Alumina Foams: Catalytic Performance and Controlling Regimes in Biogas Reforming Processes. *Catalysts* **2018**, *8* (10), 1–25. https://doi.org/10.3390/catal8100448.

(53) Ercolino, G.; Stelmachowski, P.; Specchia, S. Catalytic Performance of Pd/Co3O4 on SiC and ZrO2 Open Cell Foams for Process Intensification of Methane Combustion in Lean Conditions. *Ind. Eng. Chem. Res.* **2017**, *56* (23), 6625–6636. https://doi.org/10.1021/acs.iecr.7b01087.

(54) Ashraf, M. A.; Sanz, O.; Italiano, C.; Vita, A.; Montes, M.; Specchia, S. Analysis of Ru/La-Al2O3 Catalyst Loading on Alumina Monoliths and Controlling Regimes in Methane Steam Reforming. *Chem. Eng. J.* **2018**, *334*, 1792–1807. https://doi.org/10.1016/j.cej.2017.11.154.

(55) Huu, T. T.; Lacroix, M.; Pham Huu, C.; Schweich, D.; Edouard, D. Towards a More Realistic Modeling of Solid Foam: Use of the Pentagonal Dodecahedron Geometry. *Chem. Eng. Sci.* **2009**, *64* (24), 5131–5142. https://doi.org/10.1016/j.ces.2009.08.028.

(56) Thomson, W. LXIII. On the Division of Space with Minimum Partitional Area . *London, Edinburgh, Dublin Philos. Mag. J. Sci.* **1887**, *24* (151), 503–514. https://doi.org/10.1080/14786448708628135.

(57) Favata, A. On the Kelvin Problem. *J. Elast.* **2012**, *109* (2), 189–204. https://doi.org/10.1007/s10659-012-9375-4.

(58) Podio-Guidugli, P.; Favata, A. Elasticity for Geotechnicians. *Solid Mech. its Appl.* **2014**, *204*, 149–157. https://doi.org/10.1007/978-3-319-01258-2.

(59) Kelvin, Lord; Thomson, W. Note on the Integration of the Equations of Equilibrium of an Elastic Solid. *Math. Phys. Pap.* **2015**, No. 4, 97–99. https://doi.org/10.1017/cbo9780511996009.038.

(60) Weaire, D.; Phelan, R. A Counter-Example to Kelvin's Conjecture on Minimal Surfaces. *Philos. Mag. Lett.* **1994**, *69* (2), 107–110. https://doi.org/10.1080/09500839408241577.

(61) Zhu, H. X.; Mills, N. J.; Knott, J. F. Analysis of the High Strain Compression of Open-Cell Foams. *J. Mech. Phys. Solids* **1997**, *45* (11–12), 1875–1899. https://doi.org/10.1016/S0022-5096(97)00027-6.

(62) Roberts, A. P.; Garboczi, E. J. Elastic Moduli of Model Random Three-Dimensional Closed-Cell Cellular Solids. *Acta Mater.* **2001**, *49* (2), 189–197. https://doi.org/10.1016/S1359-

6454(00)00314-1.

(63) Habisreuther, P.; Djordjevic, N.; Zarzalis, N. Statistical Distribution of Residence Time and Tortuosity of Flow through Open-Cell Foams. *Chem. Eng. Sci.* **2009**, *64* (23), 4943–4954. https://doi.org/10.1016/j.ces.2009.07.033.

(64) Lucci, F.; Della Torre, A.; von Rickenbach, J.; Montenegro, G.; Poulikakos, D.; Dimopoulos Eggenschwiler, P. Performance of Randomized Kelvin Cell Structures as Catalytic Substrates: Mass-Transfer Based Analysis. *Chem. Eng. Sci.* **2014**, *112*, 143–151. https://doi.org/10.1016/j.ces.2014.03.023.

(65) Skibinski, J.; Cwieka, K.; Kowalkowski, T.; Wysocki, B.; Wejrzanowski, T.; Kurzydlowski, K. J. The Influence of Pore Size Variation on the Pressure Drop in Open-Cell Foams. *Mater. Des.* **2015**, *87*, 650–655. https://doi.org/10.1016/j.matdes.2015.08.079.

(66) Maliaris, G.; Michailidis, N. Modeling of Open Cell Structures Geometry and Mechanical Response Applying the Voronoi Tessellation Algorithm; Bouzakis, K.-D., Ed.; EEAM and PCCM: Thessaloniki, 2014; pp 393–402. https://doi.org/10.13140/2.1.2342.3689.

(67) Nie, Z.; Lin, Y.; Tong, Q. Modeling Structures of Open Cell Foams. *Comput. Mater. Sci.* **2017**, *131*, 160–169. https://doi.org/10.1016/j.commatsci.2017.01.029.

(68) Randrianalisoa, J.; Baillis, D.; Martin, C. L.; Dendievel, R.; Roberts, A. P.; Garboczi, E. J. Microstructure Effects on Thermal Conductivity of Open-Cell Foams Generated from the Laguerre-Voronoï Tessellation Method. *J. Mech. Phys. Solids* **2002**, *50* (1), 33–55. https://doi.org/10.1016/j.ijthermalsci.2015.07.016.

(69) Gibson, L. J.; Ashby, M. F. *Cellular Solids: Structure and Properties*; 1988; Vol. 22. https://doi.org/10.1016/0021-9290(89)90056-0.

(70) Kraynik, A. M.; Reinelt, D. A.; van Swol, F. Structure of Random Monodisperse Foam. *Phys. Rev. E* **2003**, *67*, 031403. https://doi.org/10.1103/PhysRevE.67.031403.

(71) Wejrzanowski, T.; Skibinski, J.; Szumbarski, J.; Kurzydlowski, K. J. Structure of Foams Modeled by Laguerre-Voronoi Tessellations. *Comput. Mater. Sci.* **2013**, *67*, 216–221. https://doi.org/10.1016/j.commatsci.2012.08.046.

(72) Montminy, M. D.; Tannenbaum, A. R.; MacOsko, C. W. The 3D Structure of Real Polymer Foams. *J. Colloid Interface Sci.* **2004**, *280* (1), 202–211. https://doi.org/10.1016/j.jcis.2004.07.032.

(73) Saadatfar, M.; Garcia-Moreno, F.; Hutzler, S.; Sheppard, A. P.; Knackstedt, M. A.; Banhart, J.; Weaire, D. Imaging of Metallic Foams Using X-Ray Micro-CT. *Colloids Surfaces A Physicochem. Eng. Asp.* **2009**, *344* (1–3), 107–112. https://doi.org/10.1016/j.colsurfa.2009.01.008.

(74) Nacucchi, M.; De Pascalis, F.; Scatto, M.; Capodieci, L.; Albertoni, R. Structural Analysis of Advanced Polymeric Foams by Means of High Resolution X-Ray Computed Tomography. In *AIP Conference Proceedings*; 2016; Vol. 1749. https://doi.org/10.1063/1.4954492.

(75) Neethirajan, S.; Karunakaran, C.; Jayas, D. S.; White, N. D. G. X-Ray Computed Tomography Image Analysis to Explain the Airflow Resistance Differences in Grain Bulks. *Biosyst. Eng.* **2006**, *94* (4), 545–555. https://doi.org/10.1016/j.biosystemseng.2006.04.013.

(76) Maire, E.; Colombo, P.; Adrien, J.; Babout, L.; Biasetto, L. Characterization of the Morphology of Cellular Ceramics by 3D Image Processing of X-Ray Tomography. *J. Eur. Ceram. Soc.* **2007**, *27* (4), 1973–1981. https://doi.org/10.1016/j.jeurceramsoc.2006.05.097.

(77) Schmierer, E. N.; Razani, A.; Keating, S.; Melton, T. Characterization of High Porosity Open-Celled Metal Foam Using Computed Tomography. *ASME Int. Mech. Eng. Congr. Expo.* **2016**, 1–10.

(78) Papetti, V.; Dimopoulos Eggenschwiler, P.; Della Torre, A.; Lucci, F.; Ortona, A.; Montenegro, G. Additive Manufactured Open Cell Polyhedral Structures as Substrates for Automotive Catalysts. *Int. J. Heat Mass Transf.* **2018**, *126*, 1035–1047. https://doi.org/10.1016/j.ijheatmasstransfer.2018.06.061.

(79) Kim, T. B.; Yue, S.; Zhang, Z.; Jones, E.; Jones, J. R.; Lee, P. D. Additive Manufactured Porous Titanium Structures: Through-Process Quantification of Pore and Strut Networks. *J. Mater. Process. Technol.* **2014**, *214* (11), 2706–2715. https://doi.org/10.1016/j.jmatprotec.2014.05.006.

(80) Ou, X.; Zhang, X.; Lowe, T.; Blanc, R.; Rad, M. N.; Wang, Y.; Batail, N.; Pham, C.; Shokri, N.; Garforth, A.; Withers, P.; Fan, X. X-Ray Micro Computed Tomography Characterization of Cellular SiC Foams for Their Applications in Chemical Engineering. *Mater. Charact.* **2017**, *123*, 20–28. https://doi.org/10.1016/j.matchar.2016.11.013.

(81) Petit, C.; Maire, E.; Meille, S.; Adrien, J. Two-Scale Study of the Fracture of an Aluminum Foam by X-Ray Tomography and Finite Element Modeling. *Mater. Des.* **2017**, *120*, 117–127. https://doi.org/10.1016/j.matdes.2017.02.009.

(82) Lanik Foam Ceramics https://www.lanik.eu/en/ (accessed Feb 21, 2021).

(83) Twigg, M. V.; Richardson, J. T. Fundamentals and Applications of Structured Ceramic Foam Catalysts. *Ind. Eng. Chem. Res.* **2007**, *46* (12), 4166–4177. https://doi.org/10.1021/ie061122o.

(84) Richard Ketcham. X-ray Computed Tomography (CT) https://serc.carleton.edu/research_education/geochemsheets/techniques/CT.html (accessed Feb 12, 2021).

(85) Otsu, N. A Threshold Selection Method from Gray-Level Histograms. *IEEE Trans. Syst. Man Cybern. Syst.* **1979**, *smc-9* (1), 62–66. https://doi.org/0018-9472/79/0100-0062$00.75.

(86) Ridler, T. W.; Calvard, S. Picture Thresholding Using an Iterative Selection Method. *IEEE Trans. Syst. Man Cybern.* **1978**, *smc-8* (8), 630–632. https://doi.org/0018-9472/78/0800-0632$00.75.

(87) Lacroix, M.; Nguyen, P.; Schweich, D.; Pham Huu, C.; Savin-Poncet, S.; Edouard, D. Pressure Drop Measurements and Modeling on SiC Foams. *Chem. Eng. Sci.* **2007**, *62* (12), 3259–3267. https://doi.org/10.1016/j.ces.2007.03.027.

(88) Plateau, J. *Experimental and Theoretical Statics of Liquids Subject to Molecular Forces Only*; Gauthier-Villars, Paris, 1873.

(89) Hernandez Camacho, J. N.; Lecrivain, G.; Schubert, M.; Hampel, U. Droplet Retention Time and Pressure Drop in SiSiC Open-Cell Foams Used as Droplet Separation Devices: A Numerical Approach. *Ind. Eng. Chem. Res.* **2019**. https://doi.org/10.1021/acs.iecr.9b04247.

(90) Visiocell® | Recticel Flexible Foams https://recticelflexiblefoams.com/consumergoods/visiocell (accessed Mar 8, 2021).

(91) Mancin, S.; Zilio, C.; Cavallini, A.; Rossetto, L. Heat Transfer during Air Flow in Aluminum Foams. *Int. J. Heat Mass Transf.* **2010**, *53* (21–22), 4976–4984. https://doi.org/10.1016/j.ijheatmasstransfer.2010.05.033.

(92) Mancin, S.; Zilio, C.; Diani, A.; Rossetto, L. Air Forced Convection through Metal Foams: Experimental Results and Modeling. *Int. J. Heat Mass Transf.* **2013**, *62* (1), 112–123. https://doi.org/10.1016/j.ijheatmasstransfer.2013.02.050.

(93) Dietrich, B.; Schabel, W.; Kind, M.; Martin, H. Pressure Drop Measurements of Ceramic Sponges-Determining the Hydraulic Diameter. *Chem. Eng. Sci.* **2009**, *64* (16), 3633–3640. https://doi.org/10.1016/j.ces.2009.05.005.

(94) Kumar, P. Investigation of Kelvin-like Solid Foams for Potential Engineering Applications : An

Attractive Set of Geometrical and Thermo-Hydraulic Properties, Aix-Marseille University, 2015.

(95) Ahmad, R.; Ha, J.-H.; Song, I.-H. Processing Methods for the Preparation of Porous Ceramics. *J. Korean Powder Metall. Inst.* **2014**, *21* (5), 389–398. https://doi.org/10.4150/kpmi.2014.21.5.389.

(96) Liang, X.; Li, Y.; He, Z.; Wang, Q.; Chen, Y.; Xu, X.; Li, B.; Aneziris, C. G. Design of Three-Layered Struts in SiC Reticulated Porous Ceramics for Porous Burner. *Ceram. Int.* **2019**, *45* (7), 8571–8576. https://doi.org/10.1016/j.ceramint.2019.01.175.

(97) Bracconi, M.; Ambrosetti, M.; Okafor, O.; Sans, V.; Zhang, X.; Ou, X.; Da Fonte, C. P.; Fan, X.; Maestri, M.; Groppi, G.; Tronconi, E. Investigation of Pressure Drop in 3D Replicated Open-Cell Foams: Coupling CFD with Experimental Data on Additively Manufactured Foams. *Chem. Eng. J.* **2019**, *377*, 120123. https://doi.org/10.1016/j.cej.2018.10.060.

(98) Ghazi, A.; Berke, P.; Tiago, C.; Massart, T. J. Computed Tomography Based Modelling of the Behaviour of Closed Cell Metallic Foams Using a Shell Approximation. *Mater. Des.* **2020**, *194*, 108866. https://doi.org/10.1016/j.matdes.2020.108866.

(99) Ghosh, I. How Good Is Open-Cell Metal Foam as Heat Transfer Surface? *J. Heat Transfer* **2009**, *131* (10), 1–8. https://doi.org/10.1115/1.3160537.

(100) Calmidi, V. V.; Mahajan, R. L. The Effective Thermal Conductivity of High Porosity Fibrous Metal Foams. *J. Heat Transfer* **1999**, *121* (2), 466–471. https://doi.org/10.1115/1.2826001.

(101) Ghosh, I. Deterioration in Heat Transfer Due to Axial Conduction of Heat in Open Cell Metal Foam. *AIP Conf. Proc.* **2010**, *1254*, 254–259. https://doi.org/10.1063/1.3453820.

(102) Bernard, P.; Stelmachowski, P.; Broś, P.; Makowski, W.; Kotarba, A. Demonstration of the Influence of Specific Surface Area on Reaction Rate in Heterogeneous Catalysis. *J. Chem. Educ.* **2021**, *98*, 935–940. https://doi.org/10.1021/acs.jchemed.0c01101.

(103) Mirdrikvand, M.; Sadeghi, M.; Karim, M. N.; Thöming, J.; Dreher, W. Pore-Scale Analysis of Axial and Radial Dispersion Coefficients of Gas Flow in Macroporous Foam Monoliths Using NMR-Based Displacement Measurements. *Chem. Eng. J.* **2020**, *388*, 124234. https://doi.org/10.1016/j.cej.2020.124234.

(104) Poryles, R.; Gland, N.; King, A.; Rosenberg, E.; Barré, L.; Chevalier, T. Foam Trapping in a 3D Porous Medium:: In Situ Observations by Ultra-Fast X-Ray Microtomography. *Soft Matter* **2020**, *16* (27), 6354–6361. https://doi.org/10.1039/d0sm00392a.

# CHAPTER VII

(*PAPER VII*)

Combined silicon carbide and zirconia open cell foams for the process intensification of catalytic methane combustion in lean conditions: impact on heat and mass transfer

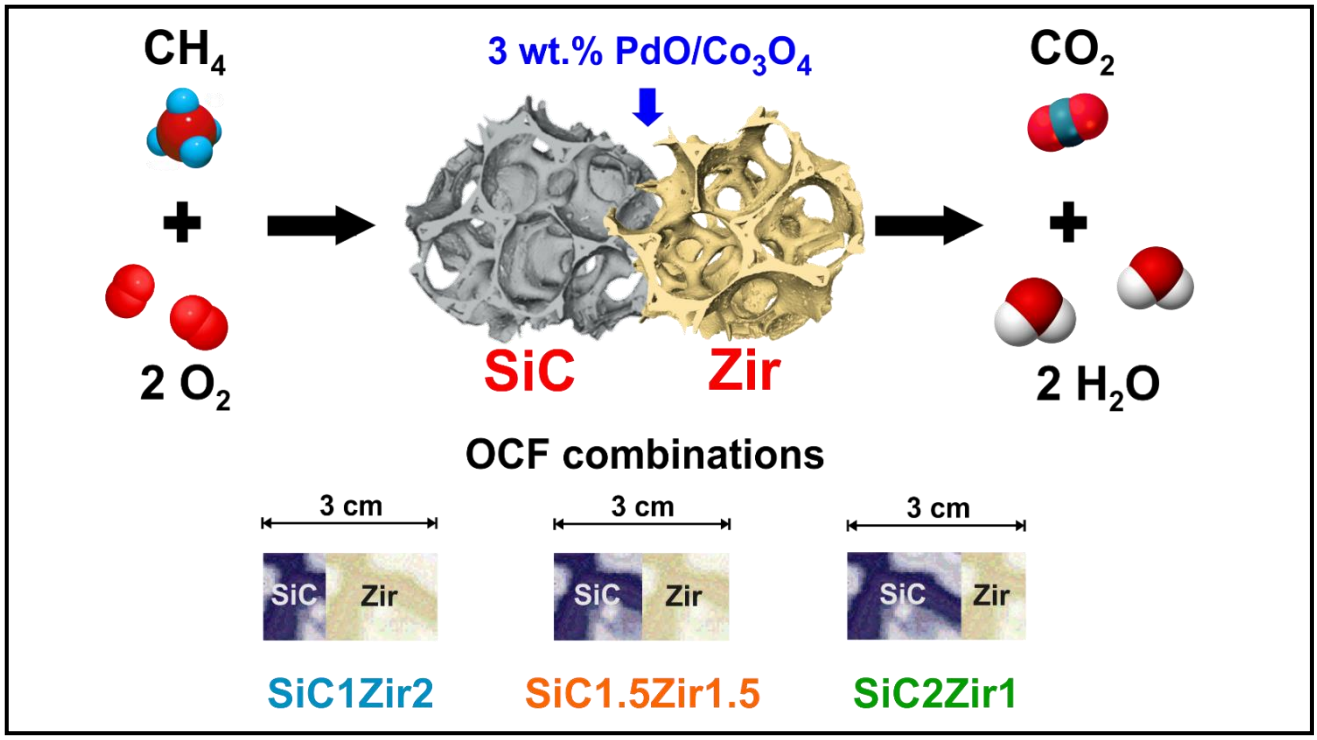


*Chemical Engineering Journal, 429,* 132448.

DOI: 10.1016/j.cej.2021.132448

Chemical Engineering Journal 429 (2022) 132448

Contents lists available at ScienceDirect

Chemical Engineering Journal

journal homepage: www.elsevier.com/locate/cej

# Combined silicon carbide and zirconia open cell foams for the process intensification of catalytic methane combustion in lean conditions: Impact on heat and mass transfer

Carmen W. Moncada Quintero *, Giuliana Ercolino, Stefania Specchia *

*Politecnico di Torino, Department of Applied Science and Technology, Corso Duca degli Abruzzi 24, 10129 Torino, Italy*

ARTICLE INFO

*Keywords:*
Open cell foams
Palladium
Cobalt spinel
Kinetic and mass transfer regimes
Heat transfer effects

ABSTRACT

For catalytic process intensification, a series of open cell foams (OCFs) made of silicon carbide (SiC) and zirconia (Zir) with pore density of 30 ppi coated with 3 wt% $PdO/Co_3O_4$ as catalyst were combined together and tested toward methane oxidation in lean conditions. In each combination, the SiC OCF was positioned in the reactor on the inlet side of the reactant gases followed by the Zir OCF. The reactor was fed at different weight hourly space velocities (WHSV, 30 and 90 NL $h^{-1}$ $g_{cat}^{-1}$) and inlet methane concentrations (0.5 and 1 vol%). The best results are obtained with the combination where two supports of same length but with different thermal conductivity (higher at the inlet of the reactor, SiC, and lower at the outlet, Zir) are used in series. For all OCF combinations, mass transfer effects were evaluated using the characteristic resistances (kinetic, internal and external mass transfer). The external and internal heat transfer effects were analyzed using the Mears and Anderson criteria. Furthermore, a comparison in terms of volumetric heat transfer coefficient and heats of removal/reaction was performed.

## 1. Introduction

Methane ($CH_4$), the main component of natural gas, is one of the most important gases that contributes to the greenhouse effect. Although $CH_4$ is about 200 times less abundant in the atmosphere than carbon dioxide ($CO_2$), its ability to absorb thermal infrared radiation is much more effective and, as a consequence, its impact on the greenhouse effect is much stronger compared to that of $CO_2$ [1,2]. In fact, the global warming potential (GWP) of $CH_4$ is 86 over a 20-year period, and 28 over a 100-year period (by definition, the GWP $CO_2$ is 1) [3]. Indeed, $CH_4$ emissions recorded an increase of more than 150% since 1750 as a result of human activities [4]. By the end of 2019, the global average concentration of $CH_4$ in the atmosphere reached about 1875 parts per billion (ppb), more than two and a half times pre-industrial levels [5]. Methane emissions come mainly from anthropogenic sources such as agriculture, energy, industry and waste management processes [6,7]. Most of the human-induced emissions have low $CH_4$ concentrations, generally between 0.1 and 1 vol% [8–10]. Reducing $CH_4$ emissions could offer a great opportunity to mitigate global climate change leading to significant environmental and economic benefits.

Despite the high stability of the $CH_4$ molecule, the catalytic combustion is considered one of the most efficient and promising technologies to eliminate $CH_4$ emissions and maximize the use of rational and clean low-temperature energy. Therefore, the development of a catalyst with outstanding catalytic activity (the lowest possible shut-down temperature) and high stability even at low temperature operations remains a challenge for chemical engineers. So far, Pd-based catalysts have been reported to be the most active catalytic systems for total oxidation of $CH_4$, due to their high activity at low temperature [11–15]. However, because of the relatively high cost associated with Pd, researchers have paid much attention to the study of alternative catalytic systems with a reduced amount of Pd, such as oxides or mixed oxides [16–18] and perovskites [19–21], because of their much lower cost and relatively abundant availability. In all cases, the nature of the catalyst carrier as well as the active phase-support interactions play a crucial role in the catalytic properties of Pd-based catalysts Recently, spinel cobalt oxide ($Co_3O_4$) has proven to be one of the best multifunctional materials for a wide variety of technological applications thanks to its surface redox reactivity properties, strong oxygen mobility and lower Co–O binding energy [23–27]. Specifically, when $CH_4$ is oxidized, $Co_3O_4$ favors the removal of hydroxyl species from the PdO surface [28]. In this way, the active sites are more prone to $CH_4$ activation [15]. Besides,

* Corresponding author.
*E-mail addresses:* carmen.moncada@polito.it (C.W. Moncada Quintero), stefania.specchia@polito.it (S. Specchia).

https://doi.org/10.1016/j.cej.2021.132448
Received 1 June 2021; Received in revised form 8 September 2021; Accepted 10 September 2021
Available online 16 September 2021

$Co_3O_4$ provides lattice oxygen to the PdO phase, favoring again the recreation of active sites afterwards [29]. This makes $Co_3O_4$ an optimal catalytic support, especially for the complete $CH_4$ oxidation in lean conditions, in comparison with other carriers such as $Al_2O_3$ or perovskites [11,12,22].

Currently, the attention has been focused on structured reactors as a potential way to facilitate the intensification of the process, thanks to the possibility of enhancing transport phenomena (increased mass and heat transfer rates [30–39]), bringing to significant benefits in terms of process efficiency, improved safety, and lower capital costs [40,41]. Open cell foams (OCFs) have become promising candidates owing to their attractive characteristics such as large specific surface area, high porosity, great mechanical strength and light-weight, as well as reduced pressure drops when compared to classical fixed-bed reactors [42–51]. In addition, their particular structural geometry produces a tortuous flow path that allows improving the reactive mixing and thus the transport properties.

Recently, we investigated the catalytic oxidation of $CH_4$ under lean conditions of 3 wt% $PdO/Co_3O_4$ catalyst supported on individual OCFs made of silicon carbide (SiC), alumina (Alu) and zirconia (Zir) [52–55] with different pore density. Furthermore, a mass and heat transfer analysis was performed for each catalytic support [52]. We found that the best catalytic performance towards complete $CH_4$ conversion was obtained with the Zir OCF system [54]. Nevertheless, the higher thermal conductivity of the SiC OCF led to higher volumetric heat exchange coefficients, which help to hold the reaction heat and, consequently, provide the necessary energy to maintain the reaction during the extinction by delaying the shut-down temperature of the reactor [54], thanks to the existence of multiple steady-states [56–59]. In fact, although the best catalytic performance was obtained with the Zir OCF, the reaction kinetics was favored by the SiC OCF showing a lower temperature range under kinetic control [52]. In the present work, we exploited the results obtained in our previous research by evaluating the catalytic performance of 3 wt% $PdO/Co_3O_4$ catalyst towards $CH_4$ oxidation in lean conditions using three different combinations of OCFs made of SiC and Zir. The total length of each foam combination was 3 cm (as in our previous works [52–55]), while the lengths of each single OCF (SiC and Zir) were varied from 1, 1.5, and 2 cm. Each combination was placed inside the reactor with the SiC OCF always at the inlet side of the reactant gases. Thus, we tried three different bed configurations: SiC1-Zir2, SiC1.5Zir1.5, SiC2Zir1. The idea of using the SiC OCF in the front matured from our previous experience, comparing the performance of $PdO/Co_3O_4$ on single Zir or SiC. We noticed that the reactor configuration with the SiC was able to guarantee a very good performance at low temperature, that is at the extinction of the combustion reaction [54]. In fact, recently, the study of ignition and extinction pathways in non-isothermal reactors is gaining importance to reach a better reactor's thermal management [59,60]. In this work, the reactor was fed at different weight hourly space velocities (WHSV) and inlet $CH_4$ concentrations. Moreover, the overall catalytic process resistance was evaluated in terms of kinetic, external, and internal mass transfer resistance allowing the identification of the operating regime of each OCF combination. Finally, heat transfer effects both within the catalyst and associated to the gas phase were analyzed.

## 2. Materials and methods

### 2.1. Open cell foams and chemicals

Ceramic OCFs made of zirconia (Vukopor® HT30, labelled Zir OCF) and silicon carbide (Vukupor® S30, labelled SiC OCF) with pore density of 30 ppi (pore per inch) were purchased from Lanik s.r.o (Czech Republic) in dimensions of 0.9 cm as in diameter and 3 cm as length. For experimental purposes, the length of the foams was carefully reduced to 1, 1.5, and 2 cm, obtaining the following OCF pieces: SiC1, SiC1.5, SiC2, Zir1, Zir1.5, and Zir2 (where each value indicates the foam length in cm). Table 1 lists the textural properties of single SiC and Zir OCF of 30 ppi measured in our previous work using the X-ray computed microtomography technique [61].

**Table 1**
Textural properties of individual SiC and Zir OCF with pore density of 30 ppi [61].

| | SiC OCF | Zir OCF |
|---|---|---|
| Pore diameter, $d_p$ (mm) | 2.22 | 2.87 |
| Strut diameter, $d_s$ (mm) | 0.35 | 0.51 |
| Open porosity, $\varepsilon_o$ (-) | 0.79 | 0.84 |
| Specific surface area, $S_{ga}$ ($mm^{-1}$) | 0.90 | 1.09 |

All reagents were purchased from Sigma-Aldrich: Cobalt(II) nitrate hexahydrate $Co(NO_3)_2{\cdot}6H_2O$ (≥98% purity), palladium(II) nitrate hydrate $Pd(NO_3)_2{\cdot}xH_2O$ (≥99% purity), glycine $NH_2CH_2COOH$ (≥99% purity), ethanol $CH_3CH_2OH$ (≥99.8% purity), and acetone $CH_3COCH_3$ (≥99.8% purity). Ultrapure water obtained from a Millipore Milli-Q system with resistivity of ~ 18 MΩ cm was used to prepare all aqueous solutions. Catalytic tests were carried out using pure methane, oxygen and nitrogen gases (99.999% purity) supplied in cylinders provided by SIAD S.p.A.

### 2.2. Preparation of the foam structured catalysts

Prior to use, all foam pieces were washed in a water/acetone solution (50:50, v/v) for 30 min using an ultrasonic bath at room temperature and dried at 140 °C for 60 min. The deposition of $PdO/Co_3O_4$ catalyst on each foam piece was performed in two consecutive steps, described in detail in our previous works [52–55]: i) solution combustion synthesis (SCS) method to deposit the $Co_3O_4$ carrier and ii) wetness impregnation (WI) of the PdO active phase. Briefly, each OCF piece was immersed in a 3 M aqueous solution of cobalt nitrate and glycine (with an amount of glycine equal to 0.25 of the stoichiometric amount) for 3 min. The excess solution was removed from the foams with a flow of compressed air. Then, the wet OCFs were introduced into a muffle furnace preheated to 250 °C for 20 min to allow ignition of the combustion reaction. The coating operation was repeated several times until the desired $Co_3O_4$ carrier amount was achieved on each OCF. Once the foams were coated, they were calcined at 600 °C for 4 h in static air. Subsequently, 3 wt% PdO was deposited on the $Co_3O_4$-coated OCF pieces by WI. Through WI, each OCF was dipped several times in an aqueous solution containing the targeted amount of PdO. For each dipping, the OCF was rotated with tweezers, to ensure homogeneous absorption, and dried in a muffle at 140 °C for 1 h to remove water. The dipping/drying steps were repeated till the becker containing the aqueous solution was fully empty. Finally, the $PdO/Co_3O_4$ OCFs were calcined at 600 °C for 4 h in static air. Considering that the three SiCZir OCF combinations were different in the length of each single foam (SiC1Zir2, SiC1.5Zir1.5, SiC2Zir1), but equal in terms of overall length (3 cm), for sake of comparison we deposited on each entire system a targeted amount of $Co_3O_4$ + PdO equal to approx. 250 mg (PdO: 3 wt% of the $Co_3O_4$ amount [52–55]), proportionally shared on the two single SiC or Zir OCF depending on their respective lengths in the SiCZir configuration.

### 2.3. Catalytic tests toward $CH_4$ combustion

Fig. 1 shows the test rig we used for testing the $CH_4$ catalytic activity. A fixed bed reactor consisting of a straight quartz tube (10 mm inner diameter) placed inside a PID-controlled electric furnace was used for this purpose. The total length of all foam configurations was 3 cm, with the SiC OCF positioned always at the inlet of the reactive gases followed by the Zir one. Each foam configuration was wrapped all along the length in a thin vermiculite foil to avoid channeling and heat dispersion phenomena at the reactor's wall/OCF boundary, especially at the SiCZir

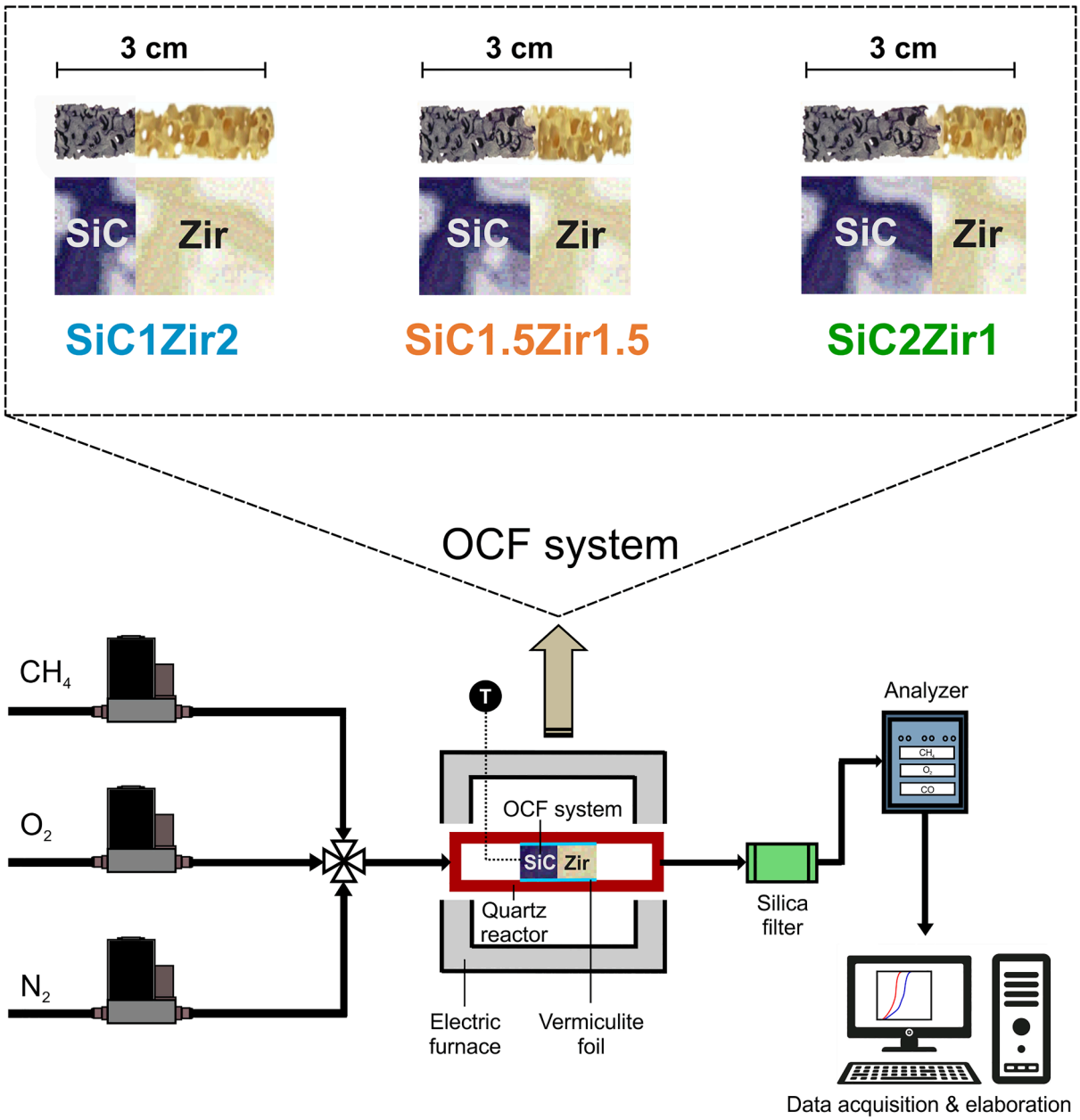


**Fig. 1.** Schematic diagram of the lab-scale plant for $CH_4$ oxidation and the three combinations of ceramic OCFs made of SiC and Zir with pore density of 30 ppi used in this study.

junction.

The reactor was fed with a reactive $CH_4/O_2/N_2$ gas mixture, at methane concentrations of 0.5 or 1 vol%, with a constant molar ratio of $O_2/CH_4$ equal to 8 to ensure lean conditions. First, the reactor was heated to 700 °C (10 °C $min^{-1}$) while the reactant gas mixture was fed, to favor the ignition and the achievement of stationary conditions. Once the steady state conditions were reached (hold time at 700 °C for 1 h), the reactor was cooled to room temperature (5 °C $min^{-1}$), while the outlet dry gas concentration was monitored as a function of the temperature (measured by a K-type thermocouple located a few mm inside the inlet side of each foam configuration) using an ABB analyzer equipped with a Uras 14 NDIR module for $CO/CO_2/CH_4$ and a Magnos 106 paramagnetic module for $O_2$. Consequently, all the conversion versus temperature curves presented in this work are extinction curves, because of the more favorable $CH_4$ conversion profiles due to the presence of the ignition/extinction hysteresis (multiple steady states conditions [53,59]). The water vapor generated by the reaction was removed before entering the analyzer in a condenser set at 3 °C. The reagent flow rate was varied to allow the catalytic tests to be carried out at WHSV of 30 and 90 NL $h^{-1}$ $g_{cat}{}^{-1}$. All catalytic runs were repeated at least three times to ensure reproducibility of the results.

### 2.4. Determination of the apparent kinetic parameters

The kinetics of $CH_4$ combustion can be approximated as a pseudo-first order reaction ($R^{obs} = k{\cdot}C_{CH_4}$) considering that all catalytic tests towards $CH_4$ oxidation performed on each $PdO/Co_3O_4$/SiCZir combination were conducted in a large excess of oxygen ($C_{O2} \gg C_{CH4}$). Thus, assuming a plug flow reactor model, the observed rate constant per unit of catalyst bulk density ($k^{'}$) for a first-order reaction was determined as:

$$k^{'}(T) = \frac{1}{\tau}\ln\left(\frac{1}{1 - X_{CH4}}\right) \quad (1)$$

$$\tau = \frac{W_{cat} \cdot C_{CH4}^{in}}{F_{CH4}^{in}} \quad (2)$$

where $\tau$ is the contact time ($g_{cat}$ s $m^{-3}$), $X_{CH4}$ is the $CH_4$ conversion, $W_{cat}$ is the weight of PdO/$Co_3O_4$ catalyst ($g_{cat}$), and $C_{CH4}^{in}$, $F_{CH4}^{in}$ are the inlet concentration (mol $m^{-3}$), and molar flow of methane (mol $s^{-1}$), respectively.

Then, the $k'$ was plotted as a function of inverse temperature using the logarithmic form of the Arrhenius equation (**Equation (3)**). The pre-exponential factor ($A_o$) and the apparent activation energy ($E_{app}$) were determined using the experimental data points with $CH_4$ conversion below 10%, that is, in kinetic regime.

$$k' = A_o \cdot e^{-\frac{E_{app}}{R_g \cdot T}}; ln(k') = ln(A_o) - \frac{E_{app}}{R_g} \cdot \frac{1}{T} \quad (3)$$

### 2.5. External and internal mass transfer evaluation

The overall mass transfer process in a structured catalyst is usually bounded by two limits: external mass transfer from the bulk of the fluid phase to the external catalyst surface and internal mass transfer with chemical reaction into the catalytic thickness [30,31,33,40,49,62–68]. The external mass transfer is simplified using the classical concept of mass transfer coefficient, based on the assumption that all the resistance to mass transfer resides in a fictitious thin film in which the concentration gradients occur, while the diffusion and reaction processes are simplified using the concept of effectiveness factor [40,63]. Balakotaiah in 2008 [69], demonstrated that it was possible to use an internal mass transfer coefficient to simplify the diffusion and reaction process in a catalyst particle utilizing a hypothetical film model similar to that of external mass transfer. Later, Joshi et al. [70–73] extended this approach by developing a low dimensional model to describe convection processes with diffusion and reaction in washcoated monoliths of arbitrary shape. The main advantage of this model is that it allows the inclusion of intraparticle diffusional effects without explicitly solving the multicomponent diffusion–reaction problem within the catalyst layer.

Recently, we adapted the model developed by Joshi et al. [70–73] to evaluate the mass transfer effects that occur from the bulk of the gas phase to the outer catalyst surface and to the inside of the catalytic layer in single coated OCFs made of alumina, silicon carbide, and zirconia [52]. Briefly, the total mass transfer resistance ($R_m{}^t$) can be described as the combined effect of two diffusive contributions using a series approach, as follows [52,53,71,72]:

$$R_m{}^t = R_m{}^e + R_m{}^i \quad (4)$$

$$R_m{}^t = \frac{1}{k_m{}^t}; \; R_m{}^e = \frac{1}{k_m{}^e} = \frac{4 \cdot R_{\Omega e}}{Sh_{OCF} \cdot D_f}; \; R_m{}^i = \frac{1}{k_m{}^i} = \frac{R_{\Omega,i}}{Sh_c \cdot D_e} \quad (5)$$

where $R_m{}^e$, $R_m{}^i$ are the gas phase film and intraparticle (within the PdO/$Co_3O_4$ catalyst layer) mass transfer resistances (s $m^{-1}$); $k_m{}^t$, $k_m{}^e$, $k_m{}^i$ are the total, external and internal mass transfer coefficients (m $s^{-1}$); $R_{\Omega e}$, $R_{\Omega,i}$ are the characteristic length scales for the transverse diffusion associated with the gas phase and the catalytic layer (m); $D_f$, $D_e$ are the molecular and effective diffusivity of $CH_4$ in the fluid phase and within the catalyst layer ($m^2$ $s^{-1}$), and $Sh_{OCF}$, $Sh_c$ are the external and internal Sherwood numbers.

The characteristic length scales are defined as the ratio of the flow or coated layer cross-sectional area to the gas–solid interfacial perimeter (wetted surface, assuming a continuous catalyst layer), which are expressed as:

$$R_{\Omega,e} = \frac{A_{\Omega,e}}{P_\Omega} = \frac{d_h}{4} \quad (6)$$

$$R_{\Omega,i} = \frac{A_{\Omega,i}}{P_\Omega} = \delta_c \quad (7)$$

where $P_\Omega$ is the wetted gas–coated layer interfacial perimeter (m); $d_h$ is the hydraulic diameter of the foam (m); $\delta_c$ is the catalytic thickness (m); $A_{\Omega,e}$ and $A_{\Omega,i}$ are the cross sectional areas for the gas phase and coated catalyst layer ($m^2$), respectively.

To estimate the dimensionless external mass transfer coefficient ($Sh_{OCF}$), we use the correlation derived by Garrido et al. [74] for ceramic OCFs with circular strut shape valid for a voidage range of $0.75 \leq \varepsilon_{ocf} \leq 0.85$ and pore diameter of $0.87 \leq d_{p,c} \leq 3.13$ mm:

$$Sh_{OCF} = 1.0 \cdot Re^{0.47} \cdot Sc^{\frac{1}{3}} \cdot F_g \quad (8)$$

where $Re$ is the Reynold number, $Sc$ is the Smith number and $F_g$ is the geometrical factor which depends on the pore diameter ($d_{p,c}$) and the OCF voidage ($\varepsilon_{ocf}$).

On the other hand, the dimensionless mass transfer coefficient within the catalyst layer ($Sh_c$) was estimated using the correlation derived by Joshi et al. [71] on washcoated monolith for first order reactions as:

$$Sh_c = Sh_{c,\infty} + \frac{\Lambda \cdot \phi^2}{1 + \Lambda \cdot \phi} \quad (9)$$

where $Sh_{c,\infty}$ is the asymptotic internal Sherwood number (where the pore diameter and coated layer shape was assumed to be circular, thus, $Sh_{c,\infty} = 3.013$) [75], $\Lambda$ is a constant that depends on the coated layer geometry (for a circular coated layer shape with circular crown ratio of 1.1, $\Lambda = 0.38$) [71,72], and $\phi$ is the Thiele modulus for a first order reaction.

### 2.6. Overall catalytic performance: Kinetic and mass transfer regimes

To evaluate the operating regimes (kinetic, internal and external mass transfer) of the catalytic process, we used the low-dimensional model developed by Joshi et al. [70–72], considering the following assumptions: i) fully developed laminar flow; ii) very high axial Peclet number; iii) isothermal foam; and iv) first order reaction kinetics. In this way, the operating regime of each catalytic OCF combination was evaluated as the sum of the total mass transfer resistance and the reaction resistance as:

$$R^{ov} = R_m{}^t + R_r \quad (10)$$

Substituting the **Equation (4)** in **10**, we obtain that:

$$R^{ov} = R_m{}^e + R_m{}^i + R_r \quad (11)$$

$$\frac{1}{k^{ov}} = \frac{1}{k_m{}^e} + \frac{1}{k_m{}^i} + \frac{1}{k \cdot R_{\Omega,i}} \quad (12)$$

where **Equations (11) and (12)** describe the overall resistance of the catalytic process.

The Thiele modulus ($\phi$) and the effectiveness factor ($\eta$) for a first order reactions were estimated as follows [71,72]:

$$\phi = \sqrt{\frac{k \cdot R_{\Omega i}{}^2}{D_e}} \quad (13)$$

$$\eta = \frac{1}{1 + \frac{\phi^2}{Sh_c}} \quad (14)$$

### 2.7. External and internal heat transfer evaluation

In highly exothermic reactions, such as $CH_4$ combustion, additional to mass transfer limitations, temperature gradients can also originate both between the bulk fluid phase and the external catalyst surface (external heat transfer) and within the catalyst layer (internal heat transfer), causing catalyst deactivation due to thermal sintering [60]. Therefore, heat management becomes a key aspect for both reactor

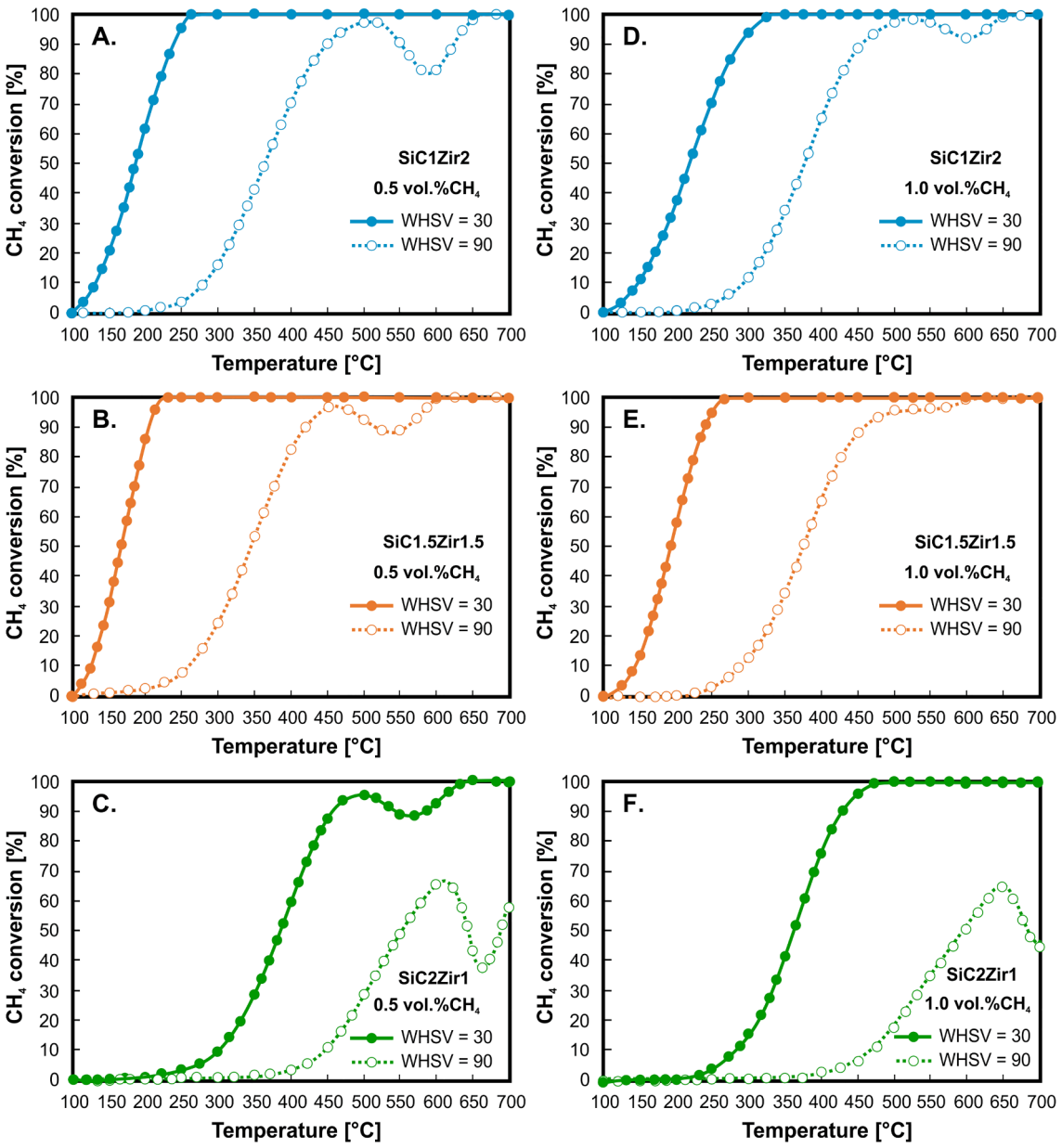


**Fig. 2.** Extinction curves of $CH_4$ oxidation on 3 wt% $PdO/Co_3O_4$ catalyst coated on SiC1Zir2 (A, D), SiC1.5Zir1.5 (B, E) and SiC2Zir1 (C, F) OCF combinations at WHSV of 30 and 90 NL $h^{-1}$ $g_{cat}^{-1}$ and intel $CH_4$ concentration of 0.5 and 1 vol%.

design and catalytic process control.

First of all, we estimated the volumetric heat transfer coefficients ($h_e^v$) of each OCF combination, which take into account the heat exchange between the fluid and outer catalyst surface. These are also influenced by the foam solid network that, as reported in our previous work [61], are composed of circular hollow struts, showing a macro/microporous skeleton with irregular and tortuous pathways. Thus, the $h_e^v$ values were estimated using the correlation derived by Younis and Viskanta in 1993 [76] valid for ceramic OCFs with pore densities up to 70 ppi, as:

$$Nu = \frac{h_e^v \cdot d_{p,c}^2}{\lambda_f} = C \cdot Re^m \tag{15}$$

$$C = 0.819 \cdot \left[1 - 7.33 \cdot \left(\frac{d_{p,c}}{L}\right)\right] \tag{16}$$

$$m = 0.36 \cdot \left[1 + 15.5 \cdot \left(\frac{d_{p,c}}{L}\right)\right] \tag{17}$$

where $Nu$ is the Nusselt number, $\lambda_f$ is the gas phase thermal conductivity (W $m^{-1}$ $K^{-1}$), $C$ and $m$ are geometrical parameters that depend on the OCFs, and $L$ is the total length of each OCF combination (0.03 m)

To evaluate the effects of external heat transfer, we used the criterion proposed by Mears in 1971 [77], which assumes that the fluid phase heat transfer resistance is lumped at the surface, according to the following expression:

$$\chi = \left|\frac{(-\triangle H_r)\cdot R^{obs}\cdot R_{\Omega e}}{h_e \cdot T_b}\right| < \frac{0.15}{\gamma_b} \quad ; \qquad \gamma_b = \frac{E_{app}}{R_g \cdot T_b} \tag{18}$$

where $\Delta H_r$ is the heat of $CH_4$ combustion reaction (J $mol^{-1}$), $h_e$ is the heat transfer coefficient associated for the gas phase (W $m^{-2}$ $K^{-1}$), $T_b$ is the temperature in the bulk of the gas phase (K); $\gamma_b$ is the Arrhenuis number evaluated at the bulk of the gas phase, $R_g$ is the universal gas constant (J $mol^{-1}$ $K^{-1}$), and $\chi$ is the Damköhler for interphase heat transport [63,77].

Thermal gradients within the catalyst layer were evaluated using the

criterion proposed by Anderson in 1963 [78]:

$$\psi = \left| \frac{\left( - \triangle H_r \cdot R^{obs} \cdot R_{\Omega i}^2 \right)}{\lambda_e \cdot T_s} \right| < \frac{0.75}{\gamma_s}; \qquad \gamma_s = \frac{E_{app}}{R_g \cdot T_s} \tag{19}$$

where $\lambda_e$ is the effective thermal conductivity (W m$^{-1}$ K$^{-1}$), $T_s$ is the temperature at the surface of the catalyst layer (K), $\gamma_s$ is the Arrhenuis number evaluated at the surface of the gas phase, and $\psi$ is the Damköhler for intraparticle heat transport [63].

Furthermore, the reaction and removal heats were evaluated at steady state conditions. Under these conditions, the heat released by the combustion reaction on any element on the outer surface of the PdO/$Co_3O_4$ catalyst layer must be transported from the catalyst surface to the bulk gas. Therefore, the heat analysis in steady state conditions, assuming a pseudo-first order reaction, is given as follows [40]:

$$Q_r = Q \tag{20}$$

$$Q_r = (R_{CH4}^{'}) \cdot ( - \Delta H_r) = A_o^{'} \cdot e^{\left( \frac{\gamma_b}{\theta + 1} \right)} \cdot C_{CH4} \cdot ( - \Delta H_r) \tag{21}$$

$$Q = h_e \cdot a_m \cdot (T_s - T_b) = h_e \cdot a_m \cdot T_b \cdot \theta \tag{22}$$

$$\theta = \frac{T_s - T_b}{T_b} \tag{23}$$

where $Q_r$ is the heat generation rate per unit mass of catalyst (J Kg$^{-1}$ s$^{-1}$), $Q$ is the heat removal rate per unit mass of catalyst (J Kg$^{-1}$ s$^{-1}$), $R_{CH4}^{'}$ is the reaction rate expressed with respect to $CH_4$ per unit mass of catalyst (mol Kg$^{-1}$ s$^{-1}$), $A_o^{'}$ is the pre-exponential factor per unit of the catalyst bulk density (m$^3$ Kg$^{-1}$ s$^{-1}$), $a_m$ is the external surface area per unit mass of catalyst (m$^2$ Kg$^{-1}$), and $\theta$ is the dimensionless temperature.

Further, the relationship between the degree of external mass transfer control and the temperature difference between the bulk gas phase and the outer catalyst surface can be easily derived for steady-state conditions. Under such conditions, the $CH_4$ external mass transfer rate must be equal to the $CH_4$ conversion rate by surface reaction. Thus, assuming that the outer surface of the catalytic layer is uniformly accessible to the reactive gases, each section of the surface behaves kinetically the same:

$$k_m^{'} \cdot a_m \cdot \left( C_{CH_4,b} - C_{CH_4,s} \right) \cdot ( - \Delta H_r) = h_e \cdot a_m \cdot (T_s - T_b) \tag{24}$$

Hence, solving for the temperature difference and considering the Chilton-Colburn analogies between heat and mass transfer by means of the j-factor correlations ($j_H \approx j_D$) leads to [79–81]:

$$(T_s - T_b) = \left( \frac{-\Delta H_r}{\rho_f \cdot c_{p,f}} \right) \cdot \left( C_{CH_4,b} - C_{CH_4,s} \right) \tag{25}$$

$$(T_s - T_b) = \left( \frac{-\Delta H_r \cdot C_{CH_4,b}}{\rho_f \cdot c_{p,f}} \right) \cdot Ca \tag{26}$$

where $\rho_f$ is the density of gas mixture (kg m$^{-3}$), $c_{p,f}$ is the heat capacity per unit mass of gas mixture (J Kg$^{-1}$ K$^{-1}$), $C_{CH_4,b}$ and $C_{CH_4,s}$ are the bulk gas and surface concentration of $CH_4$ and $Ca$ is the Carberry number [63].

Now, introducing the definition of adiabatic temperature, **Equation (26)** can be written as:

$$(T_s - T_b) = \Delta T_{ad} \cdot Ca \tag{27}$$

$$\Delta T_{ad} = \frac{-\Delta H_r \cdot C_{CH_4,b}}{\rho_f \cdot c_{p,f}}; \quad Ca = \frac{C_{CH_4,b} - C_{CH_4,s}}{C_{CH_4,b}} \tag{28}$$

Note that $(T_s - T_b)$ is maximum for reactions limited by mass transfer $Ca \geq 1$.

## 3. Results and discussion

The physical–chemical characterization of the combined OCFs, as well as the adhesive properties of the coated 3 wt% PdO/$Co_3O_4$ on both SiC and Zir supports have been fully performed and reported in our previous works [52–55,61]. In fact, a series of sonication tests (not reported here, but available in our above-mentioned works) demonstrated that the layer of PdO/$Co_3O_4$ remains well attached to the ceramic OCFs, with practically no loss of catalyst from the surface of the foams after 2 h of sonication at 40 kHz. Thus, here we can affirm that the SCS + WI methods allowed us to line on the two OCFs the desired PdO/$Co_3O_4$ catalyst, realizing a structured catalyst.

### 3.1. Catalytic tests toward $CH_4$ combustion

Fig. 2 shows the extinction curves of $CH_4$ combustion for all flow conditions and coated SiCZir combinations studied. An increase in WHSV reduces the contact time between the reactants and the catalyst, which leads to a worsening of the catalytic performance. Thus, the $CH_4$ conversion cannot be maintained at low temperature and the extinction temperature shifts to slightly higher values. For both inlet $CH_4$ concentrations, when the reactor was operated at WHSV of 30, all SiCZir OCF combinations achieved complete conversion. Particularly, the SiC1.5Zir1.5 started the extinction of the reaction at 221 °C (0.5 vol% inlet $CH_4$ concentration) or 266 °C (1 vol% inlet $CH_4$ concentration), followed by the SiC1Zir2 at 259 or 328 °C, respectively, and the SiC2-Zir1 at 496 or 484 °C, respectively. By increasing the WHSV to 90, only the combinations SiC1Zir2 and SiC1.5Zir1.5 were able to maintain full $CH_4$ conversion, while the SiC2Zir1 combination, did not reach full conversion, showing a maximum conversion of 67.3% and 65.2% at inlet $CH_4$ concentrations of 0.5 and 1 vol% respectively.

On the other hand, it is worth mentioning the drop, and further recovery, in the catalytic activity due to the PdO-Pd-PdO phase transformation during the reactor cooling ramp, at around 550–600 °C, as also reported in several other studies on $CH_4$ oxidation over Pd-based catalyst [82–87]. Recently, we also reported a decrease in $CH_4$ conversion at medium/high temperatures when the PdO/$CO_3O_4$ catalyst amount coated on the single Zir OCF was varied [53]. The decrease in the catalytic activity was observed for all flow conditions studied (WHSV = 30, 60, 90 and inlet $CH_4$ concentration of 0.5 and 1 vol% [53]). Interestingly, in this work, when carrying out the catalytic $CH_4$ oxidation combining the coated SiCZir OCFs at the lowest WHSV of 30, the $CH_4$ conversion remains constant at 100% till very low temperature values, without being affected by the PdO-Pd-PdO phase transformation, except for the SiC2Zir1 combination at the inlet $CH_4$ concentration of 0.5 vol%. However, as the WHSV increases to 90, the drop in the catalytic activity becomes evident in all OCF combinations, occurring at higher temperatures respect to the previous series of tests. Attractively, in terms of $CH_4$ conversion, the SiC1.5Zir1.5 combination showed the smallest performance drop due to the PdO-Pd-PdO phase transformation (from 100% to 90%) compared to the other foams combinations, even with those reported in our previous work at the same flow conditions on the coated Zir OCF [53]. Furthermore, it is important to note that at WHSV of 90, when the reactor operates with a higher $CH_4$ concentration and, hence, with a higher oxygen concentration ($O_2$/$CH_4$ molar ratio constant and equal to 8), the shift of the curve is less accentuated (from 100% to 95%).

Such a feature has also been reported in our previous work [53] and by other authors for highly exothermic reactions [57,59,87,88]. Various studies have pointed out that the increase in the partial pressure of $O_2$ favors the stabilization of the PdOx system by promoting the formation of PdO during the cooling phase (Pd ↔ PdO phase transformation) [29,83,86,87,89–92]. Farrauto et al. [93] also reported that as $O_2$ concentration increases, the hysteresis of the PdO-Pd-PdO phase transformation is shifted towards higher temperatures. Such an effect is also observed here, particularly during the catalytic tests performed at

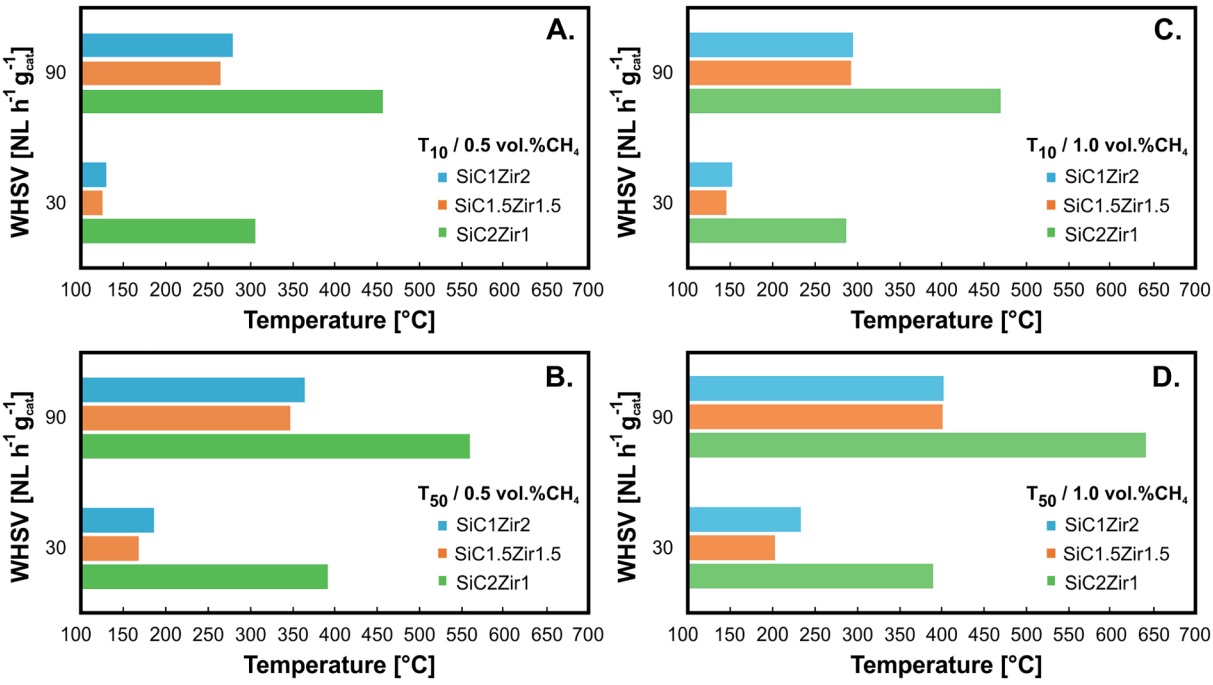


**Fig. 3.** $T_{10}$ and $T_{50}$ of the three OCF combinations for all flow conditions studied during the extinction curves.

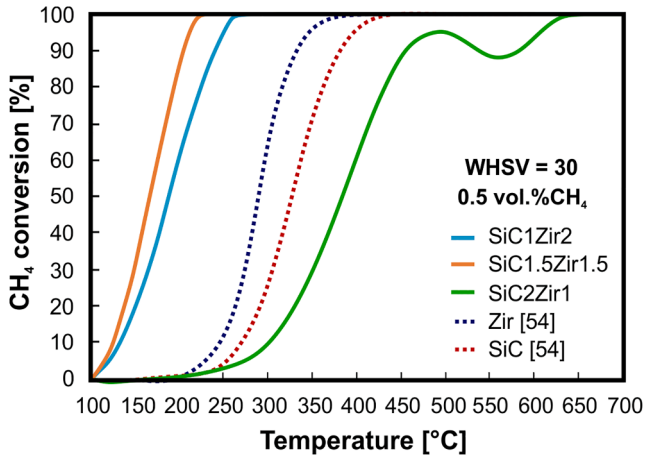


**Fig. 4.** Extinction curves of $CH_4$ oxidation for 3 wt% $PdO/Co_3O_4$ catalyst coated on individual SiC and Zir OCF (from our previous work Ercolino et al. [54]) and combinations of them at WHSV of 30 NL $h^{-1}$ $g_{cat}^{-1}$ and inlet $CH_4$ concentration of 0.5 vol%.

WHSV of 90 on the SiC2Zir1 combination (Fig. 2**C and 2F**).

Fig. 3 shows a comparison of the three coated SiCZir OCF combinations in terms of temperature at 10% ($T_{10}$) and 50% ($T_{50}$) methane conversion, for all flow conditions investigated. Specifically, when analyzing the shut-down temperature ($T_{10}$), the extinction of the reaction occurs at lower temperatures in the SiC1.5Zir1.5 and SiC1Zir2 combinations, showing a $T_{10}$ difference between them below 15 °C at both WHSV and inlet $CH_4$ concentrations. On the other hand, the extinction for the SiC2Zir1 combination is anticipated, obtaining a $T_{10}$ difference with respect to the SiC1.5Zir1.5 combination greater than 140 °C, at the same flow conditions. Regarding the $T_{50}$, at WHSV of 90, the SiC1Zir2 and SiC1.5Zir1.5 configurations exhibited similar values with a $T_{50}$ difference below 15 °C. However, when operating the reactor at the lowest WHSV (30), the $T_{50}$ difference between the latter increased to about 30 °C. Similar to the $T_{10}$ results, the SiC2Zir1 combination showed the highest $T_{50}$ values. Thus, according to the catalytic test results, it is possible to deduce that combining equal lengths of the coated SiC and Zir OCF pieces in the SiC1.5Zir1.5 configuration favors the catalytic performance of $CH_4$ oxidation, since it allows maintaining the reaction and the complete $CH_4$ conversion at lower temperatures. This result can be explained considering the difference in thermal conductivity of both foams. In fact, as we reported in our previous work [54], the volumetric heat transfer coefficient for the individual SiC OCF is about 25 times higher than that of the Zir OCF. This could suggest a lower resistance to external heat transfer favoring the catalytic process.

In order to highlight the effect on the catalytic performance towards $CH_4$ combustion in lean conditions when using different combinations of SiC and Zir OCFs, we compared the extinction curves of all the OCF combinations studied here with those obtained in our previous work on individual SiC and Zir OCFs [54], as shown in Fig. 4. All of them were lined with 3 wt% $PdO/Co_3O_4$ as catalyst and carried out at the same flow conditions (WHSV = 30 NL $h^{-1}$ $g_{cat}^{-1}$ and inlet $CH_4$ concentration of 0.5 vol%).

Clearly, the SiC1Zir2 and SiC1.5Zir1.5 combinations offer a marked

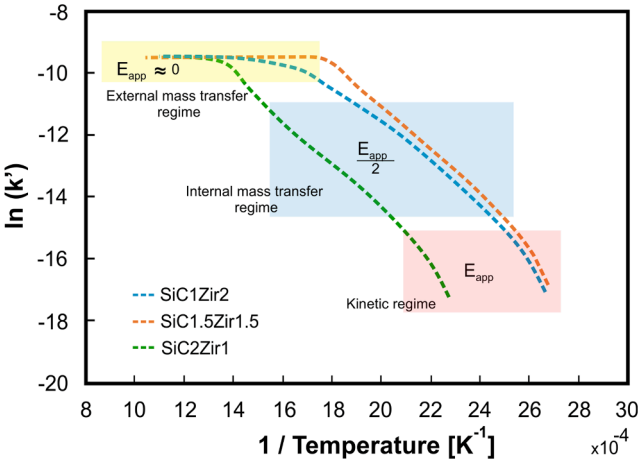


**Fig. 5.** Arrhenius plots for the various OCF combinations (SiC1Zir2, SiC1.5-Zir1.5, and SiC2Zir1) at WHSV of 30 and inlet $CH_4$ concentration of 1 wt%.

**Table 2**
Apparent kinetic parameters estimated for the three OCF combinations at WHSV of 30 and 90 NL $h^{-1}$ $g_{cat}^{-1}$ and inlet $CH_4$ concentration of 1 vol%.

| | 30 WHSV (NL $h^{-1}$ $g_{cat}^{-1}$) | | 90 WHSV (NL $h^{-1}$ $g_{cat}^{-1}$) | |
|---|---|---|---|---|
| | $E_{app}$ (kJ $mol^{-1}$) | $A_o$ ($m^3$ $g^{-1}$ $s^{-1}$) | $E_{app}$ (kJ $mol^{-1}$) | $A_o$ ($m^3$ $g^{-1}$ $s^{-1}$) |
| SiC1Zir2 | 104.30 | $3.78{\cdot}10^4$ | 96.30 | $8.65{\cdot}10^3$ |
| SiC1.5Zir1.5 | 102.42 | $1.14{\cdot}10^7$ | 113.90 | $8.03{\cdot}10^5$ |
| SiC2Zir1 | 108.82 | $1.68{\cdot}10^5$ | 109.06 | $1.17{\cdot}10^2$ |

improvement in holding on the $CH_4$ conversion at low temperature. Particularly, the SiC1.5Zir1.5 combination allowed combustion extinction at 150 and 90 °C less than those obtained for the individual SiC and Zir OCFs, respectively. Furthermore, this OCF combination showed a decrease of the temperature of approximately 175 and 135 °C, with respect to the individual SiC and Zir OCFs. That is, the SiC1.5Zir1.5 combination maintained full $CH_4$ combustion till to the temperature of 215 °C (for 30 as WHSH and 0.5 vol% as inlet $CH_4$ concentration), which is a remarkable result. This result shows a promising performance in heterogeneous catalysis for the complete oxidation of methane in lean conditions and at low temperature. Such outcome is of utmost importance especially for the intensification of processes where it is required to abate methane emissions at the lowest possible temperature [8–10].

### 3.2. Apparent kinetic parameters

Fig. 5 shows the Arrhenius plot for all SiCZir OCF combinations studied at WHSV of 30 and inlet $CH_4$ concentration of 1 vol%. The SiC2Zir1 combination curve shifts towards higher temperatures (lower 1/T values), indicating slower ignition of the reaction. On the other

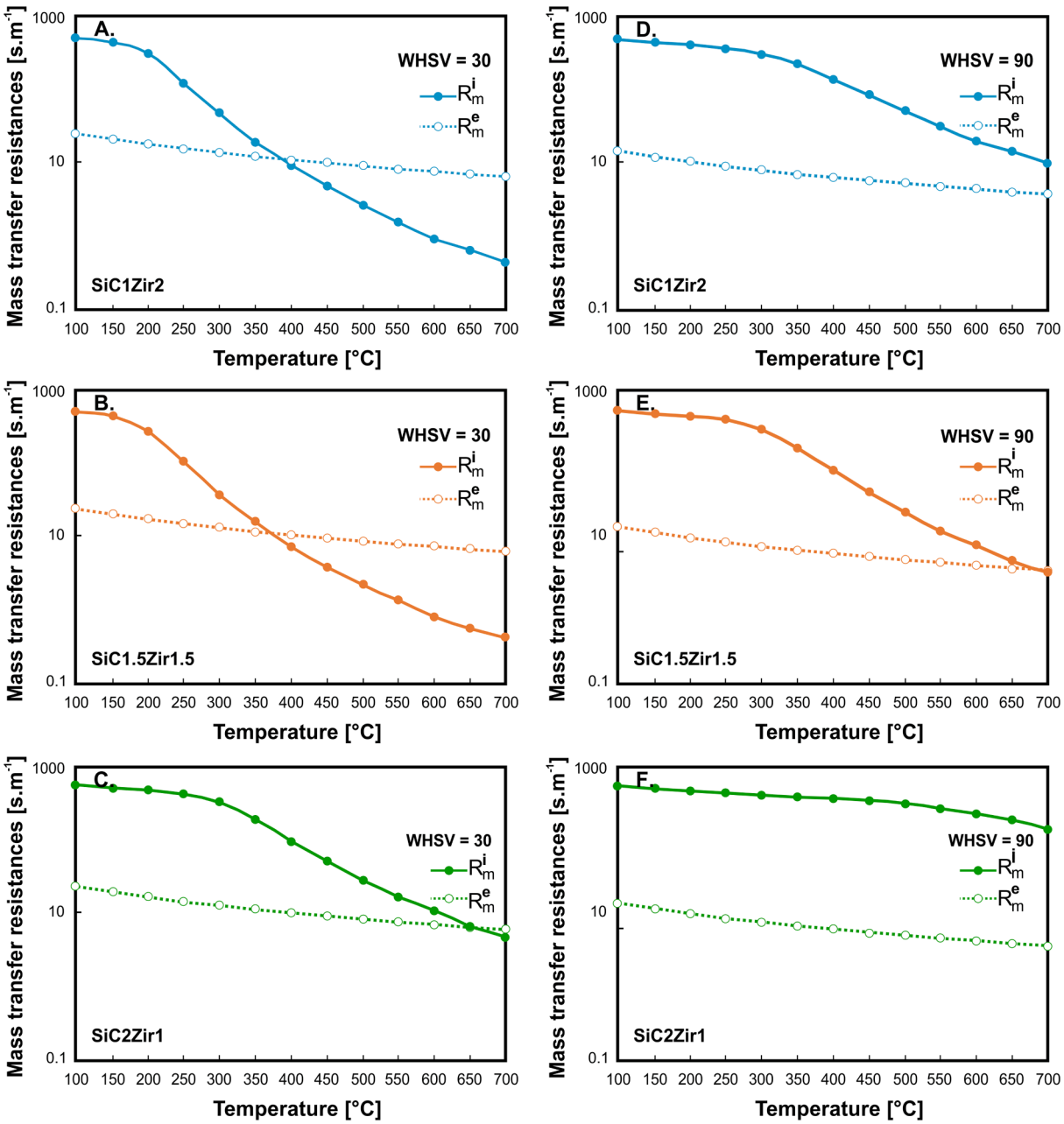


**Fig. 6.** Mass transfer resistance as a function of temperature at inlet $CH_4$ concentration of 1 vol% and WHSV of 30 and 90 NL $h^{-1}$ $g_{cat}^{-1}$ for all OCF combinations: SiC1Zir2 (A, D); SiC1.5Zir1.5 (B, E) and SiC2Zir1 (C, F).

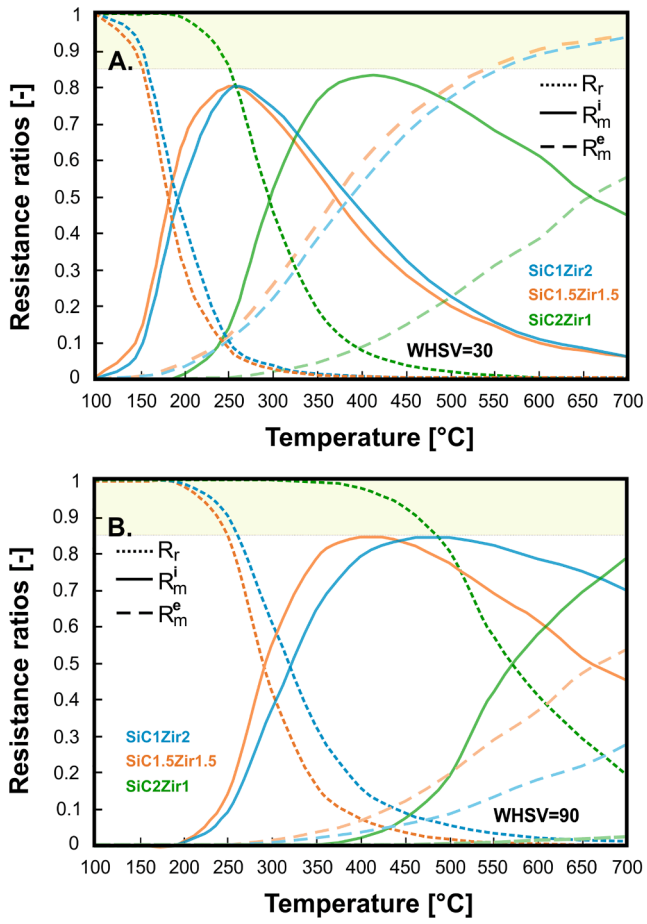


**Fig. 7.** Various resistance ratios as a function of temperature showing the different operating regimes for the three OCF combinations at inlet $CH_4$ concentration of 1 vol% and WHSV of 30 (A) and 90 (B) NL $h^{-1}$ $g_{cat}^{-1}$.

hand, the curves for the SiC1Zir2 and SiC1.5Zir1.5 configurations are quite close, with a slight shift towards lower temperatures for the SiC1.5Zir1.5 combination. The apparent activation energy ($E_{app}$) and the pre-exponential factor $A_o$ were estimated at $CH_4$ conversions below 10 % to guarantee a kinetic regime in all structured catalysts (see Table 2). The kinetic parameters, also calculated for the three OCFs at WHSV of 90, were in line with the values obtained at the lower WHSV and with those we calculated for the 3% $PdO/Co_3O_4$ lined on single Zir and SiC foams in one of our previous paper ($E_{app}$ = 85.9 kJ $mol^{-1}$ for Zir, and 191.6 kJ $mol^{-1}$ for SiC at WHSV 30, inlet $CH_4$ concentration 0.5% [52], instead of 1%).

At higher temperature, the reaction rate increases and the reaction resistance decreases, thus the diffusional effects become important. This is observed in all the curves displayed in Fig. 5, where it is possible to visualize the change in the slope ($-E_{app}/R_g$) of the Arrhenius plot as the temperature varies. At intermediate temperatures, a slope of about half compared to that obtained in the kinetic regime was found ($E_a^{id} \approx E_{app}/2$), evidencing the relevance of diffusional effects inside the catalyst. Finally, at very high temperatures the slope of the curve drops to a value close to zero, indicating the dominance of external diffusive effects ($E_a^{ed} \approx 0$).

### 3.3. External and internal mass transfer resistances

In Fig. 6, the external ($R_m{}^e$ or $1/k_m{}^e$) and internal ($R_m{}^i$ or $1/k_m{}^i$) mass transfer resistances are plotted as a function of temperature at inlet $CH_4$ concentration of 1 vol% and the two WHSV examined, for the three catalytic OCF combinations. At lower WHSV, SiC1Zir2 and SiC1.5Zir1.5 showed a dominance of $R_m{}^i$ at temperatures below 400 °C (see Fig. 6**A and 6B**). Thereafter, diffusional effects related to the fluid phase ($R_m{}^e$) start to become significant as the temperature continues to increase. For SiC2Zir1 the dominance of $R_m{}^i$ remains up to temperatures of approximately 690 °C, covering practically the entire temperature range studied (Fig. 6**C**). On the other hand, with the increase of WHSV to 90, the external mass transfer coefficient increases as well, due to the enhancement of mixing (higher turbulence) in the gas phase. This leads to a remarkable decrease of the $R_m{}^e$, being irrelevant during almost the whole temperature range investigated and thus the $R_m{}^i$ becomes the crucial point for the catalyst performance. Both resistances show monotonic behavior with temperature, although the resistance to external mass transfer is almost independent of temperature.

### 3.4. Overall catalytic performance: Kinetic and mass transfer regimes

We evaluated the operating regime (kinetic, internal and external mass transfer) of each SiCZir combination. For this purpose, we plotted the ratio of each resistance with respect to the total resistance ($\frac{R_r}{R^{ov}}; \frac{R_m{}^i}{R^{ov}}; \frac{R_m{}^e}{R^{ov}}$) as a function of gas temperature, at WHSV of 30 and 90 and inlet $CH_4$ concentration of 1 vol%, as shown in Fig. 7.

As a general trend, the increase of temperature leads to a sharp drop of the $\frac{R_r}{R^{ov}}$ ratio due to the increase of the reaction rate, which is strongly dependent on the Arrhenius equation. On the other hand, as the temperature increases, the $\frac{R_m{}^i}{R^{ov}}$ ratio progressively increases (the intraparticle effects become more and more significant), reaching a maximum value, for then decreasing gradually with temperature. As for the external diffusional effects, the $\frac{R_m{}^e}{R^{ov}}$ ratio shows a progressive increase with increasing temperature, becoming much more significant at lower

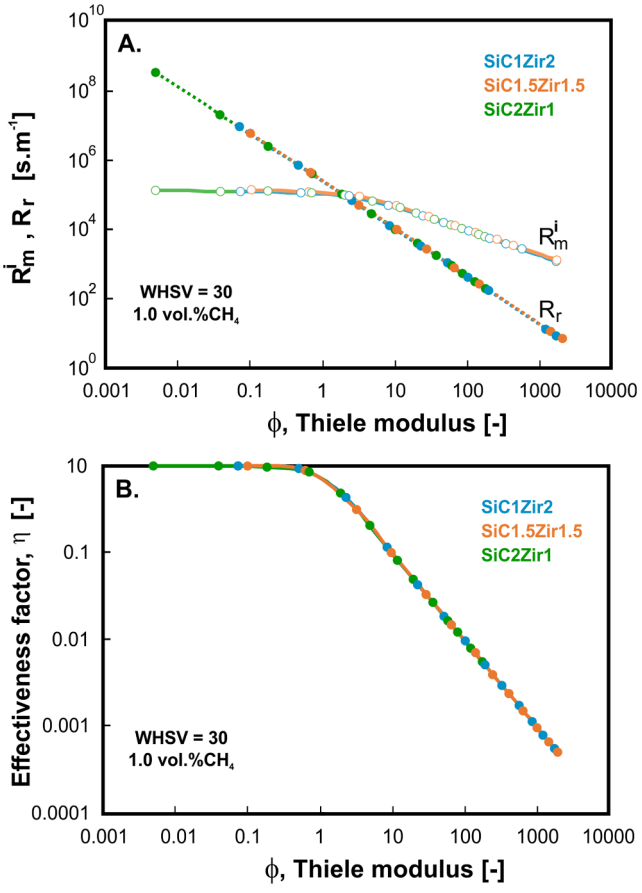


**Fig. 8.** Evolution of $R_r$ and $R_m{}^i$ (A) and effectiveness factor (B) as a function of the Thiele modulus ($\phi$) at WHSV of 30 and inlet $CH_4$ concentration of 1 vol%.

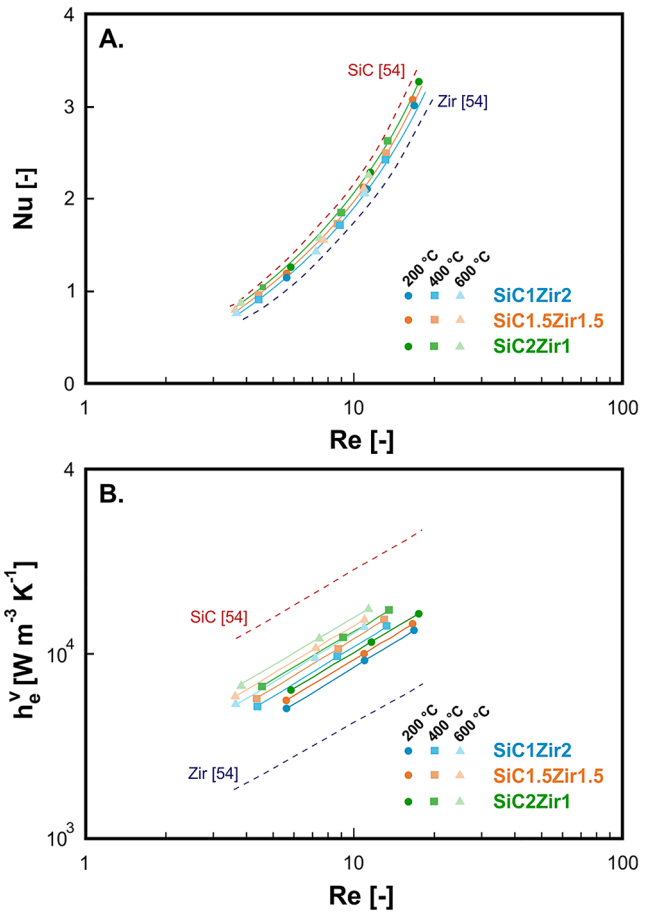


**Fig. 9.** Nusselt number (A) and volumetric heat transfer coefficient (B) as a function of Reynolds number defined at temperatures of 200, 400, and 600 °C for the three OCF combinations and for each individual SiC and Zir OCF reported in our previous work [54].

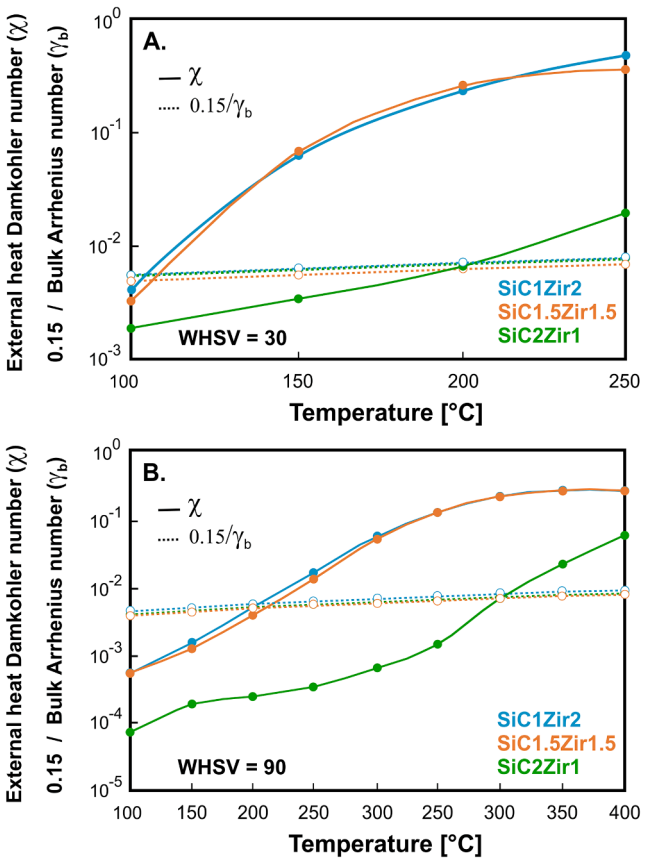


**Fig. 10.** Mears criterion to evaluate external heat transfer for all OCF combinations at inlet $CH_4$ concentration of 1 vol% and WHSV of 30 (A) and 90 (B).

WHSV and very high temperatures.

When analyzing the operating regimes at WHSV of 30 (see Fig. 7**A**), at temperatures below 148, 160, and 255 °C for SiC1.5Zir1.5, SiC1Zir2 and SiC2Zir1, respectively, the reaction kinetics dominates the process ($\frac{R_r}{R^{ov}} > 0.85$), being the reaction resistance controlling, thus the catalyst operates in a kinetic regime. As the temperature increases, the reaction rate becomes increasingly faster, thus internal diffusion effects start to become significant. In particular, at temperatures between 180 and 370 °C, 190–395 °C and 295–660 °C the diffusion inside the $PdO/Co_3O_4$ layer becomes the pivotal resistance of the catalytic process for the OCF combinations of SiC1.5Zir1.5, SiC1Zir2 and SiC2Zir1, respectively. However, considering that by convention a reaction is defined under internal resistance control regime for a thresold limit value of 85% [71,72], in our case the structured catalysts cannot be considered under internal resistance control (all the curves show a $\frac{R_m{}^i}{R^{ov}} < 0.85$). On the other hand, only the coated SiC1Zir2 and SiC1.5Zir1.5 structures exhibit an external diffusive regime at temperature above roughly 550 °C.

When operating the reactor at the higher WHSV (see Fig. 7**B**), the kinetic regime ($\frac{R_r}{R^{ov}} > 0.85$) shifts towards higher temperatures, due to the shorter contact time. Specifically, at temperatures below 250, 260, and 485 °C the catalyst operates in the kinetic regime for OCF combinations of SiC1.5Zir1.5, SiC1Zir2 and SiC2Zir1, respectively. As mentioned above, the increase in gas velocity produces an enhancement of mixing and thus an increase of the external mass transfer coefficient. In this way, the dominant resistance at medium–high temperatures becomes the $R_m{}^i$. Nevertheless, the $\frac{R_m{}^i}{R^{ov}}$ ratios are not higher than 0.85 to be considered as a controlling regime. Therefore, once the kinetic control is overcome (as the temperature increases), the catalyst operates in a mixture of regimes where $R_r$ and $R_m{}^i$ are comparable at low/medium temperatures, while $R_m{}^i$ and $R_m{}^e$ at medium/high temperatures.

For further analysis, we plotted the effectiveness factor, $\eta$ (Fig. 8**B**), and the evolution of $R_r$ and $R_m{}^i$ (Fig. 8**A**) as a function of the Thiele modulus ($\phi$) at WHSV of 30 and 1 vol% as inlet $CH_4$ concentration. Clearly, in the case of very slow reactions, $\phi \ll 1$ and $\eta \rightarrow 1$. At this point, the $R_r$ controls the catalytic combustion and $R_m{}^i$ tends to the asymptotic value of $\frac{R_{\Omega,i}}{Sh_{c,\infty} \cdot D_e}$, being independent of the reaction kinetics and catalytic thickness dependent [71]. On the contrary, in the limit of very fast reactions (for $\phi \gg 1$; $\eta \rightarrow \frac{1}{\phi}$), the $R_r$ is negligible and thus, the diffusional effects control the process, where the $R_m{}^i$ tends to the value of $\frac{1}{\sqrt{k \cdot D_e}}$ [72]. Therefore, $R_m{}^i$ is independent of the catalytic thickness and depends only on the combustion kinetics and the effective diffusivity inside the catalyst [40,63,72,73,94].

### 3.5. External and internal heat transfer evaluation

Fig. 9 shows the Nusselt number and volumetric heat transfer coefficient as a function of Reynolds number defined at temperatures of 200, 400, and 600 °C for the three OCF combinations and for each individual SiC and Zir OCF reported in our previous work [54]. Clearly, the higher the gas velocity, the greater the fluid turbulence in the foam flow paths, and hence the convective heat transfer increases. At the same flow conditions, the gas surface velocity is higher with increasing SiC OCF length in the combinations. This is because the SiC OCF has a lower average pore diameter value [61], thus as the SiC OCF length increases in each combination, more of the reactive flow passes through the entire

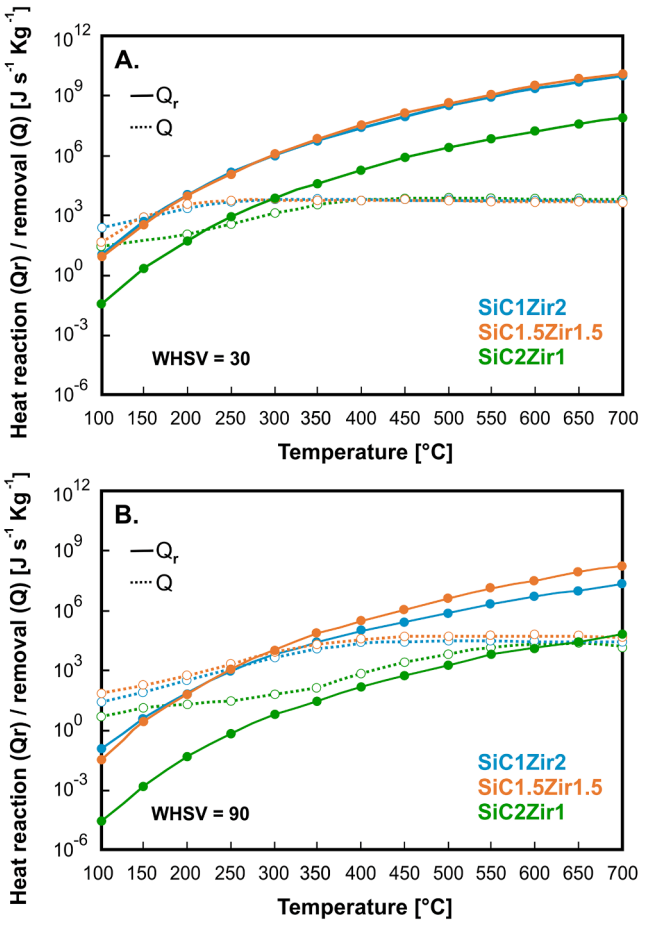


**Fig. 11.** Heat reaction and removal rates as a function of bulk temperature for all the OCF combinations at WHSV of 30 (A) and 90 (B) and inlet $CH_4$ concentration of 1 vol%

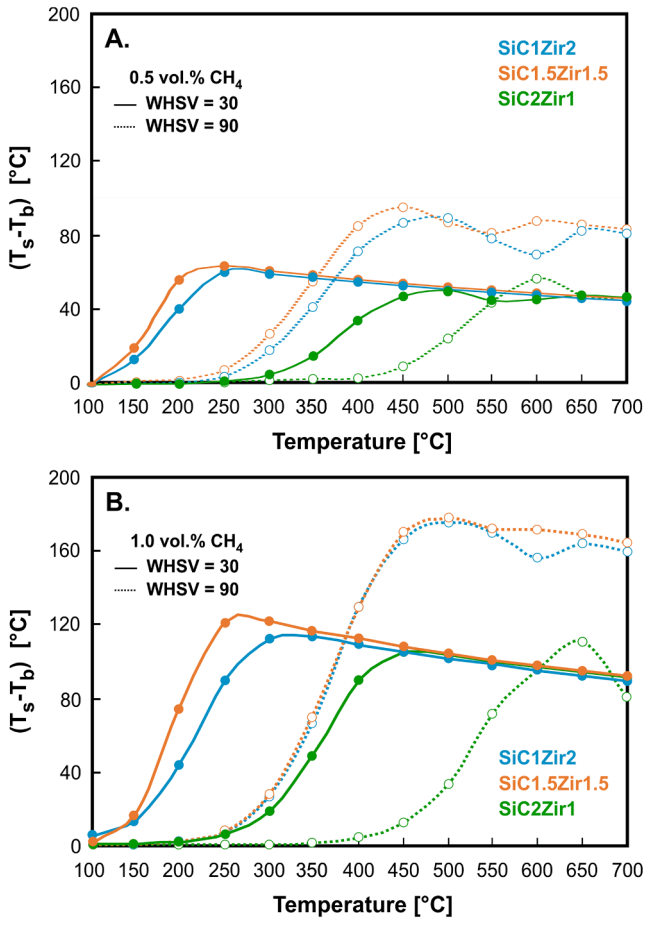


**Fig. 12.** Temperature difference between the bulk gas phase and the external catalyst surface as a function of temperature at WHSV of 30 and 90 and inlet $CH_4$ concentration of 0.5 (A) and 1 vol% (B) for all the OCF combinations investigated.

configuration at a higher velocity. Examining the effect of temperature, at 200 °C higher *Nu* values are obtained by increasing the length of the SiC OCF (SiC2Zir1 > SiC1.5Zir1.5 > SiC1Zir2). However, increasing the temperature up to 600 °C led to very similar *Nu* values for all OCF combinations, due to the decrease in viscosity of the reactive mixture. These effects play a key role in the volumetric heat transfer coefficients, which, at same flow conditions are higher for the combinations with longer SiC foam length, thanks to the higher thermal conductivity that they offer compared to Zir OCF. Thus, by combining SiCZir OCFs, a remarkable increase of the volumetric heat transfer coefficient is obtained. The $h_e^v$ values are in line with those reported by Dietrich [95] and Xia et. al [96] for OCFs, and also other reactor configurations, such as packed bed reactors and monoliths [45,97–99].

To evaluate the effects of external heat transfer in all SiCZir OCF combinations, we used the Mears criterion according to **Equation (18)**, for both WHSV studied and inlet $CH_4$ concentration of 1 vol%.

At lower reactive gas flow and hence low WHSV (Fig. 10**A**), external heat transfer limitations are present at higher temperatures of 105, 115, and 200 °C for the combinations of SiC1Zir2, SiC1.5Zir1.5, and SiC2-Zir1, respectively. On the other hand, by increasing the WHSV to 90, a higher gas turbulence is obtained and hence higher heat transfer coefficients (Fig. 9), which leads to shift the external heat transfer limitations to higher temperatures, as shown in Fig. 10**B**. Such limitations could be due to the rapid ignition of the reaction, which results in a higher heat production due to the exothermicity of the combustion process, with respect to the heat removed by the flue gases. By analyzing the heats of removal ($Q$) and reaction ($Q_r$) as a function of temperature at the two WHSV and inlet $CH_4$ concentration of 1 vol% (see Fig. 11), the SiC1Zir2 and SiC1.5Zir1.5 combinations show similar values of $Q_r$ and $Q$ (at both space velocities), with slightly higher values for SiC1.5Zir1.5. In particular, the latter exhibits a $Q > Q_r$ (stable operating zone) at lower temperatures of 160 and 272 °C at WHSV of 30 and 90, respectively. In contrast, the SiC2Zir configuration displays the lowest $Q$ and $Q_r$ when compared to the other combinations, operating in a stable zone at temperatures below 230 and 650 °C at WHSV of 30 and 90 NL $h^{-1}$ $g_{cat}^{-1}$, respectively. Once the catalyst reaches conversions above 90 % (Fig. 2), that is, when the reaction rate constant is sufficiently high and hence the $R_r$ is negligible ($R_r \ll R_m^e + R_m^i$), the heat removal becomes stable reaching similar values at elevated temperatures for the three OCF combinations.

The presence of SiC OCF at the inlet of the reactor, which has a higher thermal conductivity compared to that of Zir OCF, is helpful to retain the heat of reaction for boosting the ignition of the first reacting molecules on the surface of the catalyst at low temperature during the heating ramp, and to hold the reaction on during the cooling ramp of the tests [54,99]. The optimal configuration is reached in the SiC1.5Zir1.5 combination, where the kinetics and thermal effects of the two foams are synergetically enhanced by combining two supports with different thermal conductivity but equal length. The OCF in front, with a higher thermal conductivity, to boost the ignition of the catalytic reaction at low temperature, the following one with a lower thermal conductivity, to reach and maintain full combustion at the lowest possible temperature.

For further analysis, we plotted the temperature difference between the bulk gas phase and the external catalyst surface (according to

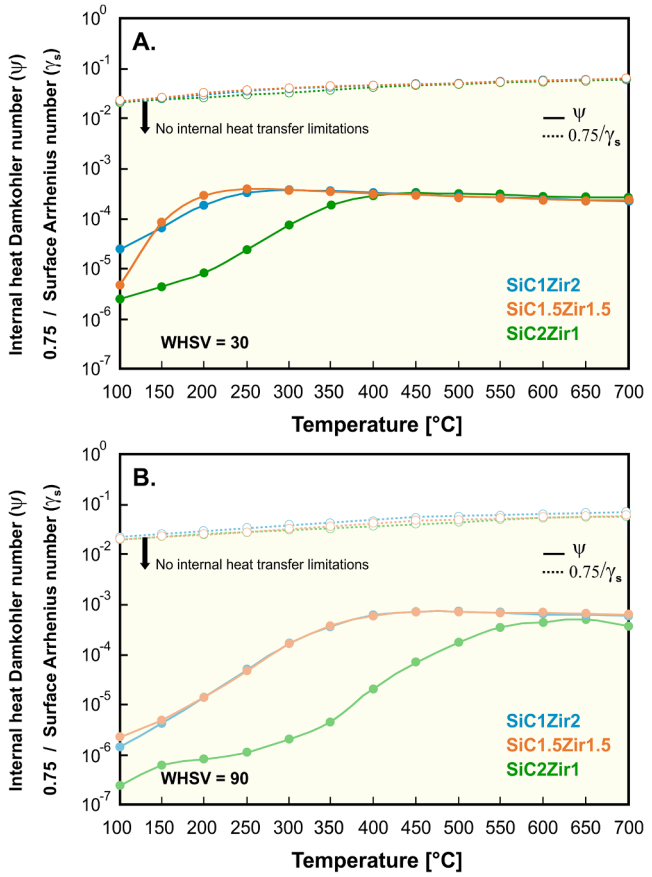


**Fig. 13.** Anderson criterion to evaluate internal heat transfer for all OCF combinations at inlet $CH_4$ concentration of 1 vol% and WHSV of 30 (A) and 90 (B).

**Equation (27)**) as a function of temperature for all the conditions examined (Fig. 12). This is a purely qualitatively analysis, since the $T_s$ is a theoretical average temperature calculated taking into account the different properties of the two OCFs and their relative lengths, and it does not represent any real surface temperature. Moreover, in the tests we made on single OCFs [54], we measured a temperature gradient between the inlet and outlet of the foams, being the $\Delta(T_{in} - T_{out})$ values of the Zir foams very limited, representative of an isothermal system, while the $\Delta(T_{in} - T_{out})$ values of the SiC slightly more positive, representative of a quasi-isothermal system, at various temperatures and WHSV. Consequently, in our SiCZir configurations we expect inlet/outlet temperature gradients. Thus, the following considerations are purely speculative, but helpful in understanding what is happening in the catalytic systems during reaction.

As observed from our calculations, the increase in $CH_4$ concentration leads to a higher adiabatic temperature ($\Delta T_{ad}$) in the catalytic system and thus a greater $(T_s - T_b)$. The temperature difference increases rapidly until the catalyst reaches full $CH_4$ conversion. At this point, the $(T_s - T_b)$ starts to decay gradually as the gas temperature increases. The highest temperature difference was found for the SiC1.5Zir1.5 combination for all flow conditions studied. A greater $(T_s - T_b)$, that is a higher $T_s$, should hold the combustion reaction, thus exploiting the extinction temperature at lower values. However, at higher WHSV, the contact time decreases, and the Carberry values increase with temperature, reaching maximum values approaching full methane conversion, thus shifting the extinction temperature to greater values. This is also visible by the significative increase of the diffusional effects related to the fluid phase as the temperature raises, as visible from Fig. 6. These two effects combined together prevail on the advantage of a greater $(T_s - T_b)$, with the consequence that at higher WHSV and higher $CH_4$ inlet concentration, the combustion reaction worsen.

Regarding internal heat transfer, we plotted in Fig. 13 the Anderson criterion for all OCF combinations at inlet $CH_4$ concentration of 1 vol% and the two WHSV. No heat limitations were found within the catalyst layer thickness, indicating the absence of intraparticle temperature gradients in all OCF configurations.

## 4. Conclusions

The main contribution of this work is to evaluate the catalytic performance towards complete $CH_4$ combustion in lean conditions by using three different OCF combinations made of SiC and Zir with pore densities of 30 ppi coated with 3 wt% $PdO/Co_3O_4$ as catalyst. The reactor was fed with a large excess of oxygen ($O_2/CH_4$ molar ratio equal to 8), with inlet $CH_4$ concentrations of 0.5 and 1 vol% and WHSV of 30 and 90 NL $h^{-1}$ $g_{cat}^{-1}$. The apparent kinetic parameters of the structured catalysts were determined in order to estimate the reaction resistance. In addition, external and internal mass transfer effects were evaluated using a theoretical model adapted to the OCF geometry, which allowed the determination of the mass transport resistances. The operating regime of each OCF combination was determined by varying the temperature of the reactive gas. Furthermore, an analysis of heat transfer effects was carried out in terms of volumetric heat transfer coefficients, possible heat limitations using theoretical criteria (Mears and Anderson criteria), heats of removal and reaction, and theoretical evaluation of the temperature difference between the gas bulk and the external catalyst surface. The following major conclusions can be drawn from this study:

- Among the three foam combinations, SiC1.5Zir1.5 exhibited complete methane conversion at the lowest temperatures for all flow conditions studied.
- The remarkable catalytic performance of the SiC1.5Zir1.5 configuration, which maintained full methane conversion at the lowest extinction temperature of 215 °C (WHSV of 30 and 0.5 vol% as inlet $CH_4$ concentration), can be explained considering the different thermal conductivity of the SiC and Zir used as supports for the $PdO/Co_3O_4$ catalyst. The presence of SiC OCF at the inlet of the reactor, which has a higher thermal conductivity compared to that of Zir OCF, is helpful to hold on the heat of reaction, thus shifting the extinction temperature at lower values. The optimal configuration is reached in the SiC1.5Zir1.5 system combination, where two supports of same length but with different thermal conductivity are used in series. With such a configuration, we reached a favorable balance of heat and mass transfers acting synergistically to drive and hold the combustion reaction even at low temperature.
- The temperature difference between the bulk of the fluid phase and the external catalyst surface increases rapidly in the combinations with faster ignition of the reaction, until the catalyst reaches near full conversion and then gradually decreases as the gas temperature increases.
- The mass transport limitations, ignition/extinction behavior, and presence of multiple steady-state conditions of a catalytic system are of utmost importance to design new compact catalytic reactors for process intensification of highly exothermic reactions.

## CRediT authorship contribution statement

**Carmen W. Moncada Quintero:** Conceptualization, Methodology, Investigation, Data curation, Formal analysis, Validation, Writing – original draft, Writing – review & editing. **Giuliana Ercolino:** Conceptualization, Investigation, Data curation. **Stefania Specchia:** Conceptualization, Methodology, Validation, Supervision, Writing – review & editing, Funding acquisition, Resources.

## Declaration of Competing Interest

The authors declare that they have no known competing financial interests or personal relationships that could have appeared to influence the work reported in this paper.

## Acknowledgements

This work was supported by the Italian Ministry of Education, University and Research (MIUR, Italy), via the ERANETMED network (SOLCARE project, grant number ENERG-065).

## References

[1] Understanding Global Warming Potentials | Greenhouse Gas (GHG) Emissions | US EPA, (n.d.). https://www.epa.gov/ghgemissions/understanding-global-warming-potentials.
[2] E.J. Dlugokencky, E.G. Nisbet, R. Fisher, D. Lowry, Global atmospheric methane: Budget, changes and dangers, Philos. Trans. R. Soc. A Math. Phys. Eng. Sci. 369 (1943) (2011) 2058–2072, https://doi.org/10.1098/rsta.2010.0341.
[3] IPCC, Climate Change 2014 Part A: Global and Sectoral Aspects, 2014. papers2://publication/uuid/B8BF5043-C873-4AFD-97F9-A630782E590D.
[4] R.K. Pachauri, L. Meyer. Climate Change 2014: Synthesis Report. Contribution of Working Groups I, II and III to the Fifth Assessment Report of the Intergovernmental Panel on Climate Change, IPCC, Geneva, Switzerland, 2014.
[5] Dlugokencky E.J., Global Monitoring Laboratory - Carbon Cycle Greenhouse Gases, US Dep. Commer. NOAA, Glob. Monit. Lab. (2019). https://www.esrl.noaa.gov/gmd/ccgg/trends_ch4/ (accessed September 28, 2020).
[6] Global Methane Initiative, Global methane emissions by sector, 2020 (2010) 1–4. www.globalmethane.org.
[7] Methane Tracker 2020 – Analysis - IEA, (n.d.). https://www.iea.org/reports/methane-tracker-2020.
[8] J.K. Stolaroff, S. Bhattacharyya, C.A. Smith, W.L. Bourcier, P.J. Cameron-Smith, R. D. Aines, Review of methane mitigation technologies with application to rapid release of methane from the arctic, Environ. Sci. Technol. 46 (12) (2012) 6455–6469, https://doi.org/10.1021/es204686w.
[9] P. Gélin, L. Urfels, M. Primet, E. Tena, Complete oxidation of methane at low temperature over Pt and Pd catalysts for the abatement of lean-burn natural gas fuelled vehicles emissions: Influence of water and sulphur containing compounds, Catal. Today. 83 (1-4) (2003) 45–57, https://doi.org/10.1016/S0920-5861(03)00215-3.
[10] I. Karakurt, G. Aydin, K. Aydiner, Mine ventilation air methane as a sustainable energy source, Renew. Sustain. Energy Rev. 15 (2) (2011) 1042–1049, https://doi.org/10.1016/j.rser.2010.11.030.
[11] N.M. Kinnunen, J.T. Hirvi, M. Suvanto, T.A. Pakkanen, Methane combustion activity of Pd–$PdO_x$–Pt/$Al_2O_3$ catalyst: the role of platinum promoter, J. Mol. Catal. A Chem. 356 (2012) 20–28, https://doi.org/10.1016/j.molcata.2011.12.023.
[12] W.R. Schwartz, L.D. Pfefferle, Combustion of methane over palladium-based catalysts: Support interactions, J. Phys. Chem. C. 116 (15) (2012) 8571–8578, https://doi.org/10.1021/jp2119668.
[13] M. Monai, T. Montini, R.J. Gorte, P. Fornasiero, Catalytic oxidation of methane: Pd and beyond, Eur. J. Inorg. Chem. 2018 (25) (2018) 2884–2893, https://doi.org/10.1002/ejic.201800326.
[14] H. Stotz, L. Maier, A. Boubnov, A.T. Gremminger, J.D. Grunwaldt, O. Deutschmann, Surface reaction kinetics of methane oxidation over PdO, J. Catal. 370 (2019) 152–175, https://doi.org/10.1016/j.jcat.2018.12.007.
[15] G. Ercolino, P. Stelmachowski, G. Grzybek, A. Kotarba, S. Specchia, Optimization of Pd catalysts supported on $Co_3O_4$ for low-temperature lean combustion of residual methane, Appl. Catal. B Environ. 206 (2017) 712–725, https://doi.org/10.1016/j.apcatb.2017.01.055.
[16] L.F. Liotta, G. Di Carlo, G. Pantaleo, G. Deganello, Catalytic performance of $Co_3O_4$/$CeO_2$ and $Co_3O_4$/$CeO_2$–$ZrO_2$ composite oxides for methane combustion: Influence of catalyst pretreatment temperature and oxygen concentration in the reaction mixture, Appl. Catal. B Environ. 70 (1-4) (2007) 314–322, https://doi.org/10.1016/j.apcatb.2005.12.023.
[17] M.M. Fiuk, A. Adamski, Activity of $MnO_x$–$CeO_2$ catalysts in combustion of low concentrated methane, Catal. Today. 257 (2015) 131–135, https://doi.org/10.1016/j.cattod.2015.01.029.
[18] G. Ercolino, P. Stelmachowski, A. Kotarba, S. Specchia, Reactivity of mixed iron-cobalt spinels in the lean methane combustion, Top. Catal. 60 (17-18) (2017) 1370–1379, https://doi.org/10.1007/s11244-017-0826-9.
[19] S. Specchia, A. Civera, G. Saracco, V. Specchia, Palladium/perovskite/zirconia catalytic premixed fiber burners for efficient and clean natural gas combustion, Catal. Today. 117 (4) (2006) 427–432, https://doi.org/10.1016/j.cattod.2006.06.041.
[20] N. Miniajluk, J. Trawczyński, M. Zawadzki, P.E. Tomaszewski, W. Miśta, Solvothermal synthesis and characterization of mixed oxides with perovskite-like structure, Catal. Today. 257 (1) (2015) 26–34, https://doi.org/10.1016/j.cattod.2015.03.029.
[21] Z. Ren, V. Botu, S. Wang, Y. Meng, W. Song, Y. Guo, R. Ramprasad, S.L. Suib, P.-X. Gao, Monolithically integrated spinel $M_xCo_{3-x}O_4$ (M=Co, Ni, Zn) nanoarray catalysts: scalable synthesis and cation manipulation for tunable low-temperature $CH_4$ and CO oxidation, Angew Chemie. 126 (28) (2014) 7351–7355, https://doi.org/10.1002/ange.v126.2810.1002/ange.201403461.
[22] A.M. Venezia, V. La Parola, L.F. Liotta, Structural and surface properties of heterogeneous catalysts: Nature of the oxide carrier and supported particle size effects, Catal. Today. 285 (2017) 114–124, https://doi.org/10.1016/j.cattod.2016.11.004.
[23] U. Zavyalova, P. Scholz, B. Ondruschka, Influence of cobalt precursor and fuels on the performance of combustion synthesized $Co_3O_4$/γ-$Al_2O_3$ catalysts for total oxidation of methane, Appl. Catal. A Gen. 323 (2007) 226–233, https://doi.org/10.1016/j.apcata.2007.02.021.
[24] M. Verelst, T.O. Ely, C. Amiens, E. Snoeck, P. Lecante, A. Mosset, M. Respaud, J. M. Broto, B. Chaudret, Synthesis and Characterization of CoO, $Co_3O_4$, and Mixed Co/CoO, Nanoparticules 11 (1999) 2702–2708, https://doi.org/10.1021/cm991003h.
[25] E. Barrera, I. González, T. Viveros, A new cobalt oxide electrodeposit bath for solar absorbers, Sol. Energy Mater. Sol. Cells. 51 (1) (1998) 69–82, https://doi.org/10.1016/S0927-0248(97)00209-2.
[26] S. Weichel, P.J Møller, Annealing-induced microfaceting of the CoO(100) surface investigated by LEED and STM, Surf. Sci. 399 (2-3) (1998) 219–224, https://doi.org/10.1016/S0039-6028(97)00820-0.
[27] F. Švegl, B. Orel, M.G. Hutchins, K. Kalcher, Structural and Spectroelectrochemical Investigations of Sol-Gel Derived Electrochromic Spinel $Co_3O_4$ Films, J. Electrochem. Soc. 143 (1996) 1532–1539, https://doi.org/10.1149/1.1836675.
[28] G.B. Hoflund, Z. Li, Surface characterization study of a Pd/$Co_3O_4$ methane oxidation catalyst, Appl. Surf. Sci. 253 (5) (2006) 2830–2834, https://doi.org/10.1016/j.apsusc.2006.05.115.
[29] D. Ciuparu, E. Altman, L. Pfefferle, Contributions of lattice oxygen in methane combustion over PdO-based catalysts, J. Catal. 203 (1) (2001) 64–74, https://doi.org/10.1006/jcat.2001.3331.
[30] J. Votruba, J. Sinkule, V. Hlaváček, J. Skřivánek, Heat and mass transfer in monolithic honeycomb catalysts-I, Chem. Eng. Sci. 30 (1) (1975) 117–123, https://doi.org/10.1016/0009-2509(75)85122-0.
[31] M.T. Kreutzer, P. Du, J.J. Heiszwolf, F. Kapteijn, J.A. Moulijn, Mass transfer characteristics of three-phase monolith reactors, Chem. Eng. Sci. 56 (21-22) (2001) 6015–6023, https://doi.org/10.1016/S0009-2509(01)00271-8.
[32] S. Roy, A.K. Heibel, W. Liu, T. Boger, Design of monolithic catalysts for multiphase reactions, Chem. Eng. Sci. 59 (5) (2004) 957–966, https://doi.org/10.1016/j.ces.2003.12.001.
[33] L. Giani, G. Groppi, E. Tronconi, Mass-transfer characterization of metallic foams as supports for structured catalysts, Ind. Eng. Chem. Res. 44 (14) (2005) 4993–5002, https://doi.org/10.1021/ie0490886.
[34] M.V. Twigg, J.T. Richardson, Theory and applications of ceramic foam catalysts, Chem. Eng. Res. Des. 80 (2002) 183–189, https://doi.org/10.1016/S0263-8762(02)72166-7.
[35] F. Lucci, A. Della Torre, J. von Rickenbach, G. Montenegro, D. Poulikakos, P. Dimopoulos Eggenschwiler, Performance of randomized Kelvin cell structures as catalytic substrates: Mass-transfer based analysis, Chem. Eng. Sci. 112 (2014) 143–151, https://doi.org/10.1016/j.ces.2014.03.023.
[36] C. Sinn, J. Wentrup, G.R. Pesch, J. Thöming, L. Kiewidt, Structure-heat transport analysis of periodic open-cell foams to be used as catalyst carriers, Chem. Eng. Res. Des. 166 (2021) 209–219, https://doi.org/10.1016/j.cherd.2020.12.007.
[37] S. Wójcik, G. Ercolino, M. Gajewska, C.W.M. Quintero, S. Specchia, A. Kotarba, Robust $Co_3O_4$|α-$Al_2O_3$|cordierite structured catalyst for $N_2O$ abatement – Validation of the SCS method for active phase synthesis and deposition, Chem. Eng. J. 377 (2019) 120088, https://doi.org/10.1016/j.cej.2018.10.025.
[38] A. Vita, C. Italiano, L. Pino, M. Laganà, M. Ferraro, V. Antonucci, High-temperature $CO_2$ methanation over structured Ni/GDC catalysts: Performance and scale-up for Power-to-Gas application, Fuel Process. Technol. 202 (2020) 106365, https://doi.org/10.1016/j.fuproc.2020.106365.
[39] A. Egaña, O. Sanz, D. Merino, X. Moriones, M. Montes, Fischer-tropsch synthesis intensification in foam structures, Ind. Eng. Chem. Res. 57 (31) (2018) 10187–10197, https://doi.org/10.1021/acs.iecr.8b0149210.1021/acs.iecr.8b01492.s001.
[40] A. Cybulski, J.A. Moulijn, Structured catalysts and reactors, Marcel Dekker Inc, New York, 1998.
[41] A.I. Stankiewicz, J.A. Moulijn, Process intensification: transforming chemical engineering, AIChE - Chem. Eng. Prog. 96 (2000) 22–33. https://www.aiche.org/sites/default/files/docs/news/010022_cep_stankiewicz.pdf.
[42] T.J. Lu, H.A. Stone, M.F. Ashby, Heat transfer in open-cell metal foams, Acta Mater. 46 (10) (1998) 3619–3635, https://doi.org/10.1016/S1359-6454(98)00031-7.
[43] W.-Y. Jang, A.M. Kraynik, S. Kyriakides, On the microstructure of open-cell foams and its effect on elastic properties, Int. J. Solids Struct. 45 (7-8) (2008) 1845–1875, https://doi.org/10.1016/j.ijsolstr.2007.10.008.
[44] F.C. Buciuman, B. Kraushaar-Czarnetzki, Ceramic foam monoliths as catalyst carriers. 1. adjustment and description of the morphology, Ind. Eng. Chem. Res. 42 (9) (2003) 1863–1869, https://doi.org/10.1021/ie0204134.
[45] E. Tronconi, G. Groppi, C.G. Visconti, Structured catalysts for non-adiabatic applications, Curr. Opin. Chem. Eng. 5 (2014) 55–67, https://doi.org/10.1016/j.coche.2014.04.003.
[46] S. Voltolina, P. Marín, F.V. Díez, S. Ordóñez, Open-cell foams as beds in multiphase reactors: residence time distribution and mass transfer, Chem. Eng. J. 316 (2017) 323–331, https://doi.org/10.1016/j.cej.2017.01.113.
[47] A.M. Dashliborun, A. Füssel, F. Larachi, Prospect of open-cell solid foams for floating-platform multiphase reactor applications – Maldistribution susceptibility

and hydrodynamic behavior, Chem. Eng. J. 332 (2018) 596–607, https://doi.org/10.1016/j.cej.2017.09.116.
[48] A. Inayat, M. Klumpp, M. Lämmermann, H. Freund, W. Schwieger, Development of a new pressure drop correlation for open-cell foams based completely on theoretical grounds: taking into account strut shape and geometric tortuosity, Chem. Eng. J. 287 (2016) 704–719, https://doi.org/10.1016/j.cej.2015.11.050.
[49] A. Aguirre, V. Chandra, E.A.J.F. Peters, J.A.M. Kuipers, M.F. Neira D'Angelo, Open-cell foams as catalysts support: a systematic analysis of the mass transfer limitations, Chem. Eng. J. 393 (2020) 124656, https://doi.org/10.1016/j.cej.2020.124656.
[50] C.W. Moncada Quintero, R.Z. Babar, S. Specchia, Performance and controlling regimes analysis of methane steam reforming on Ru/γ-$Al_2O_3$ cordierite monoliths, Green Energy Technol. (2021) 91–131, https://doi.org/10.1007/978-981-15-5667-8_5.
[51] P. Bernard, P. Stelmachowski, P. Broś, W. Makowski, A. Kotarba, Demonstration of the influence of specific surface area on reaction rate in heterogeneous catalysis, J. Chem. Educ. 98 (3) (2021) 935–940, https://doi.org/10.1021/acs.jchemed.0c01101.
[52] C.W. Moncada Quintero, G. Ercolino, A. Poozhikunnath, R. Maric, S. Specchia, Analysis of heat and mass transfer limitations for the combustion of methane emissions on PdO/$Co_3O_4$ coated on ceramic open cell foams, Chem. Eng. J. 405 (2021) 126970, https://doi.org/10.1016/j.cej.2020.126970.
[53] C.W. Moncada Quintero, G. Ercolino, S. Specchia, Effect of the $Co_3O_4$ load on the performance of PdO/$Co_3O_4$/$ZrO_2$ open cell foam catalysts for the lean combustion of methane: kinetic and mass transfer regimes, Catal. Today. (2021), https://doi.org/10.1016/j.cattod.2021.03.014.
[54] G. Ercolino, P. Stelmachowski, S. Specchia, Catalytic performance of Pd/$Co_3O_4$ on SiC and $ZrO_2$ open cell foams for process intensification of methane combustion in lean conditions, Ind. Eng. Chem. Res. 56 (23) (2017) 6625–6636, https://doi.org/10.1021/acs.iecr.7b0108710.1021/acs.iecr.7b01087.s001.
[55] G. Ercolino, S. Karimi, P. Stelmachowski, S. Specchia, Catalytic combustion of residual methane on alumina monoliths and open cell foams coated with Pd/$Co_3O_4$, Chem. Eng. J. 326 (2017) 339–349, https://doi.org/10.1016/j.cej.2017.05.149.
[56] P.A. Carlsson, M. Skoglundh, E. Fridell, E. Jobson, B. Andersson, Induced low temperature catalytic ignition by transient changes in the gas composition, Catal. Today. 73 (2002) 307–313, https://doi.org/10.1016/j.cej.2010.10.051.
[57] R.H. Nibbelke, J.H.B.J. Hoebink, G.B. Marin, Kinetically induced multiplicity of steady states in integral catalytic reactors, Chem. Eng. Sci. 53 (12) (1998) 2195–2210, https://doi.org/10.1016/S0009-2509(98)00055-4.
[58] S. Specchia, S. Tacchino, V. Specchia, Facing the catalytic combustion of $CH_4$/$H_2$ mixtures into monoliths, Chem. Eng. J. 167 (2-3) (2011) 622–633, https://doi.org/10.1016/j.cej.2010.10.051.
[59] A. Aseem, G.G. Jeba, M.T. Conato, J.D. Rimer, M.P. Harold, Oxidative coupling of methane over mixed metal oxide catalysts: Steady state multiplicity and catalyst durability, Chem. Eng. J. 331 (2018) 132–143, https://doi.org/10.1016/j.cej.2017.08.093.
[60] L.A. Vandewalle, R. Van de Vijver, K.M. Van Geem, G.B. Marin, The role of mass and heat transfer in the design of novel reactors for oxidative coupling of methane, Chem. Eng. Sci. 198 (2019) 268–289, https://doi.org/10.1016/j.ces.2018.09.022.
[61] C.W. Moncada Quintero, M. Servel, F. Augier, Y. Haroun, J.-F. Joly, S. Specchia, Imaging ceramic open cell foams by X-ray micro computed tomography, Ind. Eng. Chem. Res. submitted (2021) ie-2021-01515w.
[62] I. Cornejo, P. Nikrityuk, R.E. Hayes, Heat and mass transfer inside of a monolith honeycomb: From channel to full size reactor scale, Catal. Today. (2020), https://doi.org/10.1016/j.cattod.2020.10.036.
[63] J.J. Carberry, Chemical and catalytic reaction engineering, McGraw-Hill, New York, 1976.
[64] J.R. Anderson, M. Boudart, Catalysis Sci. Tech. (1987), https://doi.org/10.1007/978-3-642-93278-6_1.
[65] C. McGreavy, L. Draper, E.K.T. Kam, Methodologies for the design of reactors using structured catalysts: modelling and experimental study of diffusion and reaction in structured catalysts, Chem. Eng. Sci. 49 (24) (1994) 5413–5425, https://doi.org/10.1016/0009-2509(94)00384-X.
[66] S. Roy, T. Bauer, M. Al-Dahhan, P. Lehner, T. Turek, Monoliths as multiphase reactors: a review, AIChE J. 50 (11) (2004) 2918–2938, https://doi.org/10.1002/(ISSN)1547-590510.1002/aic.v50:1110.1002/aic.10268.
[67] O.P. Klenov, S.A. Pokrovskaya, N.A. Chumakova, S.N. Pavlova, V.A. Sadykov, A. S. Noskov, Effect of mass transfer on the reaction rate in a monolithic catalyst with porous walls, Catal. Today. 144 (3-4) (2009) 258–264, https://doi.org/10.1016/j.cattod.2008.11.014.
[68] A. Gancarczyk, M. Iwaniszyn, M. Piatek, M. Korpyś, K. Sindera, P.J. Jodłowski, J. Łojewska, A. Kołodziej, Catalytic Combustion of Low-Concentration Methane on Structured Catalyst Supports, Ind. Eng. Chem. Res. 57 (31) (2018) 10281–10291, https://doi.org/10.1021/acs.iecr.8b01987.
[69] V. Balakotaiah, On the relationship between Aris and Sherwood numbers and friction and effectiveness factors, Chem. Eng. Sci. 63 (24) (2008) 5802–5812, https://doi.org/10.1016/j.ces.2008.08.025.
[70] S.Y. Joshi, M.P. Harold, V. Balakotaiah, Low-dimensional models for real time simulations of catalytic monoliths, AIChE J. 55 (7) (2009) 1771–1783, https://doi.org/10.1002/aic.v55:710.1002/aic.11794.
[71] S.Y. Joshi, M.P. Harold, V. Balakotaiah, On the use of internal mass transfer coefficients in modeling of diffusion and reaction in catalytic monoliths, Chem. Eng. Sci. 64 (23) (2009) 4976–4991, https://doi.org/10.1016/j.ces.2009.08.008.
[72] S.Y. Joshi, M.P. Harold, V. Balakotaiah, Overall mass transfer coefficients and controlling regimes in catalytic monoliths, Chem. Eng. Sci. 65 (5) (2010) 1729–1747, https://doi.org/10.1016/j.ces.2009.11.021.
[73] S.Y. Joshi, Y. Ren, M.P. Harold, V. Balakotaiah, Determination of kinetics and controlling regimes for H2 oxidation on Pt/$Al_2O_3$ monolithic catalyst using high space velocity experiments, Appl. Catal. B Environ. 102 (3-4) (2011) 484–495, https://doi.org/10.1016/j.apcatb.2010.12.030.
[74] G. Incera Garrido, F.C. Patcas, S. Lang, B. Kraushaar-Czarnetzki, Mass transfer and pressure drop in ceramic foams: a description for different pore sizes and porosities, Chem. Eng. Sci. 63 (21) (2008) 5202–5217, https://doi.org/10.1016/j.ces.2008.06.015.
[75] M. Bhattacharya, M.P. Harold, V. Balakotaiah, Mass-transfer coefficients in washcoated monoliths, AIChE J. 50 (11) (2004) 2939–2955, https://doi.org/10.1002/(ISSN)1547-590510.1002/aic.v50:1110.1002/aic.10212.
[76] L.B. Younis, R. Viskanta, Experimental determination of the volumetric heat transfer coefficient between stream of air and ceramic foam, Int. J. Heat Mass Transf. 36 (6) (1993) 1425–1434, https://doi.org/10.1016/S0017-9310(05)80053-5.
[77] D Mears, Diagnostic criteria for heat transport limitations in fixed bed reactors, J. Catal. 20 (2) (1971) 127–131, https://doi.org/10.1016/0021-9517(71)90073-X.
[78] J.B. Anderson, A criterion for isothermal behaviour of a catalyst pellet, Chem. Eng. Sci. 18 (1963) 147–148.
[79] J.M. Smith, Chemical engineering kinetics, 2nd ed., McGraw-Hill, New York, 1970.
[80] G.F. Froment, K.B. Bischoff, J. De Wilde, Chemical reactor analysis and design, 3rd ed., John Wiley & Sons, New York, 2011.
[81] B.R. Bird, W.E. Stewart, E.N. Lightfoot, Transport phenomena, 2nd ed., Wiley, 2006.
[82] G. Groppi, C. Cristiani, L. Lietti, P. Forzatti, Study of PdO/Pd transformation over alumina supported catalysts for natural gas combustion, Stud. Surf. Sci. Catal. 130 (2000) 3801–3806, https://doi.org/10.1016/s0167-2991(00)80615-1.
[83] L.M.T. Simplício, S.T. Brandão, D. Domingos, F. Bozon-Verduraz, E.A. Sales, Catalytic combustion of methane at high temperatures: Cerium effect on PdO/$Al_2O_3$ catalysts, Appl. Catal. A Gen. 360 (1) (2009) 2–7, https://doi.org/10.1016/j.apcata.2009.03.005.
[84] S. Colussi, P. Fornasiero, A. Trovarelli, Structure-activity relationship in Pd/$CeO_2$ methane oxidation catalysts, Chinese, J. Catal. 41 (6) (2020) 938–950, https://doi.org/10.1016/S1872-2067(19)63510-2.
[85] J. Lin, X. Chen, Y. Zheng, F. Huang, Y. Xiao, Y. Zheng, L. Jiang, Facile construction of ultrastable alumina anchored palladium catalysts: via a designed one pot strategy for enhanced methane oxidation, Catal Sci. Technol. 10 (14) (2020) 4612–4623, https://doi.org/10.1039/D0CY00727G.
[86] S. Nasr, N. Semagina, R.E. Hayes, Kinetic modelling of $Co_3O_4$- and Pd/$Co_3O_4$-catalyzed wet lean methane combustion, Emiss. Control Sci. Technol. 6 (2) (2020) 269–278, https://doi.org/10.1007/s40825-019-00143-0.
[87] G.S. Bugosh, V.G. Easterling, I.A. Rusakova, M.P. Harold, Anomalous steady-state and spatio-temporal features of methane oxidation on Pt/Pd/$Al_2O_3$ monolith spanning lean and rich conditions, Appl. Catal. B Environ. 165 (2015) 68–78, https://doi.org/10.1016/j.apcatb.2014.09.058.
[88] A.K. Datye, J. Bravo, T.R. Nelson, P. Atanasova, M. Lyubovsky, L. Pfefferle, Catalyst microstructure and methane oxidation reactivity during the Pd↔PdO transformation on alumina supports, Appl. Catal. A Gen. 198 (1-2) (2000) 179–196, https://doi.org/10.1016/S0926-860X(99)00512-8.
[89] D. Ciuparu, M.R. Lyubovsky, E. Altman, L.D. Pfefferle, A. Datye, Catalytic combustion of methane over palladium-based catalysts, Catal. Rev. - Sci. Eng. 44 (4) (2002) 593–649, https://doi.org/10.1081/CR-120015482.
[90] S. Colussi, A. Trovarelli, E. Vesselli, A. Baraldi, G. Comelli, G. Groppi, J. Llorca, Structure and morphology of Pd/$Al_2O_3$ and Pd/$CeO_2$/$Al_2O_3$ combustion catalysts in Pd-PdO transformation hysteresis, Appl. Catal. A Gen. 390 (1–2) (2010) 1–10, https://doi.org/10.1016/j.apcata.2010.09.033.
[91] R. Gholami, M. Alyani, K.J. Smith, Deactivation of Pd catalysts by water during low temperature methane oxidation relevant to natural gas vehicle converters 5 (2) (2015) 561–594, https://doi.org/10.3390/catal5020561.
[92] Y.-H.C. Chin, M. García-Diéguez, E. Iglesia, Dynamics and thermodynamics of Pd-PdO phase transitions: Effects of pd cluster size and kinetic implications for catalytic methane combustion, J. Phys. Chem. C. 120 (3) (2016) 1446–1460, https://doi.org/10.1021/acs.jpcc.5b0667710.1021/acs.jpcc.5b06677.s001.
[93] R.J. Farrauto, M.C. Hobson, T. Kennelly, E.M. Waterman, Catalytic chemistry of supported palladium for combustion of methane, Appl. Catal. A, Gen. 81 (2) (1992) 227–237, https://doi.org/10.1016/0926-860X(92)80095-T.
[94] H. Scott Fogler, Elements of chemical reaction engineering, 5th ed.,, Pearson Education Inc, Kendallville, Indiana (USA), 2016.
[95] B. Dietrich, Heat transfer coefficients for solid ceramic sponges-Experimental results and correlation, Int. J. Heat Mass Transf. 61 (2013) 627–637, https://doi.org/10.1016/j.ijheatmasstransfer.2013.02.019.
[96] X.L. Xia, X. Chen, C. Sun, Z.H. Li, B. Liu, Experiment on the convective heat transfer from airflow to skeleton in open-cell porous foams, Int. J. Heat Mass Transf. 106 (2017) 83–90, https://doi.org/10.1016/j.ijheatmasstransfer.2016.10.053.
[97] V. Specchia, G. Baldi, S. Sicardi, Heat transfer in packed bed reactors with one phase flow, Chem. Eng. Commun. 4 (1-3) (1980) 361–380, https://doi.org/10.1080/00986448008935916.
[98] C.G. Visconti, E. Tronconi, G. Groppi, L. Lietti, M. Iovane, S. Rossini, R. Zennaro, Monolithic catalysts with high thermal conductivity for the Fischer-Tropsch synthesis in tubular reactors, Chem. Eng. J. 171 (3) (2011) 1294–1307, https://doi.org/10.1016/j.cej.2011.05.014.
[99] O. Sanz, I. Velasco, I. Reyero, I. Legorburu, G. Arzamendi, L.M. Gandía, M. Montes, Effect of the thermal conductivity of metallic monoliths on methanolsteam

reforming, Catal. Today. 273 (2016) 131–139, https://doi.org/10.1016/j.cattod.2016.03.008.

# CO-AUTHORS STATEMENT

Warsaw, 21.05.2021

**CO-AUTHOR STATEMENT**

**I Dr. Sylwia Gudyka**, hereby confirm that my contribution to the work:

1. Wójcik, S., Ercolino, G., Gajewska, M., **Moncada Quintero, C. W.**, Specchia, S., & Kotarba, A. (2018). Robust $Co_3O_4|\alpha\text{-}Al_2O_3|$cordierite structured catalyst for $N_2O$ abatement – Validation of the SCS method for active phase synthesis and deposition. *Chemical Engineering Journal, 377*, 120088. https://doi.org/10.1016/j.cej.2018.10.025

was the execution of most of the experimental work, data processing and drafting the manuscript.

**I Dr. Sylwia Gudyka** hereby agree that this manuscript can be integrally inserted in the Ph.D. thesis of Carmen Williana Moncada Quintero.

Sylwia Gudyka

Krakow, 14.05.2021

## CO-AUTHOR STATEMENT

I, **Dr. Marta Gajewska**, hereby confirm that my contribution to the work:

1. Wójcik, S., Ercolino, G., Gajewska, M., **Moncada Quintero, C. W.**, Specchia, S., & Kotarba, A. (2018). Robust $Co_3O_4|\alpha\text{-}Al_2O_3|$cordierite structured catalyst for $N_2O$ abatement – Validation of the SCS method for active phase synthesis and deposition. *Chemical Engineering Journal, 377*, 120088. https://doi.org/10.1016/j.cej.2018.10.025

was carrying out the SEM/EDX microscopic measurements, analyzing and interpreting the obtained results and partly drafting the manuscript.

I, **Dr. Marta Gajewska,** hereby agree that this manuscript can be included in the Ph.D. thesis of Carmen Williana Moncada Quintero.

Marta Gajewska

Krakow, 12.05.2021

**CO-AUTHOR STATEMENT**

**I Prof. Andrzej Kotarba**, hereby confirm that my contribution to the work:

1. Wójcik, S., Ercolino, G., Gajewska, M., **Moncada Quintero, C. W**., Specchia, S., & Kotarba, A. (2018). Robust $Co_3O_4|\alpha\text{-}Al_2O_3|$cordierite structured catalyst for $N_2O$ abatement – Validation of the SCS method for active phase synthesis and deposition. *Chemical Engineering Journal, 377*, 120088. https://doi.org/10.1016/j.cej.2018.10.025

was supervising the work, discussing the experiment design, drafting and revising the manuscript.

**I Prof. Andrzej Kotarba** hereby agree that this manuscript can be integrally inserted in the Ph.D. thesis of Carmen Williana Moncada Quintero.

A. Kotarba

Torino, 24 May 2021

**CO-AUTHOR STATEMENT**

**Dr. Roman Z. Babar**, hereby confirm that my contribution to the work:

1. **Moncada Quintero, C. W.**, Babar, R. Z., & Specchia, S. (2021). Performance and Controlling Regimes Analysis of Methane Steam Reforming on Ru/γ-$Al_2O_3$ Cordierite Monoliths. *Green Energy and Technology*, 91–131. https://doi.org/10.1007/978-981-15-5667-8_5

was the execution of most of the experimental work.

**Dr. Roman Z. Babar** hereby agrees that this manuscript can be integrally inserted in the Ph.D. thesis of Carmen Williana Moncada Quintero.

Messina, 14/05/2021

**CO-AUTHOR STATEMENT**

**I Dr. Cristina Italiano**, hereby confirm that my contribution to the work:

1. Italiano, C., Ashraf, M. A., Pino, L., **Moncada Quintero, C. W**., Specchia, S., & Vita, A. (2018). Rh/$CeO_2$ thin catalytic layer deposition on alumina foams: Catalytic performance and controlling regimes in biogas reforming processes. *Catalysts, 8*(10), 1–25. https://doi.org/10.3390/catal8100448

was the execution of the experimental work, data processing, discussion, analysis and drafting the manuscript.

**I Dr. Cristina Italiano** hereby agree that this manuscript can be integrally inserted in the Ph.D. thesis of Carmen Williana Moncada Quintero.

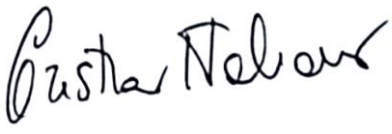

Bath (United Kingdom), 14-May-21

**CO-AUTHOR STATEMENT**

**I Dr. Arsalan Ashraf**, hereby confirm that my contribution to the work:

1. Italiano, C., Ashraf, M. A., Pino, L., **Moncada Quintero, C. W**., Specchia, S., & Vita, A. (2018). Rh/$CeO_2$ thin catalytic layer deposition on alumina foams: Catalytic performance and controlling regimes in biogas reforming processes. *Catalysts, 8*(10), 1–25. https://doi.org/10.3390/catal8100448

was the execution of partly experimental work, data processing, discussion, analysis and drafting the manuscript.

**I Dr. Arsalan Ashraf** hereby agree that this manuscript can be integrally inserted in the Ph.D. thesis of Carmen Williana Moncada Quintero.

M. Arsalan Ashraf

14/05/21

Messina, 14th of May, 2021

**CO-AUTHOR STATEMENT**

**I Dr. Lidia Pino**, hereby confirm that my contribution to the work:

1. Italiano, C., Ashraf, M. A., Pino, L., **Moncada Quintero, C. W.**, Specchia, S., & Vita, A. (2018). Rh/$CeO_2$ thin catalytic layer deposition on alumina foams: Catalytic performance and controlling regimes in biogas reforming processes. *Catalysts, 8*(10), 1-25. https://doi.org/10.3390/catal8100448

was supervising the work, analysis and revising the manuscript.

**I Dr. Lidia Pino** hereby agree that this manuscript can be integrally inserted in the Ph.D. thesis of Carmen Williana Moncada Quintero.

(Dr. Lidia Pino)

**Istituto di Tecnologie Avanzate per l'Energia "Nicola Giordano"**

Via S. Lucia sopra Contesse n.5
98126 Messina, Italy
tel: 090 624246, fax: 090 624247
e-mail: itae@itae.cnr.it
C.F. 80054330586
protocollo.itae@pec.cnr.it

Consiglio Nazionale delle Ricerche

Istituto di Tecnologie Avanzate per l'Energia "Nicola Giordano"

**CO-AUTHOR STATEMENT**

**I Dr. Antonio Vita** (Head of FPMat Team at CNR-ITAE), hereby confirm that the contribution of Carmen Williana Moncada Quintero to the work:

1. Italiano, C., Ashraf, M. A., Pino, L., **Moncada Quintero, C. W**., Specchia, S., & Vita, A. (2018). $Rh/CeO_2$ thin catalytic layer deposition on alumina foams: Catalytic performance and controlling regimes in biogas reforming processes. *Catalysts, 8*(10), 1–25. https://doi.org/10.3390/catal8100448

was supervising the work, discussion of the experimental design, critical analysis, drafting and revising the manuscript.

**I Dr. Antonio Vita** hereby agree that this manuscript can be integrally inserted in the Ph.D. thesis of Carmen Williana Moncada Quintero.

Sincerely,

Dr. Antonio Vita

Messina, 14/05/2021

CNR-ITAE Via S. Lucia sopra Contesse n. 5 - 98126 Messina, Italy

Tel: +39 090 624246 Fax: +39 090 624247 Mail: itae@itae.cnr.it PEC: protocollo.itae@pec.cnr.it http//www.itae.cnr.it/

Hillsboro, OR, USA, 05/18/2021

**CO-AUTHOR STATEMENT**

**I Dr. Abhinav Poozhikunnath**, hereby confirm that my contribution to the work:

1. **Moncada Quintero, C. W.**, Ercolino, G., Poozhikunnath, A., Maric, R., & Specchia, S. (2020). Analysis of heat and mass transfer limitations for the combustion of methane emissions on $PdO/Co_3O_4$ coated on ceramic open cell foams. *Chemical Engineering Journal, 405*, 126970. https://doi.org/10.1016/j.cej.2020.126970

was to carry out the FESEM and Raman spectra measurements, analysis, interpretation of the results and revising the manuscript.

**I Dr. Abhinav Poozhikunnath** hereby agree that this manuscript can be integrally inserted in the Ph.D. thesis of Carmen Williana Moncada Quintero.

05/18/2021

West Hartford, CT | May 18, 2021

**CO-AUTHOR STATEMENT**

**I Prof. Radenka Maric**, hereby confirm that my contribution to the work:

1. **Moncada Quintero, C. W.**, Ercolino, G., Poozhikunnath, A., Maric, R., & Specchia, S. (2020). Analysis of heat and mass transfer limitations for the combustion of methane emissions on $PdO/Co_3O_4$ coated on ceramic open cell foams. *Chemical Engineering Journal, 405*, 126970. https://doi.org/10.1016/j.cej.2020.126970

was supervising the work, project financial support and revising the manuscript.

**I Prof. Radenka Maric** hereby agree that this manuscript can be integrally inserted in the Ph.D. thesis of Carmen Williana Moncada Quintero.

Regards,

Marić Radenka

Radenka Maric, Ph.D.

Solaize, France, 17th may 2021

**CO-AUTHOR STATEMENT**

**I Dr. Frédéric Augier**, hereby confirm that my contribution to the work:

1. **Moncada Quintero, C. W.**, Servel, M., Augier, F., Haroun, Y., Joly, J.F., & Specchia, S. (2021). Imaging ceramic open cell foams by X-ray micro computed tomography. *Under preparation.*

was supervising the work, supporting, discussion of the experimental design and critical analysis of results.

**I Dr. Frédéric Augier** hereby agree that this manuscript can be integrally inserted in the Ph.D. thesis of Carmen Williana Moncada Quintero.

Frédéric Augier

Lyon, 21 may 2021

**CO-AUTHOR STATEMENT**

**I Dr. Marion Servel**, hereby confirm that my contribution to the work:

1. **Moncada Quintero, C. W.**, Servel, M., Augier, F., Haroun, Y., Joly, J.F., & Specchia, S. (2021). Imaging ceramic open cell foams by X-ray micro computed tomography. *Under preparation*.

was supervising the work, discussion of the experimental design, analysis and revising the manuscript.

**I Dr. Marion Servel** hereby agree that this manuscript can be integrally inserted in the Ph.D. thesis of Carmen Williana Moncada Quintero.

Par ordre

Lyon, May 17th , 2021

**CO-AUTHOR STATEMENT**

**I Dr. Yacine Haroun**, hereby confirm that my contribution to the work:

1. **Moncada Quintero, C. W.**, Servel, M., Augier, F., Haroun, Y., Joly, J.F., & Specchia, S. (2021). Imaging ceramic open cell foams by X-ray micro computed tomography. *Under preparation*.

was supervising the work, discussion of the experimental design, analysis and revising the manuscript.

**I Dr. Yacine Haroun** hereby agree that this manuscript can be integrally inserted in the Ph.D. thesis of Carmen Williana Moncada Quintero.

yacine Haroun

Y. Haroun.

Lyon, 18 may 2021

**CO-AUTHOR STATEMENT**

**I Dr. Jean-François Joly**, hereby confirm that my contribution to the work:

1. **Moncada Quintero, C. W.**, Servel, M., Augier, F., Haroun, Y., Joly, J.F., & Specchia, S. (2021). Imaging ceramic open cell foams by X-ray micro computed tomography. *Under preparation*.

was supervising the work, discussion of the experimental design, analysis and revising the manuscript.

**I Dr. Jean-François Joly** hereby agree that this manuscript can be integrally inserted in the Ph.D. thesis of Carmen Williana Moncada Quintero.

Torino, 17/09/2021

**CO-AUTHOR STATEMENT**

**I Dr. Giuliana Ercolino**, hereby confirm that my contributions to the work:

1. Wójcik, S.; Ercolino, G.; Gajewska, M.; **Moncada Quintero, C. W**.; Specchia, S.; Kotarba, A. (2018). Robust $Co_3O_4$|α-$Al_2O_3$|cordierite structured catalyst for $N_2O$ abatement – Validation of the SCS method for active phase synthesis and deposition. *Chemical Engineering Journal, 377*, 120088. https://doi.org/10.1016/j.cej.2018.10.025
2. **Moncada Quintero, C. W.**; Ercolino, G.; Poozhikunnath, A.; Maric, R.; Specchia, S. (2020). Analysis of heat and mass transfer limitations for the combustion of methane emissions on PdO/$Co_3O_4$ coated on ceramic open cell foams. *Chemical Engineering Journal, 405*, 126970. https://doi.org/10.1016/j.cej.2020.126970
3. **Moncada Quintero, C. W.**; Ercolino, G.; Specchia, S. (2021). Effect of the $Co_3O_4$ load on the performance of PdO/$Co_3O_4$/$ZrO_2$ open cell foam catalysts for the lean combustion of methane: kinetic and mass transfer regimes. *Catalysis Today*. https://doi.org/10.1016/j.cattod.2021.03.014
4. **Moncada Quintero, C.W.**; Ercolino, G.; Specchia, S. (2021) Combined silicon carbide and zirconia open cell foams for the process intensification of catalytic methane combustion in lean conditions: impact on heat and mass transfer. *Chemical engineering Journal* in press (16/09/2021) https://doi.org/10.1016/j.cej.2021.132448

were the execution and discussion of part of the experiments, analysis and discussion of the results.

**I Dr. Giuliana Ercolino** hereby agree that these manuscripts can be integrally inserted in the Ph.D. thesis of Carmen Williana Moncada Quintero.

Torino, 17/09/2021

**CO-AUTHOR STATEMENT**

**I Prof. Stefania Specchia**, hereby confirm that my contributions to the work:

1. Wójcik, S.; Ercolino, G.; Gajewska, M.; **Moncada Quintero, C. W**.; Specchia, S.; Kotarba, A. (2018). Robust $Co_3O_4|\alpha\text{-}Al_2O_3|$cordierite structured catalyst for $N_2O$ abatement – Validation of the SCS method for active phase synthesis and deposition. *Chemical Engineering Journal, 377*, 120088. https://doi.org/10.1016/j.cej.2018.10.025
2. Italiano, C.; Ashraf, M. A.; Pino, L.; **Moncada Quintero, C. W.**; Specchia, S.; Vita, A. (2018). $Rh/CeO_2$ thin catalytic layer deposition on alumina foams: Catalytic performance and controlling regimes in biogas reforming processes. *Catalysts*, 8(10), 1–25. https://doi.org/10.3390/catal8100448
3. **Moncada Quintero, C. W.**; Ercolino, G.; Poozhikunnath, A.; Maric, R.; Specchia, S. (2020). Analysis of heat and mass transfer limitations for the combustion of methane emissions on $PdO/Co_3O_4$ coated on ceramic open cell foams. *Chemical Engineering Journal, 405*, 126970. https://doi.org/10.1016/j.cej.2020.126970
4. **Moncada Quintero, C. W.**; Babar, R. Z.; Specchia, S. (2021). Performance and Controlling Regimes Analysis of Methane Steam Reforming on $Ru/\gamma\text{-}Al_2O_3$ Cordierite Monoliths. *Green Energy and Technology*, 91–131. https://doi.org/10.1007/978-981-15-5667-8_5
5. **Moncada Quintero, C. W.**; Ercolino, G.; Specchia, S. (2021). Effect of the $Co_3O_4$ load on the performance of $PdO/Co_3O_4/ZrO_2$ open cell foam catalysts for the lean combustion of methane: kinetic and mass transfer regimes. *Catalysis Today*. In press (18/06/2021) https://doi.org/10.1016/j.cattod.2021.03.014
6. **Moncada Quintero, C. W.**; Servel, M.; Augier, F.; Haroun, Y.; Joly, J.-F.; Specchia, S. (2021). Imaging ceramic open cell foams by X-ray micro computed tomography. *Under preparation*
7. **Moncada Quintero, C.W.**; Ercolino, G.; Specchia, S. (2021) Combined silicon carbide and zirconia open cell foams for the process intensification of catalytic methane combustion in lean conditions: impact on heat and mass transfer. *Chemical engineering Journal* in press (16/09/2021) https://doi.org/10.1016/j.cej.2021.132448

were the conceptualization and supervision of the experiments, analysis and discussion of the results, reviewing and editing the papers and figures, acquiring the resources necessary.

**I Prof. Stefania Specchia** hereby agree that these manuscripts can be integrally inserted in the Ph.D. thesis of Carmen Williana Moncada Quintero.

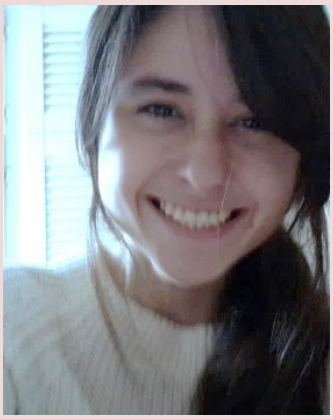

# Carmen Williana Moncada Quintero

Chemical engineer

## Contact


Via Nizza 106
Torino, Italy
10126

carmen.moncada@polito.it
carmenwilliana@hotmail.com

+39 388 496 94 56
+39 011 090 46 57


January 16, 1993
Caracas, Venezuela

## Languages

Spanish

Italian

English

## Computer Skills

**Languages:**
C++ , Visual Basic

**Softwares:**
Matlab, COMSOL, Pro II, Aspen Plus and Hysys, AutoCad, SolidWork

## Personal profile

Chemical engineer passionately focused on innovation, optimization and intensification of catalytic processes

## Eduaction

**2017-Now**
PhD student in Chemical Engineering
Ceramic open cell foams as catalytic support for exo/endothermic reaction: Focus on methane combustion
Politecnico di Torino, Italy

**2014-2016**
Msc in Chemical Engineering
Politecnico di Torino, Italy

**2009-2016**
Bsc in Chemical Engineering with Double degree
Politecnico di Torino, Italy
Central University of Venezuela, Venezuela

## Academic experience

**2018-2021**
Teaching assistance in Chemistry
Politecnico di Torino, Italy

**2020**
Erasmus PhD programme countries
Preparation and characterization of structured catalyst
University of the Basque Country, Spain

**2019**
Erasmus+ Traineeship
Modelling of open cell foams as catalytic support
IFP Energies Nouvelles, France

**2018**
20th National Congress of Catalyst
20th National Congress of the Division of Industrial Chemistry
Overall mass transfer coefficients and controlling regimes in foams
Politecnico di Milano, Italy

**2013-2014**
Teaching assistance in Chemical Reactors and Kinetic
Central University of Venezuela, Venezuela

## Social

carmenwmoncadaq

carmen-moncada-2

carmen-moncada

carmenwilliana

## Interests

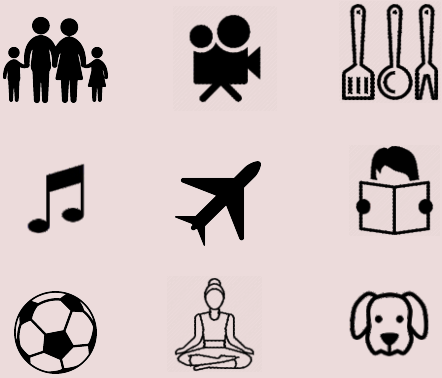

## Training courses

**2021** Gricu PhD School
Digitalization Tools for the chemical and process industries
Virtual event

**2019** ELITECAT Summer School
Heterogeneous catalyst, characterization and modelling
Claude Bernard University Lyon 1, France

**2019** Summer School on Raman Spectroscopy
Biomaterials and Food Science
Kyoto Institute of Technology Kyoto, Japan

**2019** Workshop on Fuel Cells
PGM-free catalysts for Energy Systems and Fuel Cells
Politecnico di Torino, Italy

**2018** Seminar on Energy and Low Carbon Technologies
Functional Nanostructured materials for catalysis and sensing
Politecnico di Torino, Italy

## Proceedings

Ercolino, G.; Moncada Quintero, C.W.; Gudyka, S.; Stelmachowski, P.J.; Kotarba, A.; Specchia, S.(2017). Open cell foams Pd/$Co_3O_4$/$ZrO_2$ catalyst for the lean combustion of methane. In: 8th World Congress on Oxidation Catalysis - 8WCOC, Krakow (Poland), 3-8/09/2017, pp. 174-174. ISBN: 978-83-60514-27-6

Moncada Quintero, C. W.; Ercolino, G.; Specchia, S. (2018). A combination of silicon carbide and zirconia open cell foams coated with 3% PdO/$Co_3O_4$ as structured catalysts for the lean combustion of methane. In: The 8th Tokyo Conference on Advanced Catalytic Science & Technology (TOCAT8), Yokohama (Japan), 5-10/08/2018

Moncada Quintero, C. W.; Ercolino, E.; Specchia, S. (2018). Overall mass transfer coefficients and controlling regimes in open cell foams. In: XX Congresso Nazionale di Catalisi - XX Congresso Nazionale della Divisione di Chimica Industriale, Milano, 2-5/09/2018

## Publications

Wójcik, S., Ercolino, G., Gajewska, M., Moncada Quintero, C. W., Specchia, S., & Kotarba, A. (2018). Robust $Co_3O_4$|α-$Al_2O_3$|cordierite structured catalyst for $N_2O$ abatement – Validation of the SCS method for active phase synthesis and deposition. Chemical Engineering Journal, 377, 120088
https://doi.org/10.1016/j.cej.2018.10.025

Italiano, C., Ashraf, M. A., Pino, L., Moncada Quintero, C. W., Specchia, S., & Vita, A. (2018). Rh/$CeO_2$ thin catalytic layer deposition on alumina foams: Catalytic performance and controlling regimes in biogas reforming processes. Catalysts, 8(10), 1–25. https://doi.org/10.3390/catal8100448

Amjad, U., Moncada Quintero, C.W, Ercolino, G., Italiano, C., Vita, A., & Specchia, S. (2019). Methane Steam Reforming on the Pt/$CeO_2$ Catalyst: Effect of Daily Start-Up and Shut-Down on Long-Term Stability of the Catalyst. Industrial & Engineering Chemistry Research, 58(36), 16395-16406. doi: 10.1021/acs.iecr.9b02436

Moncada Quintero, C. W., Babar, R. Z., & Specchia, S. (2021). Performance and Controlling Regimes Analysis of Methane Steam Reforming on Ru/γ-$Al_2O_3$ Cordierite Monoliths. Green Energy and Technology, 91–131
https://doi.org/10.1007/978-981-15-5667-8_5

Moncada Quintero, C. W., Ercolino, G., Poozhikunnath, A., Maric, R., & Specchia, S. (2020). Analysis of heat and mass transfer limitations for the combustion of methane emissions on PdO/$Co_3O_4$ coated on ceramic open cell foams. Chemical Engineering Journal, 405, 126970.
https://doi.org/10.1016/j.cej.2020.126970

Moncada Quintero, C. W., Ercolino, G., & Specchia, S. (2021). Effect of the $Co_3O_4$ load on the performance of PdO/$Co_3O_4$/$ZrO_2$ open cell foam catalysts for the lean combustion of methane: kinetic and mass transfer regimes. Catalysis Today.
https://doi.org/10.1016/j.cattod.2021.03.014

Moncada Quintero, C. W., Servel, M., Augier, F., Haroun, Y., Joly, J.F., & Specchia, S. (2021). Imaging ceramic open cell foams by X-ray micro computed tomography. Under preparation.

Moncada Quintero, C. W., Ercolino, G., & Specchia, S. (2021). Combined silicon carbide and zirconia open cell foams for the process intensification of catalytic methane combustion in lean conditions: impact on heat and mass transfer. Chemical Engineering Journal, 429, 132448.
https://doi.org/10.1016/j.cej.2021.132448